**RÉPUBLIQUE DU CAMEROUN**

***Paix – Travail – Patrie***

**UNIVERSITÉ DE YAOUNDÉ I**

***FACULTÉ DES SCIENCES***

**DÉPARTEMENT DE PHYSIQUE**

**REPUBLIC OF CAMEROON**

***Peace – Work – Fatherland***

**UNIVERSITY OF YAOUNDE I**

***FACULTY OF SCIENCE***

**DEPARTMENT OF PHYSICS**

LABORATORY OF MECHANICS, MATERIALS AND STRUCTURE

*LABORATOIRE DE MECANIQUE, MATERIAUX ET STRUCTURE*

# Ultra-short pulses compression and supercontinuum generation in optical waveguides : cases of SMFs, SOI-waveguides and $CS_2$-LCPCFs

# THESIS

**Submitted and defended publicly**

**By**

**LUCIEN MANDENG MANDENG**

*D.E.A in Physics (Master's degree with thesis)*

**Registration N° : 02Q076**

In fulfillment of the requirements for the awards of the degree of Doctorate/Ph.D

**Speciality :** Mechanics

*Under the supervision of*

**CLÉMENT TCHAWOUA**

***Associate Professor***

**Academic year: 2015**

# Ultra-short pulses compression and supercontinuum generation in optical waveguides : cases of SMFs, SOI-waveguides and $CS_2$-LCPCFs

by **Lucien Mandeng Mandeng**

*D.E.A in Physics (Master's degree with thesis)*

under the supervision of :

**Clément Tchawoua**

*Associate Professor*

21st December 2015

# Dedication

*This thesis is dedicated to my parents Mr. Emmanuel Mandeng and Mrs. Marie-Claire Mandeng*

# Acknowledgments

The work presented in this thesis has been made under the label of the Laboratory of Mechanics, Department of Physics, Faculty of Science, University of Yaoundé I. We sincerely thank **Pr. Timoléon Crépin Kofané**, Head of the laboratory, to have allowed this work to be realized within his research team.

A particular acknowledgement is addressed to **Pr. Clément Tchawoua** to have been our advisor. He has been our lantern, guiding us and assuming fully his role despite all the other tasks associated to his position within the University of Yaoundé I. This thesis being a result of this laborious work, no word can describe our gratitude, we just hope that he will continue this noble task for the next generation of PhD students. A sentence of our advisor still resounds in our head and has been the conductor line of this work : "Only the perseverance, the seriousness and the rigor allow to reach to the expected results...". This sentence has allowed us to be tenacious and to hope the end of this tunnel. Thank once again **Pr. Clément Tchawoua.**

We acknowledge **Pr. Mourad Zghal** from the Sup'Com Engineering School of the University of Carthage (Tunisia), for his help, useful discussions, academic support, collaboration in the study of supercontinuum generation phenomenon, and for his encouragement which has accompanied us until the end of this work. We also acknowledge the financial support that he has obtained for us, and which has allowed us to attend to the First African Summer School on Optics and Applications to Sustainable Development (ASOSD) held from 31st August to 08th September 2013 in Tunis (Tunisia).

We are also grateful to **Pr. Paul Woafo**, **Pr. Claude Marie Ngabireng**, **Dr. Laurent Nana** for having contributed to our introduction in the research work. It is also an occasion to thank all the Department of Physics of the Faculty of Science (University of Yaoundé I).

We acknowledge the jury's members of the preliminary thesis's viva voce of this work namely **Pr. Donatien Njomo**, **Pr. Beguide Bonoma**, **Pr. Serge Sylvain Zekeng** and **Pr. Bernard Essimbi Zobo** who have made the first review of this document. We continue with the anonymous experts who have subsequently allowed this document to be defended in the present form.

We acknowledge the jury's members of the final thesis's viva voce : **Pr. Timoléon Crépin Kofané**, **Pr. Clément Tchawoua**, **Pr. Paul Woafo**, **Pr. Aurélien Jiotsa Kenfack**, **Pr. François Beceau Pelap** and **Pr. Alidou Mohamadou** for their comments and suggestions allowing to improve the quality of this document.

We thank **Dr. Serge Ibraid Fewo** for having been a must in the achievement of this work, for the useful discussions, advices and collaboration in the study of the four-wave mixing process and the pulse compression mechanism. He has kindly shared his personal and academic experiences with us. He has also proofread this thesis.

We send our gratitude to **Pr. Alidou Mohamadou** for his useful help, discussions and collaboration in the modulational instability analysis and the study of supercontinuum generation phenomenon that have allowed the achievement of the thesis.

We thank **Pr. Rim Cherif** and **Dr. Amine Ben salem** from the Sup'Com Engineering School of the University of Carthage (Tunisia), for useful help in numerical simulations and comments in the investigation of the supercontinuum generation phenomenon.

We thank **Dr. Pavel Polynkin** from the College of Optical Sciences, University of Arizona (U.S.A) and **Pr. Stephen Coen** from the University of Auckland, (New-Zealand) for help in simulations of the supercontinuum phenomenon.

A special thank is addressed to **Dr. Jean-Pascal Eloundou** from the National Advanced Engineering school of Yaoundé, for his encouragement and invaluable support having contributed to the achievement of this work.

We send our gratitude to **Pr. Francesco Petruccione** and **Dr. Angela Dudley** for their

support for attendance to the Quantum Africa 2 conference held in KwaZulu-Natal (South-Africa).

The same gratitude is addressed to the **African Laser Centre** (ALC) for the participation to the 2012 short courses on Optical Fiber Technology at the Nelson Mandela Metropolitan University (NMMU) of Port-Elizabeth (P-E) (South-Africa) and to the **Optical Society of America** (O.S.A) for each grant for attendance to the FiO conferences.

This work has been done while we worked in the National Advanced Engineering school of Yaoundé as an assistant lecturer, therefore we thank all of those with who we have collaborated during this time namely **Pr. Henri Gweth**, **Pr. Pierre Meukam**, **Pr. Alain Tiedeu**, **Dr. P. S. Ngohe-Ekam**, **Dr. Marthe Boyomo**, **Dr. Elizabeth Pemha**, **Dr. Etienne Takou**, **Dr. Bridinette Thiodjio**, **Dr. Nguimbous**, **Dr. Jampong**, **Dr. Tagoudjeu**, **Dr. Jules Tewa**, **Dr. Victor Kuetche**, **Dr. Omer Tcheutchoua**, **Dr. Fabien Ndzana**, **Dr. Kaze Aloyem**, **Dr. Emmanuel Tchomgo**, **Dr. Stéphane Atok**, Mr. **Hermann Ouandji**, Mr. **Donfack**, Mr. **Brunel Biedi**, Mr. **Tchoffo**, Mrs. **Isabelle Fotsing**, Mrs. **Batiglak Roda**, Mrs. **Linda Nyeke** spouse **Njie**, Mrs. **Hawa Oumarou** and the rest of temporary assistants of the ENSP MSP department. All of them, even indirectly, have helped us with their support, encouragement and advices.

We also thank **Dr. Martin S. Siewe** for his help and advices. We continue with **Pr. Mama Foupouagnini**, **Dr. Jean-Cher Messassé**, **Dr. Blaise Nana Nbendjo**, **Dr. Rosalie Woulache**, **Dr. Germaine Djuidje Aloyem**, **Dr. David Tegankong**, **Dr. Jean-Marie Mbounga**, **Dr. Jean-Baptiste Patenou** for their encouragement.

We are profoundly grateful to our parents : our father Mr. **Emmanuel Mandeng** and our mother Mrs. **Marie-Claire Mandeng** who are always there for us in any circumstances, spiritually, financially, emotionally. Their support has been a real and decisive turning point for the achievement of this thesis. We send our thanks to Mrs. **Françoise Ndjeng** for his sincere support. We acknowledge our brothers and sisters **Antoine Olivier** and his family, **Sylvie Hortence**, **Emmanuel Patrick**, **Serge Romuald**, **John William Boris**, **Marguérite Nadège**, **Clément Luc Junior**, and **Achille Aurélien** who are always there for us in all circumstances. We also think to our large family (uncles, aunts, cousins,...).

We are indebted to our late brother **Clément Hervé Mandeng** and our late grandmother **Marguérite Ngo Likeng**. May their souls rest in peace.

We are grateful to the constructive discussions with our colleagues who belong to the Laboratory of Mechanics as **Dr. John B. Nono**, **Dr. Alain B. M. Togueu**, **Dr. David B. Tatchim**, **Joël D. T. Tchinang**, **Omar Foupouagnigni**, **Hippolyte Tagwo**, this latter having collaborated with us on two projects of supercontinuum study. Beyond those mentioned above, we also include all the rest of students under the direction of **Pr. Clément Tchawoua**, both in the PhD and MsC levels.

We also send our thanks to :

- Mr. **Joachim Djomgang**, Mr. **Bayiha**, Mrs. **Abona**, Mr. **Thomas Kanga**, Mr. **Ruben Bikoï**, Mr. **Emmanuel Babe**, Mr. **Phillipe Maemble**, Mr. **Prosper Bayebeck**,
- Mr. **Raphaël Touko** and his family, Mr. **Michel Pougoué Touko**, Mr. **Gabriel Minyemeck**, Mr. **Jacques Djon**, Mr. **Adamou Nchange**,
- our colleagues in the secondary studies : Mr. **Simon Logui Baha**, Mr. **Emmanuel Michel Manang** and the members of the french-speaking Physics-Chemistry-Technology's department of the Etoug-Ebe's Bilingual Government school in Yaoundé,
- **Dr. Bernard Azanmene** and his family, **Dr. Angéline Florence Ngomo**,
- our friends **Bernis Fomazou** for his support, **Dr. Sifeu Takougang** for useful discussions and his kindness to share when possible useful informations about conferences in optics and others.

- our tanzanian friends met in QA 2 conference : **Samwel Mwankemwa** and **Emmanuel Olutu**,
- our friends met in NMMU (P-E) : **Lili Bethulie**, **Nduduzi Mbongo**, **Evans Ojwak**, **Jean Jacques Kaboko**, **Noxolo Thabatha**,
- our friends met in ASOSD 2013 conference : **Ivon Mbesse Kongbonga**, **Olusola Oyebola**, **William Mbogning Feudjio**, **Heythem Salhi**, **Basma Khanjari**...
- our other friends **Fatima-zahra Boussetta**, **Sandrine Huet**, **Yolande Kemagoua**, **Michèle Mekena Mvondo**, **Fredy Feuzeu**, **Christian Kotta** and his family, **Dr. Remy Takogue**, **Patrick Nyandjou**, **Patrick Njonou**, **Gisèle Tchuisseu**, **Honoré Ndafeu**, **Désiré**, **Annie Caroline**,**Annie Nlend**,**Muriel Ibis**, **zéline Mouliom**, **Valérie Ouafo Meka**, **Jannesquin Djofang**, **Hervé Kokam**, **Marcel Abéga**, **Christelle Nangné**, **Placide Ombolo**,
- the members of the OSA and SPIE student chapters of the university of Yaoundé I,
- the teachers participating to "**PREPA ENSP**" project since 2011 until now,
- our students in the National Advanced Engineering School of Yaoundé for having allowed us to stay in a state of permanent work which has certainly contributed to the successful achievement of this work.
- Finally, a thought is addressed to our darling **Lynda** (and her family) for having been there for us, with her sincere affection during the last step of our thesis's work.

*To those we have forgotten, we ask you to receive our sincere thanks.*

# Grants, fellowships and financial supports of this thesis

1. Grant of excellence of Head of State of Cameroon for Higher Degree students, 2009-2010.
2. Grant of excellence of Head of State of Cameroon for Higher Degree students, 2010-2011.
3. Grant of excellence of Head of State of Cameroon for Higher Degree students, 2011-2012.
4. Grant of excellence of Head of State of Cameroon for Higher Degree students, 2013-2014.
5. OSA Student Travel Grant for attending to the FiO 2011 Conference given by OSA Foundation.
6. OSA Student Travel Grant for attending to the FiO 2012 Conference given by OSA Foundation.
7. Award of Fellowships and Financial Aid for RIAO/OPTILAS2013.
8. OSA Student Travel Grant for attending to the FiO 2013 Conference given by OSA Foundation.
9. OSA Student Travel Grant for attending to the FiO 2014 Conference given by OSA Foundation.
10. The organizations OSA, SPIE and ICTP have helped us making available research papers respectively through their databases : OpticsInfobase, SPIE library and EJDS.
11. Logistic of Pr. **Clément Tchawoua** including personal computer, books, articles ...

# Résumé

Dans cette thèse, nous étudions analytiquement et numériquement les phénomènes de compression temporelle et d'étalement spectral qui se manifestent lors de la propagation des impulsions ultra brèves dans les guides d'ondes optiques, largement utilisés, notamment les guides d'onde à silicium, les fibres classiques monomodes des systèmes de multiplexage en longueurs d'onde, les fibres à cristaux photoniques, et enfin les guides d'onde modélisés par l'équation de Schrödinger non linéaire à termes non Kerr.

Plus spécifiquement, nous analysons dans un premier temps, le mécanisme de compression temporelle dans les guides optiques à silicium en utilisant l'approche variationnelle modifiée et réaliste qui prend en compte la fonction de dissipation de Rayleigh. Cette étude permet de montrer les effets de la dispersion chromatique d'ordre 4, des coefficients non linéaires d'absorption (absorption non linéaire) et du chirp, non seulement sur les impulsions à profil compact et symétrique mais aussi sur celles qui sont asymétriques comme les impulsions d'Airy. En effet, en considérant le cas de la compression linéaire, les conditions de son apparition sont déterminées. Une relation entre la dispersion chromatique d'ordre 4, la dispersion de vitesse de groupe et le chirp est ainsi proposée. Dans le cas non linéaire, prenant les impulsions symétriques comme profil d'entrée, nous démontrons qu'une compression périodique est induite par l'interaction entre l'auto-modulation de phase et le coefficient de dispersion chromatique d'ordre 4. Ceci apparaît comme un nouveau mode de génération du phénomène de compression. Ensuite nous montrons qu'un coefficient d'absorption intrinsèque aux guides d'onde à silicium, en particulier le coefficient d'absorption à deux photons, se trouve être un facteur néfaste pour ladite compression périodique (destruction de la périodicité). Enfin, l'étude relative aux impulsions d'Airy (impulsions asymétriques) dans cette première partie, conduit plutôt à la réduction de la longueur de compression induite par l'auto-modulation de phase, l'absorption à deux photons et l'absorption des porteurs libres. Ceci permet de déduire l'influence de l'asymétrie de l'impulsion sur ce phénomène de compression.

Dans un deuxième temps, afin d'apprécier certaines influences sur le phénomène d'étalement spectral drastique en termes de génération de supercontinuum, nous nous intéressons au phénomène de mélange à quatre ondes et à l'instabilité modulationnelle. Prenant l'exemple des fibres classiques monomodes des systèmes multiplexés en longueur d'onde, et utilisant l'approche dite ABCJS principalement basée sur une propagation d'ondes quasi-solitonique au voisinage du zéro de dispersion de la fibre, nous montrons que la combinaison des ordres deux et trois de dispersion chromatique permet de réduire les effets néfastes induits par le mélange à quatre ondes dans de tels systèmes multiplexés. L'instabilité modulationnelle étudiée quant à elle dans les guides d'onde à silicium où le chirp est décrit comme un facteur adjuvant à l'amplification de l'intensité des pics principaux des trains d'onde, conduit à une indépendance du point de vue du profil d'entrée. D'un autre côté, il résulte de cette étude que les coefficients d'absorption contrecarrent l'effet du chirp re-créant ainsi la dépendance au profil d'entrée.

Finalement, dans un troisième temps pour l'étude du supercontinuum, concernant le guide d'onde modélisé par l'équation généralisée de Schrödinger incluant des termes non Kerr (provenant de la nonlinéarité quintique), nous obtenons une compression spectrale. Ceci est réalisé à travers la réduction de largeur temporelle dans le cas des nonlinéarités coopératives en lieu et place des nonlinéarités compétitives. Plus loin, avec l'impulsion d'Airy dans une fibre monomode hautement dispersive, nous étudions la propagation sous l'influence du chirp initial. Nous obtenons que l'effet du chirp initial sur le spectre de l'impulsion d'Airy est similaire à celui de l'auto-raidissement nonlinéaire menant à une sortie asymétrique. Néanmoins, le choc optique qui est ainsi créé dépend du signe du chirp et présage d'interessants avantages pour la réalisation des ultra-larges spectres de supercontinuum. Bien plus, le chirp initial agit comme la dispersion chromatique de troisième ordre produisant la

fameuse inversion asymétrique découverte plus tôt par R. Driben et al [**R. Driben, Y. Hu, Z. Chen, B. A. Malomed, and R. Morandotti, Opt. Lett. 38, 2499 (2013).**]. Dès lors, le chirp peut être utilisé pour jouer le rôle soit de l'auto-raidissement nonlinéaire, soit de la dispersion chromatique d'ordre 3, ou encore pour contrôler voir annihiler leurs effets. Durant le processus d'inversion, la compression d'impulsion a également lieu à travers la formation d'un profil Gaussien. Nous démontrons également que l'interaction entre le chirp, la dispersion de la vitesse de groupe et la dispersion chromatique d'ordre 4 permet l'amplification d'impulsion ainsi que la stabilisation d'impulsion sur une distance relativement longue. Comme application directe de cette étude, nous analysons la génération du supercontinuum dans une fibre à cristaux photoniques admise comme ayant un cœur rempli de liquide. Il s'agit d'une fibre microstructurée à cœur liquide. Dans cette étude particulière, on se sert des impulsions d'Airy chirpées et on montre qu'elles sont meilleures que leurs homologues compactes et symétriques en termes de largeur et cohérence de la bande passante spectrale, sous des conditions incluant un faible coefficient de troncation et un chirp choisi de façon optimale dans le régime anormal de dispersion proche du zero de dispersion. Le cas des guides d'ondes à silicium est également étudié dans une nouvelle modélisation analytique basée sur l'équation de la propagation d'impulsion totalement unidirectionnelle qui inclut les termes de génération de la troisième harmonique et l'effet Kerr à fréquence négative. Les effets de ces termes sur la bande passante spectrale ainsi que sur le degré de cohérence spectrale sont étudiés en comparaison avec ceux de l'absorption à deux photons. Pour des applications nécessitant d'ultra-larges spectres, on devrait réduire les effets de l'absorption à deux photons et du terme de génération de la troisième harmonique. On devrait plutôt exciter le terme de l'effet Kerr à fréquence négative afin d'obtenir des spectres explosifs en bande passante. Néanmoins, l'absorption à deux photons améliore plus la cohérence spectrale que le terme de génération de la troisième harmonique tandis que le terme d'effet Kerr à fréquence négative la réduit en comparaison avec le cas singulier de l'auto-modulation de phase seule.

**Mots clés :** Compression d'impulsions; Mélange à quatre ondes; Instabilité modulationnelle; Génération de supercontinuum; Dispersion chromatique d'ordre 4; Chirp; Approche variationnelle modifiée; Absorption à deux photons; Génération de la troisième harmonique; Effet Kerr à fréquence négative.

# Abstract

In this thesis, we study analytically and numerically the phenomena of pulse compression and spectral broadening which manifest themselves during the propagation of ultra-short pulses in common used optical waveguides, namely silicon-on-insulator (SOI) waveguides, single-mode optical fibers (SMFs) in wavelength-division multiplexing (WDM) systems, photonic crystal fibers (PCFs) and waveguides modelled by the generalized nonlinear Schrödinger equation (GNLSE) with non-Kerr terms.

More explicitly, we analyze in a first time, the pulse compression mechanism in SOI-waveguides using the modified and realistic variational approach (MVA) that involves the Rayleigh's dissipation function (RDF). This study allows to show the effects of fourth-order dispersion (FOD), the nonlinear coefficients of absorption (nonlinear absorption) and the chirp, not only on symmetric and compact pulses but also on those with asymmetric profile as the Airy pulses. Indeed, considering the case of linear compression, the conditions of their occurrence are obtained. A relation between the FOD, the group-velocity dispersion (GVD) and the chirp is proposed in this way. In the nonlinear case, using the symmetric profiles as input pulses, we demonstrate a periodic compression induced by the interplay between the self-phase modulation (SPM) and the FOD. This appears as a new mode to generate the pulse compression phenomenon. Then, we show that an absorption coefficient which generally characterizes the SOI-waveguides, particularly the two-photon absorption (TPA), is found to be detrimental to this periodic compression (destruction of the periodicity). Finally, the study relating to the Airy pulses (asymmetric pulses) in this first part, leads rather to the reduction of the compression length induced by the SPM, the TPA and the free-carrier absorption (FCA). This allows to deduce the influence of the pulse asymmetry on this phenomenon.

In a second time, in order to appreciate some influences on the drastic spectral broadening in terms of supercontinuum generation (SCG), we investigate the phenomena of the four-wave mixing (FWM) and the modulational instability (MI). Taking for instance the SMFs in WDM systems and using an approach named the ABCJS approach which is mainly based on a propagation of solitonlike pulses in the vicinity of the zero-dispersion wavelength (ZDW) of the fiber, we show that the combination of the second and the third orders of dispersion allows to reduce the crosstalk induced by the FWM in such systems. The study of the MI being done in SOI-waveguides where the chirp is described as beneficial factor to the amplification of the pulse trains main peaks, leads to an independence to the input profile. On the other hand, it emerges from this study that the coefficients of absorption counteract the chirp effect recreating so a dependence to the input profile.

Finally, in a third time for the SCG, in the case of the waveguide modelled by the GNLSE that includes non-Kerr terms (linked to the quintic nonlinearity), we obtain a spectral compression. This is achieved through the reduction of the pulse width induced by the cooperative nonlinearities instead of the competing ones. Furthermore, using the finite energy Airy pulses (FEAPs) in a highly dispersive SMF, we study the propagation under the influence of initial chirp. It is found that the initial chirp behaves as the self-steepening (SS) on the spectrum of the FEAP leading to an asymmetric output. Nonetheless, the optical shock which is created depends on the sign of the chirp parameter and omens interesting advantages for the achievement of FEAP-based broadband spectra in the SCG phenomenon. Moreover, the initial chirp acts as a chromatic third-order dispersion (TOD) leading to the asymmetric inversion (A.I) as shown earlier by R. Driben et al [**R. Driben, Y. Hu, Z. Chen, B. A. Malomed, and R. Morandotti, Opt. Lett. 38, 2499 (2013).**]. Therefore, the chirp could be used to replace the SS and TOD, or to control/cancel their effects. Pulse compression, pulse amplification and FEAP shape preserving under the interaction of the chirp, the GVD and the fourth-order dispersion (FOD) are also discussed. As a direct application of this work, we analyze the extreme spectral broadening in a PCF that is assumed to have a core filled by a liquid. Such

fiber is called a liquid-core PCF (LCPCF). In this specific study using Airy pulses, we show that they are more suitable than the common compact and symmetric pulses in terms of spectral coherence and bandwidth, under the conditions including a small truncation coefficient and a chirp value chosen optimally in the anomalous dispersion regime close the ZDW. The case of SOI-waveguides is also studied with a novel analytical modeling of a silicon waveguide based on the full unidirectional pulse propagation equation (UPPE) that includes both the third-harmonic generation (THG) and the negative-frequency Kerr (NFK) terms. The effects of these terms on the spectral bandwidth (SB) and the coherence degree (CD) are discussed in comparison to those of two-photon absorption (TPA). For applications needing wide SBs, one should reduce the TPA-THG effects and excite rather the NFK term to produce explosive ultra-broadband SCG spectra. Nonetheless, the TPA is found to enhance more the spectral coherence than the THG while the NFK effect reduces it compared with the single SPM case.

**Keywords:** Pulse compression; Four-wave mixing; Modulational instability; Supercontinuum generation; Fourth-order dispersion; Chirp; Modified variational approach; Two-photon absorption; Third-harmonic generation; Negative-frequency Kerr effect.

# Contents

# List of abbreviations and acronyms

ABCJS : Ablowitz-Biondini-Chakravarty-Jenkins-Sauer.
A.I : Asymmetric inversion.
ASC : Anti-Stokes component.
AV : Absolute value.
CD : Coherence degree.
CDP : Chromatic dispersion profile.
CKN : Cubic Kerr nonlinearity.
$CS_2$-LCPCF : LCPCF filled by $CS_2$.
CV : Collective variables.
CW : Continuous wave.
DFF : Dispersion flattened fiber.
D.M : Dispersion management.
DRR : Delayed Raman response.
DW : Dispersive wave.
FCA : Free-carrier absorption.
FCD : Free-carrier density.
FEAP : Finite energy Airy pulse.
FOD : Fourth-order dispersion.
FWHM : Full width at the half maximum.
FWM : Four-wave mixing.
GNLSE : Generalized NLSE.
GVD : Group-velocity dispersion.
HDOF : Highly dispersive optical fiber.
HOD : Higher-order dispersion.
HOS : Higher-order soliton.
HS : Hyperbolic secant.
IPRS : Intra-pulse Raman scattering.
IR : Infra-red.
KGE : Klein-Gordon equation.
LCPCF : Liquid core PCF.
LHS : Left-hand side.
MI : Modulational instability.
MP : Main peak.
MPCP : Maximal pulse compression percentage.
MPR : Maximal power reached.
MVA : Modified variational approach.
NFK : Negative-frequency Kerr.
NLS : Nonlinear Schrödinger.
NLSE : NLS equation.
NSO : Nearly symmetric output.
NSR : Non-solitonic radiation.
ODE : Ordinary differential equation.
OF : Optimal frequency.
PB : Photonic bandgap.
PCF : Photonic crystal fiber.
PDE : Partial differential equation.

PMC : Phase-matching condition.
PTG : Pulse train generation.
PTS : Polydiactylene toluene sulfonate.
QNC : Quintic nonlinearity coefficient.
RC : Raised-cosine.
RDF : Rayleigh's dissipation function.
RHS : Right-hand-side.
RIFS : Raman induced frequency shift.
RMS : Root-mean-square.
RS : Raman soliton.
SB : Spectral bandwidth.
SCG : Supercontinuum generation.
SF : Solitonic fission.
SG : Super-Gaussian.
SHAP : Self-healing Airy pulse.
SHG : Second-harmonic generation.
SI : Spectral intensity.
SMF : Single-mode fiber.
SOI : Silicon-on-insulator.
SPM : self-phase modulation.
SRS : Stimulated Raman scattering.
SS : Self-steepening.
SSF : Split-step Fourier.
SVEA : Slowly-varying envelope approximation.
TE : Transverse-electric.
TF : Tapered fiber.
THG : Third-harmonic generation.
TM: Transverse-magnetic.
TOD : Third-order dispersion.
TPA : Two-photon absorption.
UPPE : Unidirectional pulse propagation equation.
WDM : Wavelength-division multiplexing.
XPM : Cross-phase modulation.
ZDW : Zero-dispersion wavelength.

# List of Figures

# List of Tables

# General introduction

In nonlinear optics, the temporal pulse compression and the spectral broadening observed in optical waveguides are known today to have several useful applications. One can quote : high-data rate transmission in optical telecommunications, ultrafast physical processes, infrared time-resolved spectroscopy, sampling systems, coherent tomography, multiplex light sources for nonlinear spectroscopy, biomedical lasers, holography, interferometry, photonics devices applications, sub-femtosecond to attosecond researches,... [1-3]. Therefore, investigation of related topics is welcome to be apprehensive about the occurrence conditions of such processes in optical waveguides.

In the theoretical aspect of research in nonlinear optics specially in studies of propagation within nonlinear optical waveguides, many works having ended to Ph.D theses, were conducted in the Department of Physics of the Faculty of Science (University of Yaoundé I). For instance S. I. Fewo studied the dynamic of the propagation of solitons in systems modeled by the complex Ginzburg-Landau equations using the collective variables (CVs) and the classical variational approaches [4]. In this work, it was noted that a better choice of appropriate initial parameters as the initial amplitude and pulse width of the Gaussian pulse shape is important for a stable propagation inside the fiber. An overview of this work shows that the solitons dynamics could be suitably investigated through the CVs approach with more insight. Even the dual-core fibers were investigated with a focus on the interaction of solitons using the classical variational method. Bounded and unbounded elliptic trajectories separated by transitory trajectories were observed depending on the values of the coupling coefficient and parameters [4].

Subsequently, J. Atangana examined the propagation of ultra-short pulses in optical fiber systems under strongly perturbed environmental conditions [5]. This study conducted with the CVs approach, showed that when asymmetric distortions induced by the odd order terms of linear dispersion as the third-order dispersion (TOD) occur in the solitons propagation, the approach should be upgraded in order to resolve the inconsistencies of the conventional one. This does not work with the third-order nonlinear dispersion as the cubic self-steepening (SS) phenomenon, since in this case the distorted pulse translates only when one uses another ansätze calling second-order upgraded ansätze. The considered upper CVs approach was found to give accurate results and interpretation of distorted pulses dynamics [5].

Later, C. G. L. Tiofack investigated the MI phenomenon and the ultra-short pulses propagation in Erbium doped fibers modeled by GNLSE with higher order effects both in the linear and in the nonlinear part [6]. For example in this study, the equation which describes propagation of an optical soliton in an inhomogeneous Erbium doped fiber with two-level resonant atoms called the generalized inhomogeneous coupled Hirota-Maxwell-Bloch equation was analyzed. Some multi-soliton solutions of this system were obtained by employing the Darboux transformation while the MI in the complex NLSE with cubic-quintic-septic nonlinearity, the Hirota complex Ginzburg-Landau equation, the higher order NLSE with noninstantaneous nonlinear response and stochastic parameters showed interesting features in the development of the pulse train generation (PTG) [6].

After the review of these works, it was observed that with the great interest aroused by the pulse compression and the spectral broadband continua according to their wide applications, a research

path oriented on their achievement was missing considering the department of Physics of the Faculty of Science (University of Yaoundé 1). That is why, this thesis comes to be added to the previous ones with a focus on the mentioned phenomena as a study beyond the previous analyses on the solitons dynamics. Particularly, we focus on the effects of FOD and nonlinear absorption coefficients in the studies of the pulse compression and the MI. On the other hand, we study the TOD effect on the growth of the anti-Stokes component (ASC) of the FWM in the WDM solitons systems. Furthermore, the improvement of the SCG spectral bandwidth is analyzed considering the effects of the input profile, chirp and the type of the optical waveguide used. Our motivation for these works stems from the following limits :

1. a lack of a study on the linear compression in an optical system under the FOD effect that highlights the relations between the dispersion lengths associated to the GVD, the chirp and the FOD.

2. An investigation of the nonlinear compression in SOI-waveguides under FOD was still missing. The dependence of this phenomenon to the input profile was not yet highlighted.

3. In order to reduce the effect of the crosstalk induced by the FWM in WDM systems, those in the vicinity of ZDW have not yet been investigated using the ABCJS approach.

4. An investigation about the influences of the absorption coefficients (present in SOI-waveguides), chirp and input profile was missing when one considers the MI phenomenon in nonlinear optics.

5. The question of the SCG analysis in GNLSE systems with non Kerr terms stemming from quintic nonlinearity was also opened.

6. Another question concerned the analysis of propagation using the FEAPs in a highly dispersive SMF under the influence of initial chirp.

7. It remained also the analysis of the improvement of the SCG phenomenon through nanojoule (nJ)-FEAPs under the chirp effect in LCPCFs filled by the $CS_2$.

8. A SCG study in a SOI waveguide including both the THG and the NFK terms was missing.

For the compression phenomenon, the study is conducted through a MVA that involves the RDF instead of the CVs and the classical variational approaches as done in the previous studies. As discussed in these studies, the CVs focus on solitons dynamics while the present study claims to go beyond and to underline the conditions in which the compression and the SCG occur in the studied optical waveguides taking into account the initial pulse shape which is not necessarily close to a solitary wave. Moreover, the choice of the MVA is made on the basis of the recent works of Roy et al [7,8]. Indeed, they were demonstrating that considering specially the silicon waveguides, the effects of linear losses, TPA, and free-carriers dynamics are well analyzed within the framework of this MVA formalism in agreement with full numerical simulations. Therefore, it has been found interesting to use this MVA for the compression phenomenon analysis in the corresponding waveguides beyond the previous mentioned methods. The peculiarity of the FEAPs in highly dispersive SMFs, has highlighted a new feature in nonlinear dynamics as the A.I mechanism stemming from the interaction between the GVD and the initial chirp similarly to the one obtained earlier by R. Driben et al [**R. Driben, Y. Hu, Z. Chen, B. A. Malomed, and R. Morandotti, Opt. Lett. 38, 2499 (2013).**]. The problem of the famous complex phenomenon so-called the SCG in new modeled systems was set as a further part of the thesis with connection with the compression phenomenon. In addition, the introduction of specific studies on some underlying mechanisms as the FWM and

the MI in the considered optical waveguides was also found necessary as a good line to investigate the SCG. At the end of this work, we expect to have in a first part a good understanding of the impact of free-carriers absorptions, high-order dispersion, chirp, Kerr and non-Kerr nonlinearities, input profiles, harmonic generation and negative-frequency Kerr terms on the temporal compression, in a second part on the FWM and the MI mechanisms and finally, on the improvement of the SCG in the previously mentioned optical waveguides.

The presentation of the work and the results emerging from this thesis is done as follows :

- in the first chapter, we make a brief review of literature on the pulse compression phenomenon, the FWM and the SCG including the MI process. It includes a short presentation of physical descriptions, applications, the limits of these phenomena. Then, we design with concision the motivations that have conducted our work on these phenomena. Moreover, we also make a description of the different optical waveguides studied in the thesis in the last section of the chapter.

- In the second chapter, we present the analytical treatments of the different models studied. Particularly, we derive the NLSEs and the GNLSEs investigated and describe the methods used to analyze the compression, the FWM, the MI and the SCG phenomena. A short presentation of the algorithms on which the numerical simulations are based for each phenomenon is also done.

- In the last chapter, we present the results obtained in each study with the considered discussions and conclusions.

A general conclusion is done at the end of the thesis highlighting some perspectives for further researches directly linked to the results presented.

# Chapter 1

# Review of literature

## 1.1 Introduction

This chapter presents a brief overview on the physical phenomena studied in the thesis. It is organized as follows : section 1.2 deals with the pulse compression phenomenon and section 1.3 is devoted to the FWM process. The MI mechanism and the SCG phenomenon are presented in section 1.4 while section 1.5 concerns the description of the different waveguides investigated in the thesis. The last section concludes the chapter.

## 1.2 Overview on pulse compression

### 1.2.1 Theoretical and physical descriptions

The growing trend on high-data rate optical transmission because of the useful large bandwidth associated, has contributed to the studies of ultrashort optical pulses. The numerous applications of ultrashort pulses in areas such as telecommunication, ultra-fast physical processes, infrared time-resolved spectroscopy, sampling systems, sub-femtosecond to attosecond researches ..., reveal the indispensable role of such pulses [1]. The difficult generation in practice of such pulses, with the current lasers sources and amplifiers has motivated some researches on the pulse compression mechanism. The basic idea behind optical pulse compression stems from chirp radar application in which chirped pulses at microwave frequencies are compressed by passing them through a dispersive delay line [2]. In optics, as can be seen in figure 1.1, this phenomenon consists in the reduction of the width of an optical pulse during its transmission through an optical waveguide. A pulse amplification generally accompanies the compression mechanism. Moreover, the compression mechanism can be classified in two categories : linear and nonlinear pulse compression. Before we introduce the physical description about these two categories, it is necessary to present the general commonly used input pulses since they are important (in the pulse shaping approach) as discussed later.

#### Pulse shaping and input optical pulses

The pulse shaping consists to model an input profile of the propagating pulse. Practically, some shape controller devices allow to achieve this objective. In some cases, the phenomena occurring in optical waveguides are input shape dependent. So, it is necessary to know which kind of profile is appropriate in order to improve the efficiency of the considered phenomenon (the pulse compression belongs to this category of phenomena). For this purpose, we briefly present the input profiles that are generally used in the analysis of the propagation within an optical waveguide [3] :

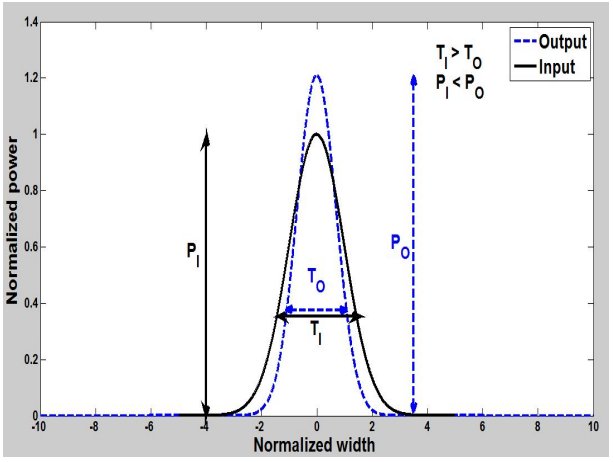


Figure 1.1: Principle of the temporal compression mechanism. $P_I$ and $T_I$ are the input normalized power and width respectively while $P_O$ and $T_O$ correspond to the output of the optical waveguide.

- **The Gaussian profile**
  It has the following analytical form

$$u(0,T) = \sqrt{P_0}\exp\big(-\frac{1}{2}\frac{T^2}{T_0^2}\big), \tag{1.1}$$

  where $u(0,T)$, T, $P_0$ and $T_0$ represent the slowly varying amplitude of the electrical field pulse envelope, the retarded frame of time, the peak power of the pulse, and the pulse half-width (at the $1/e$-intensity point), respectively. The full width at the half maximum (FWHM), $T_{FWHM}$, is commonly used instead of $T_0$. For a Gaussian pulse, it is defined by

$$T_{FWHM} = 2(\ln(2))^{1/2}T_0 \approx 1.665T_0. \tag{1.2}$$

- **The super-Gaussian (SG) profile**
  In some lightwave systems, pulses with steeper leading and trailing edges broadens more rapidly with propagation due to the input wider spectrum of pulse. So, a SG profile models the effects of the steep leading and trailing edges on the broadening. The analytical form is given as :

$$u(0,T) = \sqrt{P_0}\exp\left[-\frac{1}{2}\big(\frac{T}{T_0}\big)^{2m}\right]. \tag{1.3}$$

  The quantity m represents the coefficient which controls the degree of edge sharpness of the SG pulse. The FWHM is defined as $2\big(\ln(2)\big)^{1/2m}T_0$. The rise time $T_r$ defined as the duration on which the intensity goes from 10 to 90% of its maximal value can be written as follows :

$$T_r = (\ln(9))\frac{T_0}{2m} \approx \frac{T_0}{m}. \tag{1.4}$$

  One generally uses this relation to calculate the parameter $m$.

- **The raised-cosine (RC) ansätze profile** :
  The generation of Gaussian-shaped pulses suitable for high bit rate is not easier [9,10]. Indeed, the output of the commonly used Mach-Zehnder pulse carvers is rather close to RC profiled pulses. A RC profile could be modeled analytically as :

$$u(0,T) = \frac{\sqrt{P_0}}{2}\left[1+\cos\big(\frac{\pi T}{T_0}\big)\right] \tag{1.5}$$

Its FWHM is defined as $\left\{(4/\pi)\arccos\left[(1/2)^{1/4}\right]\right\}T_0 \approx 0.728T_0$.

- **The hyperbolic-secant or sech-type profile**
  In experiments, one uses always the Gaussian shape because many lasers emitted approximately this form of input pulses. However, in the case of some mode-locked lasers and naturally in the optical soliton context, one often reaches the hyperbolic secant of sech-type profile described as :

$$u(0,T) = \sqrt{P_0}sech(\frac{T}{T_0}). \tag{1.6}$$

  Generally, the Gaussian and the sech-type profiles are nearly identical following their features when undergoing the guide dispersion. One can also define $T_{FWHM}$ as :

$$T_{FWHM} = 2arccosh(\sqrt{2})T_0 = 2\ln(1+\sqrt{2})T_0 \approx 1.763T_0. \tag{1.7}$$

  An illustration of these profiles is shown on figure 1.2.

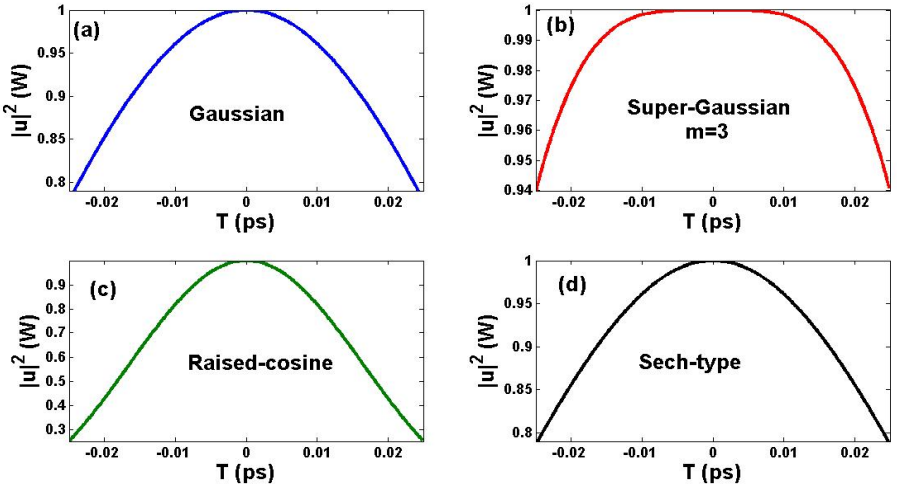


Figure 1.2: Plot of the input profiles : (a) Gaussian, (b) SG for m=3, (c) RC, (d) sech-type. Data : $P_0$=1 W, $T_0$=50 fs.

- **The Airy profile**
  Recently, a focus has been made on new optical beams known as Airy beams/pulses that are attracting a greatest interest because of their special propagation properties [11,12]. Sure enough, Airy beams/pulses are now known through their high stability properties in a stable soliton-like behavior when propagating inside a linear medium. Their origin goes back to 1979, when Berry and Balazs predicted in quantum mechanics that a wavepacket probability density propagating in free space without distortion and having a constant acceleration without external influence, should have an Airy function form [13]. These beams tend to reconstruct themselves despite the severity of perturbations that they undergo inside the medium. This reconstruction is understood through their internal transverse power flow [14-16]. The special propagation properties of Airy beams/pulses : the self-healing, the dispersion resistance and the acceleration on propagation of their dominant intensity peaks. A temporal input Airy profile is described in general as [17] :

$$u(0,T) = r\sqrt{P_0}Ai(\frac{T}{T_0})\exp(a\frac{T}{T_0}), \tag{1.8}$$

where $P_0$ is the peak power, a the truncation coefficient and r the ratio that allows to reach the same peak power with the usual input pulses. The function $Ai(T)$ represents the temporal Airy function. The presence of the parameter $a$ allows to ensure that for a positive quadratic dispersion coefficient, one shall obtain a positive dispersion [17]. The asymmetric nature of this pulse implies that, it is not interesting to define a FWHM unless one gives an interest to the main or dominant peak. Basically in practice, as discussed in [3], an input Gaussian profile propagating in a quasi-linear SMF (where the nonlinear effects are neglected comparatively to the linear ones) near its ZDW around 1.31 $\mu$m (where the TOD $\beta_3$ becomes important comparatively to the GVD $\beta_2$) transforms into an Airy profile. In [18], an input Gaussian pulse was generated by a modelocked Ti:sapphire laser oscillator operating at 800 nm center wavelength and 80 MHz pulse repetition frequency and a computer-controlled pulse shaper were used to impose a cubic spectral phase onto these transform-limited Gaussian pulses leading to the generation of an Airy pulse. So, we can suggest the design of a general set-up as illustrated in figure 1.3. Many other works have been devoted these last years on Airy beams/pulses in

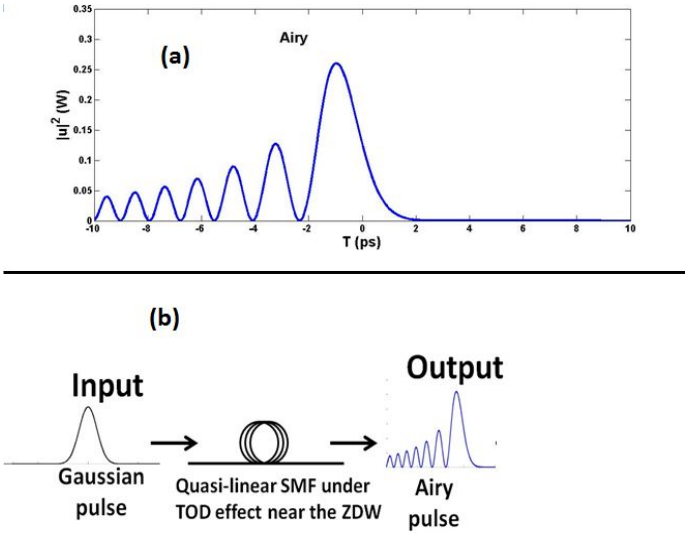


Figure 1.3: (a) Airy profile, a=0.05, $P_0 = 1$ W, r=1, $T_0 = 20$ ps; (b) Proposed experimental set-up for obtaining an Airy pulse.

different kind of systems [19-27].

### The chirping process

Generally when an optical field propagates within a waveguide, its phase varies across the pulse at any distance of propagation z, and following the time T. So, it appears a difference $\delta\omega$ between propagation induced frequency shift and the central initial frequency $\omega_0$. In this case, one says that the pulse becomes chirped [1,3]. In linear systems, the induced frequency chirp changes linearly across the pulse ie the waveguide imposes a linear frequency chirp on the pulse depending on the considered dispersion order term. However, in nonlinear systems, the chirp is induced by the well-known nonlinear Kerr effect leading to a spectral broadening of the pulse. In fact, the SPM compresses the pulse in the time domain, phenomenon which is more pronounced in the anomalous dispersion regime. Consequently, in the spectral domain, it broadens the pulse [3]. The qualitative features of these induced frequency chirps depend on the pulse shape. Often, one imposes an initial frequency chirp on an input profile. This operation is modeled analytically by multiplying the initial profile with the term $\exp\left(\pm iCT^2/2T_0^2\right)$ where the parameter $C$ is the imposed frequency chirp.

With all these basic notions in mind, we present in the next section the specific physical descriptions of the pulse compression within the two categories previously mentioned.

### 1.2.2 Linear pulse compression

In the linear case of the temporal compression mechanism, the basic theory discussed by Agrawal in [1,3] indicates that the source chirp must be opposite to the group-velocity dispersion (GVD) : $\beta_2 C < 0$. Therefore, positively chirped pulses require anomalous or negative GVD to be compressed while negatively chirped pulses require normal or positive GVD. This basic concept is mainly governed by the GVD effect as defined by the following equation [1,3] :

$$i\frac{\partial u}{\partial z} = \frac{\beta_2}{2}\frac{\partial^2 u}{\partial T^2}. \tag{1.9}$$

This equation is the basic linear part of the well-known nonlinear Schrödinger equation (NLSE) where as dispersion effect, one considers only the GVD term [1,3]. The theory mentioned above can be demonstrated analytically by using a chirped Gaussian shape through the Fourier transform method (or Marcuse formalism [28] presented for the first time in 1981) as :

$$u(z,T) = \frac{1}{2\pi}\int_{-\infty}^{+\infty} \tilde{u}(0,\omega)\exp\big(i\frac{\beta_2}{2}\omega^2 z - i\omega T\big)d\omega, \tag{1.10}$$

where $\tilde{u}(0,\omega)$ is the Fourier transform of the input Gaussian pulse (defined from Eq. (1.1) with an initial chirp C as $\sqrt{P_0}\exp\big(-0.5(1+iC)T^2/T_0^2\big)$). The obtained pulse amplitude $\tilde{u}(z,T)$ at the length z is given by :

$$u(z,T) = \left(\frac{P_0}{1 - i\frac{zs_2}{L_{GVD}}(1+iC)}\right)^{1/2}\exp\left(-\frac{(1+iC)T^2}{2T_0^2\big[1 - i\frac{zs_2}{L_{GVD}}(1+iC)\big]}\right), \tag{1.11}$$

where $L_{GVD} = T_0^2/|\beta_2|$ and $s_2$ represent the GVD length and the GVD sign, respectively. Making the comparison between the chirped version of Eq. (1.1) with Eq. (1.11) allows to define the varying width $T_p(z)$ at the length z as :

$$T_p(z) = T_0\left[\big(\frac{z}{L_{GVD}}\big)^2 + \big(1 + s_2 C\frac{z}{L_{GVD}}\big)^2\right]^{1/2}. \tag{1.12}$$

Furthermore, the varying chirp $C_p(z)$ at the length z leads to :

$$C_p(z) = C + \frac{zs_2}{L_{GVD}}(1+C^2). \tag{1.13}$$

The compression factor is therefore defined by :

$$F_c = \frac{T_p(z)}{T_0}. \tag{1.14}$$

The compression occurs only if $F_c < 1$. Mathematically, this exists only if $s_2 C < 0$ as suggested by the theory. Under this hypothesis, Eq. (1.14) shows that the specific distance on which one obtains the shortest pulse width is defined as :

$$L_{min} = \frac{|C|}{1+C^2}L_{GVD}, \tag{1.15}$$

while its maximal compression factor $F_c^{max}$ is calculated as :

$$F_c^{max} = \frac{1}{\sqrt{1+C^2}}. \tag{1.16}$$

The maximal length of compression $L_{mc}$ is generally equal to the double of $L_{min}$. We can also define the maximal pulse compression percentage (MPCP) as :

$$MPCP = 100 \times (1 - F_c^{max}). \tag{1.17}$$

For complicated pulse shapes like those defined by m>3 for the SG pulse, it is customary to use rather the broadening factor $\sigma(z)/\sigma_0$ instead of the compression factor $F_c$ [3] :

$$\sigma(z) = \left[\langle T^2\rangle - \langle T\rangle^2\right]^{1/2}, \tag{1.18}$$

with

$$\langle T^k\rangle = \frac{\int_{-\infty}^{+\infty} T^k |u(z,T)|^2 dT}{\int_{-\infty}^{+\infty} |u(z,T)|^2 dT}, \qquad k \in \mathbb{N}^*. \tag{1.19}$$

The parameter $\sigma_0$ is the root-mean-square (RMS) width of the input pulse at z = 0. Although the broadening factor $\sigma(z)/\sigma_0$ gives more accurate results when complex forms of input profile are used, it defines the same concept as the compression factor $F_c$. So, according to the complexity of the context, one of them is used. In figure 1.4, we present the compression mechanism based on the relations (1.12)-(1.14).

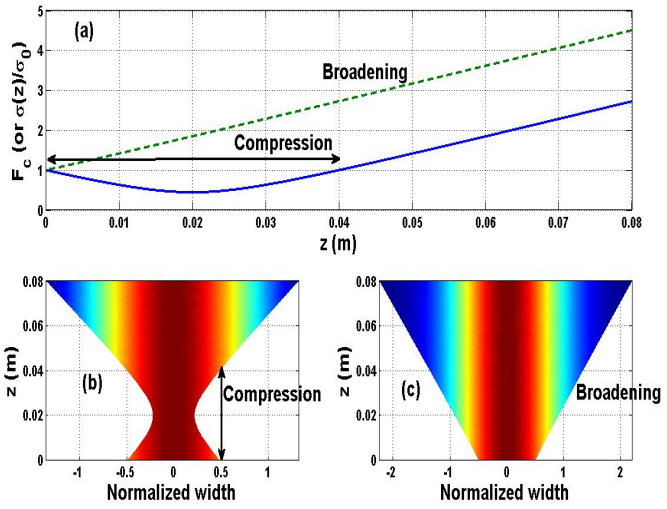


Figure 1.4: Example illustrating the linear compression mechanism of the chirped Gaussian pulse, data: $\beta_2 = -0.05\ ps^2/m$, length of the optical waveguide L=0.08 m, pulse width $T_0 = 50$ fs, $P_0 = 1$ W; (a) plot of the compression/broadening factor : compression occurrence for $C = -2$, $L_{mc} = 0.04$ m, $MPCP = 55.28$ % (solid blue line), broadening occurrence for $C = 2$; Gaussian pulse propagation : (b) contour plot of the case of compression, (c) contour plot for the case of broadening.

Beyond the basic case of the GVD effect described by Eq. (1.9), in 1977, J. D. McMullen studied the compression mechanism using the chirped Gaussian shape in a strong dispersive medium under the TOD effect [29]. This term was shown to give asymmetric broadening of the compressed pulse envelop (see figure 1.5). One should note that McMullen with the help of A. A. Maradudin suggested already at this period the Airy form of this compressed pulse under the TOD effect. The pulse

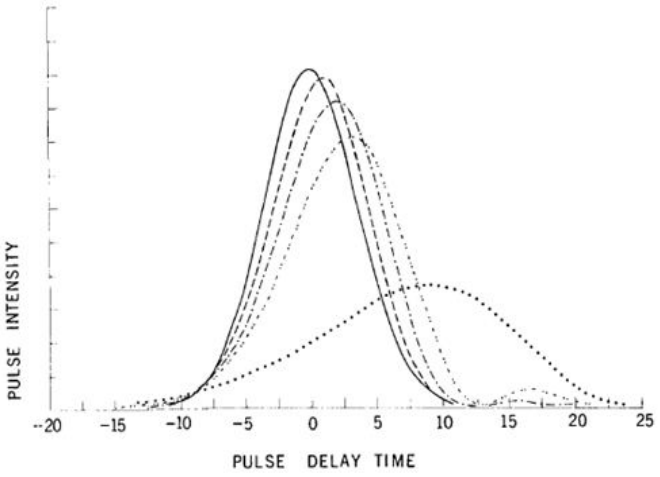


Figure 1.5: Plot of the compression mechanism : in arbitrary unit (a.u) of the TOD coefficient : $\beta_3 = 0$ (solid line), $\beta_3 = 3$ ($- - -$), $\beta_3 = 4$ ($-.-.-.-$), $\beta_3 = 5$ ($-..-..-..-..-$), $\beta_3 = 10$ (.....). Results obtained by McMullen for the compressed chirped Gaussian pulse under the TOD effect (©-1977 OSA, from [29]).

becomes more asymmetric following the increase of the TOD effect.
Later in 2002, Capmany et al [30] presented in a high-speed optical time-division multiplexed transmission line under FOD near the vanished values of GVD and TOD, a Gaussian pulse compression with a negative chirp and a positive FOD based on the Marcuse formalism. Then one year later, they presented an analysis (in [31]) of a chirped Gaussian pulse using the combination of the Marcuse formalism and the Amemiya's method [32]. The diagram that describes their model is illustrated on figure 1.6 below. The parameter $t$ represents here the retarded frame of time. The input time-

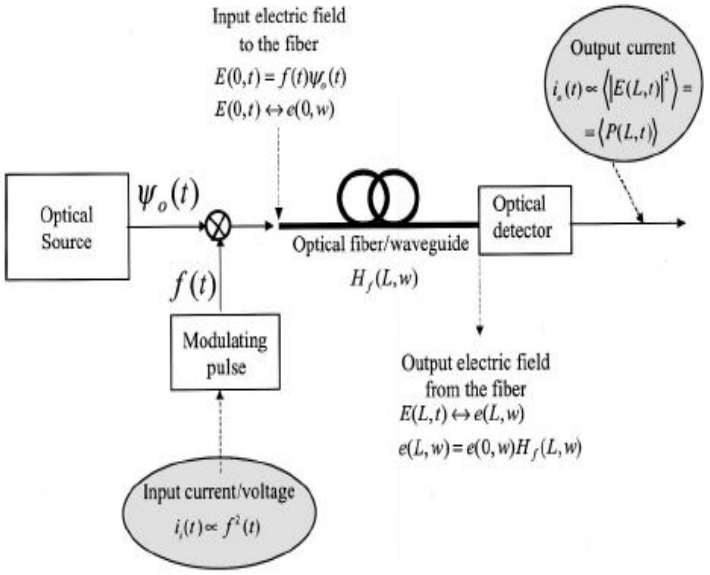


Figure 1.6: Block diagram of the Capmany et al. model (©-2003 OSA, from [31]).

domain field to the optical waveguide is given by $E_{in} = E(z = 0, t) = f(t)\psi_0(t)$ where f(t) is a slowly varying electric field envelope that corresponds to the modulating pulse defined by the width $t_0$ and

a high-frequency chirped optical carrier $\psi_0(t)$ defined as a chirped Gaussian function :

$$\psi_0(t) = A(t)\exp\left[i\left(\omega_0 t + \frac{Ct^2}{2t_0^2}\right)\right]. \tag{1.20}$$

The function $A(t)$ is the unmodulated source random-phase fluctuations that are linked to the linewidth and $\omega_0$ is the optical carrier frequency. The input modulating current $i_i$ is proportional to $f^2(t)$ and so is the output optical power from the transmitter. Then, the transmission is understood as an optical system with transfer function $H_f(L,\omega)$ that realizes a coupling between the input electrical field $E(0,t)$ to its output $E(L,t)$. The functions $e(\omega)$ and $\langle P(L,t)\rangle$ are the Fourier transform of $E(t)$ and the output electric current $(i_o)$. They showed that the pulse broadening and compression arise as a result of the interaction between dispersion orders of same parity as :$\beta_k\beta_{k+2} < 0, \quad k \geq 2$, k being an integer. For example, the GVD having an opposite sign with the FOD leads to the compression of the pump. This study assumed that the source chirp interacts only with even dispersion terms to yield pulse broadening or compression. As can be observed on figure 1.7, the compression is obtained in figure 1.7(a) by the interaction between the chirp (C=-0.5) and the positive sixth-order dispersion parameter defined by $D_6 = 2$. By contrast, the odd dispersion terms interact on figure 1.7(b) leading to the pulse asymmetry. The normalized broadening factor is represented on figure 1.7(c) showing the compression mechanism of figure 1.7(a) versus $D_6$. The figure 1.7 confirms that

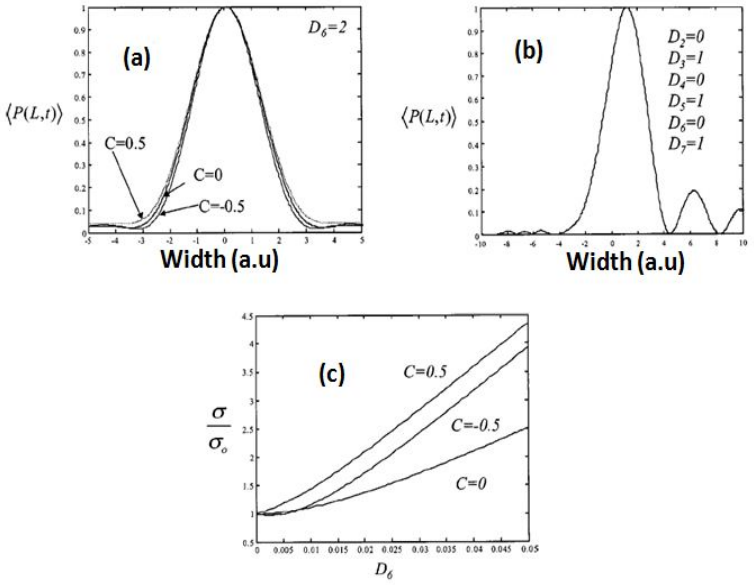


Figure 1.7: (a) Plot of chirped Gaussian pulse compression in the Capmany et al. model : interaction between the chirp and the sixth-order dispersion parameter. The compression occurs for C=-0.5; (b) Pulse asymmetry induced by the odd dispersion terms; (c) plot of the broadening factor versus $D_6$. Results obtained by Capmany et al. (©-2003 OSA, from [31]).

the dispersion terms of the same parity interact only between them and the odd ones affect only the design of the pulse, generating the asymmetry.

### 1.2.3 Nonlinear pulse compression

The compression in this specific case is obtained with the famous solitonic properties through the balance between the positive SPM (of the cubic nonlinear Kerr effect) and the anomalous dispersive

regime of the GVD [1,3,32,33,34]. The soliton order N is defined by the following relation :

$$N = \left(\frac{L_{GVD}}{L_{NL}}\right)^{1/2}, \tag{1.21}$$

where $L_{NL}$ is the nonlinear length associated to the cubic Kerr nonlinearity (CKN). It is linked to the peak power as $L_{NL} = 1/\gamma P_0$ with $\gamma$ being the CKN coefficient. An input pulse that is launched within a waveguide under the condition N=1 of the fundamental soliton (where the higher-order nonlinear effects have been neglected), transforms into a solitonic form through a progressive nonlinear compression process induced by the interaction between the GVD and the SPM. If the obtained soliton form is not seriously perturbed during its propagation, it can propagate further within the waveguide. It is this feature of solitonic robustness which creates the interest of optical solitons in communication applications. We present the transformation of an input SG pulse (m=3) to a fundamental soliton through the pulse compression mechanism on figure 1.8.

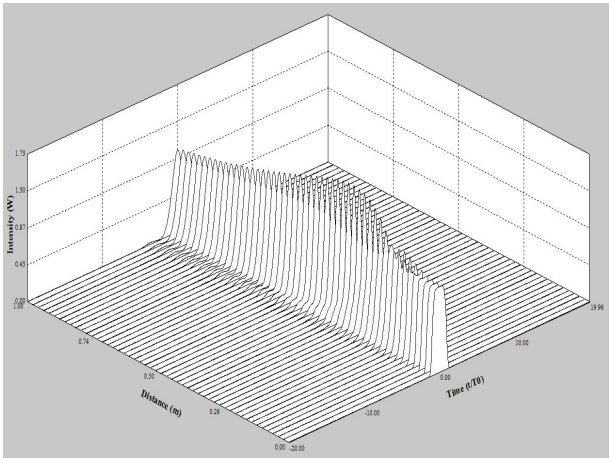


Figure 1.8: Transformation of an input SG pulse (m=3) to a fundamental soliton. Data : $P_0 = 1$ W, $\gamma = 1\ W^{-1}m^{-1}$, N=1, L=1 m. Result obtained from the NLSE Solver&Plotter software (©-2005, version 1.0 written by Nick Userchak).

The higher-order solitons (HOSs) splitting yields to the periodic compression with the well-known soliton period $z_0 = (\pi/2)L_{GVD}$. The nonlinear periodic compression mechanism is therefore understood as a fundamental property of HOSs. The HOSs undergo an initial narrowing phase at the beginning of each period. Because of this property, an appropriate choice of the optical waveguide length and input pulse peak power should be operated in order to compress the soliton by a factor that depends on its order N. We present on figure 1.9 the nonlinear compression of a third-order soliton (N=3). The evolution of this 3-OS is periodic.

### 1.2.4 Applications and experimental realizations : pulse compression techniques

As mentioned earlier, the pulse compression mechanism is very important in optics since it leads to several useful applications in a wide range of domains as in optical telecommunication, ultrafast physical processes, infrared time-resolved spectroscopy, sampling systems, sub-femtosecond to attosecond researches ... . So these last decades, the theories described above have been directly experimented for practical situations. In the linear case, negatively chirped pulses were transmitted through liquids or gases such that they experienced normal GVD [35]. For positively chirped pulses, a grating pair was found to be most suitable for providing anomalous GVD [36]. Today, this system

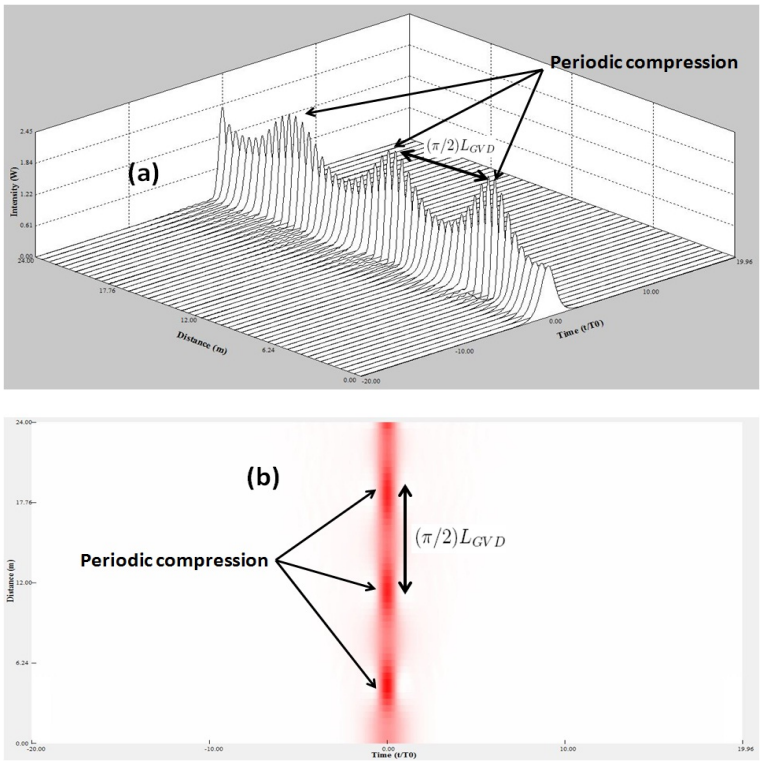


Figure 1.9: Third-order soliton evolution into a nonlinear optical waveguide. Input : sech-type pulse, $P_0 = 1$ W, $\gamma = 1\ W^{-1}m^{-1}$, N=3, L=24 m. The soliton period $z_0 \approx 4.71$ m. Result obtained from the NLSE Solver&Plotter software (©-2005, version 1.0 written by Nick Userchak).

has been introduced in fiber optics and has led on the well-known grating-fibers compressors [1]. The use of the grating-fiber compressors is efficient in the visible and the near-infrared regions. The figure 1.10 shows a diagram of a grating fiber compressor. The input pulse propagates into a SMF and then develops a positive chirp. At the output, the pulse is launched through a grating pair and undergoes an anomalous GVD. It results a linear pulse compression. After, the optical pulse is sent back through the grating pair to reconvert it to the original cross section [1]. The roles played by the mirrors $M_1$ and $M_2$ consist for the first to separate the outgoing pulse from the incoming one and for the second to deflect the compressed pulse out of the compressor in a lossless manner.
Since the optical solitons were observed in fibers by L. F. Mollenauer et al in 1980 [37] after their theoretical prediction in 1973 by A. Hasegawa and F. Tappert [38], the experimental work on SPM-based or soliton-based pulse compression has led to the so-called soliton-effect compressors. These kinds of compressors based on the nonlinear case, are useful in the range wavelengths exceeding 1.3 $\mu m$. The compression factor for a soliton-effect compressor is defined empirically by the relation [39] :

$$F_c = 4.1N, \tag{1.22}$$

and the minimal length of compression $L_{min}$ where the maximal compression occurs is linked to the soliton period $z_0$ as follows :

$$L_{min} = \frac{z_0}{N}\left(0.32 + \frac{1.1}{N}\right). \tag{1.23}$$

Several experiments have been conducted since the decades of 1980s and the compression techniques were improved. For instance in 1981, an experiment using an optical fiber was conducted [40]. Some 5.5-ps input pulses at 587 nm, with $P_0 = 10$ W, were propagated over a propagation about 70 m. The experimentation reached a compression to 1.5 ps. One year later, the femtosecond domain was

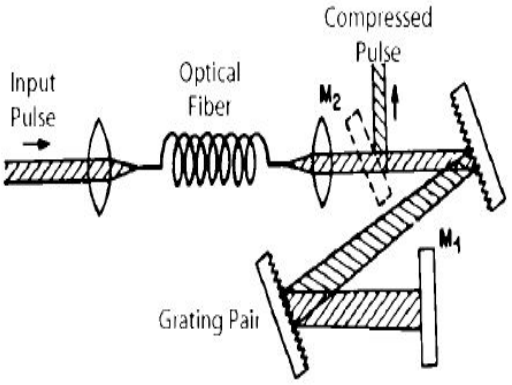


Figure 1.10: Basic diagram of a grating-fiber compressor (©-2008 AP, from [1]).

investigated by using a grating pair as a dispersive delay line [41]. In this experiment, with a 90-fs pulses at 619 nm in wavelength, the compression reaches about 30 fs. With the advent of mode-locked Ti:sapphire lasers, the pulse compression experiments leading to pulse widths under 10 fs were initiated. Since several nonlinear effects arise in this domain, the experiments encountered difficulties. The HOSs properties were needed to achieve the compression in this region. For this reason, soliton-effect compressors give high compression factors. Then, the main objective was to maximize the compression factor. Since the wavelength region near 1.3 $\mu m$ links the two kinds of compressors, two-stage compression techniques were developed in later experiments yielding large compression factors by using dispersion-shifted fibers [1]. Indeed, an experiment of the two-stage compression technique in which a grating-fiber compressor was followed by an anomalous-GVD ($\beta_2 < 0$) fiber, was used to obtain compression factors of up to 5000 [42]. By 1996, optical pulses shorter than 8 fs were generated directly from a Ti:sapphire laser [43]. Other experiments employed multiple cascaded soliton-effect compressors for the obtention of ultra-short pulses. In 1999, a 7.5-ps optical pulse was compressed down to 20 fs with $F_c \geq 3700$ [44]. More recently, in 2006, 5.4-ps parabolic pulses were compressed down to 20 fs [45]. For more details and further informations about pulse compression experiments based on both the grating-fibers and the soliton-effect compressors, the reader can consult the reference [1].
Beyond these two kinds of compressors, other techniques have been developed among which one finds fiber Bragg gratings using the cross-phase modulation (XPM) technique [1,46,47], a fiber polarization technique [48], the use of a tapered microstructure optical fiber with four layers of holes [49], gain switching technique [50-60], optical amplifiers, fiber-loops mirrors [1] ... .

### 1.2.5 Limits of the pulse compression theoretical analysis

In the theoretical aspect of the pulse compression analysis discussed in sub-sections (1.1.2) and (1.1.3), the researchers use some methods to investigate the mechanism. These methods belong both to the analytical and the numerical sides [56]. It consists to solve the dynamic equation of the optical waveguide, the so-called NLSE and so, to bring out the compression factor evolution across the length of the waveguide. In the numerical side, usually one uses the split-step Fourier (SSF) method or the finite-difference methods [3]. Although a numerical solution is necessary for accuracy, considerable physical insight is gained with the analytical or semi-analytical methods [3].

Because of this, it is therefore suitable in some theoretical studies as those of the pulse compression phenomenon to proceed through these last methods. Since in the linear case of the compression analysis, the nonlinear part is neglected, an analytical method as the Marcuse formalism (Fourier transform method) [28] gives good results for the low order dispersion systems as those under the GVD effect. For more accuracy in complex systems, Amemiya developed a method that provides integral expressions for the computation of the electric field impulse responses of an optical waveguide due to higher-order even and odd dispersion orders [32]. After, Capmany et al. combined the two methods leading to a form which describes the influences of the chirp and the linewidth [31]. They also demonstrated that, the numerical simulation of Eq. (1.9), for example using the SSF algorithm could not describe efficiently the compression mechanism when the source chirp is considered in the analysis. This result justifies why it is customary to use analytical and semi-analytical methods for the linear compression case. Among these methods, the famous quoted ones are the moment method [3], the variational approach [3,62-70], the CVs approach [71-75], the self-similar analysis on self-similar solitary waves so-called similaritons [76-78]. Considering the moment method, it can be used for approximated studies, assuming that the pulse maintains its shape as it propagates down the waveguide even though its characteristics change following the propagation distance z [3]. The basic idea behind this method is to treat the optical pulse like a particle. It is suitable in linear systems even in the nonlinear ones under certain conditions [3]. In the variational approach, the Lagrangian density of the system is constructed and a suitable trial function for the pulse is assumed. With the Lagrangian density, total Lagrangian of the system is constructed. Variation of the Lagrangian with respect to various free parameters appearing in the trial function gives ordinary differential equations (ODEs) for the parameters [75]. The CVs approach is based on the particle-like behavior of the soliton. It was first proposed by Boesh et al. for Klein Gordon equation (KGE). The CVs approach being equivalent to the Lagrangian variational method, is nonetheless more appropriate in the case of soliton dynamics [71-75]. Recently in years 2011 and 2012, for time-varying media (media with refractive index that varies with the time) a novel approach has been developed as a time-transformation approach [79-81]. This approach maps directly the input electric field to the output one, without making the slowly varying envelope approximation as done for the other methods.
Among all these semi-analytical methods, only the variational approach can be used in any system beyond the cases of the solitons (speciality of the CVs approach), particle-like waves (speciality of the moment method), and similaritons (speciality of the self-similar analysis). So, even though the compression mechanism both in the linear and the nonlinear cases has been extensively studied, some research paths remained to be explored :

- no study of the linear compression of a system under higher-order dispersion (HOD) terms as the FOD using the variational approach were conducted. The derivation of the conditions of its occurrence, highlighting the relations between the dispersion lengths associated to the GVD and the FOD was missing,

- beyond the study of Capmany et al, the linear compression mechanism was known to be generated only when two even dispersion orders interact or when one of them interacts with the chirp. It did not exist a rule that links at least two even dispersion terms with chirp in the compression process.

- One should note that for the single GVD case, the compression mechanism was studied by Roy et al in 2008 [8], using a MVA developed one year before [7] in promising optical waveguides as the SOI-waveguides. Indeed, in these waveguides beyond the SPM effect, the absorption coefficients as the TPA and the FCA should be included in the dynamics (this optical waveguide is summarily presented in section 1.5). On the other hand, the MVA involves the RDF to take into account the nonlinear part of the NLSE. However, the investigation of the nonlinear

compression in these waveguides under the FOD effect was not yet conducted. Even the impact of absorption coefficients including the chirp and the nature of the input profile on this mechanism was missing.

- The compression process of a recent input profile introduced in nonlinear optics as the Airy pulse was not yet studied in the SOI waveguide under the FOD effect.

Obviously, these points are not the only ones since the works presented in the present thesis are not exhaustive. Nonetheless, they belong to those that have attracted our attention for the present study as explained in the next sub-section.

### 1.2.6 Objective of the work done on the compression analysis : motivations and contributions

In the present thesis, our motivations are based on the need to bring some responses about the shortcomings presented above. As contributions :

- we study in a linear dispersive optical medium under FOD using the variational approach, the dynamics of the chirped pulse compression with the help of Gaussian and RC pulses in order to highlight the phenomenon's dependence on the input profile. Our numerical simulations to confirm the observed features are based on 380-fs input pulses undergoing 0.00086 $ps^4/Km$ value in the FOD.

- Then, we report the analysis of the compression mechanism for chirped femtosecond pulses in SOI waveguides under the effect of the FOD using the MVA that involves the RDF. An investigation of the effect of the absorption coefficients is also done.

- Our last work on the compression mechanism is based on the Airy pulses in the SOI-waveguides under FOD using the MVA. The obtained results concern the impact of the TPA, FCA and the SPM in the presence of the FOD.

Since in the opposite side of the temporal compression process, a spectral broadening process operates simultaneously, reaching widths of ultra-short pulses as those of the femtosecond domain allows the obtention of spectral widths about the order of 100 THz. Such extreme spectral broadening generally leads to the SCG phenomenon which is presented later in section 1.4. Before, we present briefly in the next section an overview of the FWM phenomenon which belongs generally to the whole physical processes on which the SCG is based. The case of WDM solitons systems is specially underlined since the FWM is well-known to be one of its deleterious factors.

## 1.3 Overview on FWM in WDM solitons systems

### 1.3.1 Theoretical and physical descriptions

In optical waveguides, there are two classes of nonlinear phenomena : those in which the waveguide plays an active role (such as in scattering processes) and those where it is entirely passive mediating only interaction between the different propagating optical waves. The last class of nonlinear phenomena are called parametric processes. They basically require a phase-matching condition and a modulation of a medium parameter for instance, the refractive index before occurring in the waveguide [3]. In this class, belongs the FWM phenomenon. It stems from the nonlinear response of bound

electrons of a material to an optical field. This nonlinear response is linked to the nonlinear susceptibility. Considering the third-order susceptibility $\chi^3$, one reaches the third-order parametric processes as the FWM and the third-harmonic generation (THG) as an interaction among four optical waves [3,82,83]. Concerning the FWM, its study was done soon after low-loss fibers were fabricated [84-93]. A basic theoretical illustration of the FWM can be understood from the third-order nonlinear polarization in a scalar case [3] as :

$$\mathbf{P}_{NL} = \frac{1}{2}\hat{x}\sum_{n=1}^{4} P_n \exp[i(\beta_n z - \omega_n t)] + c.c, \tag{1.24}$$

where $P_n$ (n=1 to 4), $\beta_n$, $\omega_n$ and c.c represent the polarization component of the (n)th optical field, its propagation constant, its harmonic frequency of oscillation and the conjugated complex part of Eq. (1.24), respectively. Considering the continuous waves (CWs) case, the total electrical field including the four optical fields linearly polarized along the x-axis and oscillating at frequencies $\omega_1$, $\omega_2$, $\omega_3$ and $\omega_4$ can be written as :

$$\mathbf{E} = \frac{1}{2}\hat{x}\sum_{n=1}^{4} E_n \exp[i(\beta_n z - \omega_n t)] + c.c, \tag{1.25}$$

Since the relation between $\mathbf{P}_{NL}$ and $\mathbf{E}$ is defined as $\mathbf{P}_{NL} = \varepsilon_0\chi^3\vdots\mathbf{EEE}$, the polarization $P_n$ is therefore a mixing of $E_n$. The tensorial product '$\vdots$' correspond to $\chi^{(3)}$ related to the electric field components **EEE** [3]. It is expressed with many terms involving the crossed products of three interacting fields. Note that, the constant $\varepsilon_0$ is the electrical permittivity of the vacuum. Taking for instance the component $P_4$, one obtains :

$$\begin{aligned} P_4 =& \frac{3\varepsilon_0}{4}\chi^3_{xxxx}\Big\{\left[|E_4|^2 + 2(|E_1|^2 + |E_2|^2 + |E_2|^2)\right]E_4 \\ &+ 2E_1E_2E_3\exp(i\theta_+) + 2E_1E_2E_3^*\exp(i\theta_-) + ...\Big\}, \end{aligned} \tag{1.26}$$

where $\theta_+$ and $\theta_-$ are given by :

$$\begin{aligned} \theta_+ =& (\sum_{n=1}^{3}\beta_n - \beta_4)z - (\sum_{n=1}^{3}\omega_n - \omega_4)t, \\ \theta_- =& (\beta_1 + \beta_2 - \beta_3 - \beta_4)z - (\omega_1 + \omega_2 - \omega_3 - \omega_4)t. \end{aligned} \tag{1.27}$$

The crossed terms in Eq. (1.26) including $\theta_+$ and $\theta_-$ are those related to the FWM/THG phenomenon while the first four terms are linked to the SPM and XPM.
The phase mismatch between $E_4$ and $P_4$ governed by Eq. (1.27) should nearly vanish and a phase matching condition should be realized to the occurrence of the FWM/THG. From quantum mechanic theory, FWM occurs when photons from one or more waves are annihilated and new photons are created at different frequencies such that the net energy and momentum are conserved during the parametric interaction [3]. There are two types of the FWM process according to Eq. (1.27) (as can be seen in figure 1.11) : the first type $\theta_+$ is obtained when three light pulses transfer their energy to a single fourth photon (the degenerate case corresponds to the THG phenomenon) and the second type $\theta_-$ is concerned when two photons are annihilated while two new other are created simultaneously. For the case $\theta_-$, one has $\omega_3 + \omega_4 = \omega_1 + \omega_2$. The phase-matching condition for this process to occur

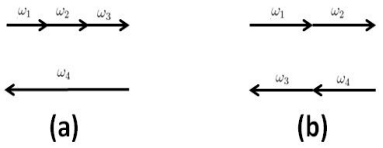


Figure 1.11: (a) case of $\theta_+$, (b) case of $\theta_-$.

correspond to the wave-number mismatch $\Delta\kappa = 0$ as :

$$\begin{aligned}\Delta\kappa =& \beta_1 + \beta_2 - \beta_3 - \beta_4, \\ =& (\tilde{n}_1\omega_1 + \tilde{n}_2\omega_2 - \tilde{n}_3\omega_3 - \tilde{n}_4\omega_4)/c,\end{aligned} \tag{1.28}$$

where $\tilde{n}_j$ is the effective mode index at the frequency $\omega_j$. Physically, it manifests as a strong pump wave at $\omega_1$ creates two sidebands located symmetrically at frequencies $\omega_3$ and $\omega_4$ with a frequency offset (or frequency shift) :

$$\Omega_s = \omega_1 - \omega_3 = \omega_4 - \omega_2. \tag{1.29}$$

If we assume that $\omega_3 < \omega_4$ and $\omega_1 = \omega_2$, the low-frequency sideband at $\omega_3$ refers to the Stokes component of FWM while the high-frequency at $\omega_4$ corresponds to the anti-Stokes component of FWM [3]. Rigorously, the mismatch of Eq. (1.28) has other contributions beyond the only material dispersion one. There are also waveguide dispersion ($\Delta\kappa_{WD}$) and nonlinear effects ($\Delta\kappa_{NE}$) :

$$\Delta\kappa = \Delta\kappa_{MD} + \Delta\kappa_{WD} + \Delta\kappa_{NE}, \tag{1.30}$$

where $\Delta\kappa_{MD}$ is defined by Eq. (1.28) and the two last contributions are defined as :

$$\Delta\kappa_{WD} = [\Delta n_3\omega_3 + \Delta n_4\omega_4 - (\Delta n_1 + \Delta n_2)\omega_1]/c, \tag{1.31}$$

and

$$\Delta\kappa_{NE} = \gamma(P_0^1 + P_0^2). \tag{1.32}$$

where $P_0^1$ and $P_0^2$ are the peak pump powers. The parameter $\Delta n_j$ is the change in the material index $n_j$ induced by the waveguiding [3].
In brief, the physical principle of the FWM is the transfer of energy from the pump to new waves. If the pump is constituted by two symmetric waves ($\omega_1 = -\omega_2$), the transfer of energy goes to the two new waves upshifted in frequency (anti-Stokes component) and downshifted in frequency (Stokes component). The general phase-matching condition in this case is given by the relation [3]:

$$\sum_{k=2}^{\infty} \frac{\beta_k(\omega_p)}{k!}\Omega_s^k + 2\gamma P_0 = 0, \tag{1.33}$$

with $\Omega_s = \omega_s - \omega_p$ being the frequency offset between the signal frequency $\omega_s$ and the pump frequency $\omega_p$.

### 1.3.2 The FWM analysis in WDM soliton systems based on the ABCJS approach

The WDM technic which consists to send many signals in a single optical fiber has increased the usefulness of the transmission of data [1,3,94-98]. This has become one of the most important techniques for high speed and high capacity requirement of optical fiber transmission systems.

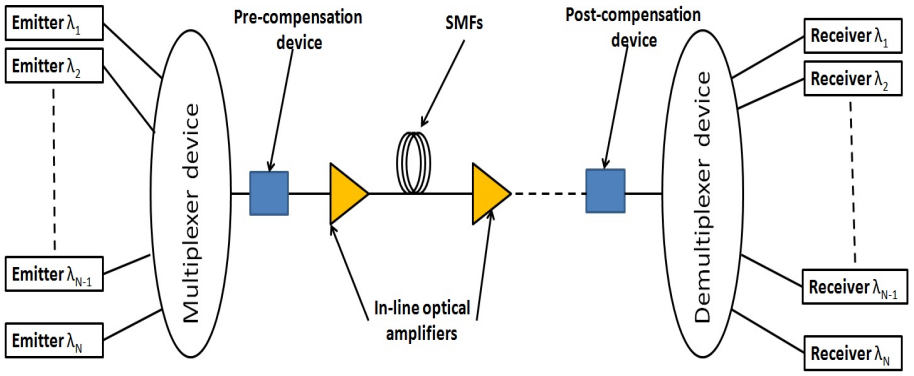


Figure 1.12: Design of the WDM principle based on SMFs. The role played by the Multiplexer and the Demultiplexer devices, is to mix and separate the wavelength channels respectively. The pre-, post and in-line compensators serve as signal regenerator (management of the dispersion link).

Nowadays, it is well-known that FWM creates deleterious effects on WDM and dense WDM communication systems [1,3,99-103]. Many technics were previously investigated in order to reduce or to quite cancel these effects such as dispersion management (DM) technic [103-107], an experimental grouping wavelength method [108], the use of weak random dispersion in second term of dispersion [109,110] and recently in frequency-division multiplexing systems [111]. The researchers Ablowitz, Biondini, Chakravarty, Jenkins and Sauer developed in 1996 a mathematical approach that describes the anti-Stokes component evolution of the second-type FWM in SMFs through the interaction between two fundamental soliton-like fields in a lossy WDM systems with periodically spaced amplifiers [99]. This approach is named as the ABCJS approach in the next. Basically, this approach starts by the following assumption : in a WDM solitons system involving two symmetric soliton-like pulses $E_1$ and $E_2$, it appears two components for the FWM as $E_{112}$ (Stokes component) and $E_{221}$ (anti-Stokes component). These waves oscillate at the frequencies : $\Omega_1$, $\Omega_2$, $\Omega_{112}$ and $\Omega_{221}$ respectively. One can define $\Omega_2 = \Omega$ and $\Omega_1 = -\Omega_2$ for the symmetry. The frequency offset $\Omega$ describes the shift between the central frequency $\omega_0$ and the corresponding component of the main pump. So, the main pump $E_{pump}$ is constituted by $E_1$ and $E_2$. Therefore, the total field propagating within the optical waveguide is written as :

$$E = E_{pump} + E_{FWM}. \tag{1.34}$$

This is the form of the field which is injected inside the NLSE modeling the system. For instance, for an anomalous GVD system of [99], we have the dimensionless equation :

$$i\frac{\partial u}{\partial z} + \frac{1}{2}\frac{\partial^2 u}{\partial t^2} + g(z)|u|^2 = 0, \tag{1.35}$$

where $u$ is the dimensionless form of $E$ and $g(z)$ the amplification function defined as :

$$g(z) = g_{max}\exp\big[-2\Gamma(z - nz_a)\big]. \tag{1.36}$$

We have $g_{max} = 2\Gamma z_a/[1-\exp(-2\Gamma z_a)]$ with $z_a$ the dimensionless amplifier spacing and $n$ the actual amplifier node. The parameter $\Gamma$ is the dimensionless losses coefficient. One obtains after this operation, four dynamic equations that describe each wave. These equations includes both the SPM and the XPM effects between the four interacting pulses. However, for the FWM Stokes and the anti-Stokes components one should neglect the small terms such as those of SPM and XPM including these components. For the anti-Stokes component (ASC), we have :

$$i\frac{\partial u_{221}}{\partial z} + \frac{1}{2}\frac{\partial^2 u_{221}}{\partial t^2} + g(z)u_2^2 u_1^* = 0, \tag{1.37}$$

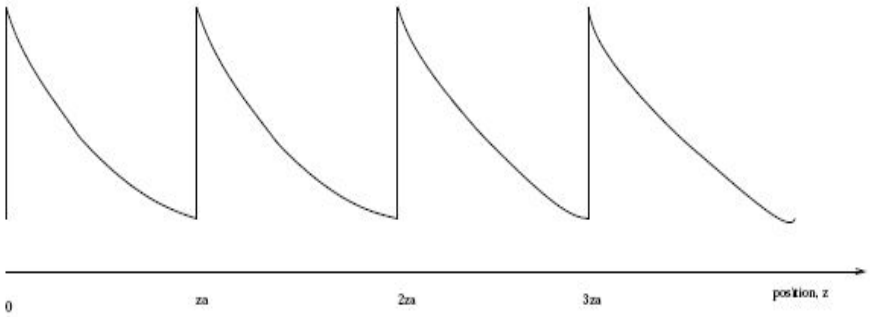


Figure 1.13: Plot of $g(z)$ versus z : a periodical evolution with the period $z_a$, (©-2001, University of Colorado at Boulder, from [103]).

where $u_{221}$ represents the dimensionless form of $E_{221}$. The input pulses are in the form :

$$u_k = A_k sech(A_k t)\exp(i\frac{A_k^2}{2}z)\exp\big[i(\Omega_k t - \frac{\Omega_k^2}{2}z)\big], \qquad k = 1,2 \tag{1.38}$$

where $A_k$ is the dimensionless amplitude of the corresponding pulse. One takes the ASC with a rapidly varying-piece as :

$$u_{221} = H(z,t)\exp\big[i(3\Omega t - \frac{\Omega^2}{2}z)\big]. \tag{1.39}$$

Introducing Eq. (1.39) into Eq. (1.37) leads to an equation for the amplitude $H(z,t)$ as :

$$i\frac{\partial H}{\partial z} + \frac{1}{2}\big[\frac{\partial^2 H}{\partial t^2} + 6i\Omega\frac{\partial H}{\partial t} - 2(2\Omega)^2 H\big] = -g(z)u_2^2 u_1^* \exp\big[i(-3\Omega t + \frac{\Omega^2}{2}z)\big]. \tag{1.40}$$

The study of the ASC growth in the system, consists to determine the function $H(z,t)$ and to draw its evolution following the propagation distance. In the reduced model of the study, one should assume that the partial derivatives in the time domain of Eq. (1.40) are nearly equal to zero. Then, one integrates the obtained ODE of $H(z,t)$. It leads to :

$$H(z,t) = i\exp\big(-i(2\Omega)^2 z\big)\int_{-\infty}^{z} g(z')u_2^2 u_1^* \exp\big[i(-3\Omega t + \frac{\Omega^2}{2}z')\big]dz'. \tag{1.41}$$

The phase-matching condition (PMC) on the frequency offset $\Omega$, for the occurrence of the maximal FWM ASC values is obtained when one considers the harmonic mismatch of the integral in the right-hand-side (RHS) of Eq. (1.41). One obtains [99] :

$$\Omega = \frac{1}{2}\sqrt{\frac{2\pi n}{z_a} - A^2}, \tag{1.42}$$

with $A_k = A$ (k=1,2). In the full model, one should consider the whole equation (1.40). The method uses the Fourier transform before making the integration on $\tilde{H}(z,\omega)$ (the Fourier transform of $H(z,t)$) to reach its spectrum in the frequency domain :

$$\begin{aligned}\tilde{H}(z,\omega) &= \frac{i\pi A}{2\omega}\exp\big(\frac{-i}{2}\phi(\omega,\Omega)z - i\omega(\Omega z - T_0)\big)sech(\frac{\pi\omega}{2A})\exp(\chi z_{coll}) \\ &\times\int_{-\infty}^{y} g(z')I(y,\frac{\omega}{A})\exp\big[i\frac{\chi}{2\Omega A}y\big]dy,\end{aligned} \tag{1.43}$$

where $\phi(\omega,\Omega) = \left[\omega^2 + 6\omega\Omega + 2(2\Omega)^2\right]$, $\chi = \frac{1}{2}\left(A^2 + \phi(\omega,\Omega)\right)$, $z_{coll}$ the position of the collision between $u_1$ and $u_2$ leading to the ASC, $I(x,s) = \left[\cosh(x) + is\sinh(x) - \exp(isx)\right]/\sinh^2(x)$ and $y = 2A(\Omega z - T_0)$. One assumes that $T_k \equiv T_0$. figure 1.14 shows a result of the collision between two soliton-like launched pulses in a basic WDM soliton system under the ABCJS approach. At the propagation distance $z = z_{coll}$, one observes the appearance of FWM components at both the two extreme sides of the emerging waves. Beyond the system under damping and amplification studied

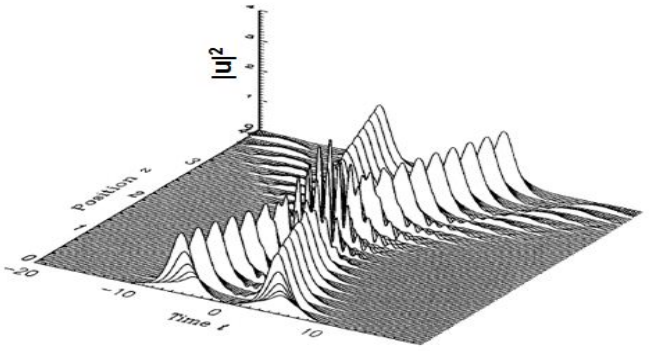


Figure 1.14: Two-soliton collision under damping and amplification described by the ABCJS approach and leading to the generation of FWM components (©-1996 OSA, from [99]).

in [99], the ideal system was studied under this approach one year later [100]. Other works based on this ABCJS approach followed describing the FWM in WDM soliton systems with methods to cancel its crosstalk [103-105,109-110]. The study of effects of higher-order dispersion terms on the FWM of the first type has been done by Singh et al [112] based on earlier works of Inoue et al [112,113]. They showed that the combination of HOD terms leads to a FWM power reduction.
However, coming back to the theoretical analysis discussed in the previous sub-section, one can consider the FWM as rather a beneficial phenomenon. Indeed from Eq. (1.28) to Eq. (1.33), another situation in which an idler signal at $\omega_3$ is launched with the strong pump $\omega_1 = \omega_2$, leads to the amplification of the initial idler signal while another one is created at $\omega_4$. Such amplification implying a parametric gain is used for several useful FWM applications.

### 1.3.3 FWM as a beneficial phenomenon

The FWM has been discovered to be useful. As examples, one can quote the measurement of the third-order nonlinear-index assuming a FWM-Based technic, FWM-Based ultrafast switches, the measurement of the ratio of the TOD over FOD coefficients, making parametric oscillators, ultrafast signal processing, FWM-induced quadrature squeezing, wavelength conversion, phase conjugation, the SCG phenomenon (which is the aim of the section 1.4)... [3,88-98]. We consider for example one of the quoted applications above such as the case of SCG. Indeed, taking into account the spectral aspect of the dynamics within an optical waveguide as a SMF, the FWM as discussed earlier generate new frequencies beyond the initial launched ones leading to an extended spectral picture. If the generation of the frequencies is done with the participation of others phenomena that also contribute as the scattering processes one can obtain extreme broadband spectra so-called SCG which has several applications in optics. For instance, considering the generation of new frequencies in the FWM phenomenon in a nearly ideal WDM solitons system of the ABCJS approach one observes nine spectral components induced by FWM from the interaction between three launched solitons (see figure 1.15). The extension of this frequencies generation to the SCG, can lead to spectral pictures

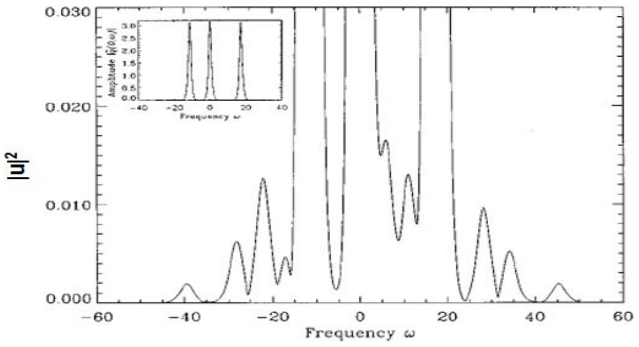


Figure 1.15: Frequencies generation in the FWM process after the interaction between three soliton-like pulses. The inset shows the location of the soliton contributions (©-1996 OSA, from [100]).

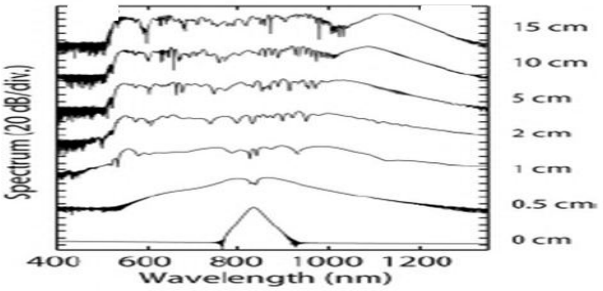


Figure 1.16: Frequencies generation in the SCG process after the pumping of a pulse within a highly nonlinear fiber (this phenomenon is presented in the next section). One observes a broadband spectral picture which takes place progressively following the propagation distance (©-2010 J. Dudley & R. Taylor, from [114]).

as shown in figure 1.16. Further details and literature about FWM applications can be found in refs. [1,3,114].

### 1.3.4 Limits of the FWM analysis

As discussed in the previous sub-sections, the FWM has been extensively studied. However, as far as the second type of the FWM process is concerned, the effects of HOD have not yet been considered in WDM soliton systems of SMFs using the ABCJS approach. In fact, since it has been shown that FWM creates new frequencies in the optical system, it is therefore a detrimental factor for communication applications such as WDM systems. It is necessary to investigate the dynamics of the generation of its components in order to operate their cancelation. In this point of view, WDM solitons systems near the ZDW have not yet been investigated. We present in the next sub-section our contribution assuming this missing investigation.

### 1.3.5 Objective of the work done on the FWM analysis in the WDM solitons system : motivations and contributions

The main purpose of the work done on the FWM analysis in the WDM solitons system in this thesis, deals with SMFs modeled by the NLSE including an additional TOD term through the ABCJS approach. We remind that the case of the NLSE with TOD is considered when the optical system has a vanishing GVD or uses high intensity peaks (short and ultrashort pulses) [1,3]. Analytical treatment of the model is based on the propagation of the ASC in the case of gain/loss. We compare the single TOD case with the combined GVD-TOD case (where a residual GVD is considered) and bring out the differences linked to the PMCs and the amplitude growth of the FWM components. The SCG being found to have the FWM as one of the numerous nonlinear effects that participate to its achievement, we present an overview in the next section of this phenomenon.

## 1.4 Overview on SCG

### 1.4.1 Theoretical and physical descriptions

The SCG phenomenon is a well-known nonlinear process today since it has been observed in bulk glasses for 200-THz light pulses [3,115]. The trend aroused has led on many works where the SCG has been extensively studied especially with the advent of the PCFs and tapered fibers (TFs) that overcame the limitations of the usual fibers because of their high malleable dispersive and nonlinear properties [1,3,13,28,115-147]. The possibility of designing the dispersive and nonlinear properties of these optical waveguides has made them as the best tools to realize the SCG process. To achieve the SCG, highly dispersive and nonlinear waveguides are required, it allows the injected optical pulses to excite these effects and therefore to undergo a large spectral broadening with the dramatic generation of side-components due to the transfer of energy from the central part of the spectrum to the pedestal part. Such extreme broadening can lead to a high temporal pulse compression as discussed by Gusakov et al [122], Schenkel et al [134]... . The combination of dispersive effects with a multitude of nonlinear effects such as SPM, XPM, FWM, stimulated Raman scattering (SRS) ..., leads to generation of new frequencies within the pulse spectrum so that it extends over a frequency range exceeding 100 THz. The properties of the optical waveguide in which a launched pulse is propagating in order to lead to the SCG phenomenon are very important. Sure enough, both the linear properties as the dispersion and the nonlinear properties as the CKN are necessary for the SCG efficient occurrence. We present basic descriptions of optical waveguides used for SCG.

### Highly nonlinear optical waveguides

A PCF is basically the best tool to create a good SCG process. It could be illustrated as shown in figure 1.17. The periodic nature of the air holes becomes important in the so-called *photonic bandgap*

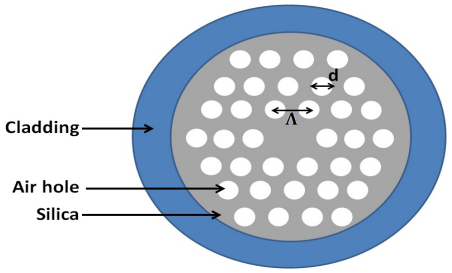


Figure 1.17: Diagram of a PCF or microstructured fiber. The parameters d and Λ represent the hole diameter and the pitch, respectively.

(PB) fibers in which the optical mode is confined to the core by periodic variations of the refractive index within the cladding. The core of such fibers often contains air to which light is confined by the PB [3]. This design allows to reach high values of nonlinearity when the air in the core is replaced with a suitable gas or liquid. Figure 1.18 shows some experimental PCFs.

The main nonlinear mechanism of the pulse splitting achievement leading to the SCG process is the

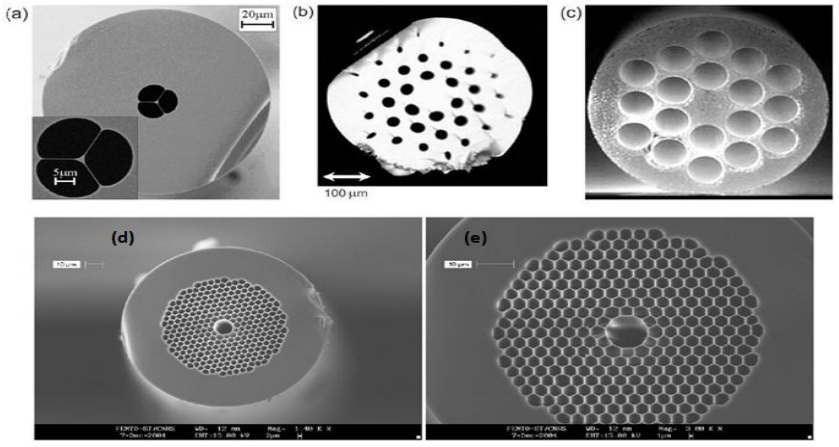


Figure 1.18: Some PCFs : Small core extruded PCF (©-2004 OSA, from Ebendorff-Heidepriem et al see [114,148]), (b) Single mode tellurite PCF with extremely large mode area (©-2008 OSA, from Feng et al see [114,149]), (c) Preform structure created by drilling (©-2004 IEEE, from Feng et al see [114,150]), (d) a Hollow core PCF fabricated by Blazephotonics, image realized in the FEMTO-ST institute of the university of Franche-Comté, France (©-2004 FEMTO-ST institute, from [151]), (e) zoomed picture of (d).

solitonic fission (SF) [114].

### The SF mechanism

The SCG occurs as a perturbation of HOS by HOD terms and high degree of nonlinearity of the medium. This implies that the SCG was firstly understood as a phenomenon which accompanies the solitons dynamics and so occurs in the anomalous dispersion regime of optical waveguide [137]. This HOS breaks into its fundamental components through the SF mechanism. Furthermore, the SF process appears at the start of HOS propagation in the medium, when the soliton spectrum extends.

The Raman scattering or HOD can perturb the constituent fundamental solitons of the main soliton signal, leading them to move with different group velocities, and therefore to split apart.
The SF process can be investigated, by considering the propagation characteristics of an ideal HOS as the 3-OS drawn in figure 1.9. In this case, the injected 3-OS evolves periodically as illustrated in this figure. In the femtosecond regime, HOD and Raman scattering are the two most significant effects that can perturb such ideal periodic evolution and induce pulse splitting through SF [137]. The dominant effect depends on the input pulse duration. The Raman effect dominates generally for input pulses exceeding 200 fs while for pulses of duration less than 20 fs, it is the HOD which dominates. So, for the two effects to operate in a balance manner in the SF process of the SCG, durations cover usually the intermediate range. The study of the SCG phenomenon through the SF mechanism has been extensively done this last decade [114,121,125-127,131,137,138,142,144]. Nearly, the whole aspects on SCG driven by SF were investigated in these works. Among these aspects, appear the emission and shedding of waves or radiations from the solitons which are themselves initially emitted from the SF mechanism. Figure 1.19 presents an illustration of the SF mechanism

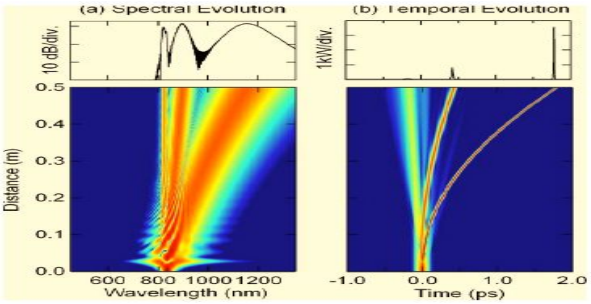


Figure 1.19: Illustration of the SF mechanism in the SCG phenomenon : results from numerical simulations showing (a) spectral and (b) temporal evolution for Raman induced fission of an incident 1.25 kW launched 3-OS. Top curves show the output profiles after 0.5 m propagation. (©-2006 APS, from [137]).

obtained by Dudley et al [137]. The SF mechanism in the temporal evolution of the 3-OS leads to a spectral broadening of the SCG. Some waves or radiations are emitted in both the time and the spectral domains. These features are briefly presented below.

### Nonsolitonic radiation (NSR) or Cherenkov radiation, dispersive waves (DWs)

The SCG phenomenon occurring in the SF mechanism is generally accompanied by the emission of waves such as the Raman solitons (RSs), and DWs... . The RSs are obviously the sub-pulses stemming from the Raman induced SF while the DWs are the light shedding from the initial soliton in the right side of the time domain picture (see figure 1.20). The radiation assembling the DWs, is emitted at a frequency at which its phase velocity matches that of the soliton. This radiation is known to be the Cherenkov radiation or a NSR similarly to those emitted by charged particles in a bulk medium [3]. These DWs are naturally due to the dispersive properties of the optical waveguide. So, SCG-Based optical waveguides with strong chromatic dispersion profile (CDP) lead to strong DWs which however occur with the satisfaction of a PMC as extensively discussed in [3,152-155] :

$$\sum_{k=2}^{\infty} \frac{\beta_k}{\left(k!|\beta_2|t_0^{k-3}\right)}\left(\omega_{DW}-\omega_S\right)=\frac{1}{2}(2N-1)^2, \tag{1.44}$$

where $\omega_{DW}$ and $\omega_S$ are the carrier frequencies associated with the DW and the soliton, respectively. Another solitonic feature known as the MI has been found to conduct to the SCG phenomenon beyond the SF mechanism.

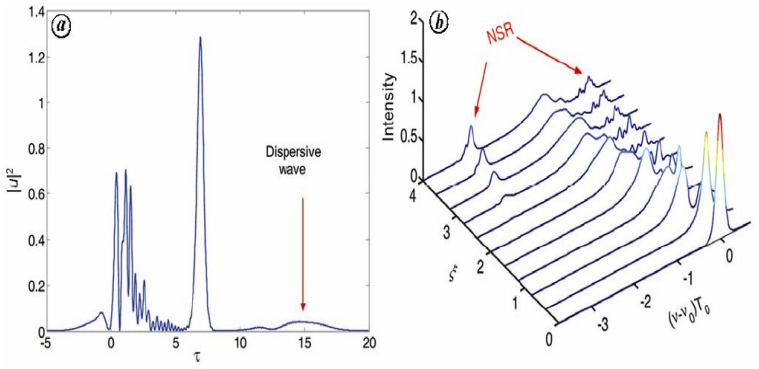


Figure 1.20: Illustration of the emission of DWs in a SCG process : (a) Low-amplitude pedestal in the form of DW, (b) NSR in spectral domain under two zero-dispersion conditions where FOD is dominant. (©-2011 CURRENT SCIENCE, from [155]).

### The MI mechanism

It is a well-known process today for the achievement of pulse trains generation (PTG). In nonlinear optics, it refers to the modulation of the steady state as a result of an interplay between the dispersive and the nonlinear effects. In other words, it is a destabilization mechanism for plane waves in an exponential manner. Since the earlier studies on the MI in 1960s [156-161], the investigation of the MI mechanism in various media and systems, has been reported and summarized in several papers and books [162-195]. Generally at a relatively low power, it leads to periodic PTG with a period of $2\pi/\Omega_{opt}$ where $\Omega_{opt}$ refers to the OFs of the MI process [3]. The OFs are given as a phase matching condition of the FWM related with the MI mechanism. It is described by two pump photons at the frequency $\omega_0$, one Stokes photon at $\omega_0 - \Omega$, and one anti-Stokes photon at $\omega_0 + \Omega$. In this view, it is often seen as a manifestation of a wider set of nonlinear processes described by the FWM [114,137,144]. Recently in 2009, Tiofack et al investigated the MI mechanism in a complex generalized Ginzburg-Landau system showing that the TOD does not intervene in the MI gain while the GVD and the FOD play an important role in this mechanism [189]. Furthermore in 2010, Dinda and Porsezian [190], studied the impact of the FOD on the MI spectra in a cubic nonlinear saturated media. Confirming the previous result of the independence to the TOD, and underlining the role played by the FOD parameter, they found that in saturated glass fibers having a negative sign of the GVD and a positive sign of the FOD, the two types of the MI mechanism are highly sensitive to the FOD magnitude. One year later, investigating a highly nonlinear system, Erkintalo et al [193] used the breather solution of Akhmediev and showed how a suitable low frequency modulation on a CW field induces higher-order MI splitting with the pulse characteristics at different phases of evolution related by a simple scaling relationship. Even the birefringent mono-core and two-core fibers have been investigated [168,169,179,191,192,194].

In the highly nonlinear media and in the high peak powers cases, the MI mechanism generally extents beyond the PTG process leading to the SCG phenomenon [114,135,137,138,142,144,145,196]. In this case, the MI brings out a multisoliton generation and a collision process whose added with the Raman-induced self-frequency shift (RIFS) cause the dramatic spectral broadening and the generation of a train of narrow high-intensity RSs. The condition in which wether the SF or the MI dominates in the SCG phenomenon was presented by Travers [144] :

$$\frac{T_0}{T_{MI}} = \frac{N}{\sqrt{2}\pi}, \tag{1.45}$$

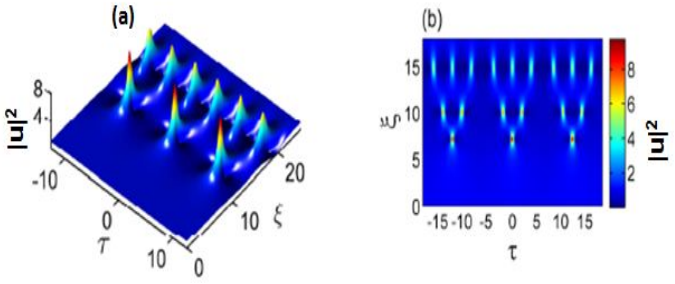


Figure 1.21: Evolution of a weakly modulated cw leading to higher-order MI (©-2011 APS, from [193]).

where $T_{MI} = 2\pi/\Delta\omega_{MI}$ is the MI period and $\omega_{MI} = (2\gamma P_0/|\beta_2|)^{1/2}$ is the modulation frequency [197]. The MI occurs if its period is sufficiently smaller than $T_0$. When the SF occurs, the MI does not exist. The cutoff for the SF mechanism has been found numerically by Genty et al [198] to be closer to $N \approx 15$. The MI FWHM is approximately $T_{MI}/5$ [114,199]. Fig. (1.22) presents a SCG

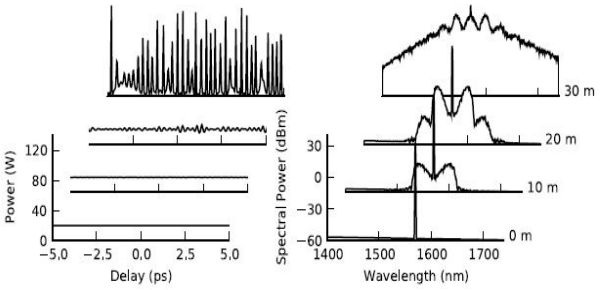


Figure 1.22: The SCG phenomenon from the development of MI using a 20 W pure CW pump laser (©-2010 J. Dudley & R. Taylor, from [114]).

picture obtained from the MI mechanism. It shows the dependence of this process on the length of the waveguide even in the MI case. The SCG spectrum becomes broad as the distance of propagation increases.

### 1.4.2 Improvement of the SCG phenomenon : spectral bandwidth enhancement

After the discovery of the SCG process, many works were conducted to improve its efficiency in nonlinear optics in two aspects : the enhancement of the spectral bandwidth obtained and the achievement of its flatness inducing a spectral coherence.

#### Based on the waveguide properties

The performing of the optical waveguide for the efficient achievement of the SCG phenomenon was the first approach developed [1,3,114,137,144]. The waveguides with a high degree of nonlinearity and strong CDP were investigated. The PCFs whose the possibility of designing the CDP and nonlinear properties has made them as the best tools to realize the SCG process. Designing characteristics of the PCFs as the effective core area, the ratio between the pitch and the hole diameter, the length ..., can properly enhance the nonlinearity and the ability of the waveguide to lead to ultra-large broadband

| Material | $SiO_2$ | Tellurite | Lead $SiO_2$ | $Bi_2O_3$ | $As_2S_3$ | $As_2Se_3$ | Si |
|---|---|---|---|---|---|---|---|
| $n_2$[1] ($\times 10^{-20}$ $m^2W^{-1}$) | 2.7[2] | 25[3] | 41[4] | 32 | $\sim 300$ | $\sim 1100$ | $500 \sim 600$ |
| $\gamma$[5] ($W^{-1}m^{-1}$) | 0.06 | 0.048 | 1.9 | 1.3 | 10 | 93.4 | $\sim 100$ |
| $\alpha$[6] ($dB/m$) | 0.001 | - | 0.3 | $2 \sim 3$ | 5 | 60 | 25 |
| TPA[7] | - | - | - | - | yes | yes | yes |

Table 1.1: Comparison of properties of some materials (©-2007 AP, from [3]; ©-2010 J. Dudley & R. Taylor, from [114]).

spectra of SCG [3]. On the other hand, materials with large values of nonlinearity were also studied in order to use them in the classical PCFs instead of the basic silica material. Today, some other materials that provide large values of CKN coefficient are known and used in the place of silica. In this category of materials one can quote heavy-metal-doped oxide glasses, semiconductors materials as the silicon material, semiconductor doped glasses, polydiactylene toluene sulfonate (PTS), chalcogenide glasses ($As_2S_3$, $As_2Se_3$), tellurite glasses, fibers based on bismuth oxide ... [3,114].
However, as seen in table 1.1 some of these materials introduce other effects as nonlinear saturation, higher-order nonlinear effects, nonlinear absorptions ... . It was therefore a challenge to manage the advantage taken on the high degree of nonlinearity against the deleterious ones raised simultaneously within the waveguide. In 2007 Yin and Agrawal studied the case of SOI-waveguides showing that they can be used to create SCG spectra extending over 400 nm by launching femtosecond pulses as HOSs through the SF mechanism [200]. The impact of absorption coefficients as the TPA and the FCA was highlighted. Furthermore, they showed that the TPA reduces the spectral bandwidth of the SCG without an effect on its flatness. The free carriers generated during the SCG process were found to have a negligible impact on the pulse. So, neither the SRS nor FCA plays a significant role during the SCG process in SOI waveguides. Therefore, these ones were considered as other suitable tools to generate efficient SCG as confirmed by Wen et al in 2011 [201e], Castelló-Lurbe et al in 2012 [202a], and Cao et al in 2015 [201g].
On the other hand, some kinds of PCFs that replace in the central core region rather a liquid were modeled [145,203-206]. The advantage to use a liquid material within the core region of the PCF consists to some special properties among which one could have large nonlinearity, ultra-flattened dispersion, broadband single-mode guidance, high birefringence, very small effective areas etc. Such PCFs are called LCPCFs.

### Based on the physical mechanisms

Another approach consists to improve the efficiency of the SCG phenomenon by using the features of the physical mechanisms on which it is based. For example, in 2002 Nikolov et al [130] demonstrated the improving of the SCG phenomenon through the degenerate FWM. Several other works followed this approach as discussed in [114,137,144].

### Based on the pulse characteristics

1. *the peak power or energy*
   Basically, the increase of the peak power enhances the Kerr effect [3,198]. So, it improves the SCG phenomenon. However, there is a serious difficulty to use laser sources with high powers in practice. On the other hand, they are expensive. Furthermore, the heating due to the use of such lasers damages the waveguide. Therefore, this approach is not the best one to improve

[0](1)Nonlinear refractive index, [2]determined at 1.06 $\mu m$, [3]determined at 1.06 $\mu m$, [4]determined a 1.05 $\mu m$, [5]CKN coefficient, [6]linear loss, [7]two-photon absorption

the efficiency of the SCG phenomenon. One should make the economy of energy. In this point of view, this approach is often avoided when possible. Other paths are explored in this case. The best method or approach to improve the SCG consists to do so without the need of high energies/powers ie an efficient achievement by reducing at the maximum the pulse energy.

2. *the pumping wavelength*
   There is a great challenge to find the suitable laser source that emit light in the proper wavelength region for the achievement of the SCG process. Since the SF mechanism drives the SCG phenomenon, the anomalous dispersion regime which is the fundamental field of the solitonic properties, is therefore more indicated for the obtaining of the broad spectra of SCG [137]. However, even the normal dispersion regime is suitable for the achievement of the SCG [207,208]. Making a proper choice of the pumping wavelength is therefore relevant to the achievement of the SCG. In the normal dispersion regime, the interaction between the SPM and the normal GVD dominates the dynamics in the SCG. Bringing the pumping wavelength closer to the ZDW of the waveguide CDP transfers the energy into the anomalous GVD regime. Figure 1.23

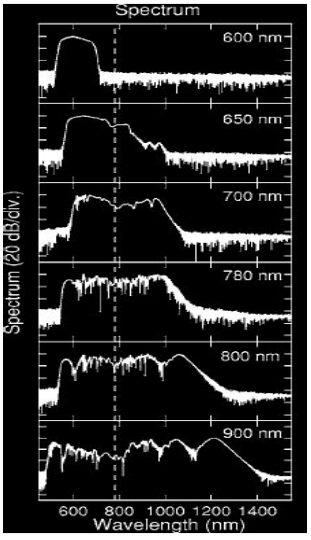


Figure 1.23: Choice of the pumping wavelength influencing the spectral bandwidth of the SCG. The dashed white line correspond to the ZDW of the waveguide. (©-2006 APS, from [137]).

   shows the influence of the pumping wavelength on the SCG spectrum.

3. *the pulse duration*
   As observed in figure 1.24, Dudley et al [137] showed the dependence of the SCG phenomenon to the pulse duration. Reducing the pulse duration also decreases the spectral bandwidth and distorts its spectrum.

4. *the pulse shape*
   Considering the pulse shaping approach in the improvement of the SCG spectra, the overwhelming majority of prior studies utilized intense optical pulses with symmetric and compact temporal profiles such as Gaussian or hyperbolic secant pulses. There have been several reports on the optimization of SCG via pulse shaping. However, the asymmetric profiles have also been investigated but more recently. Indeed, using the Airy pulses Ament et al [18], both experimentally and numerically, studied the quality of the SCG spectrum in terms of the interaction between the dominant peak and the oscillations tail through the soliton-dispersive-wave pairs

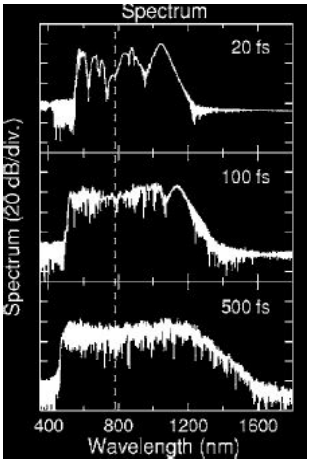


Figure 1.24: Influence of the SCG spectral bandwidth by the pulse width (©-2006 APS, from [137]).

features in a PCF. Moreover in 2012, Castelló-Lurbe et al [202a] suggested that the preshaping of the input pulse with the correct skewness (in terms of asymmetry) compensates the deleterious effect of the FCA which was assumed to highly affect the trailing edge of the propagating pulse in silicon waveguides. Then, the SCG phenomenon in terms of spectral broadening was enhanced cause of this operation. More recently in 2014, the influence of steepness of pump temporal pulse profile on spectral flatness and SCG coherence in all-solid PCFs with flattened normal dispersion has been studied by Klimczak et al [202b].

5. *the chirping process*
   Considering the pulse chirping process, it has been shown earlier that the positive chirp increases the spectral bandwidth of the SCG [137,201]. This effect is better than the one of the negative chirp as discussed in [201,209].

### Noise and coherence of SCG spectrum

The SCG spectra are accompanied by noise induced by the multitude physical processes that intervene [3]. The sensitivity to noise of SCG in both SMF and PCF has been reported by a number of authors [137]. In fact achieving broadband spectra is not the only necessity, there is also the coherence which is important. A spectrum which is enough incoherent, is not useful in practical situations ie a spectrum which is highly distorted by noise does not serve in applications. So, it is necessary to obtain broadband spectra but they should be also the most coherent as possible. One can appreciate the coherence of a SCG spectrum through the observation by considering its distortions or its flatness. Spectra which are more flattened, have a high probability to be more coherent than those which are highly distorted and less flattened. Rigorously, the spectral coherence of the SCG has been found by J. M. Dudley and S. Coen [129] to be measured through the modulus of the complex degree of first-order coherence which is defined at each wavelength in the SCG by :

$$\left|g_{12}^{(1)}(\lambda, t_1 - t_2)\right| = \left|\frac{\langle E_1^*(\lambda, t_1) E_2(\lambda, t_2)\rangle}{\langle |E_1(\lambda, t_1)|^2\rangle \langle |E_2(\lambda, t_2)|^2\rangle}\right|. \tag{1.46}$$

Here the angular brackets denote an ensemble average over independently generated pairs of SCG spectra $\left[E_1(\lambda, t), E_2(\lambda, t)\right]$ obtained from a large number of simulations, and t is the time measured at the scale of the temporal resolution of the spectrometer used to resolve these spectra [3,129,137].

### 1.4.3 Applications of the SCG

The SCG phenomenon provides light sources with broad spectral coverage. It also provides spatially coherent radiation and can provide ultrashort pulses with large compression factors. The SCG can lead to the spectral versatility of lamp based sources with the advantages of laser radiation, including higher brightness for improved signal-to-noise measurements and ultrashort pulse operation. Using the SCG allows to avoid the complexity and costs associated with tunable visible laser systems that typically involve mode-locked lasers with second harmonic generation (SHG) or optical parametric generation [114]. The SCG phenomenon has several applications in nonlinear optics and other fields using the light. These applications encompass domains like optical telecommunications, photonics, biophotonics ... . For example, the SCG output could be used in optical telecommunications as a multichannel telecommunications source (SCG-Based WDM sources) [1]. In a 2000 experiment, the supercontinuum-based WDM technique was used to produce 1000 channels with 12.5-GHz channel spacing [210]. SCG can also be useful in applications as nonlinear spectroscopy, optical coherence tomography, optical frequency metrology, biophotonic microscopy ... [1,114]. The figures 1.25 and 1.26 present some SCG-Based experiments in spectroscopy and in biophotonic microscopy, respectively [114]. In figure 1.26, the diagram presents a generalized schematic for multiphoton fluorescence

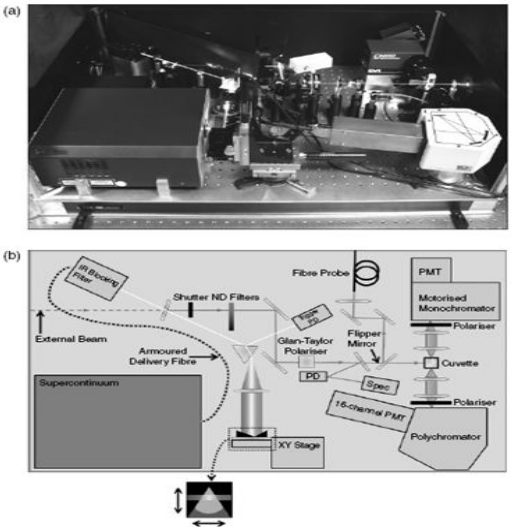


Figure 1.25: A SCG-Based experiment in spectroscopy : (a) Photograph and (b) experimental layout of a compact multidimensional spectrofluorometer based around a commercially available all-fibre SCG source (©-2010 J. Dudley & R. Taylor, from [114]).

microscopy with a SCG source, including an optional pulse compressor stage [114].

Further details and informations about the description of the presented experiments and other applications of SCG can be found in [1,114].

### 1.4.4 Limits of the previous works on the SCG analysis

Despite the great effort done these last decades in the study of the MI and the SCG phenomenon resulting on the several works, research papers, proceedings, and books, in the best of our knowledge, it still remained several paths both in the experimental and the theoretical aspects among which one can quote the following points :

- since the MI mechanism is a mean to reach to the SCG phenomenon, we have found necessary to highlight a query on its occurrence for chirped femtosecond pulses propagating in a medium

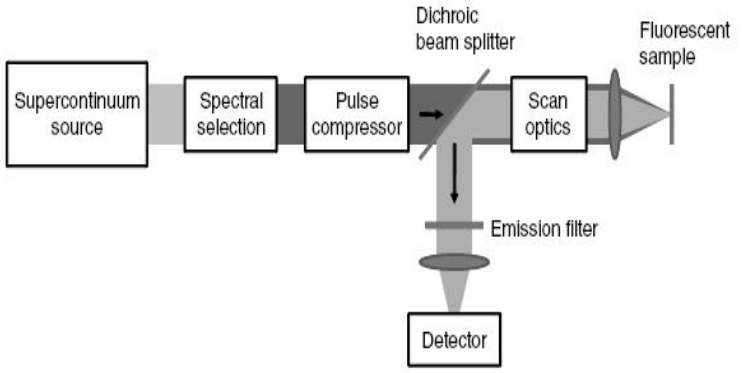


Figure 1.26: A SCG-Based experiment in biophotonic microscopy using a SCG source (©-2010 J. Dudley & R. Taylor, from [114]).

as silicon waveguides. Indeed, an investigation about the influence of the absorption coefficients present in this kind of medium was missing.

- Even the investigation of SCG phenomenon in an optical waveguide modeled by the higher-order nonlinear Schrödinger equation with non-Kerr terms using subnanojoule femtosecond pulses.
- The question of the propagation of chirped FEAPs in highly dispersive SMFs was still opened.
- Another study that was missing, concerned the SCG through femtosecond nJ-Airy pulses in the $CS_2$-LCPCFs under the influence of the initial chirp,
- A modeling that includes the TPA, the THG and the NFK effects was also found to be an interesting opened question considering the SCG analysis in SOI-waveguides.

It is worthy to notice that these paths belong to the theoretical aspect and are the only ones that have attracted our attention in the work presented in the thesis. And so, they are not exhaustive.

### 1.4.5 Objectives of SCG analysis : motivations and contributions

In the thesis, our contribution can be described as follows :

- concerning the MI analysis, we investigate the SOI-waveguides under FOD. In the PTG, we have chosen to investigate different input profiles for comparison. The effects of the input profile, chirp and absorption coefficients are highlighted.
- Then, we take an interest to the SCG phenomenon, using femtosecond pulses in the sub-nanoscale of energies through the generalized nonlinear Schrödinger equation that includes non-Kerr terms. We compare the effect of cooperative nonlinearities on the spectral bandwidth, with the one of the competing nonlinearities.
- We also analyze the role played by the pulse's shape asymmetry and the initial chirp on the propagation in highly dispersive SMFs. The A.I mechanism induced by the competition between the initial chirp and the GVD, pulse amplification and stabilization are examined.
- We study numerically the SCG in the $CS_2$-LCPCFs using femtosecond Airy and sech-type pulses in the nJ scale of energies.

- Finally, we analyze the SCG in SOI-waveguides that includes both the THG and the NFK terms.

In the next section, we describe briefly the optical waveguides that are modeled in the different systems studied in the thesis.

## 1.5 Description of the optical waveguides studied in the thesis

### 1.5.1 SMFs

These optical waveguides have been described extensively in several books and research papers. The glass waveguides are fabricated with pure silica, to get low-loss optical fibers [3]. Generally, one illustrates the optical fibers by a central glass core surrounded by a cladding layer whose refractive index $n_2$ is slightly smaller than that of the core $n_1$. The schematic illustration of the cross section and refractive index profile of a step-index fiber is given in figure 1.27. One distinguishes depending on the index profile step-index fibers and the graded-index fibers (see figure 1.28). Concerning the

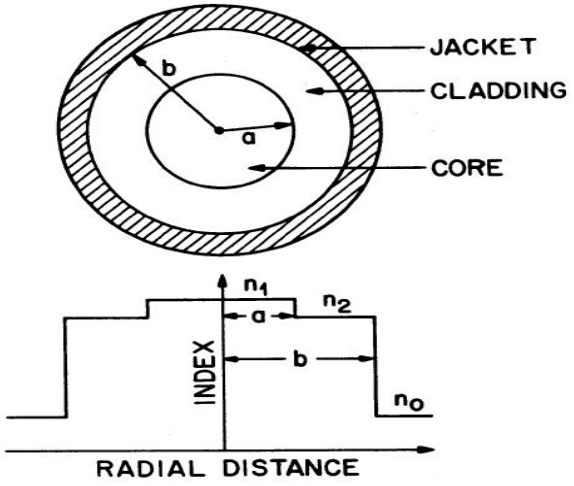


Figure 1.27: Schematic illustration of the cross section and the refractive-index profile of a step-index fiber. (©-2007 AP, from [3]).

number of modes available within a fiber, the relative core- cladding index difference $\Delta$ and the V parameter respectively given by the following relations :

$$\begin{aligned} \Delta =& \frac{n_1 - n_2}{n_2}, \\ V =& \frac{2\pi a}{\lambda_0}\sqrt{n_1^2 - n_2^2}, \end{aligned} \tag{1.47}$$

allow to distinguish the multimode fibers (large values of $a$ about 25 $\mu$m and V>2.405) to the single-mode fibers (small values of $a$ as those inferior to 5 $\mu$m with $\Delta \approx 0.003$ and V<2.405). Note that the parameter $\lambda_0$ is the wavelength of the input light. The commonly used fibers in long distances optical applications are the SMFs. In addition, the nonlinear effects are mostly studied in this last kind of fibers. Our study on the FWM mechanism is based on a SMF near the ZDW in WDM solitons system.

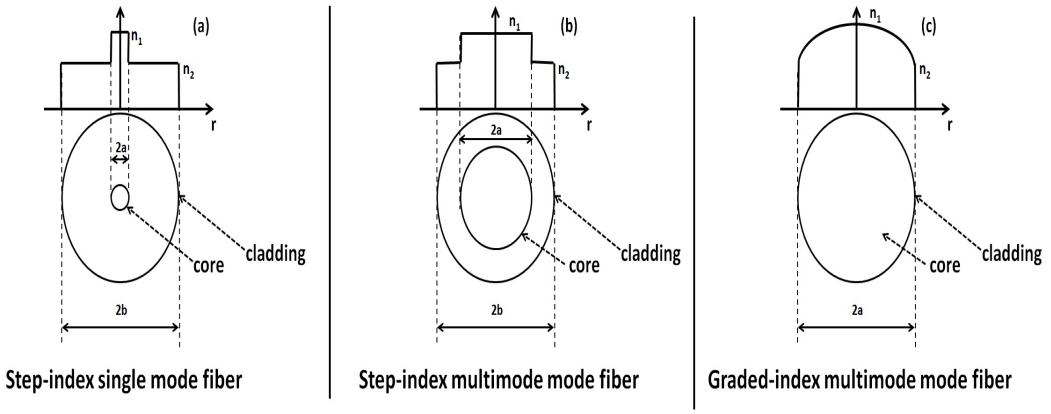


Figure 1.28: Diagram of different index profiles : (a) step-index single mode fiber, (b) step-index multimode fiber, (c) graded-index multimode fiber.

### 1.5.2 SOI-waveguides

Considering the SOI-waveguides, they are based on the silicon material which is one of the fundamental materials in the semiconductor industry. On the other hand, the interest aroused by the SOI-waveguides is due to the advantageous properties in the mid-infrared spectral region useful for the current photonics devices applications, even in the SCG process, and active opto-electronic components [7,8,200,201e,201g,202a,211-216]. The widely used SOI-waveguides may take the form of a channel waveguide, ridge waveguide, photonic-crystal waveguide, or slot waveguide, as shown in figure 1.29 [217]. The particularity of SOI-waveguides is the necessary inclusion of the absorption

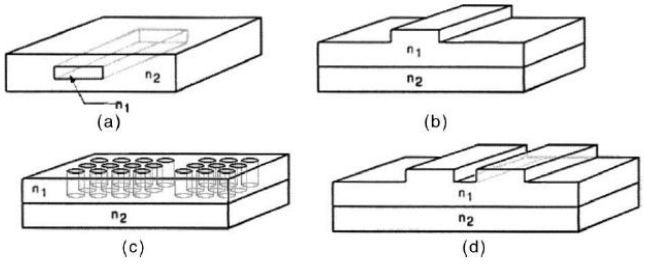


Figure 1.29: Four configurations for making waveguides in silicon: (a) Channel waveguides; (b) Rib waveguides; (c) Photonic-crystal waveguides; (d) Slot waveguides (©-2005 IEEE, from [217]).

coefficients as the TPA and the FCA in the study. They are known to have an important role in the analysis of pulse propagation within the SOI-waveguides.
The interest aroused by silicon-based (Si-based) optical devices also crosses the nanophotonics technologies and these achievements have opened up the possibility of signal performing in the field of signal processing functionalities at chip scale with relatively low optical power [202a]. The Si-based components in other hand, offer the benefits of low cost and low power consumption. Typically, a SOI-waveguide differs from a silica fiber in many aspects [200,218] : SOI-waveguides are generally smaller than silica fibers (they rarely exceed 5 cm in practice) and silicon is very nonlinear. It is about 200 times more than the silica as can be observed in table 1.1. SOI-waveguides have the property to confine light within an area so small that highly enhances the nonlinear effects. In addition, the SOI-waveguides because of the crystalline nature of silicon, have some nonlinear effects

as the stimulated-Raman-scattering which depends strongly on the waveguide geometry and mode polarization. The SOI-waveguide studied in this thesis is a rib-like waveguide. We study the pulse compression mechanism and the SCG phenomenon in the considered waveguide.

### 1.5.3 $CS_2$-LCPCFs

The PCFs in which the central core region is filled by a liquid instead of a solid (or the vacuum), are the so-called LCPCFs [145,203-206a]. The nonlinear properties of such fibers are enhanced compared with the solid/hollow core PCFs. The advantages are : a large nonlinearity, an ultra-flattened dispersion, a broadband single-mode guidance, a very small effective area etc [145,203-206a]. For instance, in the case where the liquid is the $CS_2$, one could normally obtain a nonlinearity which is one hundred (100) times larger than that of silica [145,206a,206b]. Such a LCPCF is called a $CS_2$-LCPCF [145]. We should note that, the use of the $CS_2$-LCPCF in this work just fills the need of a highly nonlinear medium without setting the problem of the practical manipulation of the $CS_2$'s liquid. Indeed, this latter is very delicate and dangerous to manipulate in practice [206c]. In addition, as noticed in [206d], the two-photon absorption (TPA) is a relevant limiting phenomenon that should be considered for the $CS_2$ material however only for the short-wavelength region $420-530$ nm. Thus for the experiment, another liquid could be chosen since the results are not directly linked to the $CS_2$ but only on the high nonlinearity of the medium. Figure 1.30(a) shows a sketch of the LCPCF's diagram. The fundamental propagation mode within the LCPCF is plotted in figure 1.30(b). This

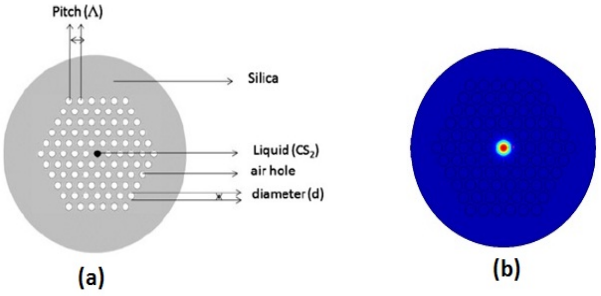


Figure 1.30: (a) Diagram of the LCPCF studied (©-2010 APS, from [145]), (b) Plot of the fundamental mode of polarization within the $CS_2-$LCPCF).

last figure shows that the considered $CS_2$-LCPCF has only one single axis of propagation. Thus, there is no birefringence in the fiber.

## 1.6 Conclusion

In summary we have presented in this chapter, a brief overview on the pulse compression mechanism through its physical descriptions, applications, limits in the theoretical analyses and the highlights of our contribution in this field of research. The FWM phenomenon has also been presented. Its basic physical description has been done, and some useful FWM-based applications were quoted. The deleterious aspect of the FWM in WDM systems was highlighted. The FWM analysis in this kind of communication systems done by Ablowitz et al in a mathematical approach that involves two launched pulses in soliton-like form was described as offering interesting paths of research among which HOD systems appear. Furthermore, a contribution in the case of TOD is presented later in the thesis. Considering the SCG phenomenon, we have done a brief presentation, highlighting its physical description and other features raised during its achievement. We have also presented the

paths of our contribution on the SCG analysis. The different waveguides studied in the thesis have been described. In the next chapter, we present the different methods used in our work.

# Chapter 2

# Analytical and numerical treatments of models

## 2.1 Introduction

This chapter presents the different methods used to obtain the results of the thesis. We start in section 2.2 by the modeling of our systems that are described in general through the NLSE. In this section, we derive the considered NLSE from the Maxwell's equations of electromagnetism. In section 2.3, the analytical treatments of the pulse compression phenomenon based on the MVA are showed while the section 2.4 concerns the FWM process. We describe in section 2.5 the MI linear analysis that allows to obtain the MI gain and PTG occurrence conditions. Section 2.6 deals with the SCG analysis while a conclusion is done in the last section of the chapter.

## 2.2 Propagation modeling : the NLSE

### 2.2.1 Modeling of the propagation in silica fibers

Beyond the experimental study, the theoretical one consists to model rather analytically this pulse propagation by a fundamental equation which simulates the dynamics within an optical waveguide. This fundamental equation well-known and widely used in different forms according to the study, is the NLSE. It has been earlier derived by Hasegawa and Tappert [38] for optical fibers, from the Maxwell's equations of electromagnetism [3] :

$$\nabla \cdot \mathbf{E} = 0, \tag{2.1a}$$

$$\nabla \times \mathbf{E} = -\frac{\partial \mathbf{B}}{\partial t}, \tag{2.1b}$$

$$\nabla \cdot \mathbf{B} = 0, \tag{2.1c}$$

$$\nabla \times \mathbf{B} = \frac{1}{c^2}\frac{\partial \mathbf{E}}{\partial t} + \mu_0 \frac{\partial \mathbf{P}}{\partial t}, \tag{2.1d}$$

where $\mathbf{E}$, $\mathbf{B}$, $\varepsilon_0$, $c$, $\mu_0$ and $\mathbf{P}$ are the electric field vector, the magnetic flux density vector, the vacuum electric permittivity, the speed of light in the vacuum, the vacuum magnetic permeability and the induced electric polarization, respectively. In this form, these equations belong to the specific case where one applies the following physical assumptions :

1. in a medium as the silica which constitutes essentially the optical fibers, there is no free charges, so the electric charge density $\rho_f$ and the current density vector $\mathbf{J}$ are equal to zero.

2. This medium is nonmagnetic, therefore the induced magnetic polarization $\mathbf{M}$ is null.

The medium of optical fibers allows to use the relation that relates $\mathbf{P}$ and $\mathbf{E}$ far from the resonances [3]. Combining Eq. (2.1b) and Eq. (2.1d) and eliminating $\mathbf{B}$ in favor of $\mathbf{E}$ and $\mathbf{P}$ we obtain

$$\nabla \times \nabla \times \mathbf{E} = -\frac{1}{c^2}\frac{\partial^2 \mathbf{E}}{\partial t^2} - \mu_0 \frac{\partial^2 \mathbf{P}}{\partial t^2}. \tag{2.2}$$

The relation between $\mathbf{P}$ and $\mathbf{E}$ is nonlinear as written below [1,3] :

$$\begin{aligned}\mathbf{P}(\mathbf{r},t) =& \varepsilon_0 \Bigg( \int_{-\infty}^{t} \chi^{(1)}(t-t') \cdot \mathbf{E}(\mathbf{r},t')dt' \\ &+ \int_{-\infty}^{t} dt_1 \int_{-\infty}^{t} dt_2 \cdot \chi^{(2)}(t-t_1, t-t_2) : \mathbf{E}(\mathbf{r},t_1)\mathbf{E}(\mathbf{r},t_2) \\ &+ \int_{-\infty}^{t} dt_1 \int_{-\infty}^{t} dt_2 \int_{-\infty}^{t} dt_3 \\ &\times \chi^{(3)}(t-t_1, t-t_2, t-t_3) \vdots \mathbf{E}(\mathbf{r},t_1)\mathbf{E}(\mathbf{r},t_2)\mathbf{E}(\mathbf{r},t_3) + ... \Bigg),\end{aligned} \tag{2.3}$$

where $\chi^{(k)}$ is the k-th order susceptibility. It is generally a tensor of rank k+1. The linear susceptibility $\chi^{(1)}$ representing the most important parameter of $\mathbf{P}(\mathbf{r},t)$, acts in the system through the refractive index $n$ and the attenuation coefficient $\alpha$ mentioned earlier. Since the silica of optical fibers is a symmetric molecule, the second-order susceptibility $\chi^{(2)}$ generally responsible for nonlinear effects as SHG and sum-frequency generation vanishes in this medium. The development of $\mathbf{P}$ should go further beyond the third-order susceptibility $\chi^{(3)}$ (presence of the suspension points in Eq. (2.3)) for highly nonlinear media, however for convenience to reach the cubic NLSE we should stop the development until order three. Reaching this order is necessary for analysis of short (picosecond domain) and ultra-short pulses (femtosecond and sub-femtosecond domains) propagation including the most nonlinear effects in optical fibers. The tensorial products '$\cdot$', ':' and ':' correspond to $\chi^{(1)}$, $\chi^{(2)}$ and $\chi^{(3)}$ related to the electric field components $\mathbf{E}(\mathbf{r},t')$, $\mathbf{E}(\mathbf{r},t_1)\mathbf{E}(\mathbf{r},t_2)$ and $\mathbf{E}(\mathbf{r},t_1)\mathbf{E}(\mathbf{r},t_2)\mathbf{E}(\mathbf{r},t_3)$, respectively. The medium response being assumed to be local, usually one should emit several hypotheses that permit to simplify the modeling :

1. the nonlinear part of $\mathbf{P}$ should be considered as a small perturbation,

2. in a scalar analysis of the pulse propagation, the polarization state should be maintained regular along the fiber length,

3. the light injected should be considered almost monochromatic : this assumption is satisfied for short and ultra-short pulses,

4. the envelope of the electromagnetic field should vary slowly approximately : it is the well-known and famous slowly varying envelope approximation (SVEA) [3].

Let us use the following form of the electrical field $\mathbf{E}(\mathbf{r},t)$ that models the dynamics into a glass fiber including all kinds of optical fibers :

$$\mathbf{E}(\mathbf{r},t) = \frac{1}{2}[E(\mathbf{r},t)\exp(-i\omega_0 t) + c.c]\hat{x}, \tag{2.4}$$

where $E(\mathbf{r},t)$, $\hat{x}$ and c.c represent the slowly varying function of time, the polarization unit vector and the complex conjugated part of $\mathbf{E}$. Similarly, one can also write the vector $\mathbf{P}$ :

$$\mathbf{P}(\mathbf{r},t) = \frac{1}{2}[P(\mathbf{r},t)\exp(-i\omega_0 t) + c.c]\hat{x} \tag{2.5}$$

Taking into account Eqs. (2.3), (2.4) and (2.5), this vector can be re-expressed explicitly by the susceptibility coefficients as follows :

$$\begin{aligned}\mathbf{P}(\mathbf{r},t) =& \varepsilon_0 \int_{-\infty}^{t} \chi_{xx}^{(1)}(t-t')E(\mathbf{r},t')\exp[-i\omega_0(t-t')]dt' \\ &+ \frac{3\varepsilon_0}{4}\chi_{xxxx}^{(3)}E(\mathbf{r},t)\int_{-\infty}^{t} R(t-t_1)E^*(\mathbf{r},t_1)E(\mathbf{r},t_1)dt_1,\end{aligned} \tag{2.6}$$

where the intensity-dependent nonlinear effects associated to third-order susceptibility have been included using [3,83]:

$$\chi^3(t-t_1,t-t_2,t-t_3) = \chi^3 R(t-t_1)\delta(t_1-t_2)\delta(t_1-t_3), \tag{2.7}$$

with $R(t)$ being the nonlinear Raman response function normalized to one because it must be zero when $t_1 > t$ with respect to the causality. The subscripts '$xx$' for $\chi^{(1)}$ and '$xxxx$' for $\chi^{(3)}$ in Eq. (2.6), represent the single polarization following the x-axis assuming that we focus only on the scalar case in which the modal birefringence (that includes the y-axis) has been neglected [3]. For pulse widths $>$ 1 ps, one should make some approximations on Eq. (2.6) that eliminate the delayed Raman response and consider the medium to have instantaneous nonlinear response. Therefore, we distinguish the two cases :

1. ***the local instantaneous medium***
   the relation (2.6) becomes :

$$\mathbf{P}(\mathbf{r},t) = \varepsilon_0\left(\chi_{xx}^{(1)} + \frac{3}{4}\chi_{xxxx}^{(3)}|E(\mathbf{r},t)|^2\right)\mathbf{E}(\mathbf{r},\mathbf{t}). \tag{2.8}$$

   Introducing Eq. (2.8) into Eq. (2.2) and taking the Fourier transform of the resulting equation leads to the following form well-known as the Helmholtz equation satisfied by the scalar field $\tilde{E}$ :

$$\nabla^2\tilde{E} + (\frac{\omega}{c})^2\big(1 + \tilde{\chi}_{xx}^{(1)}(\omega) + \frac{3}{4}\chi_{xxxx}^{3}F\big[|E(\mathbf{r},t)|^2\big]\big)\tilde{E} = 0, \tag{2.9}$$

   where $F[\ ]$ and $\tilde{E}$ are the Fourier transform operator and the Fourier transform of $E$ respectively. The operator $F[\ ]$ is defined as :

$$F[u(t)] = \tilde{u}(\omega) = \int_{-\infty}^{+\infty} u(t')\exp(i\omega t')dt'. \tag{2.10}$$

   If we set that $q(\omega) = 1 + \tilde{\chi}_{xx}^{(1)}(\omega) + (3/4)\chi_{xxxx}^{3}F\big[|E(\mathbf{r},t)|^2\big]$ and introduce two parameters $\tilde{n}$, $\tilde{\alpha}$ as $q(\omega) = (\tilde{n} + i\tilde{\alpha}c/2\omega)^2$, we normally arrive to the nonlinear-index coefficient $n_2$ and the TPA coefficient $\alpha_2$ as :

$$n_2 = \frac{3}{8n}Re(\chi_{xxxx}^{(3)}), \qquad \alpha_2 = \frac{3\omega_0}{4nc}Im(\chi_{xxxx}^{(3)}). \tag{2.11}$$

   To obtain Eq. (2.11), it is necessary to set that $\tilde{n} = n + n_2|E|^2$ and $\tilde{\alpha} = \alpha + \alpha_2|E|^2$. The coefficient $n$ is the linear index and $\alpha$ represents the linear loss parameter. Since $\chi_{xxxx}^{(3)}$ is

complex, its real and imaginary parts are represented respectively by $Re(\chi^{(3)}_{xxxx})$ and $Im(\chi^{(3)}_{xxxx})$. As $n_2$ and $\alpha_2$ link with $\chi^{(3)}_{xxxx}$, $n$ and $\alpha$ are found to link with $\chi^{(1)}_{xx}$ as following :

$$n = 1 + \frac{1}{2}Re(\tilde{\chi}^{(1)}_{xx}), \qquad \alpha = \frac{\omega}{nc}Im(\tilde{\chi}^{(1)}_{xx}). \tag{2.12}$$

Generally, $\alpha_2$ vanishes for silica that is why it is neglected in optical fibers. However, it is not the case for silicon waveguides and chalcogenide glasses (see table (1.1)). The Helmholtz equation above, can be satisfactorily solved by using the method of separation of variables in which we assume the solution of form :

$$\tilde{E}(\mathbf{r}, \omega - \omega_0) = F(x, y)\tilde{u}(z, \omega - \omega_0)\exp(i\beta_0 z), \tag{2.13}$$

where $\tilde{E}(\mathbf{r}, \omega - \omega_0)$, $F(x, y)$, $\tilde{u}(z, \omega - \omega_0)$, $\beta_0$ and $z$ are the Fourier transform of the optical field (of an envelope pulse whose frequency components $\omega$ are defined around a central one $\omega_0$), the transversal distribution function, the Fourier transform of the slowly varying amplitude function, the wave number, the axial variable which defines the propagation distance of the pulse within the waveguide.
Using Eq. (2.13) in Eq. (2.9) leads to the system :

$$\frac{\partial^2 F(x,y)}{\partial x^2} + \frac{\partial^2 F(x,y)}{\partial y^2} + \big[q(\omega)\frac{\omega_0^2}{c^2} - \tilde{\beta}^2(\omega)\big]F(x,y) = 0 \tag{2.14a}$$

$$2i\beta_0\frac{\partial \tilde{u}}{\partial z} + \big(\tilde{\beta}^2 - \beta_0^2\big)\tilde{u} = 0. \tag{2.14b}$$

The relation (2.14a) is the eigenvalue equation of the optical waveguide modes which involves the transversal distribution of the field $F(x, y)$. Solving this equation by using for example the first-order perturbation theory [219], leads to the definition of the modal field distribution [3]. For optical fibers, there are two kinds of modes : $EH_{mn}$ and $HE_{mn}$. These modes are similar to the transverse-electric (TE) and transverse-magnetic (TM) modes of planar waveguides such as SOI-waveguides for m=0. The case of SMFs is described by the fundamental mode in which m=1 and n=1. It allows to approximate the function $F(x, y)$ by a Gaussian distribution form as $\sim \exp\big[-(x^2+y^2)/w^2\big]$, where $w$ is the width parameter defined in ref. [3]. The normalized frequency $V$, given in Eq. (1.47) for SMFs stems from the solving of Eq. (2.14a). On the other hand, the dielectric constant $q(\omega)$ and the wave number $\tilde{\beta}$ could be nearly identified respectively by :

$$q(\omega) \sim n^2 + 2n\Delta n \tag{2.15}$$

and

$$\tilde{\beta}(\omega) \sim \beta(\omega) + \Delta\beta(\omega), \tag{2.16}$$

where the perturbations $\Delta n$ and $\Delta\beta(\omega)$ are themselves defined respectively as :

$$\Delta n = n_2|u|^2 + \frac{ic\tilde{\alpha}}{2\omega_0} \tag{2.17}$$

and

$$\Delta\beta(\omega) = \frac{\omega^2 n(\omega)}{c^2\beta(\omega)}\frac{\int\int_{-\infty}^{+\infty}\Delta n(\omega)|F(x,y)|^2 dxdy}{\int\int_{-\infty}^{+\infty}|F(x,y)|^2 dxdy}. \tag{2.18}$$

Let us approximate the term $\tilde{\beta}^2 - \beta_0^2$ of Eq. (2.14b) by $2\beta_0(\tilde{\beta} - \beta_0)$ and take the relation (2.16), we obtain the following modified form of Eq. (2.14b) :

$$i\frac{\partial \tilde{u}}{\partial z} + \big(\beta(\omega) - \beta_0 + \Delta\beta_0\big)\tilde{u} = 0, \tag{2.19}$$

with $\Delta\beta_0$ being an approximation of $\Delta\beta(\omega)$ as its first term in a Taylor series. It is described as follows :

$$\Delta\beta_0 \simeq \frac{\omega_0 n_2 \int\int_{-\infty}^{+\infty} |F(x,y)|^4 dxdy}{c\big(\int\int_{-\infty}^{+\infty} |F(x,y)|^2 dxdy\big)^2}|u|^2 + i\frac{\tilde{\alpha}}{2}. \tag{2.20}$$

It is observed in Eq. (2.20) the CKN $\gamma(\omega_0)$ and the effective mode area $A_{eff}$ parameters defined respectively as :

$$\gamma(\omega_0) = \frac{\omega_0 n_2}{cA_{eff}} \tag{2.21}$$

and

$$A_{eff} = \frac{\big(\int\int_{-\infty}^{+\infty} |F(x,y)|^2 dxdy\big)^2}{\int\int_{-\infty}^{+\infty} |F(x,y)|^4 dxdy}. \tag{2.22}$$

The interaction between the electromagnetic field and the bound electrons of a dielectric leads generally to dependence on the optical frequency $\omega$. This property refers to the chromatic dispersion which manifests through the frequency dependence of the refractive index $n(\omega)$. The CDP of an optical waveguide is usually approximated by expanding the mode-propagation constant $\beta(\omega)$ in a Taylor series around the pump frequency $\omega_0$ as :

$$\beta(\omega) = n(\omega)\frac{\omega}{c} = \beta_0 + \sum_{k=1}^{\infty} \frac{(\omega-\omega_0)^k}{k!}\beta_k, \tag{2.23}$$

where $\beta_k = \big(d^k\beta(\omega)/d\omega^k\big)_{\omega=\omega_0}$ is $k^{th}$ order of the CDP. Physically, the orders 1, 2, 3, 4 ... represent the group velocity, the GVD, the TOD, the FOD ... . Inserting Eqs. (2.20), (2.21), (2.22) and (2.23) in the reciprocal Fourier transform of Eq. (2.19) yields :

$$i\frac{\partial u}{\partial z} + \sum_{k=1}^{M} \frac{(i)^k\beta_k}{k!}\frac{\partial^k u}{\partial t^k} + \gamma(\omega_0)|u|^2 u + \frac{i\alpha}{2}u = 0, \tag{2.24}$$

where the term $\omega - \omega_0$ of Eq. (2.23) has been replaced in the time-domain by the differential operator $i(\partial/\partial t)$ [3]. The integer M ($\geq 2$) represents the last order reached in the CDP of the optical waveguide. Equation (2.24) is the so-called NLSE of a local instantaneous medium. The nonlinear term associated to $\gamma(\omega_0)$ corresponds to the SPM or Kerr effect. It is a manifestation of intensity dependence of the refractive index in the nonlinear optical waveguide and generally it is responsible to the spectral broadening of optical pulses. When more than one pulse is launched within the optical waveguide as done in WDM systems, the dynamic is described by coupled equations whose the number corresponds to the number of launched pulses. In this specific case, each sub-NLSE of the system is described by a similar version of Eq. (2.24) with additional terms linked to the coupling between the propagating waves. This nonlinear coupling through the CKN parameter is the so-called XPM effect. This phenomenon does not include an energy transfer between the interacting fields. Physically, XPM occurs because the effective refractive index seen by an optical pulse in a nonlinear optical waveguide depends not only on the intensity of this pulse but also on the intensity of other copropagating pulses.
Making the transformation of the well-known retarded frame of time $T$, assuming a reference frame moving with the pulse at $1/\beta_1$ as $T = t - \beta_1 z$, we obtain the following simplified form of Eq. (2.24) :

$$i\frac{\partial u}{\partial z} + \sum_{k=2}^{M} \frac{(i)^k\beta_k}{k!}\frac{\partial^k u}{\partial T^k} + \gamma(\omega_0)|u|^2 u + \frac{i\alpha}{2}u = 0. \tag{2.25}$$

2. ***The local non-instantaneous medium***

In this case, we use completely Eq. (2.6). It corresponds to the higher-order nonlinear systems since it includes the delayed response (stemming from the molecular vibrations : Raman effect) of the medium which must be added when ultra-short pulses are studied. Indeed in this specific case, the pulse spectra are wide ($> 0.1$ THz) and it leads the Raman gain to increase the intensity of the low-frequency components of the propagating optical field through an energy transfer from the high-frequency components of the same pulse : it is the description of the intra-pulse Raman scattering (IPRS) phenomenon. Considering Eq. (2.7) with Eq. (2.6) leads to a modified form of Eq. (2.9) [3,220] :

$$\begin{aligned}\nabla^2\tilde{E} + n^2(\omega)\frac{\omega_0^2}{c^2}\tilde{E} = -i\frac{\omega_0}{c} - \chi^3_{xxxx}\frac{\omega_0^2}{c^2}\int\int_{-\infty}^{+\infty}\tilde{R}(\omega_1-\omega_2) \\ \times\,\tilde{E}(\omega_1,z)\tilde{E}^*(\omega_2,z)\tilde{E}(\omega-\omega_1+\omega_2,z)d\omega_1\omega_2,\end{aligned} \tag{2.26}$$

where $\tilde{R}$ is the Fourier transform of $R(t)$. From Eq. (2.10) to Eq. (2.24), a similar process could be done in the actual case of Eq. (2.26). However a Taylor series expansion of $\gamma(\omega)$ as done for $\beta(\omega)$ in Eq. (2.23), should be included in the development (at least until to the first order of the expansion). The form of the obtained NLSE is well-known as the GNLSE [3,221] :

$$\begin{aligned}i\frac{\partial u}{\partial z} + \sum_{k=2}^{M}\frac{(i)^k\beta_k}{k!}\frac{\partial^k u}{\partial T^k} + \gamma\big(1+\frac{i}{\omega_0}\frac{\partial}{\partial T}\big)\left(u(z,T)\int_{-\infty}^{T}R(T-T')|u(z,T')|^2dT'\right) \\ + i\frac{\alpha}{2}u(z,T) = 0.\end{aligned} \tag{2.27}$$

The term with $\omega_0$ is associated to the self-steepening (SS) effect. The SS phenomenon stems from the intensity dependence of the group velocity and leads to an asymmetry in the SPM-broadened spectra of ultrashort pulses [3]. It creates an optical shock which is similar to the development of an acoustic shock on the leading edge of a sound wave [222]. The integral and the function R(t) correspond to the delayed Raman response (DRR) that includes the IPRS and the SRS. The scattering effects implicate that the optical fields transfer part of their energy to the nonlinear medium. In silica fibers and more generally, $R(t) = (1-f_R)\delta(t) + f_R h_R(t)$, where the first term governs the nearly instantaneous electronic response and $h_R(t)$ is the Raman response function [3,200]. The parameter $f_R$ represents the fractional contribution of the nuclei to the total nonlinear polarization. For silica fibers, it is found to be 0.18 while for silicon it is about 0.043 [200]. $h_R(t)$ is defined as [3,150-153] : $h_R(t) = (f_a + f_c)h_a(t) + f_b h_b(t)$ with $h_a(t) = (\tau_1^2+\tau_2^2)/(\tau_1\tau_2^2)\exp\big(-t/\tau_2\big)\sin\big(t/\tau_1\big)$ and $h_b(t) = (2\tau_3 - t)/(\tau_3^2)\exp\big(-t/\tau_3\big)$. The values of the coefficients are given as $f_a = 0.75$, $f_b = 0.21$, and $f_c = 0.04$ that quantify the relative contributions of the isotropic and the anisotropic parts of the Raman response. Considering the characteristic times $\tau_1$, $\tau_2$ and $\tau_3$, their values are generally taken as 12, 32, and 96 fs, respectively [152-155]. The Raman scattering includes optical phonons in the interaction between the propagating field and the nonlinear medium. In a quantum-mechanical view, the photon of the optical field is annihilated to create a photon at a lower frequency (the Stokes component), a photon at a longer frequency (the ASC) and a phonon allowing the conservation of the energy and the momentum. Beyond the energy transfer between the optical field and the medium, their impact depends on their nature. For instance talking about the IPRS, one observes a large temporal shift of the pulse position and a RIFS in the pulse spectrum toward the longer wavelengths [1,3]. On the other hand, the SRS exhibiting a threshold-like behavior, can transfer energy from one channel to the neighboring channels in a multichannel lightwave

system like multiplexing systems. So it is an issue for these systems while in other cases it can be useful. For example allowing the fabrication of broadband Raman amplifiers and tunable Raman lasers. On the other hand, for some fibers materials as chalcogenide or some liquid-core filled fibers the CKN coefficient exhibits a nonlinear saturation as $\gamma = \gamma_0/(1 + I|u|^2)$ with $I = 1/P_s$. The saturation power $P_s$ is the threshold power at which the CKN starts to saturate. An approximation of this CKN leads generally to the so-called cubic-quintic NLSE and then septic, neptic ... according to the degree of this approximation.

Both of these two cases (local instantaneous and non-instantaneous cases) are those which interest our study in the thesis. We do not investigate the nonlocal NLSE widely used in the case of spatial beams of planar waveguides or waveguides lattices [3]. In the next, according to the study whether for pulse compression or for SCG analyses, we use the modified forms of Eqs. (2.25) and (2.27).

### 2.2.2 Modeling of the propagation in a SOI-waveguide

Globally, the process/method is the same as done above for silica fibers. Nonetheless, there is difference in the nonlinear part of Eqs. (2.3), (2.6), (2.9), (2.11), (2.12), (2.25) and (2.27). The nonlinear refractive index of the silicon is higher than that of silica, that is why waveguides manufactured from silicon allow a tight confinement of optical pulses in the sub-microwavelength range using the technology of SOI [216]. Thus, we recall that the cubic Kerr nonlinearity is hundred times more important in SOI-waveguides than in standard silica SMFs. Subsequently, the Raman gain of SOI-waveguides is about one thousand times the one of standard SMFs. The nonlinear interaction in SOI-waveguides is therefore efficient under 5 cm-length. The silicon is a semiconductor material that includes the TPA, the FCD and free carriers as FCA. It belongs to anisotropic materials. Beyond 2.2 $\mu$m in wavelengths, there are no TPA, FCA or FCD [216]. As si-based materials exhibit a symmetry of inversion, the less important order of nonlinear effects corresponds to the third-order dielectric susceptibility $\chi^{(3)}$. In silicon the Fourier transform of the corresponding third-order polarization is given by [216]:

$$\tilde{P}_i^{(3)}(\omega_i) = \frac{3\epsilon_0}{32\pi^3} \int\int \chi_{ijkl}^{(3)}(-\omega_i, \omega_j, -\omega_k, \omega_l)\tilde{E}_j(\omega_j)\tilde{E}_k^*(\omega_k)\tilde{E}_l(\omega_l)d\omega_j d\omega_k,$$

where $\omega_l = \omega_i + \omega_k - \omega_j$.The parameter $\chi^{(3)}$ encompasses two major contributions : the electronic part $\chi_{ijkl}^e$ and the one associated to the optical phonons $\chi_{ijkl}^R$. This latter ($\chi_{ijkl}^R$) is the one that has been already discussed for silica fibers above in Eq. (2.7). The main discrepancy between the silica and silicon concerns $\chi_{ijkl}^e$ because of the semiconductor nature of the latter. The spectrum of Raman gain in silica is greater than that of silicon. Thus for silicon, the Raman scattering is more important at the first order than the Brillouin scattering which is associated to the acoustic phonons. In comparison, Brillouin scattering is negligible in silicon contrary to silica. $\chi_{ijkl}^e$ corresponds to the oscillations of bound electrons and is the part of $\chi^{(3)}$ that generates the free carriers and nonlinear absorptions as TPA, FCA and FCD when the energy of incident photon $E_p$ is higher than the half of bandgap energy $E_g$ :

$$E_p > \frac{E_g}{2}.$$

In silicon, for a wavelength as 1.1 $\mu$m, one has 1.2 $eV$ for $E_g$ [216]. When the condition above is satisfied, the bound electrons can be excited and thrown in the band of conduction through the TPA effect. For example it means that, two photons are absorbed by one bound electron whose energy is now higher than that of $E_g$ allowing its extraction from the atomic network and its free movement in the band of conduction. This kind of free charged particles moving in the band of conduction are the

so-called free carriers. That is why this process generates FCA and FCD. It is also assisted by optical phonons for the momentum conservation. Furthermore, It has been observed and demonstrated that both the Kerr and TPA effects are nearly simultaneous in silicon [216]. Let us focus now on the electronic part of $\chi^{(3)}$ [83,216] :

$$\chi^{e}_{ijkl} = \chi^{e}_{1122}\delta_{ij}\delta_{kl} + \chi^{e}_{1212}\delta_{ik}\delta_{jl} + \chi^{e}_{1221}\delta_{il}\delta_{kj} + \chi^{e}_{d}\delta_{ijkl},$$

with $\chi^{e}_{d}$ being the coefficient of the nonlinearity's anisotropy. Since $E_p < E_g$, one obtains $\chi^{e}_{1122} = \chi^{e}_{1221} = \chi^{e}_{1212}$. So :

$$\chi^{e}_{d} = \chi^{e}_{1111} - \chi^{e}_{1122} - \chi^{e}_{1221} - \chi^{e}_{1212} = \chi^{e}_{1111} - 3\chi^{e}_{1122}.$$

It yields :

$$\chi^{e}_{ijkl} = \chi^{e}_{1111}\left[\frac{\rho}{3}\big(\delta_{ij}\delta_{kl} + \delta_{ik}\delta_{jl} + \delta_{il}\delta_{kj}\big) + \big(1-\rho\big)\delta_{ijkl}\right],$$

where $\rho = 3\frac{\chi^{e}_{1122}}{\chi^{e}_{1111}} \approx 1.27$ for silicon. Therefore, the anisotropy of both the Kerr and the TPA effects is similar. The TPA generates free carriers (free electrons and holes) according to the incident light. This effect influences the nature of the propagating wave in the SOI-waveguides by modifying the refractive index in its nonlinear part. The carriers can be generated optically or electrically by the a diffusion mechanism through the rate equation :

$$\frac{\partial \bar{N}_{\nu}}{\partial t} = \bar{G} - \frac{\bar{N}_{\nu}}{\tau_0},$$

where $\bar{N}_{\nu}$, $\nu$, $\bar{G}$ and $\tau_0$ are the number of free carriers of nature $\nu$ per volume unit (free-carrier density), the nature of free carriers (free electrons or holes), a growth function (depending on the intensity of the incident light and on the effective area of the SOI-waveguide), and the effective carrier lifetime (including recombination, diffusion and drift) that depends on the geometry of the SOI-waveguide.

After the modeling done above for silicon waveguides, the coefficient of the cubic nonlinearity described in Eq. (2.21) should be rewritten as :

$$\gamma' = \gamma + i\Gamma,$$

with $\gamma$ being the Raman contribution defined in Eq. (2.21) and by $\chi^{R}_{ijkl}$ while $\Gamma$ is the electronic contribution generating the TPA and stemming from $\chi^{e}_{ijkl}$. Note that, the Raman scattering exists only for the T.E modes not for the T.M modes. The free-carrier dispersion is given by the product $\sigma\bar{N}_{\nu}$ in which $\sigma$ represents the FCA parameter. The linear absorption/losses in silicon are defined as :

$$\alpha' = \alpha + \alpha",$$

with $\alpha" = \sigma\bar{N}_{\nu}$ being the free-carrier dispersion. Taking into account $\gamma'$ and $\alpha'$ described above, one should only modify the corresponding terms in Eqs. (2.25) and (2.27) for the NLSE of SOI-waveguides.

## 2.3 The MVA that involves the RDF for the pulse compression analysis

As discussed in sub-section (1.2.5) of the first chapter, considering the theoretical aspect of the pulse compression analysis, the methods used consist to solve the dynamic equation of the optical

waveguide and so, to bring out the compression factor evolution across the length of the waveguide. In the numerical side, it is customary to use the SSF method or the finite-difference methods [3]. However, it is suitable sometimes to proceed rather through analytical or semi-analytical methods. In our studies on the pulse compression analysis, we have used the MVA that involves the RDF. We present this method in this section for the different systems studied.

### 2.3.1 In the case of linear compression of chirped femtosecond optical pulses under FOD

The linear equation describing the propagation of optical pulses in the case of FOD stems from the linear part of Eqs. (2.25) and (2.27) as follows [1,3,224,225]:

$$i\frac{\partial u}{\partial z}+\sum_{k=2}^{4}\frac{(i)^k\beta_k}{k!}\frac{\partial^k u}{\partial T^k}=0, \tag{2.28}$$

where the last order in the CDP profile, is the FOD. The TOD term is ignored in this study because it is well-known that it introduces a relatively small temporal shift of the pulse center which does not affect the purpose of our study as discussed in sub-section (1.2.2) [1,3,8,31]. The Lagrangian density function corresponding to Eq. (2.28) is taken as :

$$L_d=\frac{i}{2}(u^*\frac{\partial u}{\partial z}-u\frac{\partial u^*}{\partial z})-\sum_{k=2}^{4}\frac{(i)^k\beta_k}{k!}\frac{\partial^{k-1}u}{\partial T^{k-1}}\frac{\partial u^*}{\partial T}. \tag{2.29}$$

Since the case treated in this sub-section concerns the linear compression, the nonlinear part is therefore neglected. This does not allow to introduce the RDF. The case using the RDF is presented in the nonlinear case. Our study is conducted using the chirped Gaussian and RC profiles given respectively by [1,3,9,10,224] :

$$u(z,T)=u_p\exp\big(-\frac{1+iC_p}{2}(\frac{T}{T_p})^2+i\phi_p\big) \tag{2.30}$$

and

$$u(z,T)=\frac{u_p}{2}\big[1+\cos(\frac{\pi T}{T_p})\big]\exp\big(i\frac{C_p}{2}(\frac{T}{T_p})^2+i\phi_p\big) \tag{2.31}$$

where $u_p$, $T_p$, $C_p$ and $\phi_p$ are the amplitude, the width, the chirp and the phase, respectively. The MVA defines the Lagrangian function from its density described in Eq.(2.29) :

$$L=\int_{-\infty}^{+\infty}L_d(T')dT'. \tag{2.32}$$

The determination of the Lagrangian function for the chirped Gaussian pulse leads to :

$$L_G=-u_p^2\bigg[\frac{1}{2}(\frac{C_p}{T_p}\frac{dT_p}{dz}-\frac{1}{2}\frac{dC_p}{dz})+\frac{d\phi}{dz}\bigg]\sqrt{\pi}T_p+\frac{\sqrt{\pi}u_p^2(1+C_p^2)}{4T_p}\beta_2+\frac{\sqrt{\pi}u_p^2\beta_4}{32T_p^3}(1+C_p^2)^2, \tag{2.33}$$

and for the RC pulse we have :

$$\begin{aligned}L_{RC}=&-u_p^2T_p\bigg[a_1(\frac{1}{2}\frac{dC_p}{dz}-\frac{C_p}{T_p}\frac{dT_p}{dz})+a_2\frac{d\phi}{dz}\bigg]+\frac{u_p^2\beta_2}{2T_p}(\frac{\pi^2}{2}+a_1C_p^2)\\&-\frac{1}{24T_p^3}\big(-\frac{\pi^4}{2}+a_3C_p^2+a_4C^4\big)\beta_4u_p^2\end{aligned} \tag{2.34}$$

where $a_k$ with $k = \overline{1..4}$ are some constants defined as :

$$\begin{aligned} a_1 &= (-64 - 2\pi + 8\pi^2 + \pi^3)/8\pi^3 \\ a_2 &= (8 + 3\pi)/2\pi \\ a_3 &= -\frac{1}{4\pi}(-48 + 6\pi^2 + \pi^3) \\ a_4 &= -\frac{1}{160\pi^5}(15360 + 120\pi - 1920\pi^2 - 20\pi^3 + 40\pi^4 + 3\pi^5). \end{aligned} \tag{2.35}$$

Performing the Euler-Lagrange equation for relevant parameters of the Gaussian and the RC pulses as : The determination of the growth equations in the MVA may be done by setting :

$$\frac{\partial}{\partial T}(\frac{\partial L}{\partial q_z}) - \frac{\partial L}{\partial q} = 0, \tag{2.36}$$

where the parameter $q$ is a characteristic of pulse and $q_z$ its derivative following the parameter of propagation z. We obtain the dynamical equations respectively as :

$$\begin{aligned} \frac{du_p}{dz} &= -\frac{u_p}{2}\left\{\frac{C_p}{T_p^2}\left[\beta_2 + \frac{(1+C_p^2)}{4T_p^2}\beta_4\right]\right\} \\ \frac{dT_p}{dz} &= \frac{C_p}{T_p}\left[\beta_2 + \frac{(1+C_p^2)}{4T_p^2}\beta_4\right] \\ \frac{dC_p}{dz} &= \frac{(1+C_p^2)}{T_p^2}\left[\beta_2 + \frac{(1+C_p^2)}{4T_p^2}\beta_4\right] \\ \frac{d\phi_p}{dz} &= \frac{\beta_2}{2T_p^2} + \frac{(1+C_p^2)(3-C_p^2)}{32T_p^4}\beta_4, \end{aligned} \tag{2.37}$$

and

$$\begin{aligned} \frac{du_p}{dz} &= -\frac{u_p}{2}\left\{\frac{C_p}{T_p^2}\left[-\beta_2 + \frac{\beta_4}{12a_1T_p^2}(a_3 + 2a_4C^2)\right]\right. \\ \frac{dT_p}{dz} &= \frac{C_p}{T_p}\left[-\beta_2 + \frac{\beta_4}{12a_1T_p^2}(a_3 + 2a_4C_p^2)\right] \\ \frac{dC_p}{dz} &= \frac{1}{a_1T_p^2}\left[-\beta_2(\frac{\pi^2}{2} + C_p^2) + \frac{\beta_4}{6T_p^2}(-\frac{\pi^4}{4} + a_3C_p^2 + a_4C_p^4)\right] \\ \frac{d\phi_p}{dz} &= \frac{1}{2a_2T_p^2}\left[\pi^2\beta_2 + \frac{\beta_4}{12T_p^2}(\frac{4\pi^4}{3} - a_3C_p^3 + a_4C_p^4)\right]. \end{aligned} \tag{2.38}$$

We noted that in the absence of FOD, we obtained the previously well-known pulse characteristics in the case of single GVD. The phase is often disregarded because of its negligible role on pulse propagation characteristics.

### Assumption of the spectral width that does not change in a linear medium

It is assumed that for the Gaussian pulse, the quantity $(1+C_p^2)/T_p^2$ is assumed to be equivalent to the spectral width that is quasi-constant in the linear medium [3,224]. We make some simplifications on Eq. (2.37). In this case, this term is simply equal to its initial value $(1+C_0^2)/T_0^2$.
The same assumption applied on the RC pulse yields to set $((\pi^2/2)+C_p^2)/a_1T_p^2$ and $((-\pi^4/4)+a_3C_p^2+a_4C_p^4)/6a_1T_p^4$ as constants. We set the following parameters for the Gaussian pulse :

$$\begin{aligned}\Delta_0 &= \beta_2 + \frac{(1+C_0^2)}{4T_0^2}\beta_4 \\ \Delta &= \frac{(1+C_0^2)}{T_0^2}\Delta_0.\end{aligned} \tag{2.39}$$

We set also $\Delta_1$ and $\Delta_2$ for the RC pulse as :

$$\begin{aligned}\Delta_1 &= -\beta_2 + \frac{\beta_4}{12a_1T_0^2}(a_3+2a_4C_0^2) \\ \Delta_2 &= \frac{1}{a_1T_0^2}\Big[-\beta_2(\frac{\pi^2}{2}+C_0^2)+\frac{\beta_4}{6T_0^2}(-\frac{\pi^4}{4}+a_3C_0^2+a_4C_0^4)\Big],\end{aligned} \tag{2.40}$$

assuming that the parameters $C_0$ and $T_0$ are the initial values of the chirp $C_p$ and width $T_p$ respectively. We define $L_{FOD}=T_0^4/|\beta_4|$ as the FOD length. Then, we integrate the width and the chirp growth equations above for each pulse. The analytical approximated chirp expressions are given by :

$$\begin{aligned}C_G(z) &= C_0 + z\Delta \\ C_{RC}(z) &= C_0 + z\Delta_2.\end{aligned} \tag{2.41}$$

where the subscripts G and RC correspond to the Gaussian and RC input pulses respectively. For each corresponding dynamical equation of width, we obtained easily the analytical expressions of widths in function of the distance z :

$$\begin{aligned}T_G(z) &= T_0\left[1+2\frac{\Delta_0}{T_0^2}\big(C_0+\frac{\Delta}{2}z\big)z\right]^{\frac{1}{2}} \\ T_{RC}(z) &= T_0\left[1+2\frac{\Delta_1}{T_0^2}\big(C_0+\frac{\Delta_2}{2}z\big)z\right]^{\frac{1}{2}}\end{aligned} \tag{2.42}$$

The same process can be done with the amplitude and therefore leads to :

$$\begin{aligned}u_G(z) &= u_0\exp\left[-\frac{\Delta_0}{2T_0^2}\big(C_0+\frac{\Delta}{2}z\big)z\right] \\ u_{RC}(z) &= u_0\exp\left[-\frac{\Delta_1}{2T_0^2}\big(C_0+\frac{\Delta_2}{2}z\big)z\right],\end{aligned} \tag{2.43}$$

with $u_0$ being the initial value of the amplitude. For the Gaussian pulse, the conditions of compression are obtained for $\Delta < 0$ and $C_0 > 0$ as :

$$C_0 > 0,\ \beta_2, \beta_4 < 0 \tag{2.44a}$$

$$L_{FOD} > \frac{1+C_0^2}{4} L_{GVD},\ C_0 > 0,\ \beta_2 < 0, \beta_4 > 0 \tag{2.44b}$$

$$L_{FOD} < \frac{1+C_0^2}{4} L_{GVD},\ C_0 > 0,\ \beta_2 > 0, \beta_4 < 0, \tag{2.44c}$$

For the negative value of the initial chirp $C_0 < 0$, we have the opposite conditions :

$$C_0 < 0,\ \beta_2, \beta_4 > 0 \tag{2.45a}$$

$$L_{FOD} > \frac{1+C_0^2}{4} L_{GVD}, C_0 < 0,\ \beta_2 > 0, \beta_4 < 0 \tag{2.45b}$$

$$L_{FOD} < \frac{1+C_0^2}{4} L_{GVD}, C_0 < 0,\ \beta_2 < 0, \beta_4 > 0. \tag{2.45c}$$

The maximal pulse compression length for the Gaussian pulse is $L_{mc} = 2C_0/|\Delta|$. In the absence of FOD, Eqs. (2.44a), (2.44b), (2.45a) and (2.45b) are the well-known conditions for the linear pulse compression induced by chirp in the single GVD case requiring that $\beta_2 C_0 < 0$ [1,3]. Equations (2.44c) and (2.45c) may lead to pulse broadening in the absence of the FOD as previously known. Nevertheless, the FOD breaks this observation and we obtain a pulse compression when the additive conditions on dispersion lengths are verified. The obtained linear pulse compression when both the chirp and the GVD have the same sign or both the GVD and the FOD have the same sign, is the main feature observed, which is due to the presence of the FOD. This result encompasses the rules mentioned in [1,3,31]. In fact, they predicted a pulse broadening when $\beta_2\beta_4 > 0$ ($\beta_2, \beta_4 < 0$ or $\beta_2, \beta_4 > 0$ verified by Eq. (2.44a) and (2.45a)) and a linear compression when $\beta_2\beta_4 < 0$ (verified by Eqs. (2.44b), (2.44c), (2.45b) and (2.45c)). The results obtained in this work include the basic theory described in [1,3] and the rules set in [31]. This combination is possible with additional dispersion lengths conditions as seen in Eqs. (2.44b), (2.44c), (2.45b) and (2.45c). The study demonstrates that, it is possible to obtain a Gaussian pulse compression with the GVD having the same sign with the FOD, by adding a chirp of opposite value to the GVD and FOD. On the other hand, it is possible to compress a Gaussian pulse using an optical waveguide having a GVD which has the same sign with the chirp, in this case, one should require an opposite value of FOD.
For the RC pulse, one may notice that constants $a_3$ and $a_4$ are negative as $a_3 = -|a_3|$ and $a_4 = -|a_4|$ while $a_1$ is positive. Therefore, with $\Delta_1 < 0$ the compression conditions are given for initial positive chirp value by :

$$C_0 > 0,\ \beta_2,\ \beta_4 > 0 \tag{2.46a}$$

$$V_1' < L_{FOD} < V_2',\ \Delta_2 > 0,\ C_0 > 0\ or\ C_0 < 0,\ \beta_2 < 0, \beta_4 > 0 \tag{2.46b}$$

$$L_{FOD} < V_1',\ \Delta_2 < 0,\ C_0 > 0,\ \beta_2 < 0, \beta_4 > 0 \tag{2.46c}$$

$$L_{FOD} > V_2',\ \Delta_2 < 0,\ C_0 > 0,\ \beta_2 > 0, \beta_4 < 0 \tag{2.46d}$$

where

$$V_1' = \frac{(\frac{\pi^4}{4} + |a_3|C_0^2 + |a_4|C_0^4)}{6(\frac{\pi^2}{2} + C_0^2)} L_{GVD} \tag{2.47}$$

and

$$V_2' = \frac{(|a_3| + 2|a_4|C_0^2)}{12a_1} L_{GVD} \tag{2.48}$$

Similarly to the previous Gaussian case, for $\Delta_1 > 0$ we use the opposite relations of Eq. (2.46) and the maximal length for compression is always given by $2C_0/|\Delta_2|$. The feature previously mentioned above for the Gaussian pulse is also pointed out for the RC pulse as seen in Eqs. (2.46b), (2.46c) and (2.46d). A new condition given by (2.46a) shows that it is possible to get the RC pulse linear compression with the chirp, the GVD and the FOD all having the same sign. This condition contrasts with the previous rules known in refs. [1,3,26] and those mentioned in this work on Eqs. (2.44), (2.45), (2.46b), (2.46c) and (2.46d). It means that the linear compression conditions are greatly dependent on the input optical pulse profile.

**Description of the numerical simulations**

For the numerical simulations, we use directly the equations (2.41), (2.42) and (2.43). The MPCP for the Gaussian pulse is given by the relation $MPCP = 100\left\{1 - \left[1 - (\Delta_0/\Delta)\left((C_0/T_0)\right)^2\right]^{1/2}\right\}$ while for the RC pulse we have $MPCP = 100\left\{1 - 0.5\left[4 - (2\Delta_1/\Delta_2)\left((C_0/T_0)\right)^2\right]^{1/2}\right\}$. To obtain 3D propagation figures leading to the contour plots of the pulse compression mechanism, we use a MATLAB software code. In this code, we represent the amplitude evolution of the pulse assuming that, at each step of z (z=0..L), the chirp and the width vary respectively following Eqs. (2.41) and (2.42) under the derived conditions of Eqs. (2.44), (2.45) and (2.46).

### 2.3.2 In the case of nonlinear compression of chirped compact and symmetric femtosecond optical pulses in a SOI-waveguide under FOD

The propagation of optical pulses through a SOI-waveguide in the local instantaneous case, is governed by a modified form of Eq. (2.25) as described in subsection 2.2.2, including the effects of TPA and FCA as [7,8,202a,225]:

$$i\frac{\partial u}{\partial z} + \sum_{k=1}^{2} \frac{(-1)^k \beta_{2k}}{(2k)!} \frac{\partial^{(2k)} u}{\partial T^{(2k)}} + \gamma |u|^2 u = -i\frac{\alpha}{2}u - i\Gamma |u|^2 u - i\frac{\sigma}{2} N_C u, \tag{2.49}$$

where $\Gamma$, $\sigma$ and $N_C$ are the TPA coefficient, the FCA coefficient and the free-carrier density (FCD), respectively. Concerning the TPA, it was first reported experimentally by Kaiser and Garrett [226]. Multiphoton absorption phenomenon can lead to laser damage of optical materials and be used to write permanent refractive index structures into the interior of optical materials [1]. Therefore, the multiphoton absorption is well-known to be a nonlinear loss phenomenon that can reduce the efficiency of nonlinear optical devices such as optical switches. The TPA and FCA are linked to the FCD dynamics following the rate equation given below [7,8,215,216,218]:

$$\frac{\partial N_c(z,T)}{\partial T} = \frac{\beta_{TPA}}{2h\nu_0} \frac{|u(z,T)|^4}{a_{eff}^2} - \frac{N_c(z,T)}{\tau_c}, \tag{2.50}$$

with $\beta_{TPA} = 2\Gamma a_{eff}$ the usual TPA parameter. On the other hand, the quantities h, $\nu_0$ and $\tau_c$ represent the Planck constant, the pump frequency and the carrier lifetime, respectively. The effective carrier lifetime includes all the effects of recombination, diffusion, and drift [218]. The FCA effect is included through the coefficient $\sigma$ as :

$$\alpha_{FCA} = \sigma N_c. \tag{2.51}$$

For silicon, the coefficient $\sigma$ is equal to $1.45\times10^{-21} m^2$ [218,225]. The second term in the RHS of Eq. (2.50) is generally neglected in the case of ultra-short pulses as femtosecond pulses, since it is

well-known that carriers do not have enough time to recombine over the pulse width at this scale [8]. Our analysis is based on the chirped Gaussian, sech-type and the RC pulses. The Gaussian and the RC pulses being defined as shown in Eqs. (2.30) and (2.31), for the chirped sech-type pulse, we have [3,8,225] :

$$u = u_p sech(\frac{T}{T_p}) \exp\left(i\big[-\frac{C_p}{2}(\frac{T}{T_p})^2 + \phi_p\big]\right), \tag{2.52}$$

As discussed above, the lagrangian density and the RDF associated to Eq. (2.49) are respectively given as [7,8,225] :

$$L_d = \frac{i}{2}(u^*\frac{\partial u}{\partial z} - u\frac{\partial u^*}{\partial z}) - \sum_{k=1}^{2}\frac{(-1)^k\beta_{2k}}{(2k)!}\frac{\partial^{(2k-1)}u}{\partial T^{(2k-1)}}\frac{\partial u^*}{\partial T} + \frac{\gamma}{2}|u|^4 \tag{2.53}$$

and

$$R_d = i\left[|u|^2\Gamma + \frac{1}{2}\big(\alpha + \sigma N_c(t)\big)\right](u^*\frac{\partial u}{\partial z} - u\frac{\partial u^*}{\partial z}) \tag{2.54}$$

The determination of the Lagrangian function using Eq. (2.32) in this nonlinear case for the Gaussian pulse leads to :

$$\begin{aligned} L_G = &- u_p^2\left[\frac{1}{2}(\frac{C_p}{T_p}\frac{dT_p}{dz} - \frac{1}{2}\frac{dC_p}{dz}) + \frac{d\phi_p}{dz}\right]\sqrt{\pi}T_p + \frac{\sqrt{\pi}u_0^2(1+C_p^2)}{4T_p}\beta_2 + \frac{\sqrt{\pi}u_p^2\beta_4}{32T_p^3}(1+C_p^2)^2 \\ &+ \sqrt{\frac{\pi}{2}}\frac{\gamma u_p^4 T_p}{2}, \end{aligned} \tag{2.55}$$

for the sech-type pulse, we obtain the same form as in [8] with an additional term taking into account the FOD effect :

$$\begin{aligned} L_{sech} = &- u_p^2 T_p\left[\frac{\pi^2}{6}(\frac{C_p}{T_p}\frac{dT_p}{dz} - \frac{1}{2}\frac{dC_p}{dz}) + 2\frac{d\phi_p}{dz}\right] + \frac{\beta_2 u_p^2}{2T_p}(\frac{2}{3} + \frac{\pi^2}{6}C_p^2) + \frac{2}{3}\gamma u_p^4 T_p + \\ &\frac{1}{24T_p^3}(\frac{14}{15} + (\frac{\pi^2}{3} - 2)C_p^2 + \frac{19\pi^2}{33}C_p^4)\beta_4 u_p^2 \end{aligned} \tag{2.56}$$

and for the RC pulse we have :

$$\begin{aligned} L_{RC} = &- u_p^2 T_p\left[a_1(\frac{1}{2}\frac{dC_p}{dz} - \frac{C_p}{T_p}\frac{dT_p}{dz}) + a_2\frac{d\phi}{dz}\right] + \frac{u_p^2\beta_2}{2T_p}(\frac{\pi^2}{2} + a_1C_p^2) + a_5\gamma T_p u_p^4 \\ &- \frac{1}{24T_p^3}\big(-\frac{\pi^4}{2} + a_3C_p^2 + a_4C_p^4\big)\beta_4 u_p^2 \end{aligned} \tag{2.57}$$

where $a_k$ with $k = \overline{1..4}$ are the same constants defined as in Eq. (2.35) while the constant $a_5$

$$a_5 = \frac{5}{48\pi}(21\pi + 64). \tag{2.58}$$

The reduced form of the RDF can be derived from its density given in Eq. (2.54) as :

$$R = \int_{-\infty}^{+\infty} R_d(T')dT'. \tag{2.59}$$

For each pulse, it yields :

$$R_G = -\sqrt{\pi}u_p^2T_p\Bigg\{\Bigg[\frac{1}{2}(\frac{C_p}{T_p}\frac{dT_p}{dz}-\frac{1}{2}\frac{dC_p}{dz})+\frac{d\phi}{dz}\Bigg]\Bigg[\frac{u_0^2}{\sqrt{2}}\big(\Gamma+\frac{\sqrt{\pi}u_0^2\beta_{TPA}t_0}{4h\nu_0A_{eff}^2}\big)+\alpha\Bigg]+\frac{\sqrt{2}}{2}u_0^2\frac{\partial\phi}{\partial z}\Gamma\Bigg\}, \quad (2.60)$$

$$\begin{aligned}R_{sech} = -2u_p^2T_p\Bigg\{&\frac{4}{3}u_p^2\Gamma\Bigg[\frac{1}{2}(\frac{C}{T_p}\frac{dT_p}{dz}-\frac{1}{2}\frac{dC_p}{dz})(\frac{\pi^2}{6}-1)+\frac{d\phi}{dz}\Bigg]+\big(\alpha+\frac{1}{3}\sigma\frac{\beta_{TPA}u_p^4T_p}{h\nu_0A_{eff}^2}\big)\times\\&\Bigg[\frac{\pi^2}{12}(\frac{C_p}{T_p}\frac{dT_p}{\partial z}-\frac{1}{2}\frac{dC_p}{dz})+\frac{d\phi}{dz}\Bigg]\Bigg\}\end{aligned} \quad (2.61)$$

and

$$\begin{aligned}R_{RC} = -u_p^2T_p\Bigg\{&(\frac{1}{2}\frac{dC_p}{dz}-\frac{C_p}{T_p}\frac{dT_p}{dz})\big[b_1u_p^2\Gamma+a_1\alpha\big]+\frac{d\phi}{dz}\big[b_2u_p^2\Gamma+a_2\alpha\big]+\\&\frac{u_p^4\beta_{TPA}T_p}{1536\pi h\nu_0A_{eff}^2}\sigma\Bigg[b_3(-\frac{C}{T_p}\frac{dT_p}{dz}+\frac{1}{2}\frac{dC_p}{dz})+b_4\frac{d\phi_p}{dz}\Bigg]\Bigg\}\end{aligned} \quad (2.62)$$

where $b_k,\ k=\overline{1..4}$ are defined as :

$$\begin{aligned}b_1&=\frac{1}{\pi^3}(-\frac{1504}{27}-\frac{111\pi}{32}+\frac{20\pi^2}{3}+\frac{35\pi^3}{48})\\b_2&=\frac{80}{3}+\frac{35\pi}{4}\\b_3&=\frac{5}{8\pi^3}(-4096-1472\pi+470\pi^2+232\pi^3+21\pi^4)\\b_4&=\frac{5}{2\pi}(512+360\pi+63\pi^2).\end{aligned} \quad (2.63)$$

Using the modified form of the Euler-Lagrange equation (2.36) for relevant parameters of the pulses as :

$$\frac{\partial}{\partial T}(\frac{\partial L}{\partial q_z})-\frac{\partial L}{\partial q}+\frac{\partial R}{\partial q_z}=0. \quad (2.64)$$

Therefore, inserting Eqs. (2.60), (2.61) and (2.62) in Eq. (2.64), we determine the growth equations for each pulse :

1. Gaussian pulse :

$$\begin{aligned}
\frac{du_p}{dz} =& -\frac{u_p}{2}\left\{\frac{C_p}{T_p^2}\left[\beta_2+\frac{(1+C_p^2)}{4T_p^2}\beta_4\right]+\frac{u_p^2}{\sqrt{2}}\big(\frac{5}{2}\Gamma+\sigma\frac{\sqrt{\pi}}{4}\frac{u_p^2\beta_{TPA}}{h\nu_0 A_{eff}^2}T_p\big)+\alpha\right\},\\
\frac{dT_p}{dz} =& \frac{C_p}{T_p}\left[\beta_2+\frac{(1+C_p^2)}{4T_p^2}\beta_4\right]+\frac{\sqrt{2}}{4}u_p^2T_p\Gamma,\\
\frac{dC_z}{dz} =& \frac{(1+C_p^2)}{T_p^2}\left[\beta_2+\frac{(1+C_p^2)}{4T_p^2}\beta_4\right]+\frac{u_p^2}{\sqrt{2}}\big(\gamma+\Gamma C_p\big),\\
\frac{d\phi_p}{dz} =& \frac{\beta_2}{2T_p^2}+\frac{(1+C_p^2)(3-C_p^2)}{32T_p^4}\beta_4+\frac{5u_p^2}{4\sqrt{2}}\gamma.
\end{aligned} \tag{2.65}$$

2. Sech-type pulse :

$$\begin{aligned}
\frac{du_p}{dz} =& -\frac{u_p}{2}\left\{\frac{C_p}{T_p^2}\left[\beta_2+(\frac{1}{6}-\frac{1}{\pi^2}+\frac{19}{33}C_p^2)\frac{\beta_4}{T_p^2}\right]+4u_p^2\Gamma(\frac{1}{3}+\frac{1}{\pi^2})+\alpha+\frac{2}{3}\sigma\frac{u_p^4\beta_{TPA}T_p}{h\nu_0A_{eff}^2}\right\},\\
\frac{dT_p}{dz} =& \frac{C_p}{T_p}\left[\beta_2+(\frac{1}{6}-\frac{1}{\pi^2}+\frac{19}{33}C_p^2)\frac{\beta_4}{T_p^2}\right]+\frac{4u_p^2T_p}{\pi^2}\Gamma\\
\frac{dC_p}{dz} =& \frac{1}{T_p^2}\left[\beta_2(\frac{4}{\pi^2}+C_p^2)+\big(\frac{14}{15\pi^2}+(\frac{1}{3}-\frac{2}{\pi^2})C_p^2+\frac{19}{33}C_p^4\big)\frac{\beta_4}{T_p^2}\right]+\frac{4u_p^2}{\pi^2}(\gamma+2\Gamma C_p)\\
\frac{d\phi_p}{dz} =& \frac{1}{T_p^2}\left[\frac{\beta_2}{3}+\frac{\beta_4}{24T_p^2}\big(\frac{7}{5}+(\frac{\pi^2}{6}-1)C_p^2-\frac{19\pi^2}{66}C_p^4\big)\right]+\frac{5u_p^2}{6}\gamma.
\end{aligned} \tag{2.66}$$

3. RC pulse :

$$\frac{du_p}{dz} = -\frac{u_p}{2}\left\{\frac{C_p}{T_p^2}\left[-\beta_2+\frac{\beta_4}{12a_1T_p^2}(a_3+2a_4C_p^2)\right]+\frac{u_p^2}{2}\big(\Gamma A+\sigma\frac{u_p^2\beta_{TPA}}{h\nu_0A_{eff}^2}T_pB\big)+\alpha\right\}$$

$$\frac{dT_p}{dz} = \frac{C_p}{T_p}\left[-\beta_2+\frac{\beta_4}{12a_1T_p^2}(a_3+2a_4C_p^2)\right]+\frac{T_pu_p^2}{2}\left[\Gamma A'+\sigma\frac{\beta_{TPA}u_p^2T_p}{h\nu_0A_{eff}^2}B'\right]$$

$$\begin{aligned}\frac{dC_p}{dz} =& \frac{1}{a_1T_p^2}\left[-\beta_2(\frac{\pi^2}{2}+C_p^2)+\frac{\beta_4}{6T_p^2}(-\frac{\pi^4}{4}+a_3C_p^2+a_4C_p^4)\right]-\frac{a_5}{a_1}\gamma u_p^2\\ &+\frac{u_p^2C_p}{2}(\Gamma A'+\sigma\frac{\beta_{TPA}u_p^2T_p}{h\nu_0A_{eff}^2}B')\end{aligned} \tag{2.67}$$

$$\begin{aligned}\frac{d\phi_p}{dz} =& \frac{1}{2a_2T_p^2}\left[\pi^2\beta_2+\frac{\beta_4}{12T_p^2}(\frac{4\pi^4}{3}-a_3C_p^3+a_4C_p^4)\right]+\frac{5u_p^2}{2}\frac{a_5}{a_2}\gamma\\ &+\frac{3}{4}u_p^2(C_p\Gamma A"+\sigma\frac{\beta_{TPA}u_p^2T_p}{h\nu_0A_{eff}^2}B")\end{aligned}$$

where $A=(3b_2/a_2)-(b_1/a_1)$, $B=((3b_4/a_2)-(b_3/a_1))/1536\pi$, $A'=(b_2/a_2)-(b_1/a_1)$, $B'=((b_4/a_2)-(b_3/a_1))/1536\pi$, $A"=(b_2a_1-b_1a_2)/a_2^2$ and $B"=(b_4a_1-b_3a_2)/1536\pi a_2^2$. In the nonlinear case, there is no physical assumption about the spectral width of the pulses as discussed in the linear case in the previous sub-section.

**Description of the numerical simulations**

We take Eqs.(2.65)-(2.67), to obtain the pulse characteristics. We integrate these growth equations by using the fourth-order Runge-Kutta integration scheme. Once the integration is done at each step of the parameter z, the numerical value obtained for each characteristic is injected in the pulse evolution to model so, its 3D propagation yielding contour plots.

### 2.3.3 In the case of nonlinear compression of chirped self-healing Airy pulses (SHAPs) in a SOI-waveguide under FOD

In this sub-section, we apply the MVA on the asymmetric pulse previously presented in the first chapter of the thesis. The medium is assumed to be the same as the nonlinear one presented in the previous sub-section (2.2.2). The chirped input Airy profile can be taken as :

$$u = u_pAi(\frac{T}{T_p})\exp(a\frac{T}{T_p})\exp\big(-i\frac{C_p}{2}(\frac{T}{T_p})^2+i\phi_p\big), \tag{2.68}$$

The determination of the Lagrangian function leads to [227] :

$$\begin{aligned}L =& -u_p^2T_p\left[55.4573(\frac{C_p}{T_p}\frac{\partial T_p}{\partial z}-0.5\frac{\partial C_p}{\partial z})+\frac{9}{11}\frac{\partial\phi_p}{\partial z}\right]+\frac{u_p^2\beta_2}{2T_p}(\frac{52\pi}{31}+55.4573C_p^2)\\ &+\frac{u_p^2\beta_4}{24T_p^3}\big(78.1397+10034C_p^2+51918C_p^4\big)+\frac{3}{28}\gamma u_p^4T_p,\end{aligned} \tag{2.69}$$

The reduced form of the RDF function is obtained with an appropriate approximation of the FCD which is evaluated numerically for the truncated Airy pulse and inserted in the following relation :

$$\begin{aligned} R =& u_p^2 T_p \Big[ \big(\frac{C_p}{T_p}\frac{dT_p}{dz} - 0.5\frac{dC_p}{dz}\big)\big[u_p^2\big(\frac{12}{35}\Gamma - \frac{3u_p^2 t_p}{236}\kappa\big) - 55.4573\alpha\big] - \frac{d\phi_p}{dz}\big[u_p^2\big(\frac{3}{14}\Gamma \\ &+ \frac{\pi u_p^2 T_p}{122}\kappa\big) + \frac{9}{11}\alpha\big]\Big] \end{aligned} \tag{2.70}$$

where $\kappa = \sigma\beta_{TPA}/h\nu_0 A_{eff}^2$ is a constant related with the FCD and the FCA. Therefore, we determine the growth equations as follows :

$$\begin{aligned} \frac{du_p}{dz} =& -\frac{u_p}{2}\Big\{\frac{C_p}{T_p^2}\Big[\beta_2 + \frac{(45.233 + 468.1C_p^2)}{3T_p^2}\beta_4\Big] + 2u_p^2\big(\frac{1}{5}\Gamma + \frac{2u_p^2 T_p}{85}\kappa\big) + \alpha\Big\} \\ \frac{dT_p}{dz} =& \frac{C_p}{T_p}\Big[\beta_2 + \frac{(45.233 + 468.1C_p^2)}{3T_p^2}\beta_4\Big] + u_p^2 T_p\big(ln(\frac{8}{7})\Gamma + \frac{u_p^2 T_p}{64}\kappa\big) \\ \frac{dC_p}{dz} =& \frac{1}{T_p^2}\Big[\beta_2\big(\frac{\pi}{\exp(\frac{7}{2})} + C_p^2\big) + \big(\frac{31}{22} + 180.932C_p^2 + 936.2C_p^4\big)\frac{\beta_4}{6T_p^2}\Big] + u_p^2\big(\frac{1}{500}\gamma \\ &+ C_p\big(\frac{3}{11}\Gamma + \frac{u_p^2 T_p}{32}\kappa\big)\big) \\ \frac{d\phi_p}{dz} =& \frac{1}{T_p^2}\big[\frac{572\pi}{279}\beta_2 - \big(1010.04 + 9043.14C_p^2 - \frac{95183}{12}C_p^4\big)\frac{\beta_4}{T_p^2}\big] + u_p^2\big(\frac{55}{168}\gamma \\ &+ C_p\big(\frac{22}{105}\Gamma - \frac{11u_p^2 T_p}{1416}\kappa\big)\big). \end{aligned} \tag{2.71}$$

As it can be seen in Eq. (2.71) beyond the dispersive effects, all the characteristics of the Airy pulse are affected by both the TPA and the FCA.

### Linear compression of SHAPs induced by FOD

In this section all the nonlinear effects parameters are taken equal to zero : $\gamma = 0$, $\Gamma = 0$, $\sigma = 0$ and $\kappa = 0$. For this specific case, we use the assumption of a spectral width which does not change in the linear medium as discussed in sub-section (2.3.1). So, the terms $(45.233 + 468.1C_p^2)/3T_p^2$, $\pi\exp(-7/2) + C_p^2$ and $(31/22) + 180.932C_p^2 + 936.2C_p^4$ are constant and equal to their initial values, so that we get a linearly varying chirp for the pulse. The analytical approximated relation of the pulse width is given by :

$$T_p(z) = T_0\Big[1 + 2\frac{\Delta_1}{T_0^2}\big(C_0 + \frac{\Delta_0}{2}z\big)z\Big]^{1/2}, \tag{2.72}$$

We define the parameters $\Delta_0$ and $\Delta_1$ respectively as follows :

$$\begin{aligned}\Delta_0 =&\frac{s_2(\pi\exp(-7/2)+C_0^2)}{L_{GVD}}+\frac{s_4\big(\frac{31}{22}+180.932C_0^2+936.2C_0^4\big)}{6L_{FOD}}\\ \Delta_1 =&T_0^2\bigg[\frac{s_2}{L_{GVD}}+\frac{(45.233+468.1C_0^2)s_4}{3L_{FOD}}\bigg],\end{aligned} \tag{2.73}$$

where $s_2$ and $s_4$ are the signs of the GVD and the FOD respectively. It comes that the linear compression conditions are obtained easily by setting that the compression factor may be inferior to 1. This implies that (Note that whatever the conditions $z>0$, $L_{GVD}>0$ and $L_{FOD}>0$):

$$-0.5<\bigg[\frac{s_2}{L_{GVD}}+\frac{(45.233+468.1C_0^2)s_4}{3L_{FOD}}\bigg]\big(C_0+\frac{\Delta_0}{2}z\big)z<0. \tag{2.74}$$

So, for the compression of the SHAP to occur inside the medium under the conditions specified earlier, one must have :

$$\begin{aligned}&\frac{s_2}{L_{GVD}}+\frac{(45.233+468.1C_0^2)s_4}{3L_{FOD}}<0 \;\; and \;\; \big(C_0+\frac{\Delta_0}{2}z\big)>0\\ &\frac{s_2}{L_{GVD}}+\frac{(45.233+468.1C_0^2)s_4}{3L_{FOD}}>0 \;\; and \;\; \big(C_0+\frac{\Delta_0}{2}z\big)<0\end{aligned} \tag{2.75}$$

The resulting conditions are defined as :

$$\begin{aligned}&C_0>0, \quad \beta_2,\beta_4<0,\\ &L_{FOD}<V_1L_{GVD}, \;\; C_{lim}<C_0 \;\; \beta_2>0,\beta_4<0,\\ &L_{FOD}<V_2L_{GVD}, \;\; 0<C_0<C_{lim} \;\; \beta_2>0,\beta_4<0,\\ &L_{FOD}>V_2L_{GVD}, \;\; C_{lim}<C_0 \;\; \beta_2<0,\beta_4>0,\\ &L_{FOD}>V_1L_{GVD}, \;\; 0<C_0<C_{lim} \;\; \beta_2<0,\beta_4>0,\end{aligned} \tag{2.76}$$

where

$$\begin{aligned}V_1&=\frac{45.233+468.1C_0^2}{3},\\ V_2&=\frac{(31/22)+180.932C_0^2+936.2C_0^4}{6(\pi\exp(\frac{-7}{2})+C_0^2)},\\ C_{lim}&=2.084606293.\end{aligned} \tag{2.77}$$

We obtain the conditions of Eq.(2.76) and the definitions of Eq.(2.77) by making some basic discussions about the signs $s_2$ and $s_4$.

**Description of the numerical simulations**

For the numerical simulations, the process is the same as described in the previous cases.

## 2.4 The analysis of the FWM ASC in the WDM solitons system near the ZDW using the ABCJS approach

### 2.4.1 Analytical study of the model

We begin the analysis using the NLSE of Eq. (2.25) for the case where the TOD is considered [228] :

$$i\frac{\partial u}{\partial z} - \frac{\beta_2}{2}\frac{\partial^2 u}{\partial T^2} - i\frac{\beta_3}{6}\frac{\partial^3 u}{\partial T^3} + \gamma|u|^2 u = -i\alpha u. \tag{2.78}$$

It is admitted that, near the ZDW one should include the effect of the TOD while the GVD vanishes [3]. However, we maintain the GVD in order to make a comparison between the single TOD case of the growth of the ASC with the combined GVD-TOD case where it still remains a residual GVD effect.
We set the following dimensionless variables : $\zeta = z/L$, $\tau = T/T_0$ , $B(\zeta,\tau) = u(z,T)/\sqrt{P_0}$ where $L$ is the characteristic fiber length. Thus, we define $L_a = L_*/L$ as the dimensionless spatial amplification spacing while $|\beta_3| = T_0^3/L_{TOD}$ is the TOD average value. $L_*$ is the physical spatial amplification spacing. Introducing these dimensionless variables into Eq. (2.78) easily leads to the following form :

$$i\frac{\partial B}{\partial \zeta} - \frac{L\beta_2}{2T_0^2}\frac{\partial^2 B}{\partial \tau^2} - i\frac{L\beta_3}{6T_0^3}\frac{\partial^3 B}{\partial \tau^3} + L\gamma P_0|B|^2 B = -iL\alpha B. \tag{2.79}$$

Now we set the dimensionless terms $\beta_{GVD} = -\beta_2 L_{GVD}/T_0^2$, $\beta_{TOD} = \beta_3 L_{TOD}/T_0^3$ and $\varpi = L\alpha$ for GVD, TOD profiles and gain/loss parameter, respectively. Introducing these in Eq. (2.79) yields

$$i\frac{\partial B}{\partial \zeta} + \frac{\beta_{GVD} L}{2L_{GVD}}\frac{\partial^2 B}{\partial \tau^2} - i\frac{\beta_{TOD} L}{6L_{TOD}}\frac{\partial^3 B}{\partial \tau^3} + \frac{L}{L_{NL}}|B|^2 B = -i\varpi B. \tag{2.80}$$

It is well-known that the bright soliton solution is obtained in the regime of propagation where the dispersion length $L_{GVD}$ is similar to the nonlinear length $L_{NL}$ in the anomalous-dispersion regime. The TOD plays a significant role only if the dispersion length associated $L_{TOD}$ respects the condition $L_{TOD} \leq L_{GVD}$ [1,3,33,103,228]. Furthermore, it is well-known that the solitonic properties as the preserving shape of propagation exist in an ideal system while in realistic cases they are perturbed by higher-order effects like the TOD effect. So, in the present system, we assume that $L_{TOD} \approx L_{GVD}$. One can rewrite Eq. (2.80) in a suitable form by setting $B(\zeta,\tau) = \sqrt{h(\zeta)}E(\zeta,\tau)$ where $h(\zeta)$ is a function which will include the parameter $\varpi$. The function $h(\zeta)$ is the same as the function $g(z)$ shown in Eq. (1.36) in the first chapter. It is customary to use its expansion in Fourier series as :

$$h(\zeta) = \sum_{n=-\infty}^{n=+\infty} h_n \exp\big(-ink_{L_a}\zeta\big), \quad h_n = \frac{\varpi L_a}{\varpi L_a - in\pi} \tag{2.81}$$

where $k_{L_a} = \frac{2\pi}{L_a}$. The representation of this function is observed in figure 2.1. Equation (2.81) yields

$$i\frac{\partial E}{\partial \zeta} + \frac{\beta_{GVD}}{2}\frac{\partial^2 E}{\partial \tau^2} - i\frac{\beta_{TOD}}{6}\frac{\partial^3 E}{\partial \tau^3} + h(\zeta)|E|^2 E = 0 \tag{2.82}$$

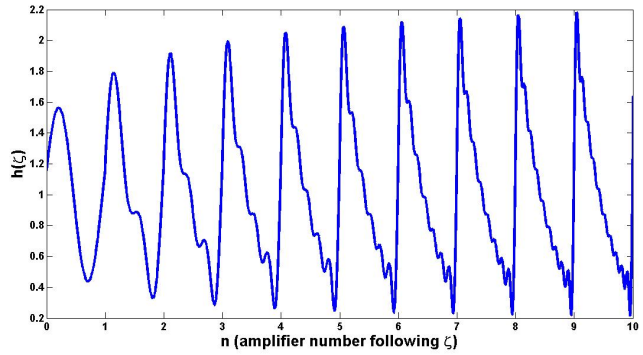


Figure 2.1: Function of amplification in the Fourier series expansion shown in Eq. (2.81). This should be compared with the definition shown in figure 1.13.

The presence or lack of the dimensionless dispersion parameter $\beta_{GVD}$ will be represented by the values 1 and 0, respectively. In the ABCJS approach [99,100,103-105,109,110,228], we should consider a signal including two pulses $E_1$ and $E_2$ such that $E_{pulse} = E_1 + E_2$. We assume that the FWM in the channels is taken as $E_{FWM} = E_{112} + E_{221}$. Then the total field in the system is

$$E(\zeta, \tau) = E_1 + E_2 + E_{112} + E_{221}, \tag{2.83}$$

where $E_1$, $E_2$, $E_{112}$ and $E_{221}$ evolve on frequencies $\Omega_1$, $\Omega_2$, $\Omega_{112} = 2\Omega_1 - \Omega_2$ and $\Omega_{221} = 2\Omega_2 - \Omega_1$, respectively. If we take $\Omega_1 = -\Omega_2 = -\Omega$, therefore $\Omega_{112} = -3\Omega$ and $\Omega_{221} = 3\Omega$. When we introduce Eq. (2.83) into Eq. (2.82), we obtain four (04) partial differential equations (PDEs) by neglecting all nonlinear terms in $E_{112}$, $E_{221}$ and the XPM terms. The system can be modeled by the diagram given in figure 2.2 where the transmission line is represented by the SMF symbolized by the ITU-T recommendation G. 652 [102]. Focusing on the growth of the ASC $E_{221}$, we choose its equation

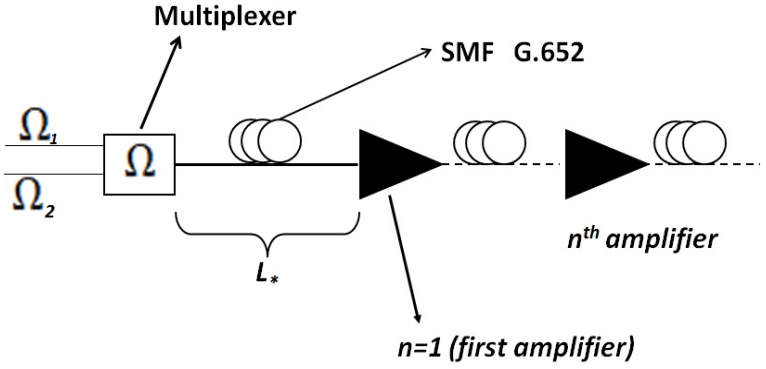


Figure 2.2: Diagram of the physical system studied in the FWM analysis (©-2013 SPRINGER EPJD, from [228]).

between the previous ones obtained after the introduction of Eq. (2.83) into Eq. (2.82). The evolution of the ASC in the system with TOD is therefore modeled by the following equation :

$$i\frac{\partial E_{221}}{\partial \zeta} + \frac{\beta_{GVD}}{2}\frac{\partial^2 E_{221}}{\partial \tau^2} - i\frac{\beta_{TOD}}{6}\frac{\partial^3 E_{221}}{\partial \tau^3} + h(\zeta)E_2^2 E_1^* = 0 \tag{2.84}$$

For simplicity, we set $v = E_{221}$ in Eq. (2.84). The present model under study (Eq. (2.84)), which includes the TOD term will be investigated in order to characterize the ASC under influence of this coefficient.

### 2.4.2 Reduced model of the FWM ASC growth

Following the assumption of Horne et al [109], the evolution of the FWM is taken in the following form including the TOD effect inside the exponential argument of the ASC :

$$v(\zeta,\tau) = G(\zeta,\tau)\exp\big[i\big(3\Omega\tau - \frac{\Omega^2}{2}\beta_{GVD}\zeta\big)\big]\exp\big[-i\frac{\Omega^3}{6}\beta_{TOD}\zeta\big] \tag{2.85}$$

When we introduce Eq. (2.85) into Eq. (2.84) we obtain the following equation for the amplitude $G(\zeta,\tau)$ :

$$\begin{aligned} i\frac{\partial G}{\partial\zeta} + \frac{\beta_{GVD}}{2}\big(\frac{\partial^2 G}{\partial\tau^2} + 6i\Omega\frac{\partial G}{\partial\tau} - 2(2\Omega)^2 G\big) - i\frac{\beta_{TOD}}{6}\big(\frac{\partial^3 G}{\partial\tau^3} + 9i\Omega\frac{\partial^2 G}{\partial\tau^2} - 27\Omega^2\frac{\partial G}{\partial\tau} \\ - 26i\Omega^3 G\big) = -h(\zeta)E_{20}^2 E_{10}^*, \end{aligned} \tag{2.86}$$

where

$$E_{20}^2 E_{10}^* = E_2^2 E_1^* \exp\left[i\big(-3\Omega\tau + \frac{\Omega^2}{2}\beta_{GVD}\zeta\big)\right]\exp\left[i\big(\frac{\Omega^2}{2}\frac{\beta_{TOD}\Omega}{3}\zeta\big)\right] \tag{2.87}$$

We set $\Delta\Omega = \Omega_2 - \Omega_1 = 2\Omega$ as the difference in the frequency offset for the case where the input pulses are well-separated, therefore in this case $\Delta\Omega \gg 1$. We assume the following simplifications $(\Delta\Omega)^2|G|,\ \ 26\Omega^3|G| \gg |\frac{\partial G}{\partial\tau}|, |\frac{\partial^2 G}{\partial\tau^2}|, |\frac{\partial^3 G}{\partial\tau^3}|$. Then Eq. (2.86) becomes

$$i\frac{\partial G}{\partial\zeta} - (\Delta\Omega)^2\big(\beta_{GVD} + \frac{13\Omega\beta_{TOD}}{12}\big)G = -h(\zeta)E_{20}^2 E_{10}^*, \tag{2.88}$$

which is considered as the reduced model. For simplicity, we set

$$\begin{aligned} \phi &= \beta_{GVD} + \tfrac{13\Omega\beta_{TOD}}{12}, \\ \psi(\zeta) &= \big(\beta_{GVD} + \tfrac{\beta_{TOD}\Omega}{3}\big)\zeta \end{aligned} \tag{2.89}$$

The input pulses are sech-type profiled in the general form of fundamental soliton as in [3,109,228] :

$$E_j = E_{max,j}\,sech[E_{max,j}(\tau - \Omega_j\zeta - T_j)]\exp\big[i(E_{max,j}^2 - \Omega_j^2)\zeta/2\big]\exp\big[i\Omega_j\tau\big] \tag{2.90}$$

where $\Omega_1 = -\Omega_2 = -\Omega$, $E_{max,1} = E_{max,2} = E_{max}$ and $T_1 = -T_2 = T_0$. The integration of Eq. (2.88) gives

$$\begin{aligned} G(\zeta,\tau) = iE_{max}^3\exp\big[-i(\Delta\Omega)^2\phi\zeta\big]\sum_{n=-\infty}^{n=+\infty} h_n\int_0^{\zeta} sech^2\big[E_{max}(\tau - \Omega\zeta' + T_0)\big] \\ \times sech\big[E_{max}(\tau + \Omega\zeta' - T_0)\big]\exp\big[i\big(-nk_{La} + \frac{E_{max}^2 - \Omega^2}{2} + (\Delta\Omega)^2\phi\big)\zeta'\big] \\ \times\exp\big[i\big(\frac{\Omega^2}{2}\psi(\zeta')\big)\big]d\zeta'. \end{aligned} \tag{2.91}$$

It is important to remind that the PMC required in order to gain the maximum FWM values is obtained by taking the argument of the imaginary exponential $\exp\left[i\big(-nk_{La}\zeta' + 0.5(E_{max}^2 - \Omega^2)\zeta'\big)\right]$ $\times\exp\big[i(\Delta\Omega)^2\phi\zeta'\big]\times\exp\big[0.5i\Omega^2\psi(\zeta')\big]$ equal to zero. This leads to some cases of the study in function of the GVD and TOD profiles.

- In the presence of constant TOD profile without the GVD parameter, the PMC leads to :

$$9\Omega^3 - \Omega^2 + E_{max}^2 - 2nk_{L_a} = 0 \tag{2.92}$$

One must solve this equation following $\Omega$ and $n$ to obtain values leading to largest amplitude of FWM.

- In the presence of both the GVD and TOD profiles, we obtain from the general reduced model the following equation :

$$9\Omega^3 + 8\Omega^2 + E_{max}^2 - 2nk_{L_a} = 0 \tag{2.93}$$

The next section deals with the full model assuming that the amplitude of the FWM component is very sensitive to the time variable (differentiated terms of $G(\zeta,\tau)$ are not negligible).

### 2.4.3 Full model of the FWM ASC growth

Considering the Fourier transform of Eq. (2.86), we obtain :

$$\begin{aligned} i\frac{\partial\tilde{G}}{\partial\zeta} - \frac{1}{2}\Big\{\beta_{GVD}\big(\omega^2 + 6\omega\Omega + 2(2\Omega)^2\big) + \frac{\beta_{TOD}}{3}\big(\omega^3 + 9\omega^2\Omega + 27\omega\Omega^2 + 26\Omega^3\big)\Big\}\tilde{G} \\ = -h(\zeta)F[E_{20}^2E_{10}^*]. \end{aligned} \tag{2.94}$$

We set :

$$\theta(\omega,\Omega) = \beta_{GVD}\big(\omega^2 + 6\omega\Omega + 2(2\Omega)^2\big) + \frac{\beta_{TOD}}{3}\big(\omega^3 + 9\omega^2\Omega + 27\omega\Omega^2 + 26\Omega^3\big) \tag{2.95}$$

Equation (2.94) leads to the following form of $\tilde{G}(z,\omega)$:

$$\begin{aligned} \tilde{G}(\zeta,\omega) =& \frac{i\pi E_{max}}{\Delta\Omega}\exp\Big[-i\big(\frac{1}{2}\theta(\omega,\Omega)\zeta + \omega\delta(\zeta)\big)\Big]sech(\frac{\pi\omega}{2E_{max}}) \\ &\times\sum_{n=-\infty}^{n=+\infty} h_n\exp\big[i\chi_n(\omega)\zeta_{coll}\big] \\ &\times\int_{-\infty}^{2E_{max}\delta(\zeta)} I(y,\frac{\omega}{E_{max}})\exp\big[-i\mu_n(\omega)y\big]dy, \end{aligned} \tag{2.96}$$

where

$$\chi_n(\omega,\Omega) = \big[-nk_{La} + \frac{E_{max}^2 - \Omega^2}{2} + \frac{1}{2}\theta(\omega,\Omega) + \frac{\Omega^2}{2}(\beta_{GVD} + \frac{\beta_{TOD}\Omega}{3})\big] \tag{2.97}$$

is related to the PMC. The function $I(y,\omega/E_{max})$ is the function mentioned in sub-section (1.2.2), $\delta(\zeta) = \Omega\zeta - T_0$, $\mu_n(\omega) = -\chi_n(\omega,\Omega)/\Delta\Omega E_{max}$ and $y = 2E_{max}\delta(\zeta)$. The PMC for the full model is given by taking $\chi_n(\omega,\Omega) = 0$. The roots $\omega_n$ obtained are only relevant, if we consider those which are equal to zero because of the presence of the function $sech(\pi\omega/2E_{max})$ inside $\tilde{G}(\zeta,\omega)$. Thus, Eq. (2.97) leads to the following polynomial equation of third degree :

$$ax^3 + bx^2 + cx + d = 0, \tag{2.98}$$

where we have set $x = \omega$, $a = \beta_{TOD}/3$, $b = \beta_{GVD} + 3\beta_{TOD}\Omega$, $c = 6\Omega\beta_{GVD} + 9\Omega^2\beta_{TOD}$ and $d = 9(\beta_{GVD} + \beta_{TOD}\Omega - 1/9)\Omega^2 + E_{max}^2 - 2nk_{La}$. Therefore, we can consider specific cases :

1. Case of the second order dispersion $\beta_{GVD} = 1, \quad \beta_{TOD} = 0$ :

$$x^2 + 6\Omega x + (8\Omega^2 + E_{max}^2 - 2nk_{La}) = 0, \tag{2.99}$$

the two solutions are $x_{n,\pm} = -3\Omega \pm \sqrt{\Omega^2 - E_{max}^2 + 2nk_{La}}$. The realistic solution is $x_{n,+}$ that must be equal to zero according to the previous hypothesis. So, we recover the single GVD PMC shown in Eq. (1.42).

2. Case of the third order dispersion $\beta_{GVD} = 0, \quad \beta_{TOD} = 1$ :

$$\frac{1}{3}x^3 + 3\Omega x^2 + 9\Omega^2 x + (9\Omega^3 - \Omega^2 + E_{max}^2 - 2nk_{La}) = 0. \tag{2.100}$$

If we take three general solutions of Eq. (2.100) as $(x - x_1)(x - x_2)(x - x_3) = 0$ and we assume one of them equal to zero, we obtain the same PMC derived from the reduced model for single TOD case given by Eq. (2.92).

3. Case of the combined GVD and TOD case $\beta_{GVD} = 1, \quad \beta_{TOD} = 1$ :

$$\frac{1}{3}x^3 + (3\Omega + 1)x^2 + (9\Omega^2 + 6\Omega)x + (9\Omega^3 + 8\Omega^2 + E_{max}^2 - 2nk_{La}) = 0. \tag{2.101}$$

Using the same process as in the previous case, we derive the PMC obtained in Eq. (2.96) for the reduced model.
So, for all these cases we obtain the same PMCs of the reduced model in the full model by taking the roots $\omega_n$ of $\chi_n(\omega, \Omega)$ equal to zero.
Considering the case where $\omega_n \neq 0$, we obtain a general form of the asymptotic solution $G(\tilde{z}, \omega)$ for long distances :

$$\begin{aligned}\tilde{G}(\zeta \to \infty, \omega) \approx & \frac{i\pi^2 Emax}{\Delta\Omega} \exp\left[ -i\big(\frac{\theta(\omega,\Omega)}{2}\zeta + \omega\delta(\zeta)\big)\right] sech(\frac{\pi\omega}{2E_{max}}) \\ & \times \sum_{n=-\infty}^{+\infty} h_n \exp\left[i\chi(\omega,\Omega)\zeta_{coll}\right] \\ & \times \frac{\mu_n(\omega,\Omega) + \omega/E_{max}}{\sinh\left[\frac{\pi}{2}\big(\mu_n(\omega,\Omega) + \omega/E_{max}\big)\right]\cosh\left(\frac{\pi\mu_n(\omega,\Omega)}{2}\right)}\end{aligned} \tag{2.102}$$

**Description of the numerical simulations**

The numerical simulations of this study of the FWM ASC, one integrates Eqs. (2.91) and (2.94) assuming physical realistic systems with amplification nodes $(n \times L_a)$ and realizing the PMC at each node in order to obtain the appropriate frequency offset to the FWM occurrence. The results are obtained by using a numerical integration scheme of trapezes between each amplifier spacing. We make the comparison between the single GVD case and the combined GVD-TOD case.

## 2.5 MI analysis of a CW in SOI-waveguides under FOD

The model equation is similar to Eq. (2.49) but including now the TOD term. In the linear analysis of the MI mechanism, we start with the steady-state solution of the CW [3,229] :

$$u = u_0 \exp\{i\phi_{NL}\} \tag{2.103}$$

where $\phi_{NL}$ represents the nonlinear phase shift. Introducing Eq. (2.103) into Eq. (2.49) leads to the following definition of $\phi_{NL}$ :

$$\phi_{NL} = \left[(\gamma + i\Gamma)u_0^2 + \frac{i}{2}(\alpha + \sigma N_c)\right]z. \tag{2.104}$$

We use a small perturbation of the steady-state solution by stating :

$$a(z,T) = a_1(z)\exp\{i(Kz - \Omega T)\} + a_2(z)\exp\{-i(Kz - \Omega T)\}, \tag{2.105}$$

where K and $\Omega$ represent the wave number and the perturbation frequency respectively. Introducing $u = (u_0 + a)\exp(i\phi_{NL})$ into Eq. (2.49) allows to define a couple of NLSEs following $a_1$ and $a_2$ (details : see appendixes). Therefore, one obtains the relation :

$$\begin{pmatrix} \frac{\partial a_1}{\partial z} \\ \\ \frac{\partial a_2}{\partial z} \end{pmatrix} = M(K) \begin{pmatrix} a_1 \\ \\ a_2 \end{pmatrix} \tag{2.106}$$

The obtained MI Matrix is given as follows :

$$M(K) = \begin{pmatrix} D_1(\Omega) - K + \gamma_1 u_0^2 + \Lambda & \gamma_1 u_0^2 \\ \gamma_1 u_0^2 & D_2(\Omega) + K + \gamma_1 u_0^2 + \Lambda \end{pmatrix} \tag{2.107}$$

where

$$\begin{aligned} D_1(\Omega) &= \sum_{k=2}^{4} \frac{\Omega^k \beta_k}{k!}, \\ \\ D_2(\Omega) &= \sum_{k=2}^{4} \frac{(-\Omega)^k \beta_k}{k!}, \\ \\ \gamma_1 &= \gamma + i\Gamma, \\ \\ \Lambda &= i\frac{(\alpha + \sigma N_c)}{2}. \end{aligned} \tag{2.108}$$

The wave number leads to :

$$K = \frac{1}{2}\left\{D_{odd} \pm \left[\big(D_{even} + 2(\Lambda + 2\gamma_1 u_0^2)\big)\big(D_{even} + 2\Lambda\big)\right]^{1/2}\right\}, \tag{2.109}$$

with $D_{even} = D_1 + D_2$ and $D_{odd} = D_1 - D_2$. The MI gain is well-known to be defined as :

$$G(\Omega) = 2|Im(K)| \equiv \frac{1}{2}\left|Im\left\{\left(\big(D_{even} + 2(\Lambda + 2\gamma_1 u_0^2)\big)\big(D_{even} + 2\Lambda\big)\right)^{1/2}\right\}\right|. \tag{2.110}$$

Since $\gamma_1$ and $\Lambda$ are complexes, it is convenient to set that :

$$G(\Omega) = 2\left|Im\big(\sqrt{A(\Omega)}\big)\right|, \tag{2.111}$$

where

$$\begin{aligned} A(\Omega) &= x(\Omega) + iy(\Omega) = r(\Omega)\exp\{i\theta(\Omega)\}, \\ x(\Omega) &= D_{even}(D_{even} + 4u_0^2\gamma) - 4|\Lambda|\big(2u_0^2\Gamma + |\Lambda|\big), \\ y(\Omega) &= 4D_{even}\big(u_0^2\Gamma + |\Lambda|\big) + 8u_0^2\gamma|\Lambda|. \end{aligned} \tag{2.112}$$

One obtains the MI gain as follows :

$$G(\Omega) = \Big[2\big(r(\Omega) - x(\Omega)\big)\Big]^{1/2}. \tag{2.113}$$

The relation in Eq. (2.113), confirms that the TOD does not intervene in the MI gain as previously discussed in the introduction section. The optimal frequencies (OFs) are given for $dG(\Omega)/d\Omega = 0$ as a PMC of the FWM related with the MI mechanism. It is described by two pump photons at the frequency $\omega_0$, one Stokes photon at $\omega_0 - \Omega$, and one ASC photon at $\omega_0 + \Omega$ [3,190]. The following relations define the obtained OFs :

$$\begin{aligned} \Omega_0 &= 0, \\ \Omega_{1,\pm} &= \pm\frac{\sqrt{-6\beta_4\beta_2}}{\beta_4}, \\ \Omega_{2,\pm} &= \pm\sqrt{\frac{-6\Gamma\beta_2 + 2\sqrt{9\Gamma^2\beta_2^2 + 6\Gamma\beta_4\gamma|\Lambda|}}{\Gamma\beta_4}}, \\ \Omega_{3,\pm} &= \pm\sqrt{-\frac{6\gamma\beta_2 + 2\sqrt{9\gamma^2\beta_2^2 - 6\gamma\beta_4U_0^2\Gamma^2 - 6\Gamma\beta_4\gamma|\Lambda| - 6\gamma^3\beta_4U_0^2}}{\gamma\beta_4}}. \end{aligned} \tag{2.114}$$

When the TPA and the FCA vanish, the OFs in Eq. (2.114) are similar with those obtained in [190] for glass fibers where $\gamma$ was linked with the saturable nonlinearity. So, we do not focus on the role played by the FOD since it has been extensively discussed in this reference. Our main purpose in this section consists to study the effect of the absorption coefficients on the MI gain spectrum.

**Description of the numerical simulations**

We use the relation (2.113) to plot the MI gain highlighting the impact of absorption coefficients. Then, we solve Eq. (2.25) through the SSF algorithm with the physical parameters assuming the MI gain above to obtain the PTG for each pulse. We study the effect chirp and profile in the mechanism varying values of chirp and comparing the results between the pulses.

## 2.6 SCG analysis

### 2.6.1 In a waveguide modeled by the GNLSE with non-Kerr terms

The optical waveguides as PCFs in the SCG numerical analysis are always modeled by the GNLSE that links the CKN with SS and DRR effects as discussed previously in Eq. (2.27). Considerable attentions are being paid theoretically and experimentally to analyze the dynamics of optical solitons in optical waveguides. The waveguides used in the picosecond and femtosecond domains in common nonlinear optical systems are usually of Kerr type and consequently the dynamics of light pulses are described by nonlinear Schrödinger (NLS) family of equations with cubic nonlinear terms. In present days applications, as the intensity of the incident light field becomes stronger, non-Kerr nonlinearity

effect comes into play. Because of this additional effect, the physical features and the stability of the NLS soliton can change. The influence of the non-Kerr nonlinearity on the NLS soliton propagation, is described by the NLS family of equations with higher degree of nonlinear terms [230-232]. So recently, both of the solitonic features and the MI process have been investigated by Choudhuri and Porsezian in [233], highlighting the effects of the non-Kerr terms through the GNLSE. In fact, they showed that the non-Kerr terms reduce the maximum value of the gain and the bandwidth, playing so a non-negligible role over the CKN. The investigation of this model of GNLSE is interesting since it is well-known today that, the nonlinearity arising due to fifth-order susceptibility $\chi^5$ can be obtained in many optical materials, such as semiconductor doped glasses, polydiactylene toluene sulfonate, chalcogenide glasses, and some transparent organic materials [230-233].
We derive the model equation through which, we numerically investigate the SCG phenomenon. Considering rather the GNLSE with non-Kerr terms, we have [230-233]:

$$\begin{aligned} i\frac{\partial u}{\partial z}+\sum_{k=2}^{M}\frac{(i)^k\beta_k}{k!}\frac{\partial^k u}{\partial T^k}+\gamma_1|u|^2u+\gamma_2|u|^4u=&-i\frac{\alpha}{2}u+i\delta_1\frac{\partial(|u|^2u)}{\partial T}+\delta_2\frac{\partial(|u|^2)}{\partial T}u \\ &+i\delta_3\frac{\partial(|u|^4u)}{\partial T}+\delta_4\frac{\partial(|u|^4)}{\partial T}u, \end{aligned} \tag{2.115}$$

where $\gamma_1$, $\gamma_2$, $\alpha$, $\delta_1$, $\delta_2$, $\delta_3$ and $\delta_4$ are the CKN coefficient, the quintic nonlinearity coefficient (QNC), the parameter of linear losses, the SS parameter linked to $\gamma_1$, the DRR coefficient corresponding to $\gamma_1$, the SS parameter linked to $\gamma_2$ and the DRR coefficient corresponding to $\gamma_2$, respectively. The parameters $\delta_3$ and $\delta_4$ are the so-called non-Kerr terms because they stem from the quintic nonlinearity. In this work, we assume the QNC as $\gamma_2 \approx \pm\gamma_1/P_0$ where $P_0$ is the peak power of the pump. The sign of $\gamma_2$ depends on the case where the system has cooperative nonlinearities ($\gamma_1\gamma_2 > 0$) or competing nonlinearities ($\gamma_1\gamma_2 < 0$) [76-78]. The parameter $\delta_1$ is equal to $-1/\omega_0$. In an empirical point of view in which we try to construct a model equation that should be solved in the SCG simulations, we consider similarly to the single CKN case above that, the full case given by Eq. (2.115) could be written differently as follows [234]:

$$\begin{aligned} i\frac{\partial u}{\partial z}+\sum_{k=2}^{M}\frac{(i)^k\beta_k}{k!}\frac{\partial^k u}{\partial T^k}=&-i\frac{\alpha}{2}u-\gamma_1(1+i\delta_1\frac{\partial}{\partial T})\left[u(z,T)\int_{-\infty}^{\infty}R(T')|u(z,T-T')|^2dT'\right] \\ &-\gamma_2(1+i\delta_3\frac{\partial}{\partial T})\left[u(z,T)\int_{-\infty}^{\infty}R(T')|u(z,T-T')|^4dT'\right]. \end{aligned} \tag{2.116}$$

The obtained form for our simulations is given by [234]:

$$\begin{aligned} \frac{\partial\tilde{u'}}{\partial z}=&i\omega\bar{\gamma}_1\delta_1\exp(-\hat{L}(\omega)z)F\left[u(z,T)\int_{-\infty}^{\infty}R(T')|u(z,T-T')|^2dT'\right] \\ &+i\omega\bar{\gamma}_2\delta_3\exp(-\hat{L}(\omega)z)F\left[u(z,T)\int_{-\infty}^{\infty}R(T')|u(z,T-T')|^4dT'\right], \end{aligned} \tag{2.117}$$

where $\bar{\gamma}_2 = \pm\bar{\gamma}_1/P_0$. The effects of $\delta_2$ and $\delta_4$ are assumed to be included within the corresponding block integrals in the RHS of Eqs. (2.116) and (2.117). To approximate the HOD parameters of the propagation constant, we have used the following relation derived from the calculated GVD at the corresponding pumping wavelength :

$$\beta_k(\lambda_p) \approx (-1)^k\beta_2(\lambda_p)T_0^{k-2}, \tag{2.118}$$

where k is an integer from 3 to the higher-order value of dispersion. The CDP being an important part in the SCG, we have chosen to stop up to M=10 (assuming that the orders beyond ten have a negligible influence on the results). We have used a sech-type input profile defined as defined in Eq. (1.6).

For the numerical simulations, we modify the trial MATLAB code provided by Travers et al in [114] assuming Eq. (2.117) given above.

### 2.6.2 In the $CS_2$-LCPCF

In this study, the GNLSE corresponds to Eq. (2.27). The subsequent form which is solved for the SCG by the numerical code previously discussed by Travers et al in [114] is given by :

$$\frac{\partial \tilde{u'}}{\partial z} = i\bar{\gamma}_1 \omega \delta_1 \exp(-\hat{L}(\omega)z) F\left[u(z,T)\int_{-\infty}^{\infty} R(T')|u(z,T-T')|^2 dT'\right], \tag{2.119}$$

with $\tilde{u'}$ and $\hat{L}(\omega)$ being the Fourier transform form of $u(z,T)$ and the linear operator including the linear losses and the Taylor series expansion of the propagation constant [114]. The transformation $F[\ ]$ is the Fourier transform of the block inside the squared brackets. $\hat{L}(\omega)$ is defined as shown in this reference. It is assumed that the CKN coefficient $\bar{\gamma}_1$ is almost independent to the frequency as :

$$\bar{\gamma}_1 = \frac{n_2 n_0 \omega_0}{c n_{eff} A_{eff}}, \tag{2.120}$$

where $n_0$ and $n_{eff}$ are the linear refractive index used when determining $n_2$ and the effective index of the guided mode, respectively.

In the simulations, it is essential to have the values of the HODs describing the CDP of the waveguide. It is customary the evaluate and plot the dispersion parameter $D(\lambda)$ or the GVD curve of the studied waveguide. For the considered $CS_2$-LCPCF, the refractive index of $CS_2$ versus the wavelength is given by the following Sellmeier equation [145,203,206,235,236]:

$$n(\lambda) = A + \frac{B}{\lambda^2} + \frac{C}{\lambda^4} + \frac{D}{\lambda^6} + \frac{E}{\lambda^8}, \tag{2.121}$$

where the wavelength $\lambda$ is in $\mu$m and the parameters A=1.580826, $B = 1.52389 \times 10^{-2}\mu m^2$, C=$4.8578\times10^{-4}\mu m^4$, D=-$8.2863\times10^{-5}\mu m^6$, $E = 1.4619 \times 10^{-5}\mu m^8$. To obtain the CDP, a software as COMSOL Multiphysics could be appropriate. Using this software, we present in figure 2.3(a), the CDPs of the PCF and LCPCF having the same pitch ($\Lambda = 1.8\ \mu m$), hole diameter (d=1.44 $\mu$m) and five air holes. We notice in the wavelength range that, both the PCF and $CS_2$-LCPCF have two ZDWs. Indeed, for the PCF, one obtains the first ZDW at 790 nm and the second at 2370 nm. Concerning the $CS_2$-LCPCF, the first ZDW is obtained at 1610 nm and the second at 2510 nm. For the SCG process, we show in figure 2.3(b), the choice of the pumping wavelengths. Two wavelengths are used in this work : for the normal dispersion regime $\lambda_p$ = 1550 nm while for the anomalous dispersion regime $\lambda_p$ = 2030 nm. We have also chosen to deal with femtosecond lasers that allow 100 fs and nJ scale pulses. In a practical experiment, some laser sources as the $Ho^{3+}$-doped silica fibre lasers could deliver such light in the 2030 nm-region [237]. We draw in figure 2.3(c), the nonlinear index given by Eq. (2.121) of the $CS_2$ versus the wavelength $\lambda$. As expected, the parameter $n_{CS_2}$ decreases while the wavelength $\lambda$ increases. We notice that this liquid is sufficiently transparent from the visible to the infra-red region of light. Using the relation of the CKN parameter $\gamma$, where the nonlinear index $n_2$ is given by $3\chi^3/(8n_{CS_2})$, we have calculated its values for each pumping wavelength. We have used for the simulations, the value of $1.2 \times 10^{-18}\ m^2/W$ for $n_2$ of the $CS_2$ (see [238]). This value is 100 times greater than that of the silica which are in the range of $10^{-20}\ m^2/W$

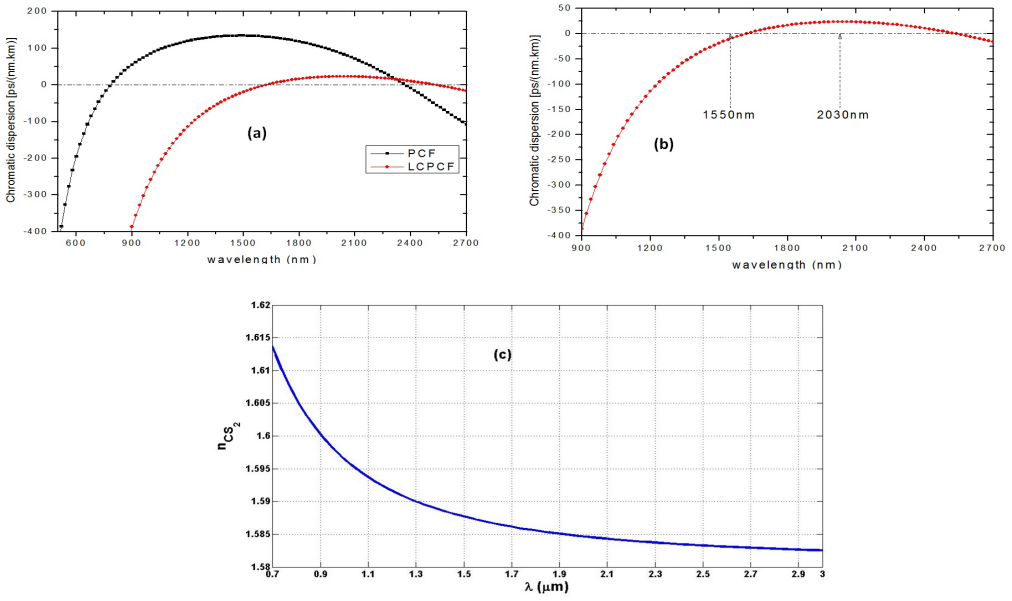


Figure 2.3: (a) Comparison of the CDPs : black curve for the standard PCF and red curve for the LCPCF. Data : Pitch $\Lambda = 1.8$ $\mu$m, hole diameter d=1.44 $\mu$m, five holes,(b) Choice of the pumping wavelengths in the CDP of the LCPCF,(c) Plot of $n_{CS_2}$ versus $\lambda$.

[3]. For this specific study, we have used a chirped Airy input profile in the numerical simulations as defined in Eq. (2.68) with a zero phase. In this work, we have also chosen to stop until the tenth order since the values beyond have a negligible influence on the results using Eq. (2.118).

### 2.6.3 In a SOI-waveguide that includes both the THG and the NFK terms

The question of SCG analysis in a SOI-waveguides should firstly concern the effects of TPA, FCA and FCD on the spectra obtained. However as fully discussed in [200,201e,201g,202a,215,216,218], the TPA is deleterious for the spectral bandwidth of the spectra. Indeed, the TPA causes a drastic reduction of the bandwidth [215]. One should also note that the effects of FCA and FCD have already been analyzed on the broadened spectra induced by the SCG [200,202a] and by the SPM only [211,215]. Moreover, for ultrashort pulses as those in the sub-picosecond domain (femtosecond pulses) for which the effective carrier lifetime should be neglected, Yin et al demonstrated that neither SRS nor FCA/FCD plays a significant role during the SCG in SOI-waveguides [200].

More recently, the impact on the SPM of both the THG process and a novel one dubbed as NFK process, were studied in a Kerr medium [239]. In this study, Loures et al found that, the THG induces additional symmetric lobes in the SPM-broadened spectrum while the amplitude of these sidebands are importantly increased by the NFK term and the SS effect so-called nonlinear shock effect. The NFK was first discussed theoretically in [240] after the pioneers experiments done in [241-243] and that have revealed the possibility of solitons to emit such negative-frequency resonant radiation. Furthermore, Conforti et al showed that the NFK term does not appear in the common GNLSE based on the SVEA. Thus, they modeled subsequently a new equation known as the full UPPE that includes the NFK in a GNLSE-like form [240]. It is well-known that, the THG necessitates a phase-matching condition to occur in a Kerr medium [3]. This is not in general satisfied for standard SMFs while phase-matching is much easier to accomplish in highly nonlinear waveguides [3].

Assuming that SOI-waveguides are media that possess high values of Kerr nonlinearity, the consideration of the THG effect could be set. If the analytical modeling of the propagation within

SOI-waveguides is not conducted through the SVEA but rather through the novel modeling introduced in [240], the NFK term could also been included. The question of such considerations has been formulated for the first time in this thesis and presented in [244]. Indeed, the following interrogations were still opened before the work described in this thesis : (i) is there an existing modeling of pulse propagation within SOI-waveguides that combines SPM, SS, TPA, THG and NFK ? (ii) What happen to the SCG when all these effects are investigated together ? (iii) What about its coherence properties ?.

In this work, we conduct for the first time to the best of our knowledge, a modeling that combines into a nonlinear equation the aforementioned nonlinear effects for a SOI-waveguide. This modeling relies on both the one of [216] and the one of [240]. Then, we derive the corresponding equation used to generate numerically the SCG spectra by a modified adapted version of the MATLAB code provided in [114]. Since, the single impacts of the mentioned nonlinear terms on the SPM-broadened spectra are known [3,137,200,202a,211,239], we focus in this thesis on their influences upon the properties of the SCG obtained through symmetric femtosecond pulses. A particular attention is given to the TPA, the THG and the NFK.

For the analytical modeling, let us start with the full UPPE expressed as follows [240]:

$$i\frac{\partial \tilde{E}(z,\omega)}{\partial z} + \beta(\omega)\tilde{E}(z,\omega) + \frac{\omega}{2cn(\omega)}\tilde{P}_{NL}(z,\omega) = 0. \tag{2.122}$$

It is a reduction of Maxwell's equations that accounts only for the forward propagating part of the electric field. $n(\omega)$ is the linear refractive index. Then similarly to the SVEA done in section 2.2, one introduces the pulse envelope as done in Eq. (2.4) that deals with frequency detuning $\Delta\omega$ from the pump frequency $\omega_0$ as $\omega_0 \pm \Delta\omega$. Nonetheless, contrary to what has been considered in subsection 2.2.1 where $|\Delta\omega| \ll \omega_0$ (SVEA), here one considers rather $supp\{\Delta\omega\} = [-\omega_0; +\infty[$ so that one could obtain negative frequencies. It is therefore a spectral extension of the SVEA. With such hypotheses, one derives the following nonlinear polarization :

$$P_{NL}(z,T) = \frac{3\chi^{(3)}}{8}\left[\frac{1}{3}\left(\big(u(z,T)\exp(i\theta)\big)^3 + \big(u^*(z,T)\exp(-i\theta)\big)^3\right) + |u(z,T)|^2\big(u(z,T)\exp(i\theta) + u^*(z,T)\exp(-i\theta)\big)\right], \tag{2.123}$$

where $u(z,T)$ represents now the pulse envelope as done in Eq. (2.4), $\theta = -\omega_0 T + \beta_0 z$, $\big(u(z,T)\exp(i\theta)\big)^3$ accounts for the THG of positive frequencies, $\big(u^*(z,T)\exp(-i\theta)\big)^3$ accounts for the THG of negative frequencies, $|u(z,T)|^2 u(z,T)\exp(i\theta)$ is for the common used positive frequencies Kerr effect inducing the SPM [3], and $|u(z,T)|^2 u^*(z,T)\exp(-i\theta)$ corresponds to the novel process dubbed as NFK effect [239,240]. Introducing Eq. (2.123) in Eq. (2.122) similarly to subsection 2.2.1, one obtains after a cumbersome calculation the following nonlinear PDE in the retarded frame of time [239,240]:

$$i\frac{\partial u(z,T)}{\partial z} + \sum_{k=2}^{M}\frac{(i)^k\beta_k}{k!}\frac{\partial^k u(z,T)}{\partial T^k} + \gamma|u|^2 u = -i\frac{\alpha}{2}u + \frac{\gamma}{3}u^3\exp(-2i\theta') + \frac{\gamma}{3}(u^*)^3\exp(2i\theta') + \gamma|u|^2u^*\exp(2i\theta'), \tag{2.124}$$

with $\theta' = \omega_0 T + \Delta\kappa z$ and $\Delta\kappa = \beta_1(\lambda_0)\omega_0 - \beta_0(\lambda_0)$. The full background of the computation used to derive the PDE in a GNLSE-like form above can be found in [240]. Assuming now a spectral filtering that allows only the THG of positive frequencies, it yields :

$$i\frac{\partial u(z,T)}{\partial z} + \sum_{k=2}^{M}\frac{(i)^k\beta_k}{k!}\frac{\partial^k u(z,T)}{\partial T^k} = -i\frac{\alpha}{2}u - \gamma u\left[|u|^2 + \frac{u^2}{3}\exp(-2i\theta') + \gamma(u^*)^2\exp(2i\theta')\right]_+. \tag{2.125}$$

Thus, only positive frequencies for THG are considered through a spectral filtering of the UPPE when the subscript "+" is written [239,240]. Such operation is important when the sub-cycle pulses are considered assuming that for them, the common SVEA is completely invalid [239].

Now for a lossless SOI-waveguide, we combine Eq. (2.125) with Eq. (2.49) to obtain the novel equation that combines the nonlinear absorptions, THG and NFK. It yields [244] :

$$\begin{aligned} i\frac{\partial u(z,T)}{\partial z}+\sum_{k=2}^{k=10}\frac{i^k\beta_k}{k!}\frac{\partial^k u(z,T)}{\partial T^k} =& -\gamma'(1+i\delta_{shock}\frac{\partial}{\partial T})\times\Big[u(z,T)\big(|u(z,T)|^2 \\ &+a_{NFK}(u^*(z,T))^2\exp(2i\theta') \\ &+\frac{a_{THG}}{3}(u(z,T))^2\exp(-2i\theta')\big)\Big]_+, \end{aligned} \tag{2.126}$$

with $a_{NFK}$ and $a_{THG}$ being the NFK coefficient and the THG coefficient, respectively. The parameter of the cubic nonlinearity is defined as described in subsection 2.2.2. Since there is a need of phase-matching satisfaction in this highly nonlinear medium for the THG to occur as extensively discussed in [3,239,240], the nearly zero-phase condition $\theta'\sim 0$ corresponds approximately to the maximal growth (or the resonance) of the THG occurrence as done for the FWM [3,228]. Under this assumption, the THG is qualified to be nearly resonant (It is underlined by the group-velocity mismatch [3]). Nevertheless, when $\theta'\neq 0$, we have :

$$\begin{aligned} \beta_1(\lambda_0) &= \frac{1}{c}\Big[n_{Si}(\lambda_0)-\lambda_0\big(\frac{dn_{Si}(\lambda)}{d\lambda}\big)\big|_{\lambda=\lambda_0}\Big], \\ \omega_0 &= \frac{2\pi c}{\lambda_0}, \\ \theta'(z,T) &= \omega_0\Big[T+\big(\beta_1(\lambda_0)-\frac{\beta_0(\lambda_0)}{\omega_0}\big)z\Big]. \end{aligned} \tag{2.127}$$

We know that $\beta_0(\lambda_0)/\omega_0=\frac{n_{Si}(\lambda_0)}{c}$, thus it yields :

$$\theta'(z,T)=2\pi\Big\{\frac{cT}{\lambda_0}-z\big(\frac{dn_{Si}(\lambda)}{d\lambda}\big)\big|_{\lambda=\lambda_0}\Big\}, \tag{2.128}$$

where $n_{Si}(\lambda)$ is the refractive index of silicon at $\lambda$. It is calculated in this work from the Sellmeier-type equation [200,245]:

$$n_{Si}(\lambda)=\Big[1+\frac{c_1\lambda^2}{\lambda^2-\lambda_1^2}+\frac{c_2\lambda^2}{\lambda^2-\lambda_2^2}\Big]^{1/2}, \tag{2.129}$$

where $c_1=9.733$, $c_2=0.936$, $\lambda_1=290.4$ nm, and $\lambda_2=366.9$ nm. It is assumed that an optical incident signal without initial phase propagating in this medium should develop a nonlinear phase shift $\theta'_{NL}(z,T)$ [3,239]. Thus, to obtain $\theta'_{NL}(z,T)$, we neglect in Eq. (2.126) the CDP and the shock term in order to have :

$$i\frac{\partial u(z,T)}{\partial z}=-\gamma'\times\Big[u(z,T)\big(|u(z,T)|^2+a_{NFK}(u^*(z,T))^2\exp(2i\theta')+\frac{a_{THG}}{3}(u(z,T))^2\exp(-2i\theta')\big)\Big]_+. \tag{2.130}$$

Let us set that $u=|u|\exp\big(i\theta'_{NL}(z,T)\big)$ and inserting this relation in Eq. (2.130) above yields two coupled PDEs for $|u|$ and $\theta'_{NL}(z,T)$ [3,239]:

$$\begin{aligned} \frac{\partial|u|}{\partial z} &= -\gamma'|u|^3(a_{NFK}-\frac{a_{THG}}{3})\sin\Big[2\big(\theta'(z,T)-\theta'_{NL}(z,T)\big)\Big] \\ \frac{\partial\theta'_{NL}(z,T)}{\partial z} &= \gamma'|u|^2\Big\{1+(a_{NFK}+\frac{a_{THG}}{3})\cos\Big[2\big(\theta'(z,T)-\theta'_{NL}(z,T)\big)\Big]\Big\}. \end{aligned} \tag{2.131}$$

The nonlinear phase is obtained from Eq. (2.131) using the MAPLE software. We assume that the modulus $|u|$ does not nearly vary following the propagation distance z as $\partial|u|/\partial z \sim 0$. As an approximation, this stems from the cases $a_{THG} = a_{NFK} = 0$ or $\theta'(z,T) \sim \theta'_{NL}(z,T)$ [3,239,244]. It is given by :

$$\theta'_{NL}(z,T) = 2\pi\left[\frac{cT}{\lambda_0} - z\big(dn_{Si}(\lambda)/d\lambda\big)\big|_{\lambda=\lambda_0}\right] - \arctan\left\{\frac{\Gamma\tanh\big[\Gamma(cte-z)\big]}{\rho_2}\right\}, \tag{2.132}$$

where $\Gamma$, $\rho_1$, $\Delta k$, $\rho_2$ and $cte$ are defined as : $\Gamma = (\rho_1\rho_2)^{1/2}$, $\rho_1 = \gamma'|u|^2(1 + a_{NFK} + a_{THG}/3) - \Delta k$, $\Delta k = -2\pi\big(dn_{Si}(\lambda)/d\lambda\big)\big|_{\lambda=\lambda_0}$, $\rho_2 = \gamma'|u|^2(-1 + a_{NFK} + a_{THG}/3) + \Delta k$, and an integration constant (taken here trivially to be zero), respectively. Note that the SRS and the FCA/FCD have been neglected in the analysis because of their weak role played on the SCG in silicon waveguides as discussed by Yin et al in [200]. The coefficients $a_{NFK}$ and $a_{THG}$ are two coefficients that can take the values 0 or 1, depending which nonlinear terms (between NFK and THG) one wishes to activate or not [239]. Since it is well-known that linear losses of the SOI-waveguides diminish only the intensity of the incident and propagated light [3], we do not consider them in this analysis : the system is lossless. Considering all these assumptions, the model equation solved in the SCG numerical code is given by :

$$\begin{aligned} i\frac{\partial\tilde{u}(z,\omega)}{\partial z} = -\bar{\gamma}'\exp(\hat{L}(\omega)z)F\Bigg(&\bar{u}(z,T)\big(|u(z,T)|^2 + a_{NFK}(u^*(z,T))^2\exp(2i\theta'_{NL}) \\ &+ \frac{a_{THG}}{3}(u(z,T))^2\exp(-2i\theta'_{NL})\big)\Bigg)_+ . \end{aligned} \tag{2.133}$$

The cubic nonlinearity parameter $\bar{\gamma}'$ is defined as in Eq. (2.120), nonetheless here it includes the TPA term as described in subsection 2.2.2. We use a symmetric initial condition as the unchirped sech-type pulse. The numerical simulations are done through a modified version (see the function in the appendixes) of the MATLAB code provided by Travers et al [114] with the following data of the fundamental TE mode through the lossless silicon waveguide having $W = 0.8$ $\mu$m and $H = 0.7$ $\mu$m [200]: pumping wavelength $\lambda_0 = 1550$ $nm$, length of the waveguide $L = 0.06$ m, $P_0 = 50$ $W$, $t_0 = 50$ $fs$, $\bar{\gamma}'(\lambda_0) = (24.322 + 2.5i)$ $W^{-1}m^{-1}$, $\beta_2(\lambda_0) = -0.1701$ $ps^2/m$. The HOD terms have calculated using Eq. (2.118): $\beta_3 = 0.0085$ $ps^3/m$, $\beta_4 = -4.2525 \times 10^{-4}$ $ps^4/m$, $\beta_5 = 2.1263 \times 10^{-5}$ $ps^5/m$, $\beta_6 = -1.0631 \times 10^{-6}$ $ps^6/m$, $\beta_7 = 5.3156 \times 10^{8}$ $ps^7/m$, $\beta_8 = -2.6578 \times 10^{-9}$ $ps^8/m$, $\beta_9 = 1.3289 \times 10^{-10}$ $ps^9/m$, $\beta_{10} = -6.6445 \times 10^{-12}$ $ps^{-10}/m$.

### 2.6.4 Analysis of the quality of the spectra

The coherence degree (CD) is defined by the parameter $g_{12}^{(1)}(\lambda, t_1 - t_2)$ of Eq. (1.46). Normally, we have $0 \leq |g_{12}^{(1)}(\lambda, t_1 - t_2)| \leq 1$. If this parameter is close to zero, the spectrum is incoherent and fundamentally noised. The opposite happens when it is rather close to 1. To numerically calculate the CD with the MATLAB SCG code, we just run N times the same simulations with some different random noise (for instance a Gaussian white noise) added to the initial condition such as one photon with random phase per spectral bin added to the initial pump pulse (see the appendixes "*Code for the simulation of the CD parameter*"). The N results are stored for each wavelength/frequency in order to get a 2D-plot [129].

## 2.7 Conclusion

In the end, the different analytical and numerical models were presented. Considering the pulse compression phenomenon, the MVA has been described analytically assuming both the linear and the

nonlinear cases of the compression. The ABCJS approach in the case of WDM solitons system near the ZDW has been applied on the ASC of the FWM. The PMCs were derived both in the reduced and the full models. Furthermore, for the MI mechanism, we have presented the linear stability analysis of the CW in the SOI-waveguide deriving the OFs from the MI gain relation.

Taking into account the SCG analyses, we have firstly investigated the system modeled by the GNLSE with non-Kerr terms. We have shown a novel analytical modeling of the SCG equation based on an analogy with the well-known cubic nonlinear case. Then, we have described the modeling of the SCG in $CS_2$-the LCPCF drawing its CDP in which two pumping wavelengths were chosen in order to generate continua both in the normal and the anomalous dispersion regimes. Moreover, another novel analytical modeling was done for the SOI-waveguides including both the THG and the NFK terms. We present in the last chapter of this thesis the numerical results obtained.

# Chapter 3

# Results and discussions

## 3.1 Introduction

This chapter presents the main results obtained in the thesis. The second section shows those of the linear pulse compression obtained numerically through the MVA while section 3.3 concerns the nonlinear compression based on both the symmetric and the asymmetric shapes. In section 3.4, we show the ASC numerical results and in section 3.5, both the MI gain and PTG are highlighted. Section 3.6 is devoted to waveguides modelled by the GNLSE with non-Kerr terms while section 3.7 deals with the role of the input profile asymmetry and the chirp both in the standard propagation and in the SCG of $CS_2$−LCPCF. It is presented in section 3.8, the results on the SCG in SOI-waveguides including both the THG and the NFK terms. We conclude the chapter in section 3.9.

## 3.2 On the linear compression of chirped femtosecond optical pulses under FOD : the case of Gaussian and the RC pulses

The results presented in this sub-section stem from [224]. The linear pulse compression as described by Eq. (2.44c) is numerically presented in figure 3.1, where we have plotted the contour plots of the Gaussian pulse propagation (see figure 3.1(a) and figure 3.1(b)) and the corresponding normalized amplitudes, normalized widths, chirps and phases in function of the distance of propagation z (see figures 3.1(c)-3.1(f)). The case where we respect the dispersion lengths condition of Eq. (44c) leads to pulse compression (figure 3.1(a) :$L_{GVD} = 6L_{FOD}/(1 + C_0^2)$) while the case where we ignore this condition leads to Gaussian pulse broadening (figure 3.1(b) :$L_{GVD} = 3.2L_{FOD}/(1 + C_0^2)$). Figures 3.1(c)-3.1(f) present the corresponding pulse characteristics of the propagating optical signals : the solid lines for the case of figure 3.1(a) and the dashed lines for the case of figure 3.1(b). The values of the initial width and the FOD are the same as in [30], with positive values of the chirp and GVD. We obtain a MPCP of 10.55% in the pulse compression of figure 3.1(a). It is clearly seen in figure 3.1 that when the condition on dispersion lengths is respected with the interaction between the chirp and the GVD having the same positive sign under the influence of an opposite value of the FOD, the compression is well obtained. In figure 3.2, we represent the compression condition of Eq. (2.45a) where both the FOD and the GVD have the same positive sign while the chirp is negative. In this case there is no condition on dispersion lengths. Figures 3.2(b-e) present the evolution of the pulse characteristics for this propagation.

Taking into account the case of the RC pulse, the pulse compression is obtained earlier at the beginning of the propagation in comparison to the Gaussian case, as can be depicted in figure 3.3. The condition of Eq. (2.46a) corresponds to the case where the parameters GVD, FOD and chirp

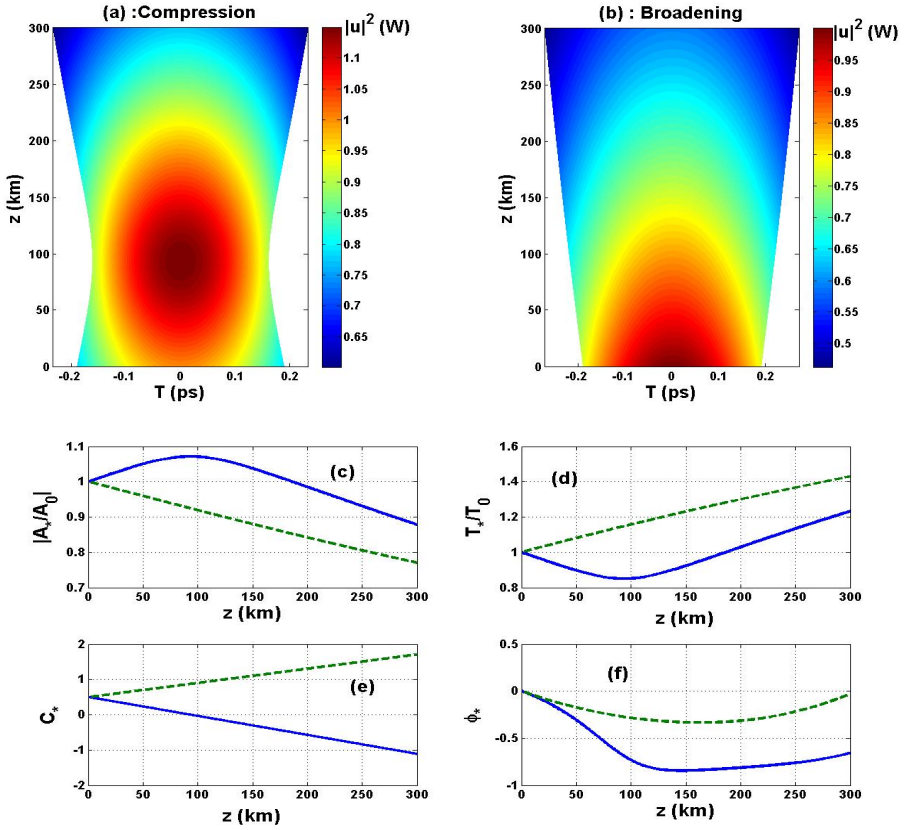


Figure 3.1: (a) Contour plot of the chirped Gaussian pulse compression of Eq. (2.44c) : assuming the dispersion lengths condition, $L_{GVD} = 120.33$ km, $L_{mc}$ =186.2075 km, MPCP=10.55 % ; (b) contour plot of the chirped Gaussian pulse broadening as expected in previous studies in the absence of verified conditions on dispersion lengths, $L_{GVD} =$ 62.78 km. For the frames (c), (d), (e) and (f) : normalized amplitude, normalized width, chirp and phase respectively (blue solid curves correspond to the case of figure 3.1(a) and green dashed curves for the case of figure 3.1(b). General parameters $\beta_4 = -0.00086\ ps^4/km$, $L_{FOD} = 24.24$ km, $T_0 = 0.38\ ps$, $T^{min} = 0.3399\ ps$, $C_0 = 0.5$.

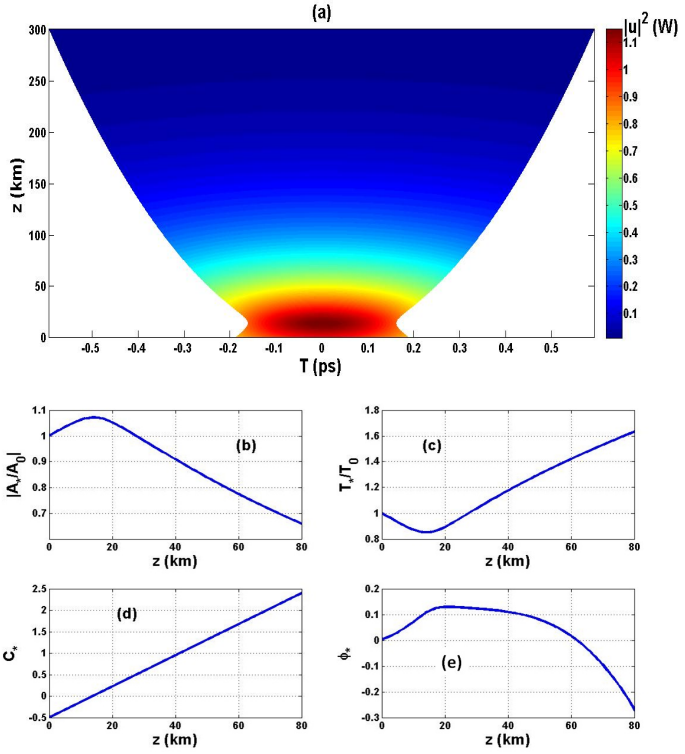


Figure 3.2: (a) Contour plot of the pulse as described by Eq. (2.45a); (b), (c), (d), (e) Evolution of the normalized pulse parameters versus the propagation distance z with parameters $\beta_4 = 0.00086\ ps^4/km$, $L_{FOD} = 24.24$ km, $T_0 = 0.38\ ps$, $T^{min} = 0.3399\ ps$, $C_0 = -0.5$, $\beta_2 = 0.0023\ ps^2/km$, $L_{mc} = 27.5863$ km.

have the same positive sign. The compression is obtained with a MPCP about 5.5767 % which is less than those obtained with the Gaussian pulse. The maximal length for the pulse compression is about 0.5041 km very far from the result obtained in figure 3.1 (about 186.2075 km) and in figure 3.2 (about 27.5863 km). Figure 3.4 presents the contour plots of the RC pulse and the evolution of its characteristics corresponding to Eq. (2.46d). In figure 3.4(a), the dispersion lengths condition is verified while in figure 3.4(b) it is ignored. Figures 3.4(b-e) present the RC pulse characteristics evolution versus z.

Recalling that the present study of dynamics of linear compression involves the GVD, the chirp and the FOD, it is important to point out that these results could be generalized to the $n^{th}-$order even dispersion terms. Our obtained results present a general description of the interaction between the chirp, the GVD and the FOD. The results recover and complete some aspects of results on pulse compression previously obtained in literature. Taking into account another type of optical light pulse, namely the raised-cosine pulse, we have obtained interesting features as concerned the dynamical behavior of the propagating pulse which are not particularly related to the major results obtained when dealing with the Gaussian pulse. For example, it comes that even when the interacting dispersion parameters and the chirp have the same sign, the pulse compression is obtained. Therefore, the description of the broadening/compression pulse is greatly dependent on the considered optical pulse.

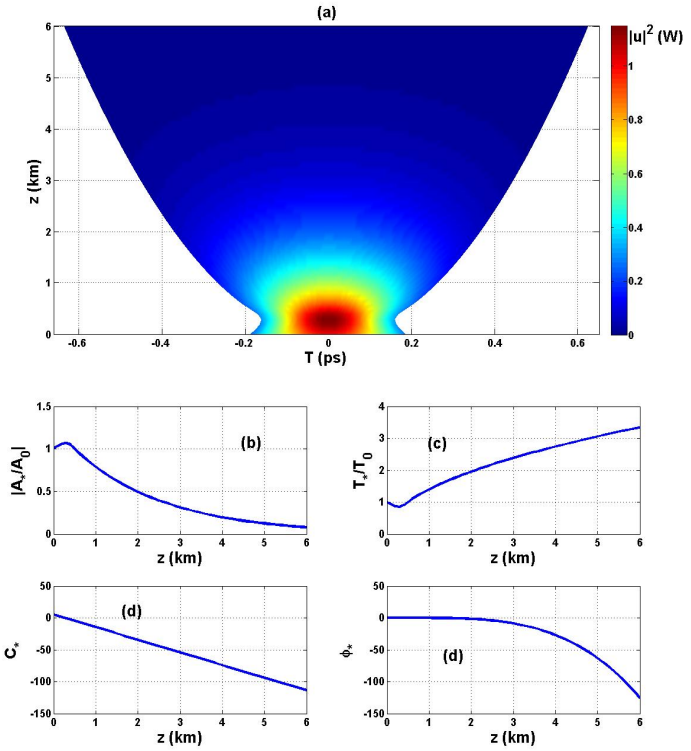


Figure 3.3: (a) Contour plot of the pulse as described by Eq. (2.46a); (b), (c), (d), (e) Evolution of the normalized pulse parameters versus the propagation distance z with parameters $\beta_4 = 0.00086\ ps^4/km$, $L_{FOD} = 24.24$ km, $T_0 = 0.38\ ps$, $T^{min} = 0.3588\ ps$, $C_0 = 5$, $\beta_2 = 0.0113\ ps^2/km$, MPCP=5.5767 %, $L_{mc} = 0.5041$ km.

## 3.3 On the nonlinear compression in SOI-waveguides under FOD

### 3.3.1 Case of compact and symmetric chirped femtosecond pulses : Gaussian, sech-type and RC pulses

The results presented in this sub-section stem from [225,246].

#### Periodic compression of femtosecond pulses in SOI-waveguide under FOD and SPM

In this sub-section, Taking Eqs. (2.65)-(2.67) we set $\gamma \neq 0$, $\Gamma = 0$, $\Lambda = \sigma N_c = 0$. We may integrate these growth equations by using the fourth-order Runge-Kutta integration scheme. It is well-known that the balanced interaction between SPM and GVD should lead to the solitonic properties of pulse propagation inside an optical medium [1,3,33,171,172,176], the solitonic features appearance being drawn within the soliton-order defined by $N^2 = L_{GVD}/L_{NL}$ where $L_{NL} = 1/\gamma P_0$. So, normally as well-known in silica optical fibers for the anomalous-GVD regime, each input pulse may lead to a solitonic form of the fundamental soliton for $N = 1$, and higher-order solitons (HOSs) for $N \geq 2$ [1,3,33,171,172,176]. However the combination of SPM effects and normal-GVD ($\beta_2 > 0$) could be used for pulse compression [3].
The HOSs have an interesting feature which is described as a periodic evolution following the distance $z$ of propagation. This property is understood within a periodic compression shaping at each times

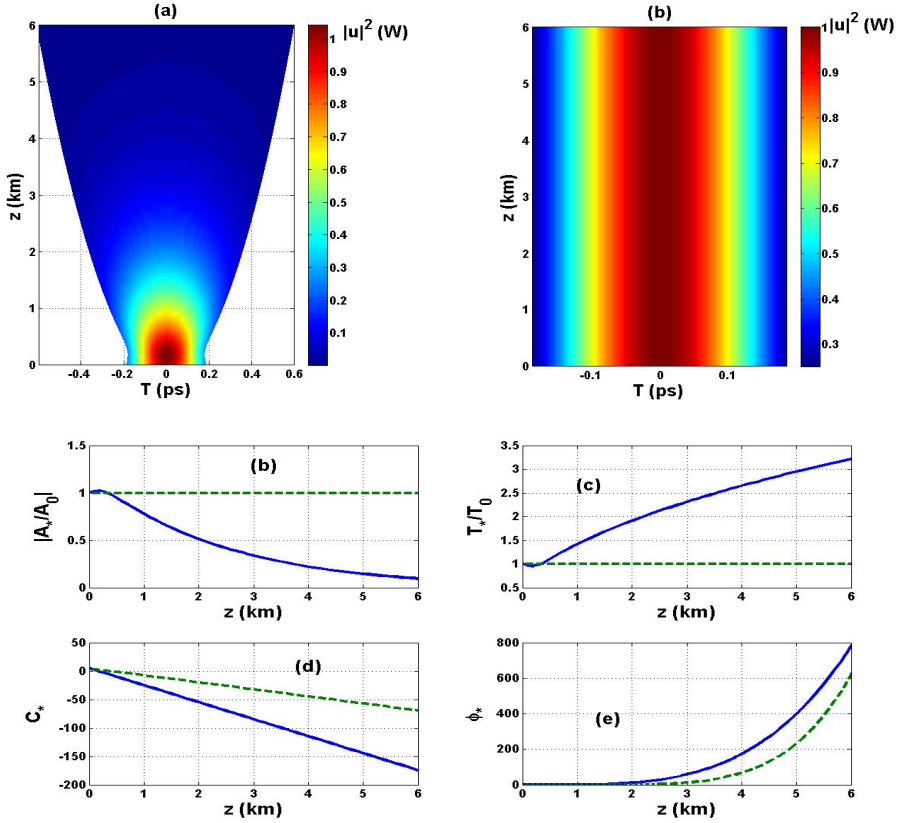


Figure 3.4: (a) Contour plot of the chirped RC pulse compression of Eq. (2.46d) : assuming the dispersion lengths condition, $L_{GVD} = 5.328$ km, $L_{mc}$ =0.3346 km, $T^{min} = 0.3725$ ps, MPCP=1.9798 % ; (b) contour plot of the chirped RC pulse in the absence of the verified condition on dispersion lengths, $L_{GVD} = 62.78$ km. For the frames (c), (d), (e) and (f) : normalized amplitude, normalized width, chirp and phase respectively (blue solid curves correspond to the case of figure 3.4(a) and green dashed curves for the case of figure 3.4(b). General parameters : $\beta_4 = -0.00086\, ps^4/km$, $L_{FOD} = 24.24\ km$, $T_0 = 0.38$ ps, $C_0 = 5$.

the solitonic profile [3,33]. Using a dimensionless definition of the propagation distance $\xi = z/L_{GVD}$, it is defined the soliton period [3] :

$$z_0 = \frac{\pi}{2} L_{GVD} \tag{3.1}$$

For HOSs with $N \geq 2$, the propagation inside the standard single-mode silica optical fibers leads generally to pulse splitting in many sub-pulses [1,3,33,171,172,176]. When N is not too large, for example $N = 3$, the splitting is made between two solitonic compression by recovering the original shape at the end of the soliton period. However, for large values of N, the propagation leads generally to pulse train generation via the modulational instability (MI) mechanism [189]. More recently, a higher-order MI soliton demonstrated the pulse train generation process [191]. The understanding of the periodic compression of HOSs is nowadays based over an interplay between the SPM and GVD effects [3].

The aim of this subsection, is to evaluate the periodic compression in SOI-waveguide from the previous input pulses in the femtosecond region via the interplay between the SPM and the FOD instead of the GVD. The regime of GVD for the achievement of this periodic compression is surprisingly normal while the SPM coefficient of Kerr nonlinearity is also positive. The chosen parameters that allow the periodic compression are $P_0 = 4.76\ W$, $\gamma = 47\ W^{-1}m^{-1}$, $\alpha = 5.06\ m^{-1}$, $t_{pulse}(0) = 50\ fs$ and $\beta_2 = 0.56\ ps^2/m$ [8]. For the parameter N, we have $N = 0.99 \approx 1$. Normally, if a single-mode silica fiber is considered in the anomalous-GVD and the FOD effect ignored ($\beta_4 = 0$), each input pulse should reshape its profile into a fundamental soliton profile while propagating inside the medium even in the presence of a small initial chirp [3,33]. Indeed, it is known that the source chirp is detrimental for soliton formation because it may disturb the exact balance between GVD and SPM [3]. We obtain rather with the given SOI-waveguide, the periodic compression induced by the balance between SPM and FOD effects instead of GVD, for the quasi-fundamental soliton order ($N \approx 1$). This interesting feature is depicted in figure 3.5. To see how pulses propagate under the conditions of figure 3.5, the

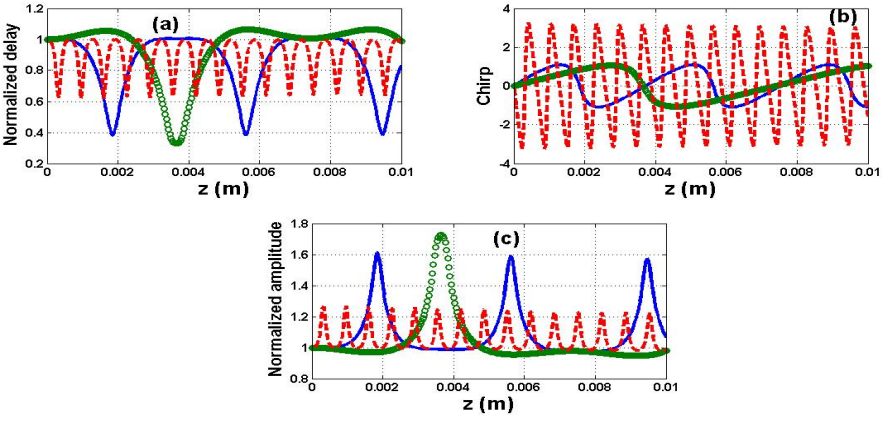


Figure 3.5: Plot of pulse characteristics, solid lines for the Gaussian pulse, circle lines for the sech-type pulse and dotted lines for the RC pulse. Parameters for each pulse $\Gamma = 0$, $\Lambda = 0$, $C_0 = 0$, SOI-waveguide length L=1 cm. Specifics results for the Gaussian pulse : $\beta_4 = -0.0051\ ps^4/m$, first peak at $z_{init} \approx 0.0019\ m$, first maximum pulse compression percentage ($MPCP$) = 61.77 %, $z_0 \approx 0.0038\ m$. Specifics results for the sech-type pulse : $\beta_4 = -0.0039\ ps^4/m$, first peak at $z_{init} \approx 0.0036\ m$, first $MPCP = 67.03$ %, $z_0 \approx 0.0075\ m$. Specifics results for the RC pulse : $\beta_4 = -0.005\ ps^4/m$, first peak at $z_{init} \approx 3.636 \times 10^{-4} m$, first $MPCP = 37.95$ %, $z_0 \approx 6.360 \times 10^{-4} m$.

illustration of their intensities and spectra propagation is done in figure 3.6 which is obtained with the convenient fourth-order Runge-Kutta scheme and the common split-step Fourier algorithm. The quantities $z_{init}$ and $z_0$ represent the initial distance at which the first compression peak is observed

and the compression spacing (spatial period), respectively. The losses were included and obviously reduce the energy of the pulses following the distance of propagation. As can be seen in figure 3.5

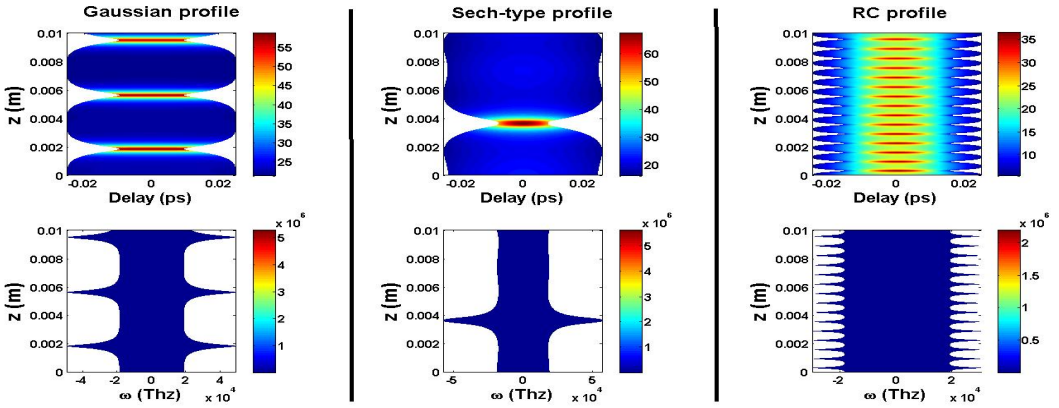


Figure 3.6: Contour plots of pulses propagation under the conditions presented in figure 3.5 : at the left-side Gaussian profile, at the middle sech-type profile and at the right-side RC profile. For each frame, at the top : intensity propagation, at the bottom : spectral propagation.

and figure 3.6, the periodic compression depends on the input pulse profile. The compression period of the sech-type pulse is greater than that of the Gaussian profile which is greater than the one of the RC profile. To explain this difference, we suggest that since the two first profiles are close to each other, they will behave nearly similarly despite some small discrepancies, while the RC profile is a periodic function in contrast to the others. It is worthy to notice that its behavior will be far different from the others which are not periodic. It is assumed that only one period of the temporal profile of this pulse is used in the dynamics. This characteristic leads the RC profile to behave differently in comparison to the other pulses which vanish intrinsically beyond the main peak. Furthermore, with the same pulse duration $t_0$, both the Gaussian and the sech-type profiles have full-widths at the half maximum intensity (respectively $t_{FWHM}^{Gauss} = 1.665t_0$ and $t_{FWHM}^{sech} = 1.763t_0$) which are nearly equal while the one of the RC pulse is approximately the half of these ones ($t_{FWHM}^{RC} = 0.728t_0$) [3,10]. Thus, its compression period is expected to be the smallest one as can be observed on figures 3.5 and 3.6. This result contrasts with the one previously mentioned about silica SMFs where the periodic compression was only obtained for HOSs, induced by the interplay between GVD and SPM. However as presented in figure 3.5 and figure 3.6, we observe that, the periodic compression not only depends on input pulse profile, but also can be obtained through the interplay of FOD and SPM in a normal-GVD regime.

We observe a pulse amplification associated to the periodic compression mechanism, with a slight reduction of pulse energy due to the losses : see for instance the blue curve of the Gaussian pulse in figure 3.5(c). Indeed, one can see that the last compression peak is smaller than the two firsts highlighting therefore the effect of the linear losses. This happens also for both the sech-type and the RC pulse for long propagation distances. It merges therefore that, for high values of losses, the compression peaks are more and more reduced (as concerned the amplitude) or more and more broadened (as concerned the temporal width). The chirp also oscillates for each pulse and the compression peaks of the amplitude (or the width) appear only at $C_{pulse}(kz_0) = 0$, k being a nonzero integer.

**Influence of the dispersion regime on the periodic compression : normal dispersion regime ($\beta_2 > 0$ and $\beta_4 < 0$) or ($\beta_2 > 0$ and $\beta_4 > 0$)**

Considering the figures 3.5 and 3.6, we remind the reader that the dispersion regime is normal according to the GVD. It corresponds to the case where we have $\beta_2 > 0$ and $\beta_4 < 0$. So, the periodicity introduced by the FOD and SPM can be linked to the values of the FOD length for each pulse following the relation $L_{FOD} = t_0^4/|\beta_4|$ (with $t_{pulse}(0) \equiv t_0$). For the Gaussian pulse, we have $L_{FOD} = (4/15)L_{NL}$. For the sech-type pulse, the relation between the nonlinear length and the FOD length is : $L_{FOD} = (16/45)L_{NL}$ while for the RC profile we have $L_{FOD} = (13/45)L_{NL}$. One should also notice that the periodic compression is obtained with the negative value of the FOD and the positive value of the SPM. If the choice of a positive value of the FOD is done while we remain

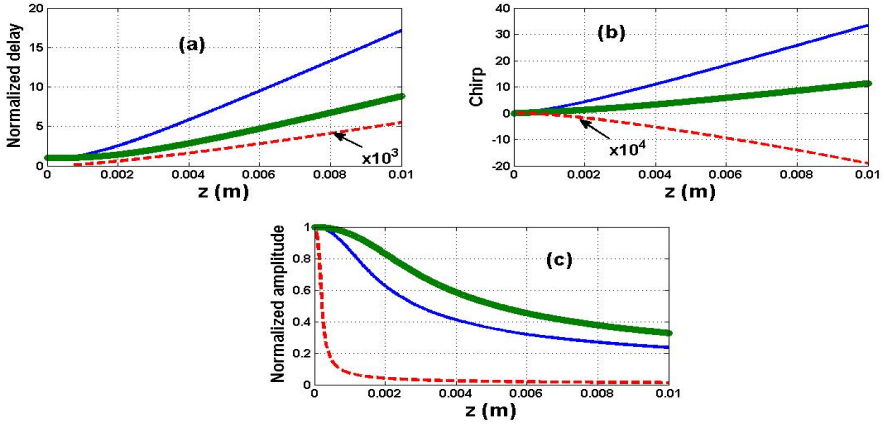


Figure 3.7: Plot of pulse characteristics, solid lines for the Gaussian pulse, circle lines for the sech-type pulse and dotted lines for the RC pulse. Parameters for each pulse $\Gamma = 0$, $\Lambda = 0$, $C = 0$, $\beta_2 = 0.56\ ps^2/m$ length L=1 cm. For the Gaussian pulse : $\beta_4 = 0.0051\ ps^4/m$. For the sech-type pulse : $\beta_4 = 0.0039\ ps^4/m$. For the RC pulse : $\beta_4 = 0.005\ ps^4/m$, the normalized delay plotted is multiplied by $10^3$ (see the red dashed curve in (a)) while the chirp is multiplied by $10^4$ (see the red dashed curve in (b)).

in the case of the normal dispersion regime (according to the GVD), the periodicity disappears as expected (see figure 3.7) [3]. It corresponds to the case where we have $\beta_2 > 0$ and $\beta_4 > 0$. As can be seen in this figure, the chirp is initially equal to zero for each pulse. With the disappearance of the periodicity, one obtains the pulse broadening. This process is more stressed for the RC pulse (see the red dashed lines in figure 3.7) than that of the other pulses.

**Influence of the dispersion regime on the periodic compression : anomalous dispersion regime ($\beta_2 < 0$ and $\beta_4 < 0$) or ($\beta_2 < 0$ and $\beta_4 > 0$)**

We plot in figure 3.8 the case where both the GVD and the FOD are negatives ($\beta_2 < 0$ and $\beta_4 < 0$). As can be observed, the periodic compression also occurs under these conditions. Nevertheless, this phenomenon is less important than that of figures 3.5 and 3.6. Indeed the MPCP for each pulse and the compression spatial period decrease. The illustration of this observation is presented in table 3.1 showing a comparison between the results obtained under the conditions $\beta_2 > 0$, $\beta_4 < 0$ (Fig.(3.5)) and $\beta_2 < 0$, $\beta_4 < 0$ (Fig.(3.8)). The main aspect coming from table 3.1, is the decrease of the MPCP for each pulse from results of figure 3.5 to those of figure 3.8. It is a surprising result when one considers the negatives values of the GVD and the FOD. Normally, one should expect that both the two dispersion orders act together in a cooperative manner to improve the periodic compression and therefore rather to increase the MPCP. Nonetheless, we observe the opposite feature. Note that

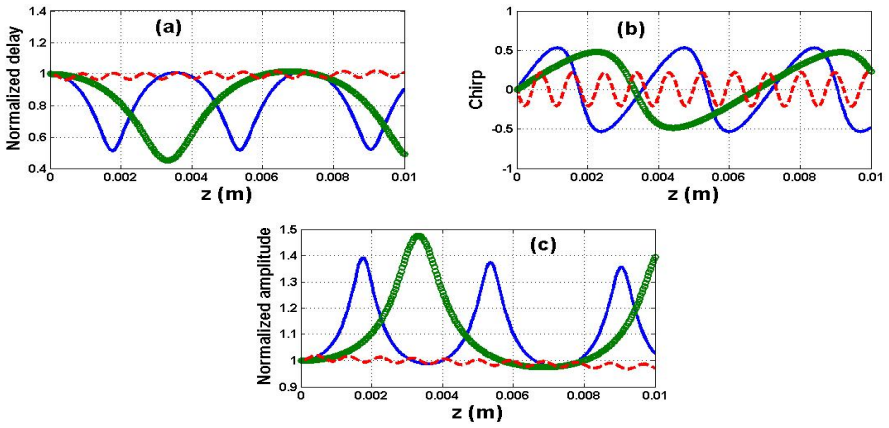


Figure 3.8: Plot of pulse characteristics, solid lines for the Gaussian pulse, circle lines for the sech-type pulse and dotted lines for the RC pulse. Parameters for each pulse $\Gamma = 0$, $\Lambda = 0$, $C = 0$, $\beta_2 = -0.56\ ps^2/m$, length L=1 cm. Specifics results for the Gaussian pulse : $\beta_4 = -0.0051\ ps^4/m$, first peak at $z_{init} \approx 0.00175\ m$, first maximum pulse compression percentage $(MPCP) = 48.84\ \%$, $z_0 \approx 0.0035\ m$. Specifics results for the sech-type pulse : $\beta_4 = -0.0039\ ps^4/m$, first peak at $z_{init} \approx 0.00325\ m$, first $MPCP = 54.86\ \%$, $z_0 \approx 0.006875\ m$. Specifics results for the RC pulse : $\beta_4 = -0.005\ ps^4/m$, first peak at $z_{init} \approx 4.375 \times 10^{-4} m$, first $MPCP = 3.91\ \%$, $z_0 \approx 8.75 \times 10^{-4} m$.

| Item | Figure 3.5 | Figure 3.8 |
|---|---|---|
| $z_{init}/z_0$ of the Gaussian profile | 0.0019 m/0.0038 m | 0.00175 m/0.0035 m |
| $z_{init}/z_0$ of the sech-type profile | 0.0036 m/0.0075 m | 0.00325 m/0.006875 m |
| $z_{init}/z_0$ of the RC profile | $3.636\times10^{-4}$ m/$6.36\times10^{-4}$ m | $4.375\times10^{-4}$ m/$8.75\times10^{-4}$ m |
| MPCP of the Gaussian profile | 61.77% | 48.84% |
| MPCP of the sech-type profile | 67.03% | 54.86% |
| MPCP of the RC profile | 37.95% | 3.91% |

Table 3.1: Comparison of results obtained in the figures 3.5 and 3.8 for each unchirped pulse. One can read as : the first item before the division symbol "/" corresponds in the same line to values before this symbol and the same procedure is done for the item behind the same symbol. For instance, for the first item "Gaussian pulse", $z_{init}$ corresponds to 0.0019 m and 0.00175 m while $z_0$ to 0.0038 m and 0.0035 m.

the parameters $z_{init}$ and $z_0$ increase for the RC from figure 3.5 to figure 3.8 in contrast to what happens to the other pulses. It is obvious that this specific feature is linked to the peculiarity of the RC pulse to be periodic and to have a small FWHM. It is highlighted in figure 3.9 where the results obtained for the sech-type pulse are plotted in the two cases. We suggest that, comparatively

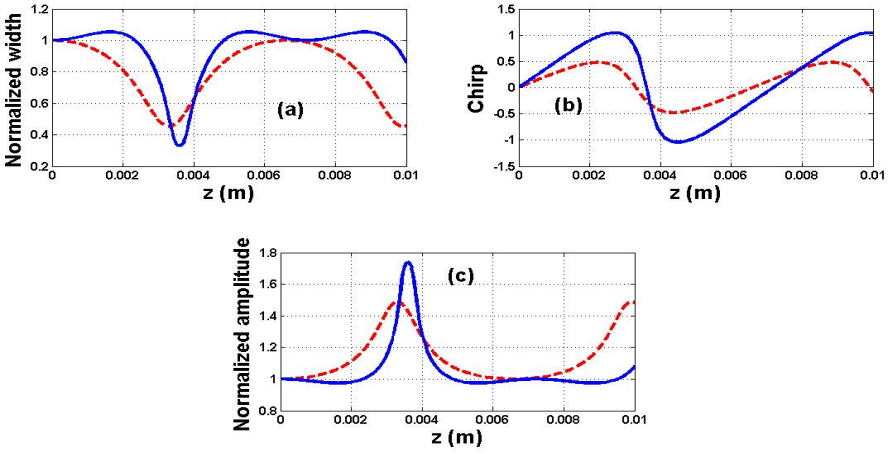


Figure 3.9: Comparison of the anomalous GVD case (red dashed curves) and the normal GVD case (blue solid curves) for the sech-type pulse : the periodic compression is enhanced in the normal GVD case. Simulation conditions are the same as in figures 3.5 and 3.8.

to the figure 3.5, the action of the anomalous GVD is in opposition with the one of the FOD, and then leads to a reduction of the periodic compression. One notices that the RC profile has its $z_{init}$ and $z_0$ which increase on contrary to what happens to the other profiles. This feature underlines the main difference between this realistic input profile and the others. For a parametric study, we

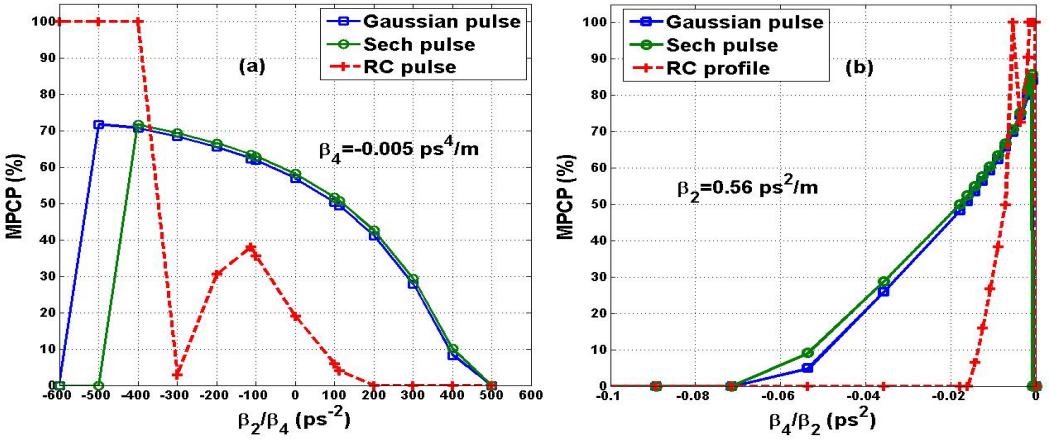


Figure 3.10: GVD and FOD managements to control the periodic compression : (a) MPCP versus the varying ratio $\beta_2/\beta_4$ with a constant negative value of FOD $-0.005\ ps^4/m$, (b) MPCP versus the varying ratio $\beta_4/\beta_2$ with a constant positive value of GVD $0.56\ ps^2/m$.

present in figure 3.10 how a management of the GVD and the FOD values can be done in order to control the periodic compression. This analysis is done by calculating the MPCP in the cases where both the GVD and the FOD vary. The range of values considered for both the GVD and the FOD is extended in order to include the realistic conditions. In figure 3.10(a), with a constant negative

| Item | Chirp | $z_{init}$ | $z_0$ | MPCP |
|---|---|---|---|---|
| Gaussian profile | 1 / 1.5 | $9.09\times10^{-4}$ m / $5.9\times10^{-4}$ m | 0.00409 m / 0.0059 m | 62.24% / 63.45% |
| Sech-type profile | 1 / 1.5 | 0.0127 m / $6.363\times10^{-4}$ m | 0.00754 m / 0.01467 m | 67.14% / 69.38% |
| RC profile | 1 / 1.5 | $3.63\times10^{-4}$ m/$3.78\times10^{-4}$ m | $6.363\times10^{-4}$ m / $6.48\times10^{-4}$ m | 38.45% / 38.88% |

Table 3.2: Comparison of results obtained with different positive values of chirp

| Item | Chirp | $z_{init}$ | $z_0$ | MPCP |
|---|---|---|---|---|
| Gaussian profile | -1 / -1.5 | 0.003 m / 0.00527 m | 0.00418 m / 0.00609 m | 62.14% / 63.16% |
| Sech-type profile | -1 / -1.5 | 0.006 m / 0.0328 m | 0.00756 m / 0.033 m | 66.9% / 67.95% |
| RC profile | -1 / -1.5 | $2.727\times10^{-4}$ m/$2.727\times10^{-4}$ m | $6.363\times10^{-4}$ m / $6.363\times10^{-4}$ m | 38.5% / 39.12% |

Table 3.3: Comparison of results obtained with different negative values of chirp

value of FOD generating the periodic compression, this latter decreases with the decrease of the GVD from the normal to the anomalous dispersion regime. We notice the special behavior of the RC pulse for the values between 3 $ps^2/m$ to 0.5 $ps^2/m$. However, the opposite feature arises for a constant positive value of GVD while the FOD varies. Indeed, as can observed in figure 3.10(b), the periodic compression phenomenon is performed by the increase of the FOD value from $-0.03$ $ps^4/m$ to $-5\times10^{-4}$ $ps^4/m$ for all the pulses. Obviously, the RC pulse still has a special behavior for the range between $-10^{-4}$ $ps^4/m$ to 0. Considering these results, the best case in which we have a highest MPCP, corresponds to the one for which a large value of FOD ($-5\times10^{-4}$ $ps^4/m$) is reached in the normal GVD regime (0.56 $ps^2/m$). The interaction that generates the periodic compression corresponds to the interplay between the negative FOD and the positive SPM. The action of the anomalous GVD is in opposition with the one of the FOD, and decreases the periodic compression phenomenon while the normal GVD is rather beneficial.

### Influence of the initial chirp on the periodic compression

As discussed earlier in [1,3], the chirp should disturb the nonlinear periodic compression phenomenon while it could lead to linear pulse compression when it is opposite to the GVD. So, introducing a small positive value of the initial chirp ($C_0 = 1$) associated with the conditions ($\beta_2 > 0$, $\beta_4 < 0$) of figure 3.5, leads to table 3.2. The main observation done concerns the beneficial effect of the positive value of the initial chirp on the periodic compression. In fact, both the MPCP and the spatial period increase for all the pulses under the effect of the positive chirp. Therefore, the periodic compression phenomenon is enhanced. However, using a relative high value as $C_0 = 2$ yields the opposite result such as the destruction of the periodicity leading rather to pulse broadening for the sech-type and the Gaussian profiles while the RC pulse still keeps its periodic compression (see figure 3.11). Numerical simulation of a high value as $C_0 = 5$, destroys the periodic compression of the RC profile. This latter needs therefore large values of positive chirp under the considered dispersion regime, for the disappearance of its periodic compression in comparison to the other input pulses.
Considering the negative values of chirp, one obtains for instance the table 3.3. As seen in this table, the negative value of chirp also enhances the periodic compression obtained under the dispersion regime of figure 3.5. It also comes that large negative values of chirp destroy the periodicity. So, one can suggest that in general the small absolute values (AVs) of chirp enhances the periodic compression induced by the interplay between the FOD and the SPM while large AVs of chirp destroy the periodicity and leads to pulse broadening. This happens when the dispersion regime is normal following the GVD, with FOD$\times$SPM$<$0. In the next subsection, we study the influence of nonlinear parameters as the TPA and the FCA on the periodic compression process.

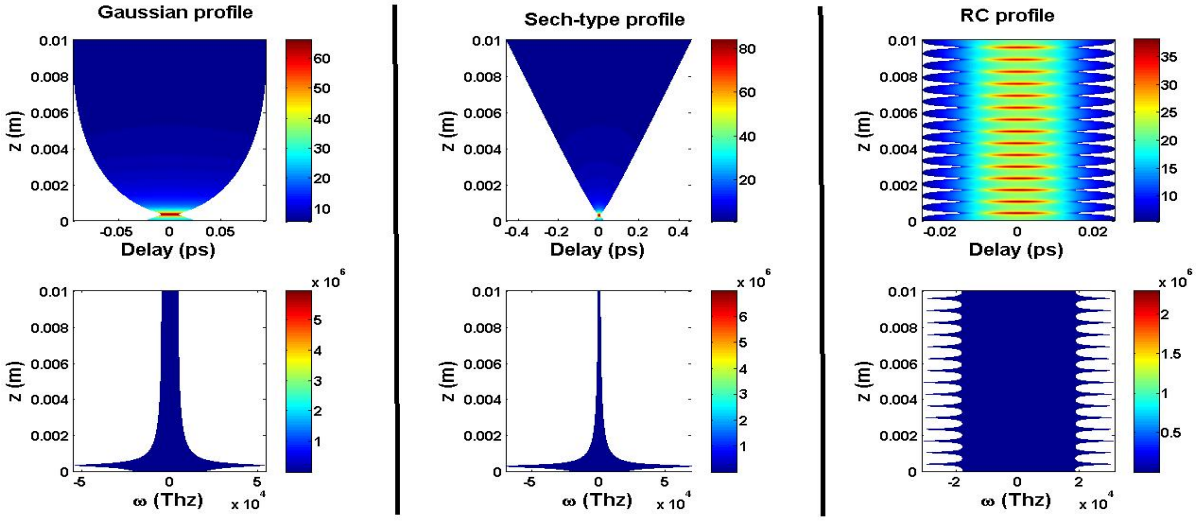


Figure 3.11: Contour plots of pulses propagation under the conditions presented in figure 3.5 with $C_0 = 2$ : at the left-side Gaussian profile, at the middle sech-type profile and at the right-side RC profile. For each frame, at the top : intensity propagation, at the bottom : spectral propagation.

### Influence of absorption coefficients on the periodic compression

In this section, the parameters are given as $\Gamma \neq 0$, $\Lambda \neq 0$, $\gamma \neq 0$. Concerning the TPA phenomenon, it was first reported experimentally by Kaiser and Garrett [226]. Multiphoton absorption phenomenon can lead to laser damage of optical materials and can be used to write permanent refractive index structures into the interior of optical materials [83]. Therefore, the multiphoton absorption is well-known to be a nonlinear loss phenomenon that can reduce the efficiency of nonlinear optical devices such as optical switches. It is known that the TPA reduces the compression factor [212].
However in the present work, we find that a small value of TPA (for instance 0.5 $W^{-1}m^{-1}$) destroys progressively the periodic compression. The spatial period is increased following the propagation distance for each pulse. As presented in figure 3.12, the effect of the small value of TPA on input

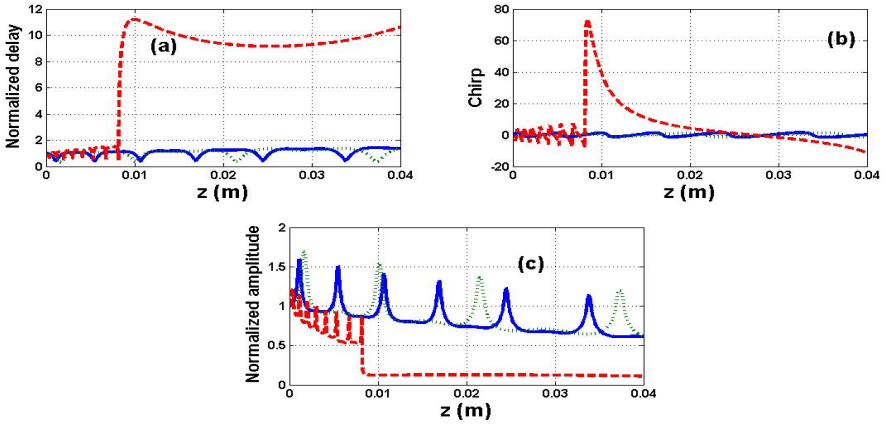


Figure 3.12: Plot of pulse characteristics, solid lines for the Gaussian, dotted lines for the sech-type pulse and dashed lines for the RC pulse. Parameters for each input pulse $C_0$=0.8, $\Gamma = 0.5\ W^{-1}m^{-1}$, $\sigma = 1.45 \times 10^{-21}\ m^2$, SOI-waveguide length L=4 cm. The other parameters are similar to those of figure 3.5.

pulse can be therefore understood as a destruction of the periodicity in the compression process

induced by the interplay between FOD and SPM.
A relative high value of TPA as 6.5 $W^{-1}m^{-1}$ as taken in [8], leads to the whole periodic compression destruction (see figure 3.13) where the effect of FCA was also included. It is observed in these figures that the large values of TPA combined to the FCA lead to pulse broadening inside the SOI-waveguide. Nonetheless, under the considered conditions, one notices at least one peak of amplification linked

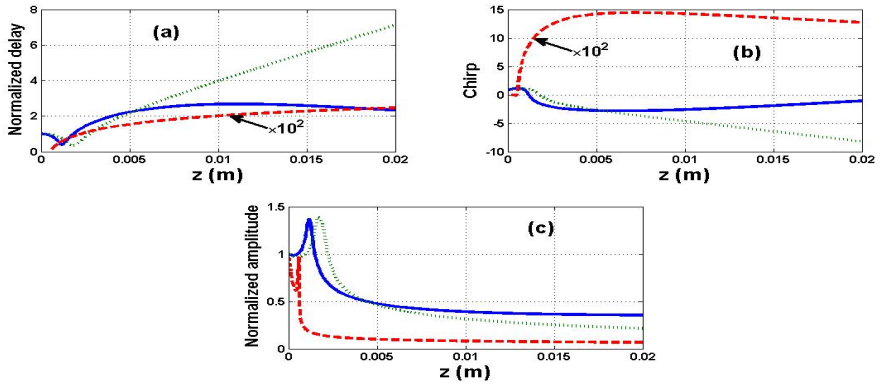


Figure 3.13: Plot of pulse characteristics, solid lines for the Gaussian, dotted lines for the sech-type pulse and dashed lines for the RC pulse. Parameters for each input pulse $C_0$=0.8, $\Gamma = 6.5\ w^{-1}m^{-1}$, $\sigma = 1.45\times10^{-21}\ m^2$, SOI-waveguide length L=2 cm. The other parameters are similar to those of figure 3.5.

to a pulse compression before the broadening. This happens for the RC at a distance smaller than that of the Gaussian pulse while the sech-type pulse is the last.

### 3.3.2 Case of SHAPs

The results presented in this sub-section stem from [227,247].

#### Linear compression

The values of the parameters used in numerical simulations are defined as [8] : the waveguide length L=4 cm - 5 cm, the linear losses $\alpha = 5.06\ m^{-1}$, the initial peak power $P_0$ =4.76 W, the TPA coefficient $\Gamma = 6.5\ W^{-1}m^{-1}$, the GVD $\beta_2 = 0.56\ ps^2m^{-1}$, the FOD $\beta_4 = -1.2843\ ps^4m^{-1}$, the FCD-FCA associated coefficient $\kappa = 5\ W^{-4}ps^{-1}m^{-1}$, the initial chirp $C_0$ =0.8, the SPM coefficient $\gamma = 47\ W^{-1}m^{-1}$, the pulse width $t_0$ =50 fs
and the wavelength $\lambda_0 = 1550$ nm, respectively.
We represent in figure 3.14 the pulse compression under the third condition of Eq. (2.76). The FOD parameter is obtained by setting that $L_{FOD} = 0.96b$ where $b = V_2L_{GVD}$. This may be obtained from a realistic value of the FOD $\beta_4$ and for the numerical simulations, we show how the obtained compression conditions work. It is convenient to choose an approximated realistic value of the FOD which verifies the third compression condition of Eq. (2.76) for example. We have chosen to draw the analytical result (see the solid line in figure 3.14(a) and figure 3.14(b)) with the numerical result obtained with a fourth-order Runge-Kutta integration scheme (see the dashed line in figure 3.14(a) and figure 3.14(c)). The analytical result here is based on Eq. (2.72) and the numerical result comes from the direct integration of the growth equation of the width in Eq. (2.71). Considering the obtained pictures, it comes that the quasi-spectral assumption that governs the analytical result can approximately satisfy the pulse compression in the linear case because the difference between the two results is not enough important for the small distances of propagation. Therefore, the assumption

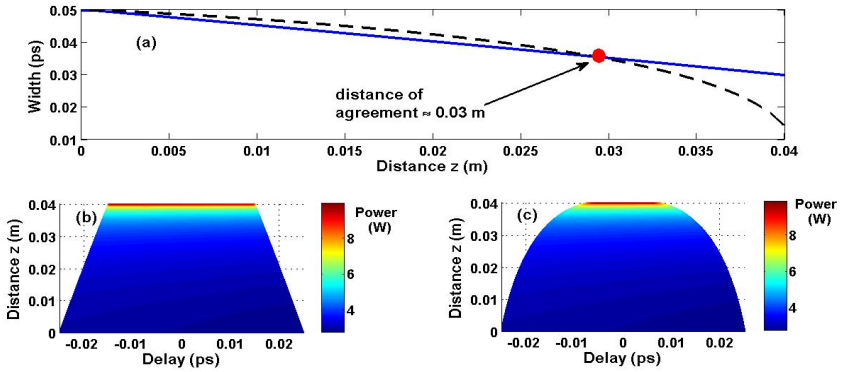


Figure 3.14: (a) Solid line for the analytical result of the width and dashed line for the numerical result versus z, (b) contour plot of the Airy pulse propagation for the analytical result and (c) contour plot of the Airy pulse propagation for the numerical result. The peak power $P_0 = 4.76$ W, $\beta_2 = 0.56\ ps^2/m$, $C_0 = 0.8$, $\alpha = 5.06\ m^{-1}$, $\beta_4 = -1.2843 \times 10^{-5}\ ps^4/m$ and SOI-waveguide length L=0.04 m.

of a spectral bandwidth approximately constant during the propagation inside the linear medium leads to admit the compression factor given in Eq. (2.72) only for short distance. It is certainly sure that Eq. (2.71) and Eq. (2.72) will diverge for a long distance of propagation. As noticed in figure 3.14, the critical distance of agreement that emerges from the simulations done is about 3 cm. The MVA being validated to be a good mean to study short pulse propagation within SOI-waveguides [8], translates cleanly in figure 3.14 the linear approximation of the waveguide dynamics.
Beyond this notice, the main feature observed here is the fact that this compression is obtained with $\beta_2 C_0 > 0$ and $\beta_2 \beta_4 < 0$. As the others conditions defined in Eq. (2.76), these results are entirely in agreement with those previously discussed in [31] while the fact that the chirp is similarly signed like the GVD contrasts with the basic admitted theory of linear compression induced by chirp with grating pairs [1,3]. The figure 3.14(b) is the contour plot of the Airy pulse for the analytical result of Eq. (2.72) and Fig. (3.14c) is the contour plot of the Airy pulse for the numerical simulation of Eq. (2.71). These figures correspond to the pulse propagation within the SOI-waveguide under the conditions defined in the linear approximation and respecting the third compression condition of Eq. (2.76). For this figure and for the followers, the scale bar is in unit of power (W) and indicates the power reached in the compression process following the distance of propagation.
Now it is convenient to analyze what happens when the nonlinear effects are considered.

## Nonlinear compression of SHAP in SOI-waveguide under FOD

Let us start firstly with the linear model that we integrate over a SOI-waveguide length about 5 cm, thus we obtain the figure 3.15. In figure 3.15, the parameters $\gamma$, $\Gamma$ and $\kappa$ ($\sigma$) are still zero. It is observed that the pulse compression really extents until a distance of propagation about 0.0409 m, after comes the pulse broadening. At this distance, one obtains obviously the maximal pulse power and compression before the broadening.
The process of the temporal compression has a peculiarity in the sense that, it is accompanied with an amplification of the pulse. The power/amplitude of the pulse amplifies during the compression process. The maximal power reached (MPR) in the compression process occurs at a distance as seen in figure 3.15 and it can be observed in the scale bar to see the corresponding value. The broadening of the Airy pulse occurs just beyond this point and is dramatically extreme as seen on the figure.
When the CKN effect is taken into account, the figure 3.16 is obtained. We can see in this picture a similar behavior as in figure 3.15, it means a pulse compression over a distance of propagation followed

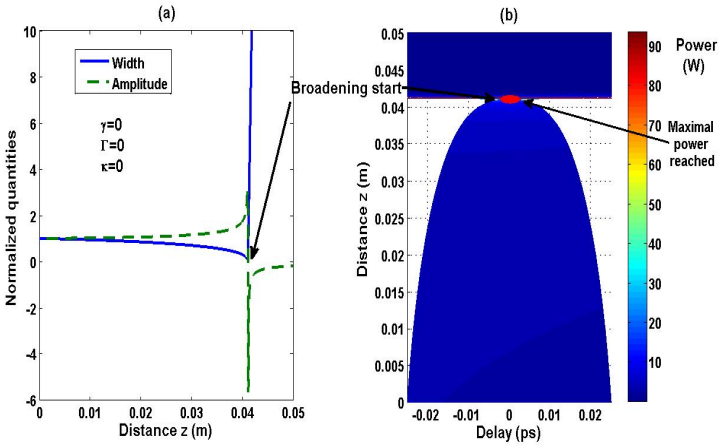


Figure 3.15: (a) Plot of the normalized width (solid line) and the normalized amplitude (dashed line) versus z. (b) Contour plot of the Airy pulse propagation. The peak power $P_0 = 4.76$ W, $\beta_2 = 0.56\ ps^2/m$, $C_0 = 0.8$, $\alpha = 5.06\ m^{-1}$, $\beta_4 = -1.2843 \times 10^{-5}\ ps^4/m$, $\gamma = 0$, $\Gamma = 0$ and $\kappa = 0$, SOI-waveguide length L=0.05 m.

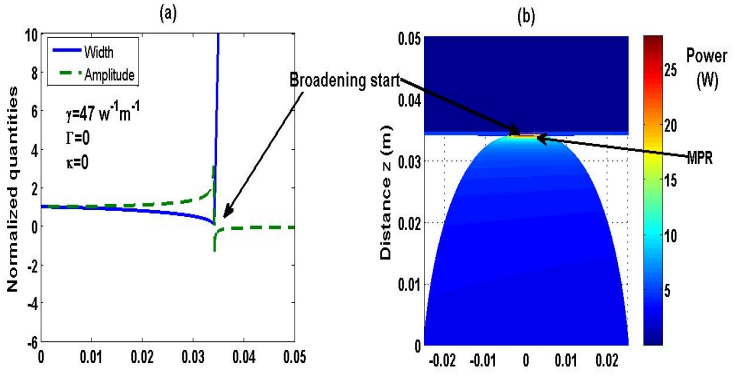


Figure 3.16: (a) Plot of the normalized width (solid line) and the normalized amplitude (dashed line) versus z. (b) Contour plot of the Airy pulse propagation. The peak power $P_0 = 4.76$ W, $\beta_2 = 0.56\ ps^2/m$, $C_0 = 0.8$, $\alpha = 5.06\ m^{-1}$, $\beta_4 = -1.2843 \times 10^{-5}\ ps^4/m$, $\gamma = 47\ W^{-1}m^{-1}$, $\Gamma = 0$ and $\kappa = 0$, SOI-waveguide length L=0.05 m.

by the pulse broadening. However, the change brought by the CKN indicates a clean reduction of the length of compression before the broadening. Indeed the pulse compression extends in this case only over 0.0340 m. Another point that must be raised, is the MPR (in the compression mechanism) which is also reduced due to the effect of $\gamma$ in combination with the negative value of the FOD. Contrary to the previous case depicted in figure 3.15 ($P_{max} \approx 90W$), the MPR $P_{max}$ here is slightly beyond 25 W only.

The consideration of the TPA inside the dynamics studied in this sub-section as the single nonlinear

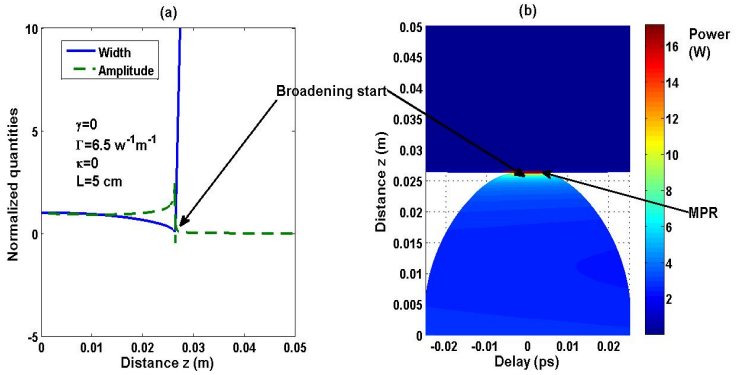


Figure 3.17: (a) Plot of the normalized width (solid line) and the normalized amplitude (dashed line) versus z. (b) Contour plot of the Airy pulse propagation. The peak power $P_0 = 4.76$ W, $\beta_2 = 0.56\ ps^2/m$, $C_0 = 0.8$, $\alpha = 5.06\ m^{-1}$, $\beta_4 = -1.2843 \times 10^{-5}\ ps^4/m$, $\gamma = 0$, $\Gamma = 6.5\ W^{-1}m^{-1}$ and $\kappa = 0$, SOI-waveguide length L=0.05 m.

process produces an important reduction of the length of compression comparatively to the cases above. This length is now about 0.0263 m with our data as seen in figure 3.17. Even the MPR is reduced about 16 W.

The FCA effect on the pulse compression mechanism of femtosecond Airy pulses in SOI-waveguide

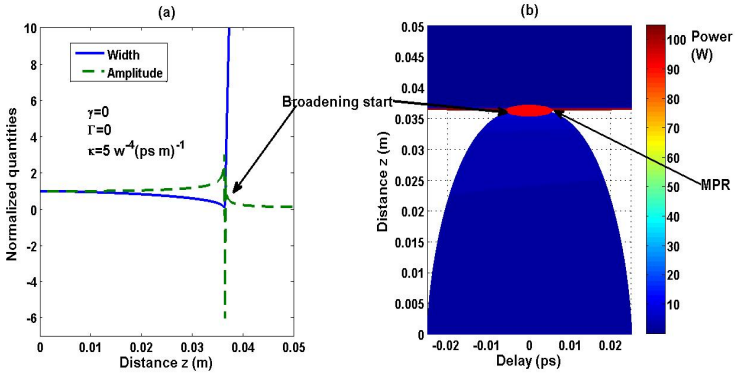


Figure 3.18: (a) Plot of the normalized width (solid line) and the normalized amplitude (dashed line) versus z. (b) Contour plot of the Airy pulse propagation. The peak power $P_0 = 4.76$ W, $\beta_2 = 0.56\ ps^2/m$, $C_0 = 0.8$, $\alpha = 5.06\ m^{-1}$, $\beta_4 = -1.2843 \times 10^{-5}\ ps^4/m$, $\gamma = 0$, $\Gamma = 0$ and $\kappa = 5\ W^{-4}(ps\ m)^{-1}$, SOI-waveguide length L=0.05 m.

presented in figure 3.18 is also described as a reduction of the length of compression about 0.0383 m. However, the contrast with all the previous reductions observed with the CKN and the TPA, concerns the MPR which is rather increased comparatively to the one of figure 3.15 about 100 W. Another point to be noticed, is the amplitude depression which is similar with the one of figure 3.15. The FCA seems to have a negligible role on this depression contrary to the TPA and the CKN.

One should notice that physically there is a dependency of free carriers to the TPA such that normally

the FCA might not be investigated without the TPA according to the relation of $\beta_{TPA}$ (presented in Eq. (2.50)). However, we stand on an approximated case where $\Gamma \ll \sigma N c(z,t)$ in order to neglect the TPA behind the FCA-FCD. Even in a pure mathematical view, the purpose is to analyze the impact of the FCA on the chirped truncated SHAP in the SOI-waveguide. This approach has the merit to underline the contribution of each nonlinear parameter in the whole behavior of the pulse when they are all considered. The same approach is done for intensity dependent nonlinear parameters in [3] such as the SPM, the SS and the IPRS for the SMFs. Indeed, the study of the impact of each nonlinear parameter is conducted separately to the others according to the purpose defined at the beginning.
Considering the combination of all these nonlinear processes namely the CKN, the TPA and the FCA to the linear parameters namely the normal GVD, the losses, the negative FOD and the positive initial chirp, we obtain for the SHAPs the figure depicted in figure 3.19. All these results are obtained with

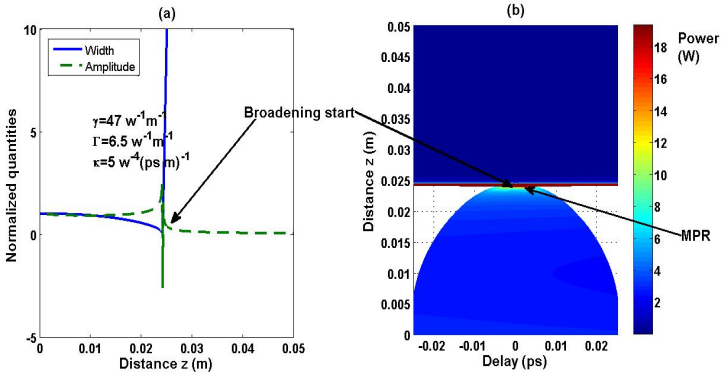


Figure 3.19: (a) Plot of the normalized width (solid line) and the normalized amplitude (dashed line) versus z. (b) Contour plot of the Airy pulse propagation. The peak power $P_0 = 4.76$ W, $\beta_2 = 0.56\ ps^2/m$, $C_0 = 0.8$, $\alpha = 5.06\ m^{-1}$, $\beta_4 = -1.2843 \times 10^{-5}\ ps^4/m$, $\gamma = 47\ W^{-1}m^{-1}$, $\Gamma = 6.5\ W^{-1}m^{-1}$ and $\kappa = 5\ W^{-4}(ps\ m)^{-1}$, SOI-waveguide length L=0.05 m.

the interaction of the negative value of the FOD, the normal GVD and positive initial chirp under the limit value defined in Eq. (2.77).
The length of compression reached is about 0.0241 m, slightly more smaller than that of figure 3.17 for the single TPA effect. All the nonlinear processes seem to cooperate in the reduction of compression length due to the combination of the negative FOD, the normal GVD and the positive chirp. Even the reduction of the MPR is observed but less dramatic than that of figure 3.17.
According to the impact of each nonlinear parameter as presented in figures 3.16-3.18, we suggest that they normally conduct to this compression length reduction, but the stressing is imposed by the TPA effect because it is the single parameter which reduces more the length of compression. If we consider the effect of the CKN and the TPA on the MPR in the compression mechanism studied, we should normally obtain a reduction more important than that of figure 3.17 (16 W). However, the result about 18 W indicates that the buffering is made by the FCA because as seen in figure 3.18, the effect of the FCA on the MPR of the SHAP allows an increase of its value comparatively to the linear case. So, while the TPA and the CKN tend to reduce this value, the FCA influences this variation in the opposite direction.
The decoupling of the effects related to $\gamma$, $\Gamma$ and $\sigma$, in a first approximation gives meaningfully a sense to the analysis. Since, in the realistic SOI-waveguide dynamic which has its process of compression via SHAPs drawn on the figure 3.19, the contribution of each parameter is underlined as additive effects that cooperate in the sense of SPM and TPA, and that compete in the sense of FCA. Sure enough, we notice that the TPA as a nonlinear loss rather acts on the chirped truncated SHAP

in the same sense than the SPM surprisingly while the FCA acts in the opposite sense. All these influences combined give an intermediate picture between those obtained with each single parameter. Thus, the FCA plays a buffer role on the dramatic effects of the SPM and TPA induced SHAP pulse broadening in the presence of the FOD.

## 3.4 On the FWM ASC growth in WDM solitons systems near the ZDW

The results presented in this section stem from [228]. Considering the PMCs obtained in both the

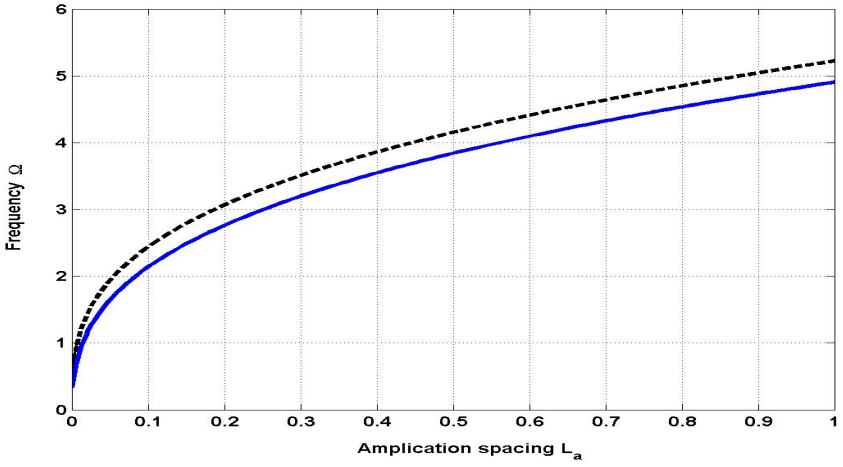


Figure 3.20: Evolution of the frequency offset of Phase-matching conditions versus the amplification spacing with $\beta_{GVD} = 1$, $\beta_{TOD} = 1$ (solid curve) and $\beta_{GVD} = 0$, $\beta_{TOD} = 1$ (dashed curve).

reduced and full models (for $\omega_n = 0$), figure 3.20 presents the evolution of the frequency offset where the FWM appears to be more important in the transmission in function of the normalized parameter of the amplification distance. In the presence of both GVD and TOD, it comes a slight reduction of the frequency offset evolution (solid curve in figure 3.20) in comparison to the single TOD case (dashed curve in figure 3.20). The addition of the GVD term is the reason of this interesting feature. The origin is linked to the polynomial equations of PMCs obtained in Eq. (2.92) and Eq. (2.93). We conclude that the combined dispersion terms reduce the frequency offset window more than a single dispersion term. Analyzing the growth function of the FWM in the reduced model, we can predict a higher growth for the most reduced frequency window.

### 3.4.1 Case of the reduced model

Figures 3.21 and 3.22 present the temporal profile evolution of the FWM versus the normalized distance $\zeta$ (for convenience $\zeta$ and $\tau$ are respectively represented by z and t in the figures) in the reduced model for the single TOD case and assuming both TOD and GVD, respectively. As can be seen in those figures, the FWM component appears along the transmission line near the first node and its amplitude increases through the following amplification nodes due to the realization of the phase-matching conditions. We notice that, in the reduced model, the FWM is reduced slightly in the single TOD case than in the combined GVD-TOD case. This feature is better observed in figure 3.23 which presents the FWM temporal profile at the first and the tenth amplification nodes for both cases (single TOD and combined GVD-TOD). Figure 3.23(a) presents identical amplitude

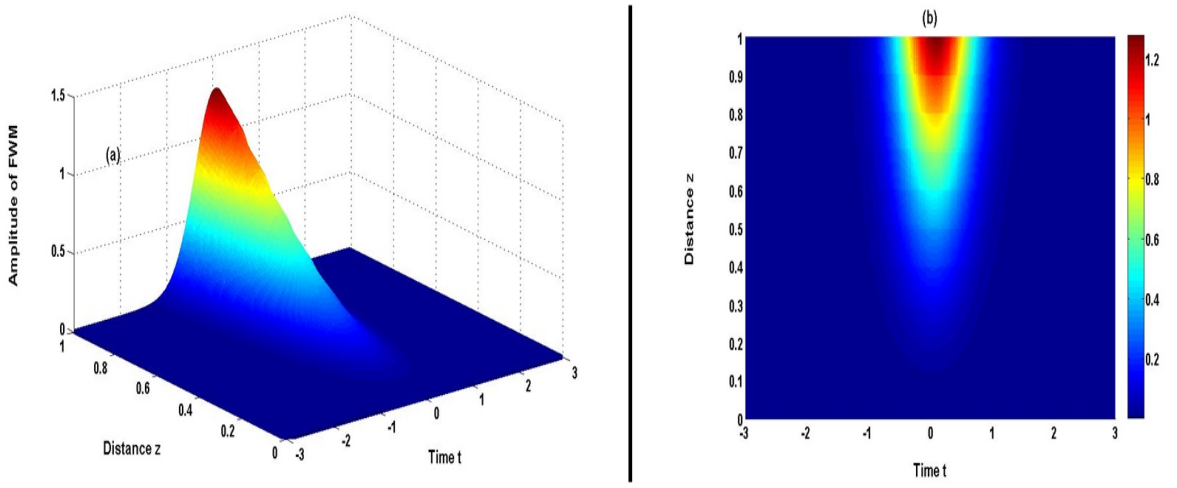


Figure 3.21: Propagation of FWM component in the reduced model, for the single TOD case $\beta_{GVD} = 0,\ \beta_{TOD} = 1$.

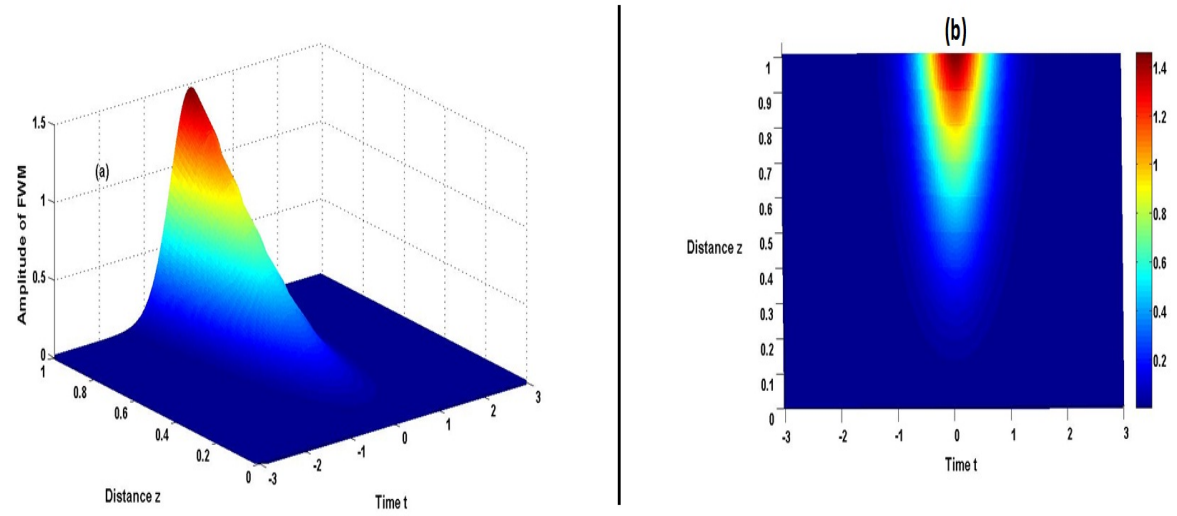


Figure 3.22: Propagation of FWM component in the reduced model, for the GVD-TOD case $\beta_{GVD} = 1,\ \beta_{TOD} = 1$.

values of the FWM at the first node for both cases under study. During the propagation along the transmission line, one observes that the amplitude of the FWM temporal profile in the single TOD case is slightly reduced in comparison with the amplitude assuming the combined GVD-TOD case (see figure 3.23(b)). Therefore, in the reduced model, the FWM grows along the transmission line and consequently a control of the FWM growth could be achieved.

### 3.4.2 Case of the full model

For the full model, the growth of the spectra profiles of the FWM versus the normalized distance $\zeta$ in the full model are presented in figures 3.24 and 3.25 for the single TOD and the combined GVD-TOD cases, respectively. The TOD introduces an asymmetry in the profile of the FWM component for both cases which is progressively reduced along the line when reaching the tenth amplification node. It is also found that in WDM soliton systems where input colliding channels $E_1$ and $E_2$ are not well-separated, the FWM is associated with slight peaks at each amplification node

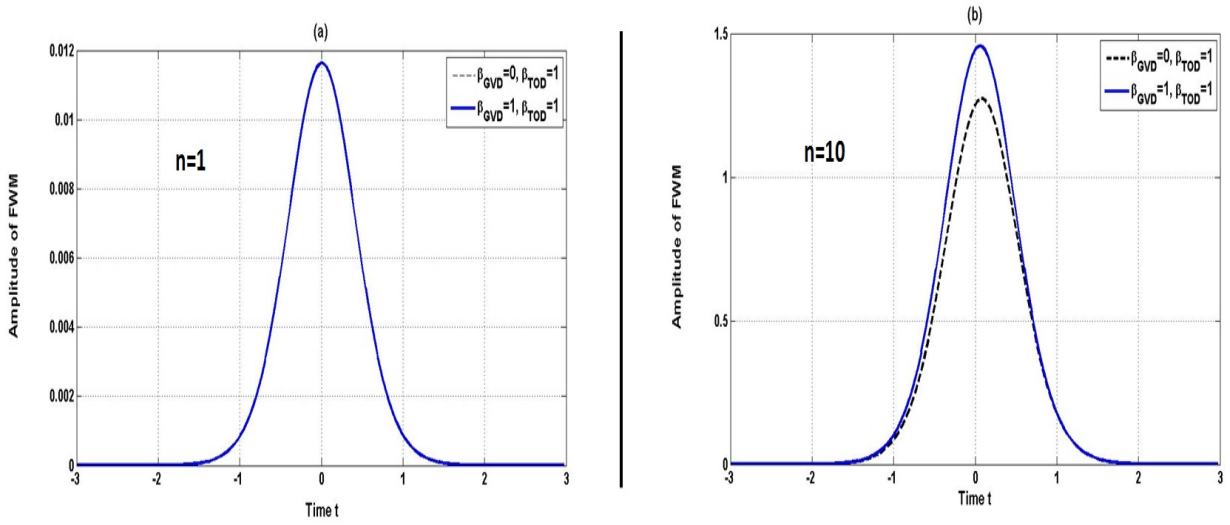


Figure 3.23: Temporal profile of FWM in the reduced model for both single TOD (dashed curve) and combined GVD-TOD (solid curve), at the first ($n = 1$ : curve **(a)**) and the tenth ($n = 10$ : curve **(b)**) nodes respectively.

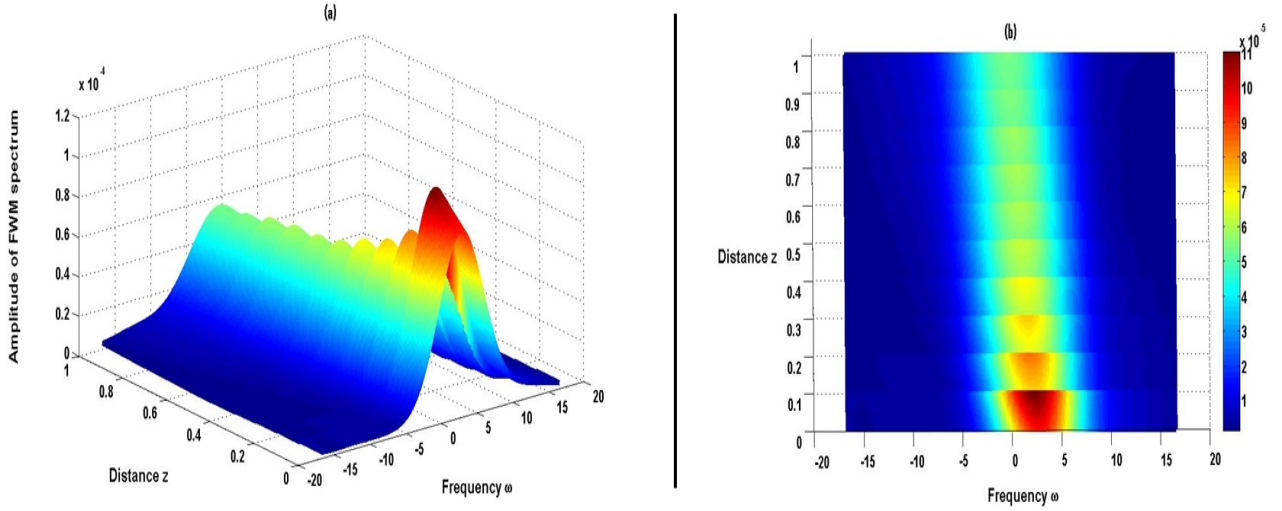


Figure 3.24: Propagation of FWM component spectrum in the full model, for the single TOD case $\beta_{GVD} = 0$, $\beta_{TOD} = 1$.

and becomes wide when $\zeta$ is increasing. It yields that, the strength of the FWM in the single TOD case is more important than in the combined GVD-TOD case. For both cases, the FWM becomes more smaller along the propagation distance $\zeta$. We present in figure 3.26, the spectrum profile of the FWM component for both cases at the first and tenth amplification nodes. This spectrum is more intense in the single TOD case (dotted lines in figure 3.26(a) and figure 3.26(b)) than in the combined GVD-TOD case (solid line in these figures). We can easily say that the combination of TOD term with the GVD term reduces the FWM crosstalk in the WDM soliton systems where input channels are closer each other (small frequency spacing). This feature is depicted by the asymptotic solution of the FWM growth presented in figure 3.27 for the full model. We obtain a high broadening of the FWM spectrum in the combined GVD-TOD case (solid lines) comparatively to the FWM spectrum in the single TOD case (dotted lines). These results show that the analytical asymptotic solution (for larger $\zeta$) is in good agreement with the previous obtained results.

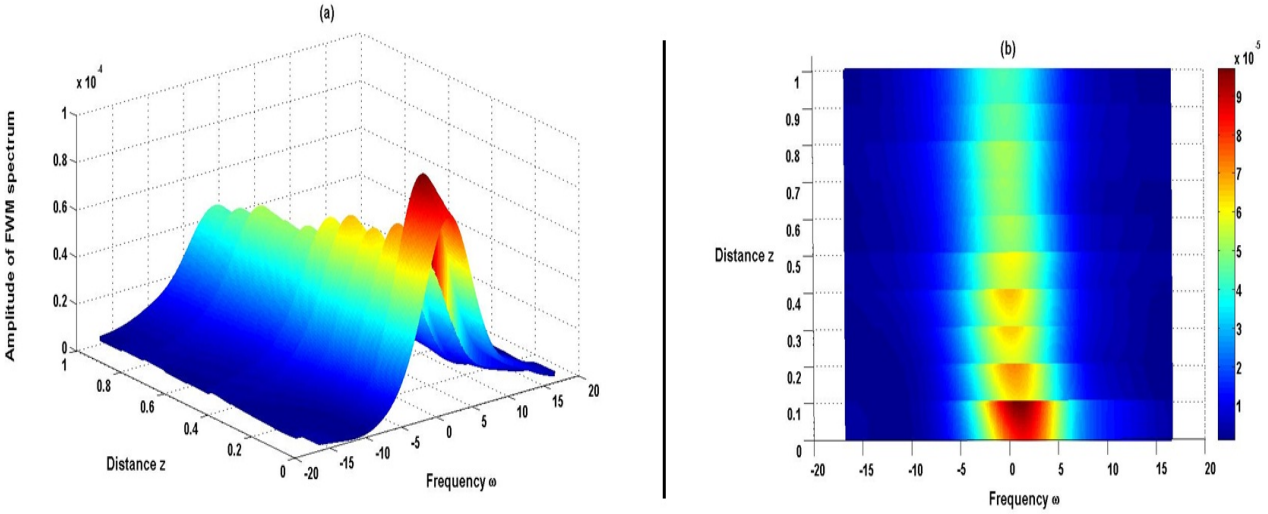


Figure 3.25: Propagation of FWM component spectrum in the full model, for the combined GVD-TOD case $\beta_{GVD} = 1,\ \beta_{TOD} = 1$.

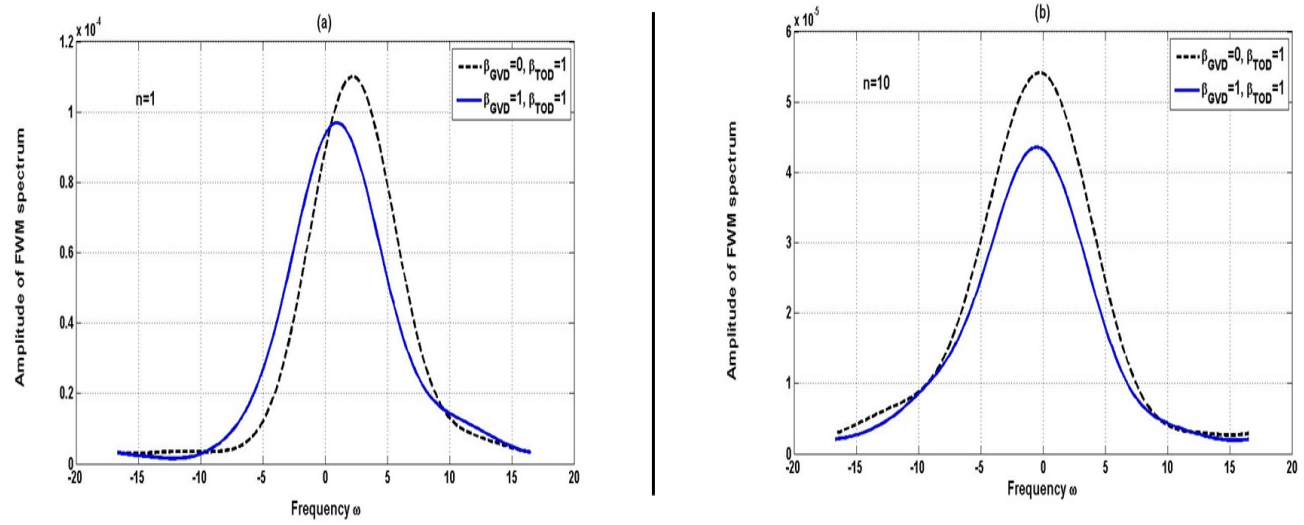


Figure 3.26: Spectral profile of FWM in the full model for both single TOD (dashed curve) and combined GVD-TOD (solid curve), at the first ($n = 1$ : curve **(a)**) and the tenth ($n = 10$ : curve **(b)**) nodes respectively.

## 3.5 On the MI mechanism in silicon waveguides under FOD

The results presented in this section stem from [229].

### 3.5.1 Effects of absorption coefficients on the MI gain

For the numerical simulations, we have set the parameter $K = \sigma N_c$ as the FCA parameter. Therefore, we choose to study separately the effects of TPA and FCA on the MI gain spectrum by controlling the value of $K$. For instance, in the case where we have $\Gamma \neq 0$, we consider that $K \sim 0$ which allows us to analyze only the single effect of TPA. On the other hand, when rather we have $K \neq 0$, we consider that $\Gamma \sim 0$ which allows us to analyze only the FCA effect.

Then, we plot in figure 3.28 the MI gain for different cases highlighting the effect of the absorption coefficients. For the case where we neglect the TPA and the FCA effects (see figure 3.28(a)), we have 2 bands of the MI gain at 2 OFs locations : -78.3443 and 78.3443 THz. These sidelobes are due to the

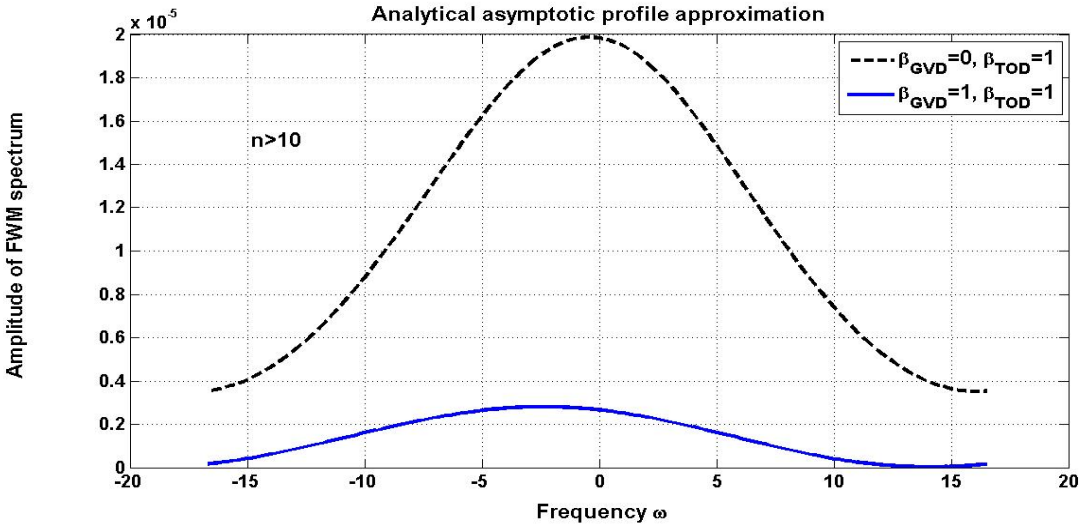


Figure 3.27: Spectral profile of FWM in the full model for both single TOD (dashed curve) and combined GVD-TOD (solid curve), asymptotic solution beyond the tenth node where the parameter $z$ is assumed to be larger.

FOD effect interacting with the GVD as discussed in [189,190] and designed by the second relation of Eq. (2.114). However, in the presence of the TPA (see figure 3.28(b)), we have 7 remarkable values of the MI gain at 7 OFs locations : -78.3443, -69.0857, -48.9898, 0, 48.9898, 69.0857 and 78.3443 THz. Among these locations, three have a zero MI gain particularly those of $\pm$69.0857 THz and 0 THz. In the presence of the FCA (see figure 3.28(c)), we have 3 OFs solutions where the one in the central frequency ($\Omega_0$=0) has an increased MI gain. It means that, the FCA enhances the value of this central MI gain point. For the full realistic case where both the TPA and the FCA effects are considered, we recover the 7 locations above of the MI gain maxima with the corresponding enhanced central peak. It is worthy to notice that, these OFs values could be directly obtained using the relations of Eq. (2.114). The figure 3.29 shows the MI gain spectra for the different cases discussed above in figure 3.28 versus the varying peak power $P_0$. The features noticed in figure 3.28 are directly observed in the contour plots of figure 3.29. It is observed in figure 3.29(b), the TPA effect on the MI gain such as the creation of the 4 OFs symmetric locations given by the two last relations of Eq. (2.114) in addition to the OFs induced by FOD and GVD interaction (see figure 3.29(a)). On the other hand, the FCA slightly increases the value of the central MI gain (see figures 3.29(c)-3.29(d)) comparatively to the cases of figures 3.29(a)-3.29(b).

### 3.5.2 Impact of pulse shape, chirp and absorption coefficients on the MI PTG

#### In the absence of chirp, TPA and FCA

We generate a map of PTG as shown in figure 3.30 for each positively chirped input pulses with the common SSF algorithm in the absence of the TPA ($\Gamma = 0$). For the sech-type and Gaussian profiles, the trails of the MI-PTG are observed around about 0.07 m while for the RC pulse, they are observed around about 0.06 m. We also observe for all the profiles with the numerical data used, about 10 main peaks of the MI-PTG process in figure 3.30. The maximum value of these mains peaks for the sech-type pulse is obtained around about 0.12 m of propagation distance with approximately the value of 9.5 W (see the colorbar in figure 3.30(b)). Concerning the Gaussian profile, we reach 11 W toward 0.115 m. For the last profile (RC pulse), we observe rather a maximal value about 12.5 W toward 0.11 m.

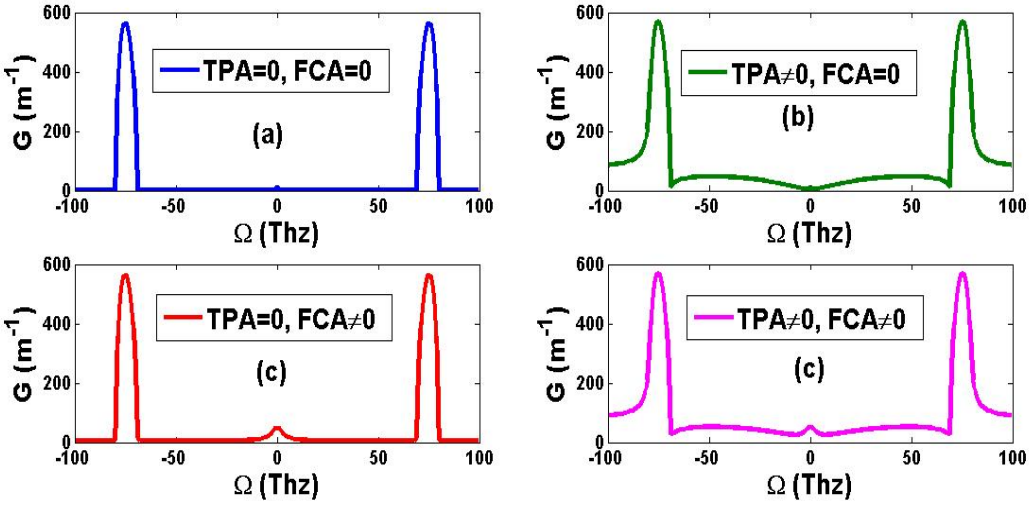


Figure 3.28: Plot of the MI gain spectrum versus Ω. (a) blue curve for TPA=0 and FCA=0, (b) green curve for $TPA \neq 0$ ($\Gamma = 6.5\ W^{-1}m^{-1}$) and $FCA \sim 0$, (c) red curve for $TPA \sim 0$ and $FCA \neq 0$ ($K = 1\ m^{-1}$) and (d) violet curve for $TPA \neq 0$ and $FCA \neq 0$. Others parameters : $\beta_2 = 0.56\ ps^2/m$, $\beta_4 = -0.0014\ ps^4/m$, $\gamma = 47\ w^{-1}m^{-1}$, $P_0 = 3\ W$.

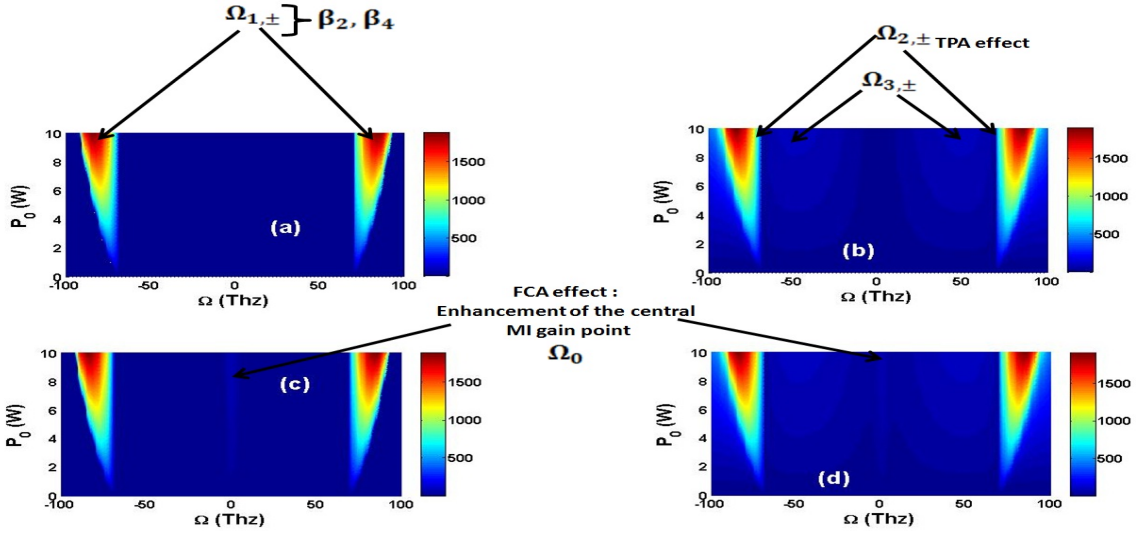


Figure 3.29: Plot of the MI gain spectrum versus $P_0$ and Ω. (a) for TPA=0 and FCA=0, (b) $TPA \neq 0$ ($\Gamma = 6.5\ W^{-1}m^{-1}$) and $FCA \sim 0$, (c) for $TPA \sim 0$ and $FCA \neq 0$ ($K = 1\ m^{-1}$) and (d) for $TPA \neq 0$ and $FCA \neq 0$. Others parameters : $\beta_2 = 0.56\ ps^2/\text{m}$, $\beta_4 = -0.0014\ ps^4/\text{m}$, $\gamma = 47\ w^{-1}m^{-1}$.

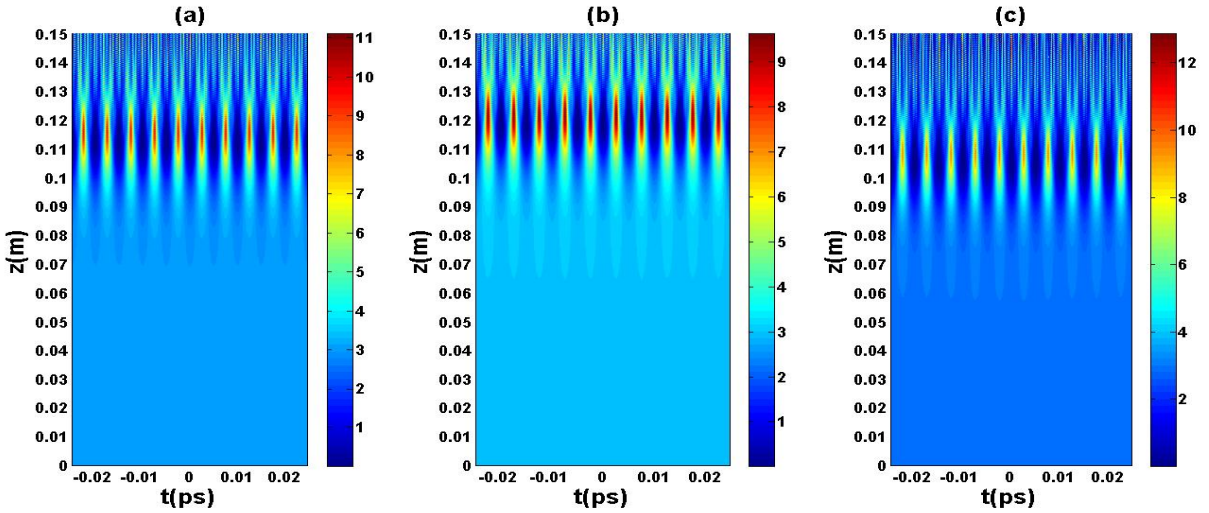


Figure 3.30: Contour plot of unchirped pulses propagation. (a) Gaussian profile, (b) Sech-type profile, (c) RC profile. Parameters : $\beta_2 = 0.56\ ps^2/\text{m}$, $\beta_4 = -0.0014\ ps^4/\text{m}$, $\gamma = 47\ w^{-1}m^{-1}$, L=0.15 m, $t_0 = 50\ fs$, $P_0 = 3\ W$, $\Gamma = 0$.

Indeed, we notice that the profiles which are close to the fundamental soliton solution (consequently more stable) as the sech-type pulse, have their main peaks of the MI-PTG trails that occur at larger propagation distances than those less stable as the RC pulse. In addition, the maximum value of these main peaks are smaller than those of the less stable input profiles. The same idea can be raised for the Gaussian pulse in comparison to the RC profile, since the first form is more close to the sech-type pulse than the latter.
More specifically, the RC pulse as a less stable input, has its main peaks of the MI-PTG trails more strong at the short propagation distances (see figures 3.31(b) and 3.31(c)). This profile is followed by the Gaussian profile, which gets strong peaks at propagation distances larger than the previous profile (see figure 3.31(d)) while the sech-type is the last with strong peaks of the MI-PTG process appearing later in the propagation (see figure 3.31(e)). Beyond these regular main peaks for all the profiles, the spontaneous breakup process continues leading to a chaotic picture for the large distances of propagation (see figures 3.30 and 3.31(f)). Another observation that can be done in figure 3.31, concerns the orientation of the undulations for each pulse. Indeed, in the absence of the source chirp, all the pulses have the same orientation in the undulations.

## Effect of chirp in the absence of TPA and FCA

Considering the initial chirping process of each pulse, we have simulated the MI-PTG process in the absence of absorption coefficients (see figure 3.32). As can be observed in this figure, the initial chirp (C=10) leads both the sech-type and the Gaussian profiles to behave similarly in the development of the MI-PTG process while the RC profile remains different. Furthermore, the chirp does not change the number of the main peaks for each profile. It shifts the occurrence of the high values of the main peaks to short propagation distances for all the input pulses (about 0.1 m). The maximum value reached in the power is the same for both the Gaussian and the sech-type pulse (about 15.25 W) while for the RC profile, one finds rather about 15 W. So, the effect of chirp consists to enhance the intensity of the MI-PTG peaks and to shift the occurrence of their maximum value to the short propagation distances than the unchirped case.
On the other hand, when we consider the figure 3.33 with the nonzero value of chirp, the pulses that

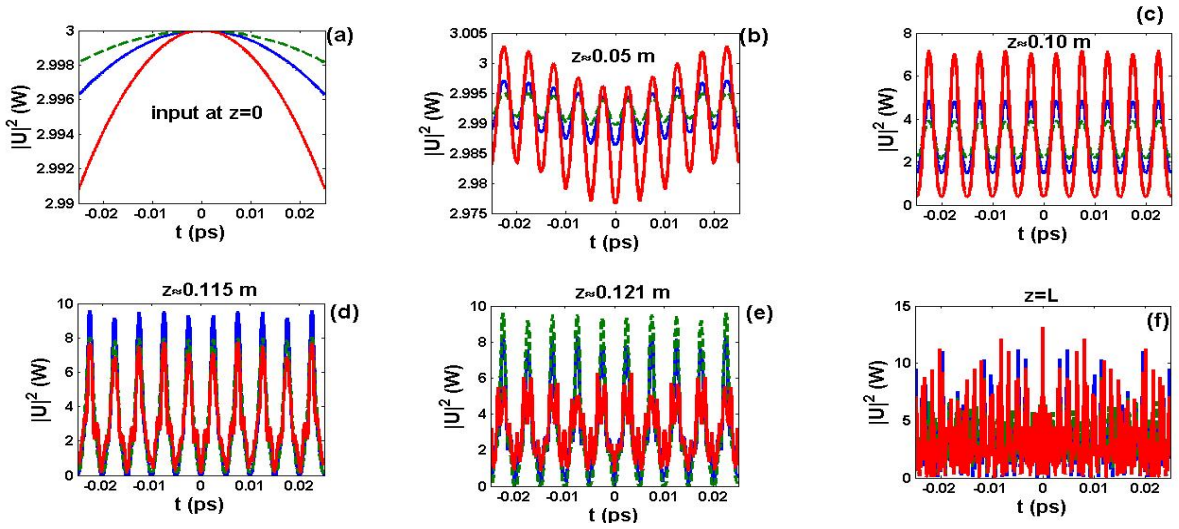


Figure 3.31: Temporal profiles of the unchirped pulses at different propagation distances: (a) input at z=0, (b) z=0.05 m, (c) z=0.1 m, (d) z=0.115, (e) z=0.121 m and (f) z=L. The parameters are the same as in figure 3.30. Solid blue curves for Gaussian profile, dashed green curves for sech-type profile and solid red curves for RC profiles.

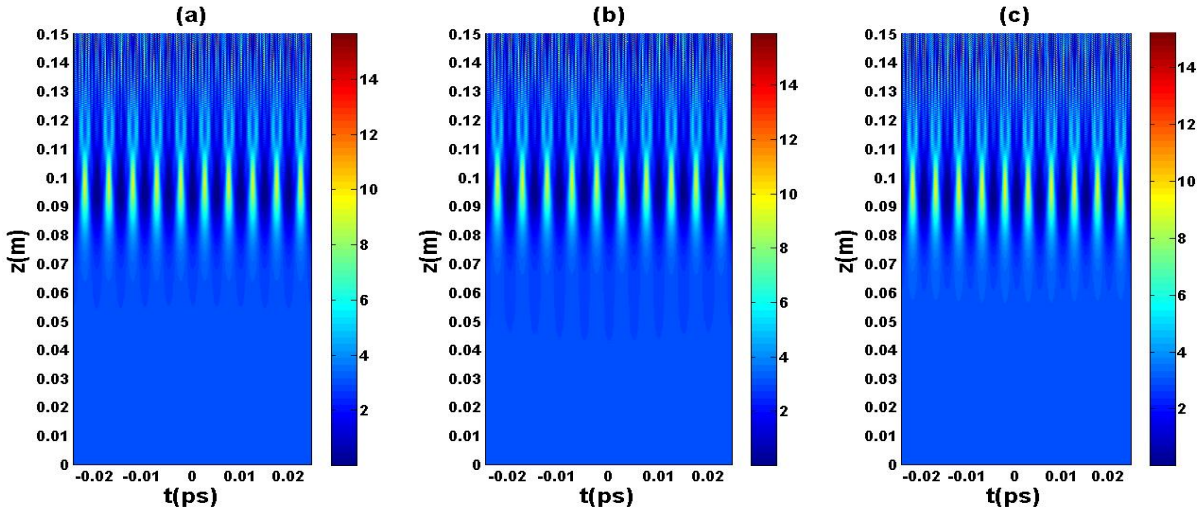


Figure 3.32: Contour plot of chirped pulses propagation. (a) Gaussian profile, (b) Sech-type profile, (c) RC profile. Parameters : C=10, $\beta_2 = 0.56\ ps^2/\text{m}$, $\beta_4 = -0.0014\ ps^4/\text{m}$, $\gamma = 47\ w^{-1}m^{-1}$, L=0.15 m, $t_0 = 50\ fs$, $P_0 = 3\ W$, $\Gamma = 0$..

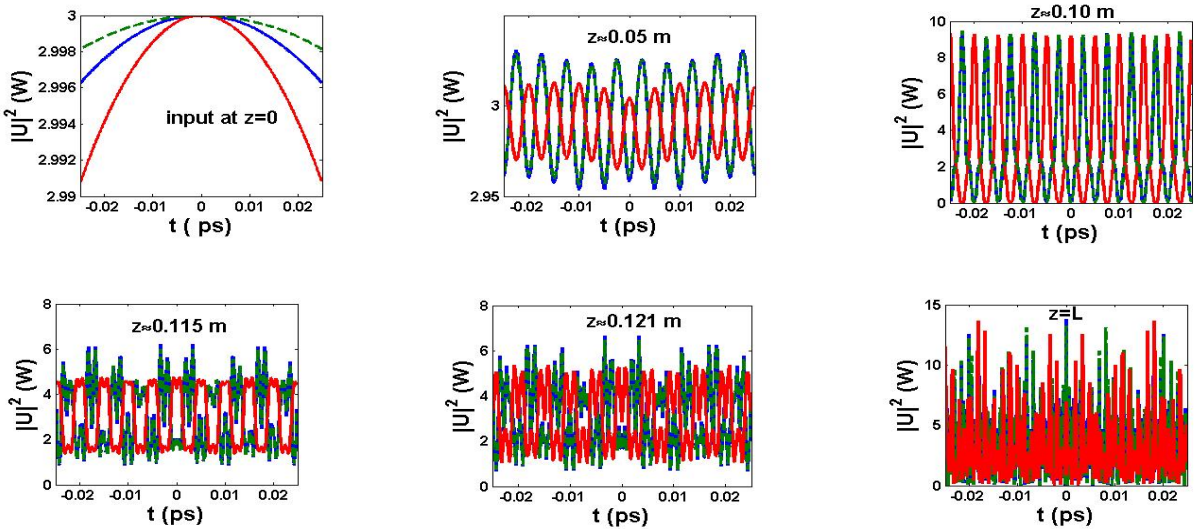


Figure 3.33: Temporal profiles of the chirped pulses at different propagation distances: (a) input at z=0, (b) z=0.05 m, (c) z=0.1 m, (d) z=0.115, (e) z=0.121 m and (f) z=L. The parameters are the same as in figure 3.32. Solid blue curves for Gaussian profile, dashed green curves for sech-type profile and solid red curves for RC profiles.

are more stable (the Gaussian and the sech-type pulses), are more amplified than those which are less stable (the RC profile). Even the orientation of the undulation changes, since the RC profile undergoes a chirp phase opposite to the one of the others. Reversing the initial chirp value of the RC pulse so that it is now chirped with a negative value while the other profiles are always chirped positively, we obtain a similar behavior for all the pulses (see figure 3.34). In this case, the chirp creates an independence of the MI-PTG process to the input profile, since it is observed that all the pulses have the same picture because of the nonzero chirp.

## Effect of absorption coefficients

The case treated in figure 3.35 concerns the chirped pulses undergoing the MI-PTG process in a SOI-waveguide having a small value of TPA about 0.1 $W^{-1}m^{-1}$ with the FCA coefficient about $1.45 \times 10^{-21}m^2$ [218]. We observe the effect of these small values of TPA and FCA on the MI-PTG picture drawn as a slight reduction of the amplified intensity comparatively to the previous cases. The chirp impact in figure 3.35 is in agreement with the one mentioned previously in figures 3.32 and 3.33. Increasing the value of the TPA parameter with a factor 5 (consequently the FCA also increases), the absorption coefficients influence significantly the MI-PTG process. In fact, in figure 3.36 we observe the influence of TPA and FCA as a real reduction of the amplified intensity of the MI-PTG peaks in which the maximum value is reached at almost the output of the considered SOI-waveguide. On the other hand, the input profiles do not interact similarly with the absorption coefficients. The RC profile is found to be more influenced by the TPA and FCA than the others, since its maximum value does not exceed the initial peak value comparatively to the whole previous cases. Concerning the sech-type and the Gaussian pulses, an important reduction is observed but it exceeds at least the double of the initial input peak power. However, the combination of the value of 6.5 $W^{-1}m^{-1}$ used previously by Roy et al [8] for the TPA effect and the FCA coefficient value of [202a], leads to the complete destruction of the MI-PTG process creating consequently an independence to the input profile (see figure 3.37). Indeed, as can be observed, all the pulses behave similarly under these conditions. The MI-PTG is destroyed in the sense that there are no peaks or any pulse splitting observed. The absorption coefficients act in this case, normally as nonlinear losses

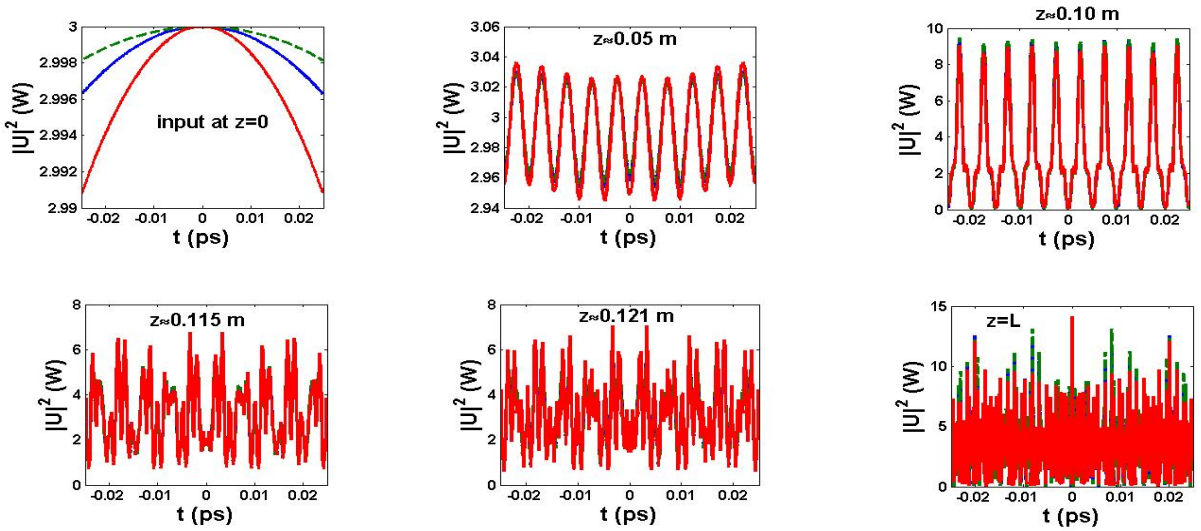


Figure 3.34: Temporal profiles of the chirped pulses at different propagation distances with a chirp inversion for the RC profile: (a) input at z=0, (b) z=0.05 m, (c) z=0.1 m, (d) z=0.115, (e) z=0.121 m and (f) z=L. The parameters are the same as in figure 3.32. Solid blue curves for Gaussian profile, dashed green curves for sech-type profile and solid red curves for RC profiles : for the RC profile $C = -10$ while for the others C=10.

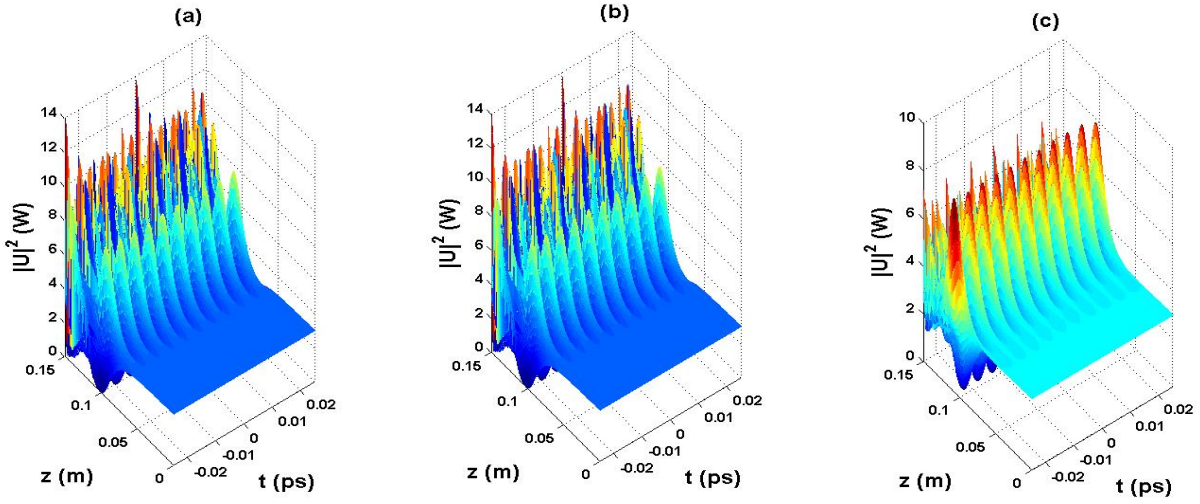


Figure 3.35: Plot of chirped pulses propagation. (a) Gaussian profile, (b) Sech-type profile, (c) RC profile. Parameters : C=10, $\beta_2 = 0.56\ ps^2/\text{m}$, $\beta_4 = -0.0014\ ps^4/\text{m}$, $\gamma = 47\ w^{-1}m^{-1}$, L=0.15 m, $t_0 = 50\ fs$, $P_0 = 3\ W$, $\Gamma = 0.1\ W^{-1}m^{-1}$, $\sigma = 1.45 \times 10^{-21}m^2$.

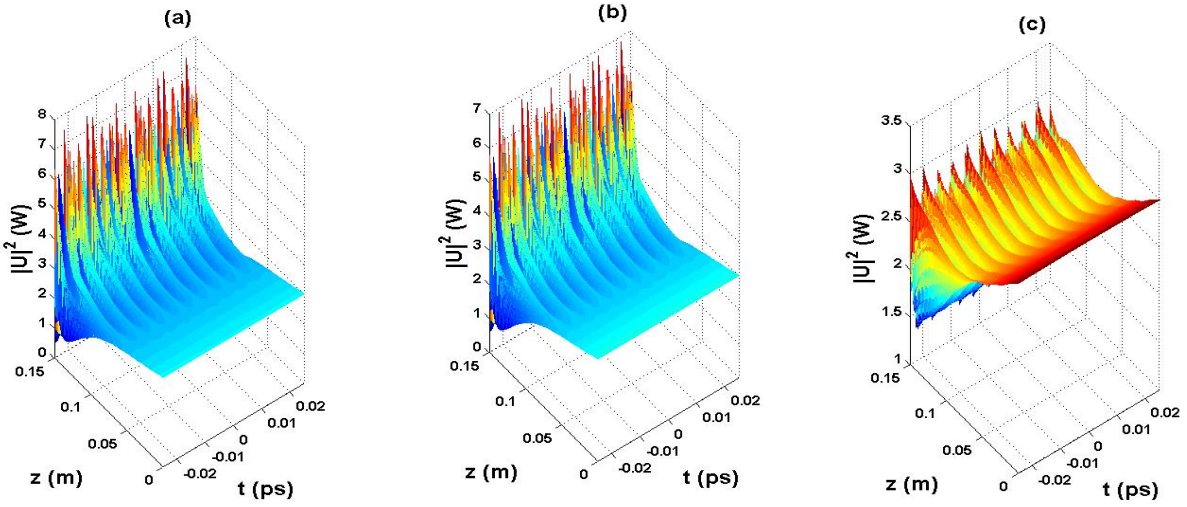


Figure 3.36: Plot of chirped pulses propagation. (a) Gaussian profile, (b) Sech-type profile, (c) RC profile. Parameters : C=10, $\beta_2 = 0.56\ ps^2/\text{m}$, $\beta_4 = -0.0014\ ps^4/\text{m}$, $\gamma = 47\ w^{-1}m^{-1}$, L=0.15 m, $t_0 = 50\ fs$, $P_0 = 3\ W$, $\Gamma = 0.5\ W^{-1}m^{-1}$, $\sigma = 1.45 \times 10^{-21}m^2$.

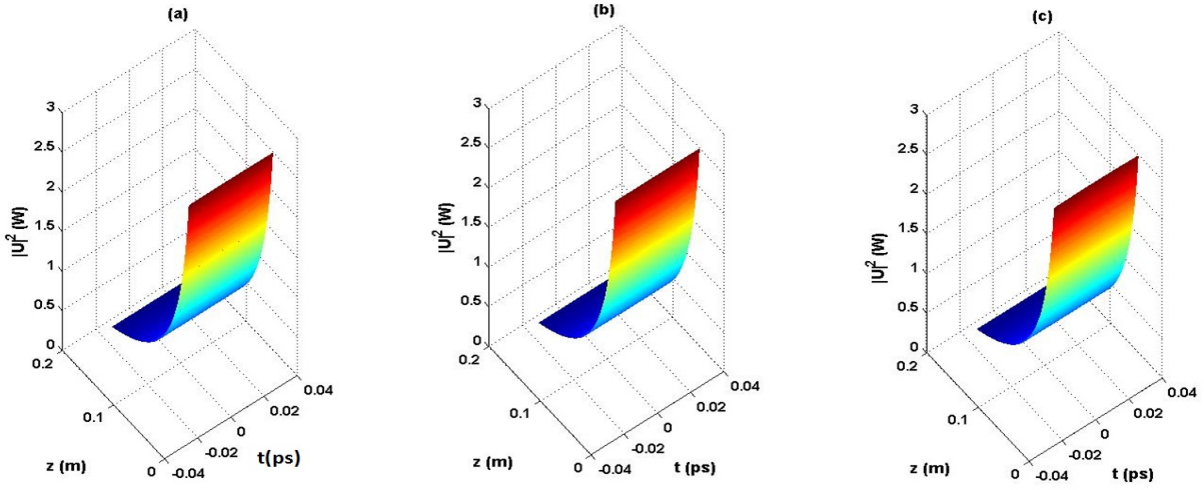


Figure 3.37: Plot of chirped pulses propagation. (a) Gaussian profile, (b) Sech-type profile, (c) RC profile. Parameters : C=10, $\beta_2 = 0.56\ ps^2/\text{m}$, $\beta_4 = -0.0014\ ps^4/\text{m}$, $\gamma = 47\ w^{-1}m^{-1}$, L=0.15 m, $t_0 = 50\ fs$, $P_0 = 3\ W$, $\Gamma = 6.5\ W^{-1}m^{-1}$, $\sigma = 1.45 \times 10^{-21}m^2$.

leading the a drastic pump depletion following the propagation distance. The half of the initial peak power is reached after a propagation of 0.04 m only. Beyond this propagation distance, the pulses are almost annihilated by the absorption coefficients whatever the value of the chirp which becomes a secondary parameter. Thus, the absorption coefficients counteract the beneficial chirp effect on the MI-PTG process.

## 3.6 On the SCG phenomenon through the higher-order NLSE with non-Kerr terms

The results presented in this section stem from [234]. The general numerical data used, are given as follows : the waveguide length $L = 1$ cm, the GVD $\beta_2 = -0.5\ ps^2m^{-1}$ (defining an anomalous dispersion regime of the modeled waveguide as taken in [237]) and the pumping wavelength $\lambda_0 = 1550$ nm.

### 3.6.1 Effects of competing and cooperative nonlinearities

Figure 3.38 shows the pulse width with $t_0 = 50fs$, the CKN coefficient $\bar{\gamma}_1 = 5\ \ W^{-1}m^{-1}$ and the incident pulse energy $E_0 = 0.1$ nJ (sub-nJ pulse). As seen in this figure, the cooperative nonlinearities (see the solid black curve in figure 3.38(a)) stress the spectral broadening of the SCG spectrum as expected since these nonlinearities have the same sign and therefore cooperate in the increase of the global nonlinearity of the media. Obviously, the opposite feature is observed for the competing nonlinearities where the quintic nonlinearity with its negative sign counteract the effect of the cubic nonlinearity in the spectral broadening of the SCG. As result of this competition, a spectral

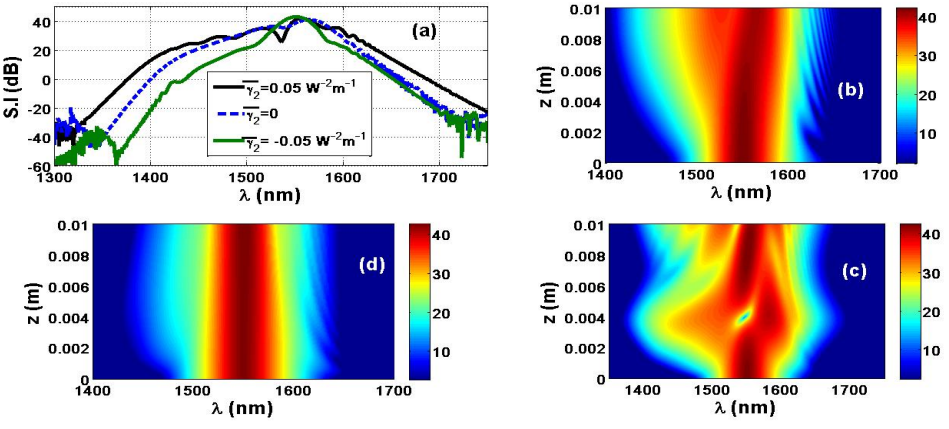


Figure 3.38: (a) SCG output spectra. Contour plots of SCG pulse spectral propagation : (b) case of single CKN $\bar{\gamma}_2 = 0$, (c) case of cooperative nonlinearities $\bar{\gamma}_2 = 0.05\ W^{-2}m^{-1}$, (d) case of competing nonlinearities $\bar{\gamma}_2 = -0.05\ W^{-2}m^{-1}$.

compression is obtained (see the solid green curve in figure 3.38(a)) in comparison to the single CKN case (see the dashed blue curve in figure 3.38(a)). The corresponding spectral propagation are showed in figures 3.38(b), 3.38(c) and 3.38(d).

### 3.6.2 Effect of the pulse width reduction in the femtosecond domain : spectral compression induced by the cooperative nonlinearities

The reduction of the pulse width in the femtosecond domain by a factor 5 leads to figure 3.39. For the spectra presented in this figure, the same data as in figure 3.39 have been used except the pulse width, which is rather $t_0 = 10fs$. Surprisingly, we notice that instead of enhancing the SCG

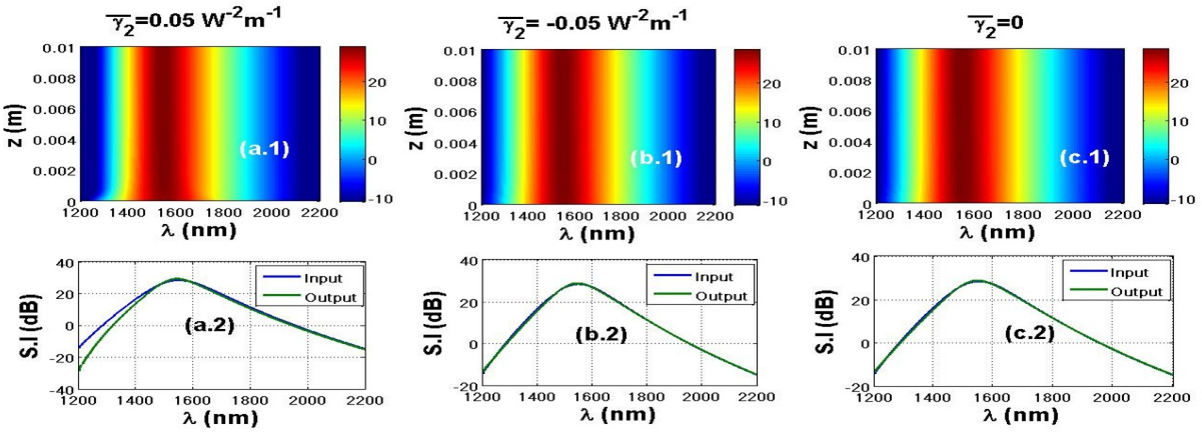


Figure 3.39: Contour plots of SCG pulse spectral propagation : (a.1), (b.1) and (c.1); SCG input and output spectra: (a.1), (b.1) and (c.1); (a.1) and (a.2) for the case of cooperative nonlinearities, (b.1) and (b.2) for the case of competing nonlinearities, (c.1) and (c.2) for the case of single CKN.

spectrum broadening (increase of the SCG bandwidth), the cooperative nonlinearities slightly lead to a spectral compression in the low wavelengths region (see figures 3.39(a1) and 3.39(a2)) while the competing ones nearly maintain unchanged the SCG spectrum (see figures 3.39(b1) and 3.39(b2)). This last feature is also observed for the single CKN case in figures. 3.39(c1) and 3.39(c2). The

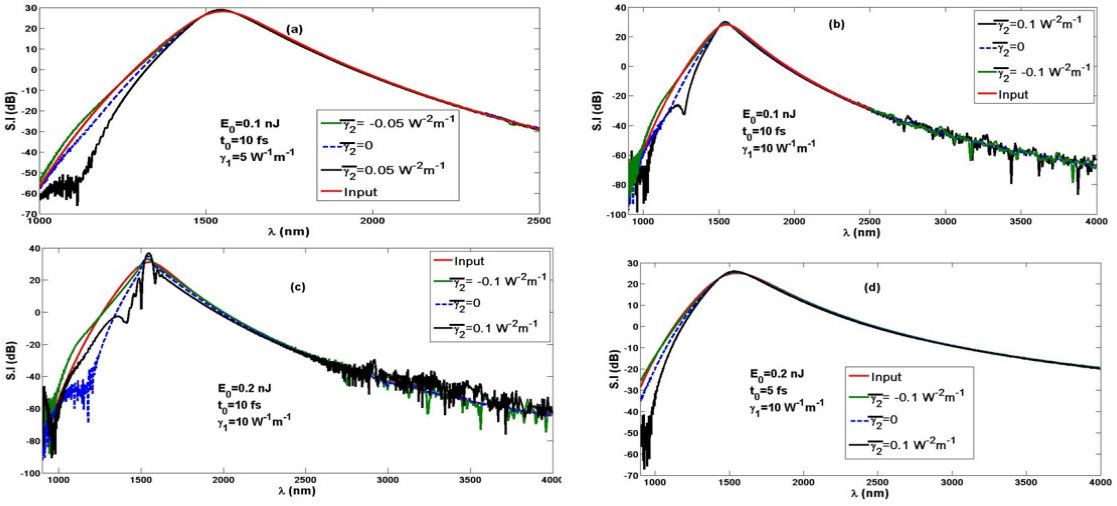


Figure 3.40: SCG spectra.

effect of this pulse width reduction induced spectral compression of the cooperative nonlinearities is highlighted in figure 3.40 where the spectral profiles of the SCG have been drawn. The three cases of figure 3.39 are presented in figure 3.40(a). Both the increase of the energy in the sub-nJ scale (as done

in figures 3.40(c) and 3.40(d)) and the nonlinearity (as done in figures 3.40(b), 3.40(c) and 3.40(d)) confirm the previous feature of the spectral compression obtained in the cooperative nonlinearities case. In these figures, the bandwidths remain nearly unchanged from the input to the output of the considered waveguide for the competing nonlinearities. Considering the figure 3.41, we have drawn

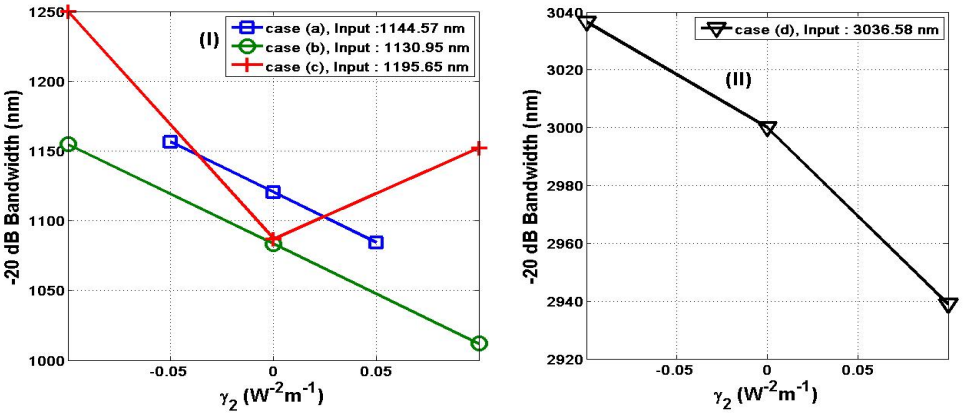


Figure 3.41: SCG -20 dB bandwidths corresponding to the cases plotted in figure 3.40 : (I) for the cases (a) input bandwidth about 1144.57 nm, (b) input bandwidth about 1130.95 nm, (c) input bandwidth about 1195.65 nm, (II) for the case (d) input bandwidth about 3026.58 nm.

the SCG bandwidths at -20 dB of the S.I for the cases shown in figure 3.40. Globally, as seen on this figure, the bandwidth decreases when one moves from the competing nonlinearities $\bar{\gamma}_2 < 0$ to the cooperative ones $\bar{\gamma}_2 > 0$. Indeed for the case (a) in figure 3.41(I), the spectral compression is obtained for the cooperative nonlinearities since one reaches about 1084.33 nm when the input was at 1144.57 nm. For the case (b), the compression is reached at 1011.90 nm for the cooperative nonlinearities while the input is at 1130.95 nm. The same feature could be observed for the cases (c) and (d) (see figure 3.41(II)).

## 3.7 On the role of the input profile asymmetry and the chirp on the propagation in highly dispersive and nonlinear fibers

The results presented in this section come from [236].

### 3.7.1 Part I : propagation of FEAPs in highly dispersive optical fibers

The model equation used to describe the dynamics within a highly dispersive optical fiber (HDOF) is the basic nonlinear NLSE defined as [3,236,248] :

$$i\frac{\partial u}{\partial \xi} - \frac{s_2}{2}\frac{\partial^2 u}{\partial \tau^2} - \frac{is_3}{6}\frac{\partial^3 u}{\partial \tau^3} + \frac{\delta_4}{24}\frac{\partial^4 u}{\partial \tau^4} + N^2|u|^2 u = 0, \tag{3.2}$$

where $u$, $\xi$ and $\tau$ are the dimensionless quantities representing the slowly varying amplitude of the electrical field, the propagation distance and the retarded frame time, respectively. The coefficients $s_2$, $s_3$ (with $s_3 = \pm\, L_{GVD}/L_{TOD}$), $\delta_4$ (with $\delta_4 = \pm\, L_{GVD}/L_{FOD}$).

**Initial chirp inducing changes in the spectral shape : the spectral asymmetric shape**

Firstly, we consider the basic nonlinear case where the GVD, TOD and FOD are neglected compared with the SPM [236,248]. This case is exhibited in figure 3.42 where we show the single effect of the

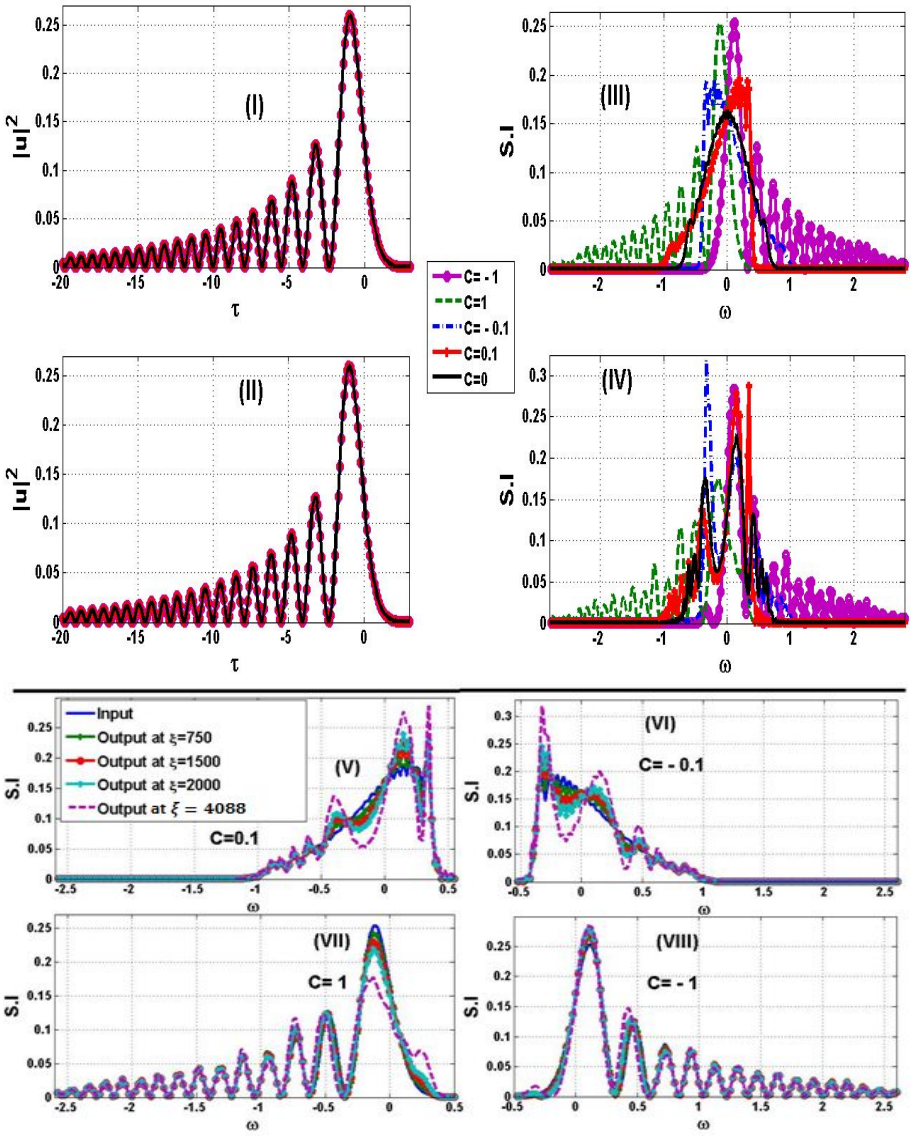


Figure 3.42: Single effect of the initial chirp without GVD, TOD and FOD and a normalized length of the HDOF $\xi_{max} = 4088$. (I) and (II) for time domain intensity versus $\tau$, (III) and (IV) for spectral intensity (S.I) versus normalized frequency $\omega$. Asymmetric spectral profiles : (V) for $C = 0.1$, (VI) for $C = -0.1$, (VII) for $C = 1$, (VIII) for $C = -1$. The truncation coefficient $a$ is 0.05.

initial chirp in the presence of the SPM. It is observed that, the chirp influences the spectral profile as seen in figures 3.42(III) and 3.42(IV), but leaves the time domain unchanged (see figures 3.42(I) and 3.42(II)). Furthermore, the chirp transforms the spectral profile into an asymmetric form with the same location of the oscillations tail when $C > 0$ (oscillations tail are in the left-hand side (LHS), see for instance the red crossed and green dashed curves of figures 3.42(III) and 3.42(IV)) and in the opposite side when $C < 0$ (oscillations tail are in the right-hand side (RHS), see for instance the violet circle and blue dot dashed curves of figures 3.42(III) and 3.42(IV)). In figure 3.42(IV), the dominant peak of C=-1 (see the violet circle curve) is amplified compared with the positive case C=1 (see the green dashed curve). Obviously, as well-known, the SPM is responsible to the distortion of

the output spectrum observed on the black solid curve of figure 3.42(IV) [3]. The spectral asymmetric profile induced chirp leads to an Airy-like form when $|C|$ increases. A comparison between the green dashed curves of C=1 and the red crossed curves of $C = 0.1$ in both figures 3.42(III) and 3.42(IV), confirms this feature. The same observation could be done on the violet circle curves of $C = -1$ and the blue dot dashed curves of $C = -0.1$ in both figures 3.42(III) and 3.42(IV). The bottom curves drawn in figures 3.42(V), 3.42(VI), 3.42(VII) and 3.42(VIII) (respectively for C=0.1, $C = -0.1$, C=1 and $C = -1$), show the dependence of the effect of chirp on the spectra obtained versus the propagation distance $\xi$. It is observed as discussed above that, for the small value of chirp cases ($|C| = 0.1$ in figures 3.42(V) and 3.42(VI)), the spectrum seems to have only one peak which is asymmetric because of chirp and distorts following $\xi$ because of the SPM. With the increase of chirp as for figures 3.42(VII) and 3.42(VIII), the spectrum takes progressively an Airy-like form which undergoes more the SPM effects when the positive chirp ($C = 1$) is used than the negative chirp ($C = -1$) (Comparison between the violet dashed curves of both figures 3.42(VII) and 3.42(VIII)).

It is well-known that, when a symmetric and compact pulse such as Gaussian, hyperbolic secant or raised-cosine profile, undergoes only the SPM effect in a dispersionless SMF, the spectrum remains symmetric as discussed in [3]. The use of an initial chirp does not change this configuration. On the other hand, it is a surprise to observe a symmetric spectral output from an asymmetric shape as the one of a FEAP (see the black solid curves in figures 3.38(III) and 3.42(IV)). Moreover it appears that the use of the initial chirp delivers an asymmetric spectral output from the asymmetric temporal shape.

One should also remind that, the effect of SS as a higher-order nonlinear effect yields an asymmetry of the SPM-broadened spectrum obtained from a symmetric pulse as a Gaussian pulse [3]. This SS effect was described as an optical shock, analogous to the development of an acoustic shock on the leading edge of a sound wave [222]. In the present work, figures 3.42(III) to 3.42(VIII) show rather that, an asymmetry of the FEAP spectrum could be obtained through the initial chirping directly at the input and can be preserved continuously under the first order SPM effects. It means that, the chirp also creates an optical shock on asymmetric pulses, analogously to the SS effect. Nonetheless, this optical shock induces a spectral asymmetry which depends on the sign of the imposed frequency chirp. For the considered simulations, the positive chirp creates the optical shock in the leading edge (blue shifted oscillations) of the spectrum leading this one to have an Airy-like form (for C=1) and just an asymmetric profile as observed (for small values of chirp as 0.1). The opposite happens for the negative chirp, in which the shock is observed on the trailing edge of the spectrum (red shifted oscillations seen on figures 3.42(VIII) for C=-1 and 3.42(VI) for C=-0.1). One can also refer to the TOD effect on the spectrum of an unchirped Gaussian pulse discussed in [3]. Indeed, it has been demonstrated that, a such symmetric profile becomes asymmetric in the spectral domain because of the TOD effect even in the presence of the SPM effects [3,249].

Thus, the chirp effect is similar to the SS and TOD effects. Subsequently, it is assumed that chirping the FEAP should increase significantly the broadening of its spectra. This result is obtained when we compare the extent of the unchirped spectrum (black solid curves in figures 3.42(III) and 3.42(IV)) with those of the chirped cases (colored curves in figures 3.42(III) and 3.42(IV)). The idea to use chirped FEAPs to produce broadband spectra is therefore well understood. A direct application to the SCG phenomenon resounds with these observations. In the literature, the spectral broadening induced by chirp has been already reported, however for the only studied symmetric profiles previously mentioned [3,137,201].

### Initial chirp inducing changes in the temporal shape : the A.I mechanism

In this subsection, we assume $\delta_4 = 0$ in Eq. (3.2) and investigate numerically the A.I mechanism. In figure 3.43 we illustrate this mechanism induced by the initial chirp in the anomalous GVD. In the

basic theory of pulse compression, considering the linear case ($N = 0$) when only the GVD governs the dynamics, the duration of the input pulse should be reduced in order to compress the pulse during its propagation with $\beta_2 C < 0$ [3,227,236,248,250]. In the present figure (figure 3.43), the interaction between the chirp and GVD, with opposite sign, influences deeply the temporal profile of the FEAP.

In order to highlight the interesting feature of the A.I mechanism obtained through the interaction between the initial chirp and the GVD, we have chosen to present in figure 3.43 different cases : (i) unchirped FEAP under anomalous GVD without TOD showed in (a.1) and (b.1), (ii) case of positively chirped FEAP under anomalous GVD without TOD showed in (a.2) and (b.2), (iii) case of positively chirped FEAP under anomalous GVD with negative TOD showed in (a.3) and (b.3), (iv) case unchirped FEAP under anomalous GVD with positive TOD (it is the result obtained by **R. Driben et al** in [251]) showed in (a.4) and (b.4), (v) case of negatively chirped FEAP under anomalous GVD with positive TOD showed in (a.5) and (b.5).

The pictures of (a.1) and (b.1) presents the acceleration of the FEAP's oscillations tail and dominant peak toward the trailing edge. Indeed, the FEAP freely accelerates as expected and bends itself to the right-side [12,251]. One can see the slight shift of the dominant peak obtained in figure 3.43(a.1) (see the green dashed curve comparatively to the input blue solid curve).

The novelty is underlined by the A.I occurring under the interplay between the positive chirp and the anomalous GVD (see figures 3.43(a.2) and 3.43(b.2)) instead of TOD effect as discussed in [251]. The oscillations tail of the temporal FEAP profile that are initially and normally in the LHS (leading edge) of the dominant peak, accelerate and collide with this last one at a certain distance of propagation from the input $\xi = 0$ (This distance is similar to the tight-focusing point or focal point discussed in [251]). This collision is found in our simulations between $\xi = 600$ and $\xi = 900$. Within the collision area $600 \leq \xi_{coll} \leq 900$, the FEAP's asymmetric shape completely collapses. After $\xi_{coll}$, the FEAP self-heals with the occurrence of the A.I : both the dominant peak and the oscillations tail regenerate themselves while in addition these last ones are recreated in the RHS (trailing edge) of the time domain instead of the regular LHS as can be observed in figure 3.43(a.2). Therefore, the A.I obtained in [251] differs from the one induced by the interaction chirp-GVD presented here : in [251] the tight-focusing of the FEAP is induced by TOD while in the present case, it is rather induced by the chirp effect. The oscillations tail collide with the dominant peak then, induce a FEAP collapse before its regeneration in the opposite side. As a result, it is found that the A.I mechanism occurs only when the GVD regime is opposite to the initial chirp : $chirp \times GVD < 0$. Under these conditions, a compact and symmetric profile as Gaussian, hyperbolic secant or raised-cosine pulse should be only compressed [3,224,227] while an asymmetric profile as a FEAP beyond the temporal compression, undergoes also an A.I mechanism. This result shows again that, the chirp produces the same effects as SS and TOD.

To confirm this observation, we add in the considered positive chirp-anomalous GVD system, a negative TOD as $s_3 = -1$ so that the TOD and GVD cooperate. We obtain figures 3.43(a.3) and 3.43(b.3). The effect of chirp inducing the A.I mechanism, is now counteracted by the TOD effect cooperating with the GVD. So, the TOD destroys the A.I mechanism induced by chirp-GVD leading rather the FEAP to diverge. On the other hand, we do once the simulation obtained by **R. Driben et al** in [251] by making that the unchirped FEAP propagates under the anomalous GVD and positive GVD, as expected the A.I mechanism induced by GVD-TOD occurs because of the competition between both the two dispersion orders (see figures 3.43(a.4) and 3.43(b.4)). Adding now a chirp having the same sign with the GVD ($C = -1$ with $s_2 = -1$) and opposite to the TOD ($s_3 = 2$), destroys the A.I mechanism induced by GVD-TOD as can be observed in figures 3.43(a.5) and 3.43(b.5). From all these observations, the chirp effect can be definitely assumed as a third-order effect acting in the linear aspect of propagation as a TOD (figure 3.43) and in the nonlinear aspect of propagation as a SS (figure 3.42).

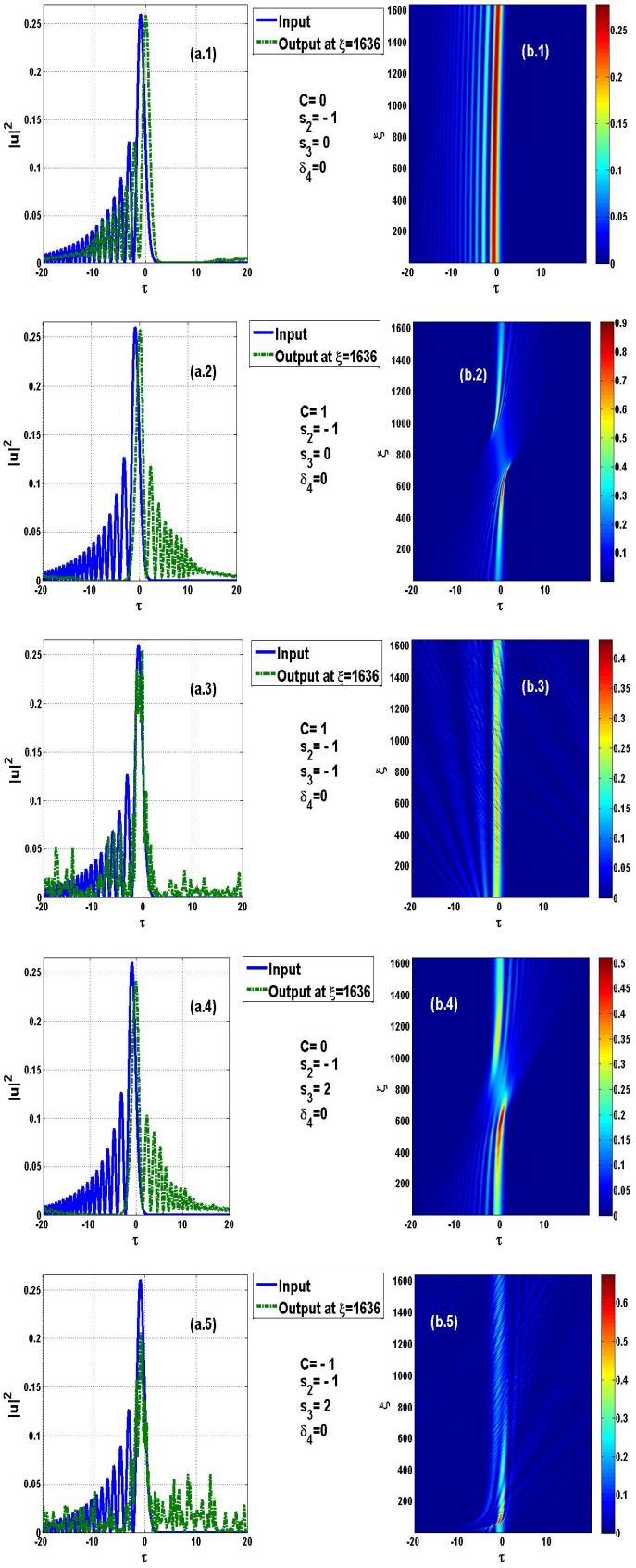


Figure 3.43: Anomalous GVD with $N = 1$, $a = 0.05$ and $\delta_4 = 0$. (a.1) and (b.1) unchirped case ($C = 0$) with $s_3 = 0$; (a.2) and (b.2) $C = 1$ with $s_3 = 0$ : A.I induced by the interaction chirp-GVD; (a.3) and (b.3) $C = 1$ with $s_3 = -1$; (a.4) and (b.4) unchirped case ($C = 0$) with $s_3 = 2$ : A.I induced by the interaction TOD-GVD; (a.5) and (b.5) $C = -1$ with $s_3 = 2$.

The confirmation of this result is given in figure 3.44 where the FEAP propagates under a negative chirp ($C = -1$) and a normal GVD regime ($s_2 = 1$). In the same figure, beyond the A.I mechanism occurring in the normal GVD with negative chirp symmetrically to the one occurring in the anomalous GVD with positive chirp in figure 3.43, the influence of the truncation coefficient $a$ is presented.

Indeed, the A.I mechanism is shown for several values of $a$ from 0.005 to 0.9. The first notice done concerns the input profiles of blue solid curves observed in figures 3.44(a.1)-(a.8) : both the number of oscillations tail and the FEAP intensity decrease when $a$ increases. Considering the decrease of the FEAP intensity with $a$, it is obvious to note that, it is exactly the role played by the truncation coefficient to gives to the Airy pulse a finite energy. On the other hand, as it can be observed in figure 3, the reduction of the number of oscillations tail leads to a symmetric shape (see for instance figure 3.44(a.8) for $a = 0.9$). Consequently, the FEAP loses its asymmetry with the increase of $a$ and then the A.I mechanism also disappears. The area of the FEAP's collapse in the A.I mechanism is reduced with the increase of $a$ (see the cases of $a = 0.1$ to $a = 0.9$ in figure 3.44). The parameter $a$ does not really affect the distance $\xi_{coll}$ over which the A.I occurs.

To see what exactly happens within the focal area (or FEAP shape's collapse area), we present in figure 3.45 the evolution of the FEAP shape after several values of the normalized propagation distance $\xi$. Here, the snapshots of (I) to (V) show how the oscillations tail collide with the dominant peak of the FEAP, merging and transferring their energy to this latter. Thus, the dominant peak amplifies and the standard FEAP shape is completely collapsed while the profile remains left-handed asymmetric. Then, the only emerging and dominant peak settles progressively from (VI) to (VIII) by a broadening and transforms into a compact and symmetric shape. In the vicinity of $\xi \approx 825$ (considering our conditions of simulation), the compact and symmetric shape for the only existing peak is completely formed (see (IX) in figure 3.45). Then, the reverse process occurs, transforming progressively the obtained nearly symmetric output (NSO) into a right-handed asymmetric output until the whole formation of the asymmetric shape (see (X) to (XII) in figure 3.45). The compact NSO obtained in (IX), can be assumed to have a Gaussian-like shape as mentioned previously by **R. Driben et al** in [251].

One observes also a temporal compression of the whole pulse which is accompanied by the amplification of the dominant peak as generally noticed in the compression process of symmetric pulses (see the red dashed curves from (I) to (V) on figure 3.45). Beyond the collapse's area, this compression is followed by a broadening-like process. Therefore, the A.I mechanism for an asymmetric pulse as a FEAP can be explained through four physical processes :

- the initial chirping gives an energy to the oscillations tail, that move faster than the dominant peak (the group-velocity of the oscillations tail increases under the chirping) in the acceleration phase (displacement from the leading edge to the trailing edge),
- the interaction between the chirp and the opposite GVD, compresses the whole pulse and amplifies the dominant peak by a fusion with the oscillations tail,
- after this initial phase, the pulse completely loses its asymmetry (in the collapse's area) and becomes continuously symmetric,
- then, the broadening occurs with the regeneration of the oscillations tail in the opposite side. The oscillations tail move faster than the dominant peak, cross this latter and reform in the opposite side.

In order to analyze the dependence of the A.I mechanism to the value of chirp, we plot on figure 3.46 the relation between the minimal distance $\xi_{sym}$ (over which the FEAP becomes nearly symmetric) and the chirp C. It is found that, this distance decreases following the increase of the

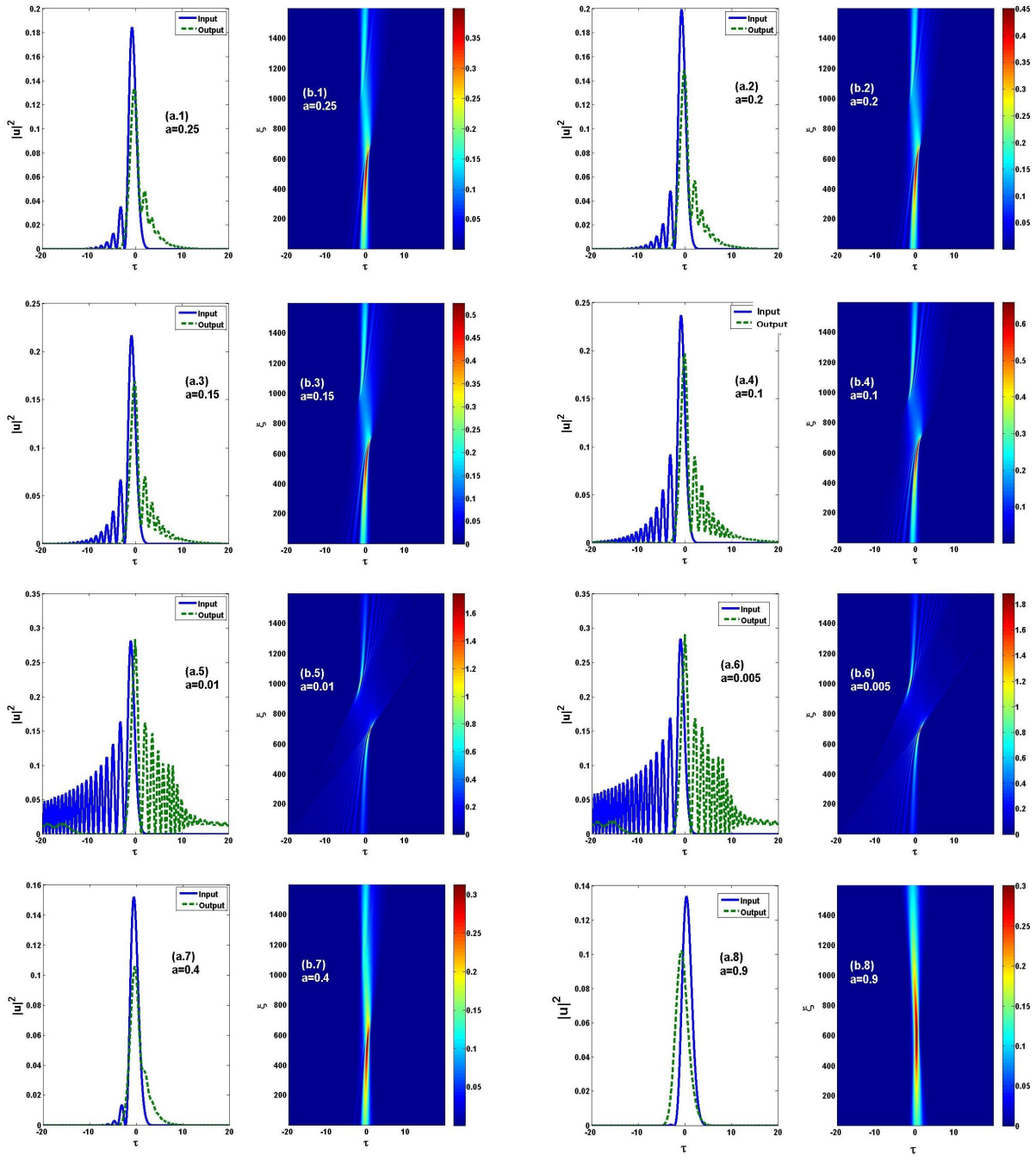


Figure 3.44: The A.I mechanism in the normal GVD regime with $C = -1$, N=1, $s_3 = 0$ and $\delta_4 = 0$: variation of the truncation coefficient. In (a.1) to (a.8) : solid blue curves are for the inputs and dashed green curves are for outputs. (a.1) and (b.1) for $a = 0.25$, (a.2) and (b.2) for $a = 0.2$, (a.3) and (b.3) for $a = 0.15$, (a.4) and (b.4) for $a = 0.1$, (a.5) and (b.5) for $a = 0.01$, (a.6) and (b.6) for $a = 0.005$, (a.7) and (b.7) for $a = 0.4$, (a.8) and (b.8) for $a = 0.9$.

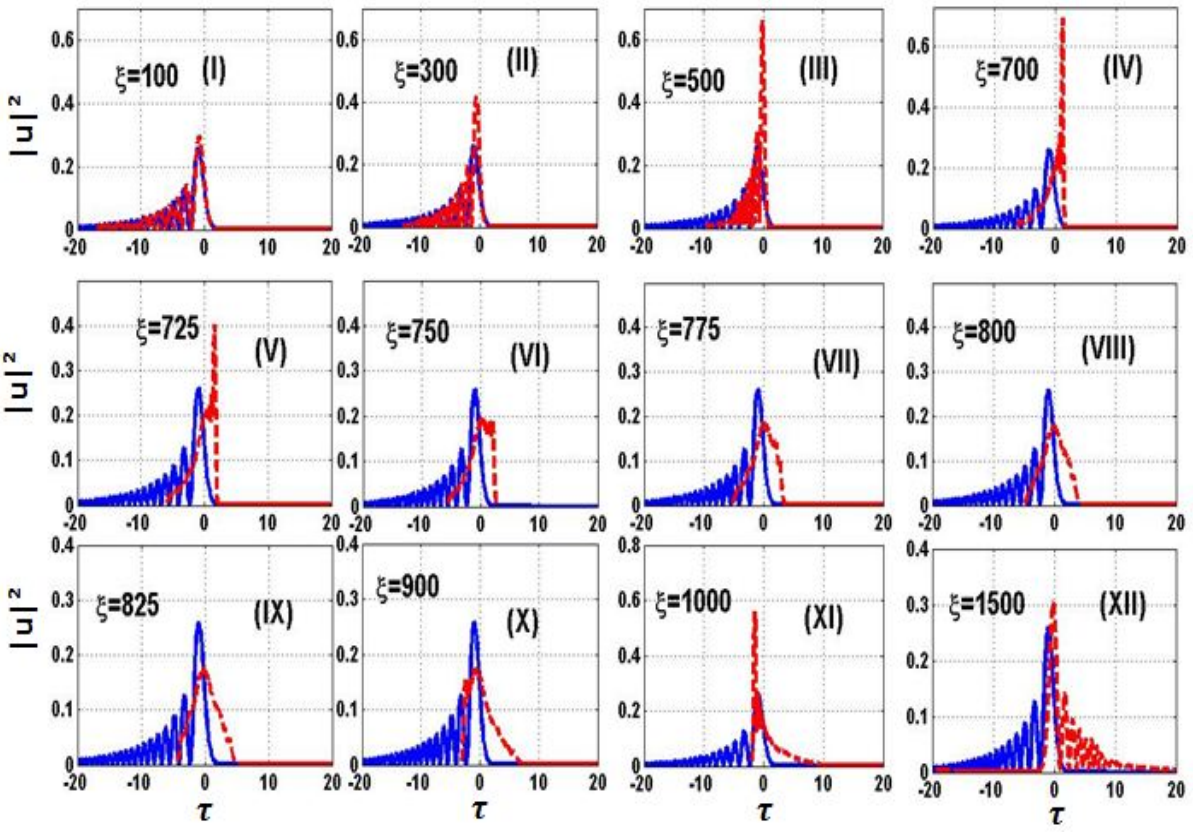


Figure 3.45: Plots of $|u|^2$ versus $\tau$ for $N = 1$, $\delta_3 = 0$ and $\delta_4 = 0$. FEAP shape's snapshots after several values of $\xi$ around the collapse area : $C = 1$, $s_2 = -1$ and $a = 0.05$. Solid blue curves for the input and dashed red curves for the output.

chirp. Note that the conditions assumes an anomalous GVD without the FOD and a first order solitonic state. We compare the blue solid curve obtained for this relation with the one in green

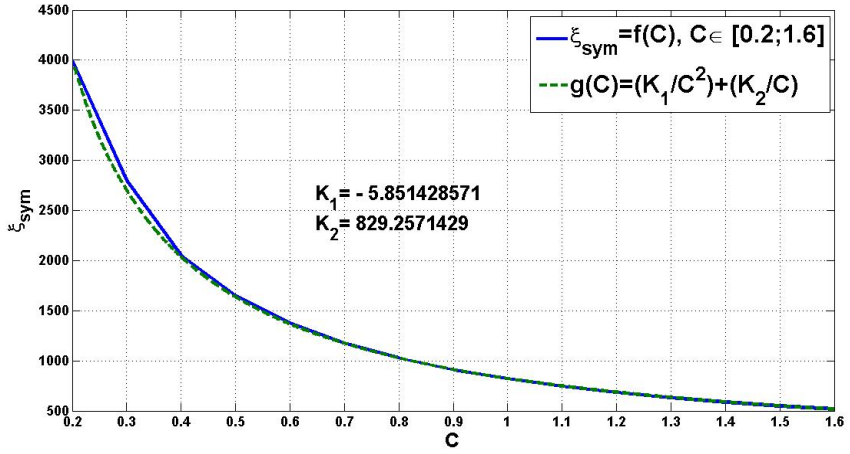


Figure 3.46: Plot of $\xi_{sym}$ versus $C$ with $a = 0.05$, $s_2 = -1$ (anomalous GVD), $s_3 = 0$ and $\delta_4 = 0$.

dashed curve of a function $g(C) = (K_1/C^2) + (K_2/C)$ where the constants $K_1$ and $K_2$ are exactly defined in figure 3.46. One observes that these curves nearly matches. Therefore, we can sketch a relation between $\xi_{sym}$ and C as :

$$\xi_{sym} = \frac{z_{sym}}{L_{GVD}} = 2\left(\frac{415C - 3}{C^2}\right), \quad C \in [0.2; 1.6], \tag{3.3}$$

with $z_{sym}$ being the physical propagation distance corresponding to $\xi_{sym}$. For small values of C, as those between 0.2 and 0.4, this relation is only an approximation as seen in figure 3.46. However, for values beyond 0.4 to 1.6, we obtain a nearly perfect match.

### FOD interacting with the GVD for unchirped FEAPs : dominant peak amplification

We recall that, the SMFs manufactured at (or near) the zero-TOD ($s_3 = 0$) are the so-called dispersion flattened fibers (DFFs) in which the GVD remains finite. Therefore, it is necessary to include the FOD effect in order to describe the dynamics [3,224,225,248,252]. The chromatic dispersion profile of such fiber could be seen in [252] compared to those of standard SMFs and dispersion-shifted fibers. The peculiarity of this HDOF is described by the following assumptions $s_2, \delta_4 \neq 0$ and $s_3 = 0$. In the unchirped case (C=0), we present on figure 3.47 the interaction between the anomalous GVD regime with the positive values of FOD meaning that $\delta_4 < 0$. The value $\delta_4 \leq -0.09$ leads to figure 3.47(a). The profile remains nearly unchanged compared to the input even though, a slight shift of the dominant peak is observed toward the leading edge. However, considering highly dispersive DFFs in which the magnitude of FOD can reach ratios $|\delta_4| \geq 0.5$, one observes an interesting feature induced by FOD on the FEAP. Varying the ratio $\delta_4$ for example from $-0.5$ to $-2$ yields the curves in figures 3.47(b)-3.47(f). The oscillations tail in the LHS accelerate and collide with the dominant peak without a collapse of the pulse (as observed during the A.I mechanism of figures 3.43-3.45), transferring their energy to this one. From this energy transfer, the resulted single peak, amplifies compared to the input dominant peak (for instance, a comparison between the dominant peaks of the cases $-0.09$ and $-0.5$, shows this feature). For values between $-0.9$ and $-2$ (and certainly beyond) the obtained single dominant peak is not stable and broadens once formed following the increase of

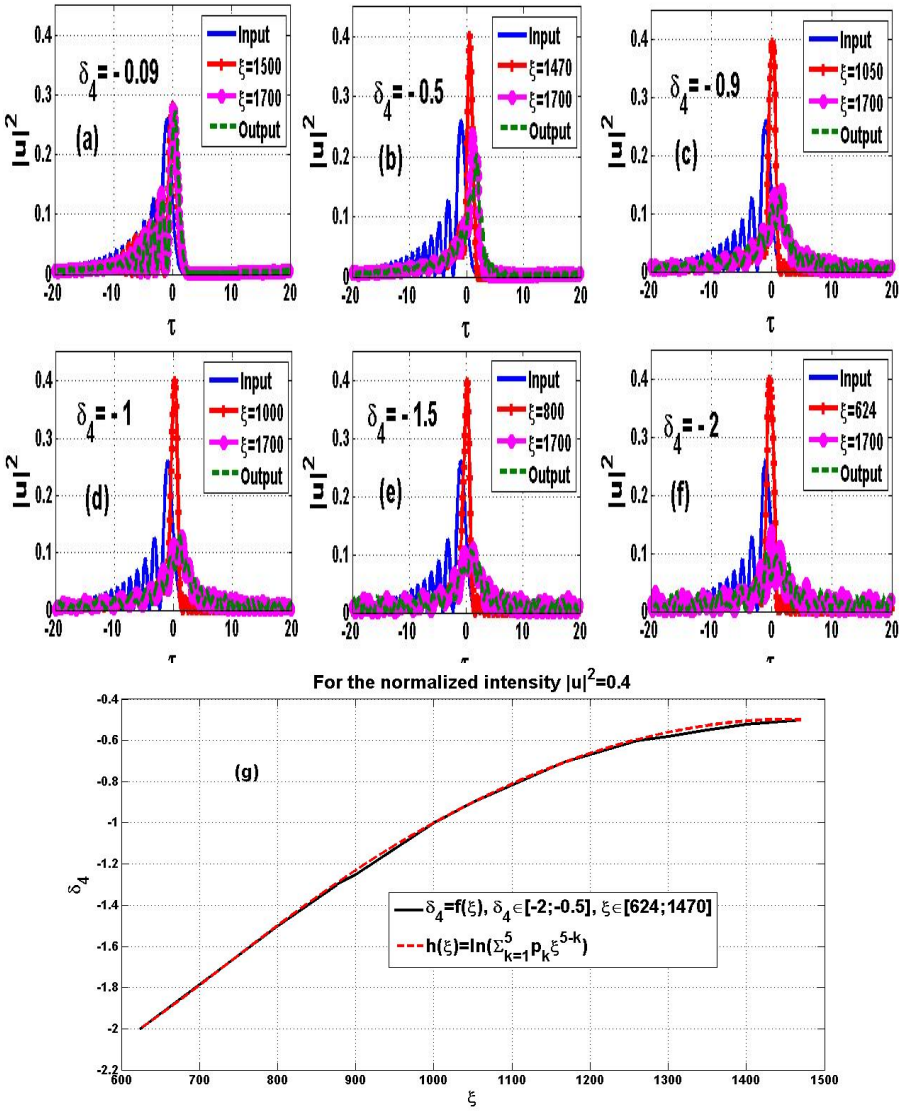


Figure 3.47: Time domain profiles : (a) input; (b)-(f) Outputs under the anomalous GVD interacting with several values of positive FOD, N=1 and $a = 0.05$. In (g), plot of $\delta_4$ versus $\xi$ for the normalized intensity $|u|^2$. For the function $h(\xi)$, the coefficients $p_k$ are defined as : $p_1 = -3.665811447 \times 10^{-13}$, $p_2 = 3.393760864 \times 10^{-10}$, $p_3 = 1.22446208710^{-6}$, $p_4 = -1.226215464 \times 10^{-3}$, $p_5 = 0.3968378758$.

the propagation distance (see the circle violet and the dashed green curves of figures 3.47(b)-(f)). Furthermore, we can see in this figure that with the increase of $|\delta_4|$, the amplification of the dominant peak is obtained sooner (see the red crossed curves in figures 3.47(b)-(f)). For example, one obtains a single amplified dominant peak of 0.4 in normalized intensity $|u|^2$ at $\xi = 1470$ for $\delta_4 = -0.5$ while for $\delta_4 = -2$ the normalized distance is 624. We plot in figure 3.47(g), the relation that draws the dominant peak amplification induced by FOD versus the propagation distance. It is noticed that, the amplification appears sooner as the FOD (defined by $\delta_4$) increases. In an analog fashion to Eq. (3.3), we sketch for the achievement of 0.4 in normalized intensity of an unchirped FEAP in a N=1-anomalous GVD-positive FOD DFF system, the relation between the parameters $\delta_4$ and $\xi = z/L_{GVD}$ as :

$$\begin{aligned}
\delta_4 =& \frac{|\beta_4|}{|\beta_2|T_0^2} = \ln\left(\sum_{k=1}^{5} p_k \left(\frac{z}{L_{GVD}}\right)^{5-k}\right), \\
p_1 =& -3.665811447 \times 10^{-13}, \\
p_2 =& 3.393760864 \times 10^{-10}, \\
p_3 =& 1.22446208710^{-6}, \\
p_4 =& -1.226215464 \times 10^{-3}, \\
p_5 =& 0.3968378758,
\end{aligned} \tag{3.4}$$

where $T_0$ is the physical pulse duration in $ps$ unit, $|\beta_2|$ the absolute value of the GVD in $ps^2/m$ and $|\beta_4|$ the absolute value of the FOD in $ps^4/m$. It is worthy to notice that in the case of GVD having the same sign as the FOD, one should obtain rather a drastic broadening : the FEAP will diverge. It means that, the oscillations tail instead of accelerate toward the leading edge, spread rather in the LHS while the dominant and secondary peaks spread in the RHS of the time domain (see figure 3.48). Figure 3.48 shows this broadening and distorted evolution (3.48(a.1) and 3.48(a.2)); The corresponding spectral evolution is depicted on figures 3.48(b.1) and 3.48(b.2).

**The FEAP shape preserving induced by the interaction between the chirp, the GVD and the FOD**

Considering the system of DFF, we use the linear chirp and we obtain the figure 3.49. In this figure, we distinguish the following cases of interaction between GVD, FOD and the small value of chirp :

- Case of FEAP shape preserving corresponds to figure 3.49(a) ($C = 0.1$, $s_2 = 1$ and $\delta_4 = 0.9$), figure 3.49(f) ($C = -0.1$, $s_2 = -1$ and $\delta_4 = -0.9$), figure 3.49(g) ($C = -0.1$, $s_2 = 1$ and $\delta_4 = -0.9$) and figure 3.49(h) ($C = 0.1$, $s_2 = -1$ and $\delta_4 = 0.9$).

- Case of the dominant peak amplification induced by the acceleration-collision with the oscillations tail corresponds to figures 3.49(b) ($C = -0.1$, $s_2 = 1$ and $\delta_4 = 0.9$) and 3.49(c) ($C = 0.1$, $s_2 = -1$ and $\delta_4 = -0.9$). It is similar to that of the unchirped GVD-FOD cases discussed in figure 3.47.

- Case in which the secondary peak amplifies instead of the dominant one. It corresponds to figure 3.49(d) ($C = 0.1$, $s_2 = 1$ and $\delta_4 = -0.9$) and figure 3.49(e) ($C = -0.1$, $s_2 = -1$ and $\delta_4 = 0.9$).

Comparing figures 3.49(a), 3.49(f), 3.49(g) and 3.49(h), we notice that for the FEAP shape preserving under the conditions of small absolute value of chirp in a highly dispersive DFF, it is

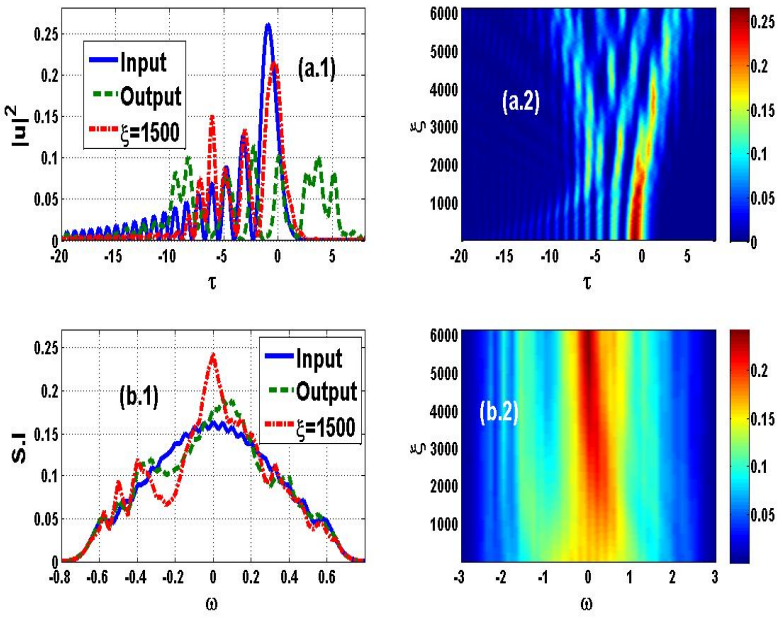


Figure 3.48: For $N = 1$, anomalous GVD and negative FOD with $\delta_4 = 0.9$, $C = 0$ and $a = 0.05$ : (a.1) temporal profile, (a.2) contour plot of the time domain propagation; (b.1) spectral profile, (b.2) contour plot of the frequency domain propagation.

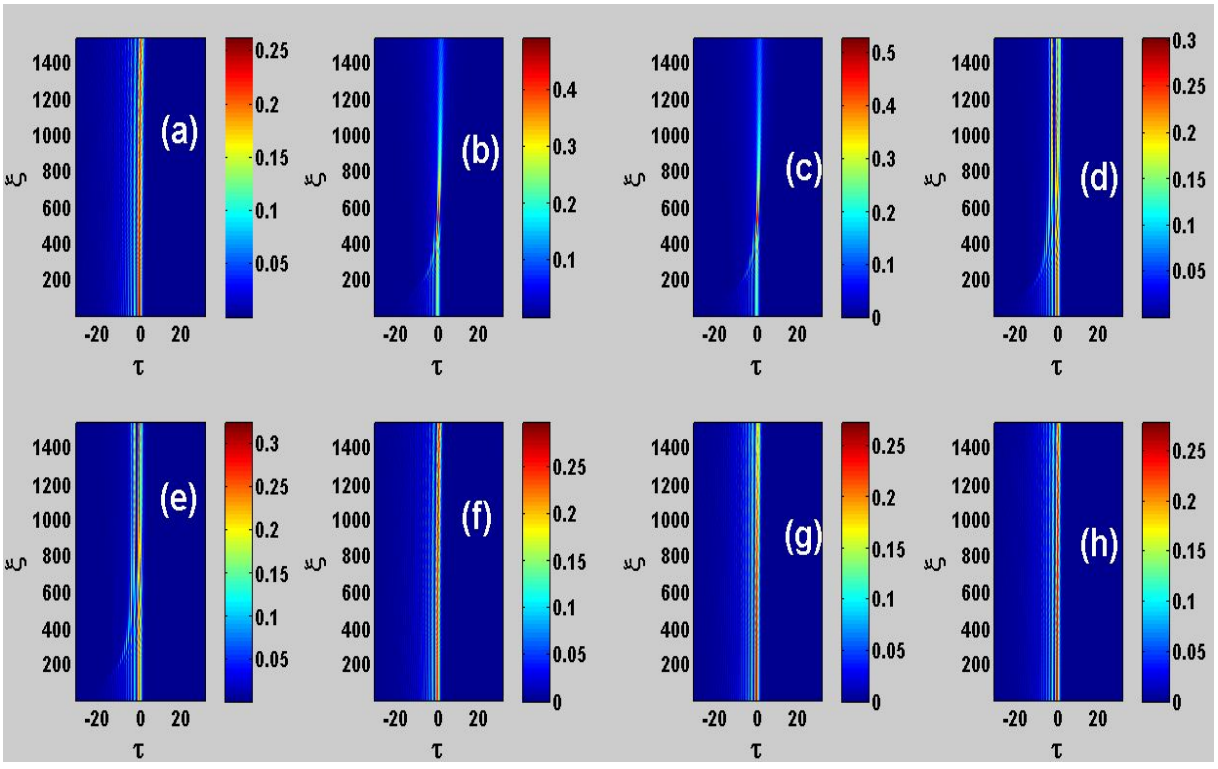


Figure 3.49: Contour plots of time domain propagation of the FEAP for N=1 and $a = 0.05$. It is presented the interaction between the FOD, the GVD and the chirp : (a) $C = 0.1$, $s_2 = 1$ and $\delta_4 = 0.9$; (b) $C = -0.1$, $s_2 = 1$ and $\delta_4 = 0.9$; (c) $C = 0.1$, $s_2 = -1$ and $\delta_4 = -0.9$; (d) $C = 0.1$, $s_2 = 1$ and $\delta_4 = -0.9$; (e) $C = -0.1$, $s_2 = -1$ and $\delta_4 = 0.9$; (f) $C = -0.1$, $s_2 = -1$ and $\delta_4 = -0.9$; (g) $C = -0.1$, $s_2 = 1$ and $\delta_4 = -0.9$; (h) $C = 0.1$, $s_2 = -1$ and $\delta_4 = 0.9$.

necessary to have the condition $C \times GVD \times FOD > 0$. The small value of chirp can therefore be used to stabilize over a certain propagation distance the FEAP shape before its distortion.

For the occurrence of the amplification of the dominant peak into a single peak that corresponds to figures 3.49(b) and 3.49(c), the condition is found to be $C \times GVD < 0$ and $FOD > 0$.

The amplification of the two dominant peaks after the collision with the oscillations tail, corresponds to the case where the condition $C \times GVD \times FOD < 0$ and $FOD < 0$ as discussed above for figures 3.49(d) and 3.49(e). We present in figure 3.50, the FEAP at different propagation distances

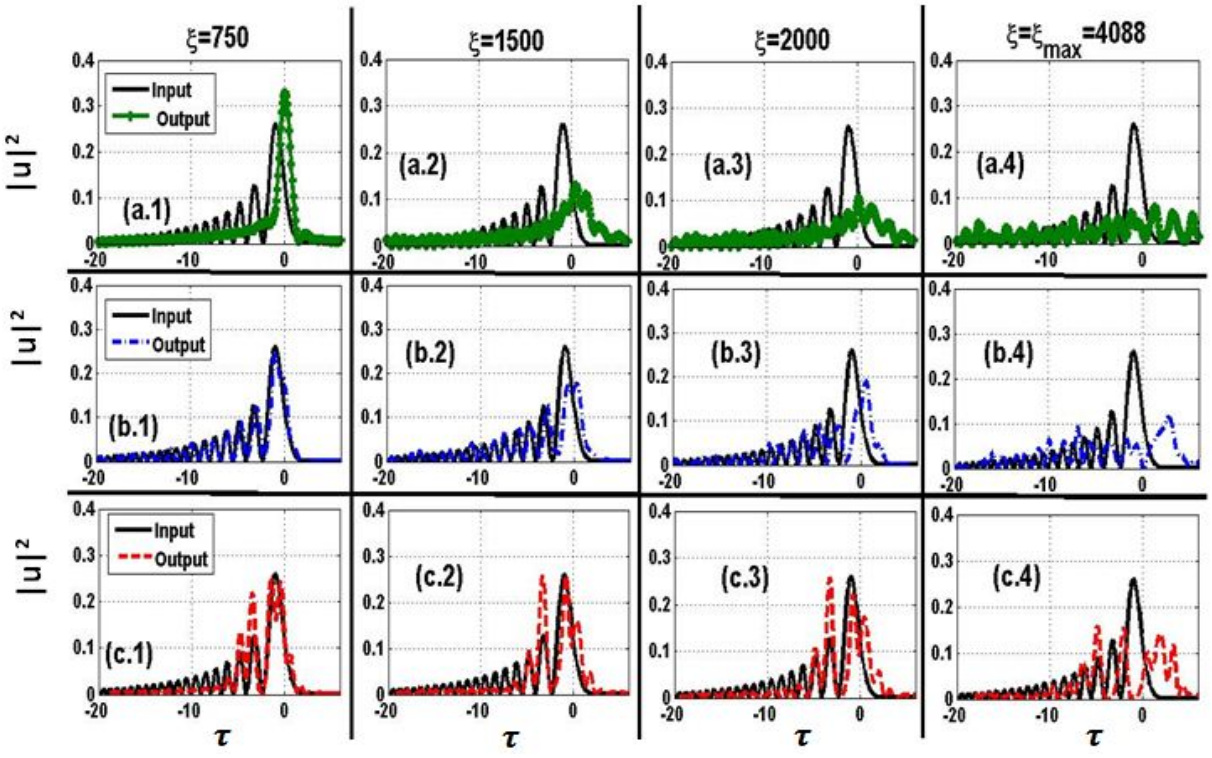


Figure 3.50: Plots of $|u|^2$ versus $\tau$ for N=1 and $a = 0.05$. The first row is for the dominant peak amplification case defined by $C = 0.1$, $s_2 = -1$ and $\delta_4 = -0.9$, the second row is for the FEAP shape preserving defined by $C = -0.1$, $s_2 = 1$ and $\delta_4 = -0.9$ and the third row is for the secondary peak amplification defined by $C = 0.1$, $s_2 = 1$ and $\delta_4 = -0.9$. The first column corresponds to the outputs at $\xi = 750$, the second column for $\xi = 1500$, the third column for $\xi = 2000$ and the fourth column for $\xi = \xi_{max} = 4088$.

for the three cases mentioned above. In the case of the dominant peak amplification depicted in figures 3.50(a.1)-(a.4), once the amplification is obtained ($\xi = 750$), the single peak broadens in an irregular manner ($\xi = 1500$ to $\xi_{max}$). Considering the case of the FEAP shape preserving induced by chirp (see the blue dot-dashed curves in figures 3.50(b.1)-(b.4)), the FEAP resists to the broadening over a long propagation distance as $\xi = 2000$ (figure 3.50(b.3)). However for very large distances as $\xi_{max}$, it undergoes distortion. We end with the case of the secondary peak amplification drawn in figures 3.50(c.1)-(c.4). In this case, the secondary amplifies continuously while the dominant one splits into sub-peaks. Progressively until the end of the waveguide, the picture becomes more and more distorted as observed in figure 3.50(c.4). Considering the values of $\delta_4 = -0.9$ and $s_2 = 1$, we show in figure 3.51 that only small values of chirp allow to stabilize the FEAP shape over a long propagation distance as observed in figures 3.50(b.1)-(b.4). Indeed, we plot under the same condition of $C \times GVD \times FOD > 0$, the case of $C = -1$ (see the red dashed curves in figure 3.51). One observes that, this case is less stable than the one of $C = -0.1$ (in black solid curves). So, figure 3.51 confirms that small values of chirp are only those which allow the FEAP to preserve its shape

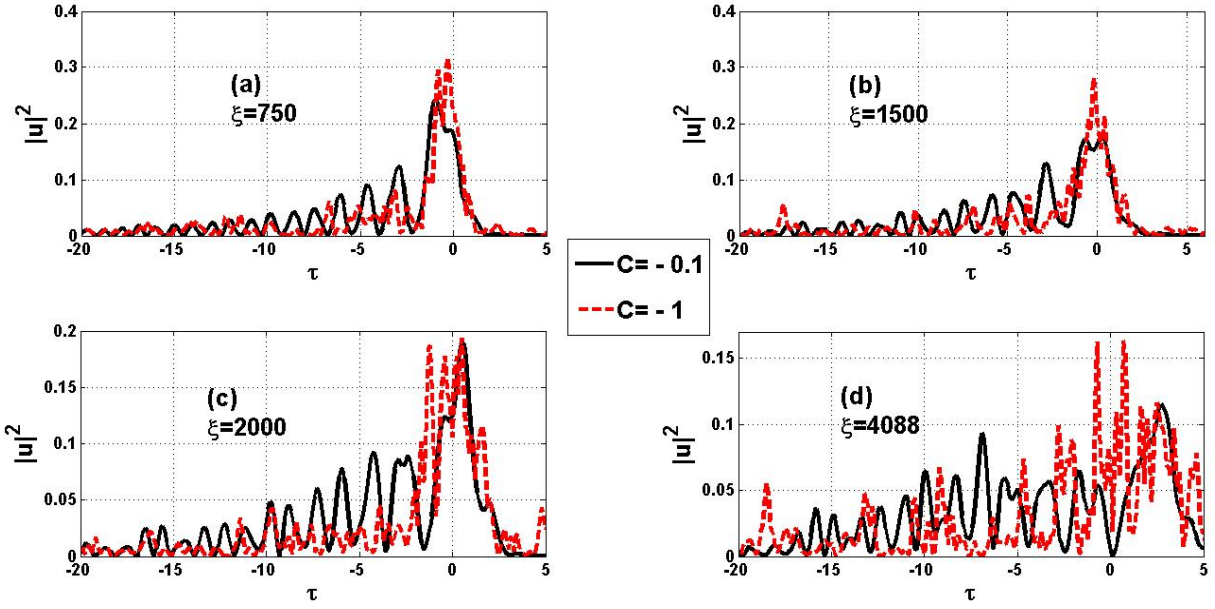


Figure 3.51: Plots of $|u|^2$ versus $\tau$ for $N = 1$, $a = 0.05$ $s_2 = 1$ and $\delta_4 = -0.9$. The black solid curves are for $C = -0.1$ and the red dashed curves are for $C = -1$. (a) $\xi = 750$, (b) $\xi = 1500$, (c) $\xi = 2000$ and $\xi = \xi_{max} = 4088$.

under the GVD-FOD effect following the condition $C \times GVD \times FOD > 0$.

### 3.7.2 Part II : SCG's analysis in the $CS_2$−LCPCF

**Pumping in the normal dispersion regime**

Let us consider first the influence of the initial chirp on the spectra ($C \neq 0$). We use an initial energy of 18 nJ that leads to an interesting broadened spectrum for the FEAP. The data are defined as : $\beta_2 = 0.0159$ $ps^2/m$ and $\gamma$=2.0495 $W^{-1}m^{-1}$ for $\lambda_p = 1550$ nm (normal dispersion regime) and $\beta_2 = -0.0547$ $ps^2/m$ and $\gamma$=1.482 $W^{-1}m^{-1}$ for $\lambda_p = 2030$ nm (anomalous dispersion regime).

- **Positive chirp :**
  We plot the spectral intensity (S.I) in dB units versus the wavelength ($\lambda$). As seen in figure 3.52, the initial chirp influences the SCG spectra for both the two profiles. Nonetheless, this effect is more important for the FEAP than for the sech-type pulse. Indeed considering the shapes, as early introduced in [248] by **Mandeng** and **Tchawoua** (with the extension done in [236]) after by **Zhang et al** [250,253], the chirp transforms the FEAP spectra into an Airy profile. It behaves as a SS effect as discussed in the present work. Then, considering the bandwidth, we notice that the FEAP is very wider than the sech-type under the effect of the chirp. The width of the FEAP's lobes increases under the chirp effect while the same feature can be observed for the sech-type pulse particularly on the input spectra. The increase of the initial chirp broadens the initial spectra of the sech-type pulse (see the dashed black curves of the left-hand side (LHS) of figure 3.52). Another observation done in figure 3.52, is the generation in the LHS of the spectrum of small oscillations tail induced by the increase of chirp (see the blue curves of (a.4) and (b.4)). The presence of these sides lobes in addition to those of the right-hand side (RHS), increases the bandwidth of the SCG compared with the cases of small values of chirp depicted in (a.1)-(a.3) and (b.1)-(b.3). The width of these chirp-induced sides lobes increases with the value of the chirp. We present in figure 3.53, the contour plots of a 2 mm-propagation of the pulses under the effect of the positive chirp. As can be observed in this figure, the initial

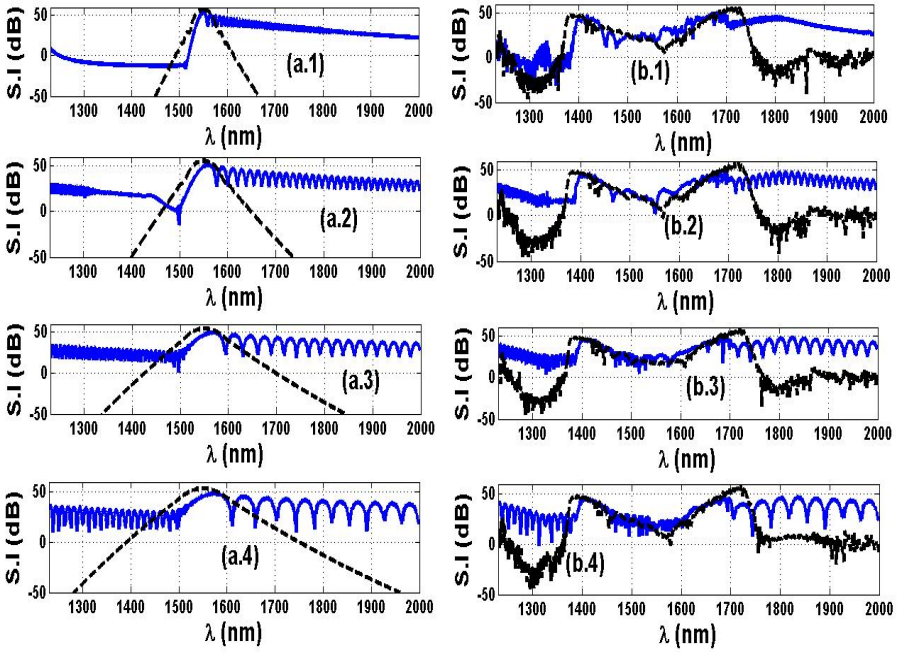


Figure 3.52: SCG spectra for the FEAP and the sech-type pulse with $t_0 = 100\ fs$, $a = 0.05$, fiber length of 1 cm and $E_0 = 18$ nJ : (a.1)-(a.4) are the inputs and (b.1)-(b2) are the outputs; (a.1) and (b.1) correspond to C=0.5, (a.2) and (b.2) to C=1, (a.3) and (b.3) to C=1.5 and (a.4) and (b.4) to C=2. Solid blue curves are for the FEAP and dashed black curves are for the sech-type pulse.

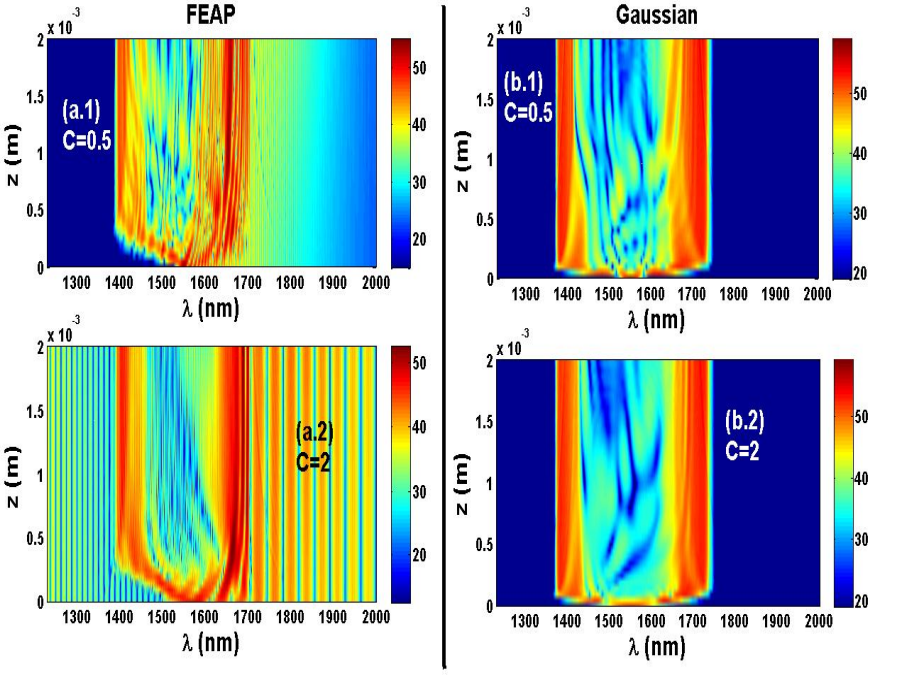


Figure 3.53: Contour plots with $t_0 = 100\ fs$, $a = 0.05$, fiber length of 2 mm and $E_0 = 18$ nJ : (a.1) C=0.5 and (a.2) C=2 for the FEAP; (b.1) C=0.5 and (b.2) C=2 for the sech-type pulse.

chirp influences significantly the spectra of the FEAP. For the value of $C = 0.5$ shown in figure 3.53(a.1), the FEAP's spectrum including the side lobes of the oscillations tail, extents about from 1400 nm to 2000 nm compared with the one of the sech-type pulse which stops only until about 1750 nm (see figure 3.53(b.1)). Considering the value $C = 2$ (see figure 3.53(a.2)), the FEAP's spectrum spreads about beyond 1300 nm toward the visible region to 2000 nm toward the infra-red region. On the contrary, the sech-type's spectrum (see figure 3.53(b.2)) after an earlier drastic spectral broadening, preserves nearly the same bandwidth. In the SCG phenomenon, it is the dominant peak of the FEAP which broadens while the side lobes of the oscillations tail keep nearly their width from input to the considered output (see figures 3.53(a.1) and 3.53(a.2)) .

- **Negative chirp :**
  When the FEAPs are chirped initially with a negative chirp, one obtains rather the figure 3.54.

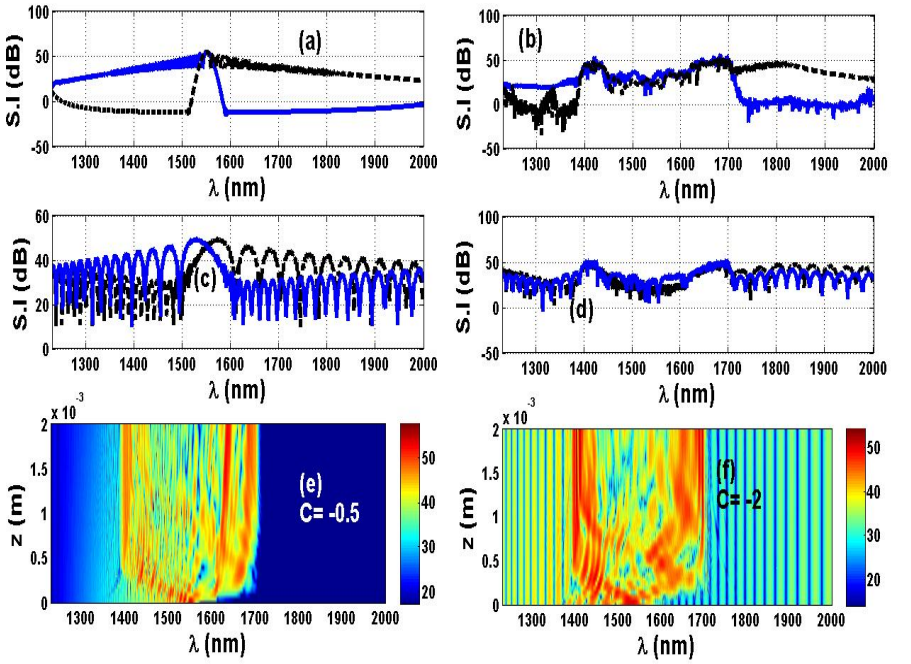


Figure 3.54: SCG spectra for the FEAP with $t_0 = 100\ fs$, $a = 0.05$ and $E_0 = 18$ nJ : (a) and (c) are the inputs while (b) and (d) are the outputs; (a) and (b) correspond to $C = \pm 0.5$, (c) and (d) to C=$\pm$2. Solid blue curves are for the negative chirp and dashed black curves are for the positive chirp. The contour plots (e) and (f) are respectively for C=-0.5 and C=-2.

The initial chirp yields the side lobes of the oscillations tail in the opposite side compared with the positive chirp symmetrically to the dominant peak [241,243]. As seen in figures 3.54(a)and 3.54(c) where both the cases of positive and negative values of chirp as $\pm 0.5$ and $\pm 2$ are plotted, there is a symmetry that appears in the input spectra obtained. Considering the outputs in figures 3.54(b)and 3.54(d), the bandwidth of the spectra are nearly the same. The contour plots drawn in figures 3.54(e) for $C = -0.5$ and 3.54(f) for $C = -2$ are nearly symmetric to those of figures 3.53(a.1) and 3.53(a.2).

The initial chirp has an important impact on the shape of the FEAP's spectrum [248,250]. The values considered in this work show that the spectra obtained both in the positively and negatively chirped cases with the FEAP, are widely more broadened than those of the sech-type pulse under the same conditions. Nonetheless, one should include the oscillations tail in the bandwidth calculation

even if only the dominant peak remains the one which is effectively broadened under the SPM (and obviously under the other processes derived from the SPM) in the considered $CS_2$-LCPCF (see figures 3.52-3.54). The side lobes of the oscillations tail in the FEAP spectra with their weak energy are not really influenced by the SPM and therefore remain nearly unchanged from the input to the chosen output. With the increase of the initial chirp, other oscillations tail are generated in the opposite side of the regular ones. The SCG-induced broadening of the FEAP's dominant peak shifts the side lobes generated by the chirp in the transversal direction and consequently, increases the spectra obtained. The increase of the initial chirp is obviously beneficial for the improvement of the spectral bandwidth as discussed in previous works [137,201,209]. However, this advantage is more developed for the FEAPs than the sech-type pulses.

We set that C=0 and show in figure 3.55, the effect of the truncation coefficient on the FEAP's SCG spectra. It is noticed that, when small values of $a$ are used as 0.005 and 0.01 (see the solid gray and dark green curves of figure 3.55, respectively), the spectra are wider than those of 0.05, 0.1, 0.5 and 0.9. Therefore, the decrease of the truncation coefficient is found to increase the spectral bandwidth of the FEAP. The colorless green curve plotted for the sech-type pulse propagating under

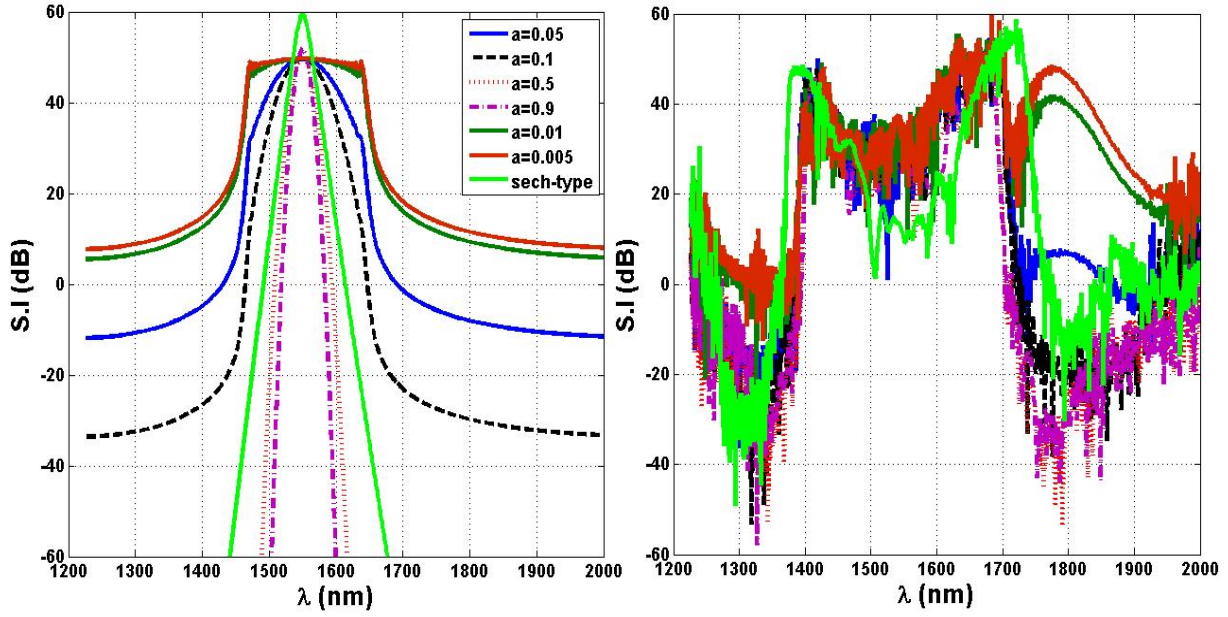


Figure 3.55: SCG spectra for 18-nJ pulses with 100 $fs$ and $C = 0$. Spectra in the LHS are for the inputs and those in the RHS are for the outputs at $L = 1$ $cm$. The decrease of $a$ improves the flatness of the input FEAP's spectrum.

the same conditions, is less wide than the $a = 0.005 - 0.01$ cases of FEAP at the output. Nonetheless, it remains wider than the $a = 0.05 - 0.9$ cases (see the curves in the RHS of figure 3.55). The effect of the truncation coefficient decay on the bandwidth of FEAP's spectra, can be explained through the physical description of the parameter $a$. Indeed, this one has been introduced earlier [11,12] to generate Airy waves with finite energy by contrast to the infinite ones defined by **Berry** and **Balazs** [13]. The role played by $a$ is to truncate the infinite energy of an Airy wave. Thus, more $a$ is high, more the Airy wave is truncated and has a weak energy. With a large value of $a$, a FEAP has a smaller energy than the case of a small value of $a$. Decreasing $a$ improves the FEAP's energy and consequently its spectral interaction with the SPM leading to broadband SCG's spectra. This justifies the result obtained in figure 3.55. However, as also observed in this figure, one should manage optimally the value of $a$ to obtain a FEAP's spectrum which is wider than the one of a sech-type

pulse taken under the same conditions. The values used in this work for this purpose are 0.01 and 0.005.

### Pumping in the anomalous dispersion regime

Considering the anomalous GVD regime, the output spectra obtained are depicted in figure 3.56. Both the unchirped case (see figure 3.56(a)) and the chirped case (see figure 3.56(b)) show that with

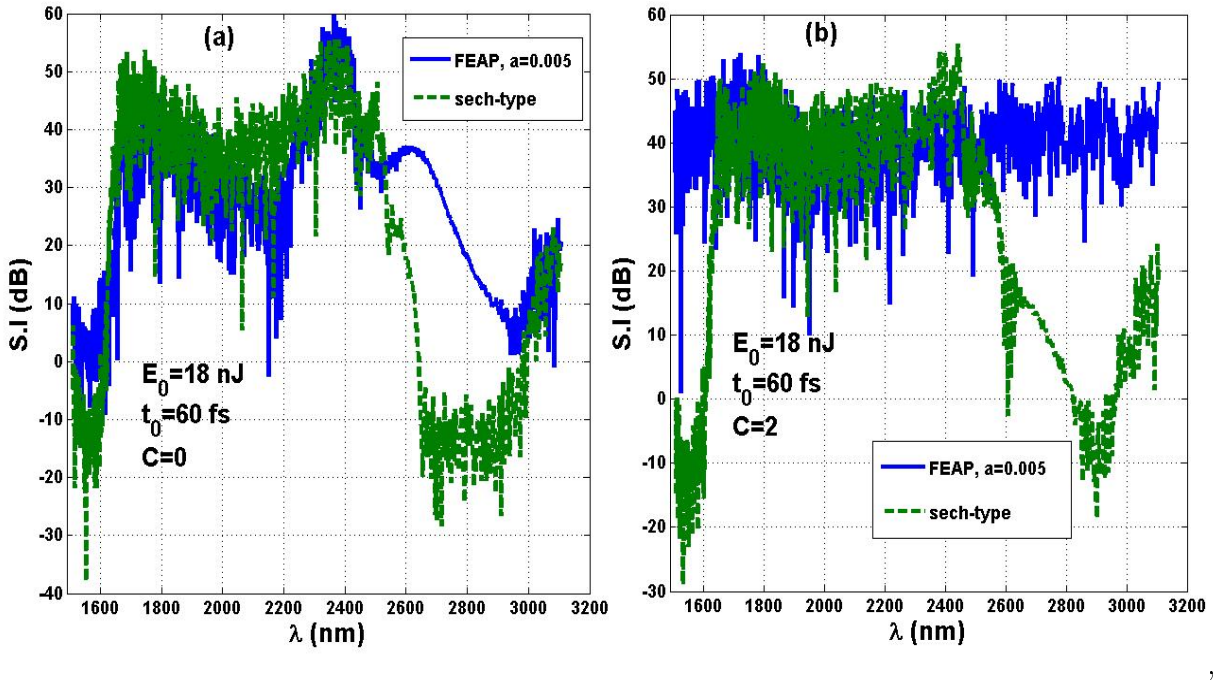


Figure 3.56: SCG's spectra at $L = 1\ cm$ obtained in the anomalous GVD regime with a pumping at $\lambda_p = 2030\ nm$. Parameters : $a = 0.005$ for the FEAP, $t_0 = 60\ fs$, $E_0 = 18$ nJ. (a) $C = 0$, (b) $C = 2$.

the considered parameters, the FEAP has a spectrum very wide than that of the sech-type pulse. The bandwidths of both the two pulses are larger than those of the normal GVD regime above (in figures 3.52-3.55). For instance, in the unchirped case depicted in figure 3.56(a), the FEAP's spectral bandwidth oversteps about 1200 nm at the 20-dB in S.I while the sech-type pulse reaches about 1000 nm. It is very significant in comparison to the bandwidths obtained for the normal dispersion regime. It is obvious to note that this is in agreement to the literature of the SCG phenomenon [114,137,144] : the pumping in the anomalous GVD regime is generally better than the normal one considering both the SF and the MI mechanisms. The key result of this simulation is not only the octave-spanning spectra better than the normal GVD regime but also the fact that, we still have the FEAP's spectra wider than those of the sech-type pulse.

A logical interpretation of the observations done both in the normal and the anomalous GVD regimes consists to focus on the main difference between the two input pulses : the FEAP has an asymmetry while the sech-type pulse is symmetric. The asymmetry of the shape plays so, a non negligible role on the spectral bandwidth of the drastic broadening obtained in the SCG phenomenon. This conclusion makes sense according to the results obtained by **Castelló-Lurbe et al** in [202a] (they model an input pulse to get a suitable skewness that enhances the SCG in silicon waveguides) and those of **Klimczak et al** in [202b] (they choose a steepness of the input pulse as a super-Gaussian pulse to improve the bandwidth and the CD of the SCG's spectra in all-solid PCFs with flattened normal dispersion). Following both these two works, the skewness and the steepness creates

an asymmetry on the input shape from which it can be deduced the SCG's improvement. In our work, we directly use an asymmetric pulse (FEAP) as suggested earlier by **Mandeng** and **Tchawoua** [248], and confirm the beneficial role played the asymmetry on the drastic spectral broadening.

### Spectral coherence

We plot in figure 3.57, the CDs of the SCG's spectra obtained for both the FEAP and the sech-type pulse in the anomalous GVD regime (with the previous parameters). For (a), (b) and (c), we present what happens with the values C=0, 2 and 4, respectively. The direct comparison between the CDs

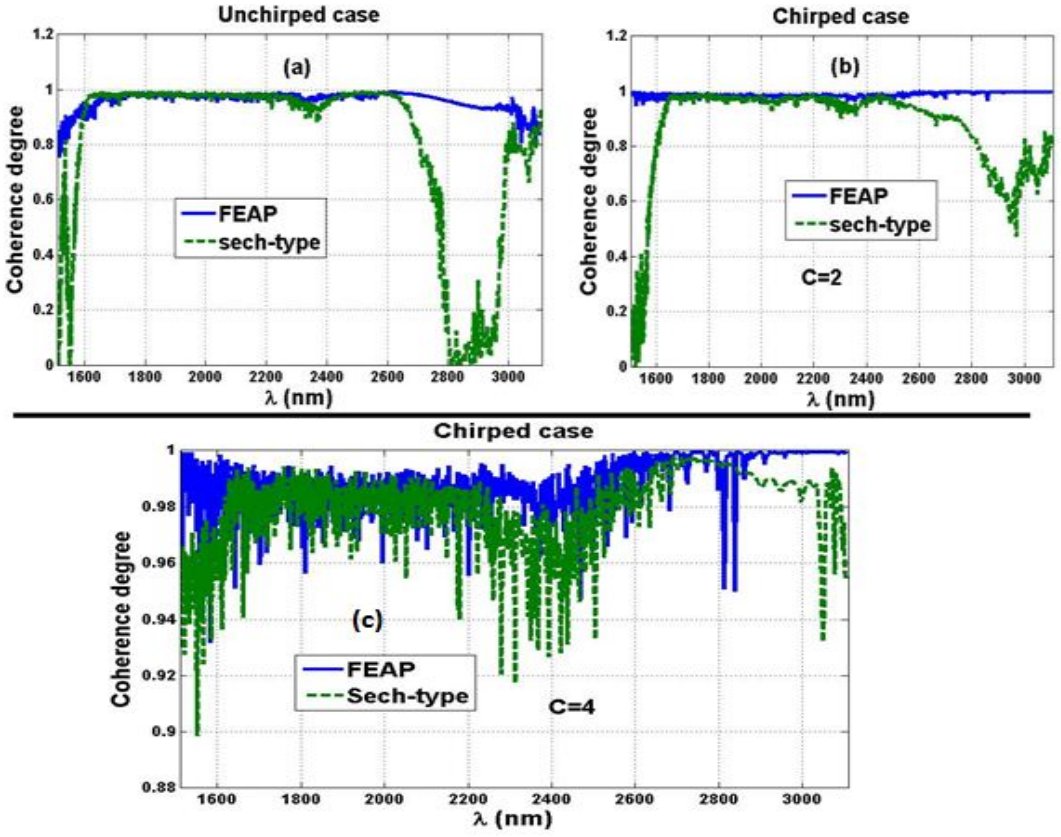


Figure 3.57: CD of the spectra obtained in the anomalous GVD regime with a pumping at $\lambda_p = 2030\,nm$. Parameters : $a = 0.005$ for the FEAP, $t_0 = 60\,fs$, $E_0 = 18$ nJ. (a) Unchirped case $C = 0$, (b) chirped case $C = 2$, (c) chirped case $C = 4$. The input profile asymmetry enhances the CD of the SCG's spectra.

obtained for the asymmetric shape and the symmetric one leads to the following result: the spectra of the FEAP are more coherent than those of the sech-type pulse since FEAP's CDs are nearly closer to 1 over the whole range of wavelengths from 1600 nm to 3200 nm than those of the sech-type pulse.

Physically, this can be explained through the SF/MI mechanisms inducing the SCG. Indeed, since these phenomena result in shedding of solitons from the propagating pulses, it is well-known that more the solitons emission is large more the CD decreases [3]. Thus, the CD is inversely related to the number of soliton emitted through the SCG. The SF is even known to be inherently noisy [3] while the MI itself is known to have weak CDs than the former mechanism ($N^{SF} \ll N^{MI} \Rightarrow CD^{SF} > CD^{MI}$) [144,145]. According to [18,27], FEAP sheds solitons as well as well-known for the HS (or sech-type) pulse. The soliton shedding from FEAPs depends strongly on its parameters as the peak power and the truncation coefficient [27]. Nonetheless, since the FEAP energy loss due to the shed soliton is not total, the remaining energy contributes to the persistence of the FEAP. It is obvious to note that this

characteristic contrasts with the soliton shedding from symmetric pulses as sech-type pulses (which is total) and consequently limits the number of emitted sub-solitons when $N = \left(P_0\gamma t_0^2/|\beta_2|\right)^{1/2}$ is large as in the case of the SCG phenomenon. Thus, the FEAP emits less solitons than the symmetric pulses and consequently its CDs should be better.

Considering the effect of chirp, the result obtained on figure 3.58, is in agreement to those of the existing works [209]. Indeed, as can be seen in this picture, the increase of the initial chirp improves

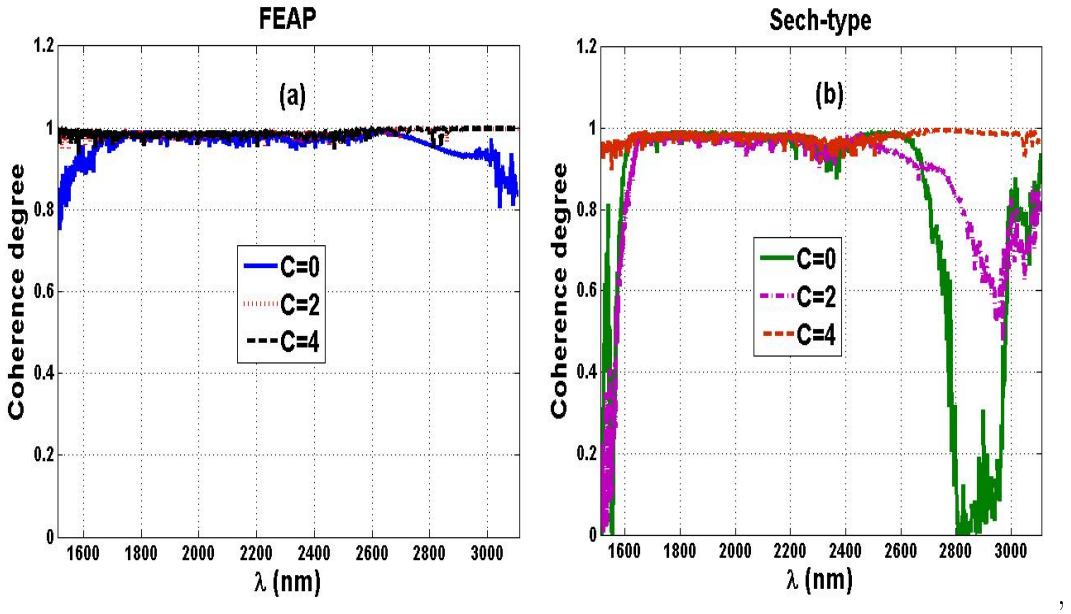


Figure 3.58: CD of the spectra obtained in the anomalous GVD regime with a pumping at $\lambda_p = 2030\,nm$. Parameters : $a = 0.005$ for the FEAP, $t_0 = 60\ fs$, $E_0 = 18$ nJ. (a) FEAP's CD, (b) sech-type's CD. The increase of the initial chirp leads to an improvement of the SCG's spectra CD.

the CD of the spectra. As well-known in the literature [3], the initial chirp does not favor the soliton formation (or emission). Thus as discussed above, it increases so the CD of SCG's spectra. The result obtained with the FEAP (see figure 3.58(a)) is better than the one of the sech-type pulse (see figure 3.58(b)).

Assuming the figures 3.57 and 3.58, one can conclude that the chirped asymmetric shapes as FEAPs have the best coherent spectra in the SCG. The whole results demonstrate the important role played by the input profile asymmetry and the initial chirp on the drastic spectral broadening of the SCG in the considered nJ's scale of energies.

## 3.8 On the SCG in a SOI-waveguide including both the THG and NFK terms

The results showed in this section stem from [244]. We present in Fig. 3.59 the contour plots of the time and spectral domains in the waveguide under the influence of the different parameters. The first novelty highlighted in this letter concerns the effect of the THG ($a_{NFK} = 0, a_{THG} = 1, \phi_{NL} = 0$) : as can be noticed in Fig. 3.59(a.1), the incident pulse diffuses dispersive waves (DWs) weakly intense and therefore leads to a spectral propagation in which after an initial increase, the SB is nearly preserved until the end of the waveguide (see Fig. 3.59(b.1)). Considering the NFK effect ($a_{NFK} = 1, a_{THG} = 0, \phi_{NL} = 0$), we observe rather the opposite feature. Indeed, it yields to intense

DWs emission (see Fig. 3.59(a.2)) and then leads to a spectral propagation in which the SB increases continuously following the propagation distance. Assuming that the NFK in our simulation has been included at 22% only, it comes that the NFK enhances importantly the SB. A full inclusion of NFK under the mentioned conditions should lead to an explosive SCG. To observe how the THG counteracts the NFK effect, we show in Figs. 3.59(a.3) and 3.59(b.3) their interaction. We notice that, the DWs emission of 3.59(a.3) is more intense than 3.59(a.1) and less than 3.59(a.2). The same comparison can be done between 3.59(b.1), 3.59(b.2) and 3.59(b.3). The single impact of the TPA as a deleterious factor for the SCG phenomenon, is highlighted in Figs. 3.59(a.4) and 3.59(b.4) in agreement with the results obtained in [200,202a,215,216]. To confirm the observations done in Fig.

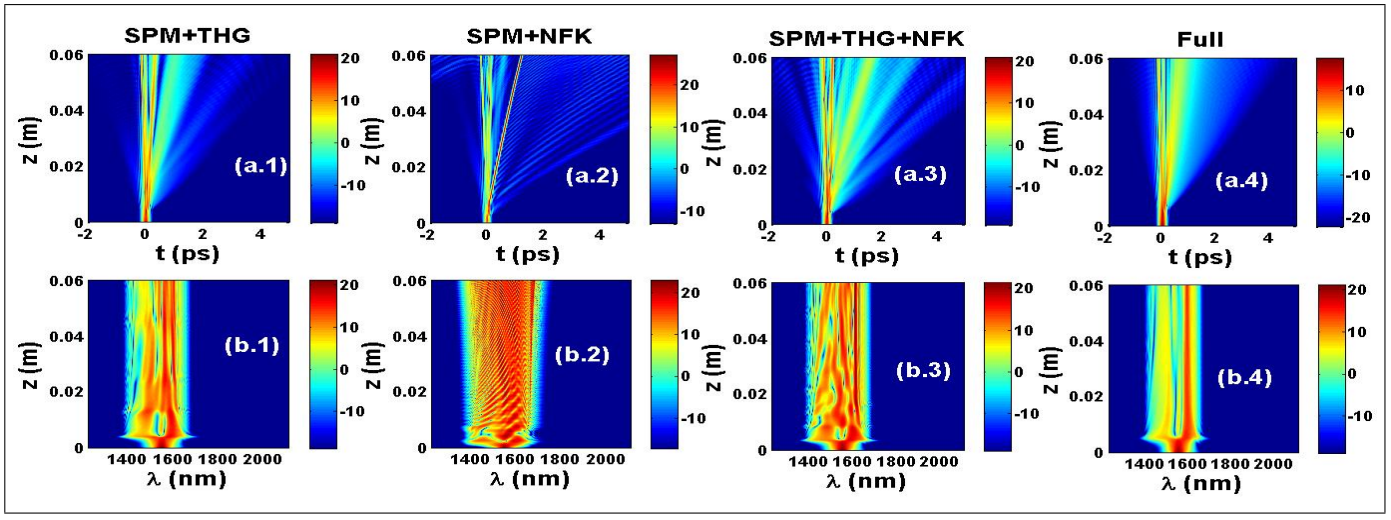


Figure 3.59: Contour plots of the pulse propagation yielding the SCG ($\phi_{NL} = 0$) : (a.1-a.4) time domain propagation, (b.1-b.4) spectral propagation. The NFK has been included at 22% of the spectral intensity (S.I).

3.59, we plot in Fig. 3.60 the 2D-plots of the output spectral profiles in the different cases. It is found that the THG reduces the SB (see the dotted-dashed green curve of Fig. 3.60(a)) compared with the single SPM case (see the dashed violet curve of Fig. 3.60(a)) while the NFK drastically enhances it (see the solid bright green curve of Fig. 3.60(a)). However, the reduction induced by TPA is greater than that of THG (see the dotted blue curve of Fig. 3.60(a)). Furthermore, when we compare the -20 dB-SB of Fig. 3.60(a), we obtain approximately the following result : input (183 nm, see the black solid curve)< SPM+TPA (234 nm, see the dotted blue curve)< Full (277 nm, see the dotted red curve)< SPM+THG (303 nm, see the dotted-dashed green curve) < SPM+THG+NFK at 22% (310 nm, see the dashed yellow curve)< single SPM (360 nm, see the dashed violet curve)< SPM+NFK at 22% (469 nm, see the solid bright green curve). Moreover, as can be observed in Figs. 3.60(b.1-6), the CD parameter $g_{12}^{(1)}$ evaluated here under the condition $0.9 \leq g_{12}^{(1)} \leq 1$ allows the following comparison : $CD_{SPM+TPA}$ (see Fig. 3.60(b.2)) $\geq CD_{Full}$ (see Fig. 3.60(b.6)) $\geq CD_{SPM+THG}$ (see Fig. 3.60(b.3)) $\geq CD_{single\ SPM}$ (see Fig. 3.60(b.1)) $\geq CD_{SPM+THG+NFK}$ (see Fig. 3.60(b.5)) $\geq CD_{SPM+NFK}$ (see Fig. 3.60(b.4)). The consideration of the nonlinear phase $\phi_{NL} \neq 0$ contributes to the improvement of the SB for both the resonant THG and NFK. It is worthy to notice that comparatively to what happens in Fig. 3.59, the nonlinear phase changes qualitatively and quantitatively the SCG in Fig. 3.61. The pulse diffuses DWs more intensively than in Fig. 3.59. The effect of $\phi_{NL}$ is evident when we compare the -20 dB-SB of Figs. 3.62(a.1,2) : Full (283 nm, see the solid bright green curve)< SPM+THG+NFK at 10% (327 nm, see the dotted-dashed green curve)< SPM+THG (360 nm, see the dashed violet curve) $\simeq$ single SPM (360 nm, see the solid black curve)< SPM+NFK at 10% (436 nm, see the dotted blue curve). Compared with the single SPM (see the solid black curve of Fig. 3.62(a.1)), the THG with $\phi_{NL} \neq 0$ does not really change the SB but only shifts slightly the

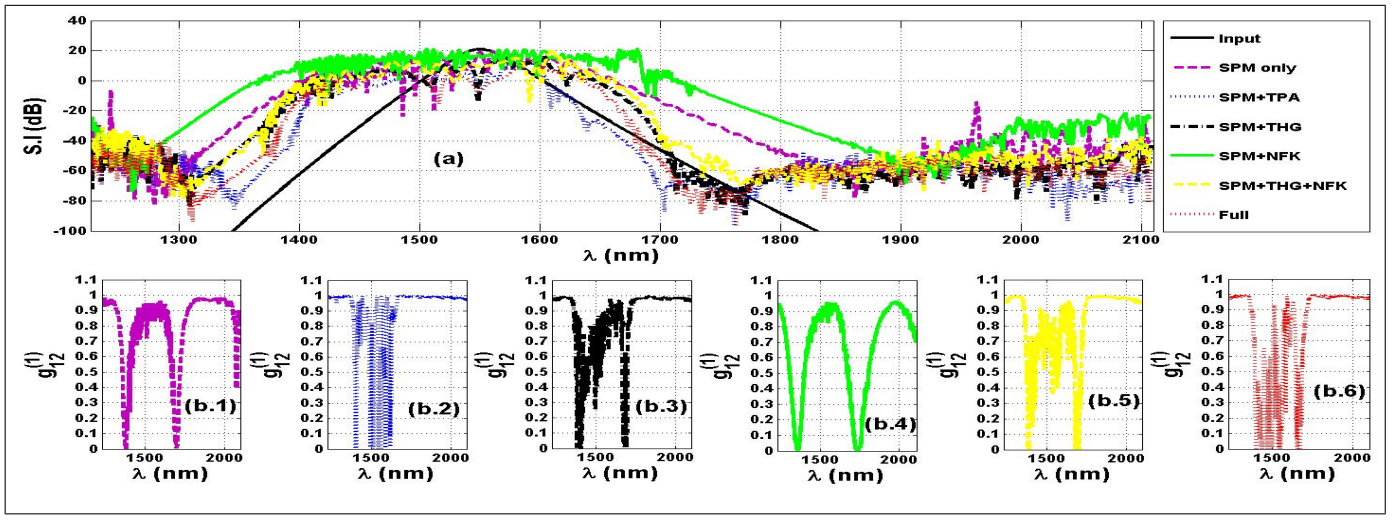


Figure 3.60: Two-dimensional (2D) plots corresponding to Fig. 1 ($\phi_{NL} = 0$) : (a) S.I in dB unit versus $\lambda$, (b.1-b.6) CD parameter $g_{12}^{(1)}$ versus $\lambda$. The full case corresponds to SPM+TPA+THG+NFK.

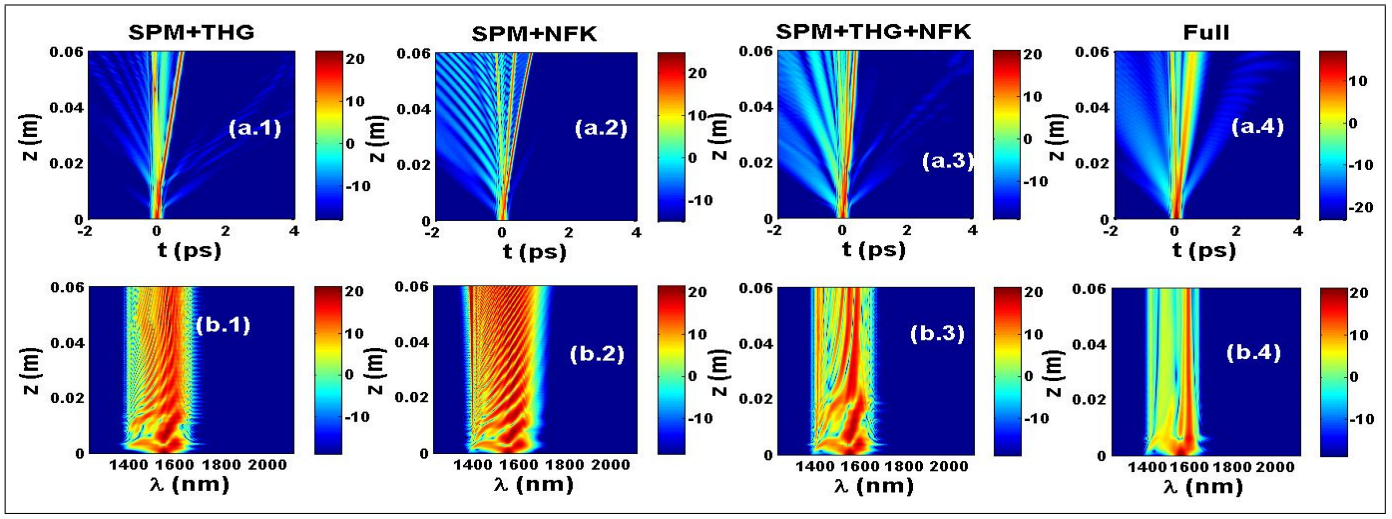


Figure 3.61: Contour plots of the pulse propagation yielding the SCG ($\phi_{NL} \neq 0$). The NFK has been included at 10% of the S.I.

spectrum towards the long wavelengths (see the dashed violet curve of Fig. 3.62(a.1)). Without the nonlinear phase, the THG is deleterious for the SCG while the NFK is found to be beneficial for the SB of the SCG in both the zero and the nonzero phase cases (Without $\phi_{NL}$, the SB under NFK at 10% gives 375 nm compared with nonzero case in which the SB is about 436 nm while the single SPM is about 360 nm). Considering the CD of the spectra with $\phi_{NL} \neq 0$ observed in

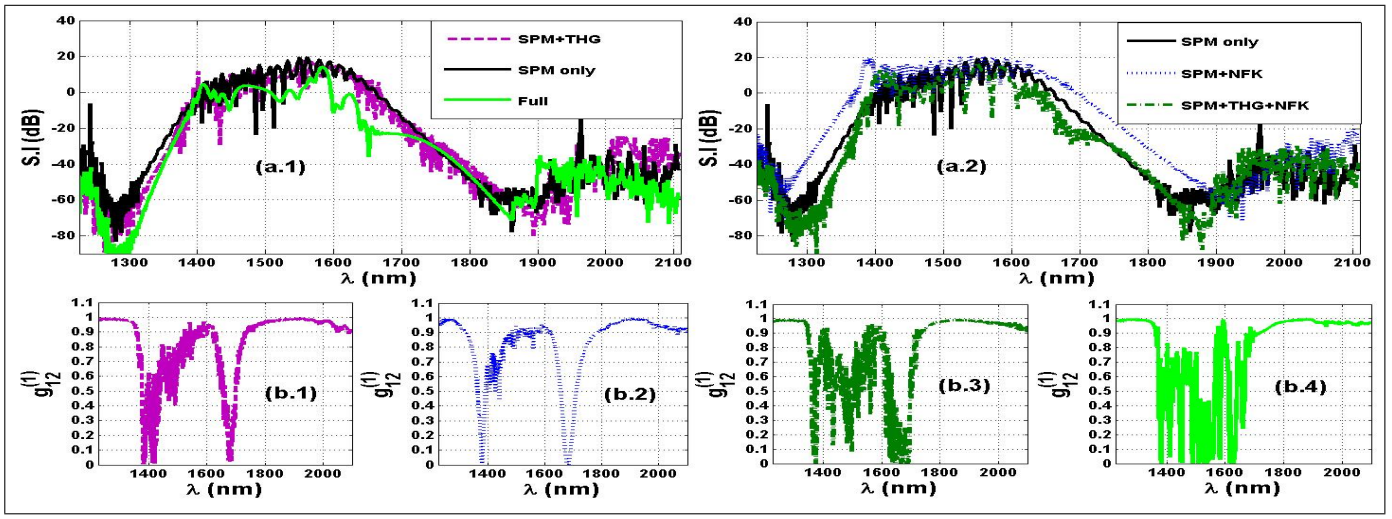


Figure 3.62: Two-dimensional (2D) plots corresponding to Fig. 3 ($\phi_{NL} \neq 0$).

Figs. 3.62(b.1-4), we obtain the same result as in Fig. 3.60. A comparison of the CD parameter under the condition $0.9 < g_{12}^{(1)} < 1$ yields : $CD_{SPM+THG}$ (see Fig. 3.62(b.1)) $\geq CD_{Full}$ (see Fig. 3.62(b.4)) $\geq CD_{SPM+THG+NFK}$ (see Fig. 3.62(b.3)) $\geq CD_{SPM+NFK}$ (see Fig. 3.62(b.2)). Thus, the THG improves the spectral coherence while the NFK reduces it. In the full case in which the TPA is included, even though the NFK reduces the CD as done in the THG-NFK case, the TPA effect allows the spectrum to be however more coherent than this latter. It means that the TPA enhances importantly the CD than the THG. Physically, this can be explained through the SF mechanism. Indeed as discussed in [3], the SF in the SCG phenomenon is inherently noisy. In addition, more the sub-solitons are emitted through the SF mechanism more the SB is wide [3,114,137]. Nonetheless, as the intensive SF mechanism improves the SB, it rather reduces the CD of spectra [3,129,137]. The TPA and THG (in $\phi_{NL} = 0$) reducing the SB of the SCG consequently limit the SF mechanism and then improves the CD of spectra while the opposite happens to the NFK effect. Thus, the TPA enhances the CD in agreement to [200] where it was found to have nearly no destructive effect on the flatness of SCG spectra. The effects of the different studied nonlinear terms are resumed in the following table :

| Item | TPA | THG | NFK |
|---|---|---|---|
| **SB** ($\phi_{NL} = 0$) | $\downarrow$ | $\downarrow$ ($<$ TPA) | $\uparrow$ |
| **SB** ($\phi_{NL} \neq 0$) | Idem | Shift to $\gg \lambda$ | $\uparrow$ enhanced |
| **CD** ($\phi_{NL} = 0$) | $\uparrow$ | $\uparrow$ ($<$ TPA) | $\downarrow$ |
| **CD** ($\phi_{NL} \neq 0$) | $\uparrow$ | $\uparrow$ ($<$ TPA) | $\downarrow$ ($> \phi = 0$) |

Table 3.4: Effects of the different terms compared with the single SPM case. **Meaning of symbols:** $\downarrow$ 'reduction', $\uparrow$ 'increase', $\gg$ 'long', $\lambda$ 'wavelengths', $<$ 'less than', $>$ 'more than'.

## 3.9 Conclusion

In summary, using the MVA with chirped Gaussian and RC pulses, we have demonstrated that optical pulse compression induced by chirp can be successfully achieved in a linear medium under GVD and FOD parameters having the same sign. The chirp parameter being of opposite sign for the case of the Gaussian pulse. The pulse compression being dependent on the input profile, for the RC pulse, new broadening/compression conditions are obtained which are quite different to the established rules on compression effect using the Gaussian pulse. These results are welcome and may complete the basic linear optical pulse compression theory induced by chirp.

In the nonlinear case of the pulse compression, the growth equations of the studied profiles show that both the sech-type and the Gaussian pulses are nearly influenced similarly by the nonlinear parameters. The characteristics of the RC pulse are more influenced by the TPA and the FCA. We have demonstrated the occurrence of a periodic compression of each pulse induced by the interplay between the SPM and the FOD instead of the GVD, in a regime of propagation that assumes a normal-GVD and a first order solitonic state. We have also shown that the anomalous GVD reduces this periodic compression phenomenon. A parametric study has been done using the MPCP parameter. We have shown that when the GVD decreases from the normal to the anomalous regime, the periodic compression phenomenon decreases. When the negative FOD increases until a maximal value for the considered conditions of simulation, the periodic compression is also performed in the presence of the constant normal GVD. The small AVs of chirp have been found to be beneficial for the periodic compression while the large ones, and whole positive dispersion orders were found to be detrimental for the studied phenomenon. Moreover, under a small value of TPA as 0.5 $W^{-1}m^{-1}$, we have shown that the periodicity is progressively destroyed with the increase of the spatial period while large values of this absorption coefficient (as 6.5 $W^{-1}m^{-1}$) combined with the FCA lead to pulse broadening. Nevertheless, we have observed one compression peak for the compression mechanism before the broadening for each pulse.

Considering the compression of the SHAPs, the derivation of the growth equations have showed that all the pulse characteristics are under the influence of the TPA and the FCA contrary to the other pulses. A comparison between the analytical relation of the compression factor and the numerical result shows a good agreement for small distances of propagation. In the nonlinear case, it has been found that the nonlinear parameters namely the CKN, the TPA and the FCA reduce the length of compression in a SOI-waveguide with normal GVD, positive chirp and a negative value of FOD. However, this reduction is more pronounced for the single TPA presence than the one obtained with the CKN only while for the FCA, it is smaller than the two first ones. We have also found that the TPA reduces the MPR in the compression mechanism than the CKN while the FCA rather increases its value comparatively to the linear case. The FCA plays therefore a buffer role on the dramatic effects of the SPM and TPA induced SHAP pulse broadening in the presence of the FOD.

For the FWM process, it comes out that the frequency offset is more important in the single TOD case than in the combined GVD-TOD case. In the case of the reduced model, the combined effect of GVD and TOD leads to a growth of the FWM in the system. We have recovered the previous mentioned results of [109] where the FWM grows along the transmission line and therefore is eliminated by the use of a weak random or DM technic for the reduced model. In addition, it has appeared that a residual GVD combined to the TOD allows a strong growth than a single TOD case. This can be seen as an interesting feature for WDM soliton systems near the ZDWs. Because of the large frequency offset difference between the two input pulses, assuming that they interact weakly, the FWM crosstalk gain in power, rising inside the line after crossing each amplification node. This feature being enhanced by the combination of dispersion terms. However, for the full model where

squeezed up channels are considered, the FWM component appears quickly along the transmission line with a high spectrum amplitude value and decreases more in the combined GVD-TOD case than in the single TOD case. This result is similar to those obtained by Singh et al [112,113] on the effect of HOD terms on the FWM of type I. However, these authors dealt with input powers of three pulses and made a conclusion that under the combined effect of second, third, fourth and fifth-order dispersion parameters, the crosstalk introduced by the FWM is reduced [112]. A relevant result obtained in the present work is that dealing with two input pulses, we have reached a reduction of the crosstalk introduced by the FWM and the frequency offset window in the case of the full model in comparison to the FWM generated by three pulses as obtained by Singh et al [112]. The weak value of the frequency offset difference between the two input pulses, lead to a great interaction. Consequently, even if the FWM crosstalk appears more quickly than in the reduced model inside the transmission line, the strong interaction between the pairwise input pulses leads them to recover their power and it follows the decreasing of the FWM power.

In the MI analysis, four symmetric OFs were created because of the TPA effect in addition to those induced by the single interaction between the FOD and the GVD. The FCA enhances the value of the central MI gain point. Considering the MI-PTG process in the unchirped case, we have demonstrated that the input pulse which is less stable such as the RC pulse, has main peaks of the MI-PTG trails more strong than the other input profiles at short propagation distances. The chirp effect consists to amplify the intensity of the main MI-PTG peaks for each profile, making the input pulses to behave similarly while it shifts the occurrence of these peaks at short distances of propagation than the unchirped case. We have finally shown that the absorption coefficients counteract the beneficial impact of the chirp as nonlinear losses, by breaking the similarity (when small values of TPA are considered), destroying drastically the MI-PTG process and leading to pump depletion when great values of TPA are reached.

The spectral compression in the SCG phenomenon through the GNLSE with non-Kerr terms using a femtosecond sech-type pulse in the sub-nJ scale of energies have been studied. Once the derivation of the SCG model equation has been done, we have investigated the analysis of the spectra obtained. The results with 50 fs-pulses in the anomalous dispersion regime have shown that, in comparison to the single CKN case, the cooperative nonlinearities improve the spectral broadening while the competing ones reduce the spectral SCG bandwidth. Surprisingly, we have obtained the opposite feature when the reduction of the pulse width was considered. In this last case, the cooperative nonlinearities induce a spectral compression when the competing ones nearly maintain constant the SCG bandwidth from the input to the output of the considered waveguide. The increase of both the energy and the nonlinearity have confirmed this feature showing that the spectral compression is also obtained in the single CKN case but less than the case of cooperative nonlinearities.

We have also shown in this chapter that the chirp behaves both as TOD and SS. As SS, it acts as a nonlinear dispersion on the spectrum of the FEAP leading to an asymmetric output whose the orientation depends on the sign of the chirp. The optical shock obtained through the chirping, suggests interesting advantages for the achievement of FEAP-based broadband spectra as in the SCG phenomenon. As TOD, the initial chirp leads to the A.I mechanism previously reported in [251]. Nonetheless, instead of TOD, the actual A.I mechanism is rather induced by the competition between the GVD and the initial chirp following when $chirp \times GVD < 0$. Beyond the numerical results presented in [248] by **Mandeng** and **Tchawoua** and in [250,253] by **Zhang et al**, the A.I is explained here through four physical processes including the increase of the group-velocity of the oscillations tail that merge with the dominant peak within the collapse area achieving both the whole pulse compression and amplification into a single peak. Then, the oscillations tail are recreated in the opposite side defined as the trailing edge of the time domain. The FEAP loses its asymmetry within the collapse area. We have found that the minimal distance $\xi_{sym}$ over which this happens decreases

with the increase of the chirp $C$ following the rule $\xi_{sym} = (K_1/C^2) + (K_2/C)$ where $K_1$ and $K_2$ have been defined in a first order solitonic state system. The reduction of the truncation coefficient has been found to increase the number of the oscillations tail, the pulse energy and the area of the FEAP's collapse during the A.I mechanism and then to improve its occurrence. In addition, in the DFFs, we have demonstrated the dominant peak amplification induced by the competition between the GVD and the FOD. This amplification is produced through the acceleration of the oscillations tail that collide and merge with the dominant peak. We have obtained a relation which shows that, this amplification appears sooner as the FOD increases in the unchirped case. The cooperating GVD and FOD were found to lead to a diverging FEAP. Considering a small value of chirp in the DFFs, has led to define a condition under which, the FEAP nearly preserves its shape over a long propagation distance with weak distortion as $chirp \times GVD \times FOD > 0$. We have also defined a condition in which the dominant peak is amplified with a small value of chirp as $C \times GVD < 0$ and $FOD > 0$. However, we have seen that the single amplified peak is not stable over a long propagation distance.

As a direct application of the study above, we have shown that the initial chirp behaving as a SS effect on FEAP's spectra, improves the bandwidth of the FEAP-based SCG more than the sech-type pulse both in the normal and the anomalous GVD regimes of the considered $CS_2$−LCPCF. The decrease of the FEAP truncation coefficient has been found to enhance the spectral bandwidth. With values of 0.01 to 0.005, the bandwidths were wider than those of the sech-type pulse. Considering the quality of spectra obtained, the CDs of the FEAPs were higher over the whole range of the wavelengths than those of the sech-type pulses. This is so because the FEAP emits less solitons than the symmetric pulses, owing to its asymmetry and its time-domain acceleration. All, these results demonstrate the important role played by the input profile asymmetry and the initial chirp on the drastic spectral broadening of the SCG in the considered nJ's scale of energies. Therefore, the choice of a FEAP with a weak truncation coefficient, a convenient high energy and initial chirp under the anomalous GVD regime, is more appropriate in a highly nonlinear medium to generate coherent and ultra-broadband SCG's spectra, instead of the common compact and symmetric profiles such as the sech-type pulses.

Finally, considering the case of SCG in SOI-waveguides that includes both the THG and the NFK terms, we have shown that the spectra have explosive SB under the NFK term despite their weak CD. The THG term has opposite features but less than the TPA. Therefore, for applications needing wide SBs, one should reduce the TPA-THG effects and excite rather the NFK term to produce explosive ultra-broadband SCG spectra.

# General conclusion and perspectives

In this thesis, we have studied the pulse compression mechanism and the SCG phenomenon for femtosecond pulses in some optical waveguides such as a SMF, SOI-waveguides, a $CS_2$-LCPCF and waveguides modeled by the GNLSE with non-Kerr terms.

As presented in the first chapter, these processes are very useful in nonlinear optics allowing so several applications. In the review of literature, a brief overview on the pulse compression, the FWM, the MI and the SCG phenomena has been done. In addition, the different waveguides studied in the thesis were described.

To achieve the purpose of the study, we have presented in the second chapter the different models with the analytical and numerical methods used for the different studied phenomena. For instance, considering the pulse compression phenomenon, the MVA has been described analytically assuming both the linear and the nonlinear cases of the compression. The ABCJS approach in the case of WDM solitons system near the ZDW has been applied on the ASC of the FWM. In the case of the MI mechanism, we have presented the linear stability analysis of the CW in the SOI-waveguide. For the SCG analyses, the different systems were also described including a relation (Eq. 118) giving their higher-order CDP.

In the last chapter, we have shown the analytical and numerical results obtained. Specifically, for the temporal compression process for both symmetric and asymmetric input pulses, the studies have highlighted the effects of the FOD, free-carriers absorptions and the chirp. Assuming the linear case of compression, conditions that link the FOD, the GVD and the chirp have been obtained. Based on the previous mentioned results, a possible experimental set-up could be suggested using a quasi-linear dispersion-flattened fiber, in which the pulse would experience normal/anormalous dispersion to obtain respective sign of the chirp [1,3], and get compressed when passing through a grating pair with dispersion of same sign. In the nonlinear case, using compact and symmetric input profiles, we have demonstrated that a periodic compression could be generated by the interplay between the SPM and the FOD. We have also showed that this dynamical process is destroyed by the presence of large AVs of chirp and absorption coefficients in the nonlinear medium. In other side, an asymmetric pulse as the Airy pulse, was shown to undergo a reduction of its compression length induced by the SPM, the TPA and the FCA. The combination of all these nonlinear parameters with the linear dispersion terms in a realistic SOI-waveguide, confirms these results that allow to characterize the peculiarity of the Airy input pulses comparatively to the symmetric and compact commonly used profiles.

The path leading to the study of the SCG phenomenon in this thesis crossing the ones of some processes as the FWM and the MI, these latter have been investigated firstly. The study concerning the FWM has been done in WDM systems using SMFs near the ZDW. The related analysis through the ABCJS approach has proved that the combination of the GVD and the TOD reduce the deleterious crosstalk induced by the FWM in such WDM systems. We can mention that if one purpose in WDM soliton systems near the ZDW is to reduce the impact of the FWM crosstalk, therefore

the choice of squeezed up input pulses under a combination of GVD-TOD is suitable to quite cancel the FWM crosstalk. Thus, the propagation of signals could be optimized in WDM soliton systems near the ZDW when the growth of the FWM could be well controlled. Moreover, in the MI study, we have found that the chirp amplifies the intensity of the main pulse trains peaks, leading to the input profile independence while the absorption coefficients counteract its effect recreating rather a dependence to the input profile. For an efficient process of the MI-PTG in a SOI-waveguides under the FOD, a good control of the values of absorption coefficients, dispersive effects and source chirp of more stable input profiles, should be operated.

The thesis has also encompassed the study of the SCG in the case of the waveguides modeled by the GNLSE with non-Kerr terms. Indeed, in this specific part of the work done in thesis, we have obtained a spectral compression induced by the cooperative nonlinearities instead of the competing ones. Assuming that this modified GNLSE with non-Kerr terms linked to the quintic nonlinearity could model a highly nonlinear optical waveguide for the achievement of the SCG phenomenon, the values of the energy and the pulse width should be chosen taking into account the conditions where the spectral compression occurs.

Using chirped FEAPs in HDOFs, we have shown in this thesis that the chirp behaves both as TOD and SS. As SS, it acts as a nonlinear dispersion on the spectrum of the FEAP leading to an asymmetric output interesting for the achievement of the SCG phenomenon. As TOD, the initial chirp leads to the A.I mechanism previously reported by **R. Driben et al** in [244]. This feature has been completely characterized as well as the effects of FOD interacting with the GVD and chirp in DFFs. In this last case, we have demonstrated the dominant peak amplification induced by the competition between the GVD and the FOD. A shape preserving was also observed in the DFFs for the weakly chirped FEAP over a long propagation distance under the condition $chirp \times GVD \times FOD > 0$.

Finally, we investigated the SCG phenomenon in $CS_2$-LCPCFs and in waveguides modeled by GNLSE with non-Kerr terms. Considering the $CS_2$-LCPCFs, we have shown that the initial chirp behaving as a SS effect on FEAP's spectra, improves the bandwidth of the FEAP-based SCG more than the sech-type pulse both in the normal and the anomalous GVD regimes. The decrease of the FEAP truncation coefficient has been found to enhance the spectral bandwidth. With values of 0.01 to 0.005, the bandwidths were wider than those of the sech-type pulse. Considering the quality of spectra obtained, the CDs of the FEAPs were higher over the whole range of the wavelengths than those of the sech-type pulses. Therefore, the choice of a FEAP with a weak truncation coefficient, a convenient high energy and initial chirp under the anomalous GVD regime, was found to be more appropriate in a highly nonlinear medium to generate coherent and ultra-broadband SCG's spectra, instead of the common compact and symmetric profiles such as the sech-type pulses. In SOI-waveguides that includes both the THG and the NFK terms, the resonant THG was found to be deleterious for the SCG by a reduction of the SB. Its reduction being weaker than that of TPA, it has been shown surprisingly that the TPA rather enhances the CD of the SCG spectra more than the THG term. Through the nonlinear phase, the THG term just shifts slightly the spectrum toward the long wavelengths while the effect of the NFK term is rather beneficial for the SCG in both the zero and the nonzero phase cases leading to explosive but less coherent spectra. Thus, for applications needing wide SBs, one should reduce the TPA-THG effects and excite rather the NFK term to produce explosive ultra-broadband SCG spectra.

At the end of this work, we expect that we have got a good understanding of the impact of free-carriers absorptions, HOD, chirp, Kerr and non-Kerr nonlinear effects, input profiles, in a first part on the temporal compression, in a second part on the FWM and the MI, and finally on the spectral bandwidth enhancement of the SCG in the studied optical waveguides.

As perspectives, we should in future works conduct the experimental part of the theoretical and numerical studies presented in this thesis for practical confirmations. Furthermore, several paths

of research raise from the thesis among which one can quote the investigation of birefringent (or polarized) optical waveguides, a nonlinear scattering process as the stimulated Brillouin scattering in the case of mechanisms and phenomena studied in the thesis, the investigation of actual promising waveguides as those based on chalcogenide glasses, the study of metamaterials. Future researches should also focus both theoretically and experimentally on production of explosive and coherent SB of SCG under the NFK term in SOI-waveguides. The influence of NFK and THG effects on propagation of symmetric and asymmetric pulses interacting with the other nonlinear phenomena will also be considered as well as the quantification of the whole systems studied in the thesis etc.

# Bibliography


[1] G. P. Agrawal, *Applications of Nonlinear Fiber Optics*, (Academic Press, 2nd Ed., 2008).

[2] J. R. Klauder et al., Bell Syst. Tech. J. **39**, 745 (1960).

[3] G. P. Agrawal, *Nonlinear Fiber Optics*, (Academic Press, 4th Ed., 2007).

[4] S. I. Fewo, "*Ultrashort optical solutions in doped nonlinear optical fibers*," (Ph.D thesis, Cameroon, Laboratory of Mechanics, Department of Physics, Faculty of Science, University of Yaoundé, 2008).

[5] J. Atangana, "*Dynamique des impulsions lumineuses ultra-brèves dans les fibres optiques fortement perturbées*," (Ph.D thesis, Cameroon, Laboratory of Electronics, Department of Physics, Faculty of Science, University of Yaoundé, 2009).

[6] C. G. L. Tiofack, "*Modulational instability and ultrashort pulse propagation in Erbium doped fiber*," (Ph.D thesis, Cameroon, Laboratory of Mechanics, Department of Physics, Faculty of Science, University of Yaoundé, 2011).

[7] S. Roy, S. K. Bhadra, Physica D-Nonlinear Phenomena **232**, 103 (2007).

[8] S. Roy, S. K. Bhadra and G. P. Agrawal, Optics Communications **281**, 5889 (2008).

[9] K. Nakkeeran et al., J. Opt. Soc. Am. B **21**, 1901 (2004).

[10] C. M. Ngabireng et al., Phys. Rev. E **72**, 036613 (2005).

[11] G. A. Siviloglou and D. N. Christodoulides, Opt. Lett. **32**, 979 (2007).

[12] G. A. Siviloglou et al., Phys. Rev. Lett. **99**, 213901 (2007); G. A. Siviloglou et al., Opt. Lett. **33**, 207 (2008).

[13] M. V. Berry and N. L. Balazs, Am. J. Phys. **47**, 264 (1979).

[14] P. Saari, Opt. Express **16**, 10303 (2008).

[15] P. Saari, Laser Physics **19**, 725 (2009).

[16] I. M. Besieris and A. M. Shaarawi, Opt. Lett. **32**, 2447 (2007).

[17] R. Bekenstein and M. Segev, Opt. Express **19**, 23706 (2011).

[18] C. Ament, P. Polynkin, and J. V. Moloney, Phys. Rev. Lett. **107**, 243901 (2011).

[19] M. A. Bandres and J. C. Gutiérrez-Vega, Opt. Express **15**, 16719 (2007).

[20] H. I. Sztul and R. R. Alfano, Opt. Express **16**, 9411 (2008); J. Broky et al., Opt. Express **16**, 12883 (2008).

[21] M. Asorey et al., Phys. Rev. A. **77**, 042115 (2008); H. T. Dai et al., Opt. Express **17**, 19365 (2009); P. Polynkin et al., Science **324**, 229 (2009); A. V. Novitsky and D. V. Novitsky, Opt. Lett. **34**, 3430 (2009); A. Salandrino and D. N. Christodoulides, Opt. Lett. **35**, 2082 (2010).

[22] A. V. Gorbach and D. V. Skryabin, Opt. Express **16**, 4858 (2008).

[23] T. J. Eichelkraut et al., Opt. Let. **35**, 3655 (2010); Y. Kaganovsky and E. Heyman, J. Opt. Soc. Am. A **28** , 1243 (2011); A. Minovich et al., Phys. Rev. Lett. **107**, 116802 (2011); L. Li et al., Phys. Rev. Lett. **107**, 126804 (2011); W. Liu et al., Opt. Lett. **36**, 1164 (2011); P. Zhang et al., Opt. Lett. 36, 3191 (2011).

[24] I. Kaminer, M. Segev, and D. N. Christodoulides, Phys. Rev. Lett. **106**, 213903 (2011).

[25] I. Kaminer et al., Opt. Express **19**, 23132 (2011).

[26] A. Rudnick and D. M. Marom, Opt. Express **19**, 25570 (2011).

[27] Y. Fattal, A. Rudnick, and D. M. Marom, Opt. Express **19**, 17298 (2011); G. Zhou, R. Chen, and X. Chu, Appl. Phys. B **109**, 549 (2012); P. Piksarv et al., Opt. Express **20**, 17220 (2012); N. Voloch-Bloch et al., Nature **494**, 331 (2013); R. Driben and T. Meier, Phys. Rev. A **89**, 043817 (2014);

[28] D. Marcuse, Appl. Opt. **20**, 3573 (1981).

[29] J. D. McMullen, J. Opt. Soc. Am. **67**, 1575 (1977).

[30] J. Capmany et al., Opt. Lett., **27**, 960 (2002).

[31] J. Capmany et al., J. Opt. Soc. Am. B, **20**, 2523 (2003).

[32] M. Amemiya, J. Lightwave Technol. **20**, 591 (2002).

[33] Y. S. Kivshar and G. P. Agrawal, *Optical Solitons: From Fibers to Photonic Crystals* (Academic Press, San Diego, 2003).

[34] M. Peyrard and T. Dauxois, *Physique des solitons*, (Savoirs actuels, EDP sciences&CNRS editions, 2004).

[35] M. A. Duguay and J. W. Hansen, Appl. Phys. Lett. **14**, 14 (1969).

[36] E. B. Treacy, IEEE J. Quantum Electron. **QE-5**, 454 (1969).

[37] L. F. Mollenauer, R. H. Stolen, and J. P. Gordon, Phys. Rev. Lett. **45**, 1095 (1980).

[38] A. Hasegawa and F. Tappert, Appl. Phys. Lett. **23**, 142 (1973).

[39] E. M. Dianov et al., Sov. Tech. Phys. Lett. **12**, 311 (1986).

[40] H. Nakatsuka, D. Grischkowsky, and A. C. Balant, Phys. Rev. Lett. **47**, 910 (1981).

[41] C. V. Shank et al., Appl. Phys. Lett. **40**, 761 (1982).

[42] A. S. Gouveia-Neto, A. S. L. Gomes, and J. R. Taylor, J. Mod. Opt. **35**, 7 (1988).

[43] L. Xu et al., Opt. Lett. **21**, 1259 (1996).

[44] Y. Matsui, M. D. Pelusi, and A. Suzuki, IEEE Photon. Technol. Lett. **11**, 1217 (1999).

[45] B. Kibler et al., IEEE Photon. Technol. Lett. **18**, 1831 (2006).

[46] N. G. R. Broderick et al., Phys. Rev. Lett. **79**, 4566 (1997).

[47] S. Jien et al., in Proceedings of SPIE, S. Shen, S. Jian, K. Okamoto, K. L. Walker, eds. (SPIE, 2004), 404.

[48] XU Wen-Cheng et al., Chin. Phys. Lett. **18**, 1211 (2001).

[49] J. Hu, B. S. Marks, and C. R. Menyuk, Opt. Express **14**, 4026 (2006).

[50] A. Takada, T. Suigi, and M. Saruwatari, Electron. Lett. **22**, 1347 (1986).

[51] M. Nakazawa, K. Suzuki, and Y. Kimura, Opt. Lett. **15**, 588 (1990); IEEE Photon. Technol. Lett. **2**, 216 (1990).

[52] R. T. Hawkins, Electron. Lett. **26**, 292 (1990).

[53] H. F. Liu et al., IEEE J. Quantum Electron. **27**, 1655 (1991).

[54] J. T. Ong et al., IEEE J. Quantum Electron. **29**, 1701 (1993).

[55] A. Galvanauskas, P. Blixt, and J. A. Tellefsen, Appl. Phys. Lett. **63**, 1742 (1993).

[56] L. Chusseau, IEEE J. Quantum Electron. **30**, 2711 (1994).

[57] K. A. Ahmed, K. C. Chan, and H. F. Liu, IEEE J. Sel. Topics Quantum Electron. **1**, 592 (1995).

[58] L. Chusseau and E. Delevaque, IEEE J. Sel. Topics Quantum Electron. **2**, 500 (1996).

[59] R. Yatsu, K. Taira, and M. Tsuchiya, Opt. Lett. **24**, 1172 (1999).

[60] P. M. Anandarajah et al., IEEE J. Sel. Topics Quantum Electron. **12**, 255 (2006).

[61] M. J. Potasek, G. P. Agrawal and S. C. Pinault, J. Opt. Soc. Am. B **3**, 205 (1986).

[62] D. Anderson, Phys. Rev. A **27**, 3135 (1983).

[63] D. Anderson, IEEE proceedings. Part J. Optoelectronics **132**, 122 (1985).

[64] D. Anderson and M. Lisak, Opt. lett. **11**, 569 (1986).

[65] D. Anderson and M. Lisak, Phys. Rev. A **35**, 184 (1987).

[66] M. Karlsson et al., Phys. Scr. **50**, 265 (1994).

[67] S. K. Turitsyn and E. G. Shapiro, Optical Fiber Technology **4**, 151 (1998).

[68] S. K. Turitsyn et al., Opt. Comm. **151**, 117 (1998).

[69] M. F. Mahmood and S. Brooks, International Journal of Mathematics and Mathematical Sciences **49**, 3143 (2003).

[70] A. V. Ramprasad and M. Murugappan, Academic Open Internet Journal **18**, 1311 (2006).

[71] P. T. Dinda, A. B. Moubissi, and K. Nakkeeran Phys. Rev. E **64**, 016608 (2001).

[72] S. I. Fewo et al., Opt. Comm. **252**, 138 (2005).

[73] S. I. Fewo, A. Kenfack-Jiotsa and T.C. Kofané, Journal of Physics A: Mathematical and General **39**, 1449-1461 (2006).

[74] S. I. Fewo and T.C. Kofané, Opt. Commun. **281**, 2893 (2008).

[75] Shwetanshumala and A. Biswas, Int. J. Theor. Phys. **47**, 1699 (2008).

[76] K. Senthilnathan et al., P.I.E.R.S. [Online] **3**, 531 (2007).

[77] K. Senthilnathan et al., Phys. Rev. A **78**, 033835 (2008).

[78] Q. Li et al., J. Opt. Soc. Am. B **26**, 432 (2009).

[79] Y. Xiao, G. P. Agrawal, and D. N. Maywar, Opt. Lett. **36**, 505 (2011).

[80] Y. Xiao, G. P. Agrawal, and D. N. Maywar, Opt. Lett. **37**, 1271 (2012).

[81] Y. Xiao, D. N. Maywar, and G. P. Agrawal, J. Opt. Soc. Am. B **29**, 2958 (2012).

[82] P. N. Butcher and D. Cotter, *Elements of Nonlinear Optics* (Cambridge University Press, Cambridge, UK, 1990).

[83] R. Boyd, *Nonlinear Optics*, (Academic Press, San Diego, CA, 3rd Ed., 2008).

[84] N. Shibata et al., Opt. Lett. **10**, 154 (1985).

[85] H. G. Park, J. D. Park, and S. S. Lee, Appl. Opt. **26**, 2974 (1987).

[86] N. Shibata, R. P. Braun, and R. G. Waarts, IEEE J. Quantum Electron. **23**, 1205 (1987).

[87] P. L. Baldeck and R. R. Alfano, J. Lightwave Technol. **5**, 1712 (1987).

[88] P. W. Smith, A. Ashkin, and W. J. Tomlinson, Opt. Lett. **6**, 284 (1981).

[89] O. Aso, M. Tadakuma, and S. Namiki, Furukawa Review **19**, 68 (2000).

[90] B. Batagelj, 6th Optical Fibre Measurement Conference, Girton College Cambridge, September 26-28, (2001).

[91] J. Hansryd et al., IEEE J. Quantum Electron. **8**, 506 (2002).

[92] T. -T. Kung et al., Journ. of Lightwave Techn. **21**,1164 (2003).

[93] T. Hornung et al., Opt. Lett. **29**,2052 (2004).

[94] G. P. Agrawal, *Ligthwave Technology: Components and Devices* (Wiley-Interscience, New York, 2005).

[95] J. M. C. Boggio and H. L. Fragnito, J. Opt. Soc. Am. B **24**, 2046 (2007).

[96] S. P. Singh and N. Singh, Prog. Electromagn. Res. **73**, 249 (2007).

[97] Y. Zhao et al., J. Opt. Soc. Am. B **27**,863 (2010).

[98] J. Fatome et al., Opt. Commun. **283**, 2425 (2010).

[99] M. J. Ablowitz et al., Opt. Lett. **21**, 1646 (1996).

[100] M. J. Ablowitz et al., J. Opt. Soc. Am. B **14**, 1788 (1997).

[101] L. F. Mollenauer and P. V. Mamyshev, J. Quantum Electron. **34**, 2089 (1998).

[102] P. B. Harboe, E. Silva and J. R. Souza, World Acad. Sci. Eng. Tech. **48**, 77 (2008).

[103] R. L. Horne, "*Collision-induced timing jitter and four-wave mixing in wavelength-division multiplexing soliton systems*" (Ph.D thesis, U.S.A, University of Colorado at Boulder, 2001).

[104] M. J. Ablowitz et al., in Nonlinear Optics Conference, Vol. 1 of 2000 OSA Technical Digest Series (Optical Society of America), paper ThB6 (2000).

[105] M. J. Ablowitz et al., J. Opt. Soc. Am. B **20**, 831 (2003).

[106] S. Gao, C. Yang and G. Jin, Appl. Opt. **42**, 7126 (2003).

[107] K. Nakajima et al., IEEE J. Lightw. Technol. **17**, 1814 (1999).

[108] T. Katagiri et al., in Optical Fiber Communication Conference, Vol. 2 of 2003 OSA Technical Digest Series (Optical Society of America), paper FE6 (2003).

[109] R. L. Horne, C. K. R. T. Jones and T. Schäfer, Physica D **205**, 70 (2005).

[110] R. L. Horne, C. K. R. T. Jones and T. Schäfer, J. Appl. Math. **69**, 690 (2008).

[111] Y. Ito, T. Tamo and T. Numai, Opt. Commun. **282**, 3989 (2009).

[112] A. Singh, A. K. Sharma and T. S. Kamal, Optik **119**, 788 (2008).

[113] A. Singh, A. K. Sharma and T. S. Kamal, IEEE Int. J. Comput. Appl. Technol. **34**, 165 (2009).

[114] J. M. Dudley and J. R. Taylor, *Supercontinuum Generation in optical fibers* (Cambridge University Press, 1st ed., Cambridge, 2010).

[115] R. R. Alfano, *The Supercontinuum Laser Source* (Springer-Verlag, New York, 1989).

[116] K. Mori et al., Electron. Lett. **33**, 1806 (1997).

[117] J. K. Ranka, R. S. Windler, and A. J. Stentz, Opt. Lett. **25**, 25 (2000).

[118] T. A. Birks, W. J. Wadsworth, and P. St. J. Russell, Opt. Lett. **25**, 1415 (2000).

[119] S. Coen et al., Opt. Lett. **26**, 1356 (2001).

[120] K. Mori, H. Takara, and S. Kawanishi, J. Opt. Soc. Am. B **18**, 1780 (2001).

[121] A. V. Husakou and J. Herrmann, Phys. Rev. Lett. **87**, 203901 (2001).

[122] A. V. Gusakov, V. P. Kalosha, and J. Herrmann, QELS, pp. 29 (2001).

[123] J.M. Dudley et al., J. Opt. Soc. Am. B **19**, 765 (2002).

[124] S. Coen et al., J. Opt. Soc. Am. B **19**, 753 (2002).

[125] J. Herrmann et al., Phys. Rev. Lett. **88**, 173901 (2002).

[126] A. Husakou and J. Herrmann, J. Opt. Soc. Am. B **19**, 2171 (2002).

[127] A. O. Blanch, J. C. Knight, and P. St. J. Russell, J. Opt. Soc. Am. B **19**, 2567 (2002).

[128] J. M. Dudley et al., Opt. Express **10**, 1215 (2002).

[129] J. M. Dudley and S. Coen, Opt. Let. **27**, 1180 (2002).

[130] N. I. Nikolov et al., J. Opt. Soc. Am. B **20**, 2329 (2003).

[131] L. Tartara, I. Cristiani, and V. Degiorgio, Appl. Phys. B **77**, 309 (2003).

[132] K. M. Hilligsøe et al., J. Opt. Soc. Am. B **20**, 1887 (2003).

[133] G. Genty, M. Lehtonen, and H. Ludvigsen, Opt. Express **12**, 4614 (2004).

[134] B. Schenkel, R. Paschotta, and U. Keller, J. Opt. Soc. Am. B **22**, 687 (2005).

[135] A. Demircan and U. Bandelow, Opt. Commun. **244**, 181 (2005).

[136] A. M. Zheltikov, Phys-Uspekhi **49**, 605 (2006).

[137] J. M. Dudley, G. Genty, and S. Coen, Rev. Mod. Phys. **78**, 1135 (2006).

[138] A. Demircan and U. Bandelow, Appl. Phys. B **86**, 31 (2007).

[139] V. L. Kalashnikov, E. Sorokin, and I. T. Sorokina, Appl. Phys. B **87**, 37 (2007).

[140] R. Cherif et al., in Proceeding of SPIE on Photonic Crystal Fibers II **6990**, 69900-O (2008).

[141] L. Tartara et al., Journal of Telecommunications and Information Technology, (invited paper,2009), pp. 34-37.

[142] J. M. Dudley and J. R. Taylor, Nature Photonics **3**, 85 (2009).

[143] F. Poletti and P. Horak, Opt. Exp. **17**, 6134 (2009).

[144] J. C. Travers, IOP J. Opt. **12**, 113001 (2010).

[145] R. J. R. Vasantha, K. Porsezian, and K. Nithyanandan, Phys. Rev. A **82**, 013825 (2010).

[146] M. Kolesik, L. Tartara, and J. V. Moloney, Phys. Rev. A **82**, 045802 (2010).

[147] R. Cherif et al., Opt. Comm. **283**, 4378 (2010).

[148] H. Ebendorff-Heidepriem et al., Opt. Express **12**, 5082 (2004).

[149] X. Feng et al., Opt. Express **16**, 13651 (2008).

[150] X. Feng et al., IEEE Journal of Lightwave Technology **23**, 2046 , (2005).

[151] B. Kibler, "*Propagation non-linéaire d'impulsions ultracourtes dans les fibres optiques de nouvelle génération*," (Ph.D thesis, France, University of Franche-Comté, Doctoral school of physical sciences for engineers and microtechnics, FEMTO-ST institut, departement of Optics P. M. Duffieux, 2007).

[152] S. Roy, S. K. Bhadra and G. P. Agrawal, Phys. Rev. A **79**, 023824 (2009).

[153] S. Roy, S. K. Bhadra and G. P. Agrawal, Opt. Comm. 282, 3798 (2009).

[154] S. Roy, S. K. Bhadra and G. P. Agrawal, Opt. Lett. **34**, 2072 (2009).

[155] S. Roy, S. K. Bhadra and G. P. Agrawal, Current Science **100**, 321 (2011).

[156] L. A. Ostrovsky, Sov. Phys. Tech. Phys. **8**, 679 (1964).

[157] V. I. Talanov, JETP Lett. **2**, 138 (1965).

[158] T. B. Benjamin and J. E. Feir, J. Fluid Mech. **27**, 417 (1967).

[159] T. Taniuti and H. Washimi, Phys. Rev. Lett. **21**, 209 (1968).

[160] V. I. Karpman and E. M. Krushkal, Sov. Phys. JETP **28**, 277 (1969).

[161] A. Hasegawa, Phys. Rev. Lett. **24**, 1165 (1970).

[162] A. Hasegawa, Opt. Lett. **9**, 288 (1984).

[163] K. Tai, A. Hasegawa, and A. Tomita, Phys. Rev. Lett. **56**, 135 (1986).

[164] G. P. Agrawal, Phys. Rev. Lett. **59**, 880 (1987).

[165] J. E. Rothenberg, Phys. Rev. Lett. **64**, 813 (1987).

[166] E. J. Greer et al., Electron. Lett. **25**, 1246 (1989).

[167] S. Sudo et al., Appl. Phys. Lett. **54**, 993 (1989).

[168] S. Trillo et al., J. Opt. Soc. Am. B **6**, 889 (1989).

[169] P. Drummond, T. Kennedy, and J. Dudley, Opt. Commun. **78**, 137 (1990).

[170] C. C. Mei, *The Applied Dynamics of Ocean Surface Waves*, (Singapore: World Scientific, 1989).

[171] V. B. Matveev and M. A. Salle, *Darboux Transformations and Solitons, Series in Nonlinear Dynamics* (Berlin: Springer Verlag, 1991).

[172] J. R. Taylor, *Optical Solitons: Theory and Experiments*, (London: Cambridge University Press, 1992).

[173] Y. Kodama, A. Maruta, and A. Hasegawa, Quantum Optics: Journal of the European Optical Society Part B **6**, 463 (1994).

[174] N. D. Dalt et al., Opt. Commun. **121**, 69 (1995).

[175] S. B. Cavalcanti, and M. Lyra, Phys. Lett. A **211**, 276 (1996).

[176] N. Akhmediev and A. Ankiewicz, *Solitons. Nonlinear Pulses and Beams*, (London: Chapman and Hall, 1997).

[177] F. Kh. Abdullaev et al., J. Opt. Soc. Am. B **14**, 27 (1997).

[178] M. Karlsson, J. Opt. Soc. Am. B **15**, 2269 (1998).

[179] R. S. Tasgal, and B. A. Malomed, Phys. Scr. **60**, 418 (1999).

[180] S. C. Wen et al., Chin. Phys. Lett. **20**, 852 (2003).

[181] E. Brainis, D. Amans, and S. Massar, Phys. Rev. A **71**, 023808 (2005).

[182] M. Nurhuda and E. Van Groesen, Phys. Rev. E **71**, 066502 (2005).

[183] R. E. Kennedy , S. V. Popov, and J. R. Taylor, Opt. Lett. **31**, 167 (2006).

[184] F. Ndzana II, A. Mohamadou, and T. C. Kofané, Opt. Commun. **275**, 421 (2007).

[185] X. Liu, J. W. Haus, and S. M. Shahriar, Opt. Commun. **281**, 2907 (2008).

[186] A. M. Kamchatnov and M. Salerno, J. Phys. B: At. Mol. Opt. Phys. **42**, 185303 (2009).

[187] P. Das, M. Vyas, and P. K. Panigrahi, J. Phys. B: At. Mol. Opt. Phys. **42**, 245304 (2009).

[188] V. E. Zakharov, and L. A. Ostrovsky, Physica D **238**, 540 (2009).

[189] C. G. L. Tiofack et al., Phys. Rev. E **80**, 066604 (2009).

[190] P. T. Dinda and K. Porsezian, J. Opt. Soc. Am. B **27**, 1143 (2010).

[191] C. M. Ngabireng et al., J. Opt. **13**, 085201 (2011).

[192] J. H. Li, K. S. Chiang, and K. W. Chow, J. Opt. Soc. Am. B 28, 1693 (2011).

[193] M. Erkintalo et al., Phys. Rev. Lett. **107**, 253901 (2011).

[194] J. H. Li et al., J. Phys. B: At. Mol. Opt. Phys. **45**, 165404 (2012).

[195] P. H. Tatsing et al., J. Opt. Soc. Am. B **29**, 3218 (2012).

[196] E. J. R. Kelleher et al., J. Opt. Soc. Am. B **29**, 502 (2012).

[197] A. Hasegawa and W. F. Brinkman, IEEE J. Quantum Electron. **16**, 694 (1980).

[198] G. Genty, S. Coen, and J. M. Dudley, J. Opt. Soc. Am. B **24**, 1771 (2007).

[199] E. Dianov et al., *Non-linear transformations of laser radiation and generation of Raman solitons in optical fibers*, (Cambridge Studies in Modern Optics, 1992).

[200] L. Yin, Q. Lin, and G. P. Agrawal, Opt. Lett. **32**, 391 (2007).

[201] (a) Z. Zhu and T. G. Brown, Opt. Express **12**, 689 (2004); (b) M. Tianprateep, J. Tada, and F. Kannari, Opt. Rev. **12**, 179 (2005); (c) H. Zhang et al., Opt. Express **15**, 1147 (2007); (d) X. Hu et al., Applied Optics **49**, 4984 (2010);(e) J. Wen et al., Appl. Phys. B **104**, 867 (2011); (f) S. Gao et al., Opt. Express **22**, 24697 (2014); (g) Y. Cao et al., Opt. Communications **334**, 190 (2015).

[202] (a) D. Castelló-Lurbe et al., Opt. Lett. **37**, 2757 (2012); (b) M. Klimczak et al., J. Opt. **16**, 085202 (2014).

[203] R. Zhang, J. Teipel, and H. Giessen, Opt. Express **14**, 6800 (2006).

[204] C. Yu et al., Opt. Express **16**, 4443 (2008).

[205] H. Zhang et al., Optik **121**, 783 (2010).

[206] (a) R. J. R. Vasantha et al., J. Opt. Soc. Am. B **27**, 1763 (2010); (b) Y. Sato, R. Morita, and M. Yamashita, Jpn. J. Appl. Phys. **36**, 2109 (1997); (c) N. Bonnard et al., [online] **www.inrs.fr**, Form written by the "Institut National de Recherche et de Sécurité" (INRS), last update on 2013 ; (d) Z. Liu et al., J. Opt. Soc. Am. B **24**, 1101 (2007).

[207] A. M. Heidt, J. Opt. Soc. Am. B **27**, 550 (2010).

[208] H. Tu et al., Opt. Express **20**, 1113 (2012).

[209] Z. Zhu and T. G. Brown, Opt. Express **12**, 689 (2004); X. Hu et al., Applied Optics **49**, 4984 (2010).

[210] H. Takara et al., Electron. Lett. **36**, 2089 (2000).

[211] H. K. Tsang, C. S. Wong, and T. K. Liang, Appl. Phys. Lett. **80**, 416 (2002).

[212] G. P. Agrawal, Phys. Rev. E **48**, 2316 (1993).

[213] B. Jalali, and S. Fathpour, IEEE J. Lightwave Technol. **24**, 4600 (2006).

[214] R. Soref, IEEE J. Sel. Top. Quantum Electronics. **12**, 1678 (2006).

[215] L. Yin, and G. P. Agrawal, Opt. Lett. **32**, 2031 (2007).

[216] Q. Lin, O. J. Painter, and G. P. Agrawal, Opt. Express **15**, 16604 (2007).

[217] M. Lipson, IEEE J. Lightwave Technol. **23**, 4222 (2005).

[218] L. Yin, "*Study of Nonlinear Optical Effects in Silicon Waveguides*," (PhD thesis, U.S.A, The Institute of Optics Arts, Sciences and Engineering Edmund A. Hajim School of Engineering and Applied Sciences, University of Rochester, New York, 2009).

[219] P. M. Morse and H. Feshbach, *Methods of Theoretical Physics* (McGraw-Hill, New York, 1953), Chap. 9.

[220] P. V. Mamyshev and S. V. Chernikov, Opt. Lett. **15**, 1076 (1990).

[221] S. V. Chernikov and P. V. Mamyshev, J. Opt. Soc. Am. B **8**, 1633 (1991).

[222] F. DeMartini et al., Phys. Rev. **164**, 312 (1967).

[223] L. F. Mollenauer and J. P. Gordon, *Solitons in Optical Fibers: Fundamentals and Applications* (Academic Press, San Diego, 2006).

[224] L. M. Mandeng et al., Journal of Modern Optics **61**, 662 (2014).

[225] L. M. Mandeng et al., Journal of Optics **16**, 085204 (2014).

[226] W. Kaiser and C.G.B. Garrett, Phys. Rev. Lett. **7**, 229 (1961).

[227] L. M. Mandeng and C. Tchawoua, Journal of Modern Optics **60**, 359 (2013).

[228] L. M. Mandeng, S. I. Fewo and C. Tchawoua, The European Physical Journal D **67**, 30511 (2013).

[229] L. M. Mandeng and C. Tchawoua, J. Opt. Soc. Am. B. **30**, 1382 (2013).

[230] R. Radhakrishnan, A. Kundu, and M. Lakshmanan, Phys. Rev. E **60**, 3314 (1999).

[231] R. J. R. Vasantha et al., Opt. Comm. **283**, 5000 (2010).

[232] A. Choudhuri and K. Porsezian, Opt. Comm. **285**, 364 (2012).

[233] A. Choudhuri and K. Porsezian, Phys. Rev. A **85**, 033820 (2012).

[234] L. M. Mandeng et al., J. Opt. Soc. Am. B **30**, 2555 (2013).

[235] Samoc, J. Appl. Phys. **94**, 6167 (2003).

[236] L. M. Mandeng et al., "*Role of the input profile asymmetry and the chirp on the propagation in highly dispersive and nonlinear fibers*," submitted (under review, 2015).

[237] J. D. Stuart, IEEE Electron. Lett. **40**, 1474 (2004).

[238] S. Couris et al., Chem. Phys. Lett. **369**, 318 (2003).

[239] C. R. Loures, A. Armaroli and F. Biancalana, Opt. Lett. **40**, 613 (2015).

[240] M. Conforti et al., Opt. Express **21**, 31239 (2013).

[241] E. Rubino et al., Phys. Rev. Lett. **108**, 253901 (2012).

[242] E. Rubino et al., Sci. Rep. **2**, 932 (2012).

[243] M. Conforti et al., Phys. Rev. A **88**, 013829 (2013).

[244] L. M. Mandeng and C. Tchawoua, "*Supercontinuum in a silicon waveguide including third-harmonic generation and negative-frequency Kerr terms*," submitted (under review, 2015).

[245] H. H. Li, J. Phys. Chem. Ref. Data **9**, 561 (1980).

[246] L. M. Mandeng and C. Tchawoua, in Frontiers in Optics Conference, OSA Technical Digest (online) (Optical Society of America, 2012), paper FTh1D.6.

[247] L. M. Mandeng and C. Tchawoua, in Frontiers in Optics Conference, OSA Technical Digest (online) (Optical Society of America, 2012), paper FW3A.36.

[248] L. M. Mandeng and C. Tchawoua, in Frontiers in Optics Conference, OSA Technical Digest (online) (Optical Society of America, 2014), paper FTh4B.5.

[249] G. P. Agrawal and M. J. Potasek, Phys. Rev. A **33**, 1765 (1986).

[250] L. Zhang et al., Opt. Express **23**, 2566 (2015).

[251] R. Driben et al., Opt. Lett. **38**, 2499 (2013).

[252] R. Paschotta, *Dispersion-shifted Fibers* ([online], RP Photonics Consulting GmbH,http://www.rp-photonics.com/dispersion_shifted_fibers.html, last update on 22nd March 2013).

[253] Y. Zhang et al., Opt. Express **23**, 10467 (2015).

# Appendixes

## Some integrals used in the MVA analysis of subsection 2.3.2

1.

$$\int_{-\infty}^{+\infty}\Big(xsech(x)tanh(x)\Big)^2dx = -\frac{2}{3}\Big\{\frac{sech^3(x)}{8}\big[e^x(3x^2+4x+2)$$
$$+2e^{-x}(x+1)+e^{-3x}(x^2+1)\big]+xln(2cosh(x))-\frac{1}{2}\int_0^{+\infty}\frac{t}{1-e^{t-2x}}dt\Big\}\Big|_{-\infty}^{+\infty}$$
$$\approx 1.215 = \frac{2}{3}+\frac{\pi^2}{18}$$

2.

$$\int_{-\infty}^{+\infty}\big(xsech(x)\big)^2\Big[tanh^2(x)-sech^2(x)\Big]dx = -\frac{2}{3}\Big\{\frac{sech^3(x)}{8}\big[e^x(3x^2+4x+2)$$
$$+e^{-x}(-6x^2+4x+4)+e^{-3x}(-x^2+2)\big]-xln\big(cosh(x)\big)-\frac{1}{2}\int_0^{+\infty}\frac{t}{1-e^{t-2x}}dt\Big\}\Big|_{-\infty}^{+\infty}$$
$$\approx 0.7850 = \frac{4}{3}-\frac{\pi^2}{18}$$

3.

$$\int_{-\infty}^{+\infty}x^4sech^2(x)dx = \Big\{-x^3\Big[x\big(e^xsech(x)+2\big)+4ln\big(2cosh(x)\big)\Big]$$
$$-6x^2\int_0^{+\infty}\frac{t}{1-e^{t-2x}}dt+3x\int_0^{+\infty}\frac{t^2}{1-e^{t-2x}}dt-\frac{1}{2}\int_0^{+\infty}\frac{t^3}{1-e^{t-2x}}dt\Big\}\Big|_{-\infty}^{+\infty}$$
$$\approx 5.6822$$

## Derivation of the couple NLSEs in the MI analysis of section 2.5

We start with the GNLSE given in Eq. (2.49) taking into account the parameters defined in Eq. (2.108) and the TOD term as :

$$i\frac{\partial u}{\partial z}-\frac{\beta_2}{2}\frac{\partial^2u}{\partial T^2}-\frac{i\beta_3}{6}\frac{\partial^3u}{\partial T^3}+\frac{\beta_4}{24}\frac{\partial^4u}{\partial T^4}+\gamma_1|u|^2u=-\Lambda u.$$

Using the definition of a perturbed CW as :

$$u(z,T)=\big(u_0+a(z,T)\big)exp(i\phi_{NL}),$$

with $\phi_{NL}$ and $a(z,T)$ defined by Eqs. (2.104) and (2.105), respectively, we obtain in the linear analysis of $a(z,T)$ :

$$-\frac{\partial\phi_{NL}}{\partial z}+i\frac{\partial a}{\partial z}-\frac{\beta_2}{2}\frac{\partial^2 a}{\partial T^2}-\frac{i\beta_3}{6}\frac{\partial^3 a}{\partial T^3}+\frac{\beta_4}{24}\frac{\partial^4 u}{\partial T^4}+\gamma_1 u_0^3+\gamma_1 u_0^2(a+a_*)=-\Lambda(u_0+a).$$

Obviously, the condition $a \ll u_0$ was used. The simplification of this equation above assuming Eq. (2.104) leads to :

$$i\frac{\partial a}{\partial z}-\frac{\beta_2}{2}\frac{\partial^2 a}{\partial T^2}-\frac{i\beta_3}{6}\frac{\partial^3 a}{\partial T^3}+\frac{\beta_4}{24}\frac{\partial^4 u}{\partial T^4}+\gamma_1 u_0^2(a+a_*)=-\Lambda a.$$

Introducing Eq. (2.105) inside this equation of $a(z,T)$ yields :

$$\begin{aligned}&\left[i\frac{\partial a_1}{\partial z}-Ka_1+\frac{\beta_2\Omega^2}{2}a_1+\frac{\beta_3\Omega^3}{6}a_1+\frac{\beta_4\Omega^4}{24}a_1+\gamma_1 u_0^2(a_1+a_2)+\Lambda a_1\right]exp(i\varphi)\\&+\left[i\frac{\partial a_2}{\partial z}+Ka_2+\frac{\beta_2\Omega^2}{2}a_2-\frac{\beta_3\Omega^3}{6}a_2+\frac{\beta_4\Omega^4}{24}a_2+\gamma_1 u_0^2(a_1+a_2)+\Lambda a_2\right]exp(-i\varphi)=0,\end{aligned}$$

where $\varphi = Kz-\Omega t$. To solve this equation, we should set that the terms in $exp(i\varphi)$ and $exp(-i\varphi)$ are equal to zero separately as :

$$\begin{aligned}&i\frac{\partial a_1}{\partial z}-Ka_1+\frac{\beta_2\Omega^2}{2}a_1+\frac{\beta_3\Omega^3}{6}a_1+\frac{\beta_4\Omega^4}{24}a_1+\gamma_1 u_0^2(a_1+a_2)+\Lambda a_1=0,\\&i\frac{\partial a_2}{\partial z}+Ka_2+\frac{\beta_2\Omega^2}{2}a_2-\frac{\beta_3\Omega^3}{6}a_2+\frac{\beta_4\Omega^4}{24}a_2+\gamma_1 u_0^2(a_1+a_2)+\Lambda a_2=0.\end{aligned}$$

These NLSEs are the couple of equations used in Eq. (2.106).

# NLSE numerical simulation

To solve the NLSE given by the following NLSE :

$$\frac{\partial u}{\partial z}=-\frac{i\beta_2}{2}\frac{\partial^2 u}{\partial T^2}+\frac{\beta_3}{6}\frac{\partial^3 u}{\partial T^3}-\frac{\alpha}{2}u+i\gamma_1\left[|u|^2u+\frac{i}{\omega_0}\frac{\partial(|u|^2u)}{\partial T}-T_R\frac{\partial(|u|^2)}{\partial T}u\right].$$

One can use the program developed by Nick Usechak ©-2005 (The reader can consult the web site of Rochester university, web page of the Professor Agrawal's team of research). $T_R$ provides an approximate way of incorporating the Raman response. This treatment is valid for many TelCom based pulse propagation simulations, however, fails in the case of SCG. $s = 1/\omega_0$ provides an approximate way to incorporate the effect of SS. "s" is the parameter the user supplies in the program's interface. This program is called "**NLSE Solver**". One obtains figures as those presented in the first chapter of this thesis (see figures 1.8 and 1.9). A trial MATLAB code is also given by G. P. Agrawal on pages 516-518 of [3].

# Trial MATLAB numerical code of the SCG simulation

The reader can consult the following link kindly provided by J. C. Travers, M. H. Frosz and J. M. Dudley [114] for the updates of the SCG numerical code : ***www.scgbook.info***.
Please cite these authors in the corresponding reference in any publication using this code. The full code is also given by these authors on pages 46-49 in [114].

# A trial MATLAB numerical code for the MI analysis

We give in the next a full version of the MATLAB numerical code for the MI analysis in a SOI waveguide as discussed in sections 2.5 and 3.5.2. Please cite this thesis in any publication using this code as : L. M. Mandeng, (Ph.D thesis, Laboratory of Mechanics, Department of Physics, Faculty of Science, University of Yaoundé I, Cameroon, 2015).

```
%MATLAB Numerical code for the achievement of the MI PTG in a SOI waveguide
%for three profiles as Gaussian, sech-type and the RC shapes.
%Please cite this thesis in any publication using this code as : L. M. Mandeng,
%(PhD thesis, Laboratory of Mechanics, Department of Physics,
%Faculty of Science, University of Yaoundé I, Cameroon, 2015).
%%%%%%%%%%%%%%%%%%%%%%%%%%%%%%%%%%%%%%%%%%%%%%%%%%%%%%%%%%%%%%%%%%%%%%%%%%%%%%%
clear all; %clean the database allowed to the code
beta2=0.56; %GVD in ps^2/m
t0=50e-3; % pulse width in ps
beta4=-beta2*(t0^2); %FOD coefficient in ps^4/m
nt=400; %number of points in time
dt=(t0/nt); % stepsize in time in ps
t=(-nt/2:(nt/2)-1)*dt; %time window in ps
w=(pi/t0)*[(0:(nt/2)-1) (-nt/2:-1)]; %frequency window in 1/ps
gamma=47; %CKN coefficient in 1/(W.m)
G=0; %G=6.5; TPA coefficient 1/(W.m)
sigma=1.45e-21; %FCA coefficient in m^2
alpha=0.2/4.343; %linear loss coefficient in 1/m
h=(6.62e-34)*(1e24); %planck constant in J.ps
Aeff=(1e-6)^2; %effective mode area
c=3e8/(1e12); %light in m/ps
lambda0=1.55e-6; %wavelength in m
nu0=c/lambda0; % pump frequency in 1/ps
P0=3; % peak power in W
C=10; % chirp
ug=sqrt(P0)*exp(-(t.^2)).*exp(-1i*C*(t.^2)/2); %initial temporal Gaussian shape
us=sqrt(P0)*sech(t).*exp(-1i*C*(t.^2)/2); % temporal sech-type shape
uRC=sqrt(P0)*(1+cos(pi*t)).*exp(1i*C*(t.^2)/2)/2; % temporal RC shape
betaTPA=2*G*Aeff; % TPA parameter
Ng=sqrt(pi/2)*((P0^2)*betaTPA*t0/(4*h*nu0*(Aeff^2)))*(1+erf(sqrt(2)*t)); %FCD
%coefficient of the Gaussian pulse
terme0=1-(((tanh(t)).^2)/3);
Ns=(betaTPA*(P0^2)*t0/(h*nu0*(Aeff^2)))*((2/3)+(tanh(t).*terme0)); %FCD coefficient
%of the sech-type pulse
terme=2*sin(pi*t).*(160+(81*cos(pi*t))+(32*((cos(pi*t)).^2))+(6*((cos(pi*t)).^3)));
NRC=((P0^2)*betaTPA*t0/(1536*pi*h*nu0*(Aeff^2)))*(320+(105*pi)+(210*t/t0)+terme);
%FCD coefficient of the RC pulse
tabug=[];% initializing the data table that registers the time-domain intensity
%of the Gaussian pulse
tabus=[];% initializing the data table that registers the time-domain intensity
%of the sech-type pulse
tabuRC=[];% initializing the data table that registers the time-domain intensity
```

```
%of the RC pulse
tabvg=[];% initializing the data table that registers the spectral-domain intensity
%of the Gaussian pulse
tabvs=[];% initializing the data table that registers the spectral-domain intensity
%of the sech-type pulse
tabvRC=[];% initializing the data table that registers the spectral-domain intensity
%of the RC pulse
tabz=[]; % initializing the data table that registers the propagation distance z
L=0.15; % length of the SOI waveguide in m
nz=nt; % number of points in the space (following the parameter z)
dz=L/nz; %stepsize following z in m
vg=fft(ug); %initial spectral Gaussian
vs=fft(us); %initial spectral sech-type shape
vRC=fft(uRC); %initial spectral RC shape
for z=0:dz:L %start of the propagation
tabug=[tabug;abs(ug).^2]; %Registration of the time-domain intensity
%of the Gaussian pulse
tabus=[tabus;abs(us).^2]; tabuRC=[tabuRC;abs(uRC).^2];
tabvg=[tabvg;abs(vg).^2]; tabvs=[tabvs;abs(vs).^2];
tabvRC=[tabvRC;abs(vRC).^2]; Pg=abs(ug).^2; Ps=abs(us).^2;
PRC=abs(uRC).^2;
NLg=(1i*gamma*Pg)-(sigma*Ng/2)-(G*Pg);%Nonlinear operator in the SSF for
%the Gaussian pulse
NLs=(1i*gamma*Ps)-(sigma*Ns/2)-(G*Ps);%Nonlinear operator in the SSF for
%the sech-type
%pulse
NLRC=(1i*gamma*PRC)-(sigma*NRC/2)-(G*PRC);%Nonlinear operator in the SSF for
%the RC pulse
D=(1i*(w.^2)*0.5.*(beta2+(beta4*(w.^2)/12)))-(alpha/2);%Linear operator
%in the SSF
%start of the SSF code
vg=fft(exp(NLg*dz).*ug); vs=fft(exp(NLs*dz).*us);
vRC=fft(exp(NLRC*dz).*uRC);
vg=exp(D*dz).*vg;%spectral-domain intensity at z for the Gaussian pulse
vs=exp(D*dz).*vs;%spectral-domain intensity at z for the sech-type pulse
vRC=exp(D*dz).*vRC;%spectral-domain intensity at z for the RC pulse
ug=ifft(vg);%time-domain intensity at z for the Gaussian pulse
us=ifft(vs);%time-domain intensity at z for the sech-type pulse
uRC=ifft(vRC);%time-domain intensity at z for the RC pulse
tabz=[tabz;ones(1,nt)*z]; %table of z values
 fprintf('%05.1f %% complete\n', (z/L)*100);%percentage of progression of
%the code execution
end
subplot(1,3,1),pcolor(t,tabz,tabug);shading interp;%Contour plot
%of the Gaussian pulse
%propagation in the time domain
xlabel('t (ps)'); ylabel('z (m)'); title('Gaussian pulse');
subplot(1,3,2),pcolor(t,tabz,tabus);shading interp; %Contour plot
```

```
%of the sech-type pulse
%propagation in the time domain
xlabel('t (ps)'); ylabel('z (m)'); title('sech-type pulse');
subplot(1,3,3),pcolor(t,tabz,tabuRC);shading interp; %Contour plot
%of the RC pulse
%propagation in the time domain
xlabel('t (ps)'); ylabel('z (m)'); title('RC pulse');
```

# Code for the simulation of the CD parameter

We give below a piece of MATLAB code for the simulation of the CD parameter in the SCG's analysis.

```
  for n1=1:NBRE    % NBRE is the number of loops for the simulation of the SCG based
      %on the pair of photons
      % one photon is a normal signal and the other is the one with random/noised
      % phase
      g_numerator(n1)=0; %initialization of the term characterizing the numerator
      % of the
      % RHS of Eq. (1.46)
      g_TE1sq(n1)=0; %initialization of the term characterizing the first factor
      % of the
      % RHS's denominator of Eq. (1.46)
      g_TE2sq(n1)=0; %initialization of the term characterizing the second factor
      % of the
      % RHS's denominator of Eq. (1.46)
  end
   for n1=1:NBRE
  for k=1:N
  for l=1:N
  E1=tabE(k,n1); %tabE is the array in which the intensities of the photons
  % pair have been registered NBRE times
  E2=tabE(l,n1);
  TE1=fft(E1);
  TE2=fft(E2);
  g_numerator(n1) = g_numerator(n1) + conj(TE1).*TE2;
  g_TE1sq(n1) = g_TE1sq(n1) + abs(TE1).^2;
  g_TE2sq(n1) = g_TE2sq(n1) + abs(TE2).^2;
  end
  end
  g12(n1)=abs(g_numerator(n1)./sqrt(g_TE1sq(n1).*g_TE2sq(n1))); %Calculation
  %of the CD given by Eq. (1.46)
   end
  figure();
  plot(WL(iis),g12); %Plot of the CD parameter versus the wavelength
```

# List of publications

## Regular journal papers

1. **Lucien M. Mandeng, Serge I. Fewo, Clément Tchawoua**, "*Four-wave mixing growth in wavelength-division multiplexing solitons systems near the zero-dispersion wavelength*" The European Physical Journal D **67**, 30511 (©-Springer, 2013).

2. **Lucien M. Mandeng and Clément Tchawoua**, "*Chirped self-healing Airy pulses compression in silicon waveguides under fourth-order dispersion*," Journal of Modern Optics **60**, 359 (©-Taylor& Francis, 2013).

3. **Lucien M. Mandeng and Clément Tchawoua**, "*Impact of input profile, absorption coefficients and chirp on modulational instability of femtosecond pulses in silicon waveguides under fourth-order dispersion*," J. Opt. Soc. Am. B. **30**, 1382 (©-OSA, 2013).

4. **Lucien M. Mandeng, Alidou Mohamadou, Clément Tchawoua, and Hippolyte Tagwo**, "*Spectral compression in the supercontinuum generation through the higher-order nonlinear Schrödinger equation with non-Kerr terms using subnanojoule femtosecond pulses*," J. Opt. Soc. Am. B **30**, 2555 (©-OSA, 2013).

5. **Lucien M. Mandeng, Serge I. Fewo, Clément Tchawoua and Timoléon C. Kofané**, "*Dynamics of linear compression of chirped femtosecond optical pulses under fourth-order dispersion*," Journal of Modern Optics **61**, 662 (©-Taylor & Francis, 2014).

6. **Lucien M. Mandeng, Serge I. Fewo, Clément Tchawoua and Timoléon C. Kofané**, "*Periodic compression of chirped femtosecond pulses in silicon waveguides under fourth-order dispersion*," Journal of Optics **16**, 085204 (©-IOP Publishing, 2014).

7. **Lucien M. Mandeng, Clément Tchawoua, Hippolyte Tagwo, Mourad Zghal, Rim Cherif, and Alidou Mohamadou**, "*Role of the input profile asymmetry and the chirp on the propagation in highly dispersive and nonlinear fibers*," submitted (under review,2015).

8. **Lucien M. Mandeng and Clément Tchawoua**, "*Supercontinuum in a silicon waveguide including third-harmonic generation and negative-frequency Kerr terms*," submitted (under review, 2015).

## Posters session in Conferences

1. **Lucien M. Mandeng, Serge I. Fewo, Clément Tchawoua**, "*Four-wave mixing products in WDM soliton systems near the zero-dispersion wavelength: case of two well-separated input*

*pulses*" presented during the ICTP meeting entitled SMR 2286: International School on Non-linear Dynamics in Complex Systems held in the University of Yaoundé I from 31st October to 11th November 2011.

2. **Lucien M. Mandeng, Serge I. Fewo, Clément Tchawoua**, "*Pulses compression induced by chirp in optical media under fourth-order dispersion*" presented during the ICTP meeting entitled SMR 2286: International School on Non-linear Dynamics in Complex Systems held in the University of Yaoundé I from 31st October to 11th November 2011.

3. **Lucien M. Mandeng and Clément Tchawoua**, "*Modulational instability analysis for chirped ultra-short pulses in silicon waveguides under fourth-order dispersion*" presented during the ASOSD 2013 held in Tunis (Tunisia) from 31st August to 08th September 2013.

# Conference papers

1. **L. Mandeng Mandeng and C. Tchawoua**, "*Periodic compression induced by the interplay of fourth-order dispersion and self-phase modulation in silicon waveguides*," in Frontiers in Optics Conference, OSA Technical Digest (online) (Optical Society of America, 2012), paper FTh1D.6.

2. **L. Mandeng Mandeng and C. Tchawoua**, "*Nonlinear compression of self-healing Airy pulses in silicon-on-insulator waveguides*," in Frontiers in Optics Conference, OSA Technical Digest (online) (Optical Society of America, 2012), paper FW3A.36.

3. **L. Mandeng Mandeng, S. Ibraid Fewo, and C. Tchawoua**, "*Full model analysis of the four-wave mixing anti-Stokes component growth in the wavelength-division multiplexing solitons systems near the zero-dispersion wavelength*," 8th Iberoamerican Optics Meeting and 11th Latin American Meeting on Optics, Lasers, and Applications, edited by Manuel Filipe P. C. Martins Costa, (Proc. of SPIE Vol. 8785, 8785AL, 2013), doi: 10.1117/12.2021714.

4. **L. Mandeng Mandeng, S. Ibraid Fewo, C. Tchawoua and T. C. Kofané**, "*A note on ultra-short pulses compression in silicon optical waveguides under fourth-order dispersion*," Proc. SPIE 9286, Second International Conference on Applications of Optics and Photonics, Manuel Filipe P. C. Martins Costa; Rogério Nunes Nogueira (Aveiro, Portugal), 92863C (August 22, 2014); doi:10.1117/12.2063573.

5. **L. Mandeng Mandeng and C. Tchawoua**, "*Asymmetric inversion of Airy pulses induced by the interaction between the initial chirp and the group-velocity dispersion in a single mode fiber*," in Frontiers in Optics Conference, OSA Technical Digest (online) (Optical Society of America, 2014), paper FTh4B.5.

# Oral presentation in conferences

- **L. Mandeng Mandeng, S. Ibraid Fewo, C. Tchawoua, T. C. Kofané, H. Tagwo, and A. Mohamadou**, "*Compression of ultrashort optical pulses in waveguides*" presented during the ICTP school entitled SMR 2639: School on Cooperative Phenomena in Condensed Matter : From Bose-Eistein Condensates to Quantum Optics held in the University of Buea from 02nd November to 13th November 2015.

EPJ D
Atomic, Molecular, Optical and Plasma Physics
EPJ.org
your physics journal

Eur. Phys. J. D (2013) 67: 10 DOI: 10.1140/epjd/e2012-30511-8

# Four-wave mixing growth in wavelength-division multiplexing solitons systems near the zero-dispersion wavelength

Lucien Mandeng Mandeng, Serge Ibraid Fewo and Clément Tchawoua

edp sciences
Società Italiana di Fisica
Springer

Eur. Phys. J. D (2013) 67: 10
DOI: 10.1140/epjd/e2012-30511-8

THE EUROPEAN PHYSICAL JOURNAL D

Regular Article

# Four-wave mixing growth in wavelength-division multiplexing solitons systems near the zero-dispersion wavelength

Lucien Mandeng Mandeng, Serge Ibraid Fewo[a], and Clément Tchawoua

Laboratory of Mechanics, Department of Physics, Faculty of Science, University of Yaounde I, P.O. Box 812, Yaounde, Cameroon

Received 17 August 2012 / Received in final form 2 November 2012
Published online 31 January 2013 – 

**Abstract.** The growth of the four-wave mixing (FWM) near the zero-dispersion wavelength (ZDWL) is analyzed in wavelength-division multiplexing (WDM) solitons systems. The phase-matching conditions lead to a slight reduction of the frequency offset. Numerical analysis of the reduced model predicts a variation of appearance of the FWM along the transmission line, and comparison of the FWM crosstalk is presented in the case of well-separated input channels approximation. Considering the full model, the FWM decreases along the transmission line. For long distances, an analytical asymptotic solution of the FWM is used and confirms this feature beyond the tenth amplification node.

## 1 Introduction

The wavelength-division multiplexing technic which consists to send many signals in a single optical fiber has increased the usefulness of the transmission of data [1,2]. This has become one of the most important technics for high speed and high capacity requirement of optical fiber transmission systems [1,2]. However, it is well-known that interactions between the propagating fields leads to new waves under appropriate conditions through several nonlinear phenomena such as harmonic generation, stimulated Raman scattering (SRS), stimulated Brillouin scattering (SBS) and parametric processes as four-wave mixing and third-harmonic generation [2–6]. The origin of FWM is linked to the nonlinear response of bound electrons of a material to an electromagnetic field [2–6]. There are two types of the FWM process: the first type is obtained when three light pulses transfer their energy to a single fourth photon (for a degenerate case, the phenomenon is called third harmonic generation) and the second type is concerned when two photons are annihilated while two new other are created simultaneously [2]. Analytical treatment of the FWM process inside a single mode line leads to a phase-matching condition in order to gain the maximum FWM values. Some works have been devoted to the study of the second type of the FWM. Particularly, Ablowitz et al. introduced an analytical model that explained the growth of the FWM in soliton systems with damping and amplification [7]. Also, they derived analytical expressions for the FWM in an ideal, lossless WDM soliton systems [8]. Their approach consisted to launch two continuous waves (CW) that interact together leading to the FWM occurrence in the system.

Nowadays, it is well-known that the FWM creates deleterious effects on WDM and dense WDM communication systems [2,7–11]. Many technics were previously investigated in order to reduce or to quite cancel these effects such as dispersion management technic [11–15], an experimental grouping wavelength method [16], the use of weak random dispersion in second term of dispersion [17,18] and recently in frequency-division multiplexing systems [19]. However, the FWM has been discovered to be also useful [20], for example when looking for the values of the third-order nonlinear-index assuming a FWM-Based technic [2]. In addition, the FWM has also been important when looking for the ratio of the third over fourth order dispersion coefficients [21], making parametric oscillators, ultrafast signal processing, FWM-induced quadrature squeezing [1,20,22] and other applications [23,24].

The study of effects of higher-order dispersion terms on the FWM of the first type has been done by Singh et al. [25] based on earlier works of Inoue et al. [25,26]. They showed that the combination of higher order dispersion terms leads to a FWM power reduction.

As far as the second type of the FWM process is concerned, the effects of higher-order dispersion have not been considered in WDM soliton systems to our knowledge. Therefore, the main purpose of the present work deals with the study of the growth of the FWM in this kind of systems modeled by the nonlinear Schrödinger equation with an additional TOD using a similar approach with the one done by Ablowitz et al. [7]. We remind that this case is considered when the optical system has a vanishing group-velocity dispersion (GVD) or uses high intensity peaks (short and ultrashort pulses) [1–6,27]. Analytical treatment of the model is based on the propagation of the anti-stokes component in the case of gain/loss. We compare the single TOD case with the combined GVD-TOD

[a] e-mail: sergefewo@yahoo.fr

case (where a residual GVD is considered) and bring out the differences as concerned the phase-matching conditions and amplitude growth of the FWM components.

The paper is organized as follows: in Section 2, a partial differential equation (PDE) for the evolution of the FWM anti-stokes component is derived. In Section 3, considering a reduced model of the FWM component assuming the third order dispersion, the associated phase-matching condition is derived. It follows a numerical integration of the equation of the FWM component. Section 4 is devoted to investigation of the full model where a generalized relation of the FWM component spectrum is obtained. Numerical analysis is presented in Section 5. The last section concludes the paper.

## 2 Analytical study of the model

We begin the analysis using the following nonlinear Schrödinger (NLS) equation for the slowly varying pulse envelope of the electrical field in the case of short pulses [1–6,27], which reads

$$i\frac{\partial A}{\partial z} - \frac{\beta_2}{2}\frac{\partial^2 A}{\partial T^2} - i\frac{\beta_3}{6}\frac{\partial^3 A}{\partial T^3} + \gamma|A|^2 A = -i\alpha A, \quad (1)$$

where $A(Z,T)$ is the optical soliton envelope of the electrical field, $Z$ is the spatial propagation variable and $T$ is the retarded time variable. The parameter $\beta_2$ is the second-order dispersion profile where $\beta_3$ is the third-order dispersion. The parameters $\gamma$ and $\alpha$ are the nonlinear and damping/amplification coefficients respectively, we set the following dimensionless variables: $\zeta = Z/L$, $\tau = T/T_0$, $B(\zeta,\tau) = A(Z,T)/\sqrt{P_0}$ where $L$ and $T_0$ are the characteristic fiber length, and the characteristic time window of the pulse, respectively. Thus, $P_0$ is the input peak power and we define $L_{GVD}$ as the length scale associated to the second-order dispersion term, $L_{NL}$ is the length scale associated to the third-order nonlinear term. We also define $L_a = L_*/L$ as the dimensionless spatial amplification spacing while $|\beta_2| = T_0^2/L_{GVD}$ and $|\beta_3| = T_0^3/L_{TOD}$ are the group-velocity dispersion (GVD) and the third-order dispersion (TOD) values, respectively. $L_*$ is the physical spatial amplification spacing. Introducing these dimensionless variables into equation (1) easily leads to the following form:

$$i\frac{\partial B}{\partial \zeta} - \frac{L\beta_2}{2\,T_0^2}\frac{\partial^2 B}{\partial \tau^2} - i\frac{L\beta_3}{6\,T_0^3}\frac{\partial^3 B}{\partial \tau^3} + L\gamma P_0|B|^2 B = -iL\alpha B. \quad (2)$$

Now we set the dimensionless terms $\beta_{GVD} = -\beta_2 L_{GVD}/T_0^2$, $\beta_{TOD} = \beta_3 L_{TOD}/T_0^3$ and $\Gamma = L\alpha$ for GVD, TOD profiles and gain/loss parameter, respectively. Introducing these in equation (2) yields

$$i\frac{\partial B}{\partial \zeta} + \frac{\beta_{GVD} L}{2L_{GVD}}\frac{\partial^2 B}{\partial \tau^2} - i\frac{\beta_{TOD} L}{6L_{TOD}}\frac{\partial^3 B}{\partial \tau^3} + \frac{L}{L_{NL}}|B|^2 B = -i\Gamma B. \quad (3)$$

It is well-known that the bright soliton solution is obtained in the regime of propagation where the dispersion length $L_{GVD}$ is similar to the nonlinear length $L_{NL}$ in the anormalous-dispersion regime. The TOD plays a significant role only if the dispersion length associated $L_{TOD}$ respects the condition $L_{TOD} \leq L_{GVD}$ [2,28–30]. Furthermore, it is well-known that the solitonic properties as the preserving shape of propagation exist in an ideal system while in realistic cases they are perturbed by higher-order effects like the TOD effect. So, in the present system, we assume that $L_{TOD} \approx L_{GVD}$. One can rewrite equation (3) in a suitable form by setting $B(\zeta,\tau) = \sqrt{h(\zeta)}E(\zeta,\tau)$ where $h(\zeta)$ is a function which will include the parameter $\Gamma$. The function $h(\zeta)$ being a periodic function expanded in Fourier series:

$$h(\zeta) = \sum_{n=-\infty}^{n=+\infty} h_n e^{-ink_{L_a}\zeta}, \quad h_n = \frac{\Gamma L_a}{\Gamma L_a - in\pi}, \quad (4)$$

where $k_{L_a} = \frac{2\pi}{L_a}$. Equation (4) yields

$$i\frac{\partial E}{\partial \zeta} + \frac{\beta_{GVD}}{2}\frac{\partial^2 E}{\partial \tau^2} - i\frac{\beta_{TOD}}{6}\frac{\partial^3 E}{\partial \tau^3} + h(\zeta)|E|^2 E = 0. \quad (5)$$

For a real physical system, we take the following parameter values: $L = 100$ Km, $\beta_3 = 1$ ps$^3$/Km. This leads to $T_0 = 4.64$ ps and $\beta_2 = -0.21$ ps$^2$/Km for the case where we consider the addition of the residual constant GVD. We also have $L_* = 10$ Km, $n = 1 \ldots 10$, $P_0 = 2$ mW and $\alpha = 0.0921$ Km$^{-1}$. The obtained values of parameters $\gamma$ and $\Gamma$ are 5 W$^{-1}$/Km and 9.21 respectively. The initial frequency offset of the pulses is given by $\Omega = 2.4392$ leading to the channel spacing $\Delta\lambda = 1.5032$ nm for a single mode fiber at $\lambda \approx 1.32$ $\mu$m. The presence or lack of the dimensionless dispersion parameter $\beta_{GVD}$ will be represented by the values 1 and 0, respectively.

The evolution of the FWM in the model is investigated through the anti-stokes component using a similar approach developed by Ablowitz et al. [7]. Therefore, we consider a signal including two pulses $E_1$ and $E_2$ such that $E_{pulse} = E_1 + E_2$. We assume that the FWM in the channels is taken as $E_{FWM} = E_{112} + E_{221}$. Then, the total field in the system is

$$E(\zeta,\tau) = E_1 + E_2 + E_{112} + E_{221}, \quad (6)$$

where $E_1$, $E_2$, $E_{112}$ and $E_{221}$ evolve on frequencies $\Omega_1$, $\Omega_2$, $\Omega_{112} = 2\Omega_1 - \Omega_2$ and $\Omega_{221} = 2\Omega_2 - \Omega_1$, respectively. If we take $\Omega_1 = -\Omega_2 = -\Omega$, therefore $\Omega_{112} = -3\Omega$ and $\Omega_{221} = 3\Omega$. The components of FWM $E_{112}$ and $E_{221}$ are the so-called stokes and anti-stokes components, respectively. When we introduce equation (6) into equation (5), we obtain a PDE by neglecting all nonlinear terms in $E_{112}$, $E_{221}$ and the cross-phase modulation (XPM) terms. The system can be modeled by the diagram given in Figure 1 where the transmission line is represented by the single mode optical fiber (SMF) symbolized by the ITU-T recommendation G.652 [9]. The evolution of the anti-stokes FWM in the system with TOD is therefore modeled by the following equation:

$$i\frac{\partial E_{221}}{\partial \zeta} + \frac{\beta_{GVD}}{2}\frac{\partial^2 E_{221}}{\partial \tau^2} - i\frac{\beta_{TOD}}{6}\frac{\partial^3 E_{221}}{\partial \tau^3} + h(\zeta)E_2^2 E_1^* = 0. \quad (7)$$

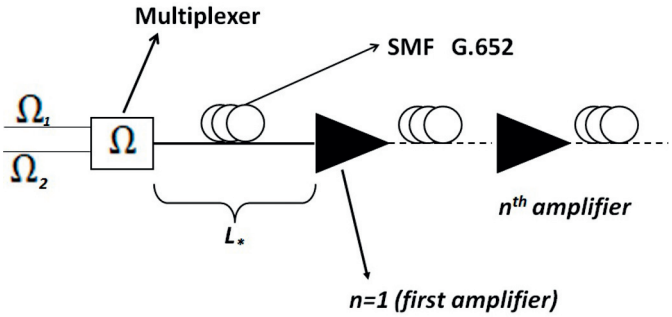


**Fig. 1.** Diagram of the physical model under study.

For simplicity, we set $v = E_{221}$ in equation (7). Many works dealing with the evolution of the FWM have been done in systems assuming only the second order dispersion term [7,8,11–13,17,18]. The present model under study (Eq. (7)), which includes the TOD term will be investigated in order to characterize the FWM under influence of this coefficient.

## 3 Reduced model of the FWM component growth

Following the assumption of Horne et al. [18], the evolution of the FWM is taken in the following form including the TOD effect inside the exponential argument of the anti-stokes component:

$$v(\zeta,\tau) = G(\zeta,\tau)\exp\left[i\left(3\Omega\tau - \frac{\Omega^2}{2}\beta_{GVD}\zeta\right)\right] \times \exp\left[-i\frac{\Omega^3}{6}\beta_{TOD}\zeta\right]. \quad (8)$$

When we introduce equation (8) into equation (7) we obtain the following equation for the amplitude $G(\zeta,\tau)$:

$$i\frac{\partial G}{\partial\zeta} + \frac{\beta_{GVD}}{2}\left(\frac{\partial^2 G}{\partial\tau^2} + 6i\Omega\frac{\partial G}{\partial\tau} - 2(2\Omega)^2 G\right) - i\frac{\beta_{TOD}}{6} \times\left(\frac{\partial^3 G}{\partial\tau^3} + 9i\Omega\frac{\partial^2 G}{\partial\tau^2} - 27\Omega^2\frac{\partial G}{\partial\tau} - 26i\Omega^3 G\right) = -h(\zeta)E_{20}^2 E_{10}^*, \quad (9)$$

where

$$E_{20}^2 E_{10}^* = E_2^2 E_1^* \exp\left[i\left(-3\Omega\tau + \frac{\Omega^2}{2}\beta_{GVD}\zeta\right)\right] \times \exp\left[i\left(\frac{\Omega^2}{2}\frac{\beta_{TOD}\Omega}{3}\zeta\right)\right]. \quad (10)$$

We set $\Delta\Omega = \Omega_2 - \Omega_1 = 2\Omega$ as the difference in the frequency offset for the case where the input pulses are well-separated, therefore in this case $\Delta\Omega \gg 1$. We assume the following simplifications $(\Delta\Omega)^2|G|$, $26\Omega^3|G| \gg |\frac{\partial G}{\partial\tau}|$, $|\frac{\partial^2 G}{\partial\tau^2}|$, $|\frac{\partial^3 G}{\partial\tau^3}|$. Then equation (9) becomes

$$i\frac{\partial G}{\partial\zeta} - (\Delta\Omega)^2\left(\beta_{GVD} + \frac{13\Omega\beta_{TOD}}{12}\right)G = -h(\zeta)E_{20}^2 E_{10}^*, \quad (11)$$

which is considered as the reduced model. For simplicity, we set

$$\phi = \beta_{GVD} + \frac{13\Omega\beta_{TOD}}{12},$$
$$\psi(\zeta) = \left(\beta_{GVD} + \frac{\beta_{TOD}\Omega}{3}\right)\zeta. \quad (12)$$

The input pulses are sech-type profiled in the general form of fundamental soliton as in [2,17]:

$$E_j = E_{max,j}\,\mathrm{sech}[E_{max,j}(\tau - \Omega_j\zeta - T_j)] \times \exp\left[i(E_{max,j}^2 - \Omega_j^2)\zeta/2\right]\exp\left[i\Omega_j\tau\right] \quad (13)$$

where $\Omega_1 = -\Omega_2 = -\Omega$, $E_{max,1} = E_{max,2} = E_{max}$ and $T_1 = -T_2 = T_*$. The integration of equation (11) gives

$$G(\zeta,\tau) = iE_{max}^3\exp\left[-i(\Delta\Omega)^2\phi\zeta\right] \times\sum_{n=-\infty}^{n=+\infty} h_n\int_0^\zeta \mathrm{sech}^2\left[E_{max}(\tau - \Omega\zeta' + T_*)\right] \times\mathrm{sech}\left[E_{max}(\tau + \Omega\zeta' - T_*)\right]\exp\left[i\left(-nk_{La}\zeta' + \frac{E_{max}^2 - \Omega^2}{2}\zeta' + (\Delta\Omega)^2\phi\zeta'\right)\right] \times\exp\left[i\left(\frac{\Omega^2}{2}\psi(\zeta')\right)\right]d\zeta'. \quad (14)$$

It is important to remind that the phase-matching condition required in order to gain the maximum FWM values is obtained by taking the argument of the imaginary exponential

$$\exp\left[i\left(-nk_{La}\zeta' + 0.5(E_{max}^2 - \Omega^2)\zeta' + (\Delta\Omega)^2\phi\zeta'\right)\right] \times\exp\left[0.5i\Omega^2\psi(\zeta')\right]$$

equal to zero. This leads to some cases of the study in function of the GVD and TOD profiles.

– In the presence of constant TOD profile without the GVD parameter, the phase-matching condition leads to:

$$9\Omega^3 - \Omega^2 + E_{max}^2 - 2nk_{L_a} = 0. \quad (15)$$

One must solve this equation following $\Omega$ and $n$ to obtain values leading to largest amplitude of FWM.

– In the presence of both the GVD and TOD profiles, we obtain from the general reduced model the following equation:

$$9\Omega^3 + 8\Omega^2 + E_{max}^2 - 2nk_{L_a} = 0. \quad (16)$$

The next section deals with the full model assuming that the amplitude of the FWM component is very sensitive to the time variable (differentiated terms of $G(\zeta,\tau)$ are not negligible).

## 4 Full model of the FWM component growth

Considering the Fourier transform of equation (9), we obtain:

$$i\frac{\partial\tilde{G}}{\partial\zeta}-\frac{1}{2}\Big\{\beta_{GVD}\Big(\omega^2+6\omega\Omega+2(2\Omega)^2\Big)+\frac{\beta_{TOD}}{3}\times\Big(\omega^3+9\omega^2\Omega+27\omega\Omega^2+26\Omega^3\Big)\Big\}\tilde{G}=-h(\zeta)F[E_{20}^2E_{10}^*]. \quad (17)$$

We set:

$$\theta(\omega,\Omega)=\beta_{GVD}\Big(\omega^2+6\omega\Omega+2(2\Omega)^2\Big)+\frac{\beta_{TOD}}{3}\Big(\omega^3+9\omega^2\Omega+27\omega\Omega^2+26\Omega^3\Big). \quad (18)$$

Equation (17) leads to the following form of $\tilde{G}(z,\omega)$:

$$\tilde{G}(\zeta,\omega)=\frac{i\pi E_{max}}{\Delta\Omega}\exp\Big[-i\Big(\frac{1}{2}\theta(\omega,\Omega)\zeta+\omega\delta(\zeta)\Big)\Big]\times\operatorname{sech}\Big(\frac{\pi\omega}{2E_{max}}\Big)\sum_{n=-\infty}^{n=+\infty}h_n\exp\Big[i\chi_n(\omega)\zeta_{coll}\Big]\times\int_{-\infty}^{2E_{max}\delta(\zeta)}I\Big(y,\frac{\omega}{E_{max}}\Big)\exp\Big[-i\mu_n(\omega)y\Big]dy, \quad (19)$$

where

$$\chi_n(\omega,\Omega)=\Big[-nk_{La}+\frac{E_{max}^2-\Omega^2}{2}+\frac{1}{2}\theta(\omega,\Omega)+\frac{\Omega^2}{2}\Big(\beta_{GVD}+\frac{\beta_{TOD}\Omega}{3}\Big)\Big], \quad (20)$$

is related to the phase-matching condition. The function $I(y,\omega/E_{max})$ is a well-known function (see Refs. [7,8]), $\delta(\zeta)=\Omega\zeta-T_*$, $\mu_n(\omega)=-\chi_n(\omega,\Omega)/\Delta\Omega E_{max}$ and $y=2E_{max}\delta(\zeta)$. The phase-matching condition for the full model is given by taking $\chi_n(\omega,\Omega)=0$. The roots $\omega_n$ obtained are only relevant, if we consider those which are equal to zero because of the presence of the function $\operatorname{sech}(\pi\omega/2E_{max})$ inside $\tilde{G}(\zeta,\omega)$. Thus, equation (20) leads to the following polynomial equation of third degree:

$$ax^3+bx^2+cx+d=0, \quad (21)$$

where we have set $x=\omega$, $a=\beta_{TOD}/3$, $b=\beta_{GVD}+3\beta_{TOD}\Omega$, $c=6\Omega\beta_{GVD}+9\Omega^2\beta_{TOD}$ and $d=9(\beta_{GVD}+\beta_{TOD}\Omega-1/9)\Omega^2+E_{max}^2-2nk_{La}$. Therefore, we can consider specific cases:

1. Case of the second order dispersion $\beta_{GVD}=1$, $\beta_{TOD}=0$:

$$x^2+6\Omega x+\big(8\Omega^2+E_{max}^2-2nk_{La}\big)=0, \quad (22)$$

the two solutions are

$$x_{n,\pm}=-3\Omega\pm\sqrt{\Omega^2-E_{max}^2+2nk_{La}}.$$

The realistic solution is $x_{n,+}$ that must be equal to zero according to the previous hypothesis. So, we recover the single GVD phase-matching condition as obtained by Ablowitz et al. [7,8]:

$$\Omega=\frac{1}{2}\sqrt{nk_{La}-\frac{E_{max}^2}{2}}. \quad (23)$$

2. Case of the third order dispersion $\beta_{GVD}=0$, $\beta_{TOD}=1$:

$$\frac{1}{3}x^3+3\Omega x^2+9\Omega^2x+(9\Omega^3-\Omega^2+E_{max}^2-2nk_{La})=0. \quad (24)$$

If we take three general solutions of equation (24) as $(x-x_1)(x-x_2)(x-x_3)=0$ and we assume one of them equal to zero, we obtain the same phase-matching condition derived from the reduced model for single TOD case given by equation (15).

3. Case of the combined GVD and TOD case $\beta_{GVD}=1$, $\beta_{TOD}=1$:

$$\frac{1}{3}x^3+(3\Omega+1)x^2+(9\Omega^2+6\Omega)x+(9\Omega^3+8\Omega^2+E_{max}^2-2nk_{La})=0. \quad (25)$$

Using the same process as in the previous case, we derive the phase-matching condition obtained in equation (16) for the reduced model.

So, for all these cases we obtain the same phase-matching conditions of the reduced model in the full model by taking the roots $\omega_n$ of $\chi_n(\omega,\Omega)$ equal to zero.

Considering the case where $\omega_n\neq 0$, we obtain a general form of the asymptotic solution $\tilde{G(z,\omega)}$ for long distances:

$$\tilde{G}(\zeta\to\infty,\omega)\approx\frac{i\pi^2E_{max}}{\Delta\Omega}\exp\Big[-i\Big(\frac{\theta(\omega,\Omega)}{2}\zeta+\omega\delta(\zeta)\Big)\Big]\times\operatorname{sech}\Big(\frac{\pi\omega}{2E_{max}}\Big)\sum_{n=-\infty}^{+\infty}h_n\exp\Big[i\chi(\omega,\Omega)\zeta_{coll}\Big]\times\frac{\mu_n(\omega,\Omega)+\omega/E_{max}}{\sinh\Big[\frac{\pi}{2}\Big(\mu_n(\omega,\Omega)+\omega/E_{max}\Big)\Big]\cosh\Big(\frac{\pi\mu_n(\omega,\Omega)}{2}\Big)}. \quad (26)$$

In the next section, we present the numerical results of the previous analytical studies.

## 5 Numerical investigations

In this section we present numerical results of the study of the FWM in the case of nonlinear Schrödinger equation assuming TOD with gain/loss. As mentioned earlier, we have worked with normalized dimensionless quantities that can be easily linked to the physical corresponding parameters. Considering the phase-matching conditions obtained in both cases for the reduced and full models (for $\omega_n=0$), Figure 2 presents the evolution of the frequency

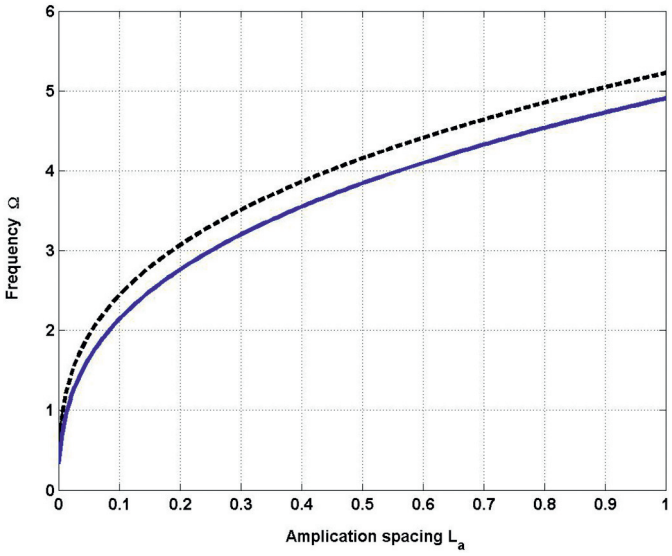


**Fig. 2.** (Color online) Evolution of the frequency offset of Phase-matching conditions versus the amplification spacing with $\beta_{GVD} = 1$, $\beta_{TOD} = 1$ (solid curve) and $\beta_{GVD} = 0$, $\beta_{TOD} = 1$ (dashed curve).

offset where the FWM appears to be more important in the transmission in function of the normalized parameter of the amplification distance. In the presence of both GVD and TOD, it comes a slight reduction of the frequency offset evolution (solid curve in Fig. 2) in comparison to the single TOD case (dashed curve in Fig. 2). The addition of the GVD term is the reason of this interesting feature. The origin is linked to the polynomial equations of phase-matching conditions obtained in equations (15) and (16). We conclude that the combined dispersion terms reduce the frequency offset window more than a single dispersion term. Analyzing the growth function of the FWM in the reduced model, we can predict a higher growth for the most reduced frequency window.

Figures 3 and 4 present the temporal profile evolution of the FWM versus the normalized distance $\zeta$ (for convenience $\zeta$ and $\tau$ are respectively represented by z and t in the figures) in the reduced model for the single TOD case and assuming both TOD and GVD, respectively. One integrates equation (14) assuming physical realistic systems with amplification nodes ($n \times L_a$) and realizing phase-matching condition at each node in order to obtain the appropriate frequency offset to the FWM occurrence. These figures are obtained by using a trapezoidal numerical integration scheme on equation (14) between each amplifier spacing and by realizing the phase-matching conditions of equations (15) and (16). As can be seen in those figures, the FWM component appears along the transmission line near the first node and its amplitude increases through the following amplification nodes due to the realization of the phase-matching conditions. We notice that, in the reduced model, the FWM is reduced slightly in the single TOD case than in the combined GVD-TOD case. This feature is better observed in Figure 5 which presents the FWM temporal profile at the first and the tenth amplification nodes for both cases (single TOD and combined GVD-TOD). Figure 5a presents identical amplitude values of the FWM at the first node for both cases under study. During the propagation along the transmission line, one observes that the amplitude of the FWM temporal profile in the single TOD case is slightly reduced in comparison with the amplitude assuming the combined GVD-TOD case (see Fig. 5b). Therefore, in the reduced model, the FWM grows along the transmission line and consequently a control of the FWM growth could be achieved.

For the full model, we have also integrated equation (19) using the same numerical scheme between each amplifier spacing and by realizing once more the phase-matching condition of the FWM on the amplifier nodes. The growth of the spectra profiles of the FWM versus the normalized distance $\zeta$ in the full model are presented in Figures 6 and 7 for the single TOD and the combined GVD-TOD cases, respectively. The TOD introduces an asymmetry in the profile of the FWM component for both cases which is progressively reduced along the line when reaching the tenth amplification node. It is also found that in WDM soliton systems where input colliding channels $E_1$ and $E_2$ are not well-separated, the FWM is associated with slight peaks at each amplification node and becomes wide when $\zeta$ is increasing. It yields that, the strength of the FWM in the single TOD case is more important than in the combined GVD-TOD case. For both cases, the FWM becomes more smaller along the propagation distance $\zeta$. We present in Figure 8, the spectrum profile of the FWM component for both cases at the first and tenth amplification nodes. This spectrum is more intense in the single TOD case (dotted lines in Figs. 8a and 8b) than in the combined GVD-TOD case (solid line in these figures). We can easily say that the combination of TOD term with the GVD term reduces the FWM crosstalk in the WDM soliton systems where input channels are closer each other (small frequency spacing). This feature is depicted by the asymptotic solution of the FWM growth presented in Figure 9 for the full model. We obtain a high broadening of the FWM spectrum in the combined GVD-TOD case (solid lines) comparatively to the FWM spectrum in the single TOD case (dotted lines). These results show that the analytical asymptotic solution (for larger $\zeta$) is in good agreement with the previous obtained results.

## 6 Conclusion

Using the NLS equation for an optical WDM solitons system near the ZDWL, we have obtained the model equation for the anti-stokes component of the FWM. Then, after some simplifications, we have obtained the so-called reduced model from which has been derived the phase-matching conditions that lead to the FWM high values occurrence. The full model has also been considered for the study in the single TOD case and the combined GVD-TOD case. It comes that the frequency offset is more important in the single TOD case than in the combined GVD-TOD case. In the case of the reduced model, the combined effect of GVD and TOD leads to a growth of

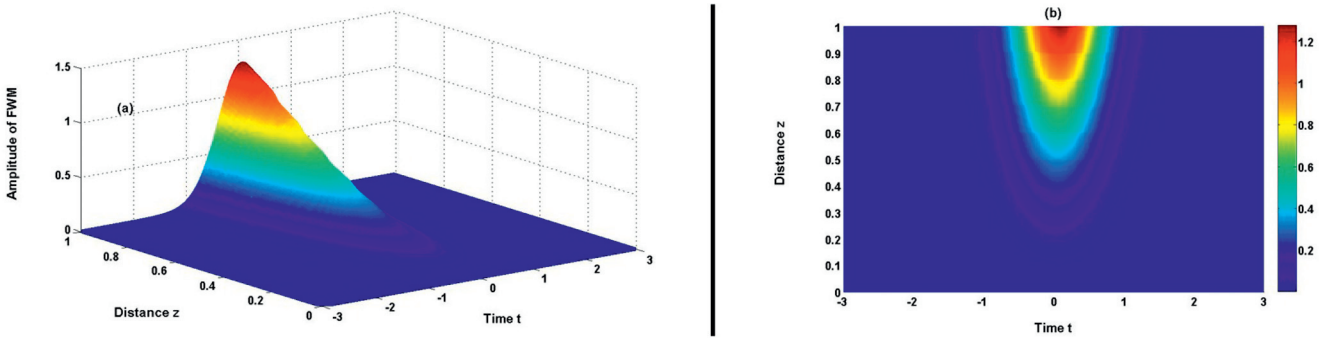


**Fig. 3.** (Color online) Propagation of FWM component in the reduced model, for the single TOD case $\beta_{GVD} = 0,\ \beta_{TOD} = 1$.

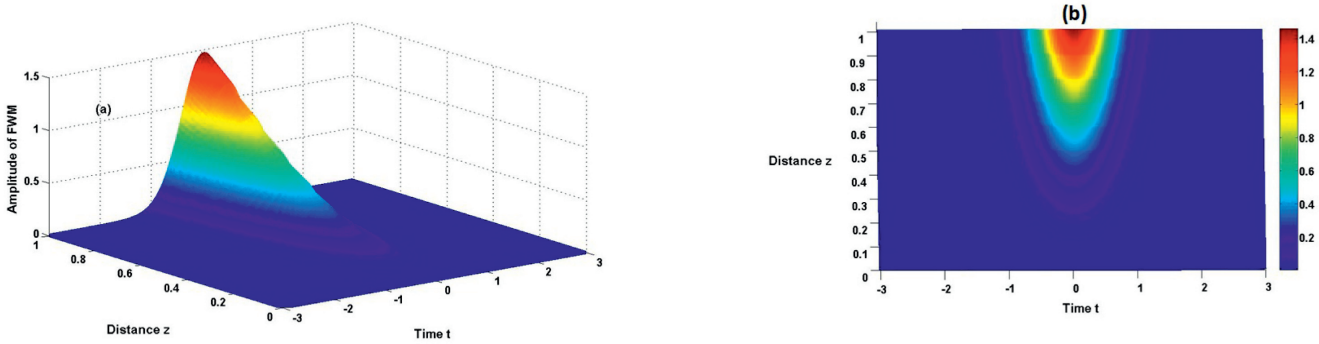


**Fig. 4.** (Color online) Propagation of FWM component in the reduced model, for the GVD-TOD case $\beta_{GVD} = 1,\ \beta_{TOD} = 1$.

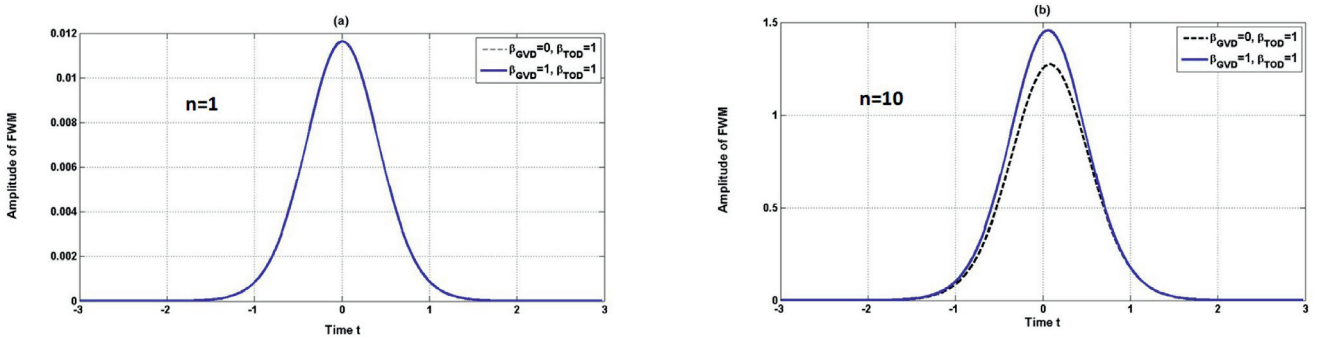


**Fig. 5.** (Color online) Temporal profile of FWM in the reduced model for both single TOD (dashed curve) and combined GVD-TOD (solid curve), at the first ($n = 1$: curve (a)) and the tenth ($n = 10$: curve (b)) nodes respectively.

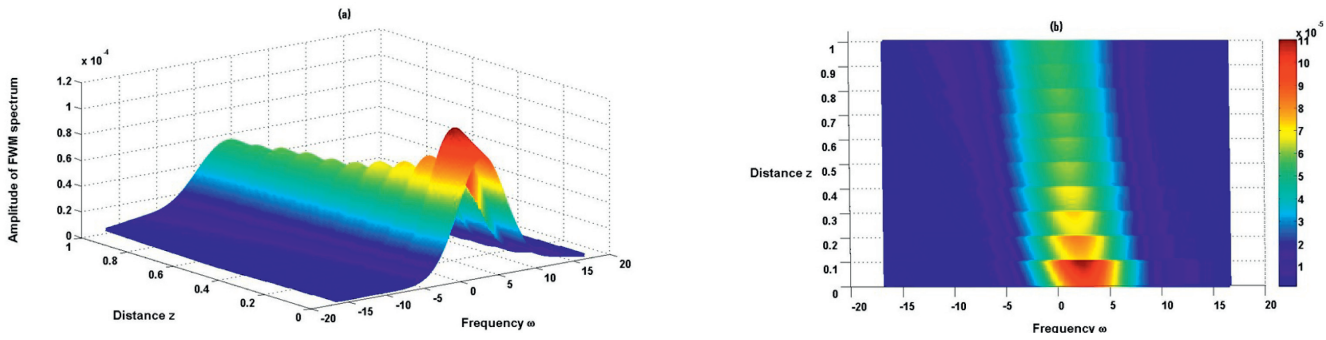


**Fig. 6.** (Color online) Propagation of FWM component spectrum in the full model, for the single TOD case $\beta_{GVD} = 0$, $\beta_{TOD} = 1$.

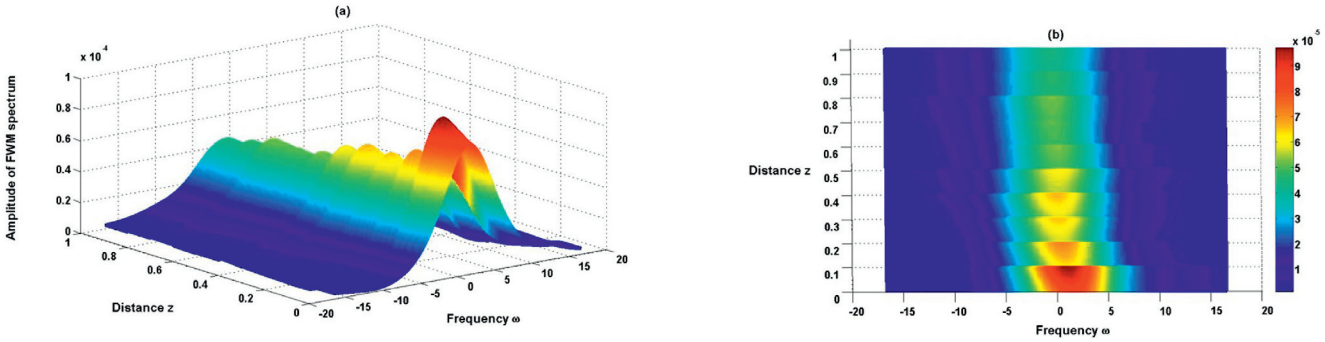


**Fig. 7.** (Color online) Propagation of FWM component spectrum in the full model, for the combined GVD-TOD case $\beta_{GVD} = 1$, $\beta_{TOD} = 1$.

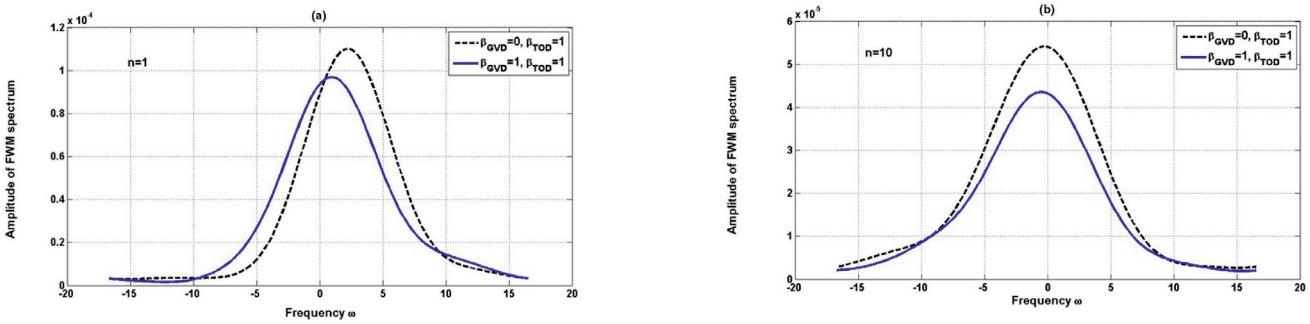


**Fig. 8.** (Color online) Spectral profile of FWM in the full model for both single TOD (dashed curve) and combined GVD-TOD (solid curve), at the first ($n = 1$: curve (a)) and the tenth ($n = 10$: curve (b)) nodes respectively.

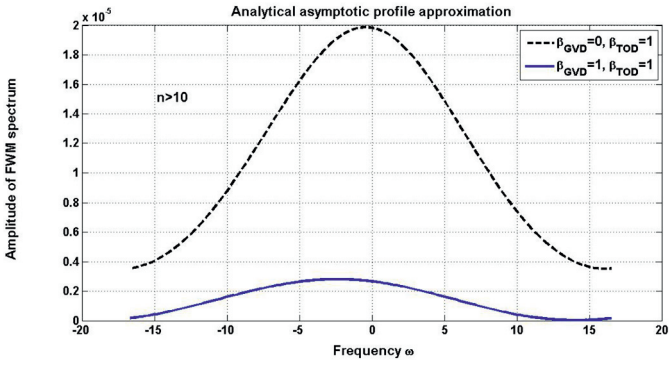


**Fig. 9.** (Color online) Spectral profile of FWM in the full model for both single TOD (dashed curve) and combined GVD-TOD (solid curve), asymptotic solution beyond the tenth node where the parameter $z$ is assumed to be larger.

the FWM in the system. We have recovered the previous mentioned results of reference [17] where the FWM grows along the transmission line and therefore is eliminated by the use of a weak random or DM technic for the reduced model. In addition, it has appeared that a residual GVD combined to the TOD allows a strong growth than a single TOD case. This can be seen as an interesting feature for WDM soliton systems near the ZDWL. Because of the large frequency offset difference between the two input pulses, assuming that they interact weakly, the FWM crosstalk gain in power, rising inside the line after crossing each amplification node. This feature being enhanced by the combination of dispersion terms.

However, for the full model where squeezed up channels are considered, the FWM component appears quickly along the transmission line with a high spectrum amplitude value and decreases more in the combined GVD-TOD case than in the single TOD case. This result is similar to those obtained by Singh et al. [25,26] on the effect of higher-order dispersion terms on the FWM of type I. However, these authors dealt with input powers of three pulses and made a conclusion that under the combined effect of second, third, fourth and fifth-order dispersion parameters, the crosstalk introduced by the FWM is reduced [25]. A relevant result obtained in the present work is that dealing with two input pulses, we have reached a reduction of the crosstalk introduced by the FWM and the frequency offset window in the case of the full model in comparison to the FWM generated by three pulses as obtained by Singh et al. [25]. The weak value of the frequency offset difference between the two input pulses, lead to a great interaction. Consequently, even if the FWM crosstalk appears more quickly than in the reduced model inside the transmission line, the strong interaction between the pairwise input pulses leads them to recover their power and it follows the decreasing of the FWM power. We can mention that if one purpose in WDM soliton systems near the ZDWL is to reduce the impact of the FWM crosstalk, therefore the choice of squeezed up input pulses under a combination of

GVD-TOD is suitable to quite cancel the FWM crosstalk. In summary, the present work demonstrates clearly the evolution of the FWM in the system under the interaction of TOD and GVD parameters. Thus, the propagation of signals could be optimized in WDM soliton systems near the ZDWL when the growth of the FWM could be well controlled.

This work has been done in the Laboratory of Mechanics, Department of Physics of the Faculty of Science of the University of Yaounde I, Cameroon. We sincerely thank Pr. T.C. Kofane, Head of the laboratory.

## References

1. G.P. Agrawal, *Application of Nonlinear Fibers Optics*, 2nd edn. (Academic Press, Boston, 2008)
2. G.P. Agrawal, *Nonlinear Fiber Optics*, 4th edn. (Academic Press, Boston, 2007)
3. Y.R. Shen, *The principles of Nonlinear Optics* (Wiley, New York, 1984)
4. M. Shubert, B. Wilhelmi, *Nonlinear Optics and Quantum Electronics* (Wiley, New York, 1986)
5. P.N. Butcher, D. Cotter, *Elements of Nonlinear Optics* (Cambridge Unversity Press, Cambridge, 1990)
6. R. Boyd, *Nonlinear Optics*, 3rd edn. (Academic Press, Boston, 2008)
7. M.J. Ablowitz, G. Biondini, S. Chakravarty, R.B. Jenkins, J.R. Sauer, Opt. Lett. **21**, 1646 (1996)
8. M.J. Ablowitz, G. Biondini, S. Chakravarty, R.B. Jenkins, J.R. Sauer, J. Opt. Soc. Am. B **14**, 1788 (1997)
9. L.F. Mollenauer, P.V. Mamyshev, J. Quantum Electron. **34**, 2089 (1998)
10. P.B. Harboe, E. Silva, J.R. Souza, World Acad. Sci. Eng. Tech. **48**, 77 (2008)
11. R.L. Horne, Ph.D. thesis, University of Colorado at Boulder, 2001
12. M.J. Ablowitz, G. Biondini, S. Chakravarty, R.L. Horne, J. Opt. Soc. Am. B **20**, 831 (2003)
13. M.J. Ablowitz, R.L. Horne, E. Spiller, G. Biondini, S. Chakravarty, *Nonlinear Optics Conference*, Vol. 1 of 2000 OSA Technical Digest Series (Optical Society of America), paper ThB6 (2000)
14. S. Gao, C. Yang, G. Jin, Appl. Opt. **42**, 7126 (2003)
15. K. Nakajima, M. Ohashi, K. Shiraki, T. Horiguchi, K. Kurokawa, Y. Miyajima, IEEE J. Lightw. Technol. **17**, 1814 (1999)
16. T. Katagiri, T. Naito, A. Miura, K. Amemiya, in *Optical Fiber Communication Conference*, Vol. 2 of 2003 OSA Technical Digest Series (Optical Society of America), paper FE6 (2003)
17. R.L. Horne, C.K.R.T. Jones, T. Schäfer, Physica D **205**, 70 (2005)
18. R.L. Horne, C.K.R.T. Jones, T. Schäfer, J. Appl. Math. **69**, 690 (2008)
19. Y. Ito, T. Tamo, T. Numai, Opt. Commun. **282**, 3989 (2009)
20. G.P. Agrawal, *Ligthwave Technology: Components and Devices* (Wiley-Interscience, New York, 2005)
21. J.M.C. Boggio, H.L. Fragnito, J. Opt. Soc. Am. B **24**, 2046 (2007)
22. J. Hansryd, P.A. Andrekson, M. Westlund, J. Lie, P.-O. Hedekvist, IEEE J. Quantum Electron. **8**, 506 (2002)
23. J. Fatome, S. Pitois, C. Fortier, B. Kibler, C. Finot, G. Millot, Opt. Commun. **283**, 2425 (2010)
24. S.P. Singh, N. Singh, Prog. Electromagn. Res. **73**, 249 (2007)
25. A. Singh, A.K. Sharma, T.S. Kamal, Optik **119**, 788 (2008)
26. A. Singh, A.K. Sharma, T.S. Kamal, IEEE Int. J. Comput. Appl. Technol. **34**, 165 (2009)
27. S.I. Fewo, T.C. Kofane, Opt. Commun. **281**, 2893 (2008)
28. V.B. Matveev, M.A. Salle, *Darboux Transformations and Solitons, Series in Nonlinear Dynamics* (Springer Verlag, Berlin, 1991)
29. N. Akhmediev, A. Ankiewicz, *Solitons. Nonlinear Pulses and Beams* (Chapman and Hall, London, 1997)
30. Y.S. Kivshar, G.P. Agrawal, *Optical Solitons: From Fibers to Photonic Crystals* (Academic Press, San Diego, 2003)

Journal of Modern Optics
Publication details, including instructions for authors and subscription information:
http://www.tandfonline.com/loi/tmop20

# Chirped self-healing Airy pulses compression in silicon waveguides under fourth-order dispersion

Lucien Mandeng Mandeng [a] & Clément Tchawoua [a]
[a] Laboratory of Mechanics, Department of Physics, Faculty of Science, University of Yaounde I, P.O. Box 812, Yaounde, Cameroon
Version of record first published: 28 Mar 2013.

To cite this article: Lucien Mandeng Mandeng & Clément Tchawoua (2013): Chirped self-healing Airy pulses compression in silicon waveguides under fourth-order dispersion, Journal of Modern Optics, DOI:10.1080/09500340.2013.777480

To link to this article: http://dx.doi.org/10.1080/09500340.2013.777480

*Journal of Modern Optics*, 2013
http://dx.doi.org/10.1080/09500340.2013.777480

Taylor & Francis
Taylor & Francis Group

# Chirped self-healing Airy pulses compression in silicon waveguides under fourth-order dispersion

Lucien Mandeng Mandeng and Clément Tchawoua*

*Laboratory of Mechanics, Department of Physics, Faculty of Science, University of Yaounde I, P.O. Box 812, Yaounde, Cameroon*

(*Received 15 November 2012; final version received 11 February 2013*)

We present the compression of Airy pulses in silicon-on-insulator (SOI) waveguides under the fourth-order dispersion (FOD) using the variational approach that involves Rayleigh's dissipation function (RDF). All the pulse characteristics are under the influence of the two-photon and the frequency-carrier absorptions. In a quasi-linear approximation, the pulse compression conditions induced by the interaction of the group-velocity dispersion (GVD), the chirp and the FOD are derived. In the nonlinear case, the self-phase modulation (SPM), the two-photon absorption (TPA) and the free-carrier absorption (FCA) reduce the length of compression in a propagation regime of normal GVD, positive chirp and a negative value of FOD. The TPA reduces the maximal power reached than the SPM while the FCA rather increases its value. These results are confirmed in the general case where they all interact with the linear dispersion terms of the SOI waveguide.

**Keywords:** pulse compression; chirp; fourth-order dispersion; temporal Airy pulse; variational approach; Rayleigh dissipation function



## 1. Introduction

The introduction in nonlinear optics of a new family of input optical profile, namely the Airy pulses, has recently attracted more attention [1–8]. Some phenomena around this profile have been investigated such as supercontinuum generation (SCG) which has revealed some interesting features confirming the particular place that the Airy pulses are taking in the pulse shaping approach [9]. The interest in Airy pulses stems from their special properties of self-healing, dispersion resistance and acceleration on propagation of their dominant intensity peaks [1–9].

Pulse compression is a famous method to obtain short pulses on scales that are more and more reduced with a very large spectral bandwidth (useful in data transmission and others applications) [10,11]. It consists of obtaining, from the propagation of a wider input pump, a smaller one after its propagation within the waveguide over a distance called the length of compression. Nowadays, this mechanism is classified as two types: linear and nonlinear compression. In the linear case, the source chirp must be opposite to the GVD: $\beta_2 C < 0$ [11,12]. Furthermore, with an analysis based on the Marcuse formalism Fourier transform method [13] and the Gaussian profile, Capmany et al. [14] showed that the linear compression could be obtained with the interaction of dispersion terms having the same parity as: $\beta_k \beta_{k+2} < 0$, $k \geq 2$, $k$ being an integer. For example, the GVD having an opposite sign with the FOD may lead to the compression of the pump. In the nonlinear case, the compression is obtained with the famous solitonic properties through the balance between the positive SPM and the anomalous dispersive regime [11,12,15–17]. The higher-order soliton (HOS) splitting yields to the periodic compression with the well-known soliton period $(\pi/2)L_{\mathrm{GVD}}$, where the parameter $L_{\mathrm{GVD}}$ is the GVD length [12].

Beyond the Marcuse formalism/Fourier transform used in the linear approximation on a temporal input profile, there are also the semi-analytical methods, such as the moment method [12], the classical variational approach [18–28], the collective variables approach [29–32], the self-similar analysis [33–35] (on self-similar solitons, the so-called similaritons), etc. More recently, Roy and Bhadra [36] showed a modified variational approach (MVA) which involves the RDF to model an optical waveguide under nonlinear absorption effects such as TPA and FCA. The RDF is incorporated in order to take account of the dissipative part, with an analogy to the non-conservative frictional problem in classical mechanics [36]. The analysis based on this MVA has been found to describe successfully the propagation of ultrashort optical pulses within SOI waveguides [37].

On the other hand, the interest aroused by the SOI waveguides is due to their advantageous properties in the mid-infrared spectral region, useful for current photonics devices applications [37–40], even in the SCG process [41,42].

A review of the literature shows that only the common symmetric and compact profiles, such as the sech-type pulse,

*Corresponding author. Email: ctchawa@yahoo.fr

Gaussian pulse (or super-Gaussian pulse) or raised-cosine ansätze pulse, are used in general for the compression mechanism analysis in optical waveguides [11–14]. Recently in a SOI waveguide, the sech-type profile has been studied [37]. The effect of TPA has been investigated on these symmetric profiles [36,37,43].

However, the problem of compression of Airy pulses in the SOI waveguide, still being opened to the best of our knowledge, is therefore investigated in this paper. Furthermore, using the MVA analysis of chirped femtosecond Airy pulses in SOI waveguides, we investigate the compression mechanism both in the linear and the nonlinear cases. The effects of the FOD and the nonlinear parameters are highlighted. The paper is designed as follows: Section 2 presents the theoretical analysis while in Section 3, we show the linear compression induced by the FOD. Section 4 presents the influence of the nonlinear parameters on the compression mechanism induced by the FOD and a conclusion is presented in the last section.

## 2. The model and the growth equations

The propagation of an optical signal inside a SOI waveguide under the FOD effect can be modeled by the lossy nonlinear Schrödinger equation (NLS) including the TPA and the FCA effects as:

$$\mathrm{i}\frac{\partial u}{\partial z} - \frac{\beta_2}{2}\frac{\partial^2 u}{\partial t^2} + \frac{\beta_4}{24}\frac{\partial^4 u}{\partial t^4} + \gamma|u|^2 u = -\mathrm{i}\alpha u - \mathrm{i}\Gamma|u|^2 u - \mathrm{i}\sigma N_c(t)u, \tag{1}$$

where $u$, $\beta_2$, $\beta_4$, $\gamma$, $\alpha$, $\Gamma$, $\sigma$ and $N_c(t)$ represent the slowly varying amplitude of the electrical field, the GVD coefficient, the FOD parameter, the cubic Kerr nonlinearity coefficient, the linear losses, the TPA coefficient, the FCA coefficient and the free-carrier density (FCD), respectively [37]. We have neglected the effect of the third-order dispersion (TOD) $\beta_3$ because it is well-known today that it introduces a relatively small temporal shift of the pulse center which is ignored here [12]. For instance, in classical nonlinear silica glass fibers, near the zero-dispersion point, one should include the effect of the TOD [12,17]. One should also note that some fibers, so-called dispersion-flattened fibers, admit rather a zero-dispersion point for the TOD, so that the whole dispersion is defined only by the GVD and the FOD which is added for ultra-short pulses [12,17]. More generally, it has been shown by Capmany et al. with the Gaussian pulse [14] that the odd order dispersion terms ($\beta_3$, $\beta_5$, $\beta_7$, etc.) introduce some oscillating tails in one side of the central part of the pulse temporal profile, in addition to the asymmetric displacement of the pulse center. Furthermore, Capmany et al. showed that the source chirp of the pulse interacts only with the even dispersion terms. This interesting feature was highlighted on the pulse compression conditions mentioned earlier in the introduction. All of these physical assumptions, lead to assume for the compression mechanism analysis, that the interaction between the GVD, the FOD and the chirp are only as described by Equation (1). The FCD is given by the following equation [37,44]:

$$Nc(z,t) = \frac{\Gamma}{2h\nu_0 A_{\mathrm{eff}}}\int_{-\infty}^{t}\left(|u(z,t')|^4\right)\mathrm{d}t'. \tag{2}$$

The relation of Equation (2) above is approximated from the one given in [37] for the short optical pulses, because we have neglected the parameter $\tau_{\mathrm{C}}$ (the carrier lifetime). It is assumed that $h$, $\nu_0$ and $A_{\mathrm{eff}}$ are the Planck constant, the pump frequency and the SOI waveguide effective core section size. The parameter $t_{\mathrm{p}}$ represents the pulse width. The Lagrangian density and the RDF of the MVA are defined as [36,37]:

$$L_d = \frac{\mathrm{i}}{2}\left(u^*\frac{\partial u}{\partial z} - u\frac{\partial u^*}{\partial z}\right) - \sum_{k=1}^{2}\frac{(-1)^k\beta_{2k}}{(2k)!}\frac{\partial^{(2k-1)}u}{\partial t^{(2k-1)}}\frac{\partial u^*}{\partial t} + \frac{\gamma}{2}|u|^4, \tag{3}$$

and

$$R_d = \mathrm{i}\left[|u|^2\Gamma + \frac{1}{2}\left(\alpha + \sigma N_c(z,t)\right)\right]\left(u^*\frac{\partial u}{\partial z} - u\frac{\partial u^*}{\partial z}\right). \tag{4}$$

One should note that the FCD intervenes within the RDF, so it may be calculated using Equation (2) before its introduction into Equation (4). The chirped input Airy profile can be taken as [8]:

$$u = u_{\mathrm{p}}A\mathrm{i}\left(\frac{t}{t_{\mathrm{p}}}\right)\exp\left(a\frac{t}{t_{\mathrm{p}}}\right)\exp\left(-\mathrm{i}\frac{C_{\mathrm{p}}}{2}\left(\frac{t}{t_{\mathrm{p}}}\right)^2 + \mathrm{i}\phi_{\mathrm{p}}\right), \tag{5}$$

with $u_{\mathrm{p}}$, $C_{\mathrm{p}}$ and $\phi_{\mathrm{p}}$ being the Airy pulse characteristics namely the amplitude, the chirp and the phase, respectively. The parameter $a$ is the truncation coefficient equal to 0.05 in this work. Its presence allows one to ensure that for a positive quadratic dispersion coefficient, one will obtain a positive dispersion [8]. One should note that the Airy pulses are not known to be a solution of the propagation equation within the SOI waveguides. In a classical nonlinear silica optical fiber at the zero-dispersion point, a chirped Gaussian pulse transforms to an Airy pulse which propagates normally into this form inside the considered media [12,45].

The MVA defines the Lagrangian and the RDF functions from their densities described in Equations (3) and (4) respectively by the following relations [12,17,36,37]:

$$L = \int_{-\infty}^{+\infty} L_d(t')\,\mathrm{d}t', \qquad R = \int_{-\infty}^{+\infty} R_d(t')\,\mathrm{d}t'. \tag{6}$$

The determination of the Lagrangian function leads to:

$$\begin{aligned} L &= -u_{\mathrm{p}}^2 t_{\mathrm{p}}\left[55.4573\left(\frac{C_{\mathrm{p}}}{t_{\mathrm{p}}}\frac{\partial t_{\mathrm{p}}}{\partial z}-0.5\frac{\partial C_{\mathrm{p}}}{\partial z}\right)+\frac{9}{11}\frac{\partial \phi_{\mathrm{p}}}{\partial z}\right] \\ &\quad+\frac{u_{\mathrm{p}}^2\beta_2}{2t_{\mathrm{p}}}\left(\frac{52\pi}{31}+55.4573C_{\mathrm{p}}^2\right) \\ &\quad+\frac{u_{\mathrm{p}}^2\beta_4}{24t_{\mathrm{p}}^3}\left(78.1397+10034C_{\mathrm{p}}^2+51918C_{\mathrm{p}}^4\right) \\ &\quad+\frac{3}{28}\gamma u_{\mathrm{p}}^4 t_{\mathrm{p}}. \end{aligned} \tag{7}$$

The reduced form of the RDF function is obtained with an appropriate approximation of the FCD (see Equation (2)) which is evaluated numerically for the apodized (truncated) Airy pulse and inserted in the following relation:

$$\begin{aligned} R &= u_{\mathrm{p}}^2 t_{\mathrm{p}}\left[\left(\frac{C_{\mathrm{p}}}{t_{\mathrm{p}}}\frac{\partial t_{\mathrm{p}}}{\partial z}-0.5\frac{\partial C_{\mathrm{p}}}{\partial z}\right)\right. \\ &\quad\times\left[u_{\mathrm{p}}^2\left(\frac{12}{35}\Gamma-\frac{3u_{\mathrm{p}}^2 t_{\mathrm{p}}}{236}\kappa\right)-55.4573\alpha\right] \\ &\quad\left.-\frac{\partial \phi_{\mathrm{p}}}{\partial z}\left[u_{\mathrm{p}}^2\left(\frac{3}{14}\Gamma+\frac{\pi u_{\mathrm{p}}^2 t_{\mathrm{p}}}{122}\kappa\right)+\frac{9}{11}\alpha\right]\right], \end{aligned} \tag{8}$$

where $\kappa = \sigma\beta_{\mathrm{TPA}}/h\nu_0 A_{\mathrm{eff}}^2$ is a constant related to the FCD and the FCA. The parameter $\beta_{\mathrm{TPA}} = 2\Gamma A_{\mathrm{eff}}$ is the usual TPA parameter [37]. The determination of the growth equations in the MVA may be done by setting:

$$\frac{\partial}{\partial t}\left(\frac{\partial L}{\partial q_z}\right)-\frac{\partial L}{\partial q}+\frac{\partial L}{\partial q_z}=0, \tag{9}$$

where the parameter $q$ is a characteristic of the pulse and $q_z$ its derivative following the parameter of propagation $z$ [12,18–21,36,37]. Therefore, we determine the growth equations as follows:

$$\begin{aligned} \frac{\partial u_{\mathrm{p}}}{\partial z} &= -\frac{u_{\mathrm{p}}}{2}\left\{\frac{C_{\mathrm{p}}}{t_{\mathrm{p}}^2}\left[\beta_2+\frac{(45.233+468.1C_{\mathrm{p}}^2)}{3t_{\mathrm{p}}^2}\beta_4\right]\right. \\ &\quad\left.+2u_{\mathrm{p}}^2\left(\frac{1}{5}\Gamma+\frac{2u_{\mathrm{p}}^2 t_{\mathrm{p}}}{85}\kappa\right)+\alpha\right\}, \\ \frac{\partial t_{\mathrm{p}}}{\partial z} &= \frac{C_{\mathrm{p}}}{t_{\mathrm{p}}}\left[\beta_2+\frac{(45.233+468.1C_{\mathrm{p}}^2)}{3t_{\mathrm{p}}^2}\beta_4\right] \\ &\quad+u_{\mathrm{p}}^2 t_{\mathrm{p}}\left(\ln\left(\frac{8}{7}\right)\Gamma+\frac{u_{\mathrm{p}}^2 t_{\mathrm{p}}}{64}\kappa\right), \end{aligned}$$

$$\begin{aligned} \frac{\partial C_{\mathrm{p}}}{\partial z} &= \frac{1}{t_{\mathrm{p}}^2}\left[\beta_2\left(\frac{\pi}{\exp(\frac{7}{2})}+C_{\mathrm{p}}^2\right)\right. \\ &\quad\left.+\left(\frac{31}{22}+180.932C_{\mathrm{p}}^2+936.2C_{\mathrm{p}}^4\right)\frac{\beta_4}{6t_{\mathrm{p}}^2}\right] \\ &\quad+u_{\mathrm{p}}^2\left(\frac{1}{500}\gamma+C_{\mathrm{p}}\left(\frac{3}{11}\Gamma+\frac{u_{\mathrm{p}}^2 t_{\mathrm{p}}}{32}\kappa\right)\right), \\ \frac{\partial \phi_{\mathrm{p}}}{\partial z} &= \frac{1}{t_{\mathrm{p}}^2}\left[\frac{572\pi}{279}\beta_2\right. \\ &\quad\left.-\left(1010.04+9043.14C_{\mathrm{p}}^2-\frac{95183}{12}C_{\mathrm{p}}^4\right)\frac{\beta_4}{t_{\mathrm{p}}^2}\right] \\ &\quad+u_{\mathrm{p}}^2\left(\frac{55}{168}\gamma+C_{\mathrm{p}}\left(\frac{22}{105}\Gamma-\frac{11u_{\mathrm{p}}^2 t_{\mathrm{p}}}{1416}\kappa\right)\right). \end{aligned} \tag{10}$$

As can be seen in Equation (10) beyond the dispersive effects, all the characteristics of the Airy pulse are affected by both the TPA and the FCA. The specificity is related to the losses and the SPM. However, the FOD impact appearing in all growth equations above suggests a non-negligible role in the linear compression induced by chirp which is investigated in the next section.

## 3. Linear temporal compression induced by FOD

In this section all the nonlinear effects parameters are taken equal to zero: $\gamma = 0$, $\Gamma = 0$, $\sigma = 0$ and $\kappa = 0$. For this specific case, we assume that the terms $(45.233 + 468.1C_{\mathrm{p}}^2)/3t_{\mathrm{p}}^2$, $\pi\exp(-7/2) + C_{\mathrm{p}}^2$ and $(31/22) + 180.932C_{\mathrm{p}}^2 + 936.2C_{\mathrm{p}}^4$ are constant and equal to their initial values, so that we get a linearly varying chirp for the pulse. This hypothesis is set similarly to the constant spectral width of the Gaussian profile as done in [12]. The analytical approximated relation of the pulse compression factor is given by:

$$F_{\mathrm{C}} = \left[1+2\frac{\Delta_1}{t_{\mathrm{p}}^2(0)}\left(C_{\mathrm{p}}(0)+\frac{\Delta_0}{2}z\right)z\right]^{1/2}, \tag{11}$$

where $F_{\mathrm{C}} = t_{\mathrm{p}}(z)/t_{\mathrm{p}}(0)$. We define the parameters $\Delta_0$ and $\Delta_1$, respectively, as follows:

$$\begin{aligned} \Delta_0 &= \frac{s_2(\pi\exp(-7/2)+C_{\mathrm{p}}^2(0))}{L_{\mathrm{GVD}}} \\ &\quad+\frac{s_4\left(\frac{31}{22}+180.932C_{\mathrm{p}}^2(0)+936.2C_{\mathrm{p}}^4(0)\right)}{6L_{\mathrm{FOD}}}, \\ \Delta_1 &= t_{\mathrm{p}}^2(0)\left[\frac{s_2}{L_{\mathrm{GVD}}}+\frac{(45.233+468.1C_{\mathrm{p}}^2(0))s_4}{3L_{\mathrm{FOD}}}\right], \end{aligned} \tag{12}$$

where $s_2$ and $s_4$ are the signs of the GVD and the FOD, respectively. The length parameter associated with the FOD is defined as $L_{\mathrm{FOD}} = t_0^4/|\beta_4|$ while the GVD length is

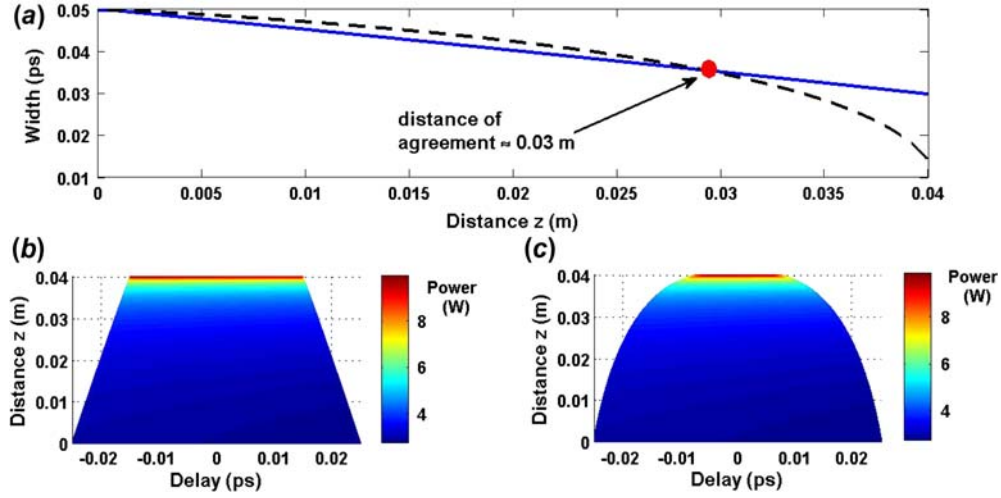


Figure 1. (*a*) Solid line for the analytical result of the width and dashed line for the numerical result versus $z$. (*b*) Contour plot of the Airy pulse propagation for the analytical result and (*c*) contour plot of the Airy pulse propagation for the numerical result. The peak power $P_0 = 4.76\,\mathrm{W}$, $\beta_2 = 0.56\,\mathrm{ps}^2\,\mathrm{m}^{-1}$, $C_0 = 0.8$, $\alpha = 5.06\,\mathrm{m}^{-1}$, $\beta_4 = -1.2843 \times 10^{-5}\,\mathrm{ps}^4\,\mathrm{m}^{-1}$ and SOI waveguide length $L = 0.04\,\mathrm{m}$. (The color version of this figure is included in the online version of the journal.)



commonly equal to $t_0^2/|\beta_2|$. It comes about that, the linear compression conditions are obtained easily by setting the compression factor inferior to 1. This implies that (note that whatever the conditions $z > 0$, $L_{\mathrm{GVD}} > 0$ and $L_{\mathrm{FOD}} > 0$):

$$-0.5 < \left[\frac{s_2}{L_{\mathrm{GVD}}} + \frac{(45.233 + 468.1C_{\mathrm{p}}^2(0))s_4}{3L_{\mathrm{FOD}}}\right] \times \left(C_{\mathrm{p}}(0) + \frac{\Delta_0}{2}\,z\right) z < 0. \tag{13}$$

So, for the compression of the self-healing Airy pulse (SHAP) to occur inside the medium under the conditions specified earlier, one must have:

$$\begin{aligned} &\frac{s_2}{L_{\mathrm{GVD}}} + \frac{(45.233 + 468.1C_{\mathrm{p}}^2(0))s_4}{3L_{\mathrm{FOD}}} < 0 \\ &\qquad \text{and} \quad \left(C_{\mathrm{p}}(0) + \frac{\Delta_0}{2}z\right) z > 0, \\ &\frac{s_2}{L_{\mathrm{GVD}}} + \frac{(45.233 + 468.1C_{\mathrm{p}}^2(0))s_4}{3L_{\mathrm{FOD}}} > 0 \\ &\qquad \text{and} \quad \left(C_{\mathrm{p}}(0) + \frac{\Delta_0}{2}z\right) z < 0. \end{aligned} \tag{14}$$

The resulting conditions are defined as:

$$\begin{aligned} &C_0 > 0,\ \beta_2, \beta_4 < 0, \\ &L_{\mathrm{FOD}} < V_1 L_{\mathrm{GVD}},\ C_{\mathrm{lim}} < C_0\ \beta_2 > 0,\ \beta_4 < 0, \\ &L_{\mathrm{FOD}} < V_2 L_{\mathrm{GVD}},\ 0 < C_0 < C_{\mathrm{lim}}\ \beta_2 > 0,\ \beta_4 < 0, \\ &L_{\mathrm{FOD}} > V_2 L_{\mathrm{GVD}},\ C_{\mathrm{lim}} < C_0\ \beta_2 < 0,\ \beta_4 > 0, \\ &L_{\mathrm{FOD}} > V_1 L_{\mathrm{GVD}},\ 0 < C_0 < C_{\mathrm{lim}}\ \beta_2 < 0,\ \beta_4 > 0, \end{aligned} \tag{15}$$

where

$$\begin{aligned} V_1 &= \frac{45.233 + 468.1C_0^2}{3}, \\ V_2 &= \frac{\frac{31}{22} + 180.932C_0^2 + 936.2C_0^4}{6(\pi \exp(\frac{-7}{2}) + C_0^2)}, \\ C_{\mathrm{lim}} &= 2.084606293. \end{aligned} \tag{16}$$

We obtain the conditions of Equation (15) and the definitions of Equation (16) by making some basic discussions about the signs $s_2$ and $s_4$. The parameters $C_0 \equiv C_{\mathrm{p}}(0)$ and $t_0 \equiv t_{\mathrm{p}}(0)$ are the initial values of the chirp and the width, respectively.

The values of the parameters used in numerical simulations are defined as [37]: the waveguide length $L = 4$–$5\,\mathrm{cm}$, the linear losses $\alpha = 5.06\,\mathrm{m}^{-1}$, the initial peak power $P_0 = 4.76\,\mathrm{W}$, the TPA coefficient $\Gamma = 6.5\,\mathrm{W}^{-1}\,\mathrm{m}^{-1}$, the GVD $\beta_2 = 0.56\,\mathrm{ps}^2\,\mathrm{m}^{-1}$, the FOD $\beta_4 = -1.2843 \times 10^{-4}\,\mathrm{ps}^4\,\mathrm{m}^{-1}$, the FCD-FCA associated coefficient $\kappa = 5\,\mathrm{W}^{-4}\,\mathrm{ps}^{-1}\,\mathrm{m}^{-1}$, the initial chirp $C_0 = 0.8$, the SPM coefficient $\gamma = 47\,\mathrm{W}^{-1}\,\mathrm{m}^{-1}$, the pulse width $t_0 = 50\,\mathrm{fs}$ and the wavelength $\lambda_0 = 1550\,\mathrm{nm}$, respectively.

We represent in Figure 1 the pulse compression under the third condition of Equation (15). The FOD parameter is obtained by setting $L_{\mathrm{FOD}} = 0.96b$, where $b = V_2 L_{\mathrm{GVD}}$. This may be obtained from a realistic value of the FOD $\beta_4$ and for the numerical simulations, we show how the obtained compression conditions work. It is convenient to choose an approximate realistic value of the FOD which verifies the third compression condition of Equation (15) for example. We have chosen to draw the analytical result (see the solid line in Figure 1(*a*) and (*b*)) with the numerical result obtained with a fourth-order Runge–Kutta integration

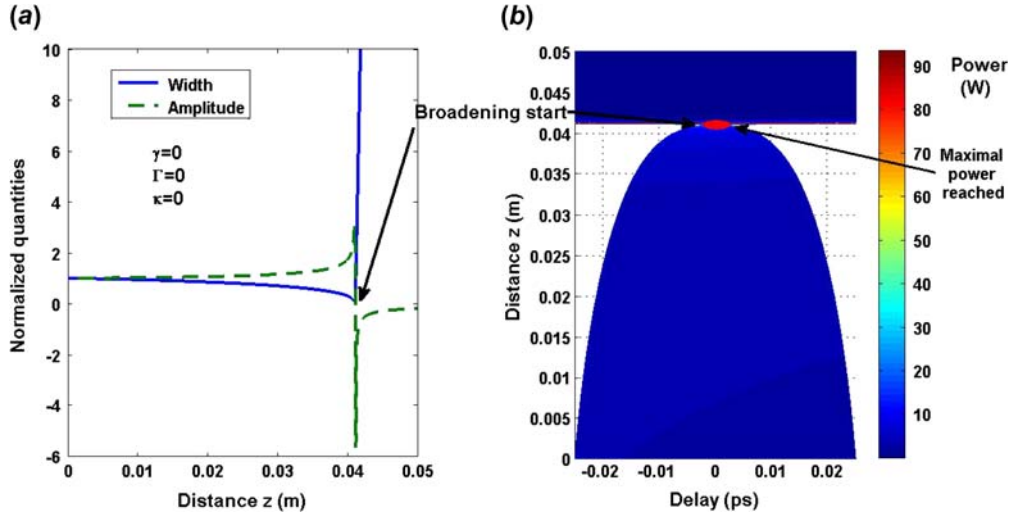


Figure 2. ($a$) Plot of the normalized width (solid line) and the normalized amplitude (dashed line) versus $z$. ($b$) Contour plot of the Airy pulse propagation. The peak power $P_0 = 4.76\,\mathrm{W}$, $\beta_2 = 0.56\,\mathrm{ps}^2\,\mathrm{m}^{-1}$, $C_0 = 0.8$, $\alpha = 5.06\,\mathrm{m}^{-1}$, $\beta_4 = -1.2843 \times 10^{-5}\,\mathrm{ps}^4\,\mathrm{m}^{-1}$, $\gamma = 0$, $\Gamma = 0$ and $\kappa = 0$, SOI waveguide length $L = 0.05\,\mathrm{m}$. (The color version of this figure is included in the online version of the journal.)



scheme (see the dashed line in Figure 1($a$) and ($c$)). The analytical result here is based on Equation (11) and the numerical result comes from the direct integration of the growth equation of the width in Equation (10). Considering the obtained pictures, it happens that the quasi-spectral assumption that governs the analytical result can approximately satisfy the pulse compression in the linear case because the difference between the two results is not important enough for the small distances of propagation. As stated at the beginning of the section, the assumption of a spectral bandwidth approximately constant during the propagation inside the linear medium leads to admit the compression factor given in Equation (11) only for a short distance. It is certain that Equations (10) and (11) will diverge for propagation distances. As shown in Figure 1, the critical distance of agreement that emerges from the simulations performed, is about 3 cm. The MVA being validated to be a good mean to study short pulse propagation within SOI waveguides [37], translates in Figure 1 the linear approximation of the waveguide dynamics.

Beyond this, notice that the main feature observed here is the compression which is obtained with $\beta_2 C_0 > 0$ and $\beta_2\beta_4 < 0$. With the other conditions defined in Equation (15), these results are entirely in agreement with those previously discussed in [14], while the fact that the chirp is similarly signed to the GVD, contrasts with the basic admitted theory of linear compression induced by chirp with grating pairs [11]. Figure 1($b$) is the contour plot of the Airy pulse for the analytical result of Equation (11) and Figure 1($c$) is the contour plot of the Airy pulse for the numerical simulation of Equation (10). These figures correspond to the pulse propagation within the SOI under the conditions defined in the linear approximation and respecting the third compression condition of Equation (15). For this figure and for the following, the scale bar is in the unit of power (W) and indicates the power reached in the compression process following the distance of propagation.

Now it is convenient to analyze what happens when the nonlinear effects are considered.

## 4. Nonlinear compression of SHAP in SOI waveguide under FOD

Let us start first with the linear model that we integrate over a SOI waveguide length of about 5 cm, thus we obtain Figure 2. In Figure 2, the parameters $\gamma$, $\Gamma$ and $\kappa$ ($\sigma$) are still zero. It is observed that the pulse compression really extends to a distance of propagation of about 0.0409 m, after which comes the pulse broadening. At this distance, obviously one obtains the maximal pulse power and compression before the broadening.

The process of the temporal compression has a particularity in the sense that it is accompanied by an amplification of the pulse [11,12,43]. The power/amplitude of the pulse amplifies during the compression process. The maximal power reached (MPR) in the compression process occurs at a distance as seen in Figure 2 and it can be referenced in the scale bar to see the corresponding value. The broadening of the Airy pulse occurs just beyond this point and is dramatically extreme as seen on the figure.

When the cubic Kerr nonlinear effect is taken into account, Figure 3 is obtained. We can see in this picture a similar behavior as in Figure 2, it means a pulse compression over a distance of propagation followed by the pulse broadening. However, the change brought by the cubic Kerr nonlinearity indicates a clean reduction of the length of compression before the broadening. Indeed the pulse

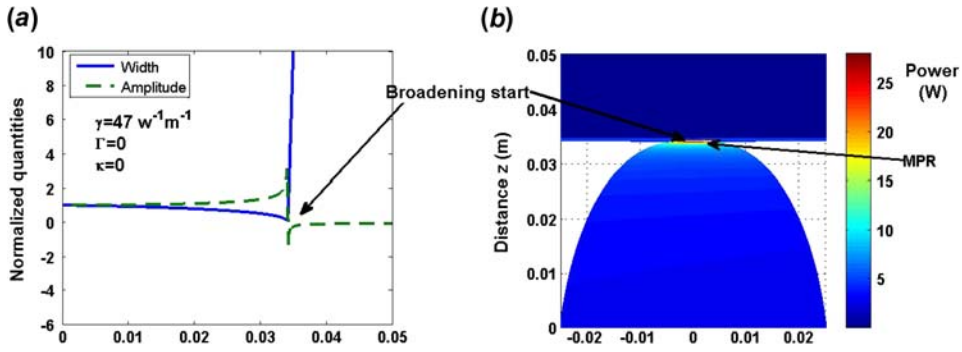


Figure 3. (*a*) Plot of the normalized width (solid line) and the normalized amplitude (dashed line) versus $z$. (*b*) Contour plot of the Airy pulse propagation. The peak power $P_0 = 4.76\,\mathrm{W}$, $\beta_2 = 0.56\,\mathrm{ps}^2\,\mathrm{m}^{-1}$, $C_0 = 0.8$, $\alpha = 5.06\,\mathrm{m}^{-1}$, $\beta_4 = -1.2843 \times 10^{-5}\,\mathrm{ps}^4\,\mathrm{m}^{-1}$, $\gamma = 47\,\mathrm{W}^{-1}\,\mathrm{m}^{-1}$, $\Gamma = 0$ and $\kappa = 0$, SOI waveguide length $L = 0.05\,\mathrm{m}$. (The color version of this figure is included in the online version of the journal.)

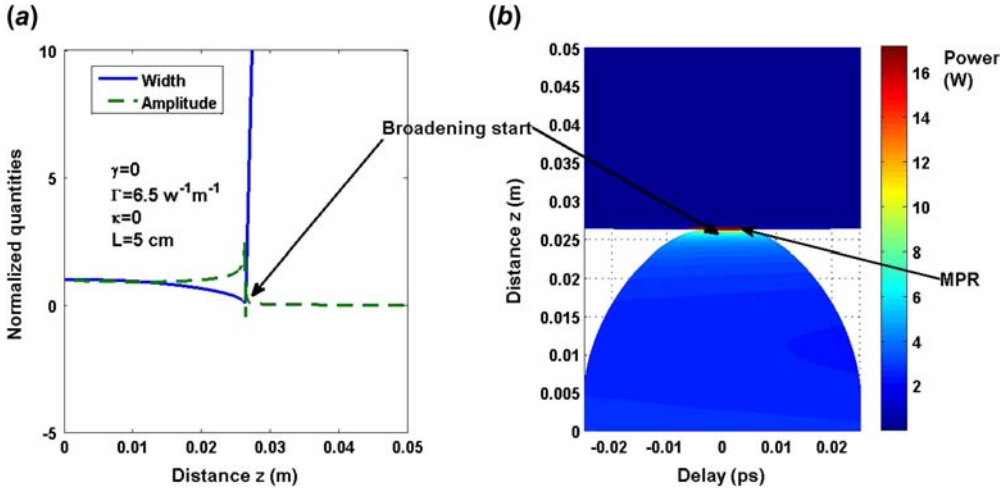


Figure 4. (*a*) Plot of the normalized width (solid line) and the normalized amplitude (dashed line) versus $z$. (*b*) Contour plot of the Airy pulse propagation. The peak power $P_0 = 4.76\,\mathrm{W}$, $\beta_2 = 0.56\,\mathrm{ps}^2\,\mathrm{m}^{-1}$, $C_0 = 0.8$, $\alpha = 5.06\,\mathrm{m}^{-1}$, $\beta_4 = -1.2843 \times 10^{-5}\,\mathrm{ps}^4\,\mathrm{m}^{-1}$, $\gamma = 0$, $\Gamma = 6.5\,\mathrm{W}^{-1}\,\mathrm{m}^{-1}$ and $\kappa = 0$, SOI waveguide length $L = 0.05\,\mathrm{m}$. (The color version of this figure is included in the online version of the journal.)



compression extends in this case only over 0.0340 m. Another point that must be raised, is the maximal pulse power reached (in the compression mechanism) which is also reduced due to the effect of $\gamma$ in combination with the negative value of the FOD. Contrarily to the previous case depicted in Figure 2 ($P_{\max} \approx 90\,\mathrm{W}$), the maximal pulse power $P_{\max}$ reached here is slightly beyond 25 W only.

The TPA has been extensively studied by others [10,36–41,43,44]. It was first reported experimentally by Kaiser and Garrett [46]. The multiphoton absorption phenomenon can lead to laser damage of optical materials and be used to write permanent refractive index structures into the interior of optical materials [10]. Therefore, the multiphoton absorption is well known to be a nonlinear loss phenomenon that can reduce the efficiency of nonlinear optical devices such as optical switches. Its consideration, inside the dynamics studied in this section as the single nonlinear process, produces an important reduction of the length of compression comparatively to the cases above. This length is now about 0.0263 m with our data as seen in Figure 4. Even the MPR is reduced by about 16 W.

The FCA effect on the pulse compression mechanism of femtosecond Airy pulses in SOI waveguide presented in Figure 5 is also described as a reduction of the length of compression by about 0.0383 m. However, the contrast with all the previous reductions observed with the cubic Kerr nonlinearity and the TPA, concerns the maximal pulse power which is rather increased comparatively to the one of Figure 2 which is about 100 W. Another point to be noticed is the amplitude depression which is similar to the one of Figure 2. It seems likely the FCA does not affect this depression contrarily to the TPA and the cubic Kerr nonlinearity.

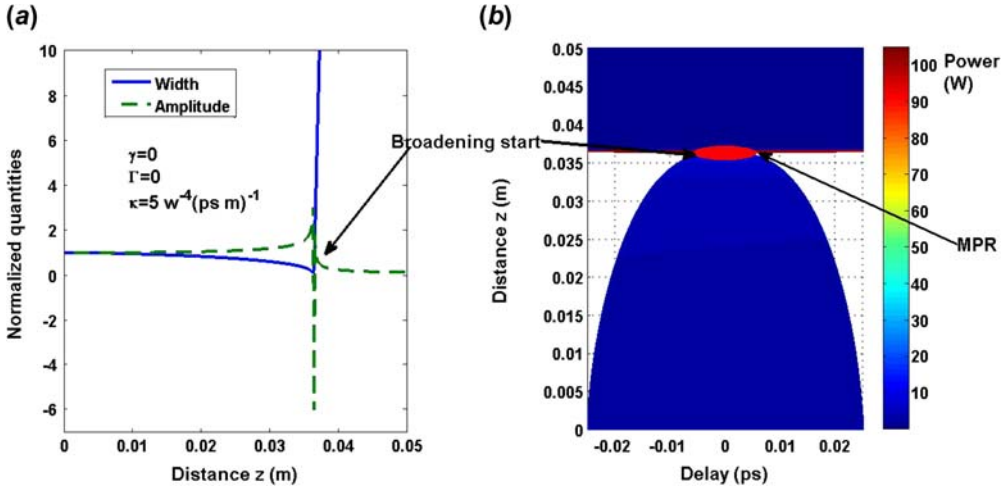


Figure 5. (*a*) Plot of the normalized width (solid line) and the normalized amplitude (dashed line) versus $z$. (*b*) Contour plot of the Airy pulse propagation. The peak power $P_0 = 4.76\,\mathrm{W}$, $\beta_2 = 0.56\,\mathrm{ps}^2\,\mathrm{m}^{-1}$, $C_0 = 0.8$, $\alpha = 5.06\,\mathrm{m}^{-1}$, $\beta_4 = -1.2843 \times 10^{-5}\,\mathrm{ps}^4\,\mathrm{m}^{-1}$, $\gamma = 0$, $\Gamma = 0$ and $\kappa = 5\,\mathrm{W}^{-4}(\mathrm{ps\,m})^{-1}$, SOI waveguide length $L = 0.05\,\mathrm{m}$. (The color version of this figure is included in the online version of the journal.)



One should notice that physically there is a dependency of free carriers to the TPA such that normally the FCA might not be investigated without the TPA according to the relation of $\beta_{\mathrm{TPA}}$ given in Section 2. However, we stand on an approximated case where $\Gamma \ll \sigma N c(z,t)$ such that we neglect the TPA behind the FCA-FCD. Even from a pure mathematical view, the purpose is to analyze the impact of the FCA on the chirped apodized SHAP in the SOI waveguide. This approach has the merit of underlining the contribution of each nonlinear parameter in the whole behaviour of the pulse when they are all considered. The same approach is performed for intensity dependent nonlinear parameters in [12] such as the SPM, the self-steepening and the intra-Raman scattering for classical silica glass fibers. Indeed, the study of the impact of each nonlinear parameter is conducted separately to the others according to the purpose defined at the beginning.

Considering the combination of all these nonlinear processes namely the cubic Kerr nonlinearity, the TPA and the FCA to the linear parameters namely the normal GVD, the losses, the negative FOD and the positive initial chirp, we obtain for the SHAPs the figure depicted in Figure 6. All these results are obtained with the interaction of the negative value of the FOD, the normal GVD and positive initial chirp under the limit value defined in Equation (16).

The length of compression reached is about 0.0241 m, slightly more smaller than that of Figure 4 for the single TPA effect. It seems like all the nonlinear processes cooperate to reduce the length of compression due to the combination of the negative FOD, the normal GVD and the positive chirp.Even the reduction of the MPR is observed but less dramatic than that of Figure 4.

According to the impact of each nonlinear parameter as presented in Figures 3–5, we suggest that they normally conduct to this length of compression reduction, but the stressing is imposed by the TPA effect because it is the single parameter which reduces more the length of compression. If we consider the effect of the cubic Kerr nonlinearity and the TPA on the MPR in the compression mechanism studied, we should normally obtain a reduction greater than that of Figure 4 16 W, however the result of about 18 W indicates that the buffering is made by the FCA because, as seen in Figure 5, the effect of the FCA on the MPR of the SHAP allows an increase of its value comparatively to the linear case. So, while the TPA and the cubic Kerr nonlinearity tends to decrease this value, the FCA influences this variation in the opposite direction.

The decoupling of the effects related to $\gamma$, $\Gamma$ and $\sigma$, to a first approximation, gives meaningfully a sense to the analysis. Since, in the realistic SOI waveguide dynamics which has its process of compression via SHAPs as drawn on Figure 6, the contribution of each parameter is underlined as additive effects that cooperate in the sense of SPM and TPA, and that compete in the sense of FCA. Sure enough, we notice that the TPA as a nonlinear loss rather acts on the chirped apodized SHAP in the same sense as the SPM surprisingly, while the FCA acts in the opposite sense. All these influences combined give an intermediary picture between those obtained with each parameter alone. Thus, the FCA plays a buffer role on the dramatic effects of the SPM and TPA induced SHAP pulse broadening in the presence of the FOD.

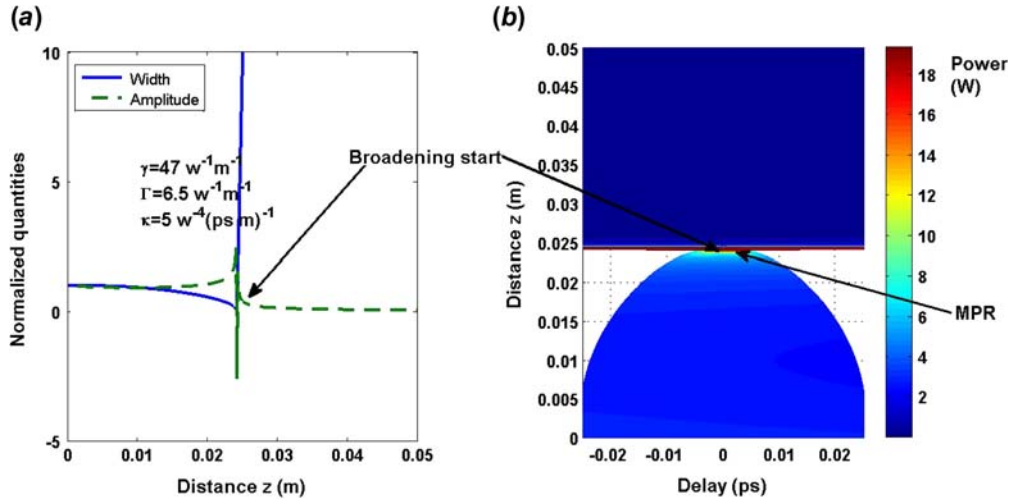


Figure 6. (*a*) Plot of the normalized width (solid line) and the normalized amplitude (dashed line) versus $z$. (*b*) Contour plot of the Airy pulse propagation. The peak power $P_0 = 4.76\,\mathrm{W}$, $\beta_2 = 0.56\,\mathrm{ps}^2\,\mathrm{m}^{-1}$, $C_0 = 0.8$, $\alpha = 5.06\,\mathrm{m}^{-1}$, $\beta_4 = -1.2843 \times 10^{-5}\,\mathrm{ps}^4\,\mathrm{m}^{-1}$, $\gamma = 47\,\mathrm{W}^{-1}\,\mathrm{m}^{-1}$, $\Gamma = 6.5\,\mathrm{W}^{-1}\,\mathrm{m}^{-1}$ and $\kappa = 5\,\mathrm{W}^{-4}(\mathrm{ps\,m})^{-1}$, SOI waveguide length $L = 0.05\,\mathrm{m}$. (The color version of this figure is included in the online version of the journal.)



## 5. Conclusion

In summary, in this paper we have presented the compression mechanism analysis of femtosecond chirped self-healing Airy pulses using the modified variational approach that involves Rayleigh's dissipation function in a SOI waveguide under fourth-order dispersion. The derivation of the growth equations shows that all the pulse characteristics are under the influence of the TPA and the FCA contrarily to the sech-type input profile analysis previously presented by Roy et al. [37]. In a quasi-linear approximation of the medium, the constant spectral width assumption leads to pulse compression conditions induced by the interaction of the GVD, the chirp and the FOD which are in good agreement with previous results obtained by Capmany et al. for the Gaussian input profile [14]. A comparison between the analytical relation of the compression factor and the numerical result shows good agreement for small distances of propagation. In the nonlinear case, it has been found that the nonlinear parameters, namely the cubic Kerr nonlinearity, the TPA and the FCA, reduce the length of compression in a SOI waveguide with normal GVD, positive chirp and a negative value of FOD. However, this reduction is more pronounced for the single TPA presence than for the one obtained with the cubic Kerr nonlinearity only, while for the FCA, it is smaller than the two first ones. We have also found that the TPA reduces the maximal power reached in the compression mechanism than the cubic Kerr nonlinearity, while for the FCA it increases its value comparatively to the linear case. Therefore, the FCA plays a buffer role on the dramatic effects of the SPM and TPA induced SHAP pulse broadening in the presence of the FOD. The combination of all these nonlinear parameters with the linear dispersion terms in a realistic SOI waveguide, confirms these results which allow one to characterize the specificity of the Airy input pulses comparatively to the symmetric and compact commonly used profiles.

## Acknowledgements

Lucien M. Mandeng acknowledges Prof. Timoléon Crépin Kofané, Dr Jean-Pascal Eloundou, Dr Serge Ibraid Fewo and Prof. Alidou Mohamadou for their support.

## References

[1] Siviloglou, G.A.; Christodoulides, D.N. *Opt. Lett.* **2007**, *32*, 979–981.
[2] Besieris, I.M.; Shaarawi, A.M. *Opt. Lett.* **2007**, *32*, 2447–2449.
[3] Siviloglou, G.A.; Broky, J.; Dogariu, A.; Christodoulides, D.N. *Phys. Rev. Lett.* **2007**, *99*, 213901.
[4] Saari, P. *Opt. Express* **2008**, *16*, 10303–10308.
[5] Broky, J.; Siviloglou, G.A.; Dogariu, A.; Christodoulides, D.N. *Opt. Express* **2008**, *18*, 12880–12891.
[6] Bekenstein, R.; Segev, M. *Opt. Express* **2011**, *19*, 23706–23715.
[7] Kaminer, I.; Lumer, Y.; Segev, M.; Christodoulides, D.N. *Opt. Express* **2011**, *19*, 23132–23139.
[8] Rudnick, A.; Marom, D.M. *Opt. Express* **2011**, *19*, 25570–25582.
[9] Ament, C.; Polynkin, P.; Moloney, J.V. *Phys. Rev. Lett.* **2011**, *107*, 243901.
[10] Boyd, R. *Nonlinear Optics*; Academic Press, San Diego, CA, 2008.
[11] Agrawal, G.P. *Applications of Nonlinear Fiber Optics*; Academic Press, San Diego, CA, 2008.
[12] Agrawal, G.P. *Nonlinear Fiber Optics*, 4th ed.; Academic Press, San Diego, CA, 2007.
[13] Marcuse, D. *Appl. Opt.* **1981**, *20*, 3573.

[14] Capmany, J.; Pastor, D.; Sales, S.; Muriel, M.A. *J. Opt. Soc. Am. B* **2003**, *20*, 2523.
[15] Matveev, V.B.; Salle, M.A. *Darboux Transformations and Solitons*; Springer Verlag, Berlin, 1991.
[16] Akhmediev, N.; Ankiewicz, A. *Solitons*; Nonlinear Pulses and Beams; Chapman and Hall, London, 1997.
[17] Kivshar, Y.S.; Agrawal, G.P. *Optical Solitons: From Fibers to Photonic Crystals*; Academic Press, San Diego, CA, 2003.
[18] Anderson, D. *Phys. Rev. A* **1983**, *27*, 3135–3145.
[19] Anderson, D. *IEEE Proc. Part J. Optoelectron.* **1985**, *132*, 122–125.
[20] Anderson, D.; Lisak, M. *Opt. Lett.* **1986**, *11*, 569–571.
[21] Anderson, D.; Lisak, M. *Phys. Rev. A* **1987**, *35*, 184–187.
[22] Karlsson, M.; Anderson, D.; Höök, A.; Lisak, M. *Phys. Scr.* **1994**, *50*, 265–270.
[23] Turitsyn, S.K.; Shapiro, E.G. *Opt. Fiber Technol.* **1998**, *4*, 151.
[24] Turitsyn, S.K.; Gabitov, I.; Laedke, E.W.; Mezentsev, V.K.; Musher, S.L.; Shapiro, E.G.; Schäfer, T.; Spatschek, K.H. *Opt. Commun.* **1998**, *151*, 117–135.
[25] Mahmood, M.F.; Brooks, S. *Int. J. Math. Math. Sci.* **2003**, *49*, 3143.
[26] Ramprasad, A.V.; Murugappan, M. *Acad. Open Internet J.* **2006**, *18*, 1311.
[27] Ndzana, F.; Mohamadou, A.; Kofané, T.C. *Opt. Commun.* **2007**, *275*, 421–428.
[28] Hakl, R.; Torres, P.J. *ZAMP* **2010**, doi:10.1007/s00033-010-0084-1.
[29] Dinda, P.T.; Moubissi, A.B.; Nakkeeran, K. *Phys. Rev. E* **2001**, *64*, 016608.
[30] Nakkeeran, K.; Kwan, Y.H.C.; Wai, P.K.A.; Labruyère, A.; Dinda, P.T.; Moubissi, A.B. *J. Opt. Soc. Am. B* **2004**, *21*, 1901–1907.
[31] Fewo, S.I.; Kofané, T.C. *Opt. Commun.* **2008**, *281*, 2893–2906.
[32] Shwetanshumala; Biswas, A. *Int. J. Theor. Phys.* **2008**, *47*, 1699.
[33] Senthilnathan, K.; Li, Q.; Wai, P.K.A.; Nakkeeran, K. *P.I.E.R.S.* [Online] **2007**, *3*, 531.
[34] Senthilnathan, K.; Li, Q.; Nakkeeran, K.; Wai, P.K.A. *Phys. Rev. A* **2008**, *78*, 033835.
[35] Li, Q.; Senthilnathan, K.; Nakkeeran, K.; Wai, P.K.A. *J. Opt. Soc. Am. B* **2009**, *26*, 432–443.
[36] Roy, S.; Bhadra, S.K. *Physica D* **2007**, *232*, 103–107.
[37] Roy, S.; Bhadra, S.K.; Agrawal, G.P. *Opt. Commun.* **2008**, *281*, 5889–5893.
[38] Tsang, H.K.; Wong, C.S.; Liang, T.K.; Day, I.E.; Roberts, S.W.; Harpin, A.; Drake, J.; Asghari, M. *Appl. Phys. Lett.* **2002**, *80*, 416–418.
[39] Emelett, S.J.; Soref, R. *IEEE J. Lightwave Technol.* **1800**, *2005*, 23.
[40] Jalali, B.; Fathpour, S. *IEEE J. Lightwave Technol.* **2006**, *24*, 4600.
[41] Yin, L.; Lin, Q.; Agrawal, G.P. *Opt. Lett.* **2007**, *32*, 391–393.
[42] Wen, J.; Liu, H.; Huang, N.; Sun, Q.; Zhao, W. *Appl. Phys. B* **2011**, *104*, 867–871.
[43] Agrawal, G.P. *Phys. Rev. E* **1993**, *48*, 2316–2318.
[44] Agrawal, G.P. *Phys. Rev. A* **1991**, *44*, 7493–7501.
[45] Fattal, Y.; Rudnick, A.; Marom, D.M. *Opt. Express* **2011**, *19*, 17298–17307.
[46] Kaiser, W.; Garrett, C.G.B. *Phys. Rev. Lett.* **1961**, *7*, 229–231.

# Impact of input profile, absorption coefficients, and chirp on modulational instability of femtosecond pulses in silicon waveguides under fourth-order dispersion

**Lucien Mandeng Mandeng and Clément Tchawoua***

*Laboratory of Mechanics, Department of Physics, Faculty of Science, University of Yaoundé I Ngoa-et-kellé, Yaoundé, P.O. Box 812, Cameroon*
**Corresponding author: ctchawa@yahoo.fr*

Received November 20, 2012; revised March 4, 2013; accepted April 1, 2013; posted April 2, 2013 (Doc. ID 179491); published May 1, 2013

We report the modulational instability (MI) analysis in silicon-on-insulator waveguides under fourth-order dispersion. The two-photon absorption (TPA) generates four symmetric optimum frequencies in the MI gain spectrum. The free-carrier absorption is found to enhance the value of the central MI gain. The chirp amplifies the intensity of the main pulse train peaks, leading to input profile independence. It shifts the occurrence of these peaks at short propagation distances. The absorption coefficients counteract the chirp, creating a pump dependence, and the high values of TPA destroy drastically the spontaneous breakup mechanism, leading to pump depletion. 

*OCIS codes:* (060.4370) Nonlinear optics, fibers; (190.5530) Pulse propagation and temporal solitons; (190.4180) Multiphoton processes.
http://dx.doi.org/10.1364/JOSAB.30.001382

## 1. INTRODUCTION

Modulational instability (MI) is a well-known process today for obtaining pulse train generation (PTG). In nonlinear optics, it refers to the modulation of the steady state as a result of an interplay between the dispersive and the nonlinear effects. In other words, it is a destabilization mechanism for plane waves. Since the earlier studies on MI [1–6], the investigation of the MI mechanism in various media and systems has been reported and summarized in several papers and books [7–45]. Generally at a relatively low power, it leads to periodic PTG with a period of $2\pi/\Omega_{\mathrm{opt}}$ where $\Omega_{\mathrm{opt}}$ refers to the optimum frequencies (OFs) of the MI process [32]. In a recent study, Tiofack *et al.* investigated the MI mechanism in a complex generalized Ginzburg–Landau system showing that the third-order dispersion (TOD) does not intervene in the MI gain while the group-velocity dispersion (GVD) and the fourth-order dispersion (FOD) play an important role in this mechanism [38]. Furthermore, Dinda and Porsezian [39], studied the impact of the FOD on the MI spectra in a cubic nonlinear saturated media. Confirming the previous result of the independence to the TOD, and underlining the role played by the FOD parameter, they found that in saturated glass fibers having a negative sign of the GVD and a positive sign of the FOD, the two types of the MI mechanism are highly sensitive to the FOD magnitude. One year later, investigating a highly nonlinear system, Erkintalo *et al.* used the breather solution of Akhmediev and showed how a suitable low frequency modulation on a continuous wave (CW) field induces higher-order MI splitting with the pulse characteristics at different phases of evolution related by a simple scaling relationship [43]. Even the birefringent two-core fibers have been investigated [13,24,42,44]. In the highly nonlinear media and in the high peak powers cases, the MI mechanism generally extends beyond the PTG process, leading to the supercontinuum generation (SCG) phenomenon [28,40,46–48].

On the other hand, the high cubic Kerr nonlinearity (CKN) values of some devices, such as nonsilica fibers and silicon-on-insulator (SOI) waveguides [49–54] could lead to interesting spontaneous breakup of pulses. Indeed, in a recent work done by Wen *et al.*, the SCG process has been obtained in an SOI waveguide following the solitonic fission mechanism [55]. They have demonstrated that good control of the initial positive chirp of pulses enhances the flatness of the SCG spectra at the communication wavelength 1.5 μm. The recent attraction to the SOI waveguides is due to their wide applications, such as the production of broadband amplifiers; tunable lasers; photonics devices in the mid-infrared region, namely the optical switching devices [49,50]; optoelectronic integration to biosensing [51–54]; and broadband optical sources through the nonlinear spectral broadening processes [55,56]. The particularity of SOI waveguides is the necessary inclusion of the absorption coefficients, such as the two-photon absorption (TPA) and the free-carrier absorption (FCA) in the study. They are known to have an important role in the analysis of pulse propagation within the SOI waveguides.

The interest aroused by silicon-based (Si-based) optical devices also crosses into nanophotonics technologies and these achievements have opened up the possibility of signal performing in the field of signal processing functionalities at chip scale with relatively low optical power [56]. The Si-based components, on other hand, offer the benefits of low cost and low power consumption. Typically, a SOI waveguide differs from a silica fiber in many aspects [57]: SOI waveguides are generally smaller than silica fibers (they rarely exceed 5 cm in

 

practice) and silicon is very nonlinear with respect to the CKN (about 200 times more than the silica). SOI waveguides have the property of confining light within an area so small that it highly enhances the nonlinear effects. In addition, the SOI waveguides, because of the crystalline nature of silicon, have some nonlinear effects, such as the stimulated-Raman-scattering, which depends strongly on the waveguide geometry and mode polarization. The structures of SOI waveguides commonly used in practice are channel waveguides, rib waveguides, photonic-crystal waveguides, and slot waveguides, whose the pictures can be found in [58].

However, among all the studies of the MI process in nonlinear optics, the question of MI analysis in highly dispersive SOI waveguides has not yet been investigated, to the best of our knowledge. Furthermore, the impact of the input profile, chirp, and absorption coefficients has not yet been conducted in this kind of waveguide. It is, therefore, the focus of this paper. The study is conducted using different input profiles as the Gaussian, the sech-type and the RC Ansätze pulses. The impact of the pulse shape is, therefore, highlighted, even those of the chirp and the absorption coefficients. The paper is designed as follows: the next section presents the model equation while in the Section 3, we do the linear MI analysis of a cw propagating within the studied waveguide. Then, we present in Section 4 the MI pulse splitting in the sense of the MI-PTG process for each input profile and the last section concludes the paper.

## 2. THE MODEL EQUATION

The propagation of the optical pulses through an SOI waveguide under the FOD effect is governed by the extended nonlinear Schrödinger equation, including the effect of the TPA and the FCA as [50,54,56]

$$i\frac{\partial U}{\partial z}+\sum_{k=2}^{4}\frac{(i)^k\beta_k}{(k)!}\frac{\partial^k U}{\partial t^k}+\gamma|U|^2U=-i\frac{\alpha}{2}U-i\Gamma|U|^2U-i\frac{\sigma}{2}N_CU, \tag{1}$$

where $U$, $\beta_k$, $\gamma$, $\alpha$, $\Gamma$, $\sigma$, and $N_C$ represent the slowly varying amplitude of the electrical field, the $(k)$th order term of dispersion, the nonlinear Kerr coefficient, the linear loss coefficient, the TPA coefficient, the FCA coefficient, and the free-carrier density (FCD), respectively. To obtain the FCD, we may use the following relation [49,50,54,56]:

$$Nc(z,t)=\frac{\Gamma}{2h\nu_0A_{\text{eff}}}\int_{-\infty}^{t}|U(z,t')|^4\mathrm{d}t', \tag{2}$$

where we have neglected the term relative to the carrier life time $\tau_C$ because we are dealing with the ultrashort pulses (femtosecond domain) [50]. It is, therefore, an approximated relation of equation 2 given in [56]. Our analysis is based on the Gaussian, sech-type and RC Ansätze trial functions, respectively defined as follows [32,59,60]:

$$U=U_0e^{\left[-\frac{1+iC}{2}\left(\frac{t}{t_0}\right)^2+i\phi\right]}, \tag{3}$$

$$U=U_0\,\mathrm{sech}\left(\frac{t}{t_0}\right)e^{i\left[-\frac{C}{2}\left(\frac{t}{t_0}\right)^2+\phi\right]}, \tag{4}$$

and

$$U=\frac{U_0}{2}\left[1+\cos\left(\frac{\pi t}{t_0}\right)\right]e^{i\left[\frac{C}{2}\left(\frac{t}{t_0}\right)^2+\phi\right]}, \tag{5}$$

where $U_0$ is the amplitude of the pulse linked with the peak input power $P_0$ as $U_0=\sqrt{P_0}$. The parameters $C$, $t_0$, and $\phi$ are the chirp, the width, and the phase, respectively. The FCD of the Gaussian and the RC pulses are given, respectively, as

$$Nc_G=\sqrt{\frac{\pi}{2}}\left(\frac{U_0^4\beta_{\text{TPA}}}{4h\nu_0A_{\text{eff}}^2}t_0\right)\left[1+\text{erf}\left(\frac{\sqrt{2}t}{t_0}\right)\right], \tag{6}$$

and

$$Nc_{\text{RC}}=\frac{U_0^4\beta_{\text{TPA}}t_0}{1536\pi h\nu_0A_{\text{eff}}^2}\left\{320+105\pi+\frac{210t}{t_0}+2\sin\left(\frac{\pi t}{t_0}\right)\times\left[160+81\cos\left(\frac{\pi t}{t_0}\right)+32\cos^2\left(\frac{\pi t}{t_0}\right)+6\cos^3\left(\frac{\pi t}{t_0}\right)\right]\right\}, \tag{7}$$

where $\beta_{\text{TPA}}$ is the usual TPA parameter [50,56] and erf the error function [61]. The parameters $h$, $\nu_0$, and $A_{\text{eff}}$ are the Planck constant, the pump frequency, and the effective core area of the SOI waveguide, respectively.

## 3. THE LINEAR MI ANALYSIS

The MI analysis of a cw is conducted in this section with the physical quantities of the SOI waveguide defined by Roy *et al.* [50]. We start with the steady-state solution of the cw [32]:

$$U=U_0e^{i\phi_{\text{NL}}}, \tag{8}$$

where $\phi_{\text{NL}}$ represents the nonlinear phase shift defined as follows:

$$\phi_{\text{NL}}=\left[(\gamma+i\Gamma)U_0^2+\frac{i}{2}(\alpha+\sigma N_c)\right]z. \tag{9}$$

We use a small perturbation of the steady-state solution by stating

$$a(z,t)=u(z)e^{i(Kz-\Omega t)}+v(z)e^{-i(Kz-\Omega t)}, \tag{10}$$

where $K$ and $\Omega$ represent the wave number and the perturbation frequency, respectively. The obtained MI matrix is given as follows:

$$M(K)=\begin{bmatrix}D_1(\Omega)-K+\gamma_1U_0^2+\Lambda & \gamma_1U_0^2\\ \gamma_1U_0^2 & D_2(\Omega)+K+\gamma_1U_0^2+\Lambda\end{bmatrix}, \tag{11}$$

where

$$D_1(\Omega)=\sum_{k=2}^{4}\frac{\Omega^k\beta_k}{k!},$$
$$D_2(\Omega)=\sum_{k=2}^{4}\frac{(-\Omega)^k\beta_k}{k!},$$
$$\gamma_1=\gamma+i\Gamma,$$
$$\Lambda=i\frac{(\alpha+\sigma N_c)}{2}. \tag{12}$$

The wave number leads to

$$K=\frac{1}{2}\left\{D_{\text{odd}}\pm[(D_{\text{even}}+2(\Lambda+2\gamma_1U_0^2))(D_{\text{even}}+2\Lambda)]^{1/2}\right\}, \tag{13}$$

with $D_{\text{even}}=D_1+D_2$ and $D_{\text{odd}}=D_1-D_2$. The MI gain is well known to be defined as

$$G(\Omega)=2|\text{Im}(K)|$$
$$\equiv\frac{1}{2}\left|\text{Im}\{((D_{\text{even}}+2(\Lambda+2\gamma_1U_0^2))(D_{\text{even}}+2\Lambda))^{1/2}\}\right|. \tag{14}$$

Since $\gamma_1$ and $\Lambda$ are complexes, it is convenient to set that

$$G(\Omega)=2\left|\text{Im}\left(\sqrt{A(\Omega)}\right)\right|, \tag{15}$$

where

$$A(\Omega)=x(\Omega)+iy(\Omega)=r(\Omega)e^{i\theta(\Omega)},$$
$$x(\Omega)=D_{\text{even}}(D_{\text{even}}+4U_0^2\gamma)-4|\Lambda|(2U_0^2\Gamma+|\Lambda|),$$
$$y(\Omega)=4D_{\text{even}}(U_0^2\Gamma+|\Lambda|)+8U_0^2\gamma|\Lambda|. \tag{16}$$

One obtains the MI gain as follows:

$$G(\Omega)=[2(r(\Omega)-x(\Omega))]^{1/2}. \tag{17}$$

The relation in Eq. (17) confirms that the TOD does not intervene in the MI gain as previously discussed in the introduction section. The OFs are given for $dG(\Omega)/d\Omega=0$ as a phase-matching condition of the four-wave mixing related with the MI mechanism. It is described by two pump photons at the frequency $\omega_0$, one Stokes photon at $\omega_0-\Omega$, and one anti-Stokes photon at $\omega_0+\Omega$ [32,39]. The following relations define the obtained OFs:

$$\Omega_0=0,$$
$$\Omega_{1,\pm}=\pm\frac{\sqrt{-6\beta_4\beta_2}}{\beta_4},$$
$$\Omega_{2,\pm}=\pm\sqrt{\frac{-6\Gamma\beta_2+2\sqrt{9\Gamma^2\beta_2^2+6\Gamma\beta_4\gamma|\Lambda|}}{\Gamma\beta_4}},$$
$$\Omega_{3,\pm}=\pm\sqrt{-\frac{6\gamma\beta_2+2\sqrt{9\gamma^2\beta_2^2-6\gamma\beta_4U_0^2\Gamma^2-6\Gamma\beta_4\gamma|\Lambda|-6\gamma^3\beta_4U_0^2}}{\gamma\beta_4}}. \tag{18}$$

When the TPA and the FCA vanish, the OFs in Eq. (18) are similar to those obtained in [39] for glass fibers where $\gamma$ was linked with the saturable nonlinearity. So, we do not focus on the role played by the FOD since it has been extensively discussed in this reference. Our main purpose in this section consists to study the effect of the absorption coefficients on the MI gain spectrum.

For the numerical simulations, we have set the parameter $K=\sigma N_c$ as the FCA parameter. Therefore, we choose to study separately the effects of TPA and FCA on the MI gain spectrum by controlling the value of $K$. For instance, in the case where we have $\Gamma\neq0$, we consider that $K\sim0$, which allows us to analyze only the single effect of TPA. On the other hand, when rather we have $K\neq0$, we consider that $\Gamma\sim0$, which allows us to analyze only the FCA effect.

Then, we plot in Fig. 1 the MI gain for different cases highlighting the effect of the absorption coefficients. For the case where we neglect the TPA and the FCA effects [see Fig. 1(a)], we have two bands of the MI gain at two OFs locations: −78.3443 and 78.3443 Thz. These sidelobes are due to the FOD effect interacting with the GVD as discussed in [38,39] and defined by the second relation of Eq. (18). However, in the presence of the TPA [see Fig. 1(b)], we have seven

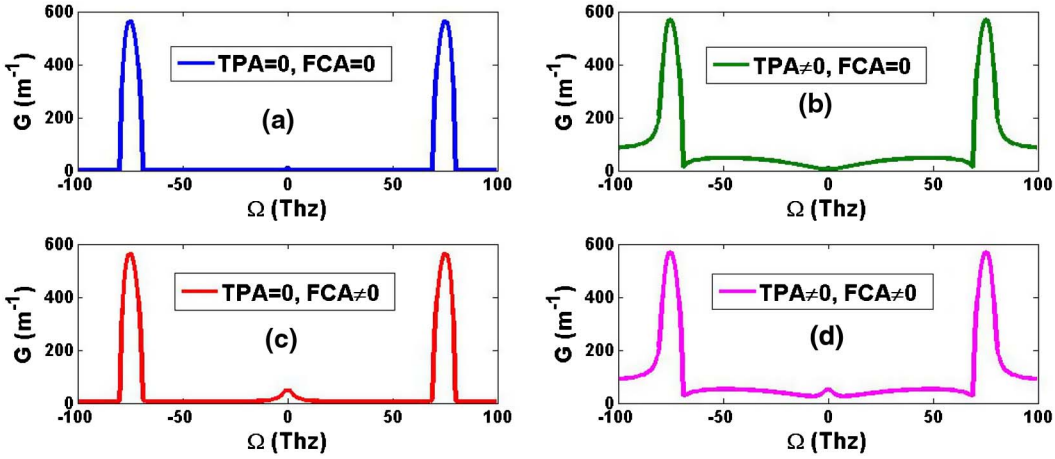


Fig. 1. Plot of the MI gain spectrum versus Ω. (a) Blue curve for TPA = 0 and FCA = 0, (b) green curve for TPA ≠ 0 ($\Gamma=6.5\ \text{W}^{-1}\,\text{m}^{-1}$) and FCA ∼ 0, (c) red curve for TPA ∼ 0 and FCA ≠ 0 ($K=1\ \text{m}^{-1}$), and (d) violet curve for TPA ≠ 0 and FCA ≠ 0. Other parameters: $\beta_2=0.56\ \text{ps}^2/\text{m}$, $\beta_4=-0.0014\ \text{ps}^4/\text{m}$, $\gamma=47\ \text{w}^{-1}\,\text{m}^{-1}$, $P_0=3$ W.

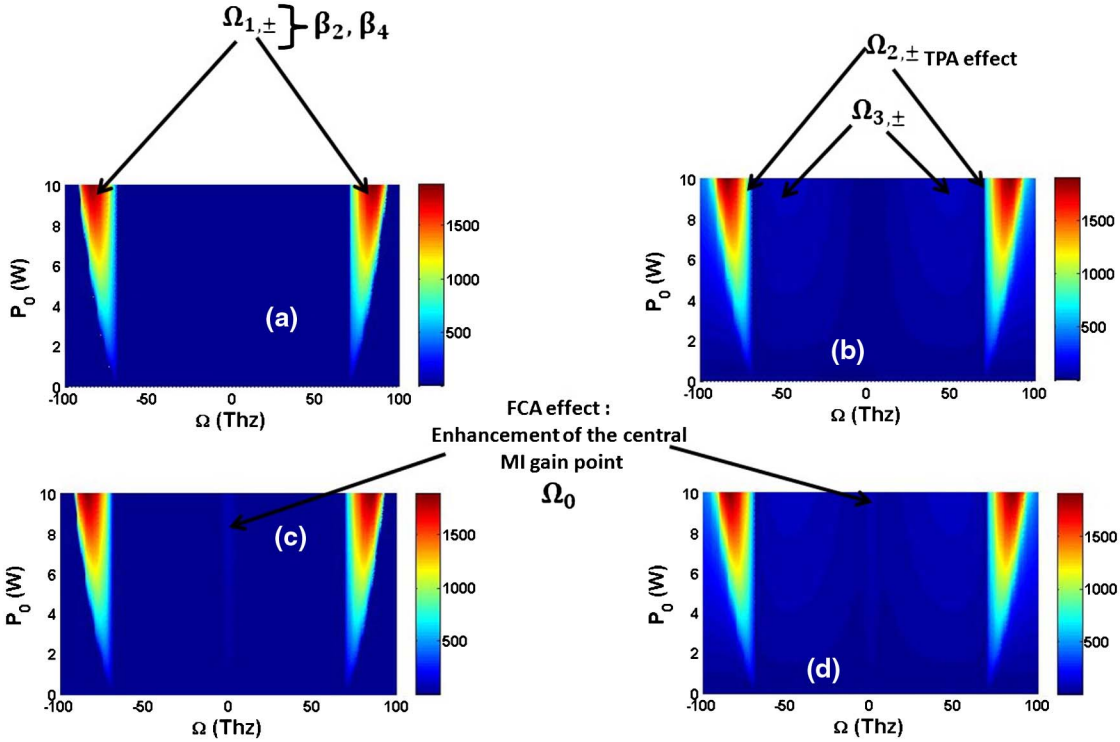


Fig. 2. Plot of the MI gain spectrum versus $P_0$ and Ω. (a) for TPA = 0 and FCA = 0, (b) TPA ≠ 0 ($\Gamma = 6.5$ W$^{-1}$ m$^{-1}$) and FCA ~ 0, (c) for TPA ~ 0 and FCA ≠ 0 ($K = 1$ m$^{-1}$), and (d) for TPA ≠ 0 and FCA ≠ 0. Other parameters: $\beta_2 = 0.56$ ps$^2$/m, $\beta_4 = -0.0014$ ps$^4$/m, $\gamma = 47$ w$^{-1}$ m$^{-1}$.

remarkable values of the MI gain at seven OF locations: −78.3443, −69.0857, −48.9898, 0, 48.9898, 69.0857, and 78.3443 Thz. Among these locations, three have a zero MI gain, particularly those of ±69.0857 Thz and 0 Thz. In the presence of the FCA [see Fig. 1(c)], we have three OF solutions where the one in the central detuning frequency ($\Omega_0 = 0$) has an increased MI gain. It means that the FCA enhances the value of this central MI gain point. For the full realistic case where both the TPA and the FCA effects are considered, we recover the seven locations above of the MI gain maxima with the corresponding enhanced central peak. It is worthy to notice that, these OF values could be directly obtained using the relations of Eq. (18). Figure 2 shows the MI gain spectra for the different cases discussed above in Fig. 1 versus the varying peak power $P_0$. The features noticed in Fig. 1 are directly observed in the contour plots of Fig. 2. It is observed in Fig. 2(b) the TPA effect on the MI gain, such as the creation of the four OF symmetric locations given by the two last relations of Eq. (18) in addition to the OFs induced by FOD and GVD interaction [see Fig. 2(a)]. On the other hand, the FCA slightly increases the value of the central MI gain [see Figs. 2(c) and 2(d) comparatively to the cases of Figs. 2(a) and 2(b)].

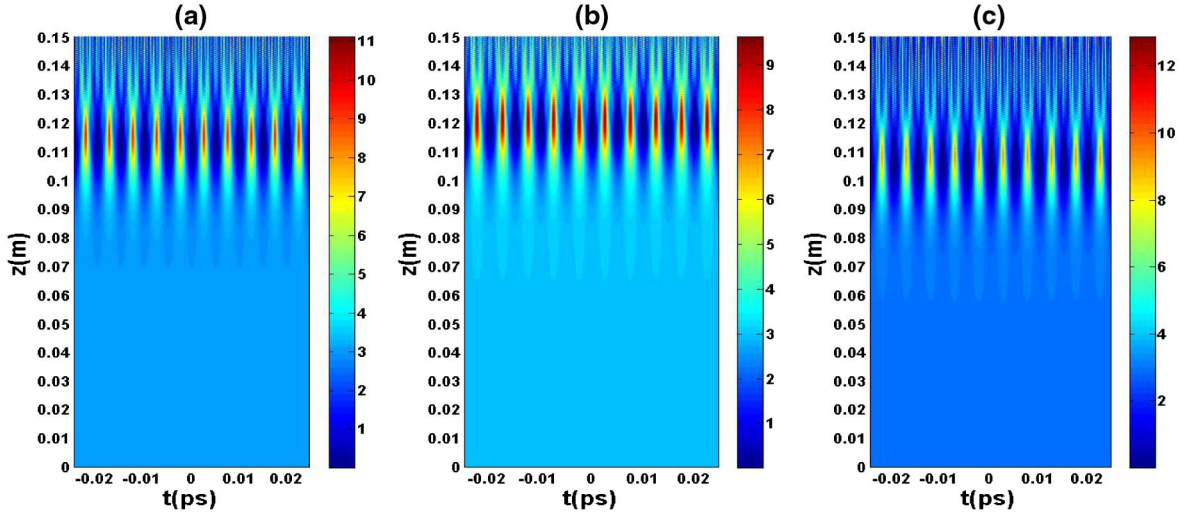


Fig. 3. Contour plot of unchirped pulses propagation. (a) Gaussian profile, (b) sech-type profile, (c) RC profile. Parameters: $\beta_2 = 0.56$ ps$^2$/m, $\beta_4 = -0.0014$ ps$^4$/m, $\gamma = 47$ w$^{-1}$ m$^{-1}$, $L = 0.15$ m, $t_0 = 50$ fs, $P_0 = 3$ W, $\Gamma = 0$.

## 4. PTG IN SOI WAVEGUIDES: IMPACT OF PULSE SHAPE, CHIRP, AND ABSORPTION COEFFICIENTS

### A. In the Absence of Chirp, TPA, and FCA

We generate a map of PTG as shown in Fig. 3 for each unchirped input pulse with the common split-Fourier algorithm in the absence of the TPA ($\Gamma = 0$). For the sech-type and Gaussian profiles, the trails of the MI-PTG are observed around about 0.07 m while for the RC pulse, they are observed around about 0.06 m. We also observe for all the profiles with the numerical data used about 10 main peaks of the MI-PTG process in Fig. 3. The maximum value of these mains peaks for the sech-type pulse is obtained around about 0.12 m of propagation distance with approximately the value of 9.5 W [see the colorbar in Fig. 3(b)]. Concerning the Gaussian profile, we reach 11 W toward 0.115 m. For the last profile (RC pulse), we observe rather a maximal value about 12.5 W toward 0.11 m.

Indeed, we notice that for the profiles that are close to the fundamental soliton solution (consequently, more stable), such as the sech-type pulse, the main peaks of the MI-PTG trails occur at larger propagation distances than those less stable, such as the RC pulse. In addition, the maximum values of these main peaks are smaller than those of the less stable input profiles. The same idea can be raised for the Gaussian pulse in comparison to the RC profile since the first form is closer to the sech-type pulse than the latter.

More specifically, the RC pulse as a less stable input has stronger main peaks of the MI-PTG trails at short propagation distances [see Figs. 4(b) and 4(c)]. This profile is followed by the Gaussian profile, which shows strong peaks at

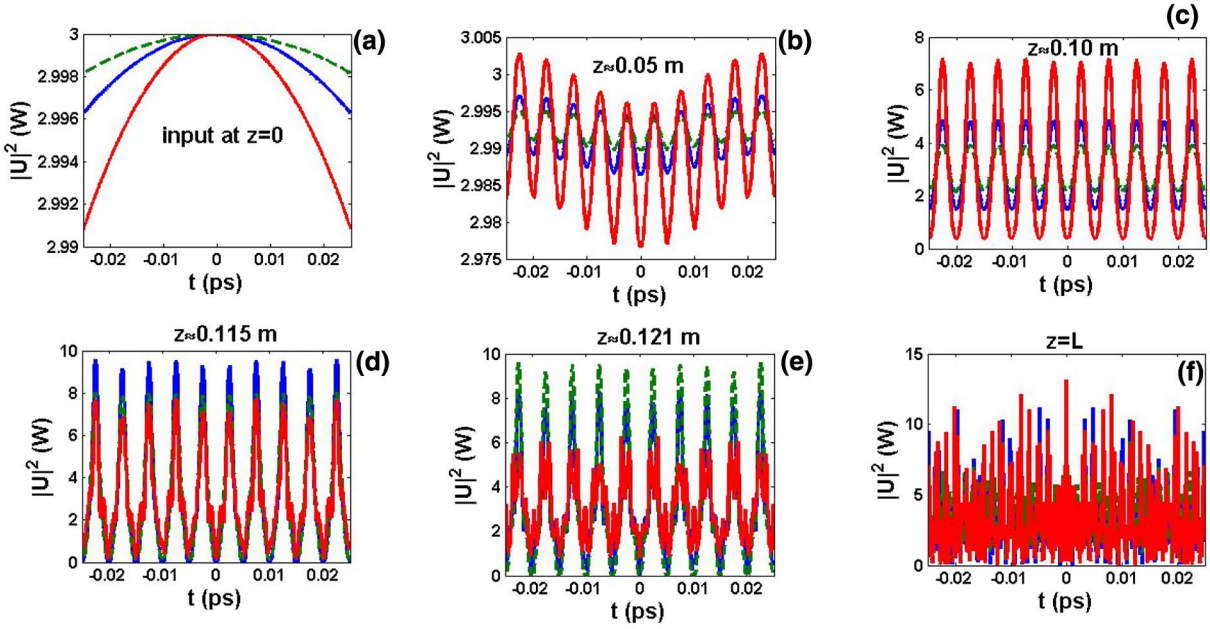


Fig. 4. Temporal profiles of the unchirped pulses at different propagation distances: (a) input at $z = 0$, (b) $z = 0.05$ m, (c) $z = 0.1$ m, (d) $z = 0.115$, (e) $z = 0.121$ m, and (f) $z = L$. The parameters are the same as in Fig. 3. Solid blue curves for Gaussian profile, dashed green curves for sech-type profile, and solid red curves for RC profiles.

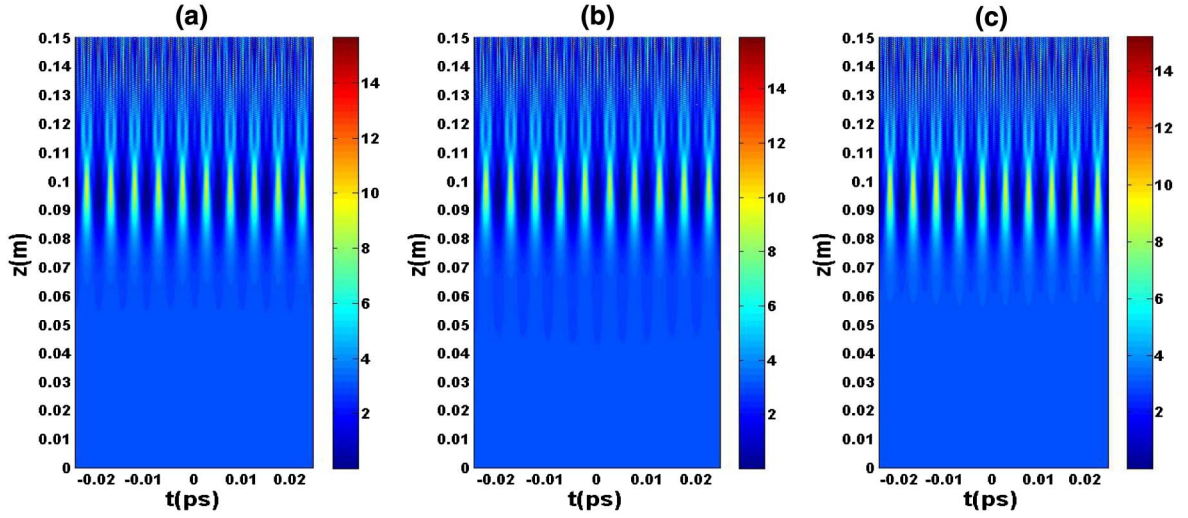


Fig. 5. Contour plot of chirped pulses propagation. (a) Gaussian profile, (b) sech-type profile, (c) RC profile. Parameters: $C = 10$, $\beta_2 = 0.56$ ps$^2$/m, $\beta_4 = -0.0014$ ps$^4$/m, $\gamma = 47$ W$^{-1}$ m$^{-1}$, $L = 0.15$ m, $t_0 = 50$ fs, $P_0 = 3$ W, $\Gamma = 0$.

propagation distances larger than those of the previous profile [see Fig. 4(d)], while the sech-type is the last, with strong peaks of the MI-PTG process appearing later in the propagation [see Fig. 4(e)]. Beyond these regular main peaks for all the profiles, the spontaneous breakup process continues, leading to a chaotic picture for large propagation distances [see Figs. 3 and 4(f)]. Another observation from Fig. 4 concerns the orientation of the undulations for each pulse. Indeed, in the absence of the source chirp, all the pulses have the same orientation in the undulations.

### B. Effect of Chirp in the Absence of TPA and FCA

Considering the initial chirping process of each pulse, we have simulated the MI-PTG process in the absence of absorption coefficients (see Fig. 5). As can be observed in this figure, the initial chirp ($C = 10$) leads both the sech-type and the Gaussian profiles to behave similarly in the development of the MI-PTG process while the RC profile remains different. Furthermore, the chirp does not change the number of the main peaks for each profile. It shifts the occurrence of the high values of the main peaks to short propagation distances for all the input pulses (about 0.1 m). The maximum value reached in the power is the same for both the Gaussian and the sech-type pulse (about 14.8 W) while for the RC profile, one finds rather about 12.8 W. So, the effect of chirp is to enhance the intensity of the MI-PTG peaks and to shift the occurrence of their maximum value to shorter propagation distances than the unchirped case.

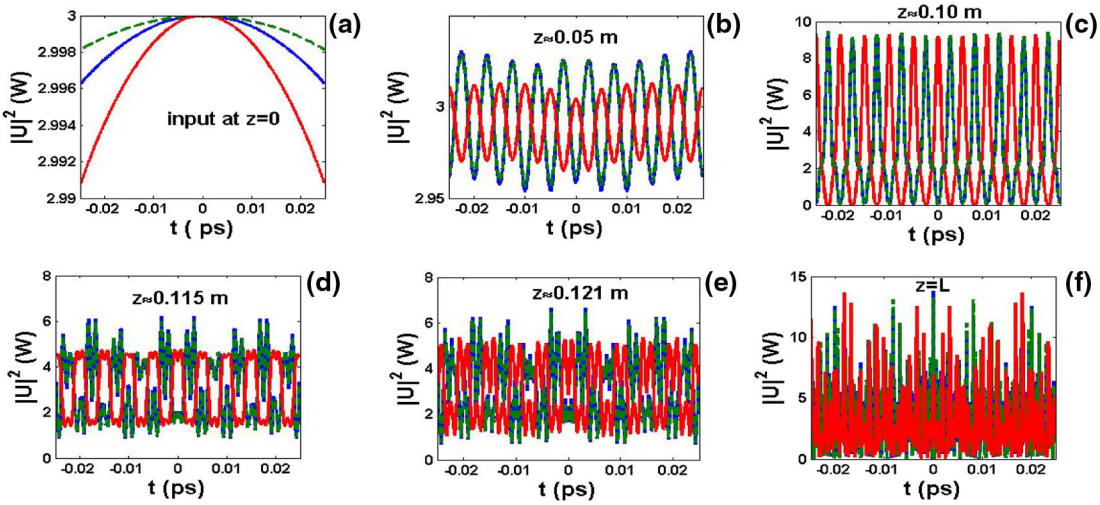


Fig. 6. Temporal profiles of the chirped pulses at different propagation distances: (a) input at $z = 0$, (b) $z = 0.05$ m, (c) $z = 0.1$ m, (d) $z = 0.115$, (e) $z = 0.121$ m, and (f) $z = L$. The parameters are the same as in Fig. 4. Solid blue curves for Gaussian profile, dashed green curves for sech-type profile, and solid red curves for RC profiles.

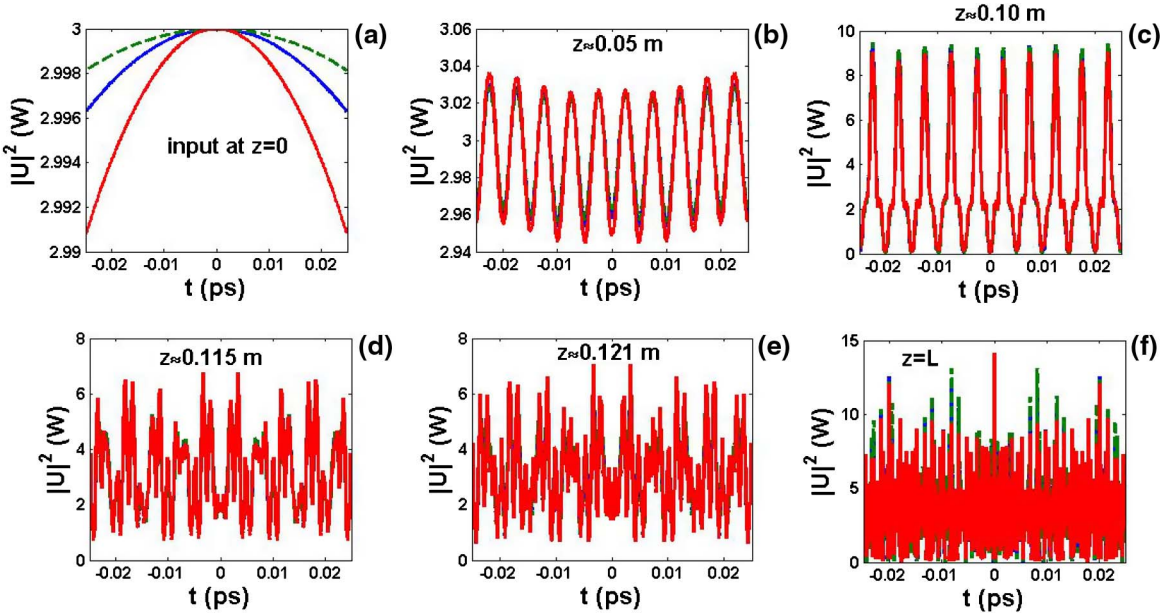


Fig. 7. Temporal profiles of the chirped pulses at different propagation distances with an chirp inversion for the RC profile: (a) input at $z = 0$, (b) $z = 0.05$ m, (c) $z = 0.1$ m, (d) $z = 0.115$, (e) $z = 0.121$ m, and (f) $z = L$. The parameters are the same as in Fig. 3. Solid blue curves for Gaussian profile, dashed green curves for sech-type profile, and solid red curves for RC profiles: for the RC profile $C = -10$ while for the others $C = 10$.

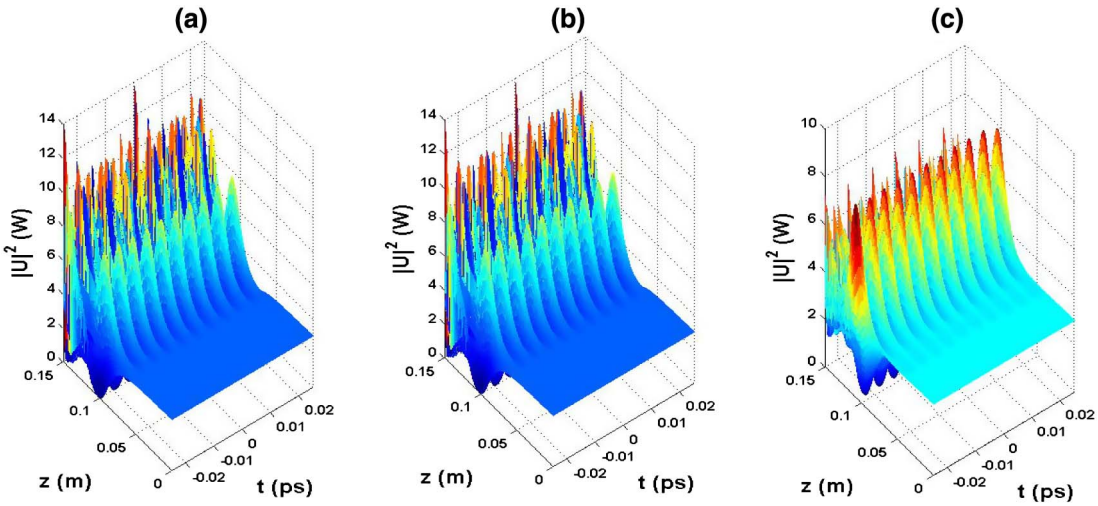


Fig. 8. Plot of chirped pulses propagation. (a) Gaussian profile, (b) sech-type profile, (c) RC profile. Parameters: $C = 10$, $\beta_2 = 0.56$ ps$^2$/m, $\beta_4 = -0.0014$ ps$^4$/m, $\gamma = 47$ w$^{-1}$ m$^{-1}$, $L = 0.15$ m, $t_0 = 50$ fs, $P_0 = 3$ W, $\Gamma = 0.1$ W$^{-1}$ m$^{-1}$, $\sigma = 1.45 \times 10^{-21}$ m$^2$.

On the other hand, when we consider the Fig. 6 with the nonzero value of chirp, the pulses that are more stable (the Gaussian and the sech-type pulses) are more amplified than those which are less stable (the RC profile). Even the orientation of the undulation changes since the RC profile undergoes a chirp phase opposite to that of the others. Reversing the initial chirp value of the RC pulse so that it is now chirped with a negative value while the other profiles are always chirped positively, we obtain a similar behavior for all the pulses (see Fig. 7). In this case, the chirp creates an independence of the MI-PTG process to the input profile since it is observed that all the pulses have the same picture because of the nonzero chirp.

### C. Effect of Absorption Coefficients on the MI-PTG in the SOI Waveguides

The case treated in Fig. 8 concerns the chirped pulses undergoing the MI-PTG process in an SOI waveguide having a small value of TPA about 0.1 W$^{-1}$ m$^{-1}$ with the FCA coefficient about $1.45 \times 10^{-21}$ m$^2$ [56]. We observe the effect of these small values of TPA and FCA on the MI-PTG picture drawn as a slight reduction of the amplified intensity comparatively to the previous cases. The chirp impact in Fig. 8 is in agreement with the one mentioned previously in Figs. 5 and 6. Increasing the value of the TPA parameter with a factor 5 (consequently, the FCA also increases), the absorption coefficients influence significantly the MI-PTG process. In fact, in Fig. 9 we observe the influence of TPA and FCA as a real reduction of the amplified intensity of the MI-PTG peaks in which the maximum value is reached at almost the output of the considered SOI waveguide. On the other hand, the input profiles do not interact similarly with the absorption coefficients. The RC profile is found to be more influenced by the TPA and FCA than the others since its maximum value does not exceed the initial peak value comparatively to the all previous cases. Concerning the sech-type and the Gaussian pulses, an important reduction is observed but it exceeds at least the double of the initial input peak power. However, the combination of the value of 6.5 W$^{-1}$ m$^{-1}$ used previously by Roy *et al.* [50] for the TPA effect and the FCA coefficient

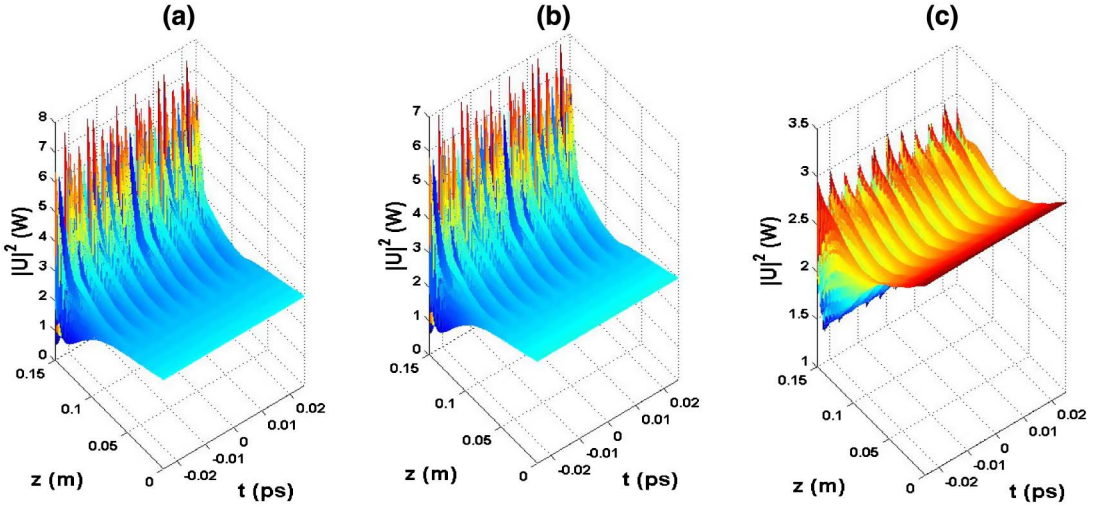


Fig. 9. Plot of chirped pulses propagation. (a) Gaussian profile, (b) sech-type profile, (c) RC profile. Parameters: $C = 10$, $\beta_2 = 0.56$ ps$^2$/m, $\beta_4 = -0.0014$ ps$^4$/m, $\gamma = 47$ w$^{-1}$ m$^{-1}$, $L = 0.15$ m, $t_0 = 50$ fs, $P_0 = 3$ W, $\Gamma = 0.5$ W$^{-1}$ m$^{-1}$, $\sigma = 1.45 \times 10^{-21}$ m$^2$.

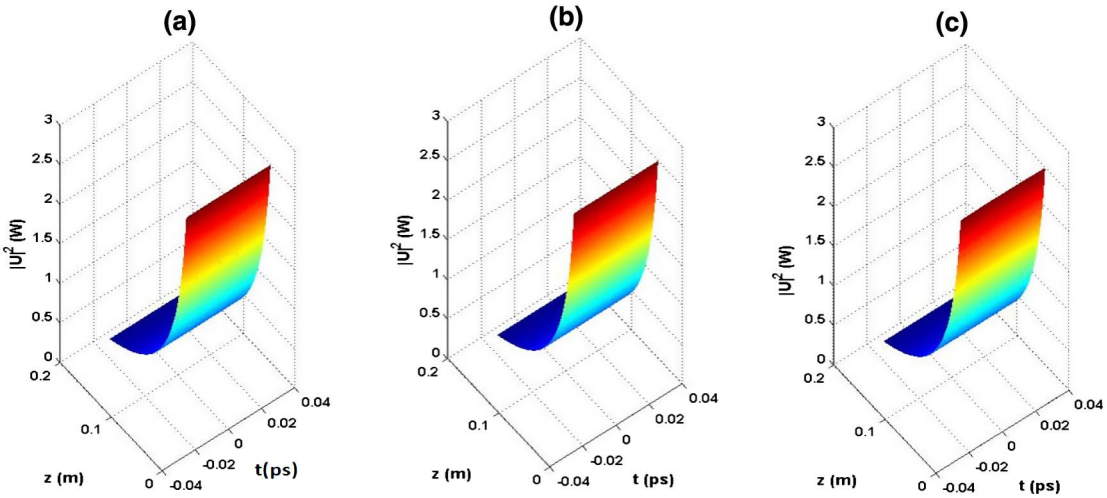


Fig. 10. Plot of chirped pulses propagation. (a) Gaussian profile, (b) sech-type profile, (c) RC profile. Parameters: $C = 10$, $\beta_2 = 0.56$ ps$^2$/m, $\beta_4 = -0.0014$ ps$^4$/m, $\gamma = 47$ w$^{-1}$ m$^{-1}$, $L = 0.15$ m, $t_0 = 50$ fs, $P_0 = 3$ W, $\Gamma = 6.5$ W$^{-1}$ m$^{-1}$, $\sigma = 1.45 \times 10^{-21}$ m$^2$.

value of [56] leads to the complete destruction of the MI-PTG process, creating, consequently, an independence to the input profile (see Fig. 10). Indeed, as can be observed, all the pulses behave similarly under these conditions. The MI-PTG is destroyed in the sense that there are no peaks or any pulse splitting observed. The absorption coefficients act in this case, normally, as nonlinear losses leading the a drastic pump depletion following the propagation distance. The half of the initial peak power is reached after a propagation of 0.04 m only. Beyond this propagation distance, the pulses are almost annihilated by the absorption coefficients whatever the value of the chirp, which becomes a secondary parameter. Thus, the absorption coefficients counteract the beneficial chirp effect on the MI-PTG process.

## 5. CONCLUSION

In summary, we have shown in this paper the MI analysis leading to PTG in SOI waveguides under the FOD using different chirped input femtosecond pulses. With the sech-type, the Gaussian and the RC pulses, we have predicted through the FCD, an almost similar behavior in the MI-PTG process between the two firsts profiles and a different one for the latter. It means that, the Gaussian and the sech-type pulses undergoing the same propagation conditions inside the SOI waveguide, lead to the MI-PTG process in a slightly similar form. In the linear analysis of the model under FOD, we have confirmed the independence of the MI gain to the TOD effect, such as any odd order of dispersion. When both the TPA and the FCA vanish, the obtained OFs encompass those of previous studies done rather on glass fibers with saturable nonlinearity. It has been shown in this work that, four symmetric OFs were created because of the TPA effect in addition to those induced by the single interaction between the FOD and the GVD. The FCA enhances the value of the central MI gain point. Considering the MI-PTG process in the unchirped case, we have demonstrated that the input pulse, which is less stable, such as the RC pulse, has main peaks of the MI-PTG trails more strong than the other input profiles at short propagation distances. The chirp effect amplifies the intensity of the main MI-PTG peaks for each profile, making the input pulses behave similarly while it shifts the occurrence of these peaks at shorter distances of propagation than the unchirped case. We have finally shown that the absorption coefficients counteract the beneficial impact of the chirp as nonlinear losses by breaking the similarity (when small values of TPA are considered), destroying drastically the MI-PTG process and leading to pump depletion when great values of TPA are reached.

For an efficient process of the MI-PTG in an SOI waveguides under the FOD, a good control of the values of absorption coefficients, dispersive effects, and source chirp of more stable input profiles should be operated.

## ACKNOWLEDGMENTS

L. M. Mandeng acknowledges Dr. Jean-Pascal Eloundou (from the National Superior Engineering School of Yaoundé, Cameroon) for his support, Dr. Serge Ibraid Fewo (from the University of Yaoundé I, Cameroon), Pr. Alidou Mohamadou (from the University of Douala, Cameroon), Prof. Mourad Zghal and Dr. Rim Cherif (from the Sup'Com Engineering School of the University of Carthage, Tunisia) for their useful discussions and encouragement. He also acknowledges Dr. Angela Dudley and Pr. Francesco Petruccione for their support for attending to Quantum Africa 2 conference held in KwaZulu-Natal (South Africa) September 3–7, 2012, and the African Laser Centre for the support for attending to short courses on optical fiber technology held September 16–22, 2012 at the Nelson Mandela Metropolitan University (South Africa). Finally, the authors acknowledge the OSA Foundation for the travel grant given to the first author for his attendance at the FiO 2012 conference (Rochester, New York, USA).

## REFERENCES

1. L. A. Ostrovsky, "Electromagnetic waves in nonlinear media with dispersion," Sov. Phys. Tech. Phys. **8**, 679–683 (1964).
2. V. I. Talanov, "Self-focusing of wave beams," JETP Lett. **2**, 138–141 (1965).
3. T. B. Benjamin and J. E. Feir, "The disintegration of wave trains on deep water. Part 1. Theory," J. Fluid Mech. **27**, 417–430 (1967).

4. T. Taniuti and H. Washimi, "Self-trapping and instability of hydromagnetic waves along the magnetic field in a cold plasma," Phys. Rev. Lett. **21**, 209–212 (1968).
5. V. I. Karpman and E. M. Krushkal, "Modulated waves in nonlinear dispersive media," Sov. Phys. JETP **28**, 277–281 (1969).
6. A. Hasegawa, "Observation of self-trapping instability of a plasma cyclotron wave in a computer experiment," Phys. Rev. Lett. **24**, 1165–1168 (1970).
7. A. Hasegawa, "Generation of a train of soliton pulses by induced modulational instability in optical fibers," Opt. Lett. **9**, 288–290 (1984).
8. K. Tai, A. Hasegawa, and A. Tomita, "Observation of modulational instability in optical fibers," Phys. Rev. Lett. **56**, 135–138 (1986).
9. G. P. Agrawal, "Modulation instability induced by cross-phase modulation," Phys. Rev. Lett. **59**, 880–883 (1987).
10. J. E. Rothenberg, "Modulational instability of copropagating frequencies for normal dispersion," Phys. Rev. Lett. **64**, 813 (1990).
11. E. J. Greer, D. M. Patrick, P. G. J. Wigley, and J. R. Taylor, "Generation of 2 THz repetition rate pulse trains through induced modulational instability," Electron. Lett. **25**, 1246–1248 (1989).
12. S. Sudo, H. Itoh, K. Okamoto, and K. Kubodora, "Generation of 5 THz repetition optical pulses by modulation instability in optical fibers," Appl. Phys. Lett. **54**, 993–994 (1989).
13. S. Trillo, S. Wabnitz, G. I. Stegeman, and E. M. Wright, "Parametric amplification and modulational instabilities in dispersive nonlinear directional couplers with relaxing nonlinearity," J. Opt. Soc. Am. B **6**, 889–900 (1989).
14. P. Drummond, T. Kennedy, and J. Dudley, "Cross-phase modulation instability in high birefringence fibers," Opt. Commun. **78**, 137–142 (1990).
15. C. C. Mei, *The Applied Dynamics of Ocean Surface Waves* (World Scientific, 1989).
16. V. B. Matveev and M. A. Salle, *Darboux Transformations and Solitons*, *Series in Nonlinear Dynamics* (Springer-Verlag, 1991).
17. J. R. Taylor, *Optical Solitons: Theory and Experiments* (Cambridge University, 1992).
18. Y. Kodama, A. Maruta, and A. Hasegawa, "Long distance communications with solitons," Quantum Opt. **6**, 463–516 (1994).
19. N. D. Dalt, C. D. Angelis, G. F. Nalesso, and M. Santagiustina, "Dynamics of induced modulational instability in waveguides with saturable nonlinearity," Opt. Commun. **121**, 69–72 (1995).
20. S. B. Cavalcanti and M. Lyra, "Modulation instability of ultrashort pulses via a generalized nonlinear Schrödinger equation with deviating argument," Phys. Lett. A **211**, 276–280 (1996).
21. N. Akhmediev and A. Ankiewicz, *Solitons. Nonlinear Pulses and Beams* (Chapman and Hall, 1997).
22. F. Kh. Abdullaev, S. A. Darmanyan, S. Bischoff, and M. P. Sorensen, "Modulational instability of electromagnetic waves in media with varying nonlinearity," J. Opt. Soc. Am. B **14**, 27–33 (1997).
23. M. Karlsson, "Four-wave mixing in fibers with randomly varying zero-dispersion wavelength," J. Opt. Soc. Am. B **15**, 2269 (1998).
24. R. S. Tasgal and B. A. Malomed, "Modulational instabilities in the dual-core nonlinear optical fiber," Phys. Scr. **60**, 418–422 (1999).
25. S. C. Wen, W. H. Su, H. Zhang, X. Q. Fu, L. J. Qian, and D. Y. Fan, "Influence of higher-order dispersions and raman delayed response on modulation instability in microstructured fibres," Chin. Phys. Lett. **20**, 852–854 (2003).
26. Y. S. Kivshar and G. P. Agrawal, *Optical Solitons: From Fibers to Photonic Crystals* (Academic, 2003).
27. E. Brainis, D. Amans, and S. Massar, "Scalar and vector modulation instabilities induced by vacuum fluctuations in fibers: numerical study," Phys. Rev. A **71**, 023808 (2005).
28. A. Dermican and U. Bandelow, "Supercontinuum generation by the modulation instability," Opt. Commun. **244**, 181–185 (2005).
29. M. Nurhuda and E. Van Groesen, "Effects of delayed Kerr nonlinearity and ionization on the filamentary ultrashort laser pulses in air," Phys. Rev. E **71**, 066502 (2005).
30. R. E. Kennedy, S. V. Popov, and J. R. Taylor, "Ytterbium gain band self-induced modulation instability laser," Opt. Lett. **31**, 167–169 (2006).
31. F. Ndzana II, A. Mohamadou, and T. C. Kofané, "Modulational instability in the cubic quintic nonlinear Schrödinger equation through the variational approach," Opt. Commun. **275**, 421–428 (2007).
32. G. P. Agrawal, *Nonlinear Fiber Optics*, 4th ed. (Academic, 2008).
33. G. P. Agrawal, *Applications of Nonlinear Fiber Optics* (Academic, 2008).
34. X. Liu, J. W. Haus, and S. M. Shahriar, "Modulation instability for a relaxational Kerr medium," Opt. Commun. **281**, 2907–2912 (2008).
35. A. M. Kamchatnov and M. Salerno, "Dark soliton oscillations in Bose–Einstein condensates with multi-body interactions," J. Phys. B **42**, 185303 (2009).
36. P. Das, M. Vyas, and P. K. Panigrahi, "Loss of superfluidity in the Bose–Einstein condensate in an optical lattice with cubic and quintic nonlinearity," J. Phys. B. **42**, 245304 (2009).
37. V. E. Zakharov and L. A. Ostrovsky, "Modulation instability: the beginning," Physica D **238**, 540–548 (2009).
38. C. G. L. Tiofack, A. Mohamadou, T. C. Kofané, and A. B. Moubissi, "Generation of pulse trains in nonlinear optical fibers through the generalized complex Ginzburg–Landau equation," Phys. Rev. E **80**, 066604 (2009).
39. P. T. Dinda and K. Porsezian, "Impact of fourth-order dispersion in the modulational instability spectra of wave propagation in glass fibers with saturable nonlinearity," J. Opt. Soc. Am. B **27**, 1143–1152 (2010).
40. R. J. R. Vasantha, K. Porsezian, and K. Nithyanandan, "Modulational-instability-induced supercontinuum generation with saturable nonlinear response," Phys. Rev. A **82**, 013825 (2010).
41. C. M. Ngabireng, S. Ambomo, P. T. Dinda, and A. B. Moubissi, "Loss effects in the spectra of polarization modulational instability in weakly birefringent optical fibers," J. Opt. **13**, 085201 (2011).
42. J. H. Li, K. S. Chiang, and K. W. Chow, "Modulation instabilities in two-core optical fibers," J. Opt. Soc. Am. B **28**, 1693–1701 (2011).
43. M. Erkintalo, K. Hammami, B. Kibler, C. Finot, N. Akhmediev, J. M. Dudley, and G. Genty, "Higher-order modulation instability in nonlinear fiber optics," Phys. Rev. Lett. **107**, 253901 (2011).
44. J. H. Li, K. S. Chiang, B. A. Malomed, and K. W. Chow, "Modulation instabilities in birefringent two-core optical fibres," J. Phys. B **45**, 165404 (2012).
45. P. H. Tatsing, A. Mohamadou, C. Bouri, C. G. L. Tiofack, and T. C. Kofané, "Modulation instability in nonlinear positive-negative index couplers with saturable nonlinearity," J. Opt. Soc. Am. B **29**, 3218–3225 (2012).
46. A. Demircan and U. Bandelow, "Analysis of the interplay between soliton fission and modulation instability in supercontinuum generation," Appl. Phys. B **86**, 31–39 (2007).
47. J. C. Travers, "Blue extension of optical fibre supercontinuum generation," J. Opt. **12**, 113001 (2010).
48. E. J. R. Kelleher, J. C. Travers, S. V. Popov, and J. R. Taylor, "Role of pump coherence in the evolution of continuous wave supercontinuum generation initiated by modulation instability," J. Opt. Soc. Am. B **29**, 502–512 (2012).
49. G. P. Agrawal, "Effect of two-photon absorption on the amplification of ultrashort optical pulses," Phys. Rev. E **48**, 2316–2318 (1993).
50. S. Roy, S. K. Bhadra, and G. P. Agrawal, "Femtosecond pulse propagation in silicon waveguides: variational approach and its advantages," Opt. Commun. **281**, 5889–5893 (2008).
51. B. Jalali and S. Fathpour, "Silicon photonics," IEEE J. Lightwave Technol. **24**, 4600–4615 (2006).
52. R. Soref, "The past, present, and future of silicon photonics," IEEE J. Sel. Top. Quantum Electron. **12**, 1678–1687 (2006).
53. H. K. Tsang, C. S. Wong, and T. K. Liang, "Optical dispersion, two-photon absorption, and self-phase modulation in silicon waveguides at 1.5 m wavelength," Appl. Phys. Lett. **80**, 416–418 (2002).
54. L. Yin and G. P. Agrawal, "Impact of two-photon absorption on self-phase modulation in silicon waveguides," Opt. Lett. **32**, 2031–2033 (2007).

55. J. Wen, H. Liu, N. Huang, Q. Sun, and W. Zhao, "Influence of the initial chirp on the supercontinuum generation in silicon-on-insulator waveguide," Appl. Phys. B **104**, 867–871 (2011).
56. D. Castelló-Lurbe, E. Silvestre, P. Andrés, and V. Torres-Company, "Spectral broadening enhancement in silicon waveguides through pulse shaping," Opt. Lett. **37**, 2757–2759 (2012).
57. L. Yin, Q. Lin, and G. P. Agrawal, "Soliton fission and supercontinuum generation in silicon waveguides," Opt. Lett. **32**, 391–393 (2007).
58. M. Lipson, "Guiding, modulating, and emitting light on silicon challenges and opportunities," J. Lightwave Technol. **23**, 4222–4238 (2005).
59. C. M. Ngabireng, P. T. Dinda, A. Tonello, K. Nakkeeran, P. K. A. Wai, and T. C. Kofané, "Radiating and nonradiating behavior of hyperbolic-secant, raised-cosine, and Gaussian input light pulses in dispersion-managed fiber systems," Phys. Rev. E **72**, 036613 (2005).
60. K. Nakkeeran, Y. H. C. Kwan, P. K. A. Wai, A. Labruyere, P. T. Dinda, and A. B. Moubissi, "Analytical design of densely dispersion-managed optical fiber transmission systems with Gaussian and raised cosine return-to-zero Ansätze," J. Opt. Soc. Am. B **21**, 1901–1907 (2004).
61. W. J. Cody, "Rational Chebyshev approximations for the error function,"Math. Comput. **23**, 631–637 (1969).

# Spectral compression in supercontinuum generation through the higher-order nonlinear Schrödinger equation with non-Kerr terms using subnanojoule femtosecond pulses

**Lucien Mandeng Mandeng,[1] Alidou Mohamadou,[2,3,*] Clément Tchawoua,[1] and Hippolyte Tagwo[1]**

[1]*Laboratory of Mechanics, Department of Physics, Faculty of Science, University of Yaoundé I, P.O. Box 812, Yaoundé, Cameroon*

[2]*Nonlinear Dynamics and Complex Systems Group, Faculty of Science, University of Douala, P.O. Box 24157, Douala, Cameroon*

[3]*The Abdus Salam International Centre for Theoretical Physics, P.O. Box 538, Strada costiera 11, I-34014 Trieste, Italy*

**Corresponding author: mohdoufr@yahoo.fr*

Received April 17, 2013; revised July 30, 2013; accepted August 7, 2013; posted August 9, 2013 (Doc. ID 188858); published August 29, 2013

We investigate numerically the supercontinuum generation (SCG) phenomenon, using femtosecond pulses in the subnanoscale of energies through the generalized nonlinear Schrödinger equation that includes non-Kerr terms. Our results with 50 fs pulses in the anomalous dispersion regime show that, in comparison to the single cubic Kerr nonlinearity (CKN) case, the cooperative nonlinearities improve the spectral broadening, while the competing ones compress the spectral SCG bandwidth. Surprisingly, with the reduction of the pulse width, the cooperative nonlinearities induce a spectral compression while the competing ones keep the SCG bandwidth nearly constant from the input to the output of the considered waveguide. The increase of both the energy and the nonlinearity confirms this feature, showing that spectral compression is also obtained in the single CKN case, but less than in the case of cooperative nonlinearities. 

*OCIS codes:* (320.6629) Supercontinuum generation; (060.5530) Pulse propagation and temporal solitons.
http://dx.doi.org/10.1364/JOSAB.30.002555

## 1. INTRODUCTION

The dramatic and extreme pulse spectral broadening induced in an optical waveguide by the combination of dispersive effects and nonlinear effects, such as self-phase modulation, cross-phase modulation, four-wave mixing, and stimulated Raman scattering, so-called supercontinuum generation (SCG), is well known today to be a very useful nonlinear phenomenon [1–6]. Indeed, the SCG has been extensively studied in different kinds of optical systems and has led to such applications as multichannel telecommunication sources (SCG-based wavelength-division multiplexing sources), nonlinear spectroscopy, optical coherence tomography, and optical frequency metrology [4,5,7]. One should note that, to achieve SCG, highly dispersive and nonlinear waveguides are required; these allow the injected optical pulses to excite these effects and therefore to undergo a large spectral broadening. The latter is accompanied by a dramatic generation of side components due to the transfer of energy from the central part of the pulse spectrum to the pedestal part. SCG does not necessarily need to use high power; even low energies could be used with microstructured fibers, such as photonic crystals fibers, tapered fibers, and other highly nonlinear fibers [3]. These optical waveguides in the SCG numerical analysis are always modeled by the generalized nonlinear Schrödinger equation (GNLSE) that links the cubic Kerr nonlinearity (CKN) with self-steepening (SS) and delayed Raman response (DRR) effects [2–6]. Considerable attention is being paid theoretically and experimentally to analyzing the dynamics of optical solitons in optical waveguides. The waveguides used in the picosecond and femtosecond domains in common nonlinear optical systems are usually of the Kerr-type, and consequently the dynamics of light pulses are described by the nonlinear Schrödinger (NLS) family of equations with cubic nonlinear terms. In present day applications, as the intensity of the incident light field becomes stronger, the non-Kerr nonlinearity effect comes into play. Because of this additional effect, the physical features and the stability of the NLS soliton can change. The influence of the non-Kerr nonlinearity on NLS soliton propagation is described by the NLS family of equations with a higher degree of nonlinear terms [8–10]. So, recently, both the solitonic features and the modulational instability mechanism were investigated by Choudhuri and Porsezian in [11], highlighting the effects of the non-Kerr terms through the GNLSE. In fact, they showed that the non-Kerr terms reduce the maximum value of the gain and the bandwidth, thus playing a non-negligible role relative to the CKN. The investigation of this model of the GNLSE is interesting, since it is well known today that the nonlinearity arising due to the fifth-order susceptibility $\chi^5$ can be obtained in many optical materials, such as semiconductor-doped glasses, polydiactylene toluene sulfonate, chalcogenide glasses, and some transparent organic materials [8–11].

In the present work, we investigate the SCG phenomenon through the GNLSE with non-Kerr terms, studying the effect

 

of the cubic–quintic nonlinearity on the SCG spectral bandwidth in the cooperative and the competing cases. Furthermore, we show that with the reduction of the pulse width, the cooperative nonlinearities induce a spectral compression of the SCG bandwidth, while the competing nonlinearities keep the input bandwidth nearly constant during the pulse propagation. A spectral compression is also obtained in the single CKN case when both the energy and the nonlinearity are increased. However, that happens with a magnitude that is less important than that in the case of cooperative nonlinearities. The presentation of this work is designed as follows: in the next section we derive the model equation through which we numerically investigate the SCG phenomenon. In Section 3, we present the results obtained, and a conclusion is stated in the last section of the paper.

## 2. DERIVATION OF SUPERCONTINUUM GENERATION MODEL EQUATION

The GNLSE for the SCG analysis in the single CKN case is commonly written as

$$i\frac{\partial u}{\partial z}+\sum_{k=2}^{M}\frac{(i)^k\beta_k}{k!}\frac{\partial^k u}{\partial T^k}+\gamma\left(1+\frac{i}{\omega_0}\frac{\partial}{\partial T}\right)\left(u(z,T)\int_{-\infty}^{t}R(T-T')|u(z,T')|^2\mathrm{d}t'\right)=-i\frac{\alpha}{2}u, \tag{1}$$

where $u(z,T)$, $z$, $T$, $\beta_k$, $\gamma$, and $\omega_0$ are the slowly varying amplitude of the optical field, the propagation distance, the retarded frame of time, the dispersion coefficient of the $k$th order, the CKN coefficient, and the pump frequency, respectively. The parameter $M$ represents the final order reached in the chromatic dispersion profile of the system. The term $1/\omega_0$ is well known to refer to the SS effect, while the integral and the function $R(t)$ correspond to the DRR. The corresponding form of Eq. (1), which is solved for the SCG by the numerical code previously discussed by Travers in [6], is given by

$$\frac{\partial\tilde{u}'}{\partial z}=i\bar{\gamma}_1\omega\delta_1\exp(-\hat{L}(\omega)z)F\left[u(z,T)\int_{-\infty}^{\infty}R(T')|u(z,T-T')|^2\mathrm{d}T'\right] \tag{2}$$

with $\tilde{u}'$ and $\hat{L}(\omega)$ being the Fourier transform form of $u(z,T)$ and the linear operator, respectively. It is assumed that $\hat{L}(\omega)$ includes the linear losses and the Taylor series expansion of the propagation constant [5]. The transformation $F[\,]$ is the Fourier transform of the block within the squared brackets. $\hat{L}(\omega)$ is defined as shown in [5]. It is assumed that the CKN coefficient $\bar{\gamma}_1$ is nearly nondependent on the frequency, as

$$\bar{\gamma}_1=\frac{n_2 n_0\omega_0}{cn_{\mathrm{eff}}A_{\mathrm{eff}}}, \tag{3}$$

where $n_2$, $n_0$, $n_{\mathrm{eff}}$, $c$, and $A_{\mathrm{eff}}$ are the nonlinear index, the linear refractive index used when determining $n_2$, the effective index of the guided mode, the light speed in vacuum, and the effective core area of the modeled waveguide, respectively.

Considering rather the GNLSE with non-Kerr terms, we have [8–11]

$$i\frac{\partial u}{\partial z}+\sum_{k=2}^{M}\frac{(i)^k\beta_k}{k!}\frac{\partial^k u}{\partial T^k}+\gamma_1|u|^2u-\gamma_2|u|^4u=-i\frac{\alpha}{2}u+i\delta_1\frac{\partial(|u|^2u)}{\partial T}+\delta_2\frac{\partial(|u|^2)}{\partial T}u+i\delta_3\frac{\partial(|u|^4u)}{\partial T}+\delta_4\frac{\partial(|u|^4)}{\partial T}u, \tag{4}$$

where $\gamma_1$, $\gamma_2$, $\alpha$, $\delta_1$, $\delta_2$, $\delta_3$, and $\delta_4$ are the CKN coefficient, the quintic nonlinearity coefficient, the parameter of linear losses, the SS parameter linked to $\gamma_1$, the DRR coefficient corresponding to $\gamma_1$, the SS parameter linked to $\gamma_2$, and the DRR coefficient corresponding to $\gamma_2$, respectively. The parameters $\delta_3$ and $\delta_4$ are the so-called non-Kerr terms because they stem from the quintic nonlinearity. In this work, we assume the quintic nonlinearity coefficient to be $\gamma_2\approx\pm\gamma_1/P_0$, where $P_0$ is the peak power of the pump. The sign of $\gamma_2$ depends on the case where the system has cooperative nonlinearities ($\gamma_1\gamma_2>0$) or competing nonlinearities ($\gamma_1\gamma_2<0$) [12]. The parameter $\delta_1$ is equal to $-1/\omega_0$. In the empirical point-of-view from which we try to construct a model equation that should be solved in the SCG simulations, we assume that, similar to in the single CKN case above, the full case given by Eq. (4) could be written differently as follows:

$$i\frac{\partial u}{\partial z}+\sum_{k=2}^{M}\frac{(i)^k\beta_k}{k!}\frac{\partial^k u}{\partial T^k}=-i\frac{\alpha}{2}u-\gamma_1\left(1+i\delta_1\frac{\partial}{\partial T}\right)\left[u(z,T)\int_{-\infty}^{\infty}R(T')|u(z,T-T')|^2\mathrm{d}T'\right]-\gamma_2\left(1+i\delta_3\frac{\partial}{\partial T}\right)\left[u(z,T)\int_{-\infty}^{\infty}R(T')|u(z,T-T')|^4\mathrm{d}T'\right]. \tag{5}$$

The form obtained for our simulations is given by

$$\frac{\partial\tilde{u}'}{\partial z}=i\omega\bar{\gamma}_1\delta_1\exp(-\hat{L}(\omega)z)F\times\left[u(z,T)\int_{-\infty}^{\infty}R(T')|u(z,T-T')|^2\mathrm{d}T'\right]+i\omega\bar{\gamma}_2\delta_3\exp(-\hat{L}(\omega)z)F\times\left[u(z,T)\int_{-\infty}^{\infty}R(T')|u(z,T-T')|^4\mathrm{d}T'\right], \tag{6}$$

where $\bar{\gamma}_2=\pm\bar{\gamma}_1/P_0$. The effects of $\delta_2$ and $\delta_4$ are assumed to be included within the corresponding block integrals in the right-hand sides of Eqs. (5) and (6). The chromatic dispersion profile being an important part in the SCG, we have chosen to stop at $M=10$ (assuming that the orders beyond ten have a negligible influence on the results). We have also defined the higher-order dispersion coefficients ($k>2$) through the approximated relation derived from the group-velocity dispersion value at the pumping wavelength $\lambda_0$:

$$\beta_k(\lambda_0)\approx(-1)^k\beta_2(\lambda_0)t_0^{k-2}, \tag{7}$$

where $k$ is an integer from 3 to 10, $t_0$ is the pulse width, and $\beta_2$ is the group-velocity dispersion coefficient. We use a sech-type input profile defined as

$$u(z,T) = \sqrt{P_0}\,\mathrm{sech}(T/t_0). \tag{8}$$

The general numerical data used are given as follows: the waveguide length is $L = 1$ cm, the group-velocity dispersion is $\beta_2 = -0.5$ ps$^2$ m$^{-1}$ (defining an anomalous dispersion regime of the modeled waveguide as taken in [11]), and the pumping wavelength is $\lambda_0 = 1550$ nm. The numerical results have been obtained by using a modified version of the MATLAB numerical code provided in [13].

## 3. NUMERICAL RESULTS AND DISCUSSION

Figure 1 has been plotted with the specific parameters of pulse width $t_0 = 50$ fs, the CKN coefficient $\bar{\gamma}_1 = 5$ W$^{-1}$ m$^{-1}$, and the incident pulse energy $E_0 = 0.1$ nJ (subnanojoule pulse). As is seen in this figure, the cooperative nonlinearities [see the solid black curve in Fig. 1(a)] improve the spectral broadening of the SCG spectrum (see the spectral intensity, S.I) as expected. Indeed, these nonlinearities have the same sign and therefore cooperate in order to increase the nonlinearity of the medium. Obviously, the opposite feature is observed for the competing nonlinearities, where the quintic nonlinearity with a negative sign counteracts the effect of the cubic nonlinearity in the spectral broadening of the SCG. As result of this competition, a spectral compression is obtained [see the solid green curve in Fig. 1(a)] in comparison to the CKN case [see the dashed blue curve in Fig. 1(a)]. Figures 1(b)–1(d) show the corresponding spectral power propagation. The reduction of the pulse width in the femtosecond domain by a factor of 5 is depicted in Fig. 2. The spectra presented in this figure were obtained with the same data of Fig. 1, except for the pulse width, which is now $t_0 = 10$ fs. Surprisingly, we notice that instead of enhancing the SCG spectrum broadening (increasing the SCG bandwidth), the cooperative nonlinearities slightly lead to a spectral

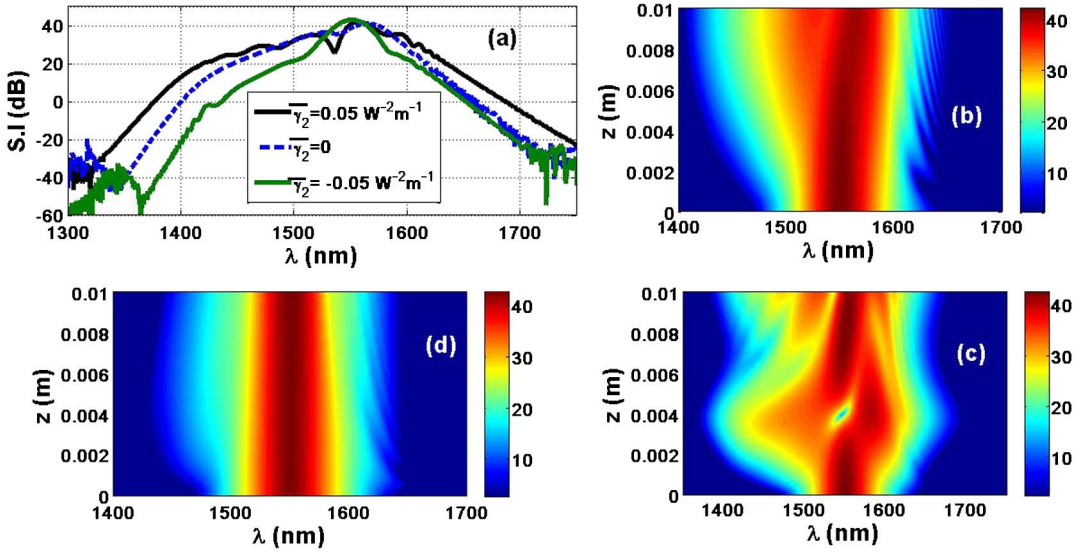


Fig. 1. (a) SCG output spectra. Contour plots of SCG pulse spectral propagation: (b) case of single CKN $\bar{\gamma}_2 = 0$, (c) case of cooperative nonlinearities $\bar{\gamma}_2 = 0.05$ W$^{-2}$ m$^{-1}$, and (d) case of competing nonlinearities $\bar{\gamma}_2 = -0.05$ W$^{-2}$ m$^{-1}$.

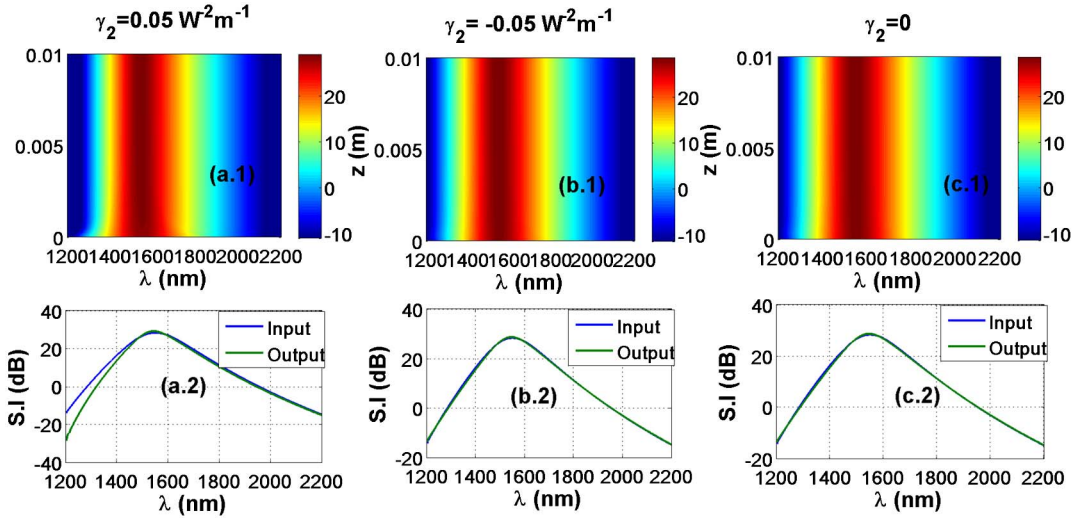


Fig. 2. Row 2, contour plots of SCG pulse spectral propagation and Row 1, SCG input and output spectra: (a.1), (a.2) for the case of cooperative nonlinearities; (b.1), (b.2) for the case of competing nonlinearities; (c.1), (c.2) for the case of single CKN.

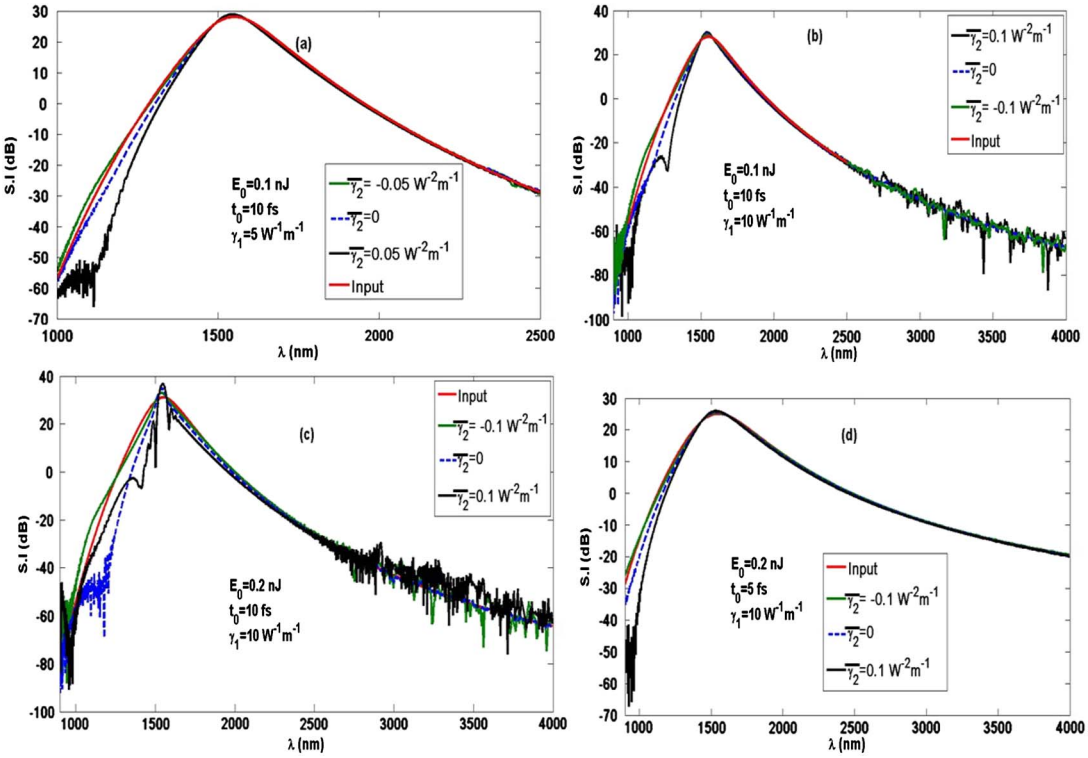


Fig. 3. SCG spectra.

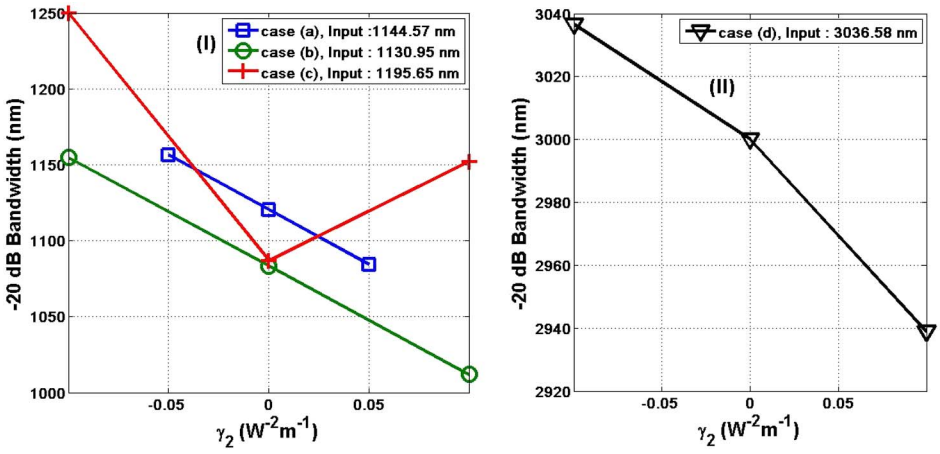


Fig. 4. SCG −20 dB bandwidths corresponding to the cases plotted in Fig. 3. (I) For input bandwidths of approximately, case (a), 1144.57 nm; case (b), 1130.95 nm; and case (c), 1195.65 nm. (II) For case (d), input bandwidth of approximately 3026.58 nm.

compression in the low wavelengths region [see Figs. 2(a.1) and 2(a.2)] while the competing ones keep the SCG spectrum nearly constant [see Figs. 2(b.1) and 2(b.2)]. This last feature is also observed for the CKN case in Figs. 2(c.1) and 2(c.2). Figure 3 shows the spectral compression profile of the SCG. One sees that the cooperative nonlinearities induce the reduction of the pulse width. The three cases of Fig. 2 are presented in Fig. 3(a). Both the increase of the energy on the subnanojoule scale [as in Figs. 3(c) and 3(d)] and the nonlinearity [as in Figs. 3(b)–3(d)] confirm the previous features of the spectral compression obtained for the cooperative nonlinearities. In these figures, the bandwidths remain nearly constant from the input to the output of the considered waveguide for the competing nonlinearities. Figure 4 depicts the SCG bandwidths at −20 dB of the spectral intensity for the cases shown in Fig. 3. Globally, as seen in this figure, the bandwidth decreases when one moves from the competing nonlinearities $\bar{\gamma}_2 < 0$ to the cooperative ones $\bar{\gamma}_2 > 0$. Figure 4(I) shows the spectral compression obtained for the cooperative nonlinearities. For case (a), one obtains 1084.33 nm when the input bandwidth is 1144.57 nm. But for case (b), the compression is observed with an output bandwidth 1011.90 nm for the cooperative nonlinearities when the input bandwidth is 1130.95 nm. The same feature could be observed for case (c) [see the red curve in Fig. 4(I)] with an input bandwidth of 1144.57 nm. For case (b), the compression is observed with an output bandwidth 1011.90 nm for the cooperative nonlinearities when the input bandwidth is 1130.95 nm. The

same feature could be observed for cases (c) [see the red curve in Fig. 4(I)] and (d) [see Fig. 4(II)].

## 4. CONCLUSION

In summary, we have studied the spectral compression in the SCG phenomenon through the GNLSE with non-Kerr terms using a femtosecond sech-type pulse on the subnanojoule scale of energies. Once the SCG model equation was derived, we investigated the analysis of the spectra obtained. The results with 50 fs pulses in the anomalous dispersion regime have shown that, in comparison to the single CKN case, the cooperative nonlinearities improve the spectral broadening, while the competing ones reduce the spectral SCG bandwidth. Surprisingly, we have obtained the opposite feature when reduction of the pulse width was considered. In this last case, the cooperative nonlinearities induce a spectral compression when the competing ones keep the SCG bandwidth nearly constant from the input to the output of the considered waveguide. Increases of both the energy and the nonlinearity have confirmed this feature, showing that the spectral compression is also obtained in the single CKN case but less so than in the case of cooperative nonlinearities. Assuming that this modified GNLSE with non-Kerr terms linked to the quintic nonlinearity could model a highly nonlinear optical waveguide for the achievement of the SCG phenomenon, the values of the energy and the pulse width should be chosen taking into account the conditions where the spectral compression occurs.

## ACKNOWLEDGMENTS

L. M. Mandeng acknowledges Amine B. Salem (from the Engineering School of Communication of Tunis, University of Carthage, Tunisia) for useful comments, Dr. Pavel Polynkin (from the College of Optical Sciences, University of Arizona, USA) for help on numerical simulations, and Dr. Jean-Pascal Eloundou and Dr. Serge Ibraid Fewo for their support.

## REFERENCES

1. R. R. Alfano, *The Supercontinuum Laser Source* (Springer-Verlag, 1989).
2. J. M. Dudley, G. Genty, and S. Coen, "Supercontinuum generation in photonics crystal fiber," Rev. Mod. Phys. **78**, 1135–1184 (2006).
3. G. P. Agrawal, *Nonlinear Fiber Optics*, 4th ed. (Academic, 2007).
4. J. M. Dudley and J. R. Taylor, "Ten years of nonlinear optics in photonic crystal fiber," Nat. Photonics **3**, 85–90 (2009).
5. J. M. Dudley and J. R. Taylor, *Supercontinuum Generation in Optical Fibers*, 1st ed. (Cambridge University Press, 2010).
6. J. C. Travers, "Blue extension of optical fibre supercontinuum generation," J. Opt. **12**, 113001 (2010).
7. G. P. Agrawal, "Supercontinuum generation," in *Applications of Nonlinear Fiber Optics* (Academic, 2008), pp. 414–431.
8. R. Radhakrishnan, A. Kundu, and M. Lakshmanan, "Coupled nonlinear Schrödinger equations with cubic-quintic nonlinearity: integrability and soliton interaction in non-Kerr media," Phys. Rev. E **60**, 3314–3323 (1999).
9. R. V. J. Raja, K. Porsezian, S. K. Varshney, and S. Sivabalan, "Modeling photonic crystal fiber for efficient soliton pulse propagation at 850 nm," Opt. Commun. **283**, 5000–5006 (2010).
10. A. Choudhuri and K. Porsezian, "Dark-in-the-bright solitary wave solution of higher-order nonlinear Schrödinger equation with non-Kerr terms," Opt. Commun. **285**, 364–367 (2012).
11. A. Choudhuri and K. Porsezian, "Impact of dispersion and non-Kerr nonlinearity on the modulational instability of the higher-order nonlinear Schrödinger equation," Phys. Rev. A **85**, 033820 (2012).
12. K. Senthilnathan, Q. Li, K. Nakkeeran, and P. K. A. Wai, "Robust pedestal-free pulse compression in cubic-quintic nonlinear media," Phys. Rev. A **78**, 033835 (2008).
13. J. C. Travers, M. H. Frosz, and J. M. Dudley, "Nonlinear fibre optics overview," in *Handbook of Supercontinuum Generation in Optical Fibers*, J. M. Dudley and J. R. Taylor, eds. (Cambridge University, 2010), Chap. 3, pp. 46–49.

Journal of Modern Optics
Publication details, including instructions for authors and subscription information:
http://www.tandfonline.com/loi/tmop20

# Dynamics of linear compression of chirped femtosecond optical pulses under fourth-order dispersion

Lucien Mandeng Mandeng[a], Serge Ibraid Fewo[a], Clément Tchawoua[a] & Timoléon Crépin Kofané[a]

[a] Faculty of Science, Laboratory of Mechanics, Department of Physics, University of Yaoundé I, Yaoundé, Cameroon.

Published online: 10 Apr 2014.

To cite this article: Lucien Mandeng Mandeng, Serge Ibraid Fewo, Clément Tchawoua & Timoléon Crépin Kofané (2014): Dynamics of linear compression of chirped femtosecond optical pulses under fourth-order dispersion, Journal of Modern Optics, DOI: 10.1080/09500340.2014.906667

To link to this article: http://dx.doi.org/10.1080/09500340.2014.906667

*Journal of Modern Optics*, 2014
http://dx.doi.org/10.1080/09500340.2014.906667

Taylor & Francis
Taylor & Francis Group

# Dynamics of linear compression of chirped femtosecond optical pulses under fourth-order dispersion

Lucien Mandeng Mandeng, Serge Ibraid Fewo*, Clément Tchawoua and Timoléon Crépin Kofané

*Faculty of Science, Laboratory of Mechanics, Department of Physics, University of Yaoundé I, Yaoundé, Cameroon*

(*Received 19 July 2013; accepted 7 March 2014*)

In a linear dispersive optical medium under fourth-order dispersion (FOD), we study the dynamics of the chirped pulse compression with the help of trial Gaussian and raised-cosine (RC) ansätze pulses. The analysis based on the variational approach leads to the occurrence of compression conditions, highlighting the cases where both the group-velocity dispersion (GVD) and the chirp could have the same sign or the case where both the FOD and the GVD have the same sign. Furthermore, we show that the compression process is dependent on the considered input profile. Particularly, a condition supposing that the GVD, the FOD and the chirp have the same sign leads to a compression only for the RC pulse in comparison to the previous results obtained for the Gaussian pulse. Numerical simulations, which confirm these features, are presented for the 380-fs input pulses undergoing 0.00086 $ps^4/Km$ value in the FOD.

**Keywords:** chirped pulses; pulse compression; group-velocity dispersion; fourth-order dispersion; variational approach



## 1. Introduction

The growing trend on high-data-rate optical transmission because of the useful large bandwidth associated has contributed to the studies of ultrashort optical pulses. The numerous applications of ultrashort pulses in areas such as telecommunication, ultrafast physical process, infrared time-resolved spectroscopy, sampling systems, etc., reveal the indispensable role of such pulses [1–4]. The difficult generation in practice of such pulses with the current laser sources and amplifiers [4] has motivated some researches on pulse compression mechanism. This phenomenon in optical fibers consists in the reduction of the width of an optical pulse during its transmission. It can be classified into two categories : linear and nonlinear pulse compression. In the linear compression, the input pulse chirped positively or negatively, experiences a group-velocity dispersion (GVD) of opposite sign with the chirp parameter and then get compressed. The dispersive delay line or grating-pair compressors allow realizing this linear compression [3,4]. In the nonlinear pulse compression with the interaction between the nonlinearity as self-phase modulation and the GVD, optical pulses get compressed in the sense of the soliton feature or adiabatic effect [1,3–5]. It has been experimentally conducted for the soliton-effect compressors [1,3]. From these basic concepts both in linear and nonlinear cases, some optical pulse compression techniques have been developed such as the cross-phase modulation technique [3,6,7], the fiber polarization technique [8], the use of a tapered microstructure optical fiber with four layers of holes [9], etc. Focusing on the linear case, Capmany et al. [10] presented in a high-speed optical time-division multiplexed transmission line under fourth-order dispersion (FOD) near the vanished values of GVD and third-order dispersion (TOD), a Gaussian pulse compression with a negative chirp and a positive FOD. In a following work [11], they presented an analysis of a chirped Gaussian pulse using a combination of Marcuse's formalism [12] and Amemiya's method [13], and showed that pulse broadening and compression arise as a result of the interaction between dispersion orders of same parity. More specifically, they demonstrated that, when dispersion orders of same parity interact, one obtains pulse compression if they are signed oppositely; otherwise pulse broadening is obtained. This is by assuming that the source chirp interacts only with even dispersion terms to yield pulse broadening or compression. In the present work, we present the dynamics of pulse compression and demonstrate the possibility to get a linear optical pulse compression for a pulse chirp having the same sign with the GVD, this being obtained in the presence of the FOD parameter of the same sign. This result, therefore, contrasts with the previous rule described in [11], and underlines an important feature on the impact of the FOD parameter. It emerges from this

*Corresponding author. Email: sergefewo@yahoo.fr

analysis that the conditions where linear chirped optical pulse compression based on trial function profiles occur are more extended than those previously reported [2–4,10,11]. Furthermore, our analysis presents analytical relations between the dispersion lengths associated with the broadening/compression occurrence conditions. The obtained results recover and complete some aspects of pulse compression of very recent works as presented by Agrawal [2,3] for the case of a chirped Gaussian pulse. The study related to the raised-cosine (RC) pulse has never been reported earlier to our knowledge. This feature is interesting and this is the first time that it is presented. The demonstration is conducted globally through the well-known Lagrangian variational approach (LVA) [2,14] on the chirped Gaussian and RC profiles. The LVA has been shown to be very useful when laser beams self-focusing were investigated [14]. In addition, Anderson showed that the determination of pulse propagation characteristics, such as width, energy, chirp and phase, could be done with this method. However, some shortcomings of the LVA exist. Sure enough, the use of trial functions through the LVA leads to forgetting of the changes in the pulse shape during the propagation even if its main parameters vary with the length parameter [14]. Furthermore, in a nonlinear pulse propagation inside an optical fiber, some effects such as higher order solitons splitting are unreachable with the LVA.

The LVA has made its proofs in the description of pulse compression mechanism and other interesting features [2,3,14]. The paper is designed as follows: in Section 2, we present the model and analytical studies while Section 3 is devoted to numerical results and discussion. The last section concludes the paper.

## 2. Analytical treatment of the model

Near the zero-dispersion wavelength of a single-mode fiber (SMF), the GVD nearly vanishes and one should take into account the effect of the odd order of dispersion as the third-order dispersion (TOD) [2]. On the other hand, as discussed in [2,15], in WDM systems special fibers have been developed, the so-called "dispersion-flattened fibers" in which the TOD is nearly equal to zero while the GVD remains finite and one should include the FOD effect to describe the dynamics inside the fiber. The chromatic dispersion profile of such fiber could be seen in [15] in comparison to those of standard SMFs and dispersion-shifted fibers. It is observed that the slope of the dispersion parameter or GVD around the communication wavelength of 1550 nm is nearly equal to zero. This shows consequently that the TOD effect vanishes in such fibers as mentioned above. We consider a fiber of this kind being manufactured to such an extent that the system is nearly linear. The linear equation describing the propagation of optical pulses in such case is the following [1–3]:

$$i\frac{\partial u}{\partial z}+\sum_{k=2}^{4}\frac{(i)^k\beta_k}{k!}\frac{\partial^k u}{\partial T^k}=0, \tag{1}$$

where $u$ and $\beta_k$ represent the dimensionless pulse amplitude, the dispersion term of the $k$th order. One should also note that odd-order dispersions such as TOD do not compress the pulse but they add rather asymmetric oscillating tails in the pulse profile [2,11,16]. So, they are not really important when one studies the variation of the pulse width in terms of compression or broadening. The Lagrangian density function corresponding to Equation (1) is given as:

$$L_d=\frac{i}{2}\left(u^*\frac{\partial u}{\partial z}-u\frac{\partial u^*}{\partial z}\right)-\sum_{k=2}^{4}\frac{(i)^k\beta_k}{k!}\frac{\partial^{k-1}u}{\partial T^{k-1}}\frac{\partial u^*}{\partial T}, \tag{2}$$

Our study is conducted using the chirped Gaussian and RC profiles given, respectively, by [2,17,18]:

$$u(z,T)=A_*\exp\left(-\frac{1+iC_*}{2}\left(\frac{T}{T_*}\right)^2+i\phi_*\right) \tag{3}$$

and

$$u(z,T)=\frac{A_*}{2}\left[1+\cos\left(\frac{\pi T}{T_*}\right)\right]\exp\left(i\frac{C_*}{2}\left(\frac{T}{T_*}\right)^2+i\phi_*\right) \tag{4}$$

where $A_*$, $T_*$, $C_*$ and $\phi_*$ are the amplitude, the width, the chirp and the phase, respectively. The parameters $T$ and $z$ are the retarded time and the propagation length, respectively. The use of the RC profile in this study stems from the difficulty that one often has to generate Gaussian-shaped pulses suitable for high bit rate. Indeed, the output of the commonly used Mach–Zehnder pulse carvers is rather close to RC-profiled pulses [17,18]. So, the RC pulse could model a rather realistic case in an experiment related to the analysis presented in this work. We plot these two profiles in Figure 1. Performing the Euler–Lagrange equation for relevant parameters of the Gaussian and the RC pulses, we obtain the dynamical equations, respectively, as:

$$\begin{aligned}
\frac{dA_*}{dz}&=-\frac{A_*}{2}\left\{\frac{C_*}{T_*^2}\left[\beta_2+\frac{(1+C_*^2)}{4T_*^2}\beta_4\right]\right\}\\
\frac{dT_*}{dz}&=\frac{C_*}{T_*}\left[\beta_2+\frac{(1+C_*^2)}{4T_*^2}\beta_4\right]\\
\frac{dC_*}{dz}&=\frac{(1+C_*^2)}{T_*^2}\left[\beta_2+\frac{(1+C_*^2)}{4T_*^2}\beta_4\right]\\
\frac{d\phi_*}{dz}&=\frac{\beta_2}{2T_*^2}+\frac{(1+C_*^2)(3-C_*^2)}{32T_*^4}\beta_4
\end{aligned} \tag{5}$$

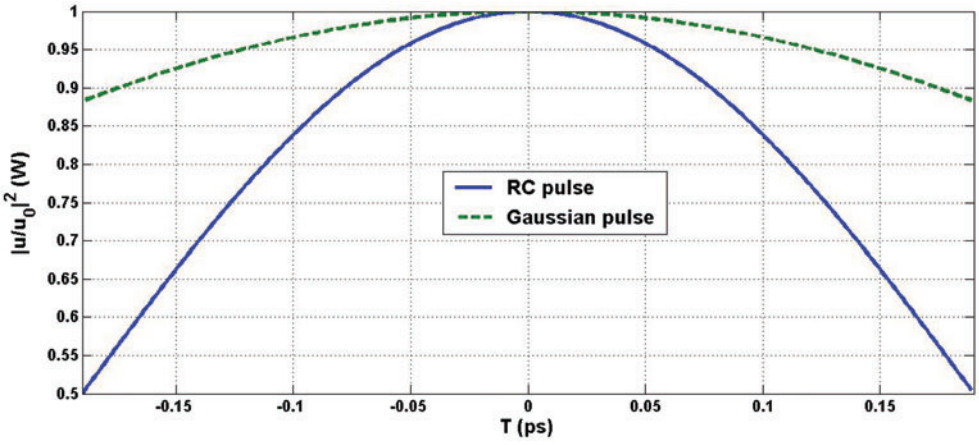


Figure 1. Illustration of the two input profiles: $T_0 = 0.38$ ps. (The colour version of this figure is included in the online version of the journal.)



and

$$\begin{aligned}
\frac{dA_*}{dz} &= -\frac{A_*}{2}\left\{\frac{C_*}{T_*^2}\left[-\beta_2 + \frac{\beta_4}{12a_1T_*^2}(a_3 + 2a_4C^2)\right]\right\}\\
\frac{dT_*}{dz} &= \frac{C_*}{T_*}\left[-\beta_2 + \frac{\beta_4}{12a_1T_*^2}\left(a_3 + 2a_4C_*^2\right)\right]\\
\frac{dC_*}{dz} &= \frac{1}{a_1T_*^2}\left[-\beta_2\left(\frac{\pi^2}{2} + C_*^2\right)\right.\\
&\qquad \left. + \frac{\beta_4}{6T_*^2}\left(-\frac{\pi^4}{4} + a_3C^2 + a_4C^4\right)\right]\\
\frac{d\phi_*}{dz} &= \frac{1}{2a_2T_*^2}\left[\pi^2\beta_2 + \frac{\beta_4}{12T_*^2}\left(\frac{4\pi^4}{3} - a_3C_*^3 + a_4C_*^4\right)\right]
\end{aligned} \tag{6}$$

where $a_k$ with $k = 1, 2, \ldots 4$ are constants defined as:

$$\begin{aligned}
a_1 &= (-64 - 2\pi + 8\pi^2 + \pi^3)/8\pi^3\\
a_2 &= (8 + 3\pi)/2\pi\\
a_3 &= -\frac{1}{4\pi}(-48 + 6\pi^2 + \pi^3)\\
a_4 &= -\frac{1}{160\pi^5}(15360 + 120\pi - 1920\pi^2 - 20\pi^3\\
&\quad + 40\pi^4 + 3\pi^5)
\end{aligned} \tag{7}$$

We noted that in the absence of FOD, we obtained the previously well-known pulse characteristics in the case of single GVD. The phase is often disregarded because of its negligible role in pulse propagation characteristics. The system being linear, the propagation of the input pulse is only affected by the dispersive properties of the waveguide interacting with the intrinsic characteristics of the considered pulse. When the chosen pulses are different, the obtained growth equations are quite different also and then the related results arise from the compression process. Equations (5)–(6) are first-order differential equations of the relevant parameters (amplitude, width, chirp and phase) of the Gaussian and RC pulses. These equations allow obtaining the evolution of these parameters as the pulse is propagating inside the medium in function of the distance z.

Recalling that for the Gaussian pulse, the quantity $(1 + C_*^2)/T_*^2$ is assumed to be equivalent to the spectral width that is quasi-constant in the linear medium [2,3], we make some simplifications on Equation (5). The same assumption applied on the RC pulse yields to set $((\pi^2/2) + C_*^2)/a_1T_*^2$ and $((-\pi^4/4) + a_3C_*^2 + a_4C_*^4)/6a_1T_*^4$ as constants. We set the following parameters for the Gaussian pulse:

$$\begin{aligned}
\Delta_0 &= \beta_2 + \frac{(1 + C_0^2)}{4T_0^2}\beta_4\\
\Delta &= \frac{(1 + C_0^2)}{T_0^2}\Delta_0.
\end{aligned} \tag{8}$$

We set also $\Delta_1$ and $\Delta_2$ for the RC pulse as:

$$\begin{aligned}
\Delta_1 &= -\beta_2 + \tfrac{\beta_4}{12a_1T_0^2}\left(a_3 + 2a_4C_0^2\right)\\
\Delta_2 &= \tfrac{1}{a_1T_0^2}\left[-\beta_2\left(\tfrac{\pi^2}{2} + C_0^2\right)\right.\\
&\qquad \left. + \tfrac{\beta_4}{6T_0^2}\left(-\tfrac{\pi^4}{4} + a_3C_0^2 + a_4C_0^4\right)\right],
\end{aligned} \tag{9}$$

assuming that the parameters $C_0$ and $T_0$ are the initial values of the chirp $C_*$ and width $T_*$, respectively. We define $L_{GVD} = T_0^2/|\beta_2|$ and $L_{FOD} = T_0^4/|\beta_4|$ as the GVD and the FOD lengths, respectively. Then, we integrate the width and the chirp growth equation above for each pulse. The analytically approximated chirp expressions are given by:

$$\begin{aligned}
C_G(z) &= C_0 + z\Delta\\
C_{\mathrm{RC}}(z) &= C_0 + z\Delta_2.
\end{aligned} \tag{10}$$

where the subscripts G and RC correspond to the Gaussian and RC input pulses, respectively. For each corresponding dynamical equation of width, we obtained easily the analytical expressions of widths in function of the distance z:

$$T_G(z) = T_0\left[1 + 2\frac{\Delta_0}{T_0^2}\left(C_0 + \frac{\Delta}{2}z\right)z\right]^{\frac{1}{2}}$$
$$T_{\mathrm{RC}}(z) = T_0\left[1 + 2\frac{\Delta_1}{T_0^2}\left(C_0 + \frac{\Delta_2}{2}z\right)z\right]^{\frac{1}{2}} \quad (11)$$

The same process can be done with the amplitude, and therefore leads to:

$$A_G(z) = A_0 \exp\left[-\frac{\Delta_0}{2T_0^2}\left(C_0 + \frac{\Delta}{2}z\right)z\right]$$
$$A_{\mathrm{RC}}(z) = A_0 \exp\left[-\frac{\Delta_1}{2T_0^2}\left(C_0 + \frac{\Delta_2}{2}z\right)z\right], \quad (12)$$

with $A_0$ is the initial value of the amplitude. For the Gaussian pulse, the conditions of compression are obtained for $\Delta < 0$ and $C_0 > 0$ as:

$$C_0 > 0, \beta_2, \beta_4 < 0 \quad (13a)$$
$$L_{\mathrm{FOD}} > \frac{1+C_0^2}{4}L_{\mathrm{GVD}}, C_0 > 0, \beta_2 < 0, \beta_4 > 0 \quad (13b)$$
$$L_{\mathrm{FOD}} < \frac{1+C_0^2}{4}L_{\mathrm{GVD}}, C_0 > 0, \beta_2 > 0, \beta_4 < 0, \quad (13c)$$

For the negative value of the initial chirp $C_0 < 0$, we have the opposite conditions:

$$C_0 < 0, \beta_2, \beta_4 > 0 \quad (14a)$$
$$L_{\mathrm{FOD}} > \frac{1+C_0^2}{4}L_{\mathrm{GVD}}, C_0 < 0, \beta_2 > 0, \beta_4 < 0 \quad (14b)$$
$$L_{\mathrm{FOD}} < \frac{1+C_0^2}{4}L_{\mathrm{GVD}}, C_0 < 0, \beta_2 < 0, \beta_4 > 0. \quad (14c)$$

The maximal pulse compression length for the Gaussian pulse is $L_{mc} = 2C_0/|\Delta|$ [2,3]. It is also important to remind that the basic idea behind optical pulse compression is borrowed from chirp radar, where chirped pulses at microwave frequencies are compressed by passing them through a dispersive delay line [19].

In the absence of FOD, Equations (13a), (13b), (14a) and (14b) are the well-known conditions for the linear pulse compression induced by chirp in the single GVD case requiring that $\beta_2 C_0 < 0$ [2,3]. Equations (13c) and (14c) may lead to pulse broadening in the absence of FOD as previously known. Nevertheless, the FOD breaks this observation and we obtain a pulse compression when the additive conditions on dispersion lengths are verified. The obtained linear pulse compression when both the chirp and the GVD have the same sign or both the GVD and the FOD have the same sign is the main feature observed, which is due to the presence of FOD. This result encompasses the rules mentioned in [2,3,11]. In fact, they predicted a pulse broadening when $\beta_2\beta_4 > 0$ ($\beta_2, \beta_4 < 0$ or $\beta_2, \beta_4 > 0$ verified by Equations (13a) and (14a)) and a linear compression when $\beta_2\beta_4 < 0$ (verified by Equations (13b), (13c), (14b) and (14c)). The results obtained in this work include the basic theory described in [2,3] and the rules set in [11]. This combination is possible with additional dispersion lengths conditions as seen in Equations (13b), (13c), (14b) and (14c). The study demonstrates that it is possible to obtain a Gaussian pulse compression with the GVD having the same sign with FOD, by adding a chirp of opposite value to the GVD and FOD. On the other hand, it is possible to compress a Gaussian pulse using an optical waveguide having a GVD which has the same sign as the chirp; in this case, one requires an opposite value of FOD.

For the RC pulse, one may notice that constants $a_3$ and $a_4$ are negative as $a_3 = -|a_3|$ and $a_4 = -|a_4|$ while $a_1$ is positive. Therefore, with $\Delta_1 < 0$ the compression conditions are given for initial positive chirp value by:

$$C_0 > 0, \beta_2, \beta_4 > 0 \quad (15a)$$
$$V_1' < L_{\mathrm{FOD}} < V_2', \Delta_2 > 0, C_0 > 0 \text{ or } C_0 < 0, \beta_2 < 0, \beta_4 > 0 \quad (15b)$$
$$L_{\mathrm{FOD}} < V_1', \Delta_2 < 0, C_0 > 0, \beta_2 < 0, \beta_4 > 0 \quad (15c)$$
$$L_{\mathrm{FOD}} > V_2', \Delta_2 < 0, C_0 > 0, \beta_2 > 0, \beta_4 < 0 \quad (15d)$$

where

$$V_1' = \frac{\left(\frac{\pi^4}{4} + |a_3|C_0^2 + |a_4|C_0^4\right)}{6\left(\frac{\pi^2}{2} + C_0^2\right)}L_{\mathrm{GVD}} \quad (16)$$

and

$$V_2' = \frac{\left(|a_3| + 2|a_4|C_0^2\right)}{12a_1}L_{\mathrm{GVD}} \quad (17)$$

Similarly to the previous Gaussian case, for $\Delta_1 > 0$ we use the opposite relations of Equation (15) and the maximal length for compression is always given by $2C_0/|\Delta_2|$. The feature previously mentioned above for the Gaussian pulse is also pointed out for the RC pulse as seen in Equations (15b), (15c) and (15d). A new condition given by (15a) shows that it is possible to get the RC pulse linear compression with the chirp, the GVD and the FOD all having the same sign. This condition contrasts with the previous rules known in [2,3,11] and those mentioned in this work on Equations (13), (14), (15b), (15c) and (15d). This means that the linear compression conditions are greatly dependent on the input optical pulse profile.

Using rather the Fourier transform method of Marcuse [12], one should obtain the pulse amplitude at the distance z as:

$$u(z,T) = \frac{T_0}{\sqrt{2\pi}} \times \int_{-\infty}^{+\infty} \exp\left\{\frac{\omega^2}{2}\left[-T_0^2 + iz(\beta_2 + \frac{\beta_4}{12}\omega^2)\right] - i\omega T\right\}d\omega. \quad (18)$$

It yields a special complex integral in the form of:

$$\int_{-\infty}^{+\infty} \exp(ax^4 + bx^2 + cx)dx, \quad (19)$$

where $a = i\beta_4 z/24$, $b = (i\beta_2 z/2) - (T_0^2/2)$ and $c = -iT$. As this primitive analytical function from this integral is not easily reachable, one should use some special mathematical assumptions to solve it as done by Amemiya

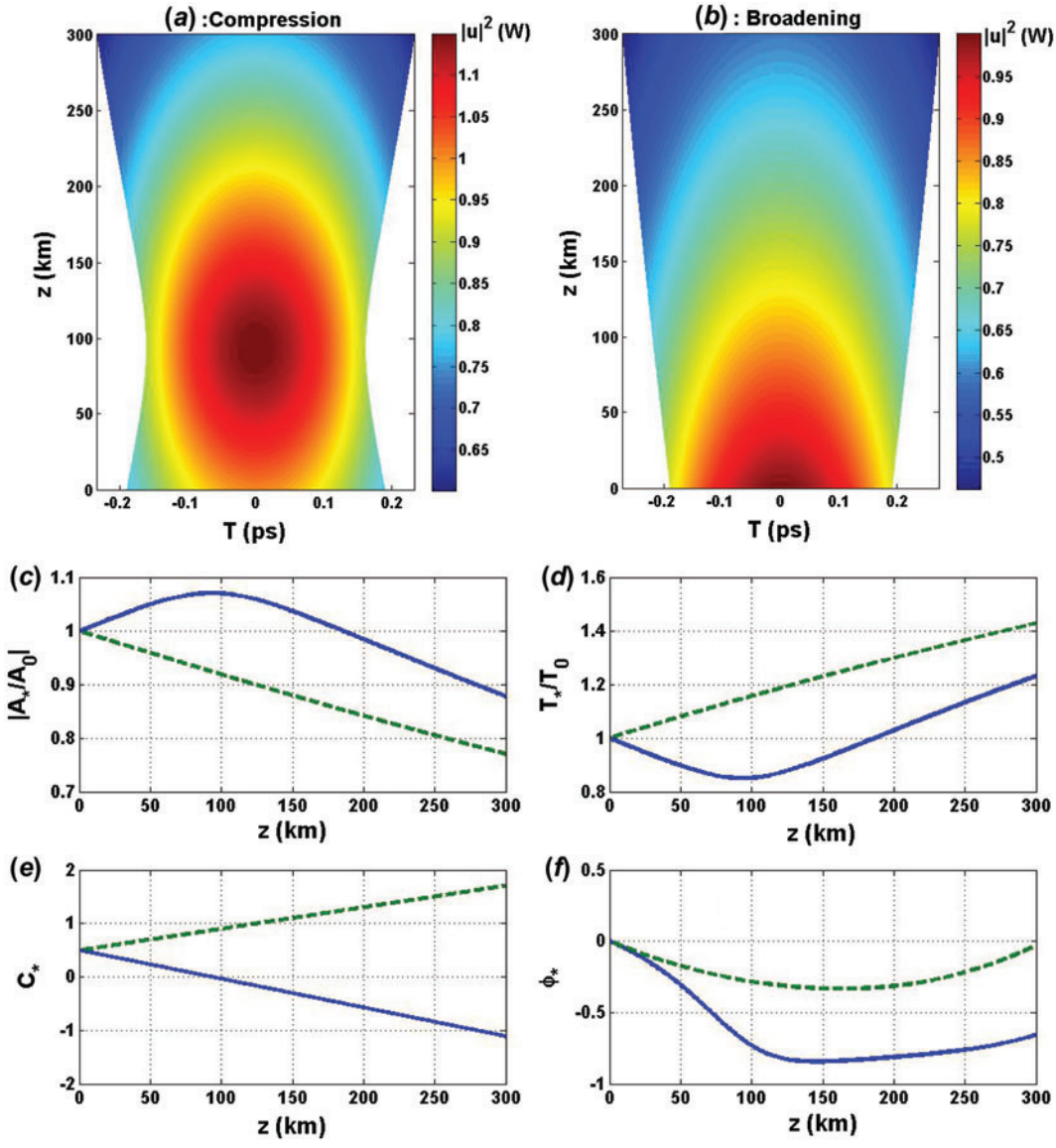


Figure 2. (*a*) contour plot of the chirped Gaussian pulse compression of Equation (13c): assuming the dispersion lengths condition, $L_{GVD} = 120.33$ km, $L_{mc} = 186.2075$ km, MPCP = 10.55%; (*b*) contour plot of the chirped Gaussian pulse broadening as expected in previous studies in the absence of verified conditions on dispersion lengths, $L_{GVD} = 62.78$ km. For the frames (*c*), (*d*), (*e*) and (*f*): normalized amplitude, normalized width, chirp and phase respectively (blue solid curves correspond to the case of Figure (2(*a*)) and green dashed curves for the case of Figure (2(*b*)). General parameters $\beta_4 = -0.00086$ ps$^4$/km, $L_{FOD} = 24.24$ km, $T_0 = 0.38$ ps, $T^{min} = 0.3399$ ps, $C_0 = 0.5$. (The colour version of this figure is included in the online version of the journal.)

or Capmany et al. [11,13]. After that, one brings out the analytical varying width as done for the single GVD case to obtain a similar relation of Equation (11). This work has been already done in these references. The variational approach being also validated as a real and efficient means to study the pulse compression mechanism as discussed by Anderson [14], Agrawal [2], Konar and Biswas [20], Roy et al. [21] and recently by Mandeng and Tchawoua [22,23], there is no question of using it in the considered model. In brief, after Equations (5)–(17), we find, therefore, the same results as discussed by Capmany et al. [11]: the even-order dispersion terms as the GVD and FOD interact to conduct the compression or broadening of the pulse. The variation allows generalizing these results highlighting the dependence of the dispersion lengths $L_{\mathrm{GVD}}$ and $L_{\mathrm{FOD}}$ on these compression conditions.

On the other hand, it is well known today that, in the case of dispersive lossless linear medium, the pulse changes only following its characteristics, but the initial shape remains the same [2,3,24]. This physical statement corresponds directly

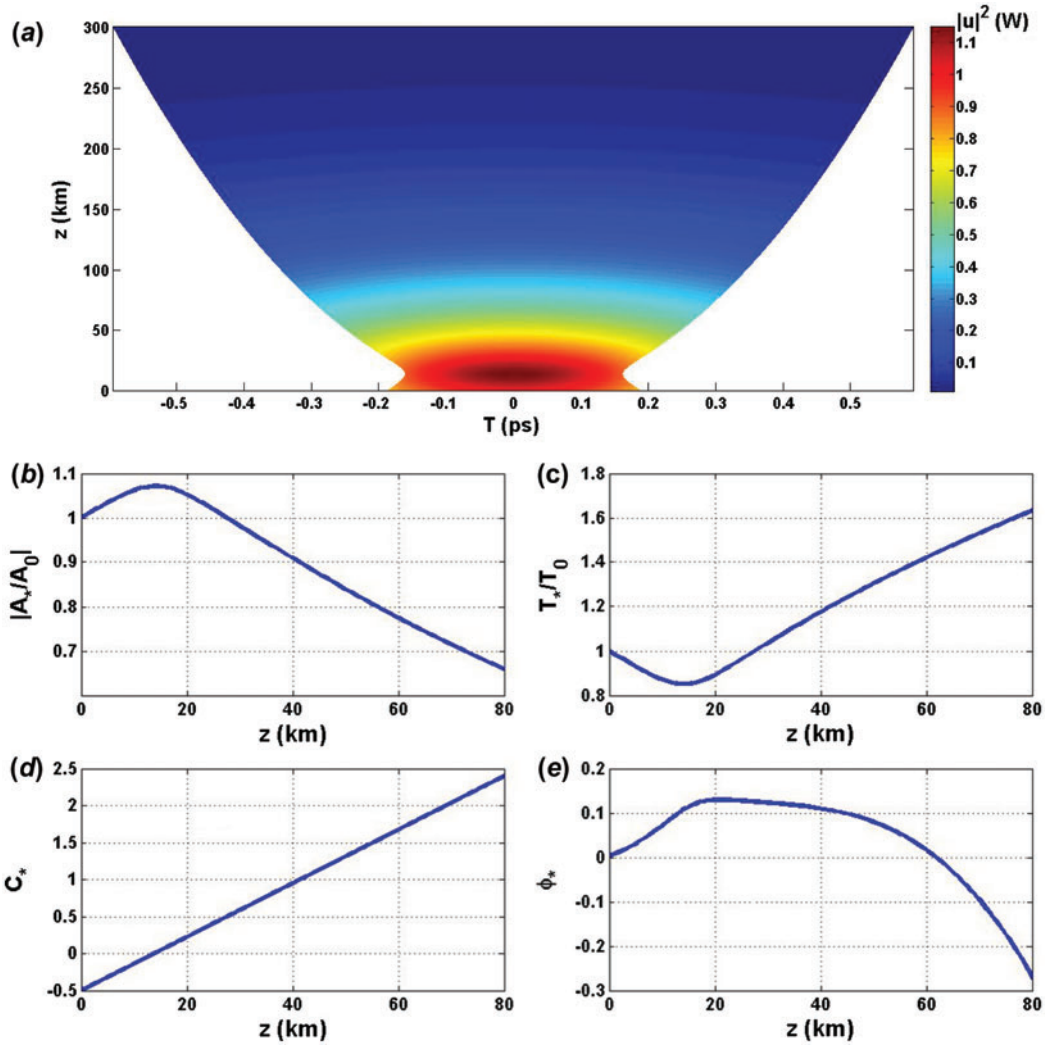


Figure 3. (*a*) Contour plot of the pulse as described by Equations (14a); (*b*), (*c*), (*d*), (*e*) Evolution of the normalized pulse parameters versus the propagation distance z with parameters $\beta_4 = 0.00086\,\mathrm{ps}^4/\mathrm{km}$, $L_{\mathrm{FOD}} = 24.24$ km, $T_0 = 0.38$ ps, $T^{\min} = 0.3399$ ps, $C_0 = -0.5$, $\beta_2 = 0.0023\,\mathrm{ps}^2/\mathrm{km}$, $L_{\mathrm{mc}} = 27.5863$ km. (The colour version of this figure is included in the online version of the journal.)

to the LVA. Therefore, if the initial shape is Gaussian, the output will be a Gaussian form but with characteristics changed according to the dispersive effects of the medium. The same thing happens for the RC profile.

## 3. Numerical results and discussion

The linear pulse compression as described by Equation (13c) is numerically presented in Figure 2, where we have plotted the contour plots of the Gaussian pulse propagation (see Figure 2(*a*) and (*b*)) and the corresponding normalized amplitudes, normalized widths, chirps and phases in function of the distance of propagation z (see Figure 2(*c*)–(*f*)). The phase term on the dynamics does not have a real impact. Its representation on Figure 2 is done as a pulse characteristic even if it does not affect really the pulse energy propagation. The case where we respect the dispersion lengths condition of Equation (13c) leads to pulse compression (Figure 2(*a*): $L_{GVD} = 6L_{FOD}/(1 + C_0^2)$) while the case where we ignore this condition leads to Gaussian pulse broadening (Figure 2(*b*): $L_{GVD} = 3.2L_{FOD}/(1 + C_0^2)$). Figures 2(*c*)–(*f*) present the corresponding pulse characteristics of the propagating optical signals: solid lines for the case of Figure 2(*a*) and dashed lines for the case of Figure 2(*b*). The values of the initial width and the FOD are the same as in [10], with positive values of the chirp and GVD. The maximal pulse compression percentage (MPCP) for the Gaussian pulse is given by the relation:

$$\mathrm{MPCP} = 100\left\{1 - \left[1 - \frac{\Delta_0}{\Delta}\left(\frac{C_0}{T_0}\right)^2\right]^{1/2}\right\} \qquad (20)$$

We obtain a MPCP of 10.55% in the pulse compression of Figure 2(*a*). It is clearly seen in Figure 2 that when

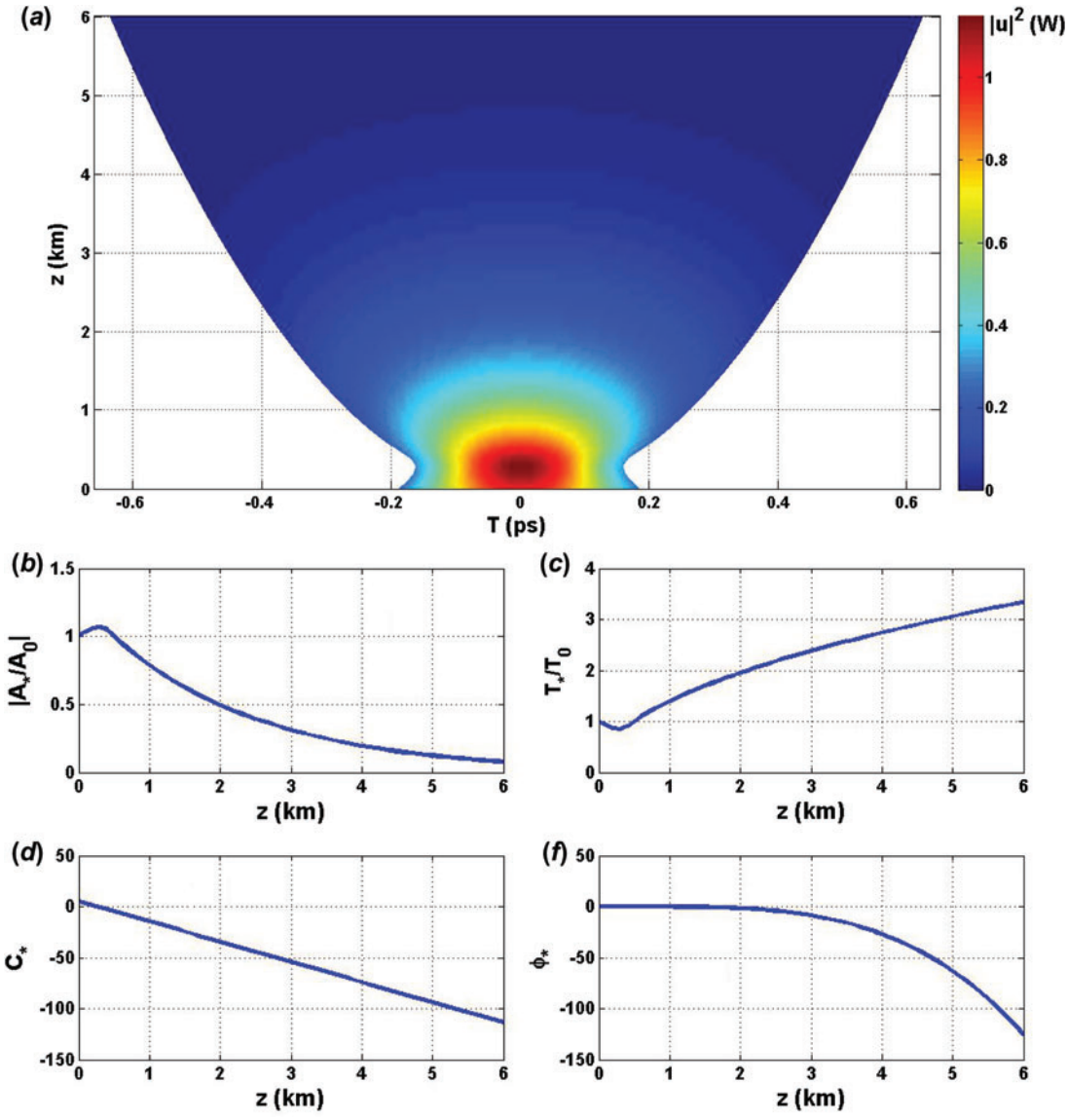


Figure 4. (*a*) Contour plot of the pulse as described by Equations (15a); (*b*), (*c*), (*d*), (*e*) Evolution of the normalized pulse parameters versus the propagation distance z with parameters $\beta_4 = 0.00086\text{ps}^4/\text{km}$, $L_{\text{FOD}} = 24.24$ km, $T_0 = 0.38$ ps, $T^{\min} = 0.3588$ ps, $C_0 = 5$, $\beta_2 = 0.0113\,\text{ps}^2/\text{km}$, MPCP = 5.5767%, $L_{\text{mc}} = 0.5041$ km. (The colour version of this figure is included in the online version of the journal.)

the condition on dispersion lengths is respected with the interaction between the chirp and the GVD having the same positive sign under the influence of an opposite value of the FOD, the compression is well obtained. In Figure 3, we represent the compression condition of Equation (14a) where both the FOD and the GVD have the same positive sign while the chirp is negative. In this case, there is no condition on dispersion lengths. Figure 3(*b*)–(*e*) present the evolution of the pulse characteristics for this propagation.

Taking into account the case of the RC pulse, the pulse compression is obtained earlier at the beginning of the propagation in comparison to the Gaussian case, as is depicted in Figure 4.

The chirped RC pulse MPCP is given by the relation:

$$\text{MPCP} = 100\left\{1 - \frac{1}{2}\left[4 - \frac{2\Delta_1}{\Delta_2}\left(\frac{C_0}{T_0}\right)^2\right]^{1/2}\right\} \quad (21)$$

The condition of Equation (15a) corresponds to the case where the parameters GVD, FOD and chirp have the same positive sign. The compression is obtained with an MPCP of about 5.5767%, which is less than those obtained with the Gaussian pulse. The maximal length for the pulse compression is about 0.5041 km, which is very far from the result obtained in Figure 2 (about 186.2075 km) and in Figure 3 (about 27.5863 km). Figure 4 presents the contour plots of

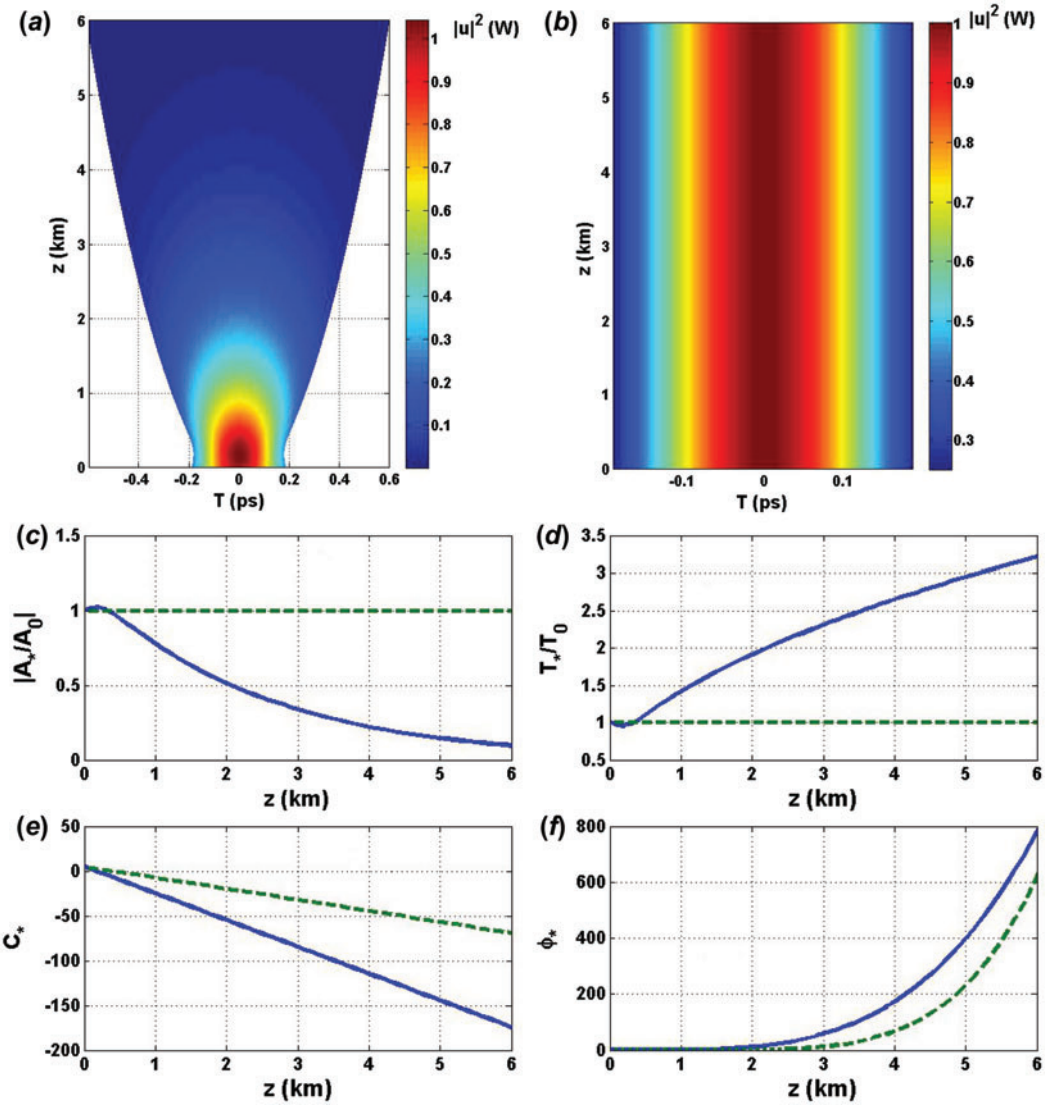


Figure 5. (*a*) contour plot of the chirped RC pulse compression of Equation (15d): assuming the dispersion lengths condition, $L_{GVD} = 5.328$ km, $L_{mc} = 0.3346$ km, $T^{min} = 0.3725$ ps, MPCP = 1.9798%; (*b*) contour plot of the chirped RC pulse in the absence of the verified condition on dispersion lengths, $L_{GVD} = 62.78$ km. For the frames (*c*), (*d*), (*e*) and (*f*): normalized amplitude, normalized width, chirp and phase respectively (blue solid curves correspond to the case of Figure 5(*a*) and green dashed curves for the case of Figure 5(*b*)). General parameters: $\beta_4 = -0.00086\,\text{ps}^4/\text{km}$, $L_{FOD} = 24.24$ km, $T_0 = 0.38$ ps, $C_0 = 5$. (The colour version of this figure is included in the online version of the journal.)

the RC pulse and the evolution of its characteristics corresponding to Equation (15d). In Figure 5(*a*), the dispersion lengths condition is verified while in Figure 5(*b*) it is ignored. Figure 5(*b*)–(*e*) present the RC pulse characteristics evolution versus z.

Recalling that the present study of dynamics of linear compression involves the GVD, the chirp and the FOD, it is important to point out that these results could be generalized to the *n*th-order even dispersion terms. Our obtained results present a general description of the interaction between the chirp, the GVD and the FOD. The results recover and complete some aspects of the results on pulse compression previously obtained in literature. Taking into account another type of optical light pulse, namely the RC pulse, we have obtained interesting features as concerning the dynamical behavior of the propagating pulse which are not particularly related to the major results obtained when dealing with the Gaussian pulse. For example, even when the interacting dispersion parameters and the chirp have the same sign, pulse compression can be obtained. Therefore, the description of the broadening/compression pulse is greatly dependent on the considered optical pulse.

## 4. Conclusion

In summary, using the LVA with chirped Gaussian and RC pulses, we have demonstrated that optical pulse compression induced by chirp can be successfully achieved in a linear medium under GVD and FOD parameters having the same sign. The chirp parameter is of opposite sign for the case of the Gaussian pulse. The pulse compression being dependent on the input profile, for the RC pulse, new broadening/compression conditions are obtained which are quite different from the established rules on compression effect using the Gaussian pulse. These results are welcome and may complete the basic linear optical pulse compression theory induced by chirp.

Based on the previous mentioned results, a possible experimental setup could be suggested using a quasi-linear dispersion-flattened fiber, in which the pulse would experience normal/anomalous dispersion to obtain the respective sign of the chirp [3], and get compressed when passing through a grating pair with dispersion of same sign.

## Acknowledgements

We acknowledge Dr. Jean-Pascal Eloundou (from National Advanced School of Engineering of the University of Yaoundé I, Cameroon) for his support.

## References

[1] Mollenauer, L.F.; Gordon, J.P. *Solitons in Optical Fibers: Fundamentals and Applications*; Academic Press: San Diego, CA, 2006.
[2] Agrawal, G.P. *Nonlinear Fiber Optics*; Academic Press: San Diego, CA, 2007.
[3] Agrawal, G.P. Pulse Compression. In *Applications of Nonlinear Fiber Optics*: Agrawal, G.P., Ed.; Academic Press: San Diego, CA, 2008; pp. 245–292.
[4] Senthilnathan, K.; Li, Q.; Nakkeeran, K.; Wai, P.K.A. *Phys. Rev. A* **2008,** *78,* 033835.
[5] Akhmediev, N.N.; Mitzkewich, N.V. *IEEE J. Quantum Electron.* **1991,** *27,* 849–857.
[6] Broderick, N.G.R.; Taverner, D.; Richardson, D.J.; Ibsen, M.; Laming, R.I. *Phys. Rev. Lett.* **1997,** *79,* 4566–4569.
[7] Jien, S.; XiaoMin, R.; YongQing, H.; GuangQiang, Y.; Yong, G.; Xue, C. In *Pulse Compression Based on Nonlinear Interaction*, Proceedings of SPIE, 2004; Shen, S., Jian, S., Okamoto, K., Walker, K.L., Eds; SPIE: Bellingham, WA, 2004; pp. 404–409.
[8] Xu, W.-C.; Chen, W.-C.; Luo, A.-P.; Guo, Q.; Liu, S.-H. *Chin. Phys. Lett.* **2001,** *18,* 1211–1213.
[9] Hu, J.; Marks, B.S.; Menyuk, C.R. *Opt. Express* **2006,** *14,* 4026–4036.
[10] Capmany, J.; Pastor, D.; Sales, S.; Ortega, B. *Opt. Lett.* **2002,** *27,* 960–962.
[11] Capmany, J.; Pastor, D.; Sales, S.; Muriel, M.A. *J. Opt. Soc. Am. B* **2003,** *20,* 2523–2533.
[12] Marcuse, D. *Appl. Opt.* **1981,** *20,* 3573–3579.
[13] Amemiya, M. *IEEE J. Lightwave Technol.* **2002,** *20,* 591–597.
[14] Anderson, D. *Phys. Rev. A* **1983,** *27,* 3135–3145.
[15] Paschotta, R. *Dispersion-shifted Fibers* [online] RP Photonics Consulting GmbH, http://www.rp-photonics.com/dispersion_shifted_fibers.html (last updated on 22 March 2013).
[16] McMullen, J.D. *J. Opt. Soc. Am.* **1977,** *67,* 1575–1578.
[17] Nakkeeran, K.; Kwan, Y.H.C.; Wai, P.K.A.; Labruyère, A.; Dinda, P.T.; Moubissi, A.B. *J. Opt. Soc. Am. B* **2004,** *21,* 1901–1907.
[18] Ngabireng, C.M.; Dinda, P.T.; Tonello, A.; Nakkeeran, K.; Wai, P.K.A.; Kofané, T.C. *Phys. Rev. E* **2005,** *72,* 036613.
[19] Klauder, J.R.; Price, A.C.; Darlington, S.; Albersheim, W.J. *Bell Syst. Tech. J.* **1960,** *39,* 745–808.
[20] Konar, S.; Biswas, A. Kluwer Academic Publishers. *Opt. Quantum Electron.* **2004,** *36,* 905–918.
[21] Roy, S.; Bhadra, S.K.; Agrawal, G.P. *Opt. Comm.* **2008,** *281,* 5889–5893.
[22] Mandeng, L.M.; Tchawoua, C. In Frontiers in Optics Conference, OSA Technical Digest. [Online], Optical Society of America, 2012, paper FW3A.36.
[23] Mandeng, L.M.; Tchawoua, C. *Journal of Modern Optics* **2013,** *60,* 359–367.
[24] Xiao, Y.; Agrawal, G.P.; Maywar, D.N. *Opt. Lett.* **2011,** *36,* 505–507.

Periodic compression of chirped femtosecond pulses in silicon waveguides under fourth-order dispersion



2014 J. Opt. 16 085204

(http://iopscience.iop.org/2040-8986/16/8/085204)

IOP Publishing Journal of Optics
J. Opt. **16** (2014) 085204 (12pp) doi:10.1088/2040-8978/16/8/085204

# Periodic compression of chirped femtosecond pulses in silicon waveguides under fourth-order dispersion

**Lucien Mandeng Mandeng[1], Serge Ibraid Fewo[1], Clément Tchawoua[1] and Timoléon Crépin Kofané[1,2,3]**

[1] Laboratory of Mechanics, Department of Physics, Faculty of Science, University of Yaoundé I, PO Box 812 Yaoundé, Cameroon
[2] The Abdus Salam International Centre for Theoretical physics, PO Box 506 Strada Costiera, II-34014 Trieste, Italy
[3] Centre d'Excellence Africain des Technologies de l'Information et de la Communication (CETIC), Université deYaoundé I, Yaoundé, Cameroon

E-mail: sergefewo@yahoo.fr

Received 20 April 2014
Accepted for publication 24 June 2014
Published 1 August 2014

**Abstract**

We report the analysis of the compression mechanism for chirped femtosecond pulses in silicon-on-insulator waveguides under the effect of fourth-order dispersion (FOD) using the modified variational approach that involves Rayleigh's dissipation function (RDF). Our results show that the nonlinear compression in these waveguides is input pulse dependent. Moreover, this study leads to a nearly periodic-like dynamic induced by the interplay between self-phase modulation and FOD in a normal group-velocity dispersion. In addition, when large values of the initial chirp and absorption coefficients present in these waveguides are considered, the compression mechanism is completely destroyed, with the observation of at least one pulse amplification over a short distance of propagation prior to pulse broadening.

Keywords: pulse compression, variational approach, fourth-order dispersion

(Some figures may appear in colour only in the online journal)

## 1. Introduction

In nonlinear optics, the pulse compression mechanism is one of the most important technologies for creating optical sources with large spectral bandwidth [1–3]. It consists of a temporal reduction of the input pulse width during its propagation inside the optical media. It is well known that there are two important ways to achieve pulse compression: linear and nonlinear. In the nonlinear case, the solitonic properties make it possible to achieve pulse compression, even adiabatically [2–7]. Recently, with analysis applied to solitary waves known as similaritons, Senthilnathan *et al* [8–10] showed pedestal-free pulse compression in optical fibers. In actual fact, many compressors, both linear and nonlinear, have been developed from these basic concepts, such as those using cross-phase modulation technology [3, 11, 12], fiber polarization technology [13], and a tapered-microstructure optical fiber with four layers of holes [14]. In addition to silica fibers, pulse compression has also been investigated in silicon-on-insulator (SOI) waveguides [15]. The high values of the Kerr nonlinearity coefficient of these media have attracted more and more attention over approximately the last decade [15–20]. Indeed, several applications use SOI waveguides as broadband amplifiers, tunable lasers, optical switching devices, and biosensors. SOI waveguides and silica fibers differ in some respects: SOI waveguides are generally smaller than silica fibers, and silicon is very nonlinear—about 200 times more so than silica. The silicon material makes it possible to confine light within an area so small that the nonlinear effects are greatly enhanced. The crystalline nature of silicon causes the Raman effect to depend strongly on the waveguide geometry and mode polarization. On the other hand, the dynamics inside SOI waveguides include two-photon absorption (TPA) and free-carrier absorption (FCA) [15–24].

 

Their impact on the pulse compression mechanism inside SOI waveguides under the influence of FOD have not yet been investigated to our knowledge.

The present work is devoted to studying the compression of chirped pulses induced by FOD in the nonlinear case, highlighting the impact of absorption coefficients. This study is conducted through the recently employed variational approach that involves Rayleigh's dissipation function (RDF) [15, 20]. RDF is associated with variational analysis to take into account the dissipative part of the system [20]. It so happens that an modified variational approach (MVA) has been found to have advantages in studies of femtosecond pulse propagation inside SOI waveguides, even in a soliton-like regime [15]. Three input pulses with Gaussian, sech-type, and raised-cosine (RC) ansätze profiles are considered for the study of this compression mechanism in order to demonstrate that this periodic compression is sensitive to an input pulse. In fact, this work is an extension of the work presented in [25].

This paper is therefore organized as follows: the next section presents the theoretical analysis of the model, whereas section 3 describes the periodic compression in the model. Sections 4 and 5 are devoted to the effects of both the dispersion regime and chirp, respectively, on periodic compression. The influence of absorption coefficients is presented in section 6. The last section concludes the paper.

## 2. Analysis of the model

The propagation of optical pulses through an SOI waveguide is governed by a generalized nonlinear Schrödinger equation that includes the effects of TPA and FCA, as in [15, 19–23]:

$$i\frac{\partial u}{\partial z} + \sum_{k=1}^{2}\frac{(-1)^k\beta_{2k}}{(2k)!}\frac{\partial^{(2k)}u}{\partial T^{(2k)}} + \gamma|u|^2u = -i\frac{\alpha}{2}u - i\Gamma|u|^2u - i\frac{\sigma}{2}N_C u \tag{1}$$

where $u$, $\beta_{2k}$, $\gamma$, $\alpha$, $\Gamma$, $\sigma$, and $N_C$ are the slowly varying amplitude of the electrical field, the $(2k)^{th}$ order term of dispersion, the nonlinear Kerr coefficient, the linear loss coefficient, the TPA coefficient, the FCA coefficient, and the free-carrier density (FCD) respectively. The third-order dispersion (TOD) term is ignored in this study because it is well known that it introduces a relatively small temporal shift of the pulse center, which has no bearing on our study [2, 3, 15]. For instance, in classical nonlinear silica fibers, near the zero-dispersion wavelength (ZDW) of the group-velocity dispersion (GVD), one should include the effect of the TOD [3]. One should also note that some fibers—so-called dispersion-flattened fibers—account for a zero-dispersion point for the TOD, and so the whole dispersion is defined only by the GVD and the FOD, which is added for ultra-short pulses. More generally, Capmany *et al* [26] have shown, with respect to the Gaussian pulse, that the odd-order dispersion terms ($\beta_3$, $\beta_5$, ...) introduce some oscillating tails in one side of the central part of the pulse temporal profile in addition to the asymmetric displacement of the pulse center. Indeed, the pulse becomes an Airy-like pulse under the TOD effect [2, 27]. Furthermore, Capmany *et al* have shown that the source chirp of the pulse interacts only with even dispersion terms. TPA and FCA are linked to the FCD dynamics following the rate equation given below [15, 27, 28]:

$$\frac{\partial N_c(z,T)}{\partial T} = \frac{\beta_{TPA}}{2\,h\nu_0}\frac{|u(z,T)|^4}{a_{eff}^2} - \frac{N_c(z,T)}{\tau_c} \tag{2}$$

where $\beta_{TPA} = 2\Gamma a_{eff}$ is the usual TPA parameter. On the other hand, the quantities h, $\nu_0$, and $\tau_c$ represent the Planck constant, the pump frequency, and the carrier lifetime, respectively. The effective carrier lifetime includes all the effects of recombination, diffusion, and drift [15]. Our analysis is based on the Gaussian, sech-type, and RC pulses, given respectively as [2, 3, 29–31]:

$$u = u_0 e^{\left[\frac{1+iC}{2}\left(\frac{T}{t_0}\right)^2 + i\phi\right]} \tag{3}$$

$$u = u_0\, sech\left(\frac{T}{t_0}\right)e^{i\left[-\frac{C}{2}\left(\frac{T}{t_0}\right)^2+\phi\right]} \tag{4}$$

and

$$u = \frac{u_0}{2}\left[1 + cos\left(\frac{\pi T}{t_0}\right)\right]e^{i\left[\frac{C}{2}\left(\frac{T}{t_0}\right)^2+\phi\right]} \tag{5}$$

where $u_0$ is the amplitude of the pulse, related to the peak input power $P_0$ as $u_0 = \sqrt{P_0}$. The parameters C, $t_0$, and $\phi$ represent the chirp, the width, and the phase respectively. The reader should notice that the generation of Gaussian-shaped pulses suitable for a high bit rate is not easier [29–31]. Indeed, the output of the commonly used Mach-Zehnder pulse carvers is rather close to RC-profile pulses. On the other hand, this pulse has a periodic profile (due to the cosine function), contrary to the other pulses. Its full width at half maximum (FWHM) is smaller than that of the other pulses.

The Lagrangian density and RDF associated with equation (1) are given respectively as [15, 20]:

$$L_d = \frac{i}{2}\left(u^*\frac{\partial u}{\partial z} - u\frac{\partial u^*}{\partial z}\right) - \sum_{k=1}^{2}\frac{(-1)^k\beta_{2k}}{(2k)!}\frac{\partial^{(2k-1)}u}{\partial T^{(2k-1)}}\frac{\partial u^*}{\partial T} + \frac{\gamma}{2}|u|^4 \tag{6}$$

and

$$R_d = i\left[|u|^2\Gamma + \frac{1}{2}(\alpha + \sigma N_c(t))\right]\left(u^*\frac{\partial u}{\partial z} - u\frac{\partial u^*}{\partial z}\right) \tag{7}$$

The determination of the Lagrangian function for the

Gaussian pulse leads to:

$$L_G = -u_0^2\left[\frac{1}{2}\left(\frac{C}{t_0}\frac{dt_0}{dz} - \frac{1}{2}\frac{dC}{dz}\right) + \frac{d\phi}{dz}\right]\sqrt{\pi}t_0 + \frac{\sqrt{\pi}u_0^2\left(1+C^2\right)}{4t_0}\beta_2 + \frac{\sqrt{\pi}u_0^2\beta_4}{32t_0^3}\left(1+C^2\right)^2 + \sqrt{\frac{\pi}{2}}\frac{\gamma u_0^4 t_0}{2}, \quad (8)$$

For the sech-type pulse, we obtain the same form as in [15], with an additional term taking into account the FOD effect:

$$L_{sech} = -u_0^2 t_0\left[\frac{\pi^2}{6}\left(\frac{C}{t_0}\frac{dt_0}{dz} - \frac{1}{2}\frac{dC}{dz}\right) + 2\frac{d\phi}{dz}\right] + \frac{\beta_2 u_0^2}{2t_0}\left(\frac{2}{3} + \frac{\pi^2}{6}C^2\right) + \frac{2}{3}\gamma u_0^4 t_0 + \frac{1}{24t_0^3}\left(\frac{14}{15} + \left(\frac{\pi^2}{3} - 2\right)C^2 + \frac{19\pi^2}{33}C^4\right)\beta_4 u_0^2 \quad (9)$$

and for the RC pulse we have:

$$L_{RC} = -u_0^2 t_0\left[a_1\left(\frac{1}{2}\frac{dC}{dz} - \frac{C}{t_0}\frac{dt_0}{dz}\right) + a_2\frac{d\phi}{dz}\right] + \frac{u_0^2\beta_2}{2t_0}\left(\frac{\pi^2}{2} + a_1C^2\right) + a_5\gamma t_0 u_0^4 - \frac{1}{24t_0^3}\left(-\frac{\pi^4}{2} + a_3C^2 + a_4C^4\right)\beta_4 u_0^2 \quad (10)$$

where $a_k$ with $k = \overline{1..5}$ are some constants defined as:

$$\begin{aligned} a_1 &= \left(-64 - 2\pi + 8\pi^2 + \pi^3\right)\Big/8\pi^3 \\ a_2 &= (8+3\pi)/2\pi \\ a_3 &= -\frac{1}{4\pi}\left(-48 + 6\pi^2 + \pi^3\right) \\ a_4 &= -\frac{1}{160\pi^5}\Big(15\,360 + 120\pi - 1920\pi^2 \\ &\quad -20\pi^3 + 40\pi^4 + 3\pi^5\Big) \\ a_5 &= \frac{5}{48\pi}(21\pi + 64) \end{aligned} \quad (11)$$

We also derive the reduced forms of the RDF function for each pulse:

$$R_G = -\sqrt{\pi}u_0^2 t_0\left\{\left[\frac{1}{2}\left(\frac{C}{t_0}\frac{dt_0}{dz} - \frac{1}{2}\frac{dC}{dz}\right) + \frac{d\phi}{dz}\right]\left[\frac{u_0^2}{\sqrt{2}}\left(\Gamma + \frac{\sqrt{\pi}u_0^2\beta_{TPA}t_0}{4\,h\nu_0 A_{eff}^2}\right) + \alpha\right] + \frac{\sqrt{2}}{2}u_0^2\frac{d\phi}{dz}\Gamma\right\}, \quad (12)$$

$$R_{sech} = -2u_0^2 t_0\left\{\frac{4}{3}u_0^2\Gamma\left[\frac{1}{2}\left(\frac{C}{t_0}\frac{dt_0}{dz} - \frac{1}{2}\frac{dC}{dz}\right)\left(\frac{\pi^2}{6} - 1\right) + \frac{d\phi}{dz}\right] + \left(\alpha + \frac{1}{3}\sigma\frac{\beta_{TPA}u_0^4 t_0}{h\nu_0 A_{eff}^2}\right) \times\left[\frac{\pi^2}{12}\left(\frac{C}{t_0}\frac{dt_0}{dz} - \frac{1}{2}\frac{dC}{dz}\right) + \frac{d\phi}{dz}\right]\right\} \quad (13)$$

and

$$R_{RC} = -u_0^2 t_0\left\{\left(\frac{1}{2}\frac{dC}{dz} - \frac{C}{t_0}\frac{dt_0}{dz}\right)\left[b_1u_0^2\Gamma + a_1\alpha\right] + \frac{d\phi}{dz}\left[b_2u_0^2\Gamma + a_2\alpha\right] + \frac{u_0^4\beta_{TPA}t_0}{1536\pi h\nu_0 A_{eff}^2}\sigma \times\left[b_3\left(-\frac{C}{t_0}\frac{dt_0}{dz} + \frac{1}{2}\frac{dC}{dz}\right) + b_4\frac{d\phi}{dz}\right]\right\} \quad (14)$$

where $b_k$, $k = \overline{1..4}$ are defined as:

$$\begin{aligned} b_1 &= \frac{1}{\pi^3}\left(-\frac{1504}{27} - \frac{111\pi}{32} + \frac{20\pi^2}{3} + \frac{35\pi^3}{48}\right) \\ b_2 &= \frac{80}{3} + \frac{35\pi}{4} \\ b_3 &= \frac{5}{8\pi^3}\left(-4096 - 1472\pi + 470\pi^2 + 232\pi^3 + 21\pi^4\right) \\ b_4 &= \frac{5}{2\pi}\left(512 + 360\pi + 63\pi^2\right) \end{aligned} \quad (15)$$

One should note that the TPA and FCA are linked to the FCD dynamics following the rate equation in which the parameter $\beta_{TPA} = 2\Gamma A_{eff}$ is the usual TPA parameter, whereas $A_{eff}$ is the the effective core area of the SOI waveguide [2, 3, 15, 19, 20]. The effective carrier lifetime has been neglected in this work because we are dealing with femtosecond pulses [15]. Using the Euler-Lagrange equations, we determine the growth equations for each pulse [31]:

(i) Gaussian pulse:

$$\frac{du_0}{dz} = -\frac{u_0}{2}\left\{\frac{C}{t_0^2}\left[\beta_2 + \frac{\left(1+C^2\right)}{4t_0^2}\beta_4\right] + \frac{u_0^2}{\sqrt{2}}\left(\frac{5}{2}\Gamma + \sigma\frac{\sqrt{\pi}}{4}\frac{u_0^2\beta_{TPA}}{h\nu_0 A_{eff}^2}t_0\right) + \alpha\right\}$$

$$\frac{dt_0}{dz} = \frac{C}{t_0}\left[\beta_2 + \frac{\left(1+C^2\right)}{4t_0^2}\beta_4\right] + \frac{\sqrt{2}}{4}u_0^2 t_0\Gamma$$

$$\frac{dC}{dz} = \frac{\left(1+C^2\right)}{t_0^2}\left[\beta_2 + \frac{\left(1+C^2\right)}{4t_0^2}\beta_4\right] + \frac{u_0^2}{\sqrt{2}}(\gamma + \Gamma C)$$

$$\frac{d\phi}{dz} = \frac{\beta_2}{2t_0^2} + \frac{\left(1+C^2\right)\left(3-C^2\right)}{32t_0^4}\beta_4 + \frac{5u_0^2}{4\sqrt{2}}\gamma \tag{16}$$

(ii) Sech-type pulse:

$$\frac{du_0}{dz} = -\frac{u_0}{2}\left\{\frac{C}{t_0^2}\left[\beta_2 + \left(\frac{1}{6} - \frac{1}{\pi^2} + \frac{19}{33}C^2\right)\frac{\beta_4}{t_0^2}\right] + 4u_0^2\Gamma\left(\frac{1}{3} + \frac{1}{\pi^2}\right) + \alpha + \frac{2}{3}\sigma\frac{u_0^4\beta_{TPA}t_0}{h\nu_0 A_{eff}^2}\right\}$$

$$\frac{dt_0}{dz} = \frac{C}{t_0}\left[\beta_2 + \left(\frac{1}{6} - \frac{1}{\pi^2} + \frac{19}{33}C^2\right)\frac{\beta_4}{t_0^2}\right] + \frac{4u_0^2 t_0}{\pi^2}\Gamma$$

$$\frac{dC}{dz} = \frac{1}{t_0^2}\left[\beta_2\left(\frac{4}{\pi^2} + C^2\right) + \left(\frac{14}{15\pi^2} + \left(\frac{1}{3} - \frac{2}{\pi^2}\right)C^2 + \frac{19}{33}C^4\right)\frac{\beta_4}{t_0^2}\right] + \frac{4u_0^2}{\pi^2}(\gamma + 2\Gamma C)$$

$$\frac{d\phi}{dz} = \frac{1}{t_0^2}\left[\frac{\beta_2}{3} + \frac{\beta_4}{24t_0^2}\left(\frac{7}{5} + \left(\frac{\pi^2}{6} - 1\right)C^2 - \frac{19\pi^2}{66}C^4\right)\right] + \frac{5u_0^2}{6}\gamma \tag{17}$$

(iii) RC pulse:

$$\frac{du_0}{dz} = \frac{u_0}{2}\left\{\frac{C}{t_0^2}\left[-\beta_2 + \frac{\beta_4}{12a_1t_0^2}\left(a_3 + 2a_4C^2\right)\right] + \frac{u_0^2}{2}\left(\Gamma A + \sigma\frac{u_0^2\beta_{TPA}}{h\nu_0 A_{eff}^2}t_0 B\right) + \alpha\right\}$$

$$\frac{dt_0}{dz} = \frac{C}{t_0}\left[-\beta_2 + \frac{\beta_4}{12a_1t_0^2}\left(a_3 + 2a_4C^2\right)\right] + \frac{t_0u_0^2}{2}\left[\Gamma A' + \sigma\frac{\beta_{TPA}u_0^2t_0}{h\nu_0 A_{eff}^2}B'\right]$$

$$\frac{dC}{dz} = \frac{1}{a_1t_0^2}\left[-\beta_2\left(\frac{\pi^2}{2} + C^2\right) + \frac{\beta_4}{6t_0^2}\left(-\frac{\pi^4}{4} + a_3C^2 + a_4C^4\right)\right] - \frac{a_5}{a_1}\gamma u_0^2 + \frac{u_0^2C}{2}\left(\Gamma A' + \sigma\frac{\beta_{TPA}u_0^2t_0}{h\nu_0 A_{eff}^2}B'\right)$$

$$\frac{d\phi}{dz} = \frac{1}{2a_2t_0^2}\left[\pi^2\beta_2 + \frac{\beta_4}{12t_0^2}\left(\frac{4\pi^4}{3} - a_3C^3 + a_4C^4\right)\right] + \frac{5u_0^2}{2}\frac{a_5}{a_2}\gamma + \frac{3}{4}u_0^2\left(C\Gamma A'' + \sigma\frac{\beta_{TPA}u_0^2t_0}{h\nu_0 A_{eff}^2}B''\right) \tag{18}$$

where $A = (3b_2/a_2) - (b_1/a_1)$, $B = ((3b_4/a_2) - (b_3/a_1))/1536\pi$, $A' = (b_2/a_2) - (b_1/a_1)$, $B' = \left((b_4/a_2) - (b_3/a_1)\right)/1536\pi$, $A'' = \left(b_2a_1 - b_1a_2\right)/a_2^2$, and $B'' = (b_4a_1 - b_3a_2)/1536\pi a_2^2$. The next section deals with the nonlinear effects on pulse compression in SOI waveguides.

## 3. Periodic compression of femtosecond pulses in an SOI waveguide under FOD and SPM

In this section, $\gamma \neq 0$, $\Gamma = 0$, $\Lambda = \sigma\beta_{TPA}/(h\nu_0 A_{eff}^2)$. We employ equations (16)–(18) to obtain the pulse characteristics. We can integrate these growth equations by using the fourth-order Runge-Kutta integration scheme. It is well known that the balanced interaction between self-phase modulation (SPM) and GVD should lead to the solitonic properties of pulse propagation inside an optical media [2–7], the appearance of the solitonic features being drawn within the soliton order defined by $N^2 = L_{GVD}/L_{NL}$, where $L_{NL} = 1/\gamma P_0$. So normally, as is well known in silica optical fibers for the anomalous-GVD regime, each input pulse may lead to a solitonic form of the fundamental soliton for $N = 1$ and to higher-order solitons (HOSs) for $N \geqslant 2$ [2–7]. However, the combination of SPM effects and normal GVD ($\beta_2 > 0$) could be used for pulse compression [2].

HOSs have an interesting feature that is described as a periodic evolution following the distance $z$ of propagation. This property is understood within a compression shaping of the solitonic profile in a periodic way [2, 7]. Using a dimensionless definition of the propagation distance $\xi = z/L_{GVD}$, the soliton period is defined [2]:

$$z_0 = \frac{\pi}{2}L_{GVD} \tag{19}$$

For HOSs with $N \geqslant 2$, the propagation inside the standard single-mode silica optical fibers leads generally to pulse splitting into many sub-pulses [2–7]. When N is not too large, for example $N = 3$, the splitting is effected between two solitonic compressions by recovering the original shape at the end of the soliton period. However, for large values of N, the propagation leads generally to pulse train generation via the modulational instability (MI) mechanism [23, 32]. More recently, a higher-order MI soliton demonstrated the pulse train generation process [33]. The understanding of the periodic compression of HOSs is based nowadays on an interplay between the SPM and GVD effects [2].

The aim of this section is to evaluate the periodic compression in an SOI waveguide from the previous input pulses in the femtosecond region via the interplay between the SPM and the FOD instead of the GVD. The regime of GVD for the achievement of this periodic compression is surprisingly normal, whereas the SPM coefficient of Kerr nonlinearity is also positive. The chosen parameters that allow the periodic compression are $P_0 = 4.76$ W, $\gamma = 47$ W$^{-1}$m$^{-1}$, $\alpha = 5.06$ m$^{-1}$, $t_{pulse}(0) = 50$ fs, and $\beta_2 = 0.56$ ps$^2$ m$^{-1}$ [15]. For the parameter N, we have $N = 0.99 \approx 1$. Normally, if a single-mode silica fiber is considered in the anomalous GVD and the FOD effect is ignored ($\beta_4 = 0$), each input pulse should reshape its profile into a fundamental soliton profile while propagating inside the media, even in the presence of a small initial chirp [2, 7]. Indeed, it is known that the source chirp is detrimental to soliton formation because it may disturb the exact balance between GVD and SPM [2]. Instead, we obtain, with the given SOI waveguide, the periodic compression induced by the balance between SPM and FOD effects instead of by

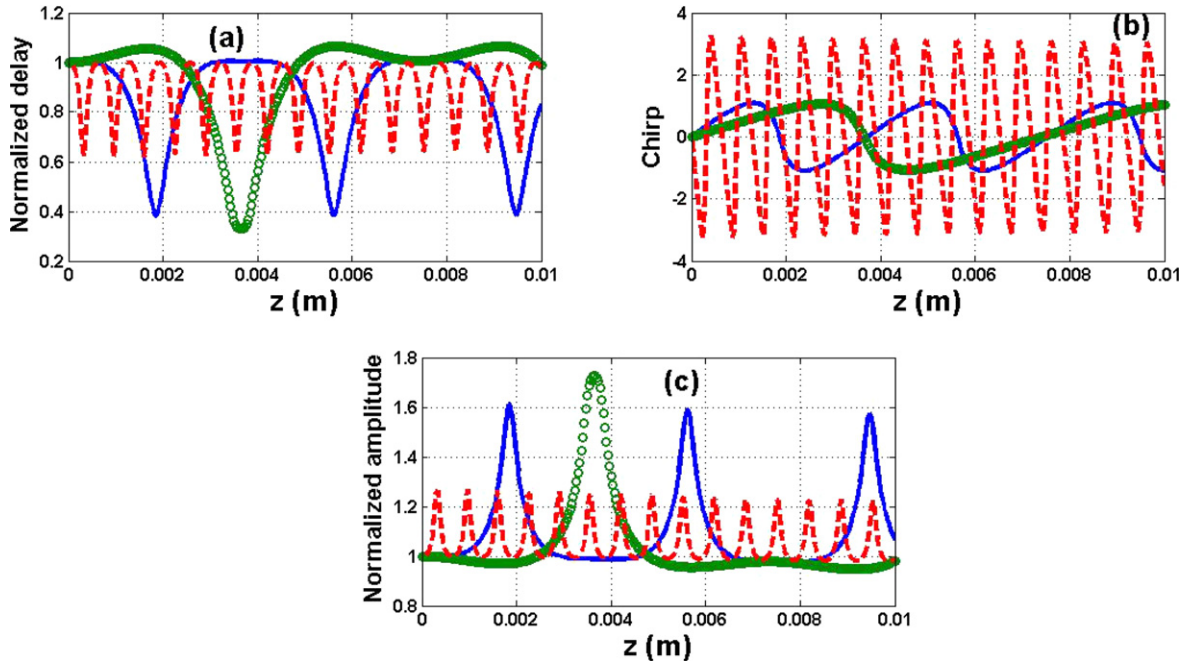


**Figure 1.** Plot of pulse characteristics: solid lines for the Gaussian pulse, circle lines for the sech-type pulse, and dashed lines for the RC pulse. Parameters for each pulse: $\Gamma = 0$, $\Lambda = 0$, $C_0 = 0$, and SOI waveguide length L = 1 cm. Specific results for the Gaussian pulse: $\beta_4 = -0.0051$ ps$^4$ m$^{-1}$, first peak at $z_{init} \approx 0.0019$ m, first maximum pulse compression percentage ($MPCP$) = 61.77%, $z_0 \approx 0.0038$ m. Specific results for the sech-type pulse: $\beta_4 = -0.0039$ ps$^4$ m$^{-1}$, first peak at $z_{init} \approx 0.0036\ m$, first $MPCP = 67.03\%$, $z_0 \approx 0.0075$ m. Specific results for the RC pulse: $\beta_4 = -0.005$ ps$^4$ m, first peak at $z_{init} \approx 3.636 \times 10^{-4}$m, first $MPCP = 37.95\%$, $z_0 \approx 6.360 \times 10^{-4}$m.

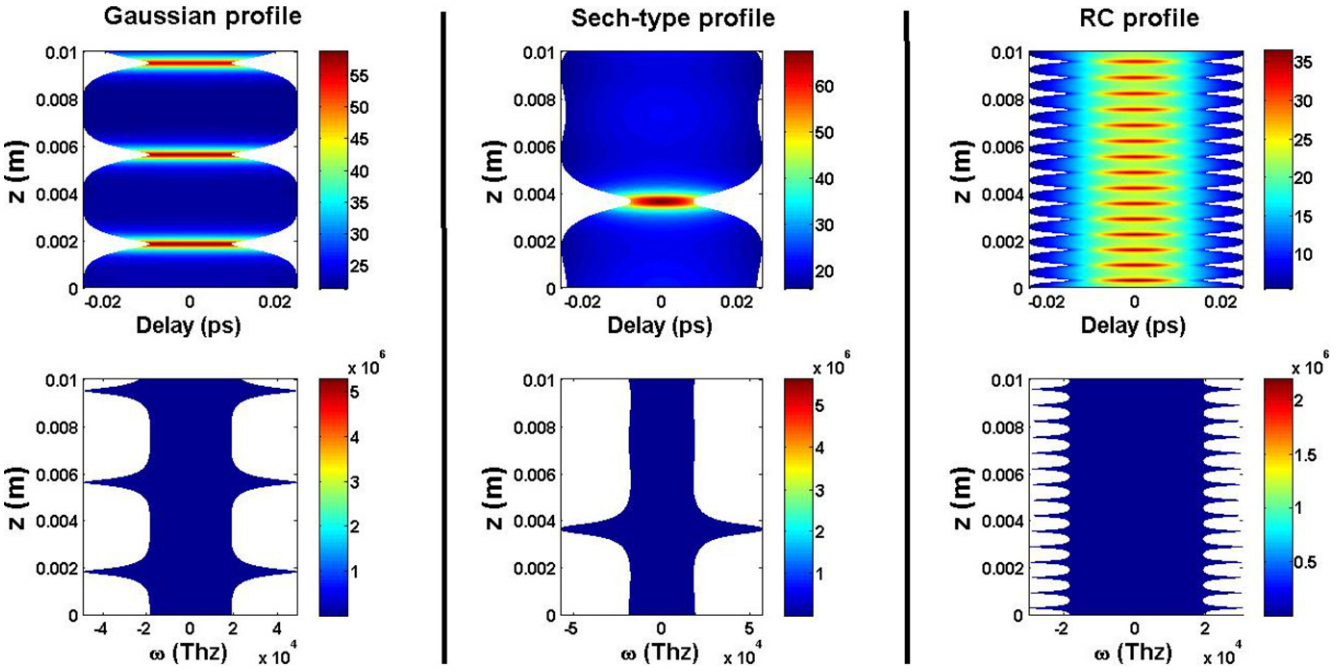


**Figure 2.** Contour plots of pulse propagation under the conditions presented in figure 1: for the left-side Gaussian profile, for the middle sech-type profile, and for the right-side RC profile. For each frame, at the top: intensity propagation; at the bottom: spectral propagation.

GVD for the quasi-fundamental soliton order ($N \approx 1$). This interesting feature is depicted in figure 1. To see how pulses propagate under the conditions of figure 1, their intensities and spectra propagation are illustrated in figure 2 and are obtained by employing the convenient fourth-order Runge-Kutta scheme and the common split-step Fourier algorithm. The quantities $z_{init}$ and $z_0$ represent the initial distance at which the first compression peak is observed and the compression spacing (spatial period), respectively. The losses are included and obviously reduce the energy of the pulses in accordance with the distance of propagation. As can be seen in figures 1 and 2, the periodic compression depends on the

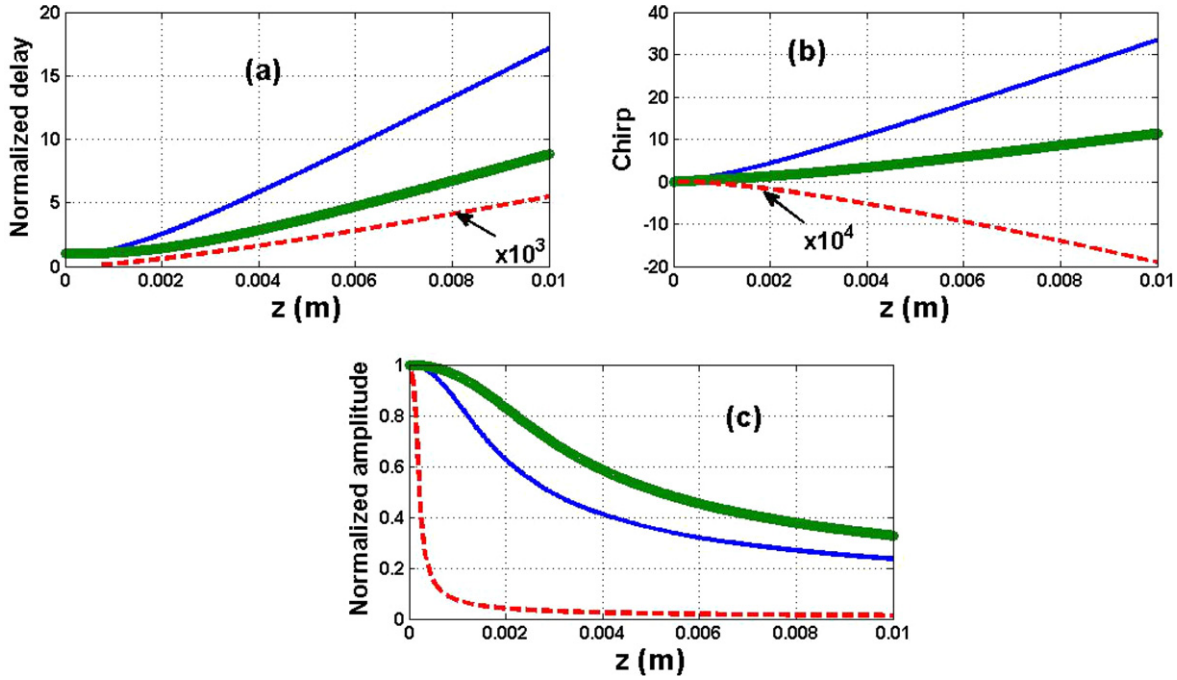


**Figure 3.** Plot of pulse characteristics: solid lines for the Gaussian pulse, circle lines for the sech-type pulse, and dashed lines for the RC pulse. Parameters for each pulse: $\Gamma = 0$, $\Lambda = 0$, $C = 0$, $\beta_2 = 0.56$ ps$^2$ m$^{-1}$, and length L = 1 cm. For the Gaussian pulse: $\beta_4 = 0.0051$ ps$^4$ m$^{-1}$ . For the sech-type pulse: $\beta_4 = 0.0039$ ps$^4$ m$^{-1}$. For the RC pulse: $\beta_4 = 0.005$ ps$^4$ m$^{-1}$; the normalized delay plotted is multiplied by $10^3$ (see the red dashed curve in (a)), whereas the chirp is multiplied by $10^4$ (see the red dashed curve in (b)).

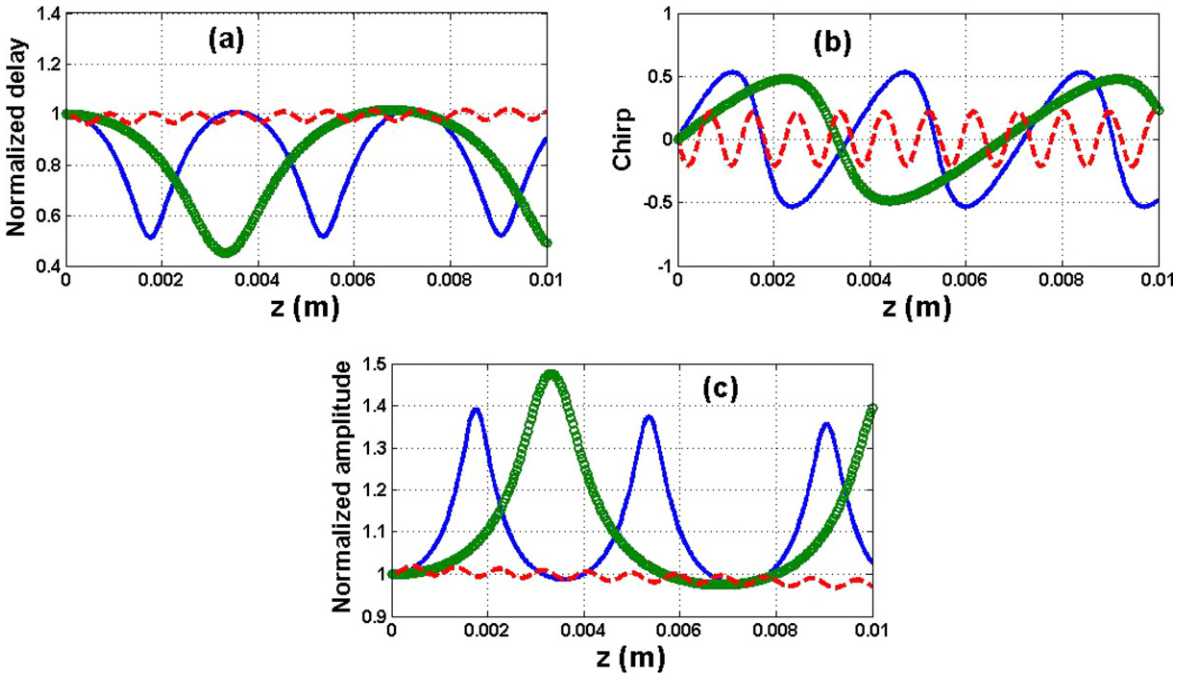


**Figure 4.** Plot of pulse characteristics: solid lines for the Gaussian pulse, circle lines for the sech-type pulse, and dashed lines for the RC pulse. Parameters for each pulse: $\Gamma = 0$, $\Lambda = 0$, $C = 0$, $\beta_2 = -0.56$ ps$^2$ m$^{-1}$, and length L = 1 cm. Specific results for the Gaussian pulse: $\beta_4 = -0.0051$ ps$^4$ m$^{-1}$, first peak at $z_{init} \approx 0.00175$ m, first maximum pulse compression percentage ($MPCP$) = 48.84%, $z_0 \approx 0.0035$ m. Specific results for the sech-type pulse: $\beta_4 = -0.0039$ ps$^4$ m$^{-1}$, first peak at $z_{init} \approx 0.00325$ m, first $MPCP = 54.86\%$, $z_0 \approx 0.006875$ m. Specific results for the RC pulse: $\beta_4 = -0.005$ ps$^4$ m$^{-1}$, first peak at $z_{init} \approx 4.375 \times 10^{-4}$m, first $MPCP = 3.91\%$, $z_0 \approx 8.75 \times 10^{-4}$m.

input pulse profile. The compression period of the sech-type pulse is greater than that of the Gaussian profile, which is greater than that of the RC profile. To explain this difference, we suggest that because the first two profiles are close to each other, they will behave almost the same despite some small discrepancies, whereas the RC profile is a periodic function, in contrast with the others. Note that the behavior of this profile will be much different from that of the others, which are not periodic. It is assumed that only one period of the temporal profile of this pulse is used in the dynamics. This

**Table 1.** Comparison of results obtained in figures 1 and 4 for each unchirped pulse. One can read these as follows as: the first item before the division symbol (/) corresponds in the same line to values before the symbol, and the same procedure is observed for the item following the same symbol. For instance, for the first item (Gaussian pulse), $z_{init}$ corresponds to 0.0019 m and 0.00175 m, whereas $z_0$ corresponds to 0.0038 m and 0.0035 m.

| Item | figure 1 | figure 4 |
|---|---|---|
| $z_{init}/z_0$ of the Gaussian profile | 0.0019 m/0.0038 m | 0.00175 m/0.0035 m |
| $z_{init}/z_0$ of the sech-type profile | 0.0036 m/0.0075 m | 0.00325 m/ 0.006875 m |
| $z_{init}/z_0$ of the RC profile | $3.636 \times 10^{-4}$ m/ $6.36 \times 10^{-4}$ m | $4.375 \times 10^{-4}$ m/ $8.75 \times 10^{-4}$ m |
| MPCP of the Gaussian profile | 61.77% | 48.84% |
| MPCP of the sech-type profile | 67.03% | 54.86% |
| MPCP of the RC profile | 37.95% | 3.91% |

characteristic leads the RC profile to behave differently in comparison with the other pulses, which vanish intrinsically beyond the main peak. Furthermore, with the same pulse duration $t_0$, both the Gaussian and the sech-type profiles have f at half maximum intensity (respectively, $t_{FWHM}^{Gauss} = 1.665t_0$ and $t_{FWHM}^{sech} = 1.763t_0$), which are nearly equal; whereas the profile of the RC pulse is approximately half that of the other profiles ($t_{FWHM}^{RC} = 0.728t_0$) [2, 29]. Thus, its compression period is expected to be the smallest, as can be observed in figures 1 and 2. This result contrasts with the one previously mentioned regarding silica single-mode optical fibers, where the periodic compression was only obtained for HOSs, induced by the interplay between GVD and SPM. However, as presented in figures 1 and 2, we observe that the periodic compression not only depends on the input pulse profile but also can be obtained through the interplay of FOD and SPM in a normal-GVD regime.

We observe a pulse amplification associated with the periodic compression mechanism, with a slight reduction in pulse energy due to the losses: see, for instance, the blue curve of the Gaussian pulse in figure 1(c). Indeed, one can see that the last compression peak is smaller than the first two, thus highlighting the effect of the linear losses. This happens also for both the sech-type and the RC pulse for long propagation distances. It follows therefore that, for high values of losses, the compression peaks are more and more reduced (with respect to amplitude) or more and more broadened (with respect to temporal width). The chirp also oscillates for each pulse, and the compression peaks of the amplitude (or the width) appear only at $C_{pulse}(kz_0) = 0$, k being a nonzero integer. In the next section, we study the influence of such nonlinear parameters as TPA and FCA on the periodic compression process.

## 4. Influence of the dispersion regime on periodic compression

### *4.1. Normal dispersion regime: ($\beta_2 > 0$ and $\beta_4 < 0$) or ($\beta_2 > 0$ and $\beta_4 > 0$)*

Considering figures 1 and 2, we remind the reader that the dispersion regime is normal according to the GVD. It corresponds to the case where we have $\beta_2 > 0$ and $\beta_4 < 0$. So the periodicity introduced by the FOD and SPM can be linked to the values of the FOD length for each pulse in accordance with the relation $L_{FOD} = t_0^4/|\beta_4|$ (with $t_{pulse}(0) \equiv t_0$). For the Gaussian pulse, we have $L_{FOD} = (4/15)L_{NL}$. For the sech-type pulse, the relation between the nonlinear length and the FOD length is $L_{FOD} = (16/45)L_{NL}$, whereas for the RC profile we have $L_{FOD} = (13/45)L_{NL}$. Also note that the periodic compression is obtained with the negative value of the FOD and the positive value of the SPM. If the choice of a positive value of the FOD is made while we remain in the normal dispersion regime (according to the GVD), the periodicity disappears as expected (see figure 3) [2]. This corresponds to the case where we have $\beta_2 > 0$ and $\beta_4 > 0$. As can be seen in this figure, the chirp is initially equal to zero for each pulse. With the disappearance of the periodicity, one obtains pulse broadening. This process is more stressed for the RC pulse (see the red dashed lines in figure 3) than for the other pulses.

### *4.2. Anomalous dispersion regime: ($\beta_2 < 0$ and $\beta_4 < 0$) or ($\beta_2 < 0$ and $\beta_4 > 0$)*

We plot in figure 4 the case where both the GVD and the FOD are negative ($\beta_2 < 0$ and $\beta_4 < 0$). As can be observed, periodic compression also occurs under these conditions. Nevertheless, this phenomenon is less important than that of figures 1 and 2. Indeed, the MPCP for each pulse and the compression spatial period decrease. The illustration of this observation is presented in table 1, showing a comparison between the results obtained under the conditions $\beta_2 > 0$, $\beta_4 < 0$ (figure 1) and $\beta_2 < 0$, $\beta_4 < 0$ (figure 4). The main aspect coming from table 1 is the decrease in the MPCP for each pulse from the results of figure 1 to those of figure 4. It is a surprising result when one considers the negative values of the GVD and the FOD. Normally, one would expect that both dispersion orders act together in a cooperative manner to improve the periodic compression and therefore to increase the MPCP. Nonetheless, we observe the opposite behavior. Note that the parameters $z_{init}$ and $z_0$ increase for the RC from figure 1 to figure 4 in contrast with what happens to the other pulses. It is obvious that this specific feature is linked to the peculiarity of the RC pulse in that it is periodic and h a small FWHM. This is highlighted in figure 5, where the results obtained for the sech-type pulse are plotted for both cases. We suggest that, comparing with figure 1, the action of the anomalous GVD is in opposition to the action of the FOD, and this leads to a reduction of the periodic compression. Note that for the RC profile, $z_{init}$ and $z_0$ increase, contrary to what happens with the other profiles. This characteristic underlines the main difference between this realistic input

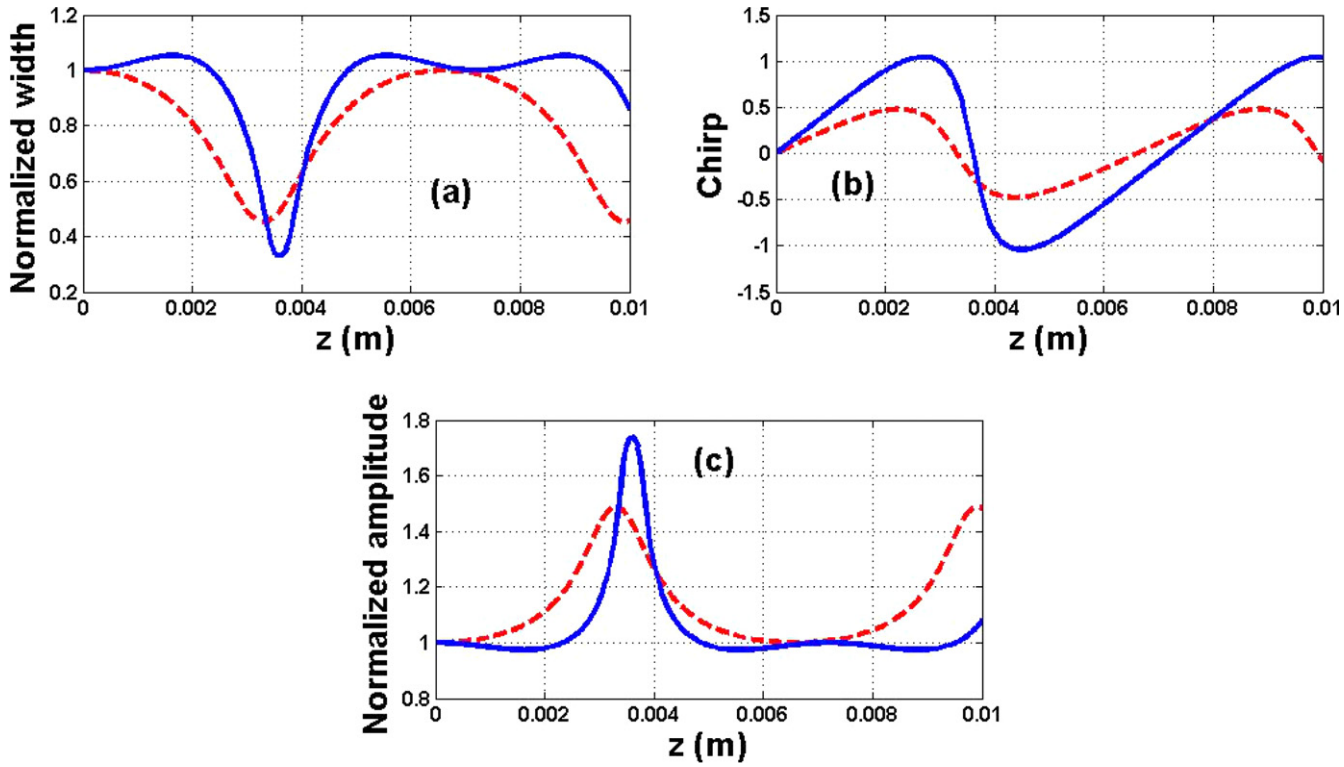


**Figure 5.** Comparison of the anomalous-GVD case (red dashed curves) and the normal-GVD case (blue solid curves) for the sech-type pulse; the periodic compression is enhanced in the case. The simulation conditions are the same as in figures 1 and 4.

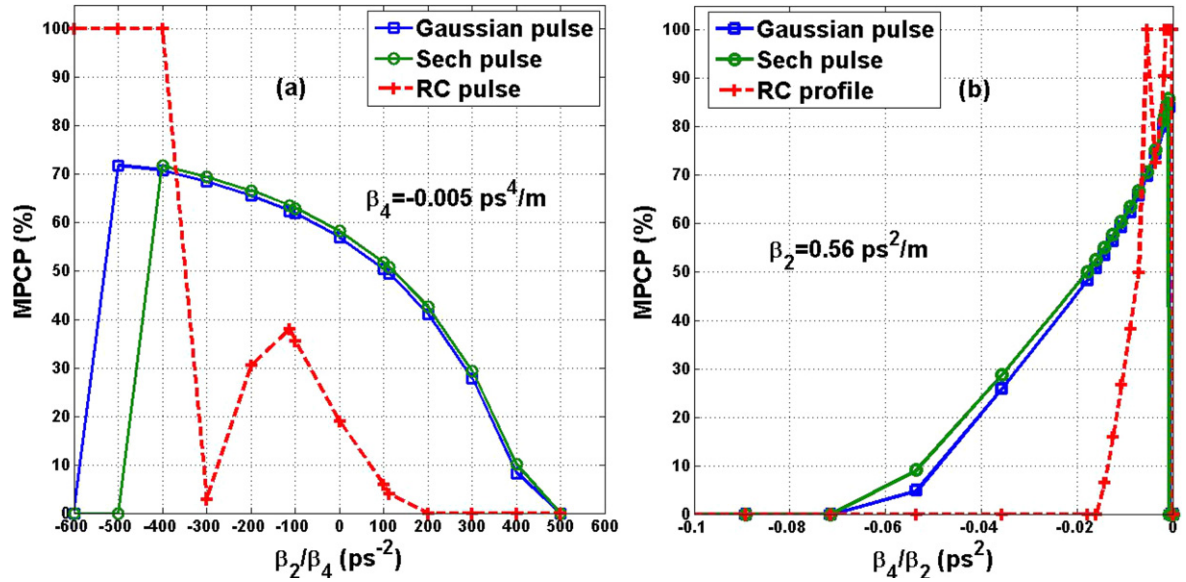


**Figure 6.** GVD and FOD management to control periodic compression: (a) MPCP versus the varying ratio $\beta_2/\beta_4$ with a constant negative value of FOD $-0.005\ \mathrm{ps}^4\ \mathrm{m}^{-1}$ ; (b) MPCP versus the varying ratio $\beta_4/\beta_2$ with a constant positive value of GVD $0.56\ \mathrm{ps}^2\ \mathrm{m}^{-1}$.

profile and the others. For a parametric study, we present in figure 6 how the GVD and FOD values can be managed to control periodic compression. This analysis is done by calculating the MPCP in the cases where both the GVD and the FOD vary. The range of values considered for both the GVD and the FOD is extended to include realistic conditions. In figure 6(a), with a constant negative value of FOD generating the periodic compression, the latter decreases with the decrease in the GVD from the normal to the anomalous dispersion regime. We notice the special behavior of the RC pulse for the values between $3\ \mathrm{ps}^2\ \mathrm{m}^{-1}$ and $0.5\ \mathrm{ps}^2\ \mathrm{m}^{-1}$. However, the opposite occurs for a constant positive value of GVD while the FOD varies. Indeed, as can be observed in figure 6(b), the periodic compression phenomenon is performed by increasing the FOD value from $-0.03\ \mathrm{ps}^4\ \mathrm{m}^{-1}$ to $-5 \times 10^{-4}\ \mathrm{ps}^4\ \mathrm{m}^{-1}$ for all pulses. Obviously, the RC pulse

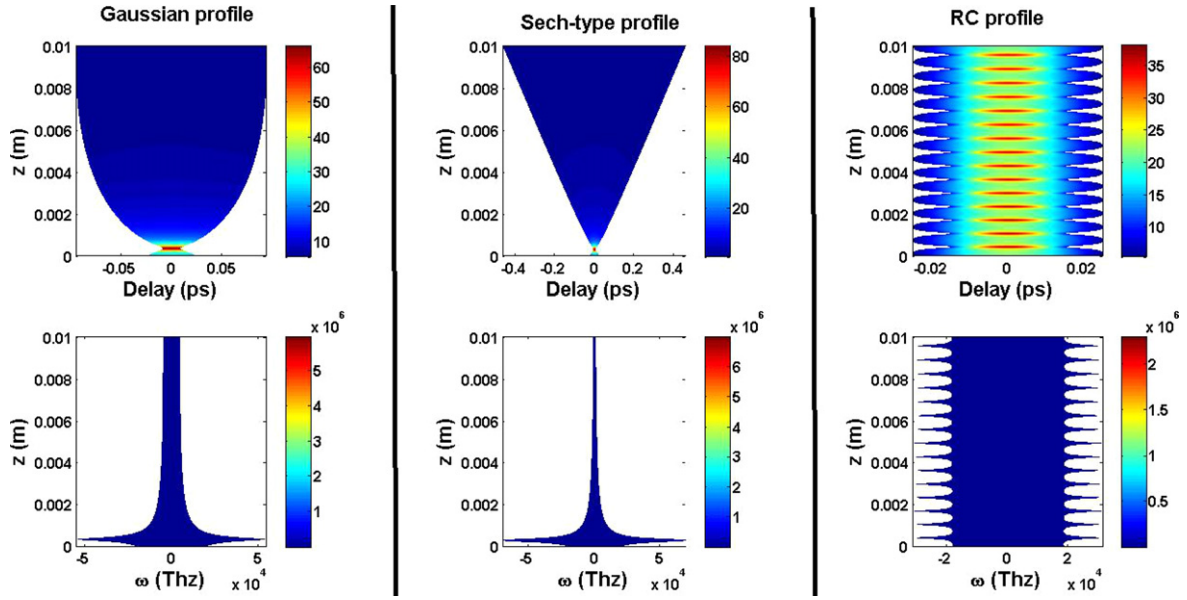


**Figure 7.** Contour plots of pulse propagation under the conditions presented in figure 1 with $C_0 = 2$: for the left-side Gaussian profile, for the middle sech-type profile, and for the right-side RC profile. For each frame, at the top: intensity propagation; at the bottom: spectral propagation.

**Table 2.** Comparison of results obtained with different positive values of chirp

| Item | Chirp | $z_{init}$ | $z_0$ | MPCP |
|---|---|---|---|---|
| Gaussian profile | 1 / 1.5 | $9.09 \times 10^{-4}$ m / $5.9 \times 10^{-4}$ m | 0.00409 m / 0.0059 m | 62.24% / 63.45% |
| Sech-type profile | 1 / 1.5 | 0.0127 m / $6.363 \times 10^{-4}$ m | 0.00754 m / 0.01467 m | 67.14% / 69.38% |
| RC profile | 1 / 1.5 | $3.63 \times 10^{-4}$ m/$3.78 \times 10^{-4}$ m | $6.363 \times 10^{-4}$ m / $6.48 \times 10^{-4}$ m | 38.45% / 38.88% |

**Table 3.** Comparison of results obtained with different negative values of chirp

| Item | Chirp | $z_{init}$ | $z_0$ | MPCP |
|---|---|---|---|---|
| Gaussian profile | −1 / −1.5 | 0.003 m / 0.00527 m | 0.00418 m / 0.00609 m | 62.14% / 63.16% |
| Sech-type profile | −1 / −1.5 | 0.006 m / 0.0328 m | 0.00756 m / 0.033 m | 66.9% / 67.95% |
| RC profile | −1 / −1.5 | $2.727 \times 10^{-4}$ m/$2.727 \times 10^{-4}$ m | $6.363 \times 10^{-4}$ m / $6.363 \times 10^{-4}$ m | 38.5% / 39.12% |

still exhibits special behavior for the range between $-10^{-4}$ ps$^4$ m$^{-1}$ and 0. Considering these results, the best case in which we have the highest MPCP corresponds to the one for which a large value of FOD ($-5 \times 10^{-4}$ ps$^4$ m$^{-1}$) is reached in the normal-GVD regime (0.56 ps$^2$ m$^{-1}$). The interaction that generates the periodic compression corresponds to the interplay between the negative FOD and the positive SPM. The action of the anomalous GVD is in opposition to the action of the FOD and decreases the periodic compression phenomenon, whereas the normal GVD is rather beneficial.

## 5. Influence of the initial chirp on periodic compression

As discussed earlier in [2, 3], the chirp should disturb the nonlinear periodic compression phenomenon, whereas it could lead to linear pulse compression when it is opposite to the GVD. So introducing a small positive value of the initial chirp ($C_0 = 1$) associated with the conditions ($\beta_2 > 0$, $\beta_4 < 0$) of figure 1 leads to table 2. The main observation concerns the beneficial effect of the positive value of the initial chirp on the periodic compression. In fact, both the MPCP and the spatial period increase for all the pulses under the effect of the positive chirp. Therefore, the periodic compression phenomenon is enhanced. However, using a relatively high value such as $C_0 = 2$ yields the opposite result, such as the destruction of periodicity, leading instead to pulse broadening for the sech-type and Gaussian profiles, whereas the RC pulse still keeps its periodic compression (see figure 7). Numerical simulation of a high value such as $C_0 = 5$ destroys the periodic compression of the RC profile. The latter therefore needs large values of positive chirp under the considered dispersion regime in comparison with the other input pulses for its periodic compression to disappear.

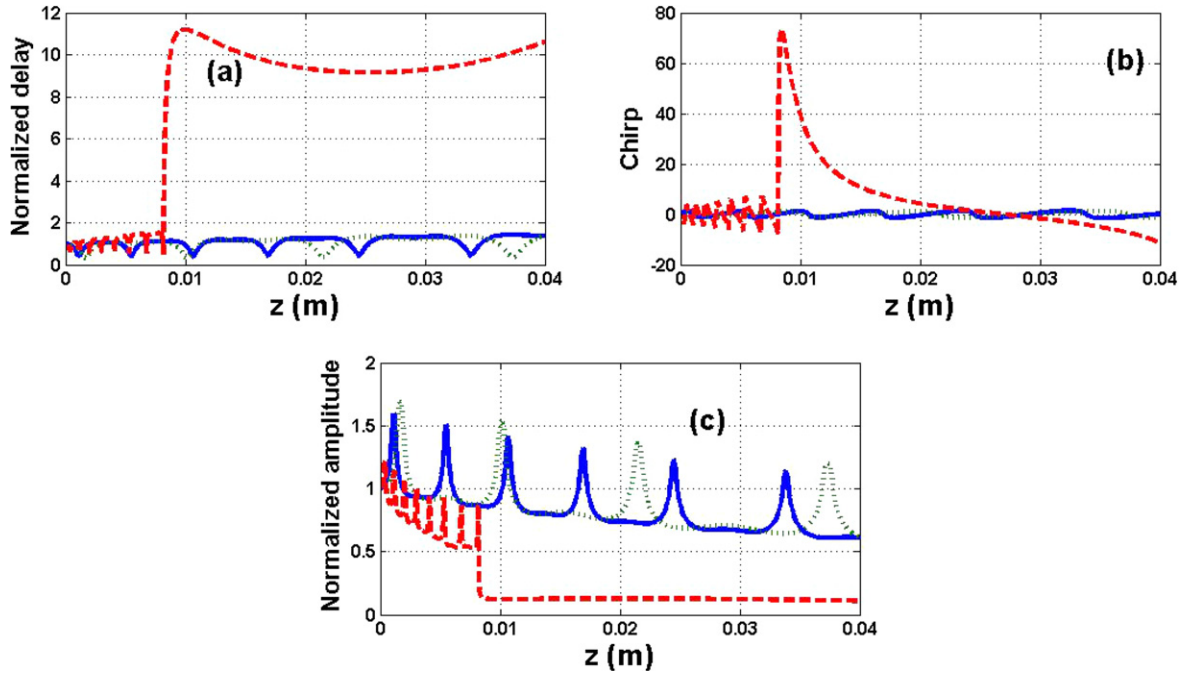


**Figure 8.** Plot of pulse characteristics: solid lines for the Gaussian, dotted lines for the sech-type pulse, and dashed lines for the RC pulse. Parameters for each input pulse: $C_0 = 0.8$, $\Gamma = 0.5\ \mathrm{W^{-1}m^{-1}}$, $\sigma = 1.45 \times 10^{-21}\ \mathrm{m^2}$, SOI waveguide length L = 4 cm. The other parameters are similar to those in figure 1.

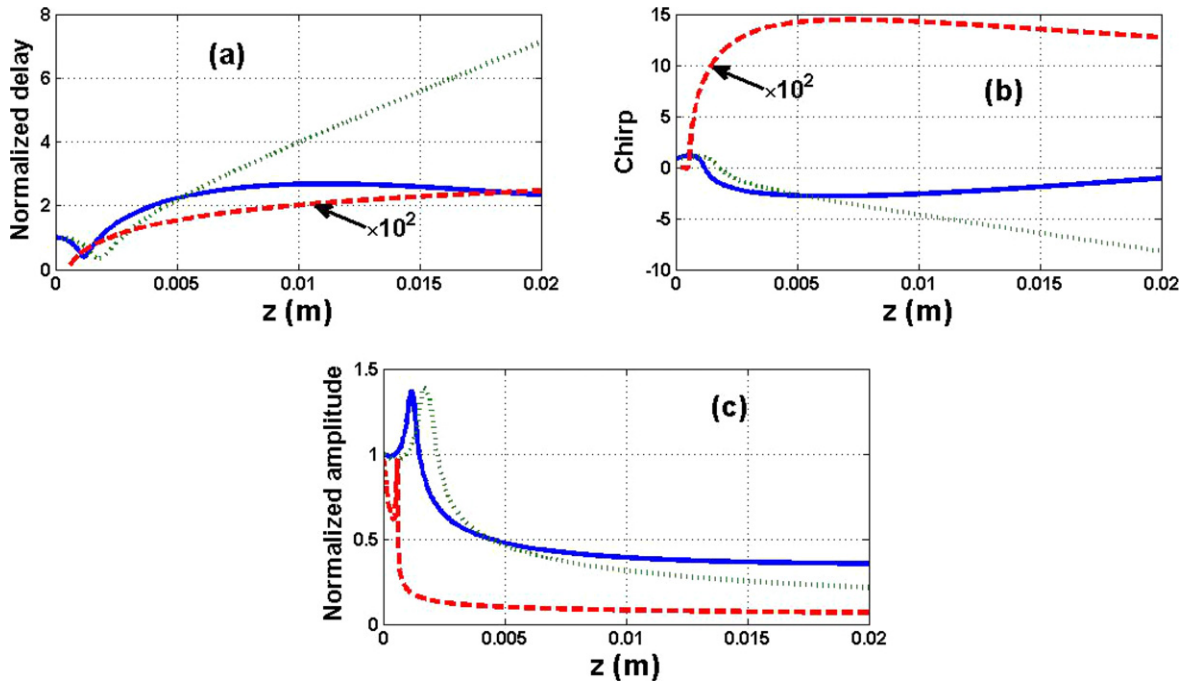


**Figure 9.** Plot of pulse characteristics: solid lines for the Gaussian, dotted lines for the sech-type pulse, and dashed lines for the RC pulse. Parameters for each input pulse: $C_0 = 0.8$, $\Gamma = 6.5\ \mathrm{w^{-1}m^{-1}}$, $\sigma = 1.45 \times 10^{-21}\ \mathrm{m^2}$, SOI waveguide length L = 2 cm. The other parameters are similar to those of figure 1.

Considering the negative values of chirp, one obtains, for instance, table 3. As seen in this table, the negative value of chirp also enhances the periodic compression obtained under the dispersion regime of figure 1. It also follows that large negative values of chirp destroy the periodicity. So one can suggest that in general small absolute values (AVs) of chirp enhance the periodic compression induced by the interplay between the FOD and the SPM, whereas large AVs of chirp destroy periodicity and lead to pulse broadening. This happens when the dispersion regime is normal following the GVD, with FOD × SPM < 0.

## 6. Influence of absorption coefficients on periodic compression

In this section, the parameters are given as $\Gamma \neq 0$, $\Lambda \neq 0$, $\gamma \neq 0$. The TPA phenomenon was first reported experimentally by Kaiser and Garrett [34]. The multiphoton absorption phenomenon can lead to laser damage of optical materials and can be used to write permanent refractive index structures into the interior of optical materials [1]. Therefore, multiphoton absorption is well known to be a nonlinear loss phenomenon that can reduce the efficiency of nonlinear optical devices such as optical switches. It is known that TPA reduces the compression factor [22].

However, in the present work, we find that a small value of TPA (for instance, 0.5 $W^{-1}m^{-1}$) progressively destroys periodic compression. The spatial period is increased following the propagation distance for each pulse. As presented in figure 8, the effect of a small value of TPA on an input pulse can therefore be understood as destruction of the periodicity in the compression process induced by the interplay between FOD and SPM.

A relatively high value of TPA, such as 6.5 $W^{-1}m^{-1}$, as assumed in [15], leads to total periodic compression destruction (see figure 9) where the effect of FCA is also included. It is observed in these figures that large values of TPA combined with FCA lead to pulse broadening inside the SOI waveguide. Nonetheless, under the considered conditions, one notices at least one peak of amplification linked to a pulse compression prior to broadening. This happens for the RC at a distance shorter than that of the Gaussian pulse, whereas the sech-type pulse broadens last.

## 7. Conclusion

To summarize, we presented in this paper the analysis of the compression mechanism for low-power chirped femtosecond input pulses in an SOI waveguide under the effect of FOD using the MVA, which involves the RDF. The growth equations of the studied profiles show that the sech-type and Gaussian pulses are influenced almost the same by nonlinear parameters. The characteristics of the RC pulse are influenced more by TPA and FCA. In nonlinear compression, we demonstrated the occurrence of a periodic compression of each pulse induced by the interplay between SPM and FOD instead of GVD, in a regime of propagation that assumes a normal GVD and a first-order solitonic state. A spatial compression period greater for the sech-type pulse than for the two other pulses was observed. We also showed that the anomalous GVD reduces this periodic compression phenomenon. A parametric study was done using the MPCP parameter. We showed that when the GVD decreases from the normal to the anomalous regime, the periodic compression phenomenon decreases. When the negative FOD increases to a maximal value for the considered conditions of simulation, the periodic compression is also performed in the presence of the constant normal GVD. Small AVs of chirp were found to be beneficial for periodic compression, whereas large ones and whole positive dispersion orders were found to be detrimental for the studied phenomenon. Moreover, under a small value of TPA, such as 0.5 $W^{-1}m^{-1}$, we showed that periodicity is progressively destroyed with the increase in spatial period, whereas large values of this absorption coefficient (such as 6.5 $W^{-1}m^{-1}$) combined with FCA lead to pulse broadening. Nevertheless, we observed one compression peak for the compression mechanism prior to broadening for each pulse.

Finally, this study showed that nonlinear compression in silicon waveguides is not only input pulse dependent but is also characterized by several dynamical processes, such as the periodicity induced by the interaction of SPM and FOD, whereas it is destroyed by the presence of absorption coefficients in the nonlinear medium.

## Acknowledgments

The authors acknowledge Dr Jean-Pascal Eloundou (from the National Advanced School of Engineering of the University of Yaoundé I, Cameroon) and the CETIC (University of Yaoundé I, Cameroon) for their helpful support.

## Appendix A

(i)

$$\int_{-\infty}^{+\infty} (xsech(x)\ tanh\ (x))^2 dx = -\frac{2}{3}\left\{\frac{sech\ ^3(x)}{8}\left[e^x\left(3x^2+4x+2\right) + 2e^{-x}(x+1) + e^{-3x}\left(x^2+1\right)\right] + xln(2\ cosh\ (x)) - \frac{1}{2}\int_0^{+\infty} \frac{t}{1-e^{t-2x}} dt\right\}\Bigg|_{-\infty}^{+\infty} \approx 1.215 = \frac{2}{3} + \frac{\pi^2}{18}$$

(ii)

$$\int_{-\infty}^{+\infty} (xsech(x))^2\left[tanh^2(x) - sech^2(x)\right] dx = -\frac{2}{3}\left\{\frac{sech\ ^3(x)}{8}\left[e^x\left(3x^2+4x+2\right) + e^{-x}\left(-6x^2+4x+4\right) + e^{-3x}\left(-x^2+2\right)\right] - xln\,(cosh\ (x)) - \frac{1}{2}\int_0^{+\infty} \frac{t}{1-e^{t-2x}} dt\right\}\Bigg|_{-\infty}^{+\infty} \approx 0.7850 = \frac{4}{3} - \frac{\pi^2}{18}$$

(iii)

$$\int_{-\infty}^{+\infty} x^4\, sech^2(x)dx$$
$$=\left\{-x^3\left[x\left(e^x\, sech\,(x)+2\right)+4\, ln\,(2\, cosh\,(x))\right]\right.$$
$$-6x^2\int_0^{+\infty}\frac{t}{1-e^{t-2x}}dt+3x\int_0^{+\infty}\frac{t^2}{1-e^{t-2x}}dt$$
$$\left.-\frac{1}{2}\int_0^{+\infty}\frac{t^3}{1-e^{t-2x}}dt\right\}\Bigg|_{-\infty}^{+\infty}\approx 5.6822$$

## References


[1] Boyd R 2008 *Nonlinear Optics* 3rd edn (San Diego: Academic Press)
[2] Agrawal G P 2007 *Nonlinear Fiber Optics* 4th edn (San Diego: Academic Press)
[3] Agrawal G P 2008 *Applications of Nonlinear Fiber Optics* 2nd edn (San Diego: Academic Press)
[4] Akhmediev N and Mitzkewich N V 1991 *IEEE J. Quantum Electron* **27** 849
[5] Matveev V B and Salle M A 1991 *Darboux Transformations and Solitons, Series in Nonlinear Dynamics* (Berlin: Springer Verlag)
[6] Akhmediev N and Ankiewicz A 1997 *Solitons. Nonlinear Pulses and Beams* (London: Chapman and Hall)
[7] Kivshar Y S and Agrawal G P 2003 *Optical Solitons: From Fibers to Photonic Crystals* (San Diego: Academic Press)
[8] Senthilnathan K, Li Q, Wai P K A and Nakkeeran K 2007 *P.I. E.R.S Online* **3** 531
[9] Senthilnathan K, Li Q, Nakkeeran K and Wai P K A 2008 *Phys. Rev.* A **78** 033835
[10] Li Q, Senthilnathan K, Nakkeeran K and Wai P K A 2009 *J. Opt. Soc. Am.* B **26** 432
[11] Broderick N G R, Taverner D, Richardson D J, Ibsen M and Laming R I 1997 *Phys. Rev. Lett.* **79** 4566
[12] Jien S, XiaoMin R, YongQing H, GuangQiang Y, Yong G and Xue C 2004 *Pulse compression based on nonlinear interaction Proc. SPIE* ed S Shen, S Jian, K Okamoto and K L Walker pp 404–9
[13] Wen-Cheng X, Wei-Cheng C, Ai-Ping L, Qi G and Song-Hao L 2001 *Chin. Phys. Lett.* **18** 1211
[14] Hu J, Marks B S and Menyuk C R 2006 *Opt. Express* **14** 4026
[15] Roy S, Bhadra S K and Agrawal G P 2008 *Optics Communications* **281** 5889
[16] Tsang H K, Wong C S, Liang T K, Day I E, Roberts S W, Harpin A, Drake J and Asghari M 2002 *Appl. Phys. Lett.* **80** 416
[17] Jalali B and Fathpour S 2006 *IEEE J. Lightwave Technol.* **24** 4600
[18] Soref R 2006 *IEEE J. Sel. Top. Quantum Electron.* **12** 678
[19] Yin L, Lin Q and Agrawal G P 2007 *Opt. Lett.* **32** 391
[20] Roy S and Bhadra S K 2007 *Physica* D **232** 103
[21] Wen J, Liu H, Huang N, Sun Q and Zhao W 2011 *Appl. Phys.* B **104** 867
[22] Agrawal G P 1993 *Phys. Rev.* E **48** 2316
[23] Mandeng L M and Tchawoua C 2013 *J. Opt. Soc. Am.* B **30** 1382
[24] Mandeng L M and Tchawoua C 2012 Nonlinear compression of self-healing Airy pulses in silicon-on-insulator waveguides *Frontiers in Optics Conf., OSA Technical Digest-online* (Optical Society of America paper) FW3A.36
[25] Mandeng L M and Tchawoua C 2012 Periodic compression induced by the interplay of fourth-order dispersion and self-phase modulation in silicon waveguides *Frontiers in Optics Conf., OSA Technical Digest-online* (Optical Society of America paper) FTh1D.6
[26] Capmany J, Pastor D, Sales S and Muriel M A 2003 *J. Opt. Soc. Am.* B **20** 2523
[27] Mandeng L M and Tchawoua C 2013 *J. Mod. Opt.* **60** 359
[28] Yin L and Agrawal G P 2007 *Opt. Lett.* **32** 2031
[29] Ngabireng C M, Dinda P T, Tonello A, Nakkeeran K, Wai P K A and Kofané T C 2005 *Phys. Rev.* E **72** 036613
[30] Nakkeeran K, Kwan Y H C, Wai P K A, Labruyère A, Dinda P T and Moubissi A B 2004 *J. Opt. Soc. Am.* B **21** 1901
[31] Mandeng L M, Fewo S I, Tchawoua C and Kofané T C 2014 *J. Mod. Opt.* **61** 662
[32] Tiofack C G L, Mohamadou A, Kofané T C and Moubissi A B 2009 *Phys. Rev.* E **80** 066604
[33] Erkintalo M, Hammami K, Kibler B, Finot C, Akhmediev N, Dudley J M and Genty G 2011 *Phys. Rev. Lett.* **107** 253901
[34] Kaiser W and Garrett C G B 1961 *Phys. Rev. Lett.* **7** 229